iSCSS 2024
INTERNATIONAL SHIP CNTROL SYSTEM SYMPOSIUM

Conference Proceedings

INSTITUTE OF MARINE
Engineering, Science & Technology

Image: © L3Harris

Sustainable, human centric and resilient control

Tuesday 5 - Thursday 7 November 2024
Spaces at the Spine, Paddington Village, Liverpool, UK

Conference Themes:

DC microgrids • Extended reality • Network Complexity • Hybrid power systems • Digital training • Reliability and availability • Novel power sources • FAIR data • Fault protection • Energy efficiency • Cooperative systems • Predictable interaction

Key Sponsors

BMT

L3HARRIS®

ROLLS ROYCE

www.imarest.org/inec

THE INSTITUTE OF MARINE ENGINEERING, SCIENCE AND TECHNOLOGY

International Ship Control Systems Symposium (iSCSS 2024)

Sustainable, human centric and resilient control

5 - 7 November 2024
Spaces at the Spine, Liverpool, UK

The Institute of Marine Engineering, Science and Technology would like to thank the following Technical Advisory Committee Members for their invaluable help and support in the organisation of this Conference:

Chairman:
Capt (E) dr. ir. Rinze Geertsma FIMarEST

Committee Members:
Jeffrey Cohen, US Navy; Dr Andrea Coraddu, TU Delft; Toby Drywood, BMT; Julian Lowe, L3Harris; Dr Michele Martelli, University of Genova; Dr Krishna Nagalingam, Kongsberg; Rudy Negenborn, TU Delft; Dr Angelo Odetti, CNR-INM; Suthakar Pakianathan, Department of National Defence, Canada; Waqas Qazi, OSM; Karl Schoder, Florida State University; Dr David Wetz, University of Texas; Prof. Mehdi Zadeh, NTNU Marine technology.

Keynote Speakers:
RAdm Rachel Durbin; Sarah Kenny OBE, BMT; V.Adm. Paul Marshall CBE; V.Adm. Martin Connell; RAdm Tom Anderson; RAdm Steve McCarthy; Marco Coli, Fincantieri; Marnix Krikke, MoD Netherlands;

Patrons:
RAdm Rachel Durbin; Sarah Kenny OBE, BMT; V.Adm. Paul Marshall CBE; V.Adm. Martin Connell; RAdm Tom Anderson; RAdm Steve McCarthy; Matt Bolton, UK NEST.

Patron Award Winners:
Neil Kapoor; Erin van Rheenen; WO2 Peter Spayne; Dr Rachel Pawling

Sir Donald Gosling Award Winners:
Lt Cdr Liam Talbot; Filippo Ponzini; Camilla Fruzzetti; Nicola Sabatino; Daisy Brooks; Henrique Faria.

THE INSTITUTE OF MARINE ENGINEERING, SCIENCE AND TECHNOLOGY

Contents

Power Management System with Load Power Regulation for Zonal Secondary DC-Grids Survivability: A Load Priority-Based Approach

B Wingelaar[1] MSc

J J Deroualle[2] MSc IEEE Member

[1] *Royal IHC, Research & Development Dept., NL*
[1] *Corresponding Author. Email: b.wingelaar@royalihc.com*

[2] *Royal IHC, FD Engineering Dept., NL*
[2] *Corresponding Author. Email: jj.deroualle@royalihc.com, jacques.deroualle@ieee.org*

Synopsis

This article proposes an algorithm based on load priorities to ensure survivability in shipboard zonal secondary DC-grids. The transition to alternative fuels introduces new opportunities and new challenges. Using inherent DC power electronics for integrating energy storage systems (ESSs) and renewable energy sources (RESs) demands novel control mechanisms for dealing with power converter overload conditions. In that sense, the power management system (PMS) has to incorporate active load management systems to ensure the continuous operation of essential loads when the ship is operating in critical missions or during abnormal power situations. This work employs the concept of a zonal DC secondary distribution network, which is based on the insertion of supercapacitors for voltage time constant enhancement. This grid concept is used to formulate the survivability objective as a DC-link voltage recovery function, with a minimum operation voltage that must not be exceeded whilst sustaining continuous operation whenever feasible. That is relevant for short-circuit currents and underestimated and unforeseen high peak loads. In these cases, the load demand may exceed the nominal ratings of the DC/DC converter that feeds the secondary zone load. Moreover, the power converter may suddenly become unavailable. Then, supercapacitors can provide the additional power, enabling the momentary survivability of the zonal secondary grid. However, in this process, the DC-link voltage value decreases while the ESS is discharged. The power imbalance can only be sustained for a limited period, determined by the supercapacitor's initial operation conditions. If the DC voltage limit is exceeded, load reduction is required to counterbalance the load mismatch and ensure voltage recoverability. A load priority approach is applied in this article to meet the load reduction objective, with essential and emergency loads having the highest priority. A study case is proposed using time-domain simulations in a Matlab-Simulink environment to demonstrate the load management functionality. The results show that supercapacitors and load management substantially increase the survivability of the zonal secondary load centre whenever one of the DC/DC converters fails during operation.

Keywords: Load management system; Zonal electrical distribution system; DC secondary distribution system; Supercapacitor network; Survivability; Multi-agent system

1. Introduction

One of the benefits of a power converter's integration into DC-grids is to optimise the power equipment space and weight constraints onboard. In that sense, it might get impractical to oversize power converters for obtaining high survivability rates under critical missions – it becomes evident that inverter-based resources (IBRs) may easily be overloaded when supplying impulsive loads for navy purposes, for example. ESS implementation is imperative for DC-grid's high performance; however, their size, weight and potential hazards limit their extensive use on ships (Du et al., 2019). To keep the system stable for a wide range of power demands (and de-rated events), it is advisable to incorporate load management to deal with the load balance in real-time and complicated fluctuating power requirements (Du et al., 2019). The present paper will discuss the implementation of such power regulation for a zonal secondary grid design based on supercapacitor's application.

This article is organised as follows. In Section 2, the supercapacitor zonal secondary DC distribution is introduced as the basis of our study. There are also some insights about the chopper controlling when energy storage devices are directly connected to the DC-link. Section 3 depicts the multi-agent system and its group objective to mind the self-restoration functionality in a secondary distribution grid. Section 4 proposes a study case for assessing the suggested power regulation – the component modelling and logic control algorithm are

given. Then, a brief discussion about the improvement in survivability is presented. Finally, conclusions and future research topics are stated in Section 5.

2. Supercapacitor zonal secondary DC distribution

This paper focuses on a secondary DC-Grid design part of a Zonal Electrical Distribution System (ZEDS). This grid type applies not only to all-electric ships but also to hospitals, airports, data centres, etc. This network concept permits the enhancement of the ship's survivability to adverse events (Bosich et al., 2023) that might be external to the electrical system itself but with direct consequences on the electrical operation (Deroualle & Vinks, 2024). A representative single-line diagram (SLD) of this network can be seen in Figure 1.

A shipboard ZEDS consists of different load zones supplied by two different connections into the primary distribution system and managed independently (Xu et al., 2022). The ring structure – from which the power generation and load subsystems are operated – is formed by port and starboard DC buses that run longitudinally along the ship and are connected by bow and stern cross-hull links (IEEE Std. 1709-2018). When a short circuit occurs in one of the main buses, the secondary loads within the zones will shift their power source of supply – automatically or manually – to the section unaffected by the electrical event (Xu et al., 2022). In that way, a ring communication network is expected to allow protection coordination and selectivity along the structure areas (Xu et al., 2022).
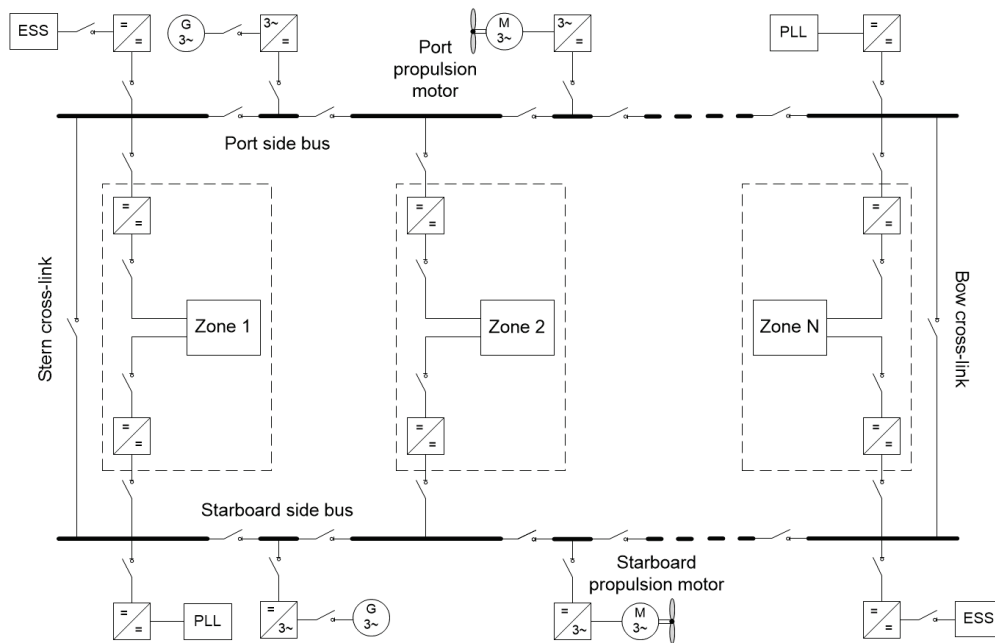
Figure 1: SLD representation of a shipboard power system based on ZEDS (Deroualle & Vinks, 2024)

In navy vessels, the emerging pulsed-power loads (PLLs) can be directly placed in the main distribution ring (Xu et al., 2022) or as part of the N load zones indicated in Figure 1. The last, at some extent of power, is achievable with DC/DC converters that would step down the voltage from 1 kV to 700 V, for example – this allows the use of ESSs to directly power the vital loads under the zones (Qazi et al., 2023).

Supercapacitors applied directly in the zonal low-voltage (LV) DC-links could provide more voltage inertia and increase the performance and stability of such PLLs. Moreover, it would unlock the possibility of implementing mechanical circuit breakers (MCBs) due to reducing the rate of change of the voltage (RoCoV) – in case of fault or transient events – and the voltage auto-recovery process once the electrical event is over (Deroualle & Vinks, 2024). This statement is valid as long as the short circuit levels are inside the withstand limits of the breaker technology, and the supercapacitor aftermath state of charge (SoC) is higher than 40% (or a pre-settled limit that enables the system to continue operation).

The zonal secondary DC distribution based on DC-link supercapacitors and MCB protection will imply some properties to the LV feeder circuits:

- The fault current will last for several seconds, making possible the time-current curve (TCC) selectivity approach between the protection apparatus;

- Once the faulty section is isolated from the rest of the grid, the voltage is automatically raised to the level in accordance with the supercapacitor SoC final condition;
- The supercapacitor's non-linearity will influence the network short-circuit currents to behave in an overdamped mode (smoothing the current waveform over time).

If a zonal DC/DC converter fails, the supercapacitor modules will continue to power the remaining base loads for a limited period (tens of seconds). That interval should be sufficient for the PMS to acknowledge the de-rated situation and proceed with countermeasures to assure the shipboard power system survivability (or at least partially). The coming sections will discuss such actions based on a zonal distribution example for the Dutch 'Seagoing Auxiliary Vessel'.

2.1. *Auxiliary vessel secondary grid design*

Figure 2 proposes the concept of a zonal secondary DC grid for the 'Seagoing Auxiliary Vessel' – this example, in particular, will not accommodate low-power PLLs. Thus, it will supply normal auxiliary loads through two 700 V busbars (open bus-tie breaker) for the principal machinery equipment (e.g., fuel transfer pumps, cooling water pumps, supply fans, heat recovery systems, etc); two 350 V busbars for lighting and DC accommodation loads; and one 700 V battery system for emergency loads (e.g., lighting, bilge/ballast pumps, etc).
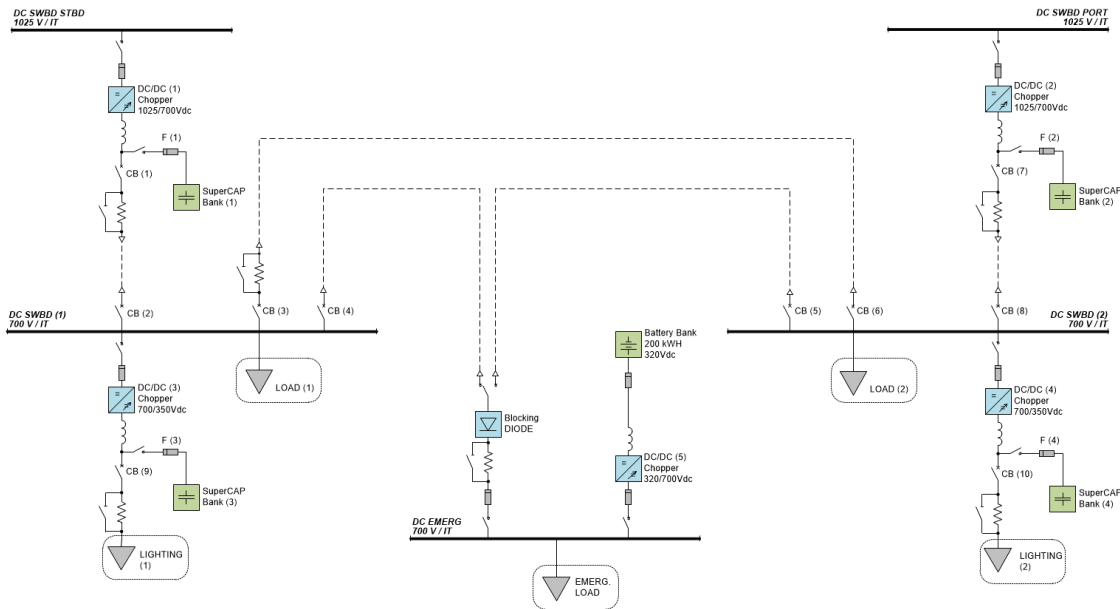
Figure 2: SLD representation for the 'Seagoing Auxiliary Vessel' secondary DC grid (Deroualle & Vinks, 2024)

The power system's data are displayed in Tables 1-3. The DC/DC choppers are expected to operate with a switching frequency of 5 kHz and an air-cooled method. The MCB feeders incorporate a switching by-pass resistance to limit the inrush currents when connecting two DC buses with different voltage levels. For example, in the 700 V bus-tie case, the power resistor has a nominal value of 0.05 Ω and a by-passing time of 3 seconds. The worst situation for closing the bus-tie 'CB (3)' would succeed when the converter 'DC/DC (1)' has failed – previously operating with full power – and when the busbar 'DC SWBD (1)' reaches the under-voltage limit of 620 V due to the 'SuperCAP Bank (1)' constant supply discharging for the local loads. The bus-tie transient current would peak at 886 A with a total energy dissipation of 65.6 kJ (Figure 3).

Table 1: Supercapacitor bank Power Ratings

Equipment	Nominal Voltage (V)	Capacitance (F)	Nominal Current (A)	ESR @25°C (mΩ)
SuperCAP (1) SuperCAP (2)	780	31.25	300	18-56
SuperCAP (3) SuperCAP (4)	390	20.83	100	27-84

Table 2: Chopper converter Power Ratings

Equipment	Input Nominal Voltage (V)	Output Voltage Range (V)	DC-link Power (kW)	Filter Inductance (µH)
DC/DC (1) DC/DC (2)	1025	640-760	149	(3x) 1640
DC/DC (3) DC/DC (4)	700	320-400	20	(3x) 3500
DC/DC (5)	320	640-760	124	(3x) 443

Table 3: Mechanical circuit breaker Power Ratings

Equipment	Number of Poles	Rated Current (A)	Operational Voltage (V)	Icu (kA) Ics (%Icu)
CB (1), CB (2) CB (7), CB (8)	4	400	750	36 (100%)
CB (3) CB (6)	4	320	750	36 (100%)
CB (4) CB (5)	4	100	750	36 (100%)
CB (9) CB (10)	2	175	500	36 (100%)
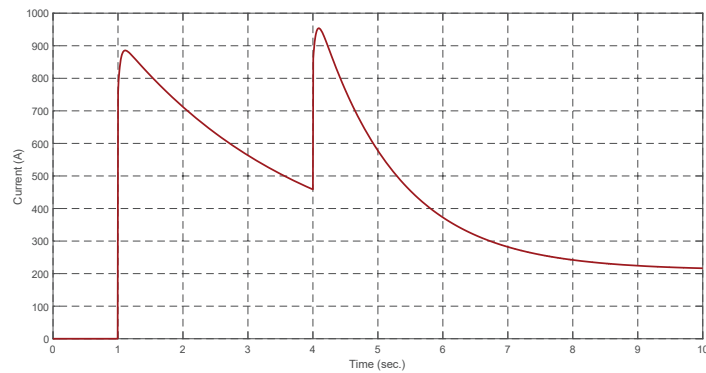
(a)
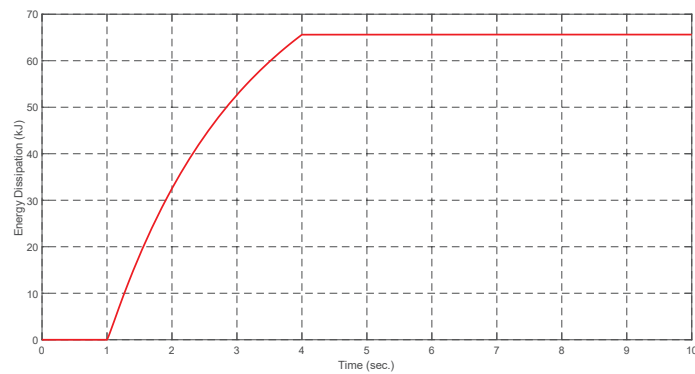
(b)

Figure 3: Bus-tie MCB by-pass closing operation
(a) DC feeder current (b) Resistor dissipated energy

Figure 4 (a) exibits the total DC fault current at 'DC SWBD (1)' when the bus-tie breaker 'CB (3)' is closed (Deroualle & Vinks, 2024). In this example, it is considered that the fault contributions from main and lighting circuits to be zero – the converters 'DC/DC (1)' and 'DC/DC (2)' have the capability of interrupting the short-circuit current at the very initial stage; the upper high-speed fuses from 'DC/DC (3)' and 'DC/DC (4)' will limit to few milliseconds the downstream contribution current. The equivalent L/R circuit constant is lower than 5 ms with a peak current of 25.7 kA. The supercapacitors presence will increase the DC-link resultant fault to several seconds, which can create considerable arc-flash levels in the front of the power cabinets (Deroualle & Vinks, 2024). Thus, backup safeguarding fuses 'F (1)', 'F (2)', 'F (3)', and 'F (4)' are implemented for limiting the let-through energy. The correct fuse size has to consider the required time for making possible selectivity between the downstream network breakers (Deroualle & Vinks, 2024).
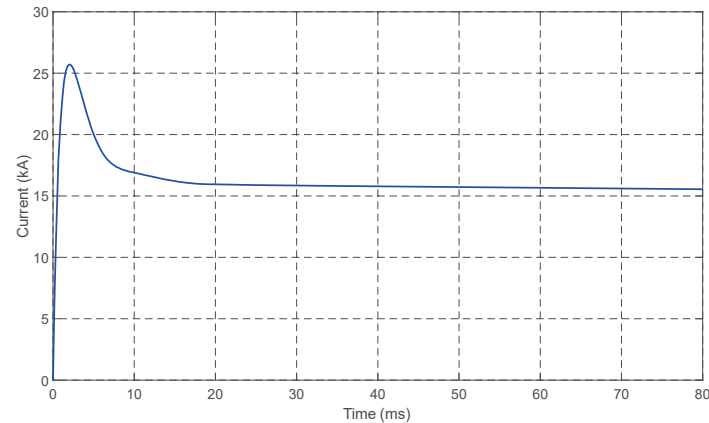
(a)
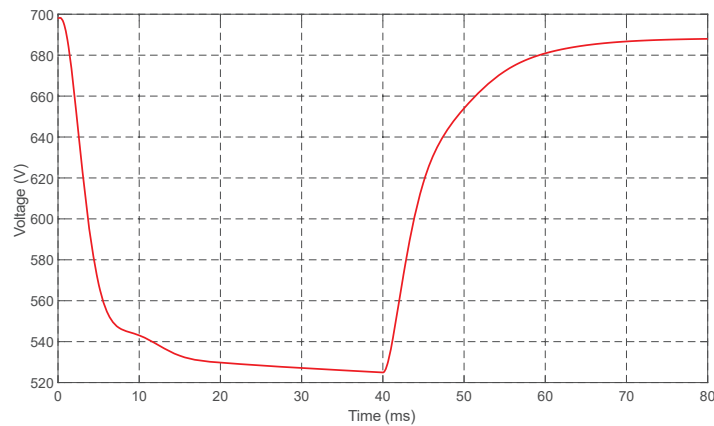
(b)

Figure 4: Fault level at DC-link 'DC SWBD (1)' (Deroualle & Vinks, 2024)
(a) Short-circuit current (b) Supercapacitor terminal voltage with 40 ms fault extinguish time

In the secondary circuit branch supplied by the bus 'DC SWBD STBD', the breaker 'CB (1)' – with a nominal current of 400 A (Table 3) – can be selected together with 'F (1)' gBat fuse-link of 500 A. The TCC chart of both protection apparatus is displayed in Figure 5. Considering the example of Figure 4, the 'SuperCAP (1)' current would merge the gBat fuse at instant ~80 ms, and instantaneously trip the 'CB (1)' – opening time estimated in the range of 20-40 ms according to common manufacturer values. The terminal voltage at the 'SuperCAP (1)' with fault extinction of 40 ms is shown in Figure 4 (b); the voltage auto-recovery property is the key feature that enables the survivability enhancement of the zonal secondary DC-grid with supercapacitors. Moreover, the chopper overload current curves – depending on the voltage trigger level – will be explained in the next sections; the breaker 'CB (1)' must be sized accordingly to allow the 'SuperCAP (1)' to supply overload conditions for a limited period of time.
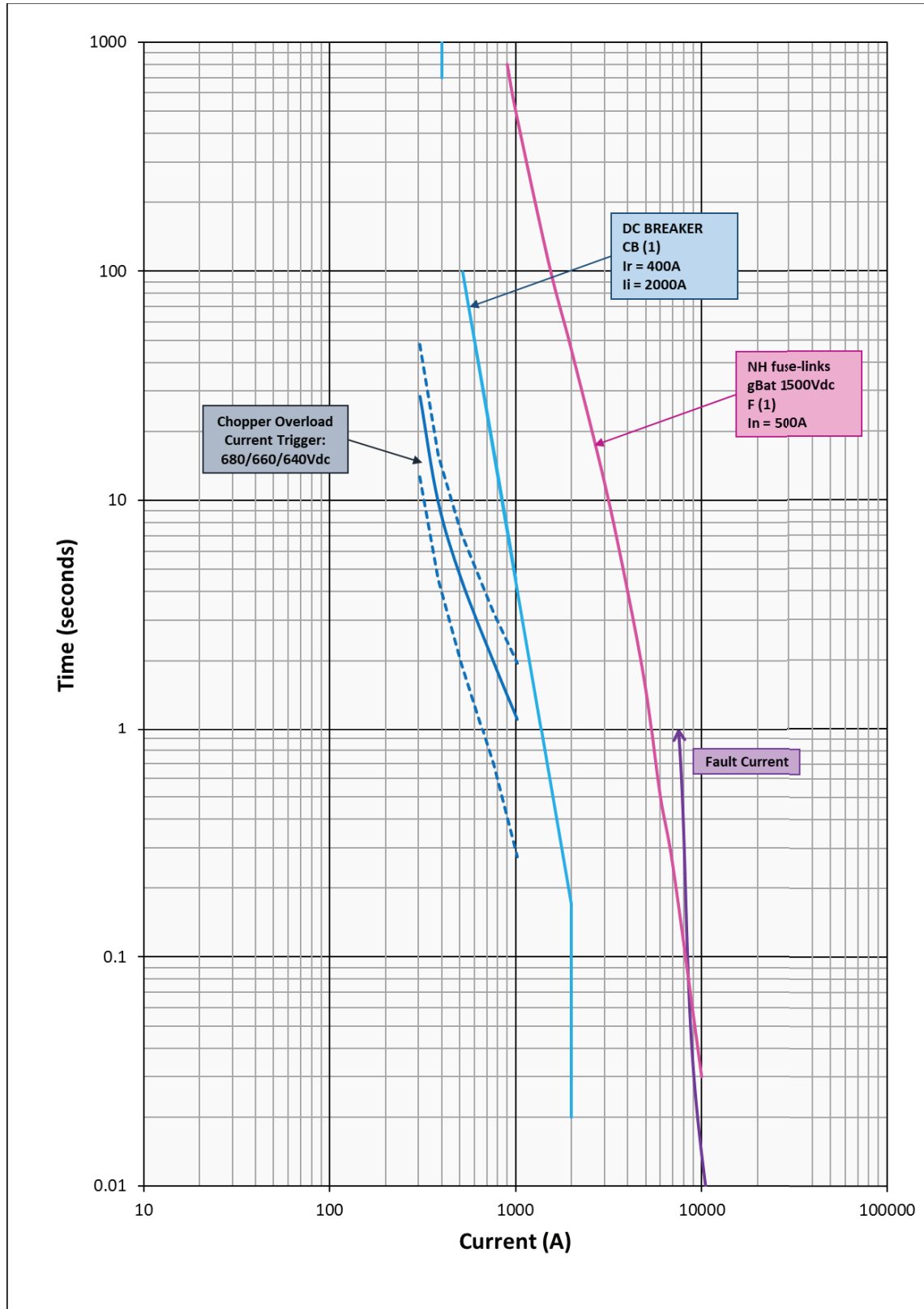
Figure 5: TCC chart for protection selectivity between 'CB (1)' and 'F (1)' protection devices.

2.2. DC/DC chopper controlling

The zonal primary chopper converters (1025/700 V) are based on the 'Average current-mode' (ACM) control philosophy. Figure 6 presents a representation of the converter controlling scheme. This popular programming technique contains an average current loop compensator around a duty-cycle-controlled converter (Erickson & Maksimović, 2020). Furthermore, an outer voltage control loop is also closed around the ACM scheme. Figure 7 shows the block diagrams that model the ACM-controlled drive (Erickson & Maksimović, 2020).
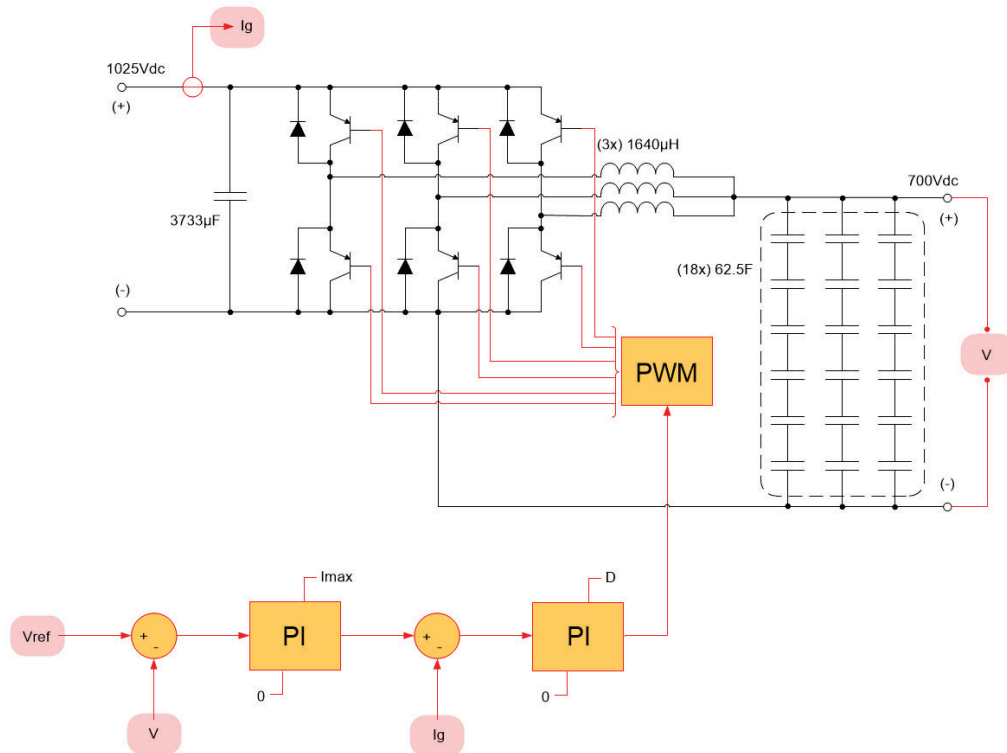
Figure 6: Zonal primary chopper converters (1025/700 V) controlling representation
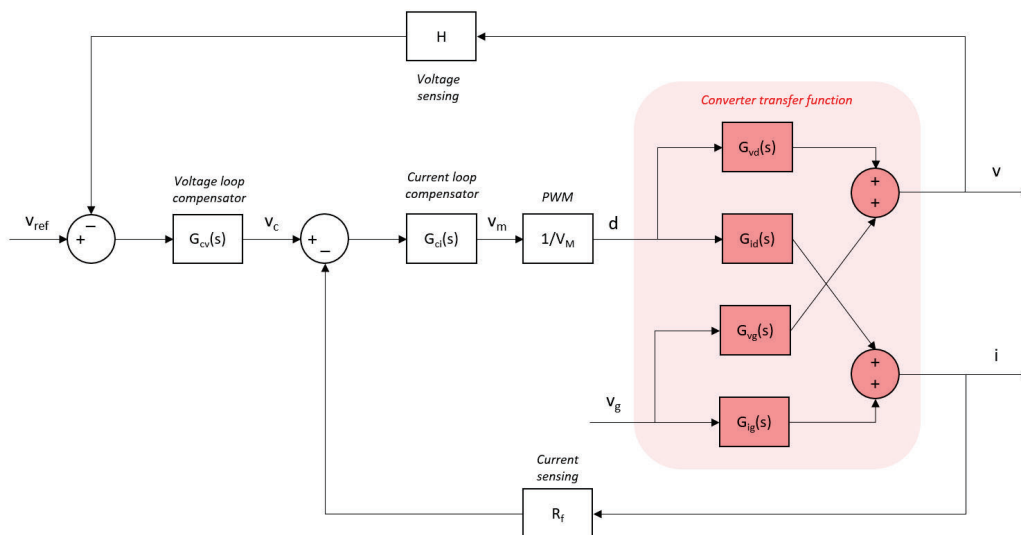
Figure 7: Block diagrams model of the ACM-controlled chopper (Erickson & Maksimović, 2020)

In Figure 7, a sensed output voltage H is compared to a reference signal V_{ref}, and the generated error signal is processed through a voltage loop compensator $G_{cv}(s)$, which will create a V_c current reference for the current control loop (Erickson & Maksimović, 2020). This reference point is compared to a sensed current signal R_f, and the outcome error is handled by a current loop compensator $G_{ci}(s)$ (Erickson & Maksimović, 2020). Finally, the Pulsed-Width Modulation (PWM) develops a switch control signal with duty cycle d to be applied to the chopper drive (Erickson & Maksimović, 2020).

The three inverter legs depicted in Figure 6 are separately controlled with a pulse-width modulation (PWM) signal that is 120° phase shifted, characterised by an 'Interleaved Current Control' mechanism. Therefore, a three-winding core choke is used to obtain a reduced ripple current at the output of the buck operating converter in the most efficient way.

The chopper is designed to have a crossover frequency of 500 Hz (one-tenth of the switching frequency) and a current loop phase margin equal to 73°. Following this reasoning, the voltage loop compensator is settled to have a crossover frequency of 50 Hz and a phase margin of 78° – the resulting voltage loop gain is shown in Figure 8.
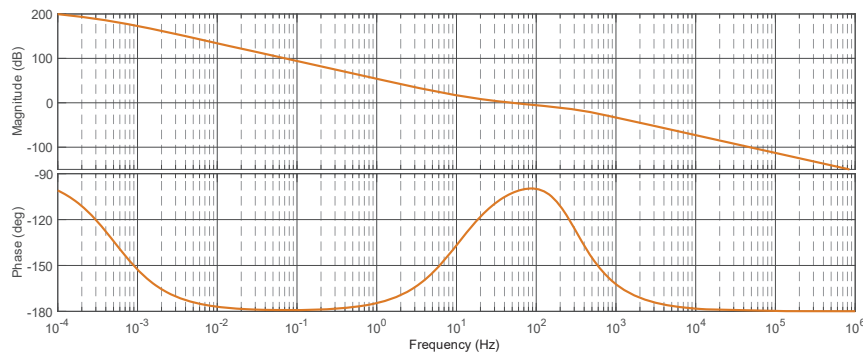
Figure 8: Loop gain in the voltage control loop around the ACM-controlled chopper converter

3. Load management for shipboard power systems

The all-electric ships are known for being 'weak' source grids. This means that such power systems possess limited generation and lower rotational inertia capacity when compared to large land-based networks (Feng et al., 2015). The consequences are translated into reduced stability margins when large portions of nonlinear and dynamic loads are included in such systems (Feng et al., 2015). Therefore, a real-time load management system might be needed to match load and generation powers (Feng et al., 2015) and enhance the system's stability under adverse situations.

In the present case of the ZEDS secondary DC Grid, converter-based resources – which present overload constraints – together with finite stored energy devices may also introduce limitations in terms of stability when supplying PLLs (for some specific mission). Thus, depending on the operational mode, the load management system should satisfy some operational constraints (Feng et al., 2015).

The real-time load management objectives can differ depending on different scenarios: operation cost reduction, profit margin maximisation, peak load contraction, and energised loads upsurge while satisfying the grid's operating constraints (Feng et al., 2012) – the latter is the target pursued for the article's zonal secondary DC-grid.

The coming sub-sections will discuss the application of the 'Multi-Agent System' (MAS) model for load management in zonal areas, but with an objective function and constraints already fixed for the local secondary loads. The MAS technology is the most popular decentralised approach, and it has already been implemented for shipload restoration, system reconfiguration, fault detection, etc. (Du et al., 2019). A centralised control scheme could also be an alternative, although it lacks adaptivity to structural changes and may become a single failure point for the entire system (Du et al., 2019).

3.1. Multi-agent system and zonal local controllers

The proposed supercapacitor secondary DC-grid has a local control system for real-time load management zonally. The load controlling behave locally in a 'Heterogeneous' way because different commands (or setting points) can be given to different agents inside the zone. Nevertheless, from the ZEDS's point of view (Figure 1),

each zone can be considered as a singular point of load – that can be supplied by port or starboard main buses – characterising a 'Homogeneous' system from that perspective. That said, the local management control can act differently in the following situations:

- **Self-restoration.** The local control can restore the normality of the secondary grid in case of failure in one of the primary chopper converters, supercapacitor banks, or 700 V main busbars. This can be accomplished by closing the bus-tie circuit breaker, changing the emergency bus selector position, and/or matching the load level with the available converter power (heterogeneous agents). This functionality is independent of the ship's automation system, so a communication failure with the port and/or starboard bus sides will not compromise performance.
- **Load limitation.** Depending on ship mission settings, the ZEDS control system will acknowledge the zone loads as a homogeneous entity and limit the total power locally – unique power indication command – if there is a need for extra power (or electrical distribution de-rated status) regarding the propulsion and PLL sub-systems. For example, in battle mode, PLLs have the highest priority, and propulsion and secondary loads can be temporarily controlled (Feng et al., 2015) to achieve the mission's requirement in a specific situation (significantly adverse ones).

The agent model formulation in ZEDS contains the physical and communication layers (Du et al., 2019). The communication network is shown in Figure 9. It becomes clear that from a local zone perspective, the agents are controlled heterogeneously, but from an outer one, the zones are treated as singular load points. It is foreseen that each zone agent locally measures its operating power and state conditions and informs the local controller (Du et al., 2019) to decide between self-restoration or load limitation actions. For the physical layer, a zonal example is illustrated in Figure 10. The local control can be chosen to determine the agent's speed or power control settings (i.e., inverter-driven motors) or turn ON/OFF lighting sections.
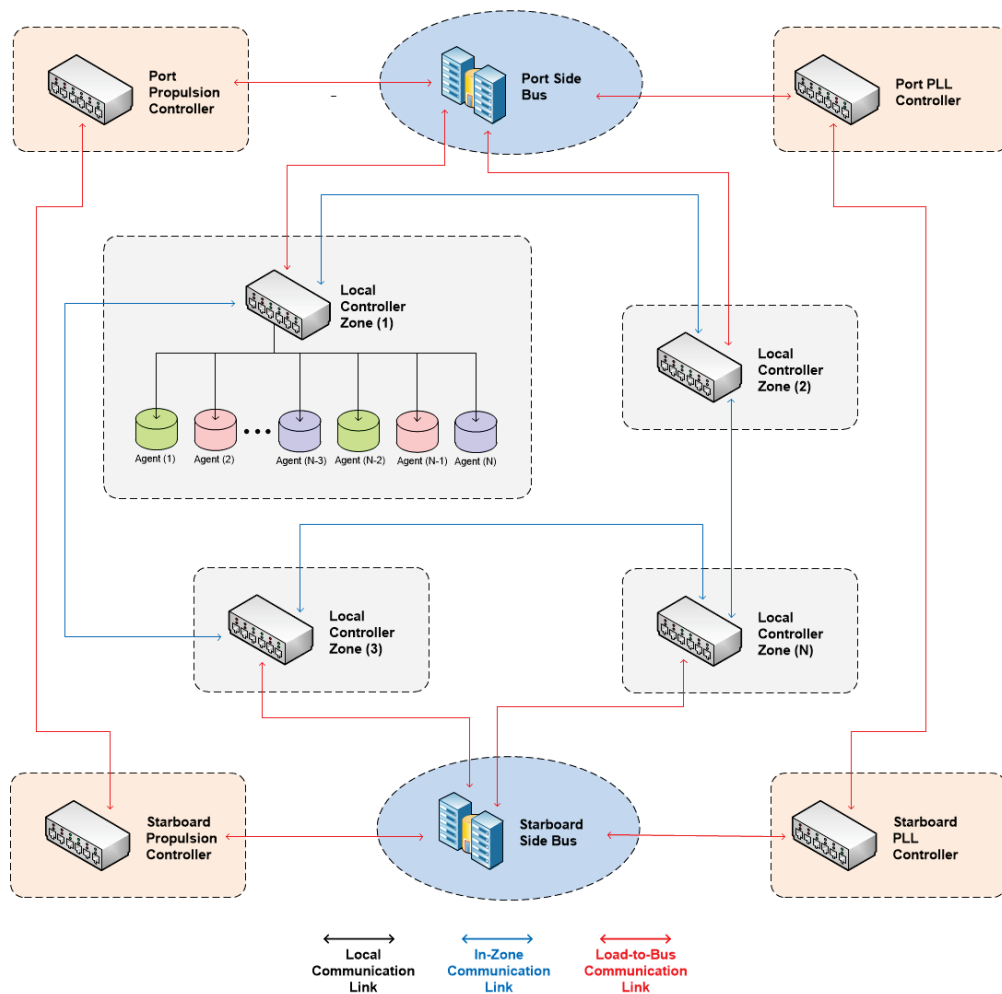
Figure 9: ZEDS communication layer regarding the MAS model for load management (Du et al., 2019)
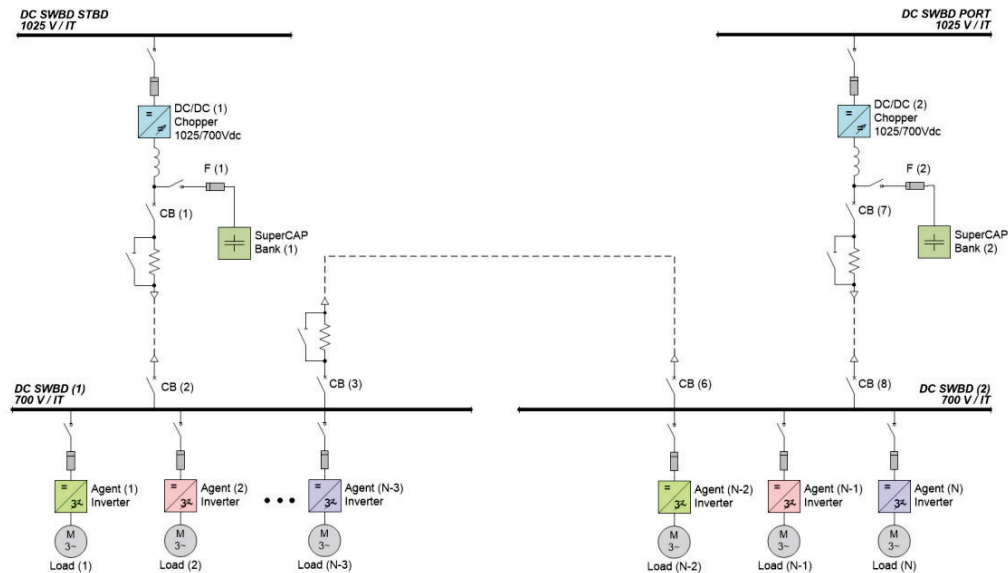
Figure 10: Zonal physical layer regarding the MAS model for load management (Du et al., 2019)

3.2. *Group objective of the secondary DC distribution*

The group objective presented from now on is related to the zonal load management's self-restoration functionality. In that case, the local controller determines each load's speed setpoints or switch status using the information provided by the secondary grid (Feng et al., 2015). In future research, the load limitation functionality would notice only the zone's total power, determining a homogeneous approach.

The 'Seagoing Auxiliary Vessel' secondary loads are classified into primary and secondary essential services, habitat loads, lighting, and emergency services. Primary services need to be maintained in continuous operation – the secondary ones do not necessarily; habitat services are intended to provide minimum comfort conditions for crew onboard; and emergency services guarantee minimum personal safety. In the table below, the loads in operation during Sailing mode are depicted for the group objective formulation in this sub-section.

Table 4: Seagoing Auxiliary Vessel active secondary loads during Sailing mode

Load Number	Component	Nominal Power (kW)	Efficiency (%)	Board	Service Level
1	FO Transfer Pump	2.2	0.843	DC SWBD (1)	Primary
2	LO Transfer Pump	0.75	0.796	DC SWBD (1)	Primary
3	Sea CW Pump	22	0.916	DC SWBD (1)	Primary
4	CW Pump Generator and FO Cooler 1	1.5	0.828	DC SWBD (1)	Primary
5	CW Pump Generator and FO Cooler 2	1.5	0.828	DC SWBD (2)	Primary
6	Fresh CW Pump (CW System)	11	0.898	DC SWBD (1)	Primary
7	Methanol Fuel Transfer Pump 1	1.5	0.828	DC SWBD (1)	Primary
8	Methanol Fuel Transfer Pump 2	1.5	0.828	DC SWBD (2)	Primary
9	Methanol Supply Pump Genset 1	15	0.906	DC SWBD (1)	Primary

Table 4: Seagoing Auxiliary Vessel active secondary loads during Sailing mode (continuation …)

Load Number	Component	Nominal Power (kW)	Efficiency (%)	Board	Service Level
10	Methanol Supply Pump Genset 2	15	0.906	DC SWBD (2)	Primary
11	Methanol Supply Pump Aux Genset	5.5	0.877	DC SWBD (1)	Primary
12	Supply Fan 1 Engine Room	15	0.906	DC SWBD (2)	Secondary
13	Supply Fan 2 Engine Room	15	0.906	DC SWBD (1)	Secondary
14	Supply Fan Cargo Hold Room	1.28	0.75	DC SWBD (2)	Habitability
15	Supply Fan Passage Way	0.4	0.65	DC SWBD (2)	Habitability
16	Supply Fan UAV Hangar	0.4	0.65	DC SWBD (2)	Habitability
17	Supply Fan Hangar	1.28	0.75	DC SWBD (2)	Habitability
18	Exhaust Fan Galley	1.25	0.75	DC SWBD (2)	Habitability
19	CH Pump Heat Recovery 1	0.86	0.65	DC SWBD (1)	Habitability
20	CH Pump Heat Recovery 2	0.86	0.65	DC SWBD (2)	Habitability
21	Lighting 1	50	0.98	DC SWBD (1)	Lighting
22	Lighting 2	50	0.98	DC SWBD (1)	Lighting
23	Lighting Emergency	50	0.98	DC SWBD (2)	Emergency
24	Bilge Ballast Pump 1	11	0.93	DC EMERG	Emergency
25	Bilge Ballast Pump 2	11	0.93	DC EMERG	Emergency

A load priority-based approach will be applied according to the different services listed above to maximise load power for the zonal centre in Figure 2 while ensuring specified operation constraints (i.e., rated output power of the chopper converters, stable voltage performance of the supercapacitors, and continuous operation of the emergency loads). The objective function and constraints of the MAS model can be expressed as:

$$\max \sum_{a=1}^{11} P_{PRI_a}(t) + \sum_{b=1}^{2} P_{SEC_b}(t) + \sum_{c=1}^{7} P_{HAB_c}(t) + \sum_{d=1}^{2} P_{LIGHT_d}(t) \tag{1}$$

$$s.t. \sum_{a=1}^{11} P_{PRI_a}(t) + \sum_{b=1}^{2} P_{SEC_b}(t) + \sum_{c=1}^{7} P_{HAB_c}(t) + \sum_{d=1}^{2} P_{LIGHT_d}(t) \leq P_{CONV} - P_{EMERG} \tag{2}$$

$$P_{PRI_a}(t) \leq P_{PRI\_MEASURED_a}(t) \qquad a = 1, 2, \cdots, 11 \tag{3}$$

$$P_{PRI_a}(t) = \alpha.P_{PRI\_NOMINAL_a} \qquad \alpha \in \{0, 0.4, 0.5, 0.6, 0.7, 0.8, 0.9, 1\} \tag{4}$$

$$P_{SEC_b}(t) \leq P_{SEC\_MEASURED_b}(t) \qquad b = 1, 2 \tag{5}$$

$$P_{SEC_b}(t) = \beta.P_{SEC\_NOMINAL_b} \qquad \beta \in \{0, 0.4, 0.6, 0.8, 1\} \tag{6}$$

$$P_{HAB_c}(t) = \gamma . P_{HAB\_MEASURED_c}(t) \qquad c = 1, 2, \cdots, 7 \mid \gamma \in \{0, 1\} \qquad (7)$$

$$P_{LIGHT_d}(t) = \delta . P_{LIGHT\_MEASURED_d}(t) \qquad d = 1, 2 \mid \delta \in \{0, 1\} \qquad (8)$$

where $P_{PRI\,a}(t)$ is the active power of the Primary load 'a', $P_{SEC\,b}(t)$ is the active power of the Secondary load 'b', $P_{HAB\,C}(t)$ is the active power of the Habitability load 'c', $P_{LIGHT\,D}(t)$ is the active power of the Lighting load 'd', P_{CONV} is the total available power for the primary chopper converters, and P_{EMERG} is the reserved power for the Emergency loads.

The load priority-based approach is based on thirteen steps that can reduce, for instance, the secondary base load up to 17% (from its initial condition) when the ship is operating in Sailing mode. The power steps reduction are not fixed values but somewhat dependent on the priority sequence disclaimed in Table 5 – based on the parameters α, β, γ, and δ, from Equations 1-8. During regular operation, the above parameters are equal to one. The sequence of step events is based on the highest priority given to Primary loads and the lowest ones to Habitability. In any case, the load management controller never affects the emergency loads when seeking self-restoration. In Figure 2, it can be seen that there is a dedicated battery system for powering the emergency busbar in case of energy loss in the zone.

Table 5: Load priority-based approach constant values

Load Step	Primary (α)	Secondary (β)	Habitability (γ)	Lighting (δ)
1st	1	1	0	1
2nd	1	0.8	0	1
3rd	1	0.6	0	1
4th	1	0.4	0	1
5th	0.9	0.4	0	1
6th	0.8	0.4	0	1
7th	0.7	0.4	0	1
8th	0.6	0.4	0	1
9th	0.5	0.4	0	1
10th	0.4	0.4	0	1
11th	0.4	0	0	1
12th	0	0	0	1
13th	0	0	0	0

4. Zonal main converter failure study case

4.1. Study case description

This section presents a study case where the chopper converter 'DC/DC (1)' completely fails. We limit ourselves to the situation where the three inverter legs of the converter fail – although partial failures are also feasible. First, the modelling of the components in the study case will be discussed. Next, the load management strategy and algorithm already mentioned to mitigate this failure will be introduced, thereby avoiding the blackout.

We simulate the failure event in the Matlab-Simulink environment, and show the results of the study case from different perspectives: switchboard busbar voltages, service level component loads and component currents.

4.2. Component modelling

For the study case, a logic load management algorithm that runs at a frequency of 1000 Hz is applied. For this particular simple case, 1000 Hz is more than sufficient. Although a lower operating frequency is also feasible due to the higher time constant dynamics that the supercapacitors provide, high-frequency load management is beneficial in situations with small supercapacitors-load power ratios or low time constant dynamics.

First, the DC/DC converters and supercapacitors are modelled precisely as described above in Section 2.2 using the Simscape Electrical toolbox. Two types of loads are considered: 1) constant power loads are used for (emergency) lighting, CH heat recovery pumps, and bilge ballast pumps – those loads have a power setpoint P^* which in this study case is either its nominal value or 0 when it is OFF; 2) the rest of the loads in Table 4 are modelled as multiple elements (i.e., namely a direct torque control space vector pulse width modulated (DTC SVPWM) controller, inverter, an induction motor and the mechanical pump element). The base equation for the pump speed and pump power relationship is defined as:

$$P \sim \omega^3 \tag{9}$$

For the actual study case, we formulate this as the following third-order polynomial, illustrated in Figure 11 – which is scaled for each pump with nominal speed and power:
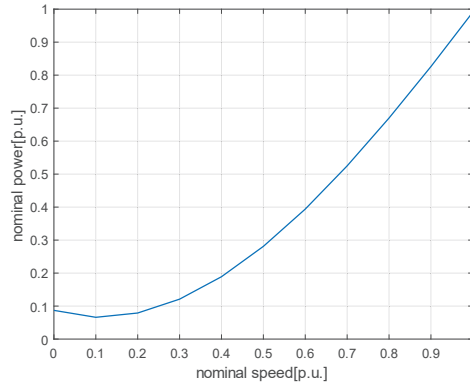
Figure 11: Nominal pump speed vs. power curve

The input of the motor load is the speed setpoint ω^*, provided in all the modelled pump elements, illustrated in Figure 12. For the sake of clarity, feedback signals have been omitted.
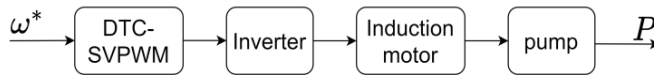
Figure 12: Simulated pump motor control blocks

Subsequently, the pump motor controller is placed in a feedback loop control, illustrated in Figure 13, to compensate for modelling errors and offset disturbances. The input of this feedback loop is a power reference setpoint P^* with a conversion to ω^* for the pump, according to Figure 11. A feedforward element is added so that the PI controller only has to compensate for the *error = $P^* – P$*. Finally, power and speed values are normalised, which is crucial as the pump is highly non-linear and non-adaptive.
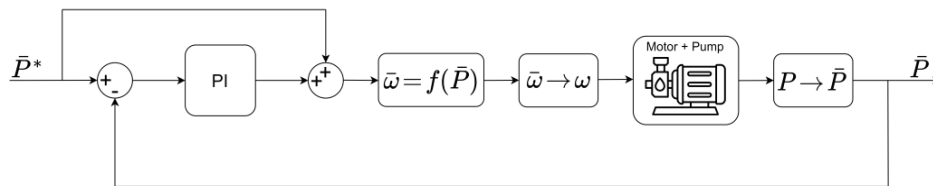
Figure 13: Pump motor control feedback loop

4.3. *Logic control algorithm*

The logic control algorithm consists of two main parts: 1) the closing of the bus-tie circuit breaker and 2) the load management algorithm.

Table 6: Bus-tie breaker trigger time for several converter overload currents and voltage thresholds

Overload Factor ($_xI_n$)	Overload Current [A]	Trigger Time 680 Vdc [sec.]	Trigger Time 660 Vdc [sec.]	Trigger Time 640 Vdc [sec.]
1.2	306	12.718	28.467	48.112
1.5	382.5	4.531	9.909	15.712
2	510	1.949	4.528	7.195
3	765	0.691	1.949	3.228
4	1020	0.273	1.109	1.949

For closing the bus-tie breaker 'CB (3)', three conditions must be satisfied:
1. The switchboard 'SWBD (1)' filtered voltage value is below the voltage threshold (i.e., 680, 660, or 640 Vdc) for 0.01 seconds;
2. There is sufficient time to close the bus-tie circuit breaker. This is based on the resultant time constant of Table 6 that depends on the overload current factor and the voltage threshold selected – the resultant time must be greater than 3 seconds; otherwise, the breaker cannot be closed;
3. There are no faults/error alarms from components 'CB (1)', 'CB (2)', 'F (1)' and 'SuperCAP (1)'.

When all conditions are assumed to be met, and a converter failure event occurs, the voltage decreases. The bus-tie circuit breaker is triggered when the voltage threshold is crossed. It closes in two steps, as described in section 2.1. If the 'DC/DC (2)' converter is still in overload condition, load management must be applied.

Load management follows the principle of reducing low-priority loads first by adjusting the factors α, β, γ, and δ, weight parameters and shedding loads. For the study case, in particular, presented in Table 5, the appropriate steps must be found to maximise loads. However, the converter's nominal power must not be exceeded, which is done by evaluating the steps until this condition (Equation 2) is satisfied.

The developed logic load management is generic and not limited to the study case. It assumes that the loads are operating at feasible values of α, β, γ, and δ, as defined in Equations 4-8. It is essential to highlight the partial overlap of reducing the secondary and primary service level loads. All secondary service level loads with $\beta > 0.4$ are first reduced to 0.4, after which any primary service level load with $\alpha > 0.4$ are reduced to 0.4. Once done, then values of $\beta = 0.4$ are reduced to $\beta = 0$. Finally, values of $\alpha = 0.4$ are reduced to $\alpha = 0$.

Using the service level priority order and the inequality of Equation 2, we can convert this into (nested) switch statement(s), creating a long list of cases. The load management algorithm is explained in Pseudocode 1, but instead of using switch case statements, we use a while loop for the sake of clarity and conciseness – but the principles are the same. The main objective of maximising the loads whilst not exceeding the converter's nominal power limit has become the condition for exiting the while loop.

4.4. *Results and discussion*

Figure 14 illustrates the busbar voltages of the switchboards 'DC SWBD (1)' and 'DC SWBD (2)'. Additionally, the main events are depicted as vertical lines corresponding to their time of occurrence. It is started in regular operation in which the loads have the nominal operating points indicated in Table 4. The (emergency) lighting loads are an exception, with loads 21, 22 and 23 operating at 55%, 55% and 30% of their nominal power, respectively. The converter 'DC/DC (1)' fails at approximately 2.7 seconds, disabling it altogether. As a result, the voltage of 'DC SWBD (1)' decreases as 'SuperCAP (1)' discharges to supply energy to the loads. At an instant of 5.3 seconds, the first part of the logic algorithm is triggered due to the voltage threshold crossing. All criteria for closing the bus-tie circuit breaker are met, and the first switch closes. Now, 'DC SWBD (1)' and 'DC SWBD (2)' are connected, and both supercapacitor banks are in the same grid. At this point, the 'DC/DC (2)' converter supplies the loads located in this zone of the ship entirely. Although the voltage in 'DC SWBD (1)' temporarily increases again, it is of short duration. Both switchboard voltages decrease again due to the overload condition of the 'DC/DC (2)' converter and the discharging of the supercapacitors. At instant 8.3 seconds, and as intended, the

bypass switch of the bus-tie circuit breaker closes. With the voltages in both switchboards still decreasing, the second stage of the logic algorithm is activated as the voltage threshold is crossed again at 11.3 seconds. At this point, Figure 14 illustrates two possibilities: 1) apply load management and restore the voltage to its nominal value, or 2) do not apply load management and eventually the voltage will lead to the failure of 'DC/DC (2)' converter due to under-voltage trip, resulting in a total zonal blackout. The remainder of this paper assumes that load management is selected and applied.

Pseudocode 1: Simplification of logic load management algorithm

---

Algorithm 1: load management

1	**input:** load power measurements vector: $P_{measured}$
2	**output:** load reference setpoints vector: U_{ref}
3	Identify weights factors $\alpha, \beta, \gamma, \delta$ for each individual load *i*. Assume load setpoints operate at weight factor $\alpha_i, \beta_i, \gamma_i, \delta_i$ of their nominal powers $P_{nom,i}$ respectively. They are placed in vectors $\vec{\alpha}, \vec{\beta}, \vec{\gamma}, \vec{\delta}$
4	define U_{ref} and copy $P_{measured}$ into it
5	define '*condition1*' as $\sum P_{measured} \leq P_{nom.converter} - P_{emergency}$
6	**while** *condition1* == false
7	**if** any γ in $\vec{\gamma} > 0$
8	set all γ in $\vec{\gamma}$ to 0; update corresponding habitability power reference setpoints to 0 in U_{ref}
9	**continue**
10	**if** any β in $\vec{\beta} > 0.4$
11	decrease all β in $\vec{\beta}$ which have value equal to $\max(\vec{\beta})$ by one step (see Eq. 6) but not smaller than 0.4; corresponding secondary service level power reference setpoints to $\beta_i \cdot P_{nom,i}$ in U_{ref}
12	**continue**
13	**if** any α in $\vec{\alpha} > 0.4$
14	decrease all α in $\vec{\alpha}$ which have value equal to $\max(\vec{\alpha})$ by one step (see Eq. 4), but not smaller than 0.4; update corresponding primary service level power reference setpoints to $\alpha_i \cdot P_{nom,i}$ in U_{ref}
15	**continue**
16	**if** all β in $\vec{\beta}$ == 0.4
17	set all β in $\vec{\beta}$ to 0; update corresponding secondary service level power reference setpoints to 0 in U_{ref}
18	**continue**
19	**if** all α in $\vec{\alpha}$ == 0.4
20	set all α in $\vec{\alpha}$ to 0; update corresponding primary service level power reference setpoints to 0 in U_{ref}
21	**continue**
22	**if** any δ in $\vec{\delta} > 0$
23	set all δ in $\vec{\delta}$ to 0 and update corresponding lighting power reference setpoints to 0 in U_{ref}
24	**continue**
25	**if** all values in $\vec{\alpha}, \vec{\beta}, \vec{\gamma}, \vec{\delta}$ == 0
26	**break**
27	for load No. *i* =12, … ,22, let power reference setpoints unchanged in U_{ref}. For load No. *i*= 1, … ,11, perform an additional in-place power setpoint reference conversion to their respective nominal value.

Figure 15 depicts the cumulative sum of each service level load over time. The initial 2 seconds represent the motor loads' starting process in the zone. Although the failure event occurs at around 2.7 seconds, this is not reflected in the loads over time. This indicates that the inclusion of supercapacitor functions as expected. Secondly, the low-priority loads are either reduced or shed during load management adjustment. For instance, habitability service level loads are shut down, and primary essential service loads are reduced to 50%. In succession, the highest priority service level loads remain operational.

Finally, Figure 16 illustrates the current flows of each power component. In regular operation, it is evident that there is negligible current flow from the supercapacitors, with all power supplied from the two chopper converters. After the failure event, one can observe that 'SuperCAP (1)' immediately takes over. Subsequently, at 5.3 seconds, the closure of the bus-tie circuit breaker illustrates two peaks in current flow, as depicted in Figure 3. The current flow through 'SuperCAP (1)' briefly becomes negative, charging it and resulting in a short-duration voltage increase, as observed in Figure 14. At an instant of 8.3 seconds, 'SuperCAP (1)' charges for a short duration due to the current outflow of 'SuperCAP (2)'. Lastly, it is notable that the short high transients at the moment of

enabling the load management in Figure 16 (i.e., sudden motor deceleration) are effectively filtered out by 'SuperCAP (1)' and 'SuperCAP (2)' – meaning higher stability for the grid.
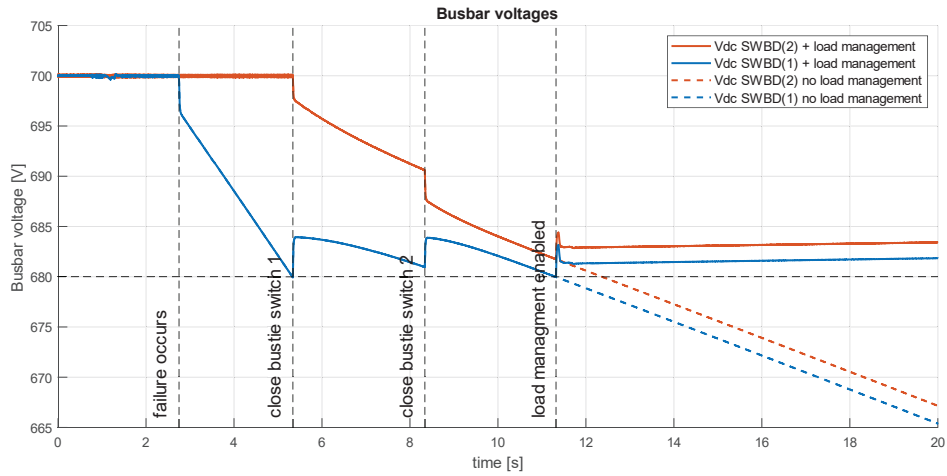
Figure 14: Study case zonal switchboard busbar voltages over time
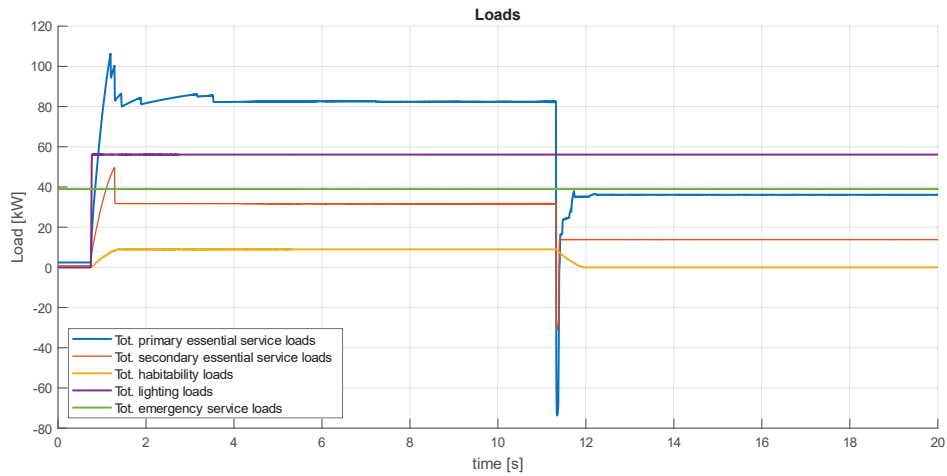
Figure 15: Service level component load sums over time
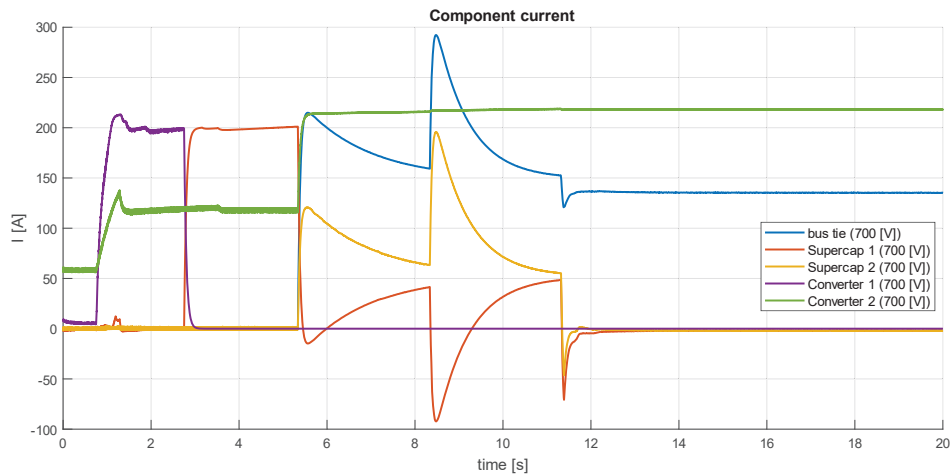
Figure 16: Power system components' current over time

The presented results come from ideal simulations in Matlab-Simulink environment. Constant nominal power loads are used, with some being reduced using a fixed set of weights or shut-down signals. Although the power components have been modelled in great detail, some imperfections are inevitable due to some assumptions and simplifications. To address these imperfections, the pump setpoint control is placed in a PI-control feedback loop for mitigation. This compensates for model imperfections and disturbances. However, this approach has limitations since the pump dynamics are highly non-linear. Despite normalising the inputs and outputs, the feedback controller is still linear and, therefore, requires cautious tuning.

Furthermore, while the logic controller design is applicable outside the study case, it is notable that assuming (approximate) constant loads is, of course, limiting with more dynamic loads expected in practice. However, the logic load management algorithm runs at a high frequency, which could mitigate the impact of such dynamic loads.

5. Conclusions

This work proposes a strategy based on load priority to enhance survivability in zonal DC-grids. A study case based on the 'Seagoing Auxiliary Vessel' was proposed to demonstrate the effectiveness of the priority-based strategy. The strategy comprises a two-stage solution in which voltage threshold triggers first enable the closing of a bus-tie circuit breaker followed by the load adjustments to ensure maximum continuous operation of high-priority loads. The study case featured a chopper converter failure in a zonal DC grid with supercapacitors. The results demonstrated that the high-priority loads continued to operate, the system's voltage was recovered (or kept at operational levels), and converter tripping due to under-voltage setting was prevented.

Incorporating a power reserve can yield faster voltage restoration and power quality improvements in future work. Furthermore, application in practice, such as dredging operations, can provide valuable insights. Finally, combinations with interzonal algorithms can be explored.

Acknowledgements

References

Bosich D., Chiandone M., Sulligoi G., Tavagnutti A. A. & Vicenzutti A.: "High-Performance Megawatt-Scale MVDC Zonal Electrical Distribution System Based on Power Electronics Open System Interfaces", IEEE Transactions on Transportation Electrification, vol. 9, no. 3, pp. 4541-4551, Sept. 2023.

Deroualle J. J., Vinks S.: "Supercapacitors for Enabling Mechanical Circuit Breakers in Shipboard Zonal Secondary DC-Grids", IEEE 6th International Conference on DC Microgrids, ICDCM 2024.

Du W., Yang G., Pan C. & Xi P.: "A Heterogeneous Multi-Agent System Model with Navigational Feedback for Load Demand Management of a Zonal Medium Voltage DC Shipboard Power System", IEEE Access, vol. 7, pp. 148073-148083, 2019.

Erickson R. W. & Maksimović D.: "Chapter 18: Current-Programmed Control", Fundamental of Power Electronics, 3rd ed., Cham, SZ: Springer, 2020, pp. 725-804.

Feng X., Butler-Purry K. L. & Zourntos T.: "Multi-Agent System-Based Real-Time Load Management for All-Electric Ship Power Systems in DC Zone Level", IEEE Transactions on Power Systems, vol. 27, no. 4, pp. 1719-1728, Nov. 2012.

Feng X., Butler-Purry K. L. & Zourntos T.: "A Multi-Agent System Framework for Real-Time Electric Load Management in MVAC All-Electric Ship Power Systems", IEEE Transactions on Power Systems, vol. 30, no. 3, pp. 1327-1336, May 2015.

"IEEE Recommended Practice for 1 kV to 35 kV Medium-Voltage DC Power Systems on Ships", IEEE Std. 1709-2018 (Revision of IEEE Std. 1709-2010), pp.1-54, 7 Dec. 2018.

Qazi S. et al.: "Powering Maritime: Challenges and prospects in ship electrification", IEEE Electrification Magazine, vol. 11, no. 2, pp. 74-87, June 2023.

Xu L. et al.: "A Review of DC Shipboard Microgrids – Part I: Power Architectures, Energy Storage, and Power Converters", IEEE Transactions on Power Electronics, vol. 37, no. 5, pp. 5155-5172, May 2022.

Development of a Low Cost Unmanned Surface Vessel for Autonomous Navigation in Shallow Water

Aiyelari Temilolorun[a], Yogang Singh [a*]

[a]*Department of Engineering and Mathematics, Sheffield Hallam University, Sheffield, S1 1WB, United Kingdom*
[*]Corresponding author. Email: y.singh@shu.ac.uk

Synopsis

Unmanned Surface Vessels (USVs) are commonly autonomous or remotely controlled, serving diverse maritime purposes such as oceanographic research, surveillance, environmental monitoring, and maritime security. These vessels exhibit variability in size, shape, and functionality, ranging from nimble crafts to specialized, larger platforms. This paper introduces the development and validation of a low-cost, agile USV tailored for autonomous navigation in shallow waters. In shallow water, the foremost challenge for USVs is maneuverability, underscoring the crucial need for cost-effective platforms as efficient monitoring systems for maritime applications. The 3D-printed twin-hull catamaran-style platform is equipped with an Inertial Measurement Unit (IMU) and a Global Navigation Satellite System (GNSS) utilizing a Raspberry Pi 4 for high-level control and Arduino MEGA for low-level control. The hovercraft-style propulsion system is designed with a differential drive configuration powered by two DC motors. The design utilizes the Robot Operating System (ROS) to develop the control framework and incorporates Extended Kalman Filter (EKF)-based sensor fusion techniques. The paper evaluates the USV's autonomy through open water captive model experiments, employing remote control methods to assess the vessel's maneuverability and overall performance characteristics in shallow water conditions.

Keywords: Unmanned Surface Vessels, Robot Operating System, Extended Kalman Filter, Autonomous Navigation, Maneuvering

1 Introduction

In recent years, unmanned vehicles have garnered significant attention from both researchers and companies. Ground, aerial, and aquatic unmanned vehicles have become the focal points of research and development efforts (Mancini et al., 2015). There is a growing interest in developing low-cost platforms for complex environmental missions involving various types of vehicles. Consequently, many researchers are exploring frameworks designed for complex scenarios in which unmanned aerial, ground, and aquatic vehicles operate collaboratively (Sotelo-Torres et al., 2023; Mendonça et al., 2013; Prats et al., 2012; Benini et al., 2012; Lewicka et al., 2022).

A particularly encouraging avenue of research focuses on employing USVs for comprehensive environmental monitoring in smaller aquatic environments. This approach facilitates the swift and secure collection of environmental data compared to methods involving human fieldwork and enables surveillance of remote and challenging-to-access areas, while also spanning a broad spectrum of spatial and temporal scales (Liu et al., 2016; Bibuli et al., 2023). Furthermore, USVs offer a precise and lightweight solution for such applications. They require lower operational investment, enhance personnel safety, extend operational range, increase autonomy, and provide greater flexibility, particularly in challenging environments such as muddy, harsh, and dangerous missions (Zappalà et al., 2017). Nevertheless, USVs encounter certain challenges in this research avenue, such as the development of fully autonomous vehicles capable of operating effectively in shallow water environments (Kum et al., 2020; Seto and Crawford, 2015; Shetty et al., 2022). Significant advances have been made in the past decade in the development of USVs, aimed at enhancing the operational efficiency of vessels in shallow water environments with a strong emphasis on design, navigation and collision avoidance capabilities (Pasculli et al., 2020; Han et al., 2020; Kebkal et al., 2014; Aissi et al., 2020; Odetti et al., 2020, 2019). However, despite the progress in these areas, there has been a noticeable dearth of research focusing specifically on comprehensively understanding the maneuvering capabilities of USVs within such environments (Li et al., 2019). This aspect remains relatively underexplored, warranting further investigation to fully grasp the maneuvering dynamics of USVs in shallow water conditions.

There are several methods available to assess the maneuvering performance and controllability of a marine vessel such as Computational Fluid Dynamics (CFD), Planar Motion Mechanism (PMM) experiment and free-running test in open water. This paper presents the design, development, and deployment of a USV, along with an assessment of its controllability performance via a series of maneuvring experiments through the free-running

---

Authors' Biographies

Aiyelari Temilolorun currently is a Research Assistant in the Department of Engineering and Mathematics at Sheffield Hallam University working on the design and development of autonomous marine robots. Aiyelari Temilolorun's research interests include Marine Robotics, Control of Autonomous Systems and Robotics.

Yogang Singh is a Lecturer (Assistant Professor) in Automation, Control and Systems Engineering at the Department of Engineering and Mathematics, Sheffield Hallam University. Dr. Singh's research interests include Autonomous Shipping and Autonomous Marine Systems with a specific interest in USVs.

test in open water. These experiments utilize a remote control approach to evaluate the vessel's maneuverability and overall performance within shallow water environments. Additionally, the USV is engineered to serve as a test platform for validating autonomous navigation techniques and integrating sensors, further enhancing its utility in advancing autonomous maritime technologies. The paper is organised as follows. In Section 2, the paper outlines the specifications of the developed USV, while Section 3 elaborates on the experimental approach to the USV along with the results obtained from field tests conducted on the developed system. Furthermore, in Section 4, a discussion is presented on the results and potential future developments for the USV platform.

2 Design and Development of USV Platform

2.1 Hardware Design and Control System

The USV features a twin-hull catamaran design, 0.72m in length, and 0.41m in width. Each hull consists of three parts, 3D printed using Polylactic acid (PLA) filaments, spray-painted for waterproofing, and then joined together using Epoxy Resin to form a single unit. Carbon fibre rods are used to connect the two hulls. This lightweight construction allows for easy assembly of the boat. Figure 1 illustrates the fully assembled CAD design along with a list of individual components. Table 1 shows the particulars of the designed USV.

Items	Value
Mass	4.88 Kg
Draft	0.045 m
Maximum Speed	4.79 m/s
Centre of Gravity	0.253 m
Length	0.720 m
Breadth	0.508 m

Table 1: Particulars of the USV
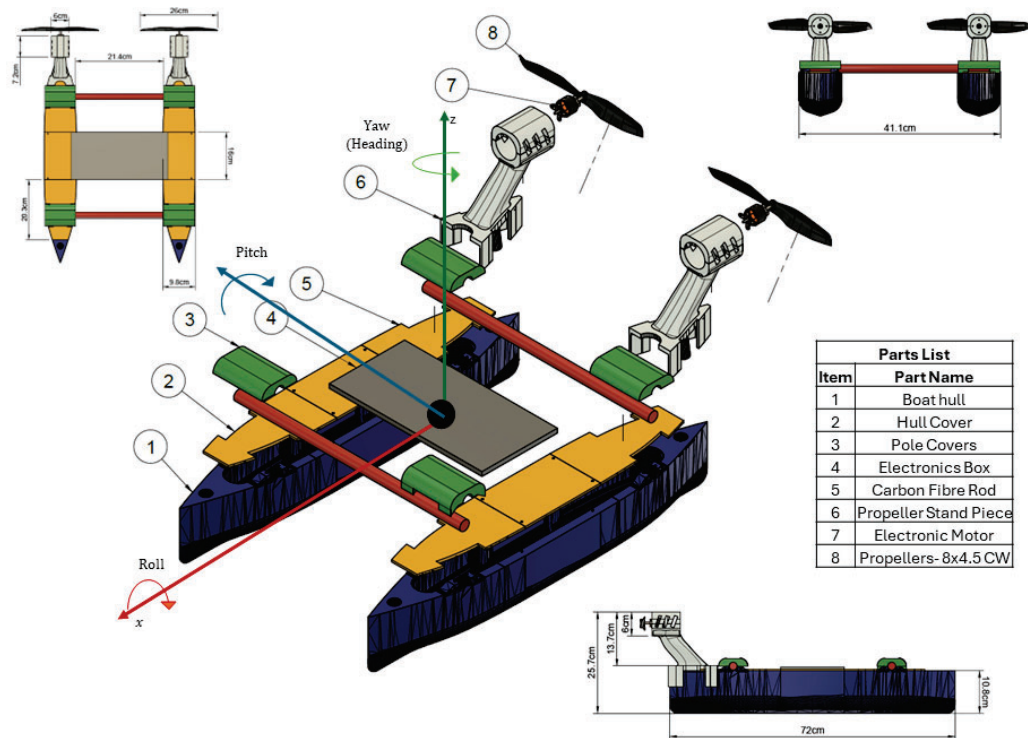
Figure 1: Assembled CAD model of the USV Platform.

The assembled design is fitted with a power system, a sensors system and a propulsion system as shown in Figure 2 with the developed prototype. Electric power is supplied to the USV via 2 channels. The first channel is a power bank that provides the 5V required by the electronic system and sensors connected via USB to the Raspberry Pi and the Arduino Mega. The second channel is the power for the propulsion system which is supplied by a Li-Po battery connected to outboard thrusters via a power distribution board and two electronic speed controllers (ESCs).

The thrusting mechanism, inspired by hovercraft technology and depicted in Figure 2, is powered by two 850Kv 2830 high-efficiency motors connected to 3D-printed propellers. This design enables the vessel to be maneuvered with precision, independent of the fixed propellers' reliance on rudders. Moreover, at very low speeds, rudders are inefficient for turning the vessel. The system employs a counter-rotating setup, with motors rotating in opposite directions, to balance forces, improve stability, and enhance maneuverability. This configuration enables the vessel to move straight, turn, or rotate in place by adjusting the relative speeds of the wheels.

The control system of the USV utilizes both high-level and low-level control mechanisms, achieved through the integration of a Raspberry Pi (RPi) 4 and an Arduino MEGA 2560, respectively. This dual-system approach allows for a comprehensive control over the USV's operations, encompassing both complex computational tasks and direct hardware interfacing. The low-level control system consists of an Arduino MEGA 2560 board as the main controller driving the ESCs, IMU and communication module. The propellers are connected with calibrated ESCs and controlled using pulse-width modulation on the Arduino MEGA. The ESCs are linked to a power distribution board (PDB), which in turn is connected to the Li-Po battery supplying power to the entire system. Figure 3 illustrates the schematic of the hardware design for the USV platform.
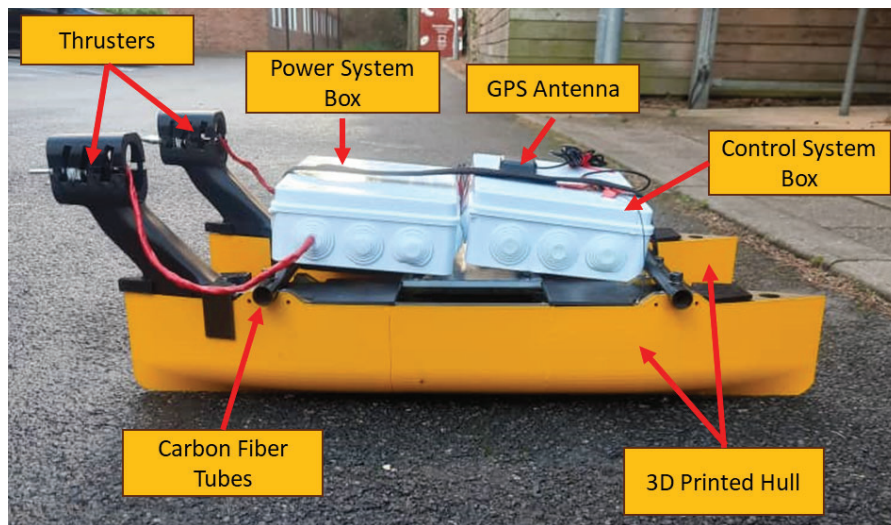
Figure 2: Developed prototype of the USV Platform

The high-level control system consists of an RPi operating the Robot Operating System (ROS) Noetic distribution within the Linux Ubuntu 20.02 environment. Through a serial connection, the GNSS module interfaces with the Arduino Uno board, while in conjunction with the IMU sensor, it establishes an *ekf_localisation* node within ROS. This node facilitates the localization of the boat within three-dimensional space.

2.2 Software Design

The software stack for the USV platform is built, utilizing a dual-layer approach that combines the strengths of both C++ and Python, in conjunction with the Robot Operating System (ROS) as shown in Figure 4. This structure ensures a robust and efficient software framework, catering to the distinct needs of both the low-level and high-level control systems of the USV.

The setup in ROS is built using nodes and launch files. Nodes are implemented to manage Arduino communication using ROSSERIAL and GNSS communication via the serial driver. In addition, we have *vel_con* and *GNSSimu2odom* nodes that take data from the GNSS and IMU publishers and transform that into odometry information. The RPi serves as the onboard computer and is responsible for running the ROS, and interfacing sensors. This setup is crucial for managing the autonomous control aspects of the USV. In ROS, the sensors connected are controlled using launch files to start them up while a subscriber is initiated to subscribe to the IMU data from the low-level controller. All this data is fed into the *robot_localization* package in the ROS which eventually contains the *ekf_localization* node to help the vessel better localize itself and perform state estimation. A detailed
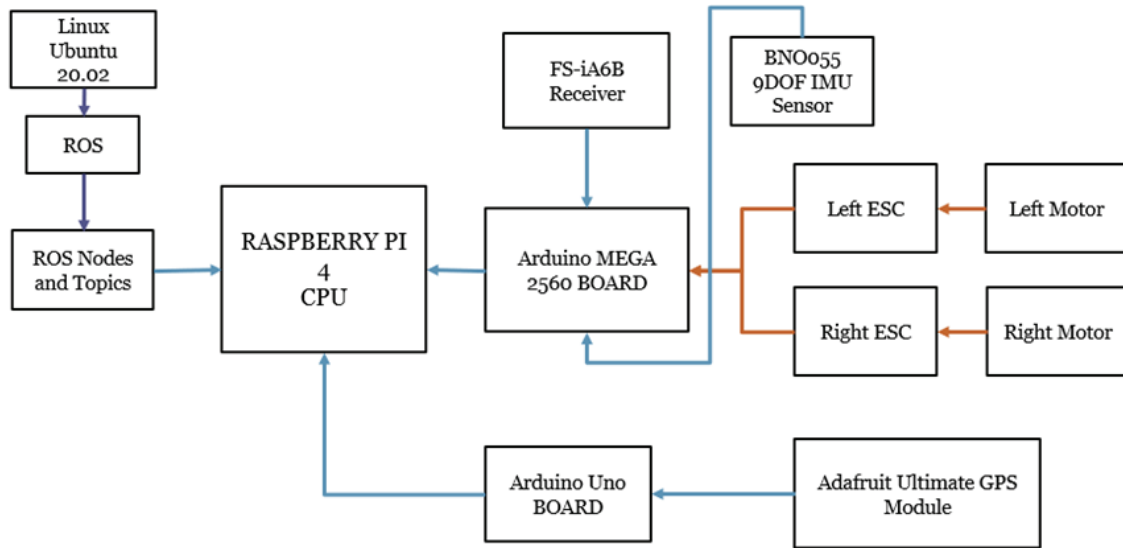
Figure 3: Schematic of the hardware design for the USV Platform
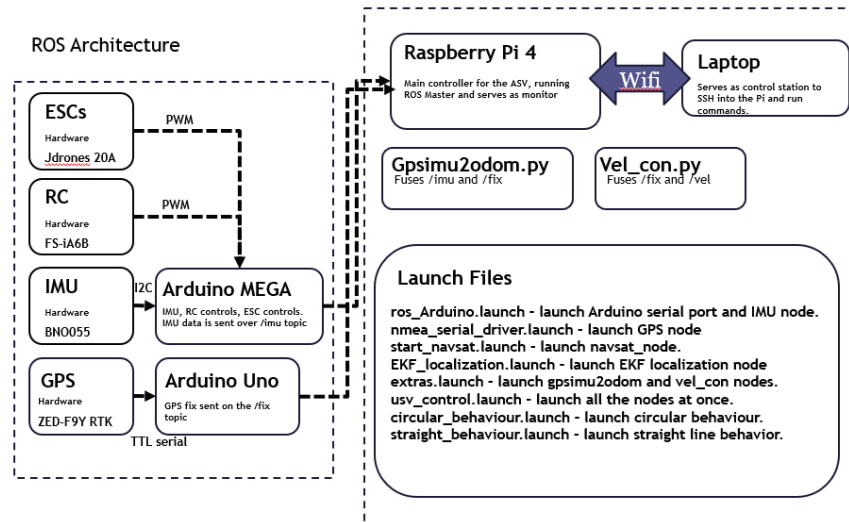
Figure 4: USV software stack

explanation of sensor fusion is explained in section 2.3.

2.3 Extended Kalman Filter based Sensor Fusion

In this study, we utilize the data fusion approach of Moore and Stouch (2016) to integrate data from an array of sensors on a USV. A *robot_localization* package developed as a part of the work has been used in the current study for the implementation of an EKF for sensor fusion. Although the original work was tested with mobile robots, this study extends its application to marine robots, adapting the methodology for use in the maritime domain. The current section details the implementation of the developed *ekf_localization* node as the component of the *robot_localization* package. The goal of the EKF is to estimate the full 3D pose and velocity of the USV over time. The non-linear dynamical system of the USV can be described with

$$x_k = f(x_{k-1}) + w_{k-1} \tag{1}$$

where x_k is the USV system state at a time k, f is a non-linear state transition function and w_{k-1} is the normally distributed noise. The USV state vector x consists of the USV's 3D pose, orientation and their respective velocities. The received measurements are expressed as

$$z_k = h(x_k) + v_k \qquad (2)$$

where z_k is the measurement at time k, h is a mapped non-linear sensor model and v_k is the normally distributed measurement noise. In the initial stage, EKF performs a prediction step, advancing the current state estimate and error covariance forward in time using equations (3) and (4) as follows:

$$\hat{x}_k = f(x_{k-1}) \qquad (3)$$

$$\hat{P}_k = FP_{k-1}F^T + Q \qquad (4)$$

In this study, f is the standard 3D kinematic model of the USV with P being the estimated error covariance, projected via F, the Jacobian of f and perturbed by Q, the process noise covariance. The correction step is then carried out using the equations (5) till (7) to calculate the Kalman gain using observation matrix H and measurement covariance R and $\hat{P}_k$ as follows:

$$K = \hat{P}_k H^T (H\hat{P}_k H^T + R)^{-1} \qquad (5)$$

$$x_k = \hat{x}_k + K(z - H\hat{x}_k) \qquad (6)$$

$$P_k = (I - KH)\hat{P}_k(I - KH)^T + KRK^T \qquad (7)$$

leading to the use of gain to update the state vector and covariance matrix. The fundamental aspect of the adopted approach is its capability for a partial update of the state vector, enabling the omission of certain variables in the state vector during the sensor data capture process. This capability is crucial for USVs, as data loss during operations is a common occurrence. In the present study, we consider the sensor configuration of fused odometry, incorporating a single IMU and a single GNSS. This configuration is chosen to effectively manage the significant interference encountered in the operational environment of the USV.

2.4 Cost Analysis

The design of our USV emphasizes low-cost construction while maintaining high functionality. Key electronic components, including a Raspberry Pi4, RTK GNSS, IMU, Arduino Uno, Arduino MEGA, and RC Controller, collectively cost £310. At the same time, the mechanical parts like propellers, an IP7 electronics box, 3D Printing and Carbon Fibre tubes add £177 to the total. This strategic selection of components results in a comprehensive, budget-friendly USV design with a total cost of £487, making it an accessible option for research and development. The table 2 summarises the cost breakdown for low-cost USV design.

Category	Items	Cost (£)
Electronics	Brushless DC Motors (x2)	35
	ESCs (x2)	20
	RTK GNSS	24
	IMU	28
	Arduino Uno	18
	RC Controller	60
	11.1V LiPo Battery	24
	Power Board	8
	Raspberry Pi4	50
	Arduino MEGA	50
Mechanical	Propellers (x2)	10
	IP7 Electronics Box	28
	Carbon Fibre Tubes	32
	3D Printing	100
	Total	487

Table 2: Cost breakdown for low-cost USV design

2.5 *Communication System*

The communication system of the USV is designed with two distinct parts namely, the Control Communications Part (CCP) and the Telemetry Communications Part (TCP) with both segments designed to employ radio communications to enhance the range and reliability of the data transmission. The CCP is primarily responsible for the remote-control operations of the USV. This system comprises two main elements: a transmitter and a receiver, both critical for the effective remote operation of the vehicle. The receiver in the CCP is intricately connected to the Arduino MEGA 2560, the core of the USV's control system and is mounted on the USV's electronics shelf. The placement of the receiver is crucial for optimal signal reception and processing, allowing for seamless communication between the remote operator and the USV. The transmitter utilized in the CCP is the FS-i6 Flysky digital proportional radio control system. The choice of the FS-i6 Flysky transmitter is based on its efficiency, reliability, and compatibility with the overall design and operational requirements of the USV.

The TCP of the USV is strategically designed around the ROS communication between two computers, one on the robot and the local base station via a local wireless network, operating at 2.4GHZ ISM (Industrial, Scientific and Medical) band. This is to ensure minimal interference and efficient telemetry data transmission for both real-time analysis on the local base station and offline analysis through recorded sensor/ROS topics information saved on the robot using ROSBAGS. With this setup, data transmitted via TCP between the two computers ensures reliable communication for the USV. The stable wireless connection between the two computers supports low-latency data exchange, which is crucial for real-time control and monitoring. Additionally, the recorded ROSBAGS enable detailed post-mission analysis, aiding in evaluating performance and diagnosing issues. This integrated system allows for precise and dependable operation of the USV, while also generating valuable data for ongoing improvements and system optimization.

3 Experimental Approach to USV

3.1 *Testing Arena*

The USV platform was tested locally at Millhouse Park in Sheffield, United Kingdom, chosen for its realistic shallow water environment as shown in Figure 5 with support from the local boating community to ensure the safety of the USV trials. Initially, a float test was conducted to test the stability and robustness of the designed platform with the vessel orientation data being recorded for the duration of the float test. Figure 6 shows the pitch, roll and heading data for the float test showing no deviation from the initial values thereby confirming the stability of the USV platform.

Figure 5: Marked testing arena for the USV Platform

3.2 *Autonomy Protocol*

The vessel's autonomy was evaluated through a series of remote-control (RC) tests, utilizing radio communication to govern its motion as described in section 2.5. Sensor data recordings were made using ROSBAGs and analyzed using the *MATLAB ROSBAG Viewer Tool* and *Foxglove Studio*. The RC setup, illustrated in Figure 7, enables the propulsion of the USV using a differential drive system. This system allows for precise movements, making the USV ideal for navigation in diverse aquatic environments. The tests were conducted using a laptop as a ground station with an Intel i7 1.90 GHz quad-core CPU and Ubuntu 20.04 as OS.
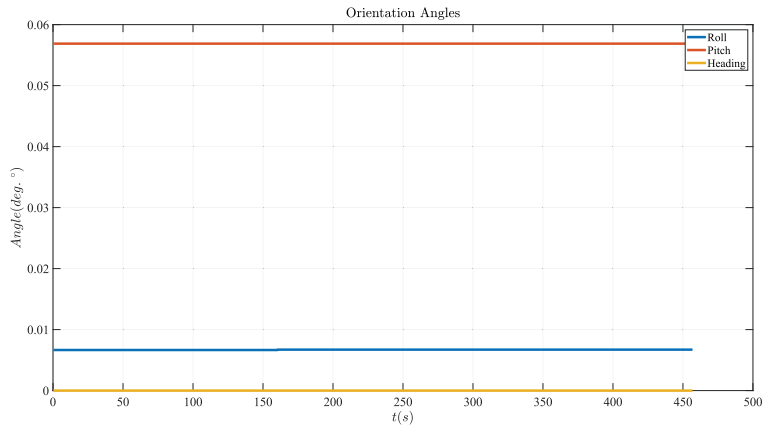
Figure 6: Orientation of the USV platform during float test
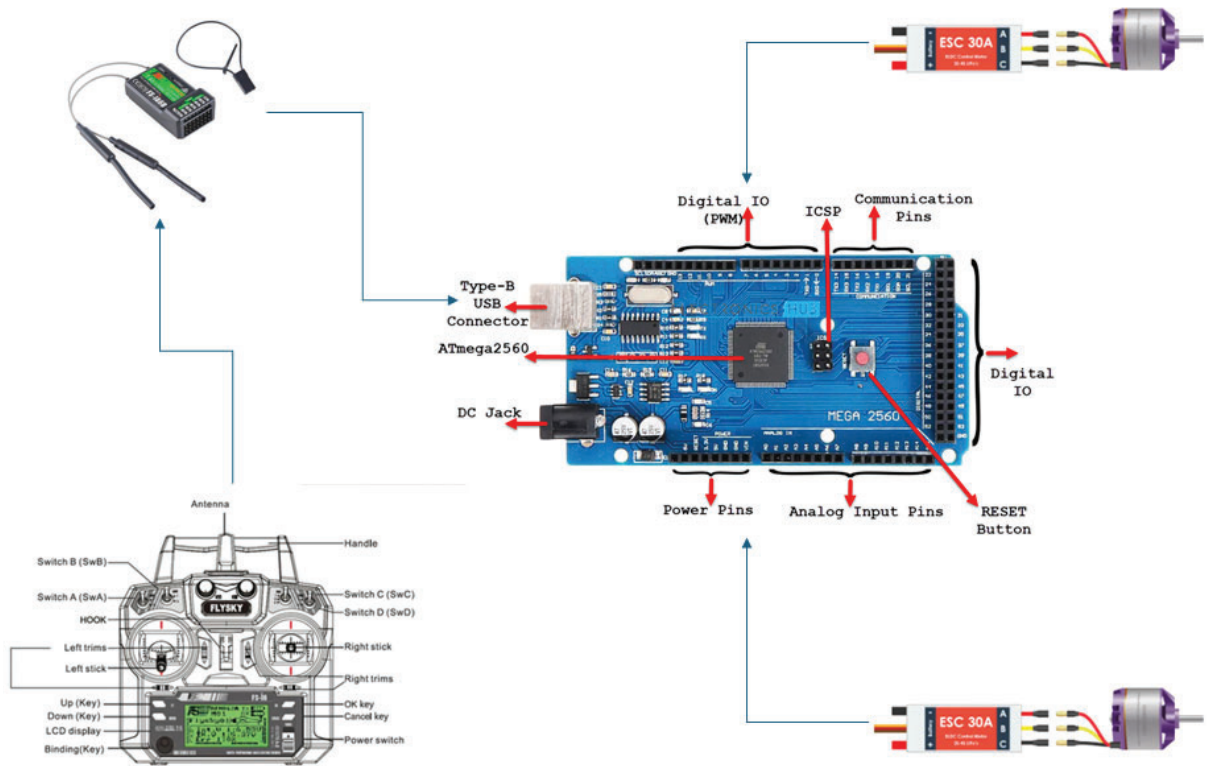
Figure 7: RC setup for the USV platform

3.3 Maneuvering Experiments and Results

The maneuvering performance of the vessel was evaluated in open water using a widely recognized captive model turning circle test. In the test, the vessel was made to do a turning circle of 540° to determine following parameters as shown in Figure 8:

- Tactical diameter

- Advance

- Transfer

- Loss of speed on a steady turn

- Time to change heading 90°

- Time to change heading 180°
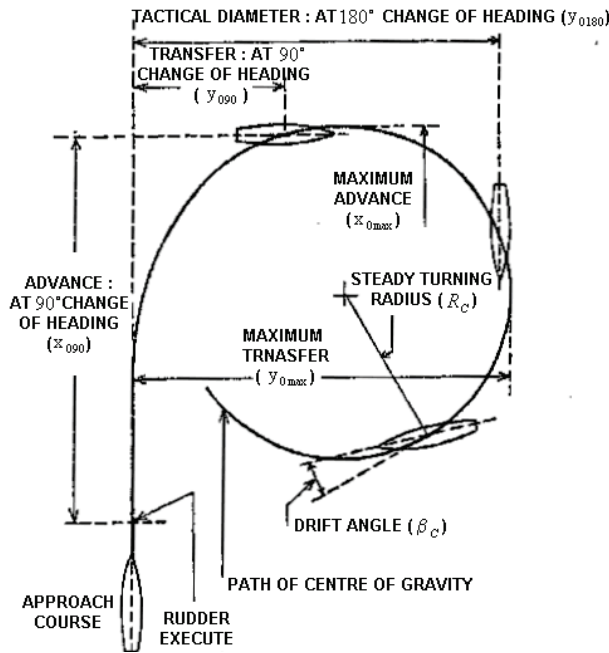
Figure 8: Turning Circle definitions

This test was conducted on a full-scale model of the USV within the testing arena depicted in Figure 5.

To perform the free-running maneuvering experiments in open water, International Maritime Organisation (IMO) Resolution A.751 stating interim standards for ship maneuverability(Kim et al., 1996; BAKAR, 2015) were adopted with suggested modifications for differential drive propulsion vessels as follows:
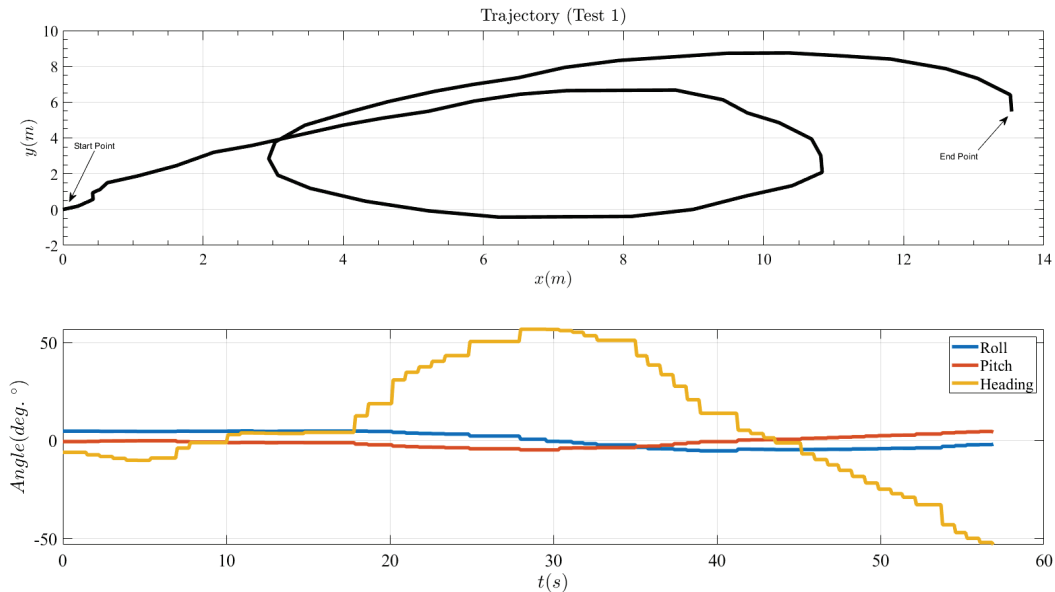
Figure 9: Turning Circle results from Test 1 (Starboard side)

Parameters	Test	Criteria
Advance	Turning Circle	< 4.5L
Tactical Diameter	Turning Circle	<5L

Table 3: IMO evaluation criteria for maneuverability

1. The approach speed should be 90% of the vessel speed corresponding to 85% of the maximum engine output.

2. Prior to executing the maneuver, the vessel must maintain a steady course at a constant setting for a minimum of one minute.

Three different tests from three different start and goal points within the testing arena were performed to determine the USV maneuverability in terms of turning circle parameters and were compared against the IMO-enforced minimum maneuverability criteria listed in Table 3 (BAKAR, 2015). The turning circle test data is summarised in the Table 4.
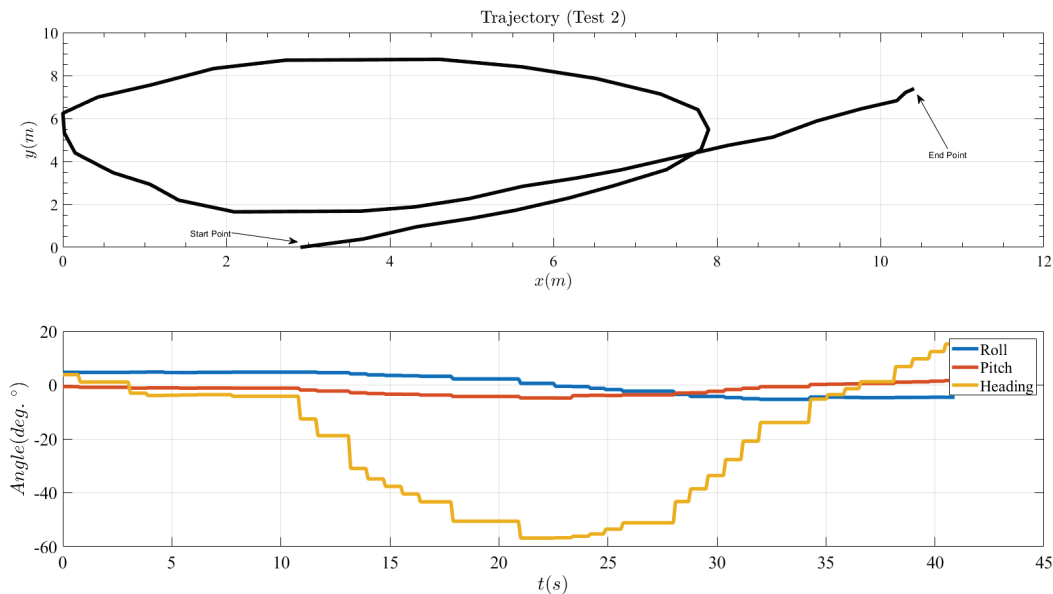
Figure 10: Turning Circle results from Test 2 (Port side)

Figure 9 and Figure 11 presents the data collected from the turning circle tests for the Starboard side while Figure 10 presents the data collected on the Port side of the USV.

Parameters	Test 1 (Starboard)	Test 2 (Port)	Test 3 (Starboard)
Advance (m)	8.4202	9.0802	5.7385
Transfer (m)	3.803	4.9336	4.4181
Tactical Diameter (m)	7.0774	7.184	6.8264
Loss of speed-steady turn (%)	7.24	5.75	8.01
Time to change heading $90°$(s)	23.12	17.24	11.12
Time to change heading $180°$(s)	31.86	24.29	18.11

Table 4: Turning Circle test results

The IMO compliance for Tactical Diameter and Advance for the three tests is detailed in Table 5. The trial data shows that the recorded values significantly exceed the specified criteria for meeting IMO standards regarding turning ability, particularly Tactical Diameter and Advance. This considerable deviation is attributed not only
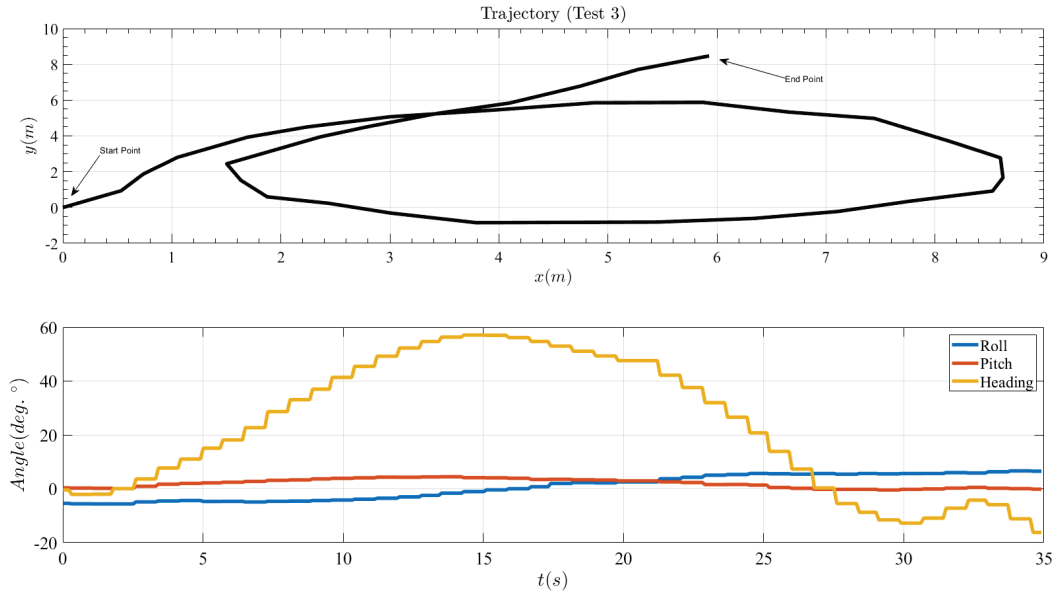
Figure 11: Turning Circle results from Test 3 (Starboard side)

Test	Parameters	Measured	Criteria	IMO Compliance (Yes or No)
1 (Starboard)	Tactical Diameter, Advance	7.0774, 8.4202	3.6, 3.24	No, No
2 (Port)	Tactical Diameter, Advance	7.184, 9.0802	3.6, 3.24	No, No
3 (Starboard)	Tactical Diameter, Advance	6.8264, 5.7385	3.6, 3.24	No, No

Table 5: IMO compliance for Turning Circle test

to the lower-cost sensor readings affecting measurement accuracy but also to external factors such as wind and surface currents in the testing area. Importantly, the measurements on the Starboard side display less variability compared to those on the Port side. The roll and pitch results from all three tests demonstrate minimal deviation, highlighting the stability and reliability of the USV, particularly in shallow waters and amidst challenging surface currents generated by wind. The recorded trials can be found at https://youtu.be/UrtKRdADDVc and the project repository can be found at https://github.com/YogangSingh/catamaranshu.

4 Lessons Learned

The dual-system approach using a Raspberry Pi and Arduino MEGA proved effective in managing both high-level computational tasks and low-level hardware interfacing. The 3D-printed hulls made from PLA filaments, reinforced with carbon fibre rods, demonstrated durability and stability in various water conditions, validating the feasibility of using cost-effective materials without compromising structural integrity. The turning circle tests highlighted significant deviations from the IMO criteria, indicating areas for improvement in sensor accuracy and propulsion control. The results showed that while the USV maintained good stability and minimal roll and pitch deviations, the tactical diameter and advance did not meet the required standards. The total cost of £487 for the USV, including electronics and mechanical parts, demonstrates that a functional USV can be developed on a low budget. Using widely available and affordable components like the Raspberry Pi, Arduino boards, and 3D-printed parts was pivotal in keeping the costs low while achieving the desired functionality. The USV achieved its aim of functional performance through successfully integrating navigation and control systems, even though the maneuverability metrics did not fully comply with IMO standards.

5 Conclusions and Future Work

The assessment of the performance and maneuverability of the designed USV was conducted through an open-water free-running turning circle test. The trial outcomes demonstrate a notable deviation from the specified IMO criteria, underscoring the imperative for further refinement in both hardware and software design for the USV.

This necessitates the incorporation of more advanced sensors and exploration of innovative design avenues. The iterative process seeks to elevate the USV's capabilities, ensuring compliance with regulatory standards while enhancing its efficiency and reliability across diverse maritime operations. Despite this, the ongoing focus on integrating CAD-designed components, 3D printed parts, and a basic sensor suite, alongside limited testing, lays a foundational framework for future enhancements.

Acknowledgement

References

Aissi, M., Moumen, Y., Berrich, J., Bouchentouf, T., Bourhaleb, M., Rahmoun, M., 2020. Autonomous solar usv with an automated launch and recovery system for uav: State of the art and design, in: 2020 IEEE 2nd International Conference on Electronics, Control, Optimization and Computer Science (ICECOCS), IEEE. pp. 1–6.

BAKAR, M.H.A.B.A., 2015. Manoeuvering analysis in free running scaled rc model on 60m multi purpose offshore support vessel (mposv).

Benini, A., Mancini, A., Minutolo, R., Longhi, S., Montanari, M., 2012. A modular framework for fast prototyping of cooperative unmanned aerial vehicle. Journal of Intelligent & Robotic Systems 65, 507–520.

Bibuli, M., Ferretti, R., Odetti, A., Aracri, S., Caccia, M., Diez, M., Serani, A., 2023. Digital twin of autonomous surface vehicles: From standard methodologies towards extended data-based models , 75–77.

Han, J., Cho, Y., Kim, J., Kim, J., Son, N.s., Kim, S.Y., 2020. Autonomous collision detection and avoidance for aragon usv: Development and field tests. Journal of Field Robotics 37, 987–1002.

Kebkal, K., Glushko, I., Tietz, T., Bannasch, R., Kebkal, O., Komar, M., Yakovlev, S., 2014. Sonobot—an autonomous unmanned surface vehicle for hydrographic surveys with hydroacoustic communication and positioning for underwater acoustic surveillance and monitoring, in: Proceedings of the 2nd International Conference and Exhibition on Underwater Acoustics, Rhodes, Greece, pp. 22–27.

Kim, M.J., et al., 1996. Assessment of ship manoeuvrability based on imo resolution no. a. 751 .

Kum, B.C., Shin, D.H., Jang, S., Lee, S.Y., Lee, J.H., Moh, T., Lim, D.G., Do, J.D., Cho, J.H., 2020. Application of unmanned surface vehicles in coastal environments: Bathymetric survey using a multibeam echosounder. Journal of Coastal Research 95, 1152–1156.

Lewicka, O., Specht, M., Stateczny, A., Specht, C., Dardanelli, G., Brčić, D., Szostak, B., Halicki, A., Stateczny, M., Widźgowski, S., 2022. Integration data model of the bathymetric monitoring system for shallow waterbodies using uav and usv platforms. Remote Sensing 14, 4075.

Li, C., Jiang, J., Duan, F., Liu, W., Wang, X., Bu, L., Sun, Z., Yang, G., 2019. Modeling and experimental testing of an unmanned surface vehicle with rudderless double thrusters. Sensors 19, 2051.

Liu, Z., Zhang, Y., Yu, X., Yuan, C., 2016. Unmanned surface vehicles: An overview of developments and challenges. Annual Reviews in Control 41, 71–93.

Mancini, A., Frontoni, E., Zingaretti, P., 2015. Development of a low-cost unmanned surface vehicle for digital survey, in: 2015 European Conference on Mobile Robots (ECMR), IEEE. pp. 1–6.

Mendonça, R., Santana, P., Marques, F., Lourenço, A., Silva, J., Barata, J., 2013. Kelpie: A ros-based multi-robot simulator for water surface and aerial vehicles, in: 2013 IEEE International Conference on Systems, Man, and Cybernetics, IEEE. pp. 3645–3650.

Moore, T., Stouch, D., 2016. A generalized extended kalman filter implementation for the robot operating system, in: Intelligent Autonomous Systems 13: Proceedings of the 13th International Conference IAS-13, Springer. pp. 335–348.

Odetti, A., Altosole, M., Bruzzone, G., Caccia, M., Viviani, M., 2019. Design and construction of a modular pump-jet thruster for autonomous surface vehicle operations in extremely shallow water. Journal of Marine Science and Engineering 7, 222.

Odetti, A., Bruzzone, G., Altosole, M., Viviani, M., Caccia, M., 2020. Swamp, an autonomous surface vehicle expressly designed for extremely shallow waters. Ocean Engineering 216, 108205.

Pasculli, L., Piermattei, V., Madonia, A., Bruzzone, G., Caccia, M., Ferretti, R., Odetti, A., Marcelli, M., 2020. New cost-effective technologies applied to the study of the glacier melting influence on physical and biological processes in kongsfjorden area (svalbard). Journal of Marine Science and Engineering 8, 593.

Prats, M., Perez, J., Fernández, J.J., Sanz, P.J., 2012. An open source tool for simulation and supervision of underwater intervention missions, in: 2012 IEEE/RSJ international conference on Intelligent Robots and Systems, IEEE. pp. 2577–2582.

Seto, M.L., Crawford, A., 2015. Autonomous shallow water bathymetric measurements for environmental assessment and safe navigation using usvs, in: OCEANS 2015-MTS/IEEE Washington, IEEE. pp. 1–5.

Shetty, D., Kotian, R., Sequeira, S.L., NR, P., Pruthviraj, U., Gangadharan, K., 2022. An economical approach towards bathymetric mapping of shallow water basins using unmanned surface vessel, in: ASME International Mechanical Engineering Congress and Exposition, American Society of Mechanical Engineers. p. V005T07A077.

Sotelo-Torres, F., Alvarez, L.V., Roberts, R.C., 2023. An unmanned surface vehicle (usv): Development of an autonomous boat with a sensor integration system for bathymetric surveys. Sensors 23, 4420.

Zappalà, G., Bruzzone, G., Azzaro, M., Caruso, G., 2017. New advanced technology devices for operational oceanography in extreme conditions. International Journal of Sustainable Development and Planning 12, 61–70.

Neuro Adaptive Integral Sliding Mode Control based on Composite Learning for Path-Following of an Underactuated Underwater Vehicle: Blucy

M Menghini[a*], S K Mallipeddi[a], P Castaldi[a], L De Marchi[a]

[a] Department of Electrical, Electronic and Information Engineering (DEI) "Guglielmo Marconi", University of Bologna, 40136 Bologna, Italy;

*Corresponding author. Email: massimilian.menghin3@unibo.it

Synopsis

This paper presents an application of an intelligent control system for an underactuated underwater vehicle called Blucy, developed for non-invasive underwater monitoring. During the monitoring, it is crucial to maintain an attitude towards the target and stay on the survey's path to improve the collected data quality, this highlights the need for developing a sophisticated guidance and control system. Specifically, intelligent controls demonstrate adaptability in challenging environments, such as sea current disturbances, and handle both unmodelled and nonlinear dynamics of the system, like the presence of the fiber optic cable during remotely operated inspections. In this work, a robust path-following algorithm is developed. A line-of-sight guidance is used to tackle the problem of under actuation, which outputs a virtual input to the control system. A composite error learning based methodology is implemented to design a control system. An integral sliding mode control that uses a radial basis neural network to estimate the unmodelled dynamics and uncertainties is developed. In addition, a disturbance observer is designed to approximate the external noise and the error made by the neural network. Furthermore, a state estimator is implemented whose error, along with the tracking error made by the controller, is used in training the neural network and disturbance observer, regarded as so-called composite error learning, which enhances the learning process, making the controller more robust against disturbances and uncertainties. The efficiency and performance of the proposed control methodology in following the desired path are studied through simulation.

Keywords: Underwater vehicles; Path-following; Composite error learning; Underactuated vehicle.

1 Introduction

The Blucy was developed in the Interreg IT-HR SUSHI DROP (Sustainable fisheries with drone data processing) project for non-invasive underwater monitoring and for preserving and restoring underwater ecosystems (Interreg, 2019). It is a hybrid Unmanned Underwater Vehicle (UUV), capable of operating either as a Remotely Operated (ROV) or Autonomous vehicle (AUV), depending on the specific mission requirements. Authors have performed missions such as close seabed monitoring and multibeam surveys to study benthic zones by generating 3D models of the habitats (Interreg, 2019, 2022; Lambertini et al., 2022). 3D models are then exploited to create digital twins of habitats, from which statistical metrics are extracted to analyze the temporal evolution of the habitat itself. These missions were performed by following a predetermined path manually by the pilot. Although depth and heading autopilots were implemented, following the desired path manually was a difficult task primarily because Blucy is an underactuated system. Secondly, external environmental disturbances and uncertainties affect the quality and accuracy of the data collected. Thus, these challenges posed by the underactuated system in the presence of variable sea currents and complex underwater terrains necessitate the importance of robust guidance and control systems that can adapt to changing conditions while maintaining paths and enhancing the capabilities of the Blucy.

Various control strategies have been explored in the literature to address the path-following challenges of UUVs. A classical PID controller is implemented in (Antonelli et al., 2003), while an adaptive integral sliding mode control for underactuated AUV with uncertain dynamics is presented in (Joe et al., 2014). A fuzzy logic observer was employed to approximate external disturbances and uncertainties in a similar context (Duan et al., 2020). A robust back-stepping control approach for underactuated AUVs was introduced in (Wang et al., 2009). A

Figure 1: Blucy UUV performing close seabed survey in Croatian waters.

self-triggered vision-based model predictive control framework to tackle trajectory tracking amidst external disturbances is proposed in (Heshmati-Alamdari et al., 2014). Disturbance observers, known for their adaptive nature, are utilized together with the controllers for robust trajectory tracking in (Guerrero et al., 2019; Duan et al., 2020; Heshmati-Alamdari et al., 2020). A thorough review of nonlinear control techniques for underactuated AUVs are provided in (Ashrafiuon et al., 2010).

Advances in computational resources have propelled the rise of Artificial Intelligence (AI) controllers, particularly Neural Networks (NN). Renowned for their adeptness in handling various uncertainties, deep learning capabilities, and universal approximation property, NNs have garnered attention among researchers. Unlike conventional controllers reliant on robustness alone, intelligent controllers employ NNs to estimate and address external disturbances and uncertainties, enhancing robustness. A recent review on intelligent controls to address the problem of trajectory tracking of underactuated UUV is presented in (Er et al., 2023). Controllers based on NNs often employ the Feedback Error Learning (FEL) strategy. However, this approach is prone to aggressive learning, and the convergence of optimal NN weights requires persistent excitation. Without it, NN parameters can drift from their optimal values, resulting in high-gain controllers. The learning efficiency is enhanced by designing a state estimator based on estimated uncertainties, and its estimation error is incorporated into the learning rule, a process known as composite learning. A composite learning-based controller for underactuated UUVs, capable of tracking desired paths amidst uncertainties and external disturbances, is proposed in (Liu and Du, 2021). In (Zhou et al., 2019), a back-stepping method with composite learning for underactuated systems is introduced, while (Makavita et al., 2015) analyzes composite model reference adaptive control for underactuated AUVs.

Based on these works, this study proposes the following contributions: 1) A look-ahead guidance law-based line-of-sight guidance system for maintaining the trajectory and attitude of a Blucy UUV in the presence of external disturbances and uncertainties. 2) Estimation of tracking error, disturbances, and uncertainties using Feed Forward Neural Networks (FFNN), along with a disturbance observer designed to calculate noise and estimation error of the NN. The state estimation error is added to the learning rule, making it composite learning to enhance the learning process. 3) Unlike previous studies, the composite error is regulated using a sliding manifold to ensure finite-time convergence. 5) Hence, a neuro-adaptive integral sliding mode control is proposed to track the reference velocities from the guidance loop.

The remainder of the paper is organized as follows: In Section 2, the mathematical model and actuator configurations of Blucy are outlined. In Section 3, the design procedure of the guidance and neuro-adaptive control is presented. Simulations and discussion on the results are reported in Section 4. Finally, conclusions drawn from the research are presented in Section 5.

2 System description

The mathematical model of the Blucy (Figure 1) is based on the Fossen model, which characterizes the UUV as a rigid body possessing a six-degree-of-freedom (DOF) motion (Fossen, 2011). It utilizes an inertial reference frame for kinematics and a body reference frame for dynamics. The model encompasses the standard equations for the translational motion of the Center of Gravity (CG) and rotational motion about the CG, which is the center of the body frame. To express these relations, the following notations are considered:

$$\eta = \begin{bmatrix} \eta_1 & \eta_2 \end{bmatrix}' \quad where \quad \eta_1 = \begin{bmatrix} x & y & z \end{bmatrix}' \quad and \quad \eta_2 = \begin{bmatrix} \phi & \theta & \psi \end{bmatrix}' \tag{1}$$

$$v = \begin{bmatrix} v_1 & v_2 \end{bmatrix}' \quad where \quad v_1 = \begin{bmatrix} u & v & w \end{bmatrix}' \quad and \quad v_2 = \begin{bmatrix} p & q & r \end{bmatrix}' \tag{2}$$

Herein, the variable η denotes the position of the body frame relative to the inertial frame, expressed through linear displacements (η_1) and Euler angles (η_2). Meanwhile, the variable v refers to the linear velocity (v_1) and angular velocity (v_2), both of which are expressed in the body axes system. Based on these notations, the 6 DOF equation of UUV can be expressed as:

$$\dot{\eta} = J_\Theta(\eta)v \tag{3a}$$
$$M\dot{v} + C(v)v + D(v)v + g(\eta) = \tau_p \tag{3b}$$

where J_Θ is the transformation matrix; $M = M_{RB} + M_A$ is the system inertia matrix including added mass (M_A); $C(v) = C_{RB}(v) + C_A(v)$ is the Coriolis-centripetal matrix (including added mass $C_A(v)$) due to the rotation of the body frame with respect to the inertial frame; $D(v)v$ is the Damping matrix, treated as the sum of a linear contribution and a nonlinear one; $g(\eta)$ is the vector of gravitational and buoyancy forces and $\tau_p = (X,Y,Z,K,M,N)^T$ is the vector of control inputs.

Actuator description

Blucy is an under-actuated UUV designed to have stability in pitch and roll, enhancing its control over the motion variables x, y, z, u, v, w, r, and ψ during various survey operations, such as multibeam and close seabed surveys (Lambertini et al., 2022). It is equipped with a propulsion system consisting of six thrusters: two horizontal, two vertical, and two lateral, strategically positioned around the CG to optimize thrust direction. These thrusters use Kaplan Ka 4-70 series ducted propellers with 19A nozzle (Kuiper, 1992), differentiated into propulsive and maneuvering types. Propulsive thrusters are optimized for high rotational speeds for surge motion. Maneuver thrusters are designed for lower speeds to handle heave, sway, or yaw motions, with blade symmetry tailored to their specific operational requirements.

Thrust and torque outputs are theoretically predicted using polynomial regression of the Ka 4-70 series, refined by experimental data to derive thrust (C_T) and torque (C_Q) coefficient curves as functions of the propeller's advance ratio J.

The overall force (F) and moment (M) generated by the thrusters are computed from the individual thrust (T_i) and torque (Q_i) of each actuator, considering their positions (l_i) and orientations (e_i) relative to the CG:

$$F = \sum_{i=1}^{6} (e_i \cdot T_i) \tag{4}$$

$$M = \sum_{i=1}^{6} (l_i \times T_i) \cdot e_i + Q_i \tag{5}$$

This setup not only ensures efficient navigation and maneuverability but also supports the vehicle's ability to perform complex underwater operations, adhering to the specific performance demands for each survey type. The overall force and moment in (4) and (5) are used as control input τ_p.

Control Objective

This work aims to develop a robust guidance and control system for Blucy UUV that guarantees precise path-following with the vehicle's nose aligned to the path direction despite uncertainties and external disturbances. The path under consideration for the simulation replicates a typical mission profile, where data collection is conducted using the onboard multibeam system. This trajectory is built through geo-located waypoints, which define the path typically undertaken during real operations.

3 Design of guidance and control system

In this section, a guidance and control system is developed in two parts. Firstly, the look-ahead guidance law, based on the line-of-sight, is designed to enable the tracking of the path. Secondly, a neuro-adaptive sliding mode control based on composite error learning is designed to track the virtual inputs for the guidance system. The schematic representation of the system is depicted in Figure 2.

To design the guidance and control system, let us consider the following synthetic model of the system (3), describing the kinematics and the dynamics:

$$\begin{aligned} \dot{x} &= u\cos\psi - v\sin\psi \\ \dot{y} &= u\sin\psi + v\cos\psi \\ \dot{z} &= w \\ \dot{\psi} &= r \end{aligned} \tag{6}$$
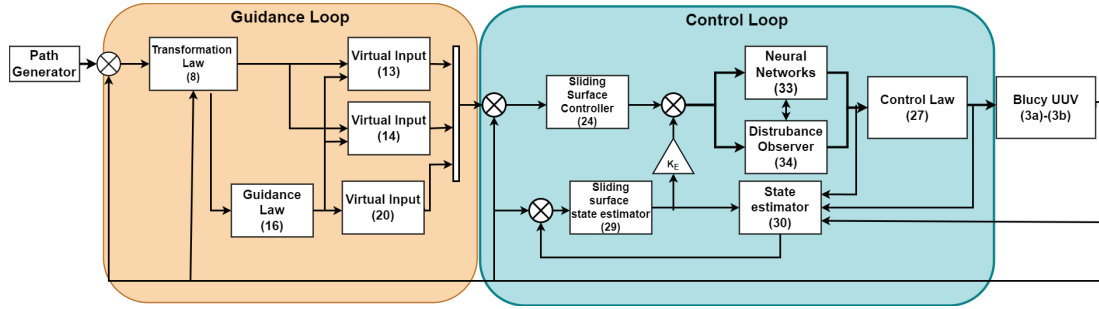
Figure 2: Guidance and control scheme.

and

$$
\begin{aligned}
\dot{u} &= \frac{1}{m_{11}}\left(m_{22}vr - d_{11}u + \tau_u + d_u(t)\right) \\
\dot{v} &= \frac{1}{m_{22}}\left(-m_{11}ur - d_{22}v + d_v(t)\right) \\
\dot{w} &= \frac{1}{m_{33}}\left(-d_{33}w + \tau_w + d_w(t)\right) \\
\dot{r} &= \frac{1}{m_{66}}\left((m_{11} - m_{22})uv - d_{66}r + \tau_r + d_r(t)\right)
\end{aligned}
\tag{7}
$$

Here in, $m_{11} = m - X_{\dot{u}}$, $m_{22} = m - Y_{\dot{v}}$, $m_{33} = m - Z_{\dot{w}}$, $d_{11} = X_u + X_{u|u|}|u|$, $d_{22} = Y_v + Y_{v|v|}|v|$, $d_{33} = Z_w + Z_{w|w|}|w|$, $d_{66} = N_r + N_{r|r|}|r|$. τ_u and τ_w are the forces along x_b and z_b respectively, while τ_r torque about z_b. The terms du, dv, dw, and dr represent the disturbance affecting the systems.

This model does not account for roll and pitch dynamics, as the separation between the CG and the Center of Buoyancy (CB) generates a substantial restoring force that inherently stabilizes roll and pitch oscillations. Moreover, the coupling motion between pitch and heave is also not considered, as they can be effectively decoupled because the depth autopilot is achieved without altering the pitch. Consequently, in practical scenarios where the UUV operates at low speeds, these assumptions hold.

3.1 Guidance

The desired path to track is assumed to be differentiable and described in a path reference frame. The tracking error respective to the inertial reference frame can be expressed in the path reference frame as follows:

$$
\begin{aligned}
x_e &= (x - x_d)cos(\psi_p) + (y - y_d)sin(\psi_p) \\
y_e &= -(x - x_d)sin(\psi_p) + (y - y_d)cos(\psi_p) \\
z_e &= z - z_d
\end{aligned}
\tag{8}
$$

where the terms x_e y_e and z_e are referred to as long tracking, cross tracking, and vertical errors, respectively. ψ_p is the path tangent angle defined as $\psi_p = atan2(\dot{y}_d, \dot{x}_d)$. The task here is to drive the x_e, y_e, and z_e to zero. To do so, take the time derivative of (8) to obtain the following error dynamics:

$$
\begin{aligned}
\dot{x}_e &= -(x - x_d)sin(\psi_p)\dot{\psi}_p + (y - y_d)cos(\psi_p)\dot{\psi}_p + (\dot{x} - \dot{x}_d)cos(\psi_p) + (\dot{y} - \dot{y}_d)sin(\psi_p) \\
\dot{y}_e &= -(x - x_d)cos(\psi_p)\dot{\psi}_p - (y - y_d)sin(\psi_p)\dot{\psi}_p - (\dot{x} - \dot{x}_d)sin(\psi_p) + (\dot{y} - \dot{y}_d)cos(\psi_p) \\
\dot{z}_e &= \dot{z} - \dot{z}_d .
\end{aligned}
\tag{9}
$$

by defining desired horizontal velocity $U_d = \sqrt{\dot{x}_d^2 + \dot{y}_d^2}$, desired vertical velocity $\dot{z}_d = w_d$ and using the kinematic relations (6), we obtain

$$
\begin{aligned}
\dot{x}_e &= y_e\dot{\psi}_p + Ucos(\psi_d - \psi_p) - U_d \\
\dot{y}_e &= -x_e\dot{\psi}_p + Usin(\psi_d - \psi_p) \\
\dot{z}_e &= w - w_d
\end{aligned}
\tag{10}
$$

where $U = \sqrt{u^2 + v^2}$ is the horizontal velocity, ψ_d is the desired yaw angle.

Now, define the following Lyapunov function candidate:

$$
V_1 = \frac{1}{2}x_e^2 + \frac{1}{2}y_e^2 + \frac{1}{2}z_e^2
\tag{11}
$$

and taking the time derivative along the trajectory, one obtains the following equation:

$$
\begin{aligned}
\dot{V}_1 &= x_e\dot{x}_e + y_e\dot{y}_e + z_e\dot{z}_e \\
&= x_e(y_e\dot{\psi}_p + Ucos(\psi_d - \psi_p) - U_d) + y_e(-x_e\dot{\psi}_p + Usin(\psi_d - \psi_p)) + z_e(w - w_d) \\
&= x_e(U_dcos(\psi_d - \psi_p) - U) + y_e(Using(\psi_d - \psi_p)) + z_e(w - w_d)
\end{aligned}
\tag{12}
$$

To this end, design the virtual inputs U_r and w_r as follows:

$$U_r = \frac{U_d}{\cos(\psi_d - \psi_p)} - \gamma_1 x_e \tag{13}$$

$$w_r = w_d - \gamma_2 z_e \tag{14}$$

where the γ_1 and γ_2 are the positive gain parameters. Under the assumption that the virtual inputs are followed, the (12) becomes:

$$\dot{V}_1 = -\gamma_1 x_e^2 + y_e(U\sin(\psi_d - \psi_p)) - \gamma_2 z_e^2 \tag{15}$$

which shows, that long tracking error (x_e) and vertical tracking error (z_e) converge to zero for positive values of γ_1 and γ_2 provided the U and w follow the virtual inputs given in (13) and (14) respectively. What remains to see is the convergence of cross-tracking error (y_e) to zero. If the system is fully actuated, a virtual input of v can be designed to make y_e converge to zero. However, the system considered is underactuated, hence the following look-ahead-based guidance law as in (Breivik and Fossen, 2005) is chosen:

$$\psi_d = \psi_p + arctan(\frac{-y_e}{\Delta}) \tag{16}$$

where the Δ is the look-ahead distance. Smaller Δ means aggressive steering, while larger Δ means slow steering. If the desired ψ_d is perfectly tracked, (15) becomes:

$$\dot{V}_1 = -\gamma_1 x_e^2 - U\frac{y_e^2}{\sqrt{y_e^2 + \Delta^2}} - \gamma_2 z_e^2 \tag{17}$$

for $U > 0$, the term y_e goes to zero. Hence, the overall system is stable according to (Lekkas and Fossen, 2014).

Now, Let us consider the error dynamics of the ψ whose error is defined as $\psi_e = \psi - \psi_d$. Let the Lyapunov candidate with respective to ψ_e defined as follows:

$$V_2 = \frac{1}{2}\psi_e^2 \tag{18}$$

with time derivative as:

$$\dot{V}_2 = \psi_e\dot{\psi}_e = \psi_e(\dot{\psi} - \dot{\psi}_d) = \psi_e(r - \dot{\psi}_d) \tag{19}$$

Similar to position tracking, to guarantee the convergence of the ψ_e to zero, the virtual input r is chosen as follows:

$$r_r = \dot{\psi}_d - \gamma_3\psi_e \tag{20}$$

for a positive γ_3 and if the r follows the given virtual command. then $\dot{V}_2 \leq 0$, thereby, guaranteeing the convergence.

3.2 Control

In light of the above discussion, it is clear that for the tracking error to converge, the virtual inputs should be followed, and hence, they are passed as a reference to the control system. To design a controller, Let us rewrite (7) as follows:

$$\begin{aligned}
\dot{u} &= f_u + \frac{1}{m_{11}}\tau_u + d_1(t) \\
\dot{v} &= f_v + d_2(t) \\
\dot{w} &= f_w + \frac{1}{m_{33}}\tau_w + d_3(t) \\
\dot{r} &= f_r + \frac{1}{m_{66}}\tau_r + d_4(t)
\end{aligned} \tag{21}$$

where

$$\begin{aligned}
f_u &= \frac{1}{m_{11}}(m_{22}vr - d_{11}u) & d_1(t) &= \frac{1}{m_{11}}d_u(t) \\
f_v &= \frac{1}{m_{22}}(-m_{11}ur - d_{22}v) & d_2(t) &= \frac{1}{m_{22}}d_v(t) \\
f_w &= \frac{1}{m_{22}}(-d_{33}w) & d_3(t) &= \frac{1}{m_{66}}d_w(t) \\
f_r &= \frac{1}{m_{66}}((m_{11} - m_{22})uv - d_{66}r) & d_3(t) &= \frac{1}{m_{66}}d_w(t)
\end{aligned} \tag{22}$$

In the above model, The sway velocity is assumed to be passively bounded in the sense that $|v| < v_m$ as it cannot be controlled but only observed, and hence, its dynamics are not considered in the control design. Furthermore, the unknown time-varying environmental disturbances are assumed to be bounded such that there exist $|d| \leq d_n$, where d_n represents an unknown constant. In addition, the system can have uncertainties due to ignored nonlinear dynamics in the synthetic model and the parameters. Therefore, the uncertain state space representation of the above system is given as follows:

$$\dot{X} = f(X) + g(X)\tau + \Delta(X) + d(t) \tag{23}$$

where $X = [u, w, r]^T$, $f(x) = [fu, fw, fr]^T$, $g(x) = [\frac{1}{m_{11}}, \frac{1}{m_{33}}, \frac{1}{m_{66}}]^T$, $\tau = [\tau_u, \tau_w, \tau_r]^T$ and $d = [d_1(t), d_2(t), d_3(t)]^T$. The term $\Delta(x) = \Delta f(x) + \Delta g(x)\tau$ represents uncertainties.

Now, considering X_r as the reference signal to the control loop and by defining the tracking error as $e = X - X_r$, a sliding manifold can be given as follows:

$$S = e + \lambda_1 \int e \, dt \tag{24}$$

where λ_1 is a positive definite matrix. By taking the time derivative of the above equation, one obtains the following equation:

$$\begin{aligned}
\dot{S} &= \dot{e} + \lambda_1 e = \dot{X} - \dot{X}_r + \lambda_1 e \\
&= f(X) + g(X)\tau + \Delta(X) + d - \dot{X}_r + \lambda_1 e
\end{aligned} \tag{25}$$

In this approach, Δ is estimated using a radial basis neural network. Assume that Δ to be approximated as $\hat{\Delta} = \hat{W}\mu(X)$, with $\hat{W}$ representing the updated output weights and μ denoting the relevant basis function matrix. Leveraging the universal approximation capability of NNs, one has:

$$\Delta = W^{*T}\mu(X) + \varepsilon, \tag{26}$$

where W^* and ε denote the optimal weight matrix and the minimal estimation error of the NN, respectively. The estimation error is assumed to be bounded based on the universal property. Essentially, the NN's role is to minimize the total estimation error by iteratively estimating W^* as $\hat{W}$.

To counterbalance the NN's estimation error and accommodate unaccounted time-dependent terms bounded disturbances (d), we introduce an adaptive disturbance observer that aims to estimate $D = d(t) + \varepsilon$ as $\hat{D}$.

To this point, the convergence of the reference tracking can be achieved by choosing the following control law:

$$\tau = g(X)^{-1}(\dot{X}_d - \lambda_1 e - f(X) - \hat{\Delta} - \hat{D} \otimes sign(E_X) - K_1 * S) \tag{27}$$

where $\otimes$ represents the element-wise multiplication and K_1 is the positive definite matrix related to the controller. The term E_x represents the composite error that is used in the updating rules of neural network and disturbance observer. It is termed as a composite error because it consists of both tracking error and error made by the state estimator to enhance the learning process. The expression for the E_X is given as follows:

$$E_x = S - K_E S_0 \tag{28}$$

where K_E is a positive definite matrix, S_0 is the sliding surface of the state estimator.

$$S_0 = e_0 + \lambda_2 \int e_0 \, dt \tag{29}$$

with $e_0 = \hat{X} - X$ is the error made by the estimator and λ_2 is a positive definite matrix.

Hence, the state estimator can be designed as follows:

$$\dot{\hat{x}} = f(X) + g(X) * u + \hat{\Delta} + \hat{D} \otimes sign(E_x) - K_0 S_0 - \lambda_2 e_0 \tag{30}$$

where the K_0 is the positive definite matrix characterising the gain of the state estimator.

To study the closed loop stability of the controller, let us consider the following Lyapunov candidate:

$$V_3 = \frac{1}{2}S^T S + \frac{1}{2}S_0^T K_E S_0 + \frac{1}{2}tr(\tilde{W}^T \Gamma^{-1} \tilde{W}) + \frac{1}{2}(\tilde{D}^T K_D^{-1} \tilde{D}) \tag{31}$$

where $\tilde{W} = \hat{W} - W^*$ and $\tilde{D} = \hat{D} - D$. Taking the time derivative, following expression is obtained:

$$\begin{aligned}
\dot{V}_3 &= S^T \dot{S} + S_0^T K_E \dot{S}_0 + tr(\tilde{W}^T \Gamma^{-1} \dot{\hat{W}}) + \tilde{D}^T K_D^{-1} \dot{\hat{D}} \\
&= S^T(-K_1 S - \tilde{W}^T \mu(X) + D - \hat{D} \otimes sign(E_X) \\
&\quad + S_0^T K_E(-K_0 S_0 + \tilde{W}^T \mu(X) - D + \hat{D} \otimes sign(E_X)) + tr(\tilde{W}^T \Gamma^{-1} \dot{\hat{W}}) + \tilde{D}^T K_D^{-1} \dot{\hat{D}} \\
&= -S^T K_1 S - S_0^T K_E K_0 S - \tilde{W}\mu(X)E_X^T - \tilde{D}^T |E_x| + tr(\tilde{W}^T \Gamma^{-1} \dot{\hat{W}}) + \tilde{D}^T K_D^{-1} \dot{\hat{D}}
\end{aligned} \tag{32}$$
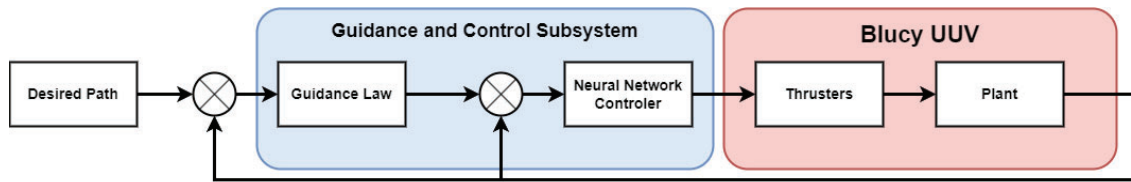
Figure 3: Architecture of the simulator.
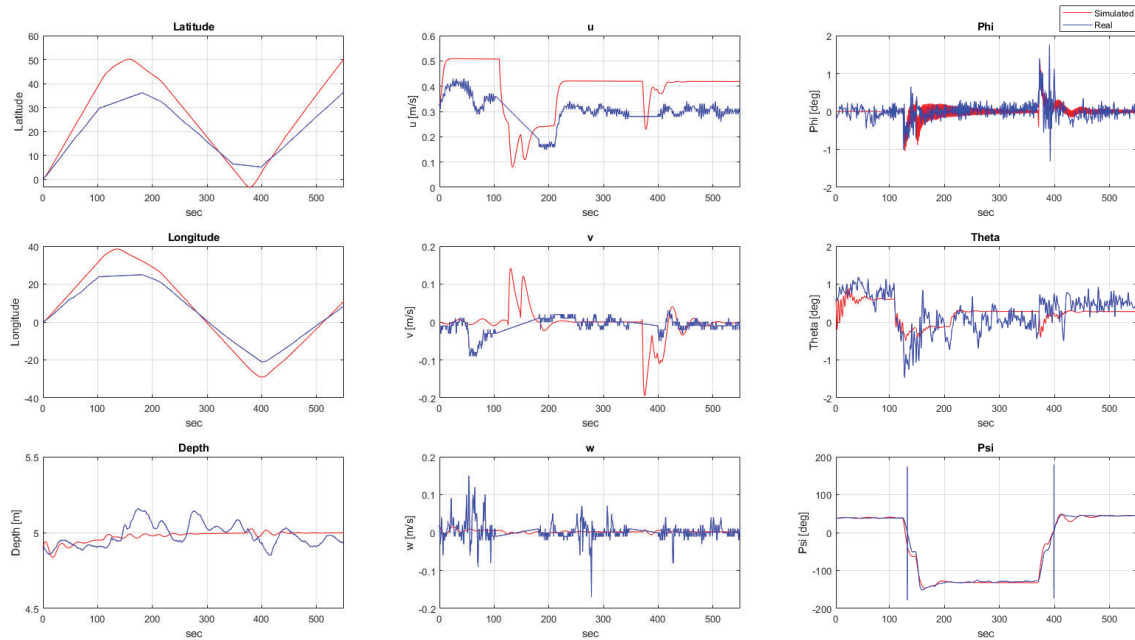
Figure 4: Validation of the simulator vs real data

Now, by choosing the following updating rules of the neural network and disturbance observer:

$$\dot{\hat{W}} = \Gamma \mu(X) E_X^T \tag{33}$$

$$\dot{\hat{D}} = K_D |E_x| \tag{34}$$

and substituting (33) and (34) in (32), one has:

$$\dot{V}_3 = -S^T K_1 S - S^T K_E K_0 S \tag{35}$$

hence, the stability of the control loop is guaranteed.

The overall closed-loop configuration of the guidance and control system adeptly ensures asymptotic stability, thereby ensuring that the vehicle follows the desired path. Although the proof is omitted here for brevity, leveraging cascade system theory and integrating neural network alongside disturbance observer into the design provides the means to establish the asymptotic stability of the overall closed-loop system (Lekkas and Fossen, 2014). Furthermore, a linear control allocation is used to map the required surge, heave forces, and yaw moment to the required rpm of the motors.

4 Simulation experiments

In this section, the reliability of the designed control scheme is tested by simulating real-life operational maneuvers through a high-fidelity simulator of Blucy implemented in Matlab/Simulink whose architecture is depicted in Figure 3. The vehicle simulator is developed from the nonlinear motion of equations (3) whose parameters are given in Tables.1 and 2.

The simulator is validated against the data acquired during previous missions of the Interreg IT-HR Techera project (Interreg, 2022). In particular, the data was recorded during a multibeam survey in the Marine Protected Area of Miramare in Trieste, Italy. The results are depicted in the Figure 4.

Blucy		Actuator	
Dry mass m	216.15 kg	propeller type	Ka 4-70 with 19A Duct
Wet mass m	216.45 kg	number of thrusters	6
I_x	11.3114 kgm^2	number of blades	4
I_y	49.2791 kgm^2	diameter D	0.145 m
I_z	41.7449 kgm^2	Pitch ratio P/D	1.28
I_{xy}	0 kgm^2	Area ratio A_e/A_o	0.7
I_{xz}	2.8636 kgm^2	Motor rpm range	$(-3000, 3000)rpm$
I_{yz}	0 kgm^2	Gear ratio	$4:1$
Center of Gravity CG	$(0,0,0)\ m$	Prop rpm range	$(-750, 750)rpm$
Center of Buoyancy CB	$(0,0,0.06)\ m$	**Propulsive**	M1, M2
Hydrodynamic Coefficients		$C_t(J)$	$-0.27J^3 + 0.33J^2 - 0.55J + 0.54$
Linear [Kg/s]	**Quadratic [Kg/m]**	$C_q(J)$	$-0.02J^3 - 0.02J^2 - 0.004J + 0.08$
$X_u = -2.61$	$X_{u|u|} = -61.82$	**Maneuver**	M3, M4, M5, M6
$Y_v = -24.72$	$Y_{v|v|} = -597.62$	$C_t(J)$	$-0.25J^3 + 0.31J^2 - 0.52J + 0.50$
$K_v = 0.83$	$K_{v|v|} = -30.05$	$C_q(J)$	$-0.02J^3 - 0.02J^2 - 0.004J + 0.08$
$N_v = -11.21$	$N_{v|v|} = -85.4$	**Position** w.r.t. CG	$l_i\ [m]$
$Z_w = -2.82$	$Z_{w|w|} = -255.86$	M1	[-0.821 0.230 -0.008]
$M_w = -1.71$	$M_{w|w|} = -38.7$	M2	[-0.821 -0.230 -0.008]
$Y_p = -1.43$	$Y_{p|p|} = -38.14$	M3	[0.615 0 -0.386]
$K_p = -0.04$	$K_{p|p|} = -23.68$	M4	[-0.835 0 -0.386]
$N_p = 0.41$	$N_{p|p|} = 9.28$	M5	[0.490 -0.113 -0.131]
$Z_q = -0.07$	$Z_{q|q|} = -37.19$	M6	[-0.660 0.124 -0.131]
$M_q = -0.06$	$M_{q|q|} = -95.69$	**Thrust versor**	e_i
$Y_r = -1.87$	$Y_{r|r|} = -342.98$	M1	[1 0 0]
$K_r = 0.14$	$K_{r|r|} = 41.28$	M2	[1 0 0]
$N_r = -0.044$	$N_{r|r|} = -375.53$	M3	[0 0 1]
Added Mass		M4	[0 0 1]
$X_{\dot{u}}$	$-28.94\ kg$	M5	[0 1 0]
$Y_{\dot{v}}$	$-166.03\ kg$	M6	[0 1 0]
$Z_{\dot{w}}$	$-94.13\ kg$		
$K_{\dot{p}}$	$-0.07\ kgm^2$		
$M_{\dot{q}}$	$-17.10\ kgm^2$		
$N_{\dot{r}}$	$-33.58\ kgm^2$		

Table 1: Blucy UUV and actuator parameters

Guidance		Controller	
γ_1	0.035	λ_1	$diag(0.1, 0.2, 0.1)$
γ_2	0.085	λ_2	$diag(2, 2, 2)$
γ_3	0.85	K_1	$diag(300, 500, 500)$
Δ	5 m	K_0	$diag(5, 5, 5)$
		Γ	$diag(10, 10, 10)$
		K_D	$diag(5, 5, 5)$
		K_E	$diag(3, 3, 3)$

Table 2: Guidance and controller parameters

The linear velocities (u, v, w) and latitude and longitude measurements are not recorded during a turn because, in multibeam surveys, data gathered during turns are not reliable for 3D reconstruction as they are distorted and act as a disturbance for the post-processing analysis. From Figure 4, it is clear that the simulated trajectory follows the actual data, except for the u velocity, because the data is also affected by the presence of the tether, which produces
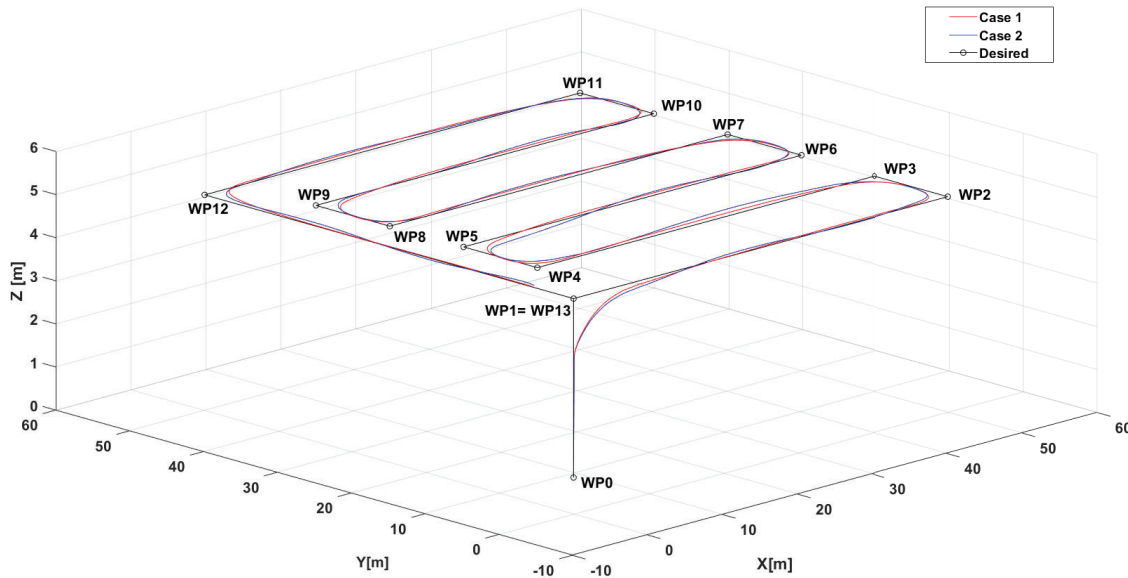
Figure 5: Simulated path of a multibeam survey: Desired path (black); Case 1 (red); Case 2 (blue).

additional drag forces that the vehicle should overcome. Although nothing can be said for data during the turn, comparing the position and ψ data, one can conclude that the simulator is still valid and can be used to design and test the new guidance and control schemes.

4.1 Operational scenario

The path used for the simulation emulates a typical operational path of underwater missions such as multibeam surveys. As shown in Figure (5), the path includes 15 waypoints (WP). The mission sequence starts with Blucy diving to $5m$ depth from WP0 to WP1. Then, the vehicle proceeds to navigate the rest of the waypoints (WP1-WP13), maintaining a constant depth. The length along the x and y directions is strategically chosen to have a good overlap of data for 3D reconstruction during a multibeam survey. The simulation accurately reflects the procedure and conditions typically encountered in a real-world mission.

Two case studies are presented in this paper: Case 1, will validate the control scheme designed using the synthetic model against the 6 DOF model to check the performance against the coupled dynamics neglected in the simplified model. Case 2, is a simulation with external disturbance of form $0.05sin(0.1t)$ and $sin(0.1t)$ are applied to translational and rotational motions, respectively. Moreover, random uncertainties of $\pm 5\%$ on Blucy parameters (Table (1)) are considered to test the robustness against disturbances and uncertainties.

4.2 Results

The 3D trajectory tracking of the two cases is depicted in Figure 5, while linear velocities, angular velocities, and attitude angles are illustrated in Figure 6. The sway velocity v (see Figure 6) is well-bounded, ensuring the assumption made in Section 3.2. Furthermore, ϕ and θ are also stable due to the restoring forces as predicted. Analysis of Figure 8 reveals that the implemented controller adeptly tracks the virtual commands u_r, w_r, and r_r with a steady state error magnitude of 10^{-3}. However, in case 2, this error magnitude rises to 10^{-2} because of the oscillations, but are well-bounded. The ψ tracks the desired command at an order of 10^{-2} and increases to the order of 10^{-1}, acting as the guiding command for the vehicle along the intended path trajectory.

The effectiveness of the designed guidance loop is evident from Figure 5, which showcases the Blucy's adherence to the desired trajectory with an error magnitude of 2 during the turning as the UUV is not capable of making sharp turns. However, the error reduces to the magnitude of 10^{-1} in the straight line paths. These magnitudes increase by an order of one in the presence of disturbance and uncertainties. These results are consistent with the general requirement of a multibeam survey mission.

Additionally, the required rpm commands are outlined in Figure 7. Initially, there is chattering (that is not depicted in the figure), an inherited problem of sliding mode control due to the discontinuity of the 'sign' function. Different approaches are proposed in the literature to tackle this problem (Gambhire et al., 2021). Nevertheless, the easiest way is to replace the sign function with a hyperbolic tangent function that smooths the chattering. Hence, in Figure 7, commands are smoother. But, in case 2, they are oscillatory because of the workload on the controller due to the disturbances and uncertainties, and these oscillations are perfectly manageable by the actuators.
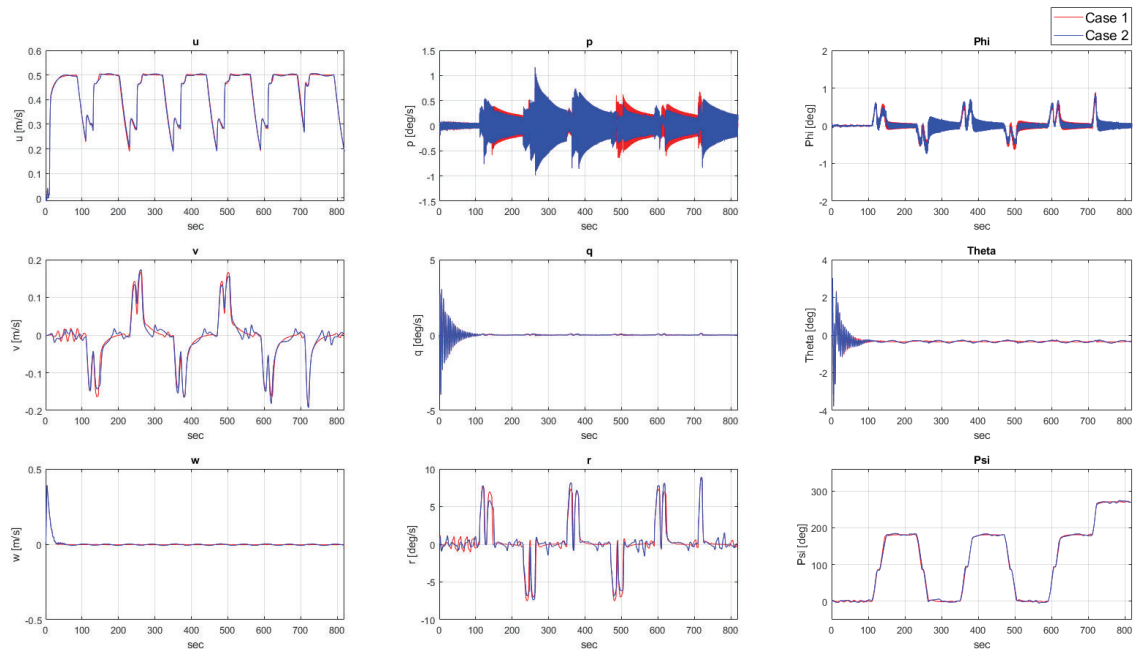
Figure 6: State variables: Case 1 (red); Case 2 (blue).
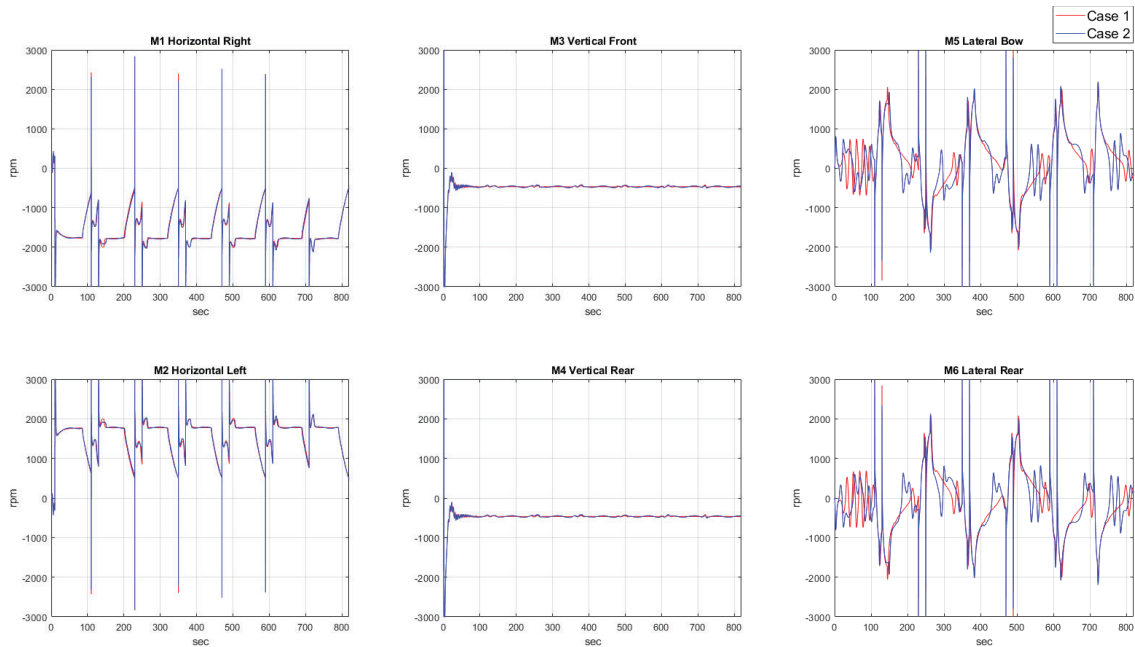
Figure 7: Thrusters rpm: Case 1 (red); Case 2 (blue).

Furthermore, the vector norms of the neural network weights in Figure 9 show that they are bounded, indicating the convergence of the neural networks. This success is due to the proposed composite learning-based neural networks, combined with a disturbance observer and state estimator. As demonstrated in Figure 10, this approach effectively estimates and compensates for complex model terms and system dynamics changes caused by various uncertainties, highlighting the robustness of the proposed methodology.

5   Conclusions

Starting from a synthetic model, A neuro-adaptive sliding mode control based on composite learning was proposed for Blucy UUV. The neural network, in conjunction with the disturbance observer and state estimator,
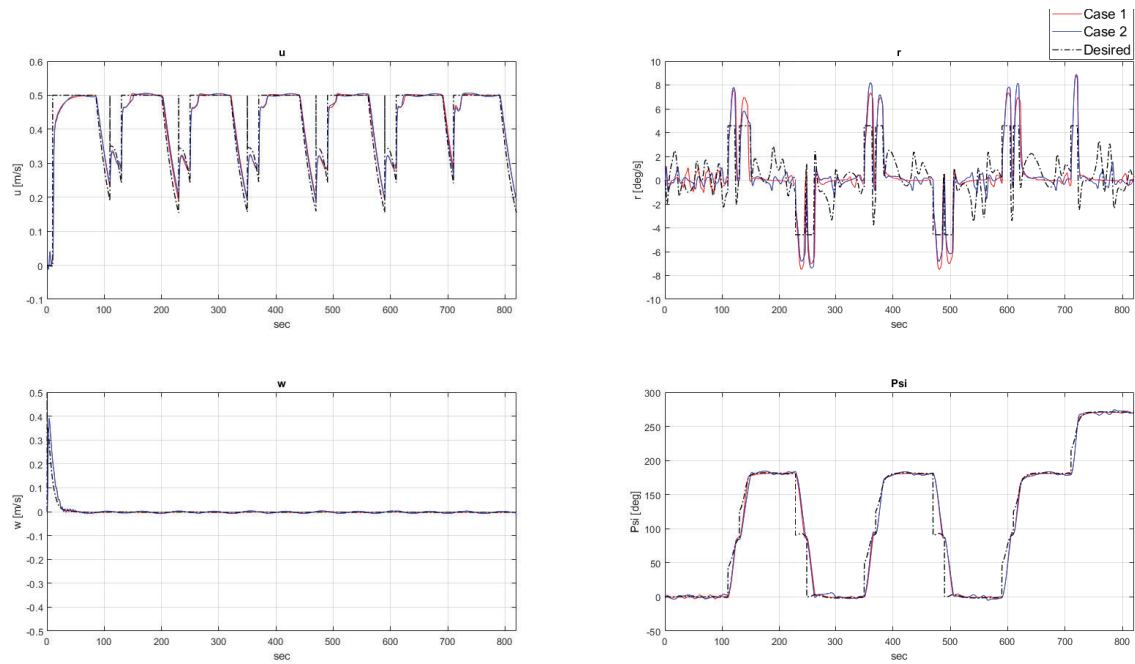
Figure 8: Controlled states (u, w, r, ψ): Case 1 (red); Case 2 (blue); Desired (black).

is trained to estimate the uncertainties and disturbances. The estimation error of the state observers is added to the learning rule of the neural network (such a learning process is called composite learning) to have a resilient and adaptive control system. Furthermore, to solve the underactuated problem, a line-of-sight guidance based on look-ahead distance is proposed. The effectiveness of the proposed guidance and control method in tracking a path of a real operational scenario was demonstrated successfully through simulations using a high-fidelity simulator of Blucy in the presence of uncertainties and disturbances. The chattering of the sliding mode control action is addressed by replacing the sign function with a hyperbolic tangent function. Notably, the composite learning process eliminates the need for prior knowledge of uncertainties and disturbances, obviating the necessity for high learning rates typical of neuro-adaptive schemes. The article's novelty lies in the design of a composite learning-based, neural adaptive sliding mode control system tailored for Blucy UUV.

Future work will focus on enhancing the robustness and adaptability of the control system in real-world operational scenarios. It includes optimising the parameters of the neural network and disturbance observer for better prediction and compensation of dynamic environmental disturbances. Additionally, efforts will be made to implement and test the proposed control strategies on the physical system to validate simulation results.

References

Antonelli, G., Caccavale, F., Chiaverini, S., Fusco, G., 2003. A novel adaptive control law for underwater vehicles. IEEE Transactions on control systems technology 11, 221–232.

Ashrafiuon, H., Muske, K.R., McNinch, L.C., 2010. Review of nonlinear tracking and setpoint control approaches for autonomous underactuated marine vehicles, in: Proceedings of the 2010 American control conference, IEEE. pp. 5203–5211.

Breivik, M., Fossen, T.I., 2005. Principles of guidance-based path following in 2d and 3d, in: Proceedings of the 44th IEEE Conference on Decision and Control, IEEE. pp. 627–634.

Duan, K., Fong, S., Chen, C.P., 2020. Fuzzy observer-based tracking control of an underactuated underwater vehicle with linear velocity estimation. IET Control Theory & Applications 14, 584–593.

Er, M.J., Gong, H., Liu, Y., Liu, T., 2023. Intelligent trajectory tracking and formation control of underactuated autonomous underwater vehicles: A critical review. IEEE Transactions on Systems, Man, and Cybernetics: Systems .

Fossen, T.I., 2011. Handbook of marine craft hydrodynamics and motion control. John Wiley & Sons.

Gambhire, S., Kishore, D.R., Londhe, P., Pawar, S., 2021. Review of sliding mode based control techniques for control system applications. International Journal of dynamics and control 9, 363–378.

Guerrero, J., Torres, J., Creuze, V., Chemori, A., 2019. Observation-based nonlinear proportional–derivative
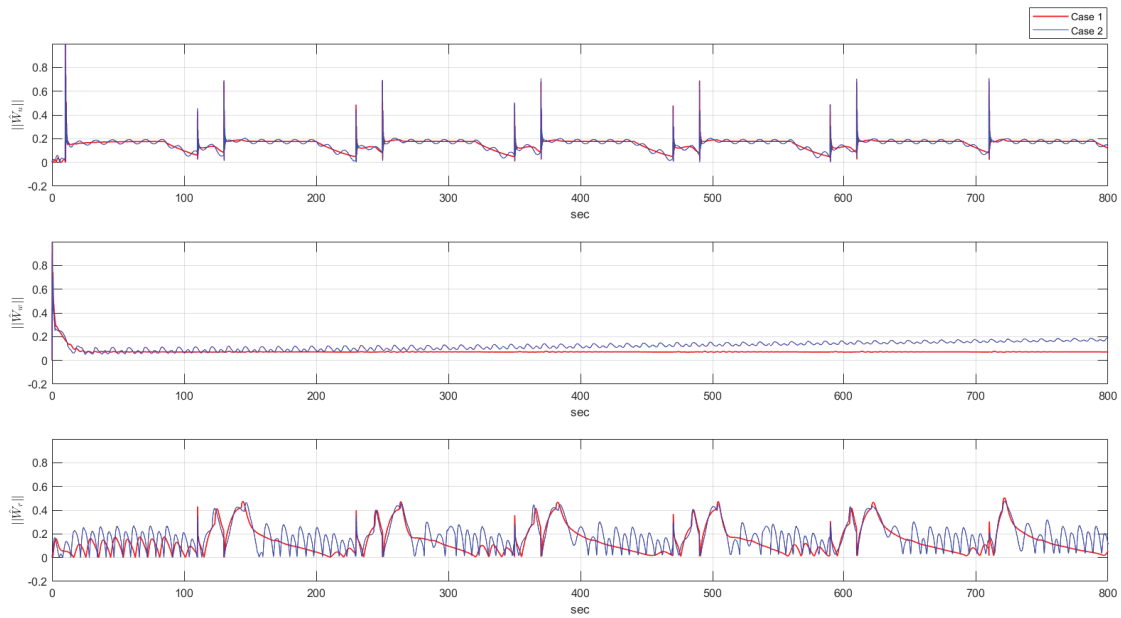
Figure 9: Vector norm of the weights of the NN.
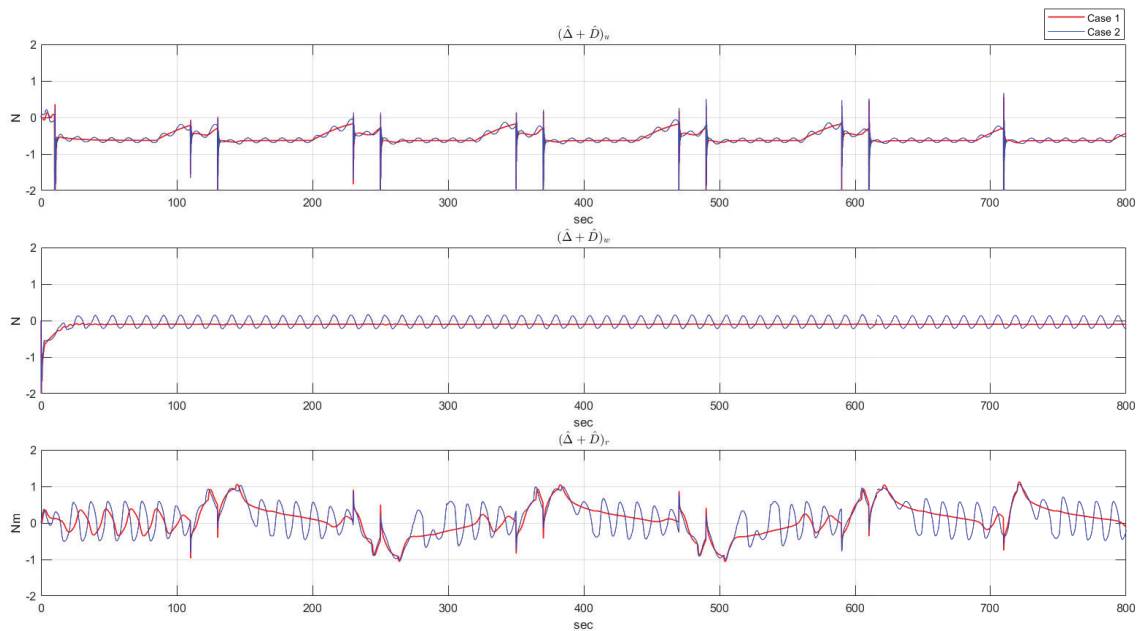
Figure 10: Uncertainties and disturbance estimated by the NN and disturbance observer combined.

control for robust trajectory tracking for autonomous underwater vehicles. IEEE journal of oceanic engineering 45, 1190–1202.

Heshmati-Alamdari, S., Eqtami, A., Karras, G.C., Dimarogonas, D.V., Kyriakopoulos, K.J., 2014. A self-triggered visual servoing model predictive control scheme for under-actuated underwater robotic vehicles, in: 2014 IEEE International Conference on Robotics and Automation (ICRA), IEEE. pp. 3826–3831.

Heshmati-Alamdari, S., Nikou, A., Dimarogonas, D.V., 2020. Robust trajectory tracking control for underactuated autonomous underwater vehicles in uncertain environments. IEEE Transactions on Automation Science and Engineering 18, 1288–1301.

Interreg, 2019. Sushi drop sustainable fisheries with drones data processing. https://www.italy-croatia.eu/web/sushidrop.

Interreg, 2022. Techera: A new technology era in the adriatic sea – big data sharing and analytics for a circular sea

economy. `https://programming14-20.italy-croatia.eu/web/techera`.

Joe, H., Kim, M., Yu, S.c., 2014. Second-order sliding-mode controller for autonomous underwater vehicle in the presence of unknown disturbances. Nonlinear Dynamics 78, 183–196.

Kuiper, G., 1992. The wageningen propeller series. MARIN Publication 91-001'Published on the occasion of its 60th anniversary, MARIN Wageningen, The Netherlands .

Lambertini, A., Menghini, M., Cimini, J., Odetti, A., Bruzzone, G., Bibuli, M., Mandanici, E., Vittuari, L., Castaldi, P., Caccia, M., et al., 2022. Underwater drone architecture for marine digital twin: Lessons learned from sushi drop project. Sensors 22, 744.

Lekkas, A.M., Fossen, T.I., 2014. Integral los path following for curved paths based on a monotone cubic hermite spline parametrization. IEEE Transactions on Control Systems Technology 22, 2287–2301.

Liu, J., Du, J., 2021. Composite learning tracking control for underactuated autonomous underwater vehicle with unknown dynamics and disturbances in three-dimension space. Applied Ocean Research 112, 102686.

Makavita, C.D., Nguyen, H.D., Ranmuthugala, D., Jayasinghe, S.G., 2015. Composite model reference adaptive control for an unmanned underwater vehicle. Underwater Technology 33, 81–93.

Wang, Y., Yan, W., Gao, B., Cui, R., 2009. Backstepping-based path following control of an underactuated autonomous underwater vehicle, in: 2009 International conference on information and automation, IEEE. pp. 466–471.

Zhou, J., Zhao, X., Chen, T., Yan, Z., Yang, Z., 2019. Trajectory tracking control of an underactuated auv based on backstepping sliding mode with state prediction. IEEE Access 7, 181983–181993.

Towards Design of an Autonomous Navigation Framework for Unmanned Surface Vessels using Marine Robotics Unity Simulator

Mohammed Shahid Umar Sanghar [a], Temilolorun Aiyelari[a], Fuat Kara [a], Yogang Singh [a*]

[a]*Department of Engineering and Mathematics, Sheffield Hallam University, Sheffield, S1 1WB, United Kingdom*
[*]Corresponding author. Email: y.singh@shu.ac.uk

Synopsis

The rising importance of Unmanned Surface Vessels (USVs) in diverse maritime contexts, such as coastal monitoring and oceanographic applications, underscores the necessity for a robust simulation environment framework. This need arises from the limited availability of sea trials and demands a high-quality simulation setup to test USV autonomy across multiple scenarios with enhanced visual fidelity. This paper describes an autonomous navigation framework for USV in a MArine Robotics Unity Simulator (MARUS), a high-fidelity simulation environment based on Unity3D to close the gap. Our approach works on coupling the MARUS simulator offering water physics and a wide array of sensors commonly used in the maritime domain with a Robot Operating System (ROS) to facilitate remotely controlled USV behaviour and motion for different navigation scenarios to assess the vessel's maneuverability and overall performance characteristics.

Keywords: Unmanned Surface Vehicle, Robot Operating System, Marine Robotics Unity Simulator, Autonomous Navigation, Unity3D

1 Introduction

Simulations, utilizing physical equations and computer algorithms, offer a means to analytically solve complex real-world problems safely and efficiently. These simulations speed up the engineering design cycle, cut costs, ensure safe and controlled testing conditions, produce extensive training data for machine learning, aid in developing intelligent robots, and allow for the supervision of real robots via digital twins.

In the marine environment, the advantages of using simulators for developing vehicle control algorithms are even more pronounced due to the high costs associated with testing vehicles at sea. The complexity and logistical challenges of conducting trials at sea necessitate high-quality simulation tools. Existing simulators, however, often fall short in providing the necessary visual fidelity and support for human-robot interaction. Gazebo, one of the most widely used general-purpose robotics simulators, offers various perception sensors through modular plugins (Koenig and Howard, 2004). Despite its extensive use in the robotics community, Gazebo lacks the realistic visual data support required for underwater and surface robotics applications (DeMarco et al., 2015). This gap is significant as the current trend in computer vision research emphasizes the need for visually realistic simulation environments.

Among the specialized simulators for marine robots, the UUV (Unmanned Underwater Vehicle) Simulator and UWSim (UnderWater Simulator) are notable (Cook et al., 2014). The UUV Simulator, integrated with the ROS framework, provides robust models for underwater vehicle dynamics and sensor simulation. However, it has not been actively maintained, resulting in numerous unresolved issues. Similarly, UWSim, while offering underwater simulation capabilities, does not fully meet the needs for high-fidelity visual data. Recently, several marine simulators like NetMarSyS (Garg et al., 2020), Simu2VITA (de Cerqueira Gava et al., 2022), VR-based simulator (Xu et al., 2021) along with a few simulation environments based on Unity3D (Katara et al., 2019; Osa and Orukpe, 2021; Szleg et al., 2022) have been proposed by research groups worldwide. However, these simulations have certain limitations, such as insufficient documentation, lack of maintenance activity, limited access to a comprehensive asset store with easy-to-interface plugins, and the absence of cross-platform deployment capabilities.

With an emphasis on such requirements in mind, this study adopts MARUS, an open-source marine simulator developed by Laboratory for Underwater Systems and Technologies (Lončar et al., 2022) based on modular

---

software framework - ROS and a cross-platform real-time game engine - Unity3D to perform the virtual captive model tests, namely the Turning Circle test on a USV platform validated by experiments. MARUS provides a set of significant features important for such testing such as accurate lighting simulation, simplicity of creating surrounding scenery, and ocean simulation with dynamic fluid-structure interaction. The current work extends the existing capabilities of MARUS by developing a new captive test module and a new control module to perform Turning Circle tests in the MARUS simulation environment validated by experiments. The paper is organized as follows: Section 2 outlines the specifications of the captive model test and discusses the performance metrics used to evaluate the USV. Section 3 elaborates on the MARUS architecture and presents simulation results for the captive tests conducted on the USV, which are detailed in Section 4. The manuscript concludes with a discussion of the results and potential future developments for the simulation framework.

2   Captive Model Tests

International Maritime Organisation (IMO) standards for captive model tests serve as a crucial step in validating the performance of marine vehicles to make a controlled assessment of their seakeeping and maneuvering capabilities (Kim et al., 1996). Captive model tests offer a cost-effective and practical means of identifying potential issues before full-scale deployment of USV, thereby saving time and resources while enhancing the overall reliability and efficiency of the USV. There are various methods for performing captive model tests, including Computational Fluid Dynamics (CFD), Planar Motion Mechanism (PMM) tests, and open-water free-running tests, to evaluate the maneuvering capabilities of USVs in different operating environments (BAKAR, 2015). In the current study, the maneuvering capabilities of the USV are assessed by a known captive model test, namely, the Turning Circle test through a set of open-water free-running tests conducted in the simulation environment of MARUS. The Turning Circle test evaluates the ship's ability to turn within a specific radius, responsiveness and stability during course changes ensuring that the vessel meets performance metrics as shown in Figure 1.

2.1   Performance Metrics

The virtual Turning Circle test are performed in the current study on the simulation environment of MARUS to determine the following performance metrics:

- Tactical diameter

- Advance

- Transfer

- Turning Radius

- Time to change heading 90° and 180°

2.2   IMO Criteria for Virtual Free Running Tests

To perform the virtual free-running maneuvering experiments in the open water simulation environment of MARUS, International Maritime Organisation (IMO) Resolution A.751 stating interim standards for ship maneuverability(Kim et al., 1996; BAKAR, 2015) was adopted with suggested modifications for differential drive propulsion vessels as follows:

1. The approach speed should be 90% of the vessel speed corresponding to 85% of the maximum engine output.

2. Before executing the maneuver, the vessel must maintain a steady course at a constant setting for a minimum of 10 seconds.

To test the performance of the USV in the simulated environment, the USV maneuverability in terms of turning circle parameters was compared against the experimental values from the test conducted in the (Aiyelari Temilolorun, 2024) whose details are explained in the separate manuscript presented in this conference.

3   MARUS Architecture and Capabilities

3.1   MARUS Architecture

The advanced simulation framework of MARUS uses gRPC networking technology, an open-source remote procedure call (RPC) framework that uses HTTP/2 for transport, Protocol Buffers as the interface description language, and provides features such as authentication, load balancing, and more, for bi-directional communication between Unity3D and ROS system. The cross-platform compatibility of Protocol Buffers has been utilised in the
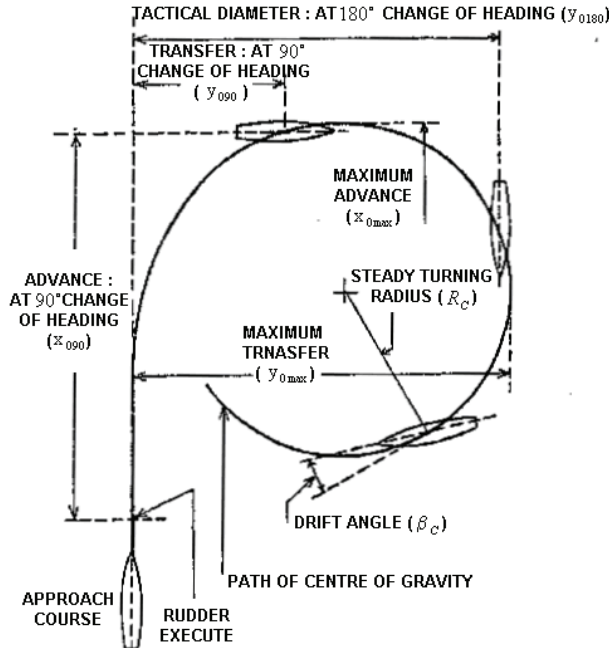
Figure 1: Schematic of Turning Circle Test with performance metrics

current work to define services and messages, due to its language-neutral, platform-neutral, extensible mechanism for serializing structured data. MARUS leverages Unity's powerful real-time 3D rendering capabilities and physics engine to create realistic marine environments through the uncoupled incorporation of water physics (buoyancy, currents, waves, etc.), sensors, robotic tools and actuators into the application backend of controllers and situational awareness. MARUS architecture with ROS backend is shown in Figure 2 where MARUS receives inputs for actuators, mission control variables, and simulation environment requests from ROS. The current study enhances the MARUS architecture by integrating a captive test module, which includes the Turning Circle behaviours, into the MARUS environment. Additionally, it incorporates a path-following control script to execute these tests, as depicted in red in Figure 2.
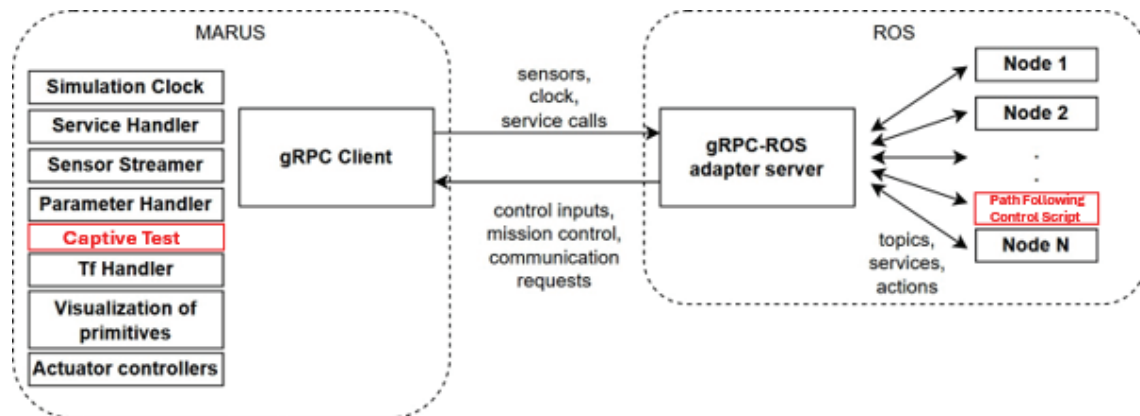
Figure 2: MARUS architecture with ROS backend (Modified from Lončar et al. (2022)) with red elements showing the new incorporated modules

3.2 MARUS Capabilities

MARUS uses Unity, a game engine for creating robotic test scenes due to its widespread popularity for offering rendering, lighting and physics solutions in 3D virtual environments. In addition to that, several virtual sensors have been integrated for the simulation of marine robots such as IMU, GNSS, Camera, 3D Lidar, Sonar and several

others required for performing critical virtual simulations. Additionally, for USV actuation, multiple controllers namely, Keyboard controller, Velocity PID controller, Go To Point controller, Open Loop controller and Thruster have been developed. The vessel's physics are approximated, considering buoyancy and hydrodynamic forces in the virtual 3D scene set up in the ocean environment as shown in Figure 3 where virtual Turning Circle tests are performed.
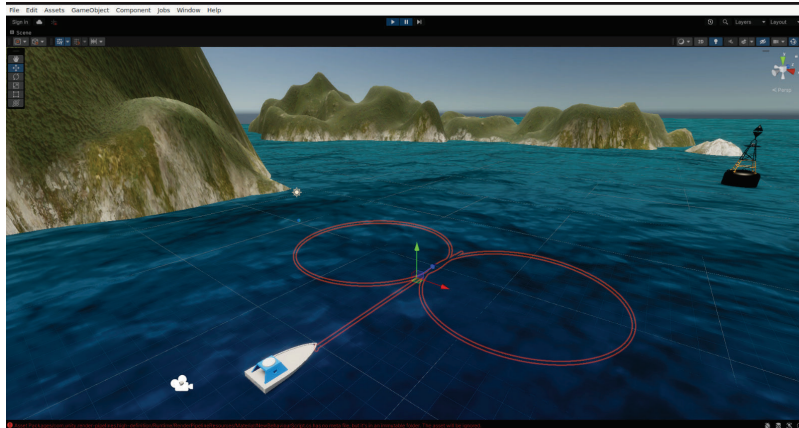
Figure 3: MARUS 3D simulation environment developed using Unity showing turning circle path in red for port and starboard side

In this study, we used Ubuntu 20.04 for running Unity3D and ROS simulations, benefiting from the stability and compatibility of the operating system. The computational demands primarily arise from Unity3D's real-time rendering and physics simulations, which require a multi-core processor, at least 16 GB of RAM, and a dedicated GPU (e.g., Nvidia GTX 960 or higher). ROS handles communication between nodes and real-time sensor data, scaling efficiently across multiple cores. The system is scalable, with ROS distributing workloads and Unity3D offering optimization options to manage graphical and physics performance. For this experiment, we utilized Ubuntu 20.04 running on a system equipped with an Nvidia GTX 960M GPU, 16GB of RAM, and 500GB of storage. Ubuntu 20.04 was chosen for its stability and compatibility, as it is the last release to officially support both ROS1 and ROS2, which are essential for setting up the docker installation of MARUS. This configuration ensured smooth integration of both ROS versions, which was a critical requirement for the simulation environment.

3.3 Thruster Controller

The MARUS architecture has several in-built controllers for the USV actuation as follows:

- Keyboard controller- keyboard-based speed generator.

- Velocity PID controller - uses position reference to generate PID parameters for velocity control.

- Go To Point controller - drives USV to a given reference point using primitive control.

- Open Loop controller - time-dependent control input.

- Thruster controller- generates force based on the datasheet available in ROS or MARUS.

The current study adopts the Thruster controller due to its ability to generate force as required for the differential drive propulsion to execute the IMO criteria for free-running turning circle tests stated in section 2.2. The current study adopts the datasheet of the T200-V16 thruster installed on the USV in the simulation framework with a maximum forward thrust of 14.65kgf and a maximum reverse thrust of 11.65kgf being utilised. This also aligns closely with the experimental set-up to validate the simulation results. This datasheet can be accessed from the docker using *Assets > marus-core > Datasheets > T200*. The schematic of the arrangements of the thrusters on the USV in the current simulation framework is shown in Figure 4.

4 Simulation Results

In the current study, the virtual turning circle test was conducted in a simulation framework for both the port and starboard sides by controlling the USV's thrusters, and the USV's path was recorded using a virtual Inertial Measurement Unit (IMU) embedded within the MARUS framework. The starboard results were validated against
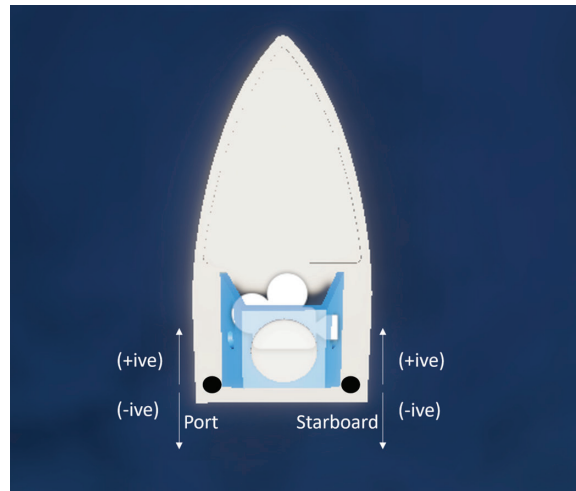
Figure 4: Schematic of the arrangement of thrusters on the USV in the current simulation framework. The positive and negative labels on the port and starboard side represent the directions of the forward and reverse thrust for the USV actuation.

the experimental results from the test conducted in the Aiyelari Temilolorun (2024). Figure 5 presents the simulation results for the port and starboard sides during the virtual Turning Circle test, alongside a comparison with the experimental results for the starboard side. Table 1 presents the performance metrics for both the port and starboard sides during the virtual Turning Circle test and the experimental results for comparison.
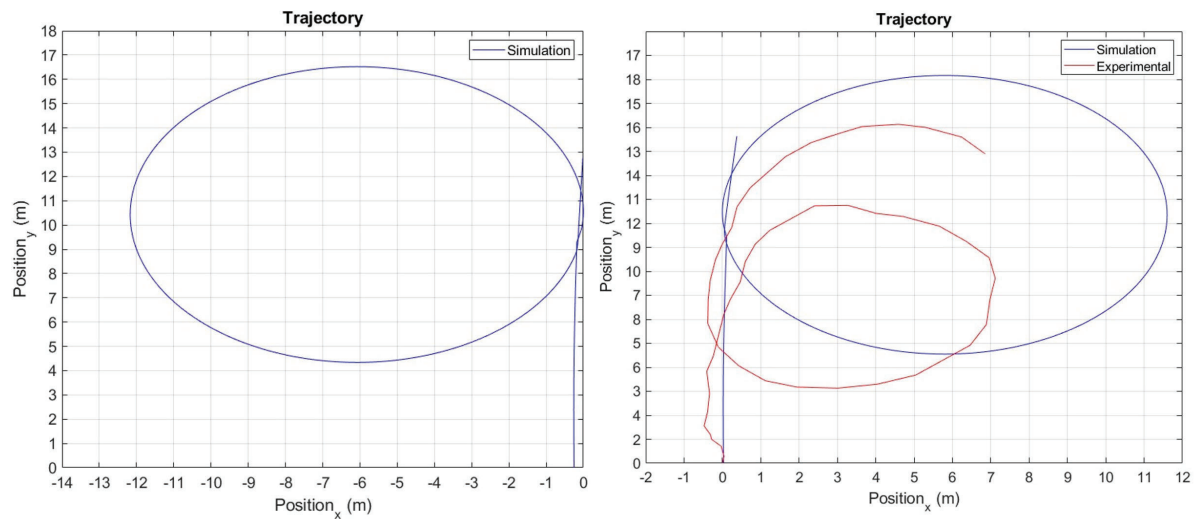
Figure 5: Simulation Turning Circle test for the port (left image) and starboard side (right image)

Parameters	Simulation(Port)	Simulation(Starboard)	Experimental(Starboard)
Advance	7.15 m	7.1 m	8.42 m
Transfer	6.11 m	5.9 m	3.8 m
Tactical Diameter	12.2 m	11.3 m	7.07 m
Time to change heading 90°	62.5 s	60.5 s	45 s
Time to change heading 180°	85 s	79 s	56 s

Table 1: Comparison of performance metrics for the virtual Turning Circle test and experimental results
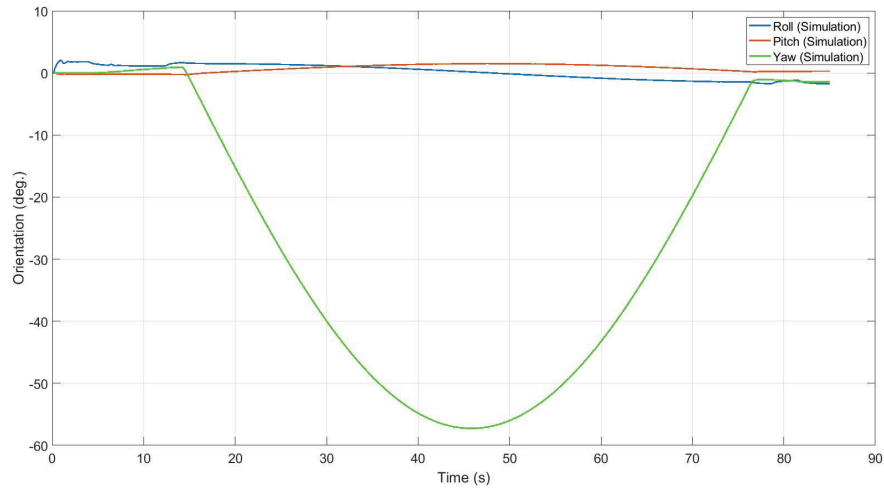
Figure 6: 3D orientation of the vessel in virtual Turning Circle test for the port side
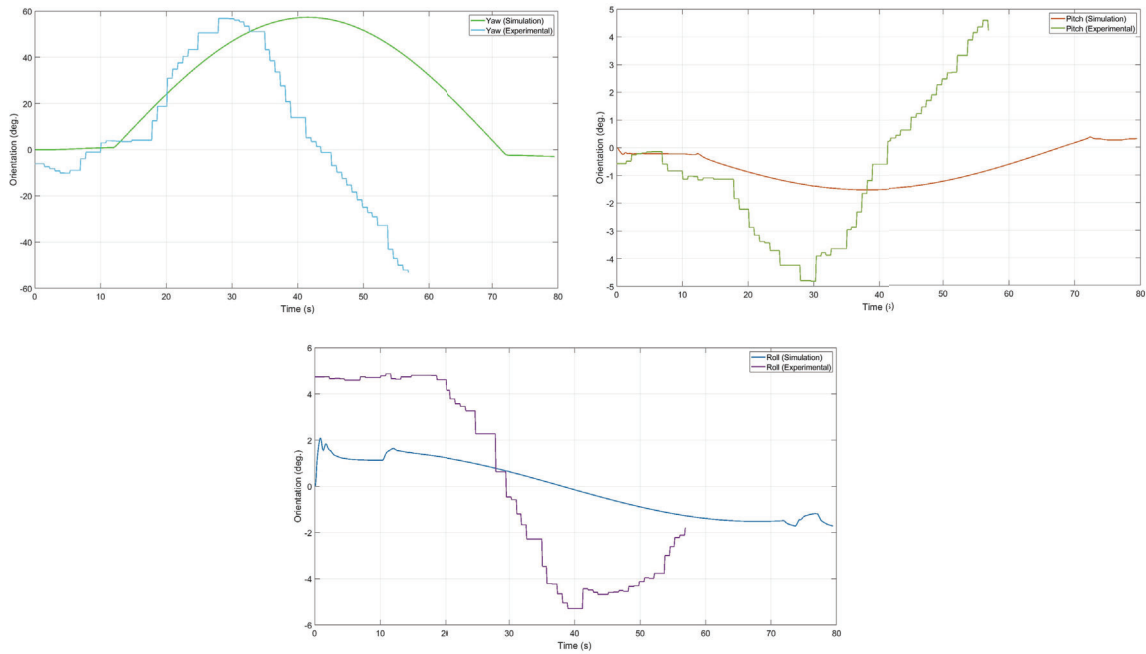
Figure 7: 3D orientation of the vessel in virtual Turning Circle test for the starboard side with comparison against the experimental values

From table 1 it is evident that manoeuvring parameters in both simulation conditions are quite similar, indicating consistency in the model's behaviour for turns in either direction. The starboard turn has a slightly lower value with a larger discrepancy from the experimental one. This discrepancy indicates that in real-life conditions vessel completes the turn in a significantly smaller area than predicted by simulations. This discrepancy arises from the fact that real-time conditions like wind and surface currents may not be accurately modelled in simulations with simulation not fully capturing all the dynamics of the vessel, such as hull interactions with water and real-time adjustments by the humans for remotely controlled vessels. Figure 6 shows the orientation of the vessel during a simulated Turning Circle test to the port side where roll and yaw remain relatively stable for the duration of the turn and the pitch relatively aligns with the behaviour of the dynamics of turning circle test. Similarly, Figure 7 depicts the 3D orientation of a vessel during a simulated and experimental turning circle test to the starboard side. The simulation predicts minor roll oscillations, while the experimental results show significant roll, with

the vessel tilting much more from side to side. This suggests that the real-life vessel experiences greater lateral instability during a starboard turn than the simulation predicts. The simulation shows a significant bow-up pitch, reaching 55 degrees, whereas the experimental results show minimal change in pitch, staying around 5 degrees. This discrepancy suggests that the simulation may overestimate the vessel's pitching behaviour during a starboard turn. Both simulation and experimental results show a similar yaw pattern, with a steady counterclockwise rotation. The experimental yaw is slightly more stable, indicating that the vessel's heading change in real-time is consistent but less variable than predicted by the simulation. The simulation appears to predict a more controlled and less dynamic turning behaviour than observed in real-life conditions. This could be due to simplifications in the simulation model or unaccounted factors in the real environment. The simulation for the port side can be accessed from https://www.youtube.com/watch?v=wJ05OrLqu$_M$ while the starboard side can be accessed from https://youtu.be/yFIsHnBdhZA.

5 Conclusions

In this study, a virtual free-running Turning circle test was performed using a MARUS simulation framework to evaluate the manoeuvering performance of a USV platform validated by experiments. The simulations provided a useful approximation of the parameters with a comparison against the experimental results providing a crucial understanding concerning the vessel's true manoeuvring capabilities. The differences highlight the need for continual refinement of simulation models to better match experimental results. The factors such as surface current, winds and hull design will be considered for the redesign of the simulation framework to reiterate on simulation results for a closer match with experimental data. A first step in this regard is to implement a non-linear feedback control strategy within MARUS to better capture the complex dynamics of vessel maneuvers during the Turning Circle test and expand the scope to more difficult manoeuvring scenarios.

Acknowledgement

References

Aiyelari Temilolorun, Y.S., 2024. Development of a low cost unmanned surface vessel for autonomous navigation in shallow water, in: iSCSS 2024, Liverpool, Institute of Marine Engineering Science and Technology.

BAKAR, M.H.A.B.A., 2015. Manoeuvering analysis in free running scaled rc model on 60m multi purpose offshore support vessel (mposv).

de Cerqueira Gava, P.D., Nascimento Júnior, C.L., Belchior de França Silva, J.R., Adabo, G.J., 2022. Simu2vita: A general purpose underwater vehicle simulator. Sensors 22, 3255.

Cook, D., Vardy, A., Lewis, R., 2014. A survey of auv and robot simulators for multi-vehicle operations, in: 2014 IEEE/OES Autonomous Underwater Vehicles (AUV), IEEE. pp. 1–8.

DeMarco, K.J., West, M.E., Howard, A.M., 2015. A computationally-efficient 2d imaging sonar model for underwater robotics simulations in gazebo, in: OCEANS 2015-MTS/IEEE Washington, IEEE. pp. 1–7.

Garg, S., Quintas, J., Cruz, J., Pascoal, A.M., 2020. Netmarsys-a tool for the simulation and visualization of distributed autonomous marine robotic systems, in: 2020 IEEE/OES Autonomous Underwater Vehicles Symposium (AUV), IEEE. pp. 1–5.

Katara, P., Khanna, M., Nagar, H., Panaiyappan, A., 2019. Open source simulator for unmanned underwater vehicles using ros and unity3d, in: 2019 IEEE Underwater Technology (UT), IEEE. pp. 1–7.

Kim, M.J., et al., 1996. Assessment of ship manoeuvrability based on imo resolution no. a. 751 .

Koenig, N., Howard, A., 2004. Design and use paradigms for gazebo, an open-source multi-robot simulator, in: 2004 IEEE/RSJ international conference on intelligent robots and systems (IROS)(IEEE Cat. No. 04CH37566), Ieee. pp. 2149–2154.

Lončar, I., Obradović, J., Kraševac, N., Mandić, L., Kvasić, I., Ferreira, F., Slošić, V., Na, ., Mišković, N., 2022. Marus-a marine robotics simulator, in: OCEANS 2022, Hampton Roads, IEEE. pp. 1–7.

Osa, E., Orukpe, P., 2021. Simulation of an underwater environment via unity 3d software, in: BOOK OF PROCEEDINGS, p. 384.

Szleg, P., Barczyk, P., Maruszczak, B., Zieliñski, S., Szymañska, E., 2022. Simulation environment for underwater vehicles testing and training in unity3d, in: International Conference on Intelligent Autonomous Systems, Springer. pp. 844–853.

Xu, F., Zhu, Q., Li, S., Song, Z., Du, J., 2021. Vr-based haptic simulator for subsea robot teleoperations, in: Computing in Civil Engineering 2021, pp. 1024–1032.

Battery Energy Storage System Sizing Strategy for Naval Vessels through Multi-Objective Optimisation

D. Belvisi [a,b*], L. Maloberti [a], R. Zaccone [a], M. Figari [a]

[a]DITEN - Department of Electrical, Electronic, Telecommunications Engineering and Naval Architecture, Polytechnic School, University of Genoa;
[b]Italian Navy, Ministry of Defence.
*Corresponding Author. e-mail: daniele.belvisi@edu.unige.it

Synopsis

Naval ship design must balance multiple conflicting requirements, including the need for fast response times and high speeds, often leading to large and complex hybrid propulsion systems. At the same time, the decarbonisation of ship operations and the shipping industry has become one of the most concerning topics for the maritime community. Even if the military sector has not been driven yet by this regulatory framework, decarbonisation is also becoming a hot topic for the navies. Additionally, short-term power loads encompass numerous demanding applications. The impact of this type of load on the performance of the shipboard power system influences power quality, and load levelling has been proven to be one of the critical power management strategies for new naval shipboard electric plants. Furthermore, decarbonisation and electric pulse management require pervasive automation systems to balance reduced crew sizes effectively.

In recent years, Battery Energy Storage Systems (*BESS*) have emerged as effective tools for reducing greenhouse gas emissions, as well as for load levelling and peak shaving. These systems support power management strategies, addressing conflicting naval ship design requirements and optimising these critical concerns. *BESS*-based hybrid propulsion is a promising solution for enhancing the energy efficiency of naval ships. It has been proven to be a reliable and flexible design option for improving the power quality of the electric grid. However, *BESS* requires space, weight tolerance, and cost expenditures to match all other military operational requirements in one convenient, optimal shipboard power plant. The paper outlines an optimisation-based approach to size a *BESS*-based hybrid propulsion architecture for naval ships, primarily focusing on reducing environmental footprint, increasing efficiency, and improving power grid reliability. The optimisation aims to minimise the ship exhaust emissions in terms of equivalent CO_2. The frontline ship type case study has been analysed while manoeuvring in restricted waters and deep seas in a given pseudo-random operating condition extracted from actual data, showing potential interest in a new, energy-efficient, and resilient solution. For comprehensive benchmarking, the case study has been further examined and discussed with different sizing configurations, and each case study has been ranked with a set of Key Performance Indicators (KPIs). The study shows that, despite the increasing size and weight of the *BESS* to reduce fuel consumption, analysing different solutions with a model-based strategy for the hybrid plant gives interesting trade-offs during the design phase while leaving space for new research directions.

Keywords: Naval ships; Hybrid Energy Systems; Battery Energy Storage System; Optimisation; Genetic Algorithm; Energy management; Load sharing; Decarbonisation

1 Introduction

The maritime world aims to reduce fuel consumption and environmental impact due to the recent ambitious targets outlined by the International Maritime Organisation (IMO) (IMO, 2023, 2024). The rules aim to drive the maritime industry to reduce Greenhouse Gas emissions and promote sustainable shipping practices.

The formulations of the Energy Efficiency Operational Indicator (EEOI), the Energy Efficiency Design Index (EEDI) and the later introduced Energy Efficiency Existing Ship Index (EEXI) (IMO, 2009, 2013, 2021) have been driving improvements in ship energy efficiency for many years. However, the EEDI formula applies exclusively to commercial vessels (e.g., bulk carriers, tankers, and container ships) and excludes military and other governmental

vessels. (IMO, 2022b,c). The Initial IMO Strategy on Reduction of Greenhouse gas (GHG) Emissions from Ships (IMO, 2018) outlined the ambitious goal of reducing emissions by at least 50% by 2050 compared to 2008 levels, with a focus on improving energy efficiency, transitioning to low-carbon fuels. This strategy provided a framework for global action, guiding the industry towards sustainable and environmentally responsible practices to combat climate change. One essential framework item is the Ship Energy Efficiency Management Plan (IMO, 2022a), a document describing the company strategy for enhancing vessel performance and reducing environmental impact. Despite the IMO's actions, the maritime industry remains responsible for approximately 3% of global greenhouse gas emissions IMO (2018), and the pace of reduction has yet to keep it on track with the UN Paris Agreement goals. The new GHG reduction paths in shipping also include the transition to alternative, low-carbon fuels, i.e., biodiesel, biomethane, methanol, ammonia, and hydrogen, as well as energy efficiency, operational measures and advice tools (Maloberti et al., 2024). In particular, methanol produced from renewable feedstocks is considered one of the most viable decarbonising options for commercial shipping (Adami and Figari, 2023; Altosole et al., 2021, 2023). Best practices for fuel-efficient operation require assessing and understanding the ship's current energy demand and energy production status. Shipboard automation, particularly the Energy Management System, plays a crucial role in monitoring electrical loads on board and can unveil opportunities for significant efficiency improvements, especially for ships with predominant non-propulsive electric loads. Energy Storage Systems (ESS) have proven their validity to optimise the load factor of the main generating sets (D'Agostino et al., 2023a). The naval sector has yet to embrace the decarbonisation strategy, primarily to uphold substantial and growing operational flexibility across diverse environmental conditions. Naval ship design involves balancing many conflicting requirements, including the need for fast response times and high speeds, which often result in large and complex hybrid propulsion plants (Belvisi et al., 2022), frequently incorporating extensive design frameworks for combined propulsion control systems (Martelli and Figari, 2022). Additionally, demanding combat system applications depend on pulse power loads, which challenge the shipboard power system's power quality and resilience performance. Therefore, load levelling has emerged as a critical power management strategy for new naval shipboard electric plants (D'Agostino et al., 2023b). Both power quality and load levelling must match pervasive automation systems that strive for continuous optimisation of personnel workload. Every alternative solution to fossil-based diesel generation and propulsion systems has peculiarities and critical issues, mainly related to the expected availability, safety measures, maturity of the technologies, and costs (Bao et al., 2021; Maloberti et al., 2022). Despite the numerous advantages of ESS, their high initial investment costs and the constrained space available for ship installation limit their widespread adoption. Therefore, it becomes imperative to tackle the issue of ESS sizing by incorporating considerations of optimal power scheduling. This aspect is closely intertwined with the overall performance of ESS (Kanellos et al., 2014). Additionally, the decision regarding the utilisation levels of different power generation technologies hinges on a variety of factors that have to be tailored to each specific scenario and typically arise from the optimisation of a cost-benefit function and the assurance of the safety and reliability of the power system (Kanellos, 2013). Despite the conflicting requirements of the frontline naval segment, which currently does not leave enough space for a full-scale implementation of ESS-based systems, Governments and Institutions have shown particular interest in multi-purpose ships with low GHG emissions, and this trend will become even more critical. This paper proposes an optimisation-based approach to size a BESS-based hybrid propulsion architecture for naval ships, primarily focusing on increasing operational flexibility, reducing environmental footprint, increasing efficiency, and improving power grid reliability. The goal is to minimise the ship exhaust emissions in terms of equivalent CO_2, thereby achieving a low environmental footprint and cost-effective operation while maintaining high levels of reliability within the specified case study. In this framework, optimising ship electric load sharing over time can enhance hybrid power plant efficiency in response to changes in electric load, providing an additional measure for controlling GHG emissions and reducing operational costs. However, this approach is constrained by factors such as redundancy and reliability, which must be carefully considered over a lifetime study that includes the systemic ageing of machinery and electric plants. The proposed optimisation approach has been tested on a frontline ship case study, considering a mission profile in deep-seas navigation with an assigned speed profile. The simulation approach proposed in this paper aims to address the design challenge of balancing multiple conflicting requirements, such as reducing environmental footprint, increasing efficiency, and improving power grid reliability.

Consequently, ESS-based technologies, while improving power management strategy, could be an interesting tool to advance endurance, reduce environmental footprint, and relax the impact on human workload for maintenance.

2 Hybrid power system modelling

In a typical naval ship electric generation system, multiple gensets, consisting of internal combustion engines coupled with alternators, are employed. A hybrid propulsion system can also integrate a *BESS* with its controller. The systems modelled in this work are the combustion engines and the batteries. The proposed modelling adopts

a static approach, neglecting the components' dynamics. It is worth noting that the models used are simplified and well-documented in the literature, integrated to build a system performance model for use in optimisation, such as comparing solutions. The ability of the model to provide accurate performance estimates under specific conditions is therefore secondary to its ability to model the physical behaviour of the system within the computational domain (Martelli, 2015). Combustion engine black-box modelling involves using Brake Specific Energy Consumption (*BSEC*) to represent fuel mass flow rate as a function of power output (Ashok et al., 2018). The specific consumption of the marine diesel oil has been calculated through the following equation:

$$BSEC = SFOC\ LHV_{MDO} \tag{1}$$

Where *SFOC* is the Specific Fuel Oil Consumption and LHV_{MDO} is the lower heating value of Marine Diesel Oil (*MDO*). The fuel mass flow rate of the generator is determined as follows:

$$\dot{m}_{MDO} = P_B\ SFOC \tag{2}$$

Where P_B represents the power delivered by the diesel engine of the generator.

The State of Charge (*SoC*) of the battery is modelled according to the following system of equations:

$$\begin{cases} SoC(t) = SoC(0) - \dfrac{\beta}{E_{BESS}} \displaystyle\int_0^T P_{BESS}(t)dt \\ \beta = \begin{cases} \eta_{charge} & \text{if } P_{BESS} \leq 0 \\ \dfrac{1}{\eta_{discharge}} & \text{if } P_{BESS} > 0 \end{cases} \end{cases} \tag{3}$$

Where $SoC(0)$ is *SoC* at time $t = 0$, $\eta_{charge} = 0,94$ and $\eta_{discharge} = 0,97$ are the battery efficiency during the *BESS* charging and discharging processes, P_{BESS} is the power delivered by the *BESS*, which can be positive or negative depending on whether it is in the discharging or charging phase, and E_{BESS} is the nominal energy stored in the battery. For technological reasons, the State of Charge of the *BESS* should be kept between 30% and 80%.

3 Operational optimisation strategy

This study aims to size a *BESS* by identifying the power split that minimises the environmental impact of the propulsive configurations, using an optimisation approach according to a rule-based procedure that depends on a specific set of performance indicators. A genetic algorithm, i.e. a method based on natural selection that drives biological evolution, is employed to find the optimal solution. The genetic algorithm repeatedly modifies a population of individuals, selecting individuals from the current population as parents at each step and using them to produce the next generation's children. Over successive generations, the population "evolves" toward an optimal solution (Goldberg, 1989). The following subsections describe all the aspects of the problem formulation, from the genetic encoding, i.e., the parametrisation of the problem, to the set-up of the cost function and constraints, based on the steady-state modelling of the ship's propulsion system (Zaccone et al., 2021).

3.1 Genetic encoding

Defining the genetic encoding is crucial when using a genetic approach to solve optimisation problems.

The inputs to the problem are the required mission power profile and the propulsive system configuration. The mission power profile is defined in discrete time, at time instants t_j, $j = 0...T$. The variables identifying the optimal solution are the powers delivered by the *BESS*, expressed as a fraction of its maximum power through an appropriate load factor α. The encoding takes the following form:

$$\mathbf{X} = \left\{ \alpha_{BESS}^0, \alpha_{BESS}^1, \cdots, \alpha_{BESS}^{T-1} \right\} \tag{4}$$

Where α_{BESS}^j are the battery load factor for each time instant. The power delivered by the generators at each time instant is calculated as the difference between the load and the power delivered by the BESS, according to the following equation:

$$P_{DG,tot}^j = P_{load}^j - P_{BESS}^j \quad ; \quad j = 0, \cdots, (T-1) \tag{5}$$

This power is then equally shared among the active generators, as they are identical and the time span considered during the simulation is large, meaning its order of magnitude is greater than the variations in electrical measures and generator loading ramps:

$$P_{DG,i}^j = \frac{P_{DG,tot}^j}{N_{active}^j} \tag{6}$$

Where N_{active} represent the number of active generators at each time instant j, which are the minimum number of generators required to support the load, and i represents the ith generator.

3.2 Cost function

In the presented application, the solution ranking after each generation in a genetic algorithm is performed using a cost function. The optimisation objective is to minimise the equivalent CO2 emissions of the power generation plant. Thus, the following function has to be minimised:

$$f(\mathbf{X} = \alpha_{BESS}^j) = EF_{fuel} \sum_{j=0}^{T} \sum_{i=1}^{N_{active}} P_{DG,i}^j SFOC_i^j \Delta t_j \qquad (7)$$

Where EF_{fuel} is the equivalent CO_2 emission factor for the MDO, $\Delta t_j = t_j - t_{j-1}$, and $SFOC_i^j$ is the specific fuel oil consumption of the ith generator at the jth time.

3.3 Constraints

Clearly defining constraints is an essential step in the proposed approach to ensure precise outcomes. First, the bounds of the solutions need to be defined:

$$\alpha_{BESS,min} \leq \alpha_{BESS}^j \leq \alpha_{BESS,max} \qquad (8)$$

Where $\alpha_{BESS,min}$ and $\alpha_{BESS,max}$ represent the maximum load that can be absorbed by the battery in the charging phase and the maximum load that can be delivered by the battery in the discharging phase, depending on the C-rate of the battery, assumed to be different for the different propulsive configurations considered.

Each generator's generated power must always be non-negative and never exceed its maximum load. Furthermore, for operational reasons, it has been decided that active generators must operate at a minimum output of 20% and a maximum of 95% of their maximum load. The lower limit ensures that diesel generators operate only within an optimal range of load factors, thereby preventing irregular functioning of the diesel engine, while the maximum load limit is set for the start of an additional diesel generator. Therefore, each generator can be kept off or on with power between 20% and 95% of their maximum power. The power balance constraint, therefore, takes the following form:

$$P_{DG,i}^j = 0 \quad \vee \quad 0.2\,P_{DG,i,max} \leq P_{DG,i}^j \leq 0.95\,P_{DG,i,max} \qquad (9)$$

Where $P_{DG,i}^j$ is the ith generator power at each time instant j, and $P_{DG,i,max}$ is the maximum power of the ith generator. A constraint has been implemented on the power balance such that, at each time instant, the power demanded by the load equals the power supplied by the system components:

$$\sum_{i=1}^{N_{active}} P_{DG,i}^j + \alpha_{BESS}^j P_{BESS} = P_{load} \qquad (10)$$

Where P_{BESS} indicates the nominal power of the BESS. Furthermore, two Battery Storage System constraints need to be set. Firstly, the SoC of the $BESS$ is is constrained to remain within specified minimum (SoC_{min}) and maximum (SoC_{max}) limits to preserve the battery state of health:

$$SoC_{min} \leq SoC_j \leq SoC_{max} \qquad (11)$$

The SoC_j at time t_j obtained by discretizing Equation 3 , is given by:

$$SoC_j = \frac{1}{E_{max}} \left(E_0 - \beta \sum_{p=0}^{j} P_{BESS_p} \Delta t_p \right) \qquad (12)$$

Where $\Delta t_p = t_p - t_{p-1}$. Secondly, the battery energy balance constraint is required to keep the results consistent:

$$SoC_0 = SoC_T \qquad (13)$$

Eventually, the fuel consumption must not exceed the fuel available on board:

$$m_{MDO} = \sum_{j=0}^{T} \sum_{i=1}^{N_{active}} \dot{m}_{i,MDO}^j \Delta t_j \leq MDO_{onboard} \qquad (14)$$

Calculations have been performed using MATLAB R2023b and the parallel computing toolbox. The average computational time to calculate six configurations ranged from around 33 minutes, performing a series calculation. The analysis has been conducted using a MacBook Pro 16 equipped with an Intel Core i7 processor running at 2,667 GHz, featuring 6 cores and 12 threads, along with 16 GB of DDR4-SDRAM.

3.4 Optimisation problem

To determine the optimal generator load sharing and, consequently, the optimal propulsion plant configuration, the following optimisation problem, which combines Equations 7, 8, 9, 10, 11, 13 and 14, needs to be solved:

$$
\begin{cases}
\min_{\alpha_{BESS}^j} \; EF_{fuel} \sum_{j=0}^{T} \sum_{i=1}^{N_{active}} P_{DG,i}^j SFOC_i^j \Delta t_j \\
s.t.: \\
\alpha_{BESS,min} \le \alpha_{BESS}^j \le \alpha_{BESS,max} \\
P_{DG,i}^j = 0 \quad \vee \quad 0.2\,P_{DG,i,max} \le P_{DG,i}^j \le 0.95\,P_{DG,i,max} \\
\sum_{i=1}^{N_{active}} P_{DG,i}^j + \alpha_{BESS}^j P_{BESS} = P_{load} \\
SoC_{min} \le SoC_j \le SoC_{max} \\
SoC_0 = SoC_T \\
m_{MDO} = \sum_{j=0}^{T} \sum_{i=1}^{N_{active}} \dot{m}_{i,MDO}^j \Delta t_j \le MDO_{onboard}
\end{cases}
\tag{15}
$$

4 Simulation methods and experiments

This paper aims to select the configuration of the electrical generating system on board and examine its performance under specific operating conditions using the simulation experiments outlined below. The mission time for sampling the time-speed profile ranges from a few hours to a day to accurately capture the load sharing trend on a daily basis. Ultimately, the time step is longer than the time required to distribute load power among diesel generators to match the power demand, and transient effects in load distribution among generators are therefore disregarded.

4.1 Case study ship

The case study is a new-generation Destroyer with an overall length of 165 meters, a maximum width of 21.80 meters, and a depth of 12.60 meters. The full-load displacement is 9170 metric tons, with a full-load draught of 5.86 meters. The operating profile necessitates steaming at low speeds for much of the vessel's lifetime.

A Combined diesel or gas or electric (CODOGOL) hybrid propulsion plant has been designed, incorporating two gas turbines and two diesel engines to ensure the required speed range, operational flexibility, power projection, survivability, and efficiency.

This configuration allows for a maximum speed of 29 knots and a cruise speed of 18 knots at the end-of-life displacement, with an operational range of 7000 nautical miles at the cruising speed. Two electric propulsion motors (EPMs) provide patrol speed. Four identical diesel generators power the electric plant. Following the "$n+1$" redundancy principle, three out of four generators provide the necessary electric power at cruising speed. A *BESS* has been proposed as a backup to meet redundancy requirements and reduce fuel consumption. The *BESS* has been initially sized to provide the required electric power in emergency conditions, acting as a spinning reserve when one of the generators fails. Specifically, the initial *BESS* sizing delivers the necessary power for 20 minutes, allowing sufficient time to start up another generator in emergency conditions. The *BESS* is divided into four Energy Storage Modules (*ESM*s) to enhance redundancy and reduce vulnerability.

The described architecture ensures high efficiency across a wide range of speeds, using the Lithium-ion battery pack to maintain the Minimum Generator Operation (*MGO*) mode at low speeds. Figure 1 illustrates the architecture, showing only the starboard shaft line, with the port side being conceptually similar. The main technical data of the machinery are reported in Table 1.

This paper introduces an alternative approach to the static sizing of the *BESS* for hybrid propulsion plants of naval ships during the design phase, leveraging a rule-based software. This model works as a decision support system that evaluates different generation plant configurations against a given set of KPIs. The proposed model-based approach offers a novel perspective for *BESS* sizing, addressing Strategic Loading (SL) or Spinning Reserve (SR) requirements.

4.2 Scenarios

The ship's mission profile has been derived from databases of a frontline ship currently in active service by scaling the measurements of time-speed trends during a typical mission. Firstly, to evaluate a typical speed range for this case study, the operating profile of the ship must be considered, as shown in Figure 2.
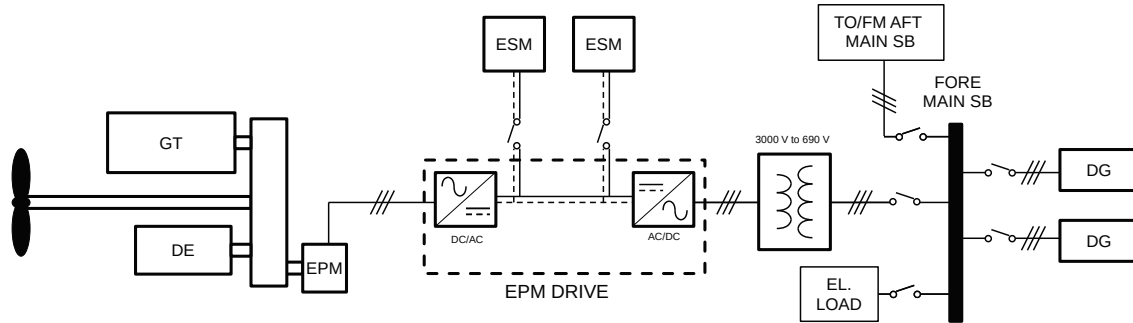
Figure 1: Layout of the proposed propulsion scheme (only the starboard shaftline is shown).

Table 1: Initial sizing of the main propulsion and generation machinery

Gas turbines	$2 \times 30600\,kW$ @ $3600\,rpm$, $220\,g/kWh$ min.
Prop. Diesel engines	$2 \times 7280\,kW$ @ $1150\,rpm$, $188\,g/kWh$ min.
EPM	$2 \times 1120\,kW$ @ $880\,rpm$
Diesel generators	$4 \times 2240\,kW\,/\,2150kWe$ @ $1800\,rpm$, $188\,g/kWh$ min.
BESS	$4\times$ ESM $(3240Ah$ @ $972V)$
ESM	$18(s) \times 54(p)$ modules $(60Ah$ @ $54V)$

According to the operating profile relationship, the ship primarily operates at low and medium speeds, using electric propulsion to achieve optimal performance at cruising and patrolling speeds. The propulsion system's efficiency in electric mode depends on the running load factor of the diesel generators. Therefore, optimising low and medium speed ranges is crucial for this propulsion plant configuration, and a typical mission profile for appropriate *BESS* dimensioning is selected accordingly.

Next, the ship's active power absorption has been analysed referring to a similar naval vessel equipped with mechanical propulsion. Consequently, the electric load of the reference ship pertains to non-propulsive loads, while for the case study, diesel generators also provide the necessary propulsion load to the electric motors. Let T be a given observation time matching a fixed mission time for the case study. Assuming $P_{ref,k}(t)$ represents a k-measured trend sample of the electric power for non-propulsive loads (e.g., hotel loads, combat systems, navigation devices, radars, and auxiliary generation plants, but excluding propulsion and ship services loads), the load factor of the generation plant of the reference ship is given by:

$$\gamma_{ref,T,k} = \frac{P_{ref,k}(t)}{P_{ref,balance}} \tag{16}$$

Where $P_{ref,k}(t)$ is a k-measured trend observed and measured from the automation plant of the reference ship, $P_{ref,balance}$ is the active power calculated from the load balance of the ship for the same type of loads as $P_{ref,k}(t)$, and T is the reference mission time. It is noteworthy that, given the mission profile and duration, $\gamma_{ref,T}$ is not significantly dependent on the specific sample analysed. At this stage of the work, fixing the mission profile (i.e. assuming $\gamma_{ref,T} = \gamma_{ref,T,k}$) implicitly neglects the stochastic nature of $\gamma_{ref,T} = \gamma_{ref,T}(t,m)$, where t is time and m is a specific, continuous variable that identifies the mission. Furthermore, in this context the stochastic nature of the electric power load over time with respect to the mean load is also disregarded.

Finally, the load profile is obtained by adding a propulsive load, which is calculated based on a typical speed-time relationship sampled from the case study's operating profile. In other words, it is assumed that the active power $P(t)$ provided by the generation plant of the case study is calculated from the load factor mentioned earlier, as expressed by the following relationship:

$$P(t) = P_{prop}(t) + \gamma_{ref,T}\,P_{balance} \tag{17}$$

Where $P_{prop}(t)$ is the active power required by the electric propulsion motors (EPMs) to ensure the necessary speed, and $P_{balance}$ is the electric load of non-propulsive loads calculated from the load balance.

A representative sample in the lower speed ranges for the time-speed relationship according to the operating profile shown in Figure 2 is illustrated in Figure 3.

4.3 Rule-based sizing strategy

The sizing strategy is based on a set of KPIs evaluated as follows in this section.
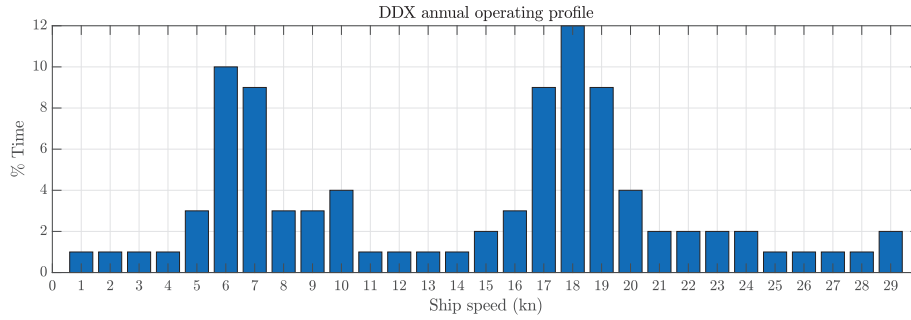
Figure 2: A typical operating profile of a new generation Destroyer with the stated mission requirements
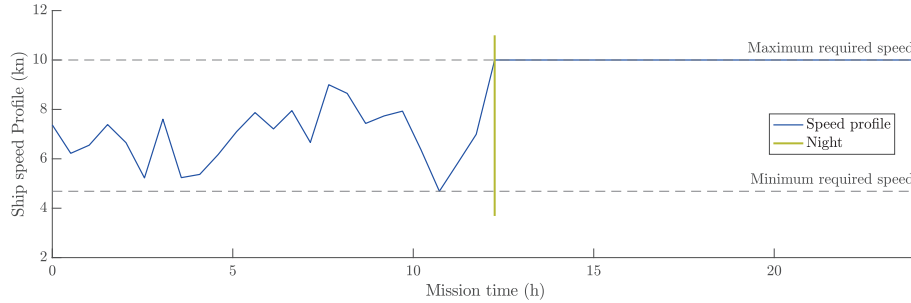
Figure 3: A sample for the speed profile of a new generation Destroyer with the stated mission requirements

The total amount of equivalent CO_2 emissions over one year of operation, representing the environmental footprint of the chosen generation plant configuration, is calculated according to the following equation:

$$CO_{2,\,eq}^{tot} = DAS\ EF_{fuel} \sum_{j=0}^{T} \sum_{i=1}^{N_{active}} P_{DG,i}^{j} SFOC_i^j \Delta t_j \tag{18}$$

Where DAS is the number of days at sea in one year calculated from the the ship's annual operational availability, i.e. 292 days.

The mean Depth of Discharge (DoD) of the battery is calculated over the mission time as follows:

$$DoD_{mean} = \frac{\sum_{i=1}\left(\boldsymbol{SoC}_{max} - \boldsymbol{SoC}_{min}\right)_i}{n_{peaks}} \tag{19}$$

where $\boldsymbol{SoC}_{max}$ is the vector of local maxima, $\boldsymbol{SoC}_{min}$ is the vector of local minima and n_{peaks} is the number of peaks of the SoC over the mission time. DoD_{mean} ranks, together with the year-based number of charge-discharge cycles of the $BESS$ (N_{cycles}), the battery system usage rate, and is related to its life cycle and duration.

The installed power for generation is strictly related to the necessary space on board the ship and the mean available power over time and is considered through the generator's rated power ($P_{DG,\,max}$).

The mean available power over the mission time T is given by:

$$P_{av,\,mean} = \sum_{i=1}^{N_{DG}} P_{DG,i,max} + P_{BESS} - \frac{\sum_{j=0}^{T}\left(\sum_{i=1}^{N_{active}} P_{DG,i}^j + \theta^j \alpha_{BESS}^j P_{BESS}\right)}{T} \tag{20}$$

in the way that the optimal load balance is satisfied with the term $\sum_{i=1}^{N_{active}} P_{DG,i}^j + \alpha_{BESS}^j P_{BESS}$ and θ^j is a Heaviside step function type

$$\theta^j = \begin{cases} 1 & \text{if } \alpha_{BESS}^j > 0 \\ 0 & \text{if } \alpha_{BESS}^j \leq 0 \end{cases}$$

In the equation 20, N_{DG} is the number of installed generators. P_{av} represents the availability and redundancy of the electric plant in case of shutdown of the main generators with the given load profile in a specific mission time.

The last indicator is the battery system volume, V_{BESS}, calculated by dimensioning the $BESS$ given the technical data of the battery modules. This volume represents the space on board the $BESS$ requires, directly proportional to its weight and cost.

Once the *KPIs* have been chosen, the sizing strategy involves the selection of a hybrid plant configuration in terms of three main parameters: the nominal power of the generators ($P_{DG,max}$), the maximum power deliverable by the battery system (P_{BESS}), and the capacity of the battery system (E_{BESS}). The rule-based sizing strategy can be outlined as follows:

Step 1: The initial configuration of the hybrid plant features diesel generators with a rated power sufficient to meet the electric load balance. For the case study, a *BESS* was then sized to ensure the necessary SR capabilities in case of a diesel generator shutdown, maintaining the same availability in *MGO* mode. This initial sizing was determined using static considerations and was supported and tested by dynamic simulations. At the same time, the *BESS* achieves the *MGO* mode, providing even better fuel consumption performance than the same system without a battery, as already highlighted in Belvisi et al. (2022). The first simulation is conducted with the proposed approach on the initial hybrid plant configuration to determine if the initial *BESS* sizing is adequate to ensure SL capabilities for load sharing;

Step 2: The three main parameters are systematically varied one at a time, beginning with the size of the diesel generator. Each hybrid plant configuration derived from these parameter combinations is assessed using the selected KPIs. All configurations must adhere to the static considerations established during the design phase, which include available space and weight, electric load balance, and the provision of spinning reserve to ensure *MGO* conditions;

Step 3: The configurations tested in the previous step are characterised by the best load sharing in terms of fuel consumption. Typically, this results in load sharings with a high rate of battery usage over the mission time or good load sharings but with frequent start and stop cycles of the diesel generators within specific speed ranges;

Step 4: The battery dimensions are refined and tested based on the previous steps to achieve both optimal load sharing and moderate battery usage, ensuring a reliable life cycle;

Step 5: The configurations achieved are tested with other speed profiles to test typical operating conditions for the fixed mission and robustness of the design solution.

4.4 Results and discussion

This section applies the proposed method to the case study to evaluate the hybrid propulsion system configuration, representing an advantageous trade-off for the specific set of KPIs chosen in Section 4.3. Given the initial configuration of the hybrid plant, in which $P_{DG,max} = 2240\ kW$, $P_{BESS} = 2240\ kW$ and $E_{BESS} = 778\ kWh$, the main parameters are modified according to the strategy described in Section 4.3, and the following configurations are analysed:

- Configuration A: $P_{DG,max} = 2400\ kW$, $P_{BESS} = 2240\ kW$ and $E_{BESS} = 1556\ kWh$, which doubles the energy of the *BESS* and increases the maximum rating of diesel generators by 7%;

- Configuration B: $P_{DG,max} = 2400\ kW$, $P_{BESS} = 2240\ kW$ and $E_{BESS} = 1167\ kWh$, which increases the energy of the *BESS* by 50% and increases the maximum rating of diesel generators by 7%;

- Configuration C: $P_{DG,max} = 2240\ kW$, $P_{BESS} = 2240\ kW$ and $E_{BESS} = 1556\ kWh$, which doubles the energy by *BESS*;

- Configuration D: $P_{DG,max} = 2240\ kW$, $P_{BESS} = 2240\ kW$ and $E_{BESS} = 1167\ kWh$, which increases the energy of the *BESS* by 50%;

- Configuration E: $P_{DG,max} = 2240\ kW$, $P_{BESS} = 1120\ kW$ and $E_{BESS} = 778\ kWh$, that decreases the power of the *BESS* by 50%;

- Configuration F: corresponding to the initial sizing to ensure enough SR for 20 minutes and the *MGO* mode for the hybrid plant;

In order to rank the differences between the six configurations, Figure 4 represents the normalised values of the chosen performance indicators according to the following relationship:

$$KPI_{i,norm} = \frac{KPI_i - KPI_{i,min}}{KPI_{i,max} - KPI_{i,min}} \tag{21}$$

where KPI_i represent the performance indicators described in Section 4.3.
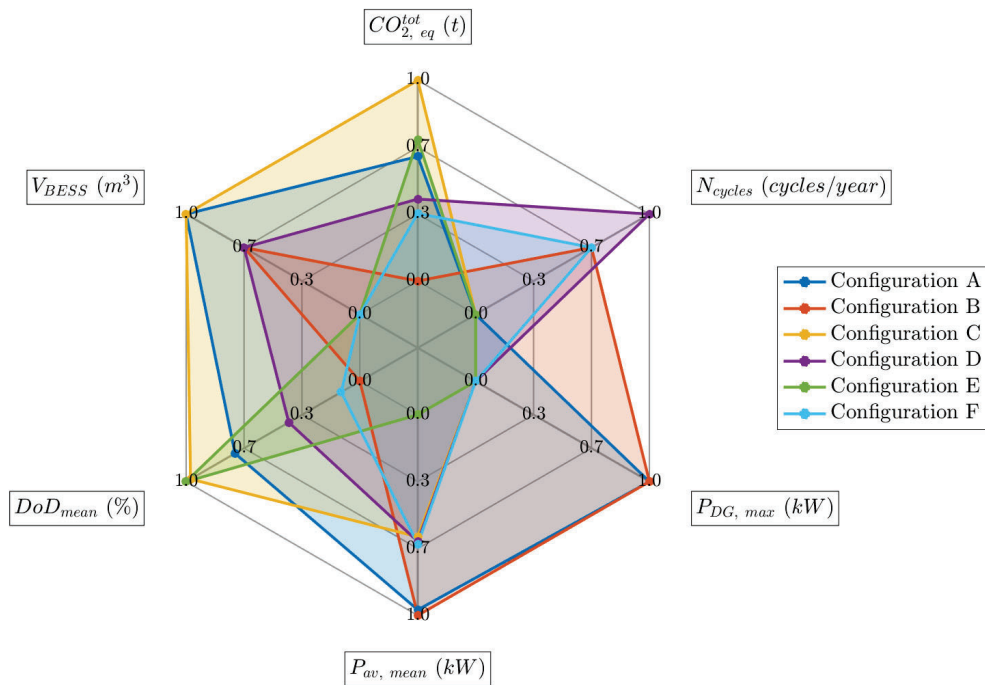
Figure 4: Normalised KPIs for the considered configurations of the *BESS* and diesel generators size

As shown in Figure 4, Configuration B provides the lowest annual-based $CO_{2\,eq}$ emissions, which are about 828 t, as calculated from the selected speed profile over a 24-hour period. Configuration B achieves a $0,4\%$ reduction in $CO_{2,\,eq}$ emissions per SL compared to Configuration C, which performs less efficiently in these respects. On the other hand, this configuration increases the volume of the *BESS* and diesel generators because of the higher energy and maximum power achievable compared to the Configuration F. The volume increase of the *BESS* is about 51% with respect to Configuration F, and with it comes an increase in weight and costs. Furthermore, Configuration C is slightly more reliable regarding SR capabilities, with a mean available power over time increased by 10% compared to Configuration F, as calculated from the load sharing with the chosen time-speed profile. This increased reliability is primarily due to the higher maximum power rating of the diesel generators. However, the predicted usage rate of the *BESS* is poor due to the low calculated Depth of Discharge with this time-speed profile.

Another interesting solution arises from Configuration D. Despite a marginal rise in annual $CO_{2\,eq}$ emissions with respect to Configuration B, Configuration D diminishes the maximum rated power of the diesel generators, albeit at the expense of a slightly higher utilisation rate of the Battery Energy Storage System compared to the optimal configuration in terms of annual cycles (up by 7%). Moreover, the DoD experiences an increase, although the average value remains approximately at 5%. Hence, Configuration D emerges as an optimal solution due to the lower volume of diesel generators and good overall performance. This is further supported by the load sharing illustrated in Figure 5a and the consistent trend observed in Figure 5b, which depicts the corresponding SoC over the mission duration. Additionally, Figure 4 shows that Configuration F has a good overall performance in terms of volume and $CO_{2\,eq}$ emissions. The genetic algorithm used in this study effectively balances conflicting objectives like minimising $CO_{2,eq}$ emissions while optimizing *BESS* volume and diesel generator performance. It consistently produces robust and reliable solutions across different configurations. However, in cases involving oversized generators or *BESS* capacities, the algorithm's performance may diverge. For oversized generators, it prioritizes reliability and power output over efficiency, leading to higher $CO_{2,eq}$ emissions. For large *BESS* capacities, it may overestimate the benefits of reduced generator use, resulting in increased costs and volume without proportional emissions or performance gains.

These observations underscore the need for well-defined bounds, constraints, and power ratings to ensure

(a) Load sharing

(b) State of Charge
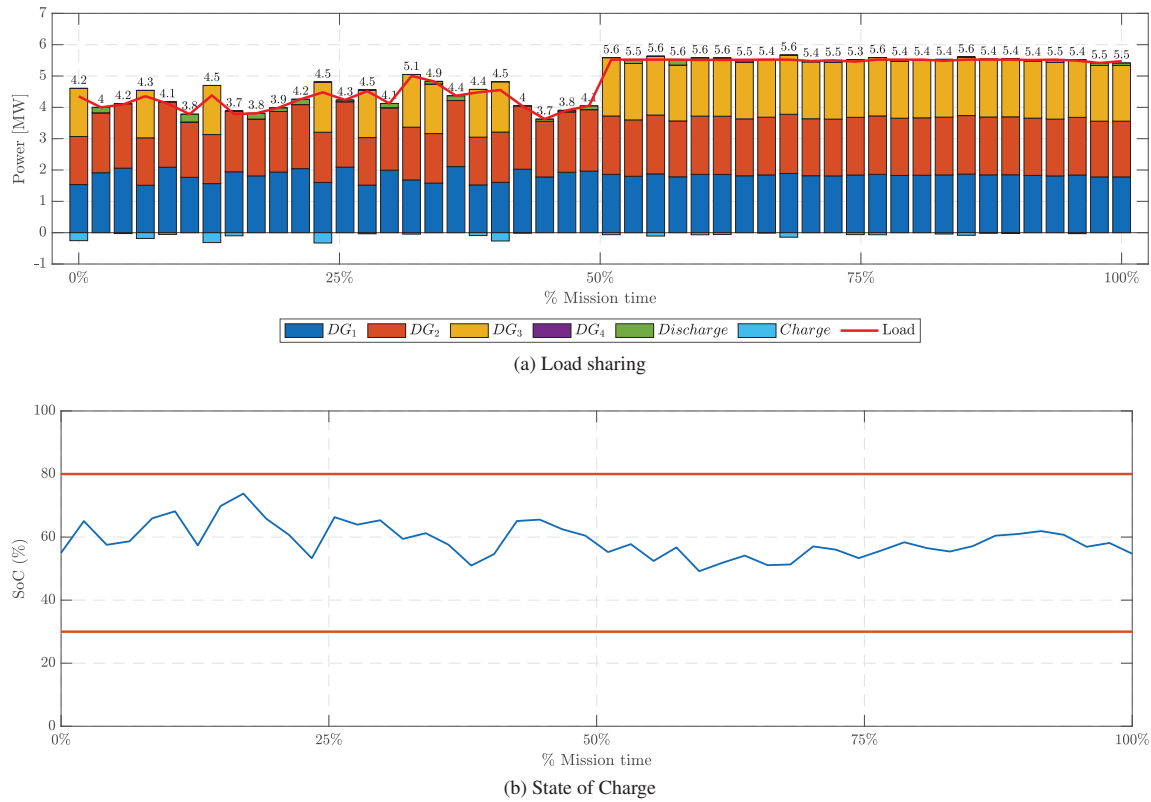
Figure 5: Calculated results for Configuration D obtained trough the CO_{2eq} emissions optimisation

balanced solutions. Overall, the algorithm performs well in preliminary design evaluations, essential for practical *BESS* sizing strategies in naval vessels.

5 Conclusions and further research

The proposed method enhances the conceptualisation phase of a *BESS* with a rule-based optimisation strategy, aiming to maintain high levels of efficiency, sufficient spinning reserve, and inherent reliability. This method offers a coherent framework for selecting the optimal configuration tailored to specific design needs by systematically analysing various configurations and their impact on key performance indicators. The method pushes the idea of *BESS* integration on board of naval ships, giving a coherent method of choice of the correct configuration concerning specific design needs, leveraging the concept of spinning reserve and strategic loading for diesel generators and ensuring optimal performance across various operational scenarios. By favouring *BESS* with strategic loading for diesel generators, the method inherently reduces diesel generator running hours under the *MGO* condition. This reduction improves operational efficiency and minimises environmental impact and maintenance requirements, contributing to overall cost savings and sustainability. A significant side effect of implementing this method is its potential to revolutionise life cycle assessment and to reduce operational workload.

While the method presented here represents a significant advancement in *BESS* integration on naval ships, there are several avenues for further research and improvement. Firstly, the dependency on the speed profile could be mitigated by conducting stochastic analyses of the ship's operating profile. By evaluating the relationship between sizing requirements and varying operating conditions, the method could be more robust and adaptable to real scenarios. Furthermore, ongoing research should explore new configurations and operational strategies to maximise *BESS* utilisation while ensuring reliability and performance standards. Although initial sizing constraints are influenced by available space on board, the choice of configuration can be generalised and applied to a broader range of *BESS* configurations, thanks to the inherent modularity of the technology. Lastly, optimisation methods should be refined to enhance calculation precision, reduce computational time, and optimise computational resources by employing advanced optimisation techniques, such as dynamic programming, metaheuristic algorithms or machine learning approaches.

In conclusion, the method outlined in this study represents a step forward in integrating *BESS* on naval ships, offering a systematic approach to configuration selection and optimisation, driving progress towards a cleaner,

more efficient, and resilient maritime fleet. As the maritime industry strives to meet ambitious emission reduction targets set by organisations like the International Maritime Organization, adopting innovative technologies and optimisation strategies will play a crucial role in shaping the future of naval propulsion systems.

Bibliography

Adami, G., Figari, M., 2023. Feasibility analysis of a methanol fuelled bulk carrier. Modelling and Optimisation of Ship Energy Systems 2023 doi:`10.59490/moses.2023.654`.

Altosole, M., Balsamo, F., Campora, U., Mocerino, L., 2021. Marine dual-fuel engines power smart management by hybrid turbocharging systems. Journal of Marine Science and Engineering 9, 663. doi:`10.3390/jmse9060663`.

Altosole, M., Balsamo, F., Mocerino, L., Scamardella, F., 2023. Methanol fuelled hybrid propulsion system for a charter yacht, in: 2023 International Conference on Clean Electrical Power (ICCEP), IEEE. pp. 810–817. doi:`10.1109/ICCEP57914.2023.10247434`.

Ashok, B., Nanthagopal, K., Sakthi Vignesh, D., 2018. Calophyllum inophyllum methyl ester biodiesel blend as an alternate fuel for diesel engine applications. Alexandria Engineering Journal 57, 1239–1247. URL: `https://www.sciencedirect.com/science/article/pii/S1110016817301357`, doi:`https://doi.org/10.1016/j.aej.2017.03.042`.

Bao, X., Xu, X., Zhang, Y., Xiong, Y., Shang, C., 2021. Optimal sizing of battery energy storage system in a shipboard power system with considering energy management optimization. Discrete Dynamics in Nature and Society 2021, 1–12. doi:`10.1155/2021/9032206`.

Belvisi, D., Zaccone, R., Figari, M., Simone, S., Spanghero, B., 2022. Bess-based hybrid propulsion: An application to a front line naval vessel preliminary design, in: Technology and Science for the Ships of the Future: Proceedings of NAV 2022: 20th International Conference on Ship & Maritime Research, p. 154 – 161. URL: `https://www.scopus.com/inward/record.uri?eid=2-s2.0-85138207713&doi=10.3233%2FPMST220020&partnerID=40&md5=ad826fe3a9d96cc05e6e098e3f1609fc`, doi:`10.3233/PMST220020`.

D'Agostino, F., Gallo, M., Saviozzi, M., Silvestro, F., 2023a. A security-constrained optimal power management algorithm for shipboard microgrids with battery energy storage system, in: 2023 IEEE International Conference on Electrical Systems for Aircraft, Railway, Ship Propulsion and Road Vehicles & International Transportation Electrification Conference (ESARS-ITEC), IEEE. pp. 1–6. doi:`10.1109/ESARS-ITEC57127.2023.10114833`.

D'Agostino, F., Kaza, D., Silvestro, F., Chiarelli, A., Olcese, F., 2023b. A survey on pulse power load applications and tools for simulation, in: 2023 IEEE Electric Ship Technologies Symposium (ESTS), IEEE. pp. 167–173.

Goldberg, D., 1989. Genetic algorithms in search, optimization and machine learning. addison-wesley longman publishing co., inc .

IMO, 2009. Guidelines for voluntary use of the ship Energy Efficiency Operational Indicator (EEOI). Resolution MEPC. 1/Circ. 684. International Maritime Organization.

IMO, 2013. 2013 Guidelines for calculation of reference lines for use with the Energy Efficiency Design Index (EEDI). Resolution MEPC. 231(65). International Maritime Organization. MEPC 65/22.

IMO, 2018. Initial IMO Strategy on Reduction of GHG Emissions from Ships. Resolution MEPC.304(72). International Maritime Organization. MEPC 72/17/Add.1.

IMO, 2021. 2021 Guidelines on survey and certification of the attained Energy Efficiency Existing Ship Index (EEXI). Resolution MEPC.334(76). International Maritime Organization. MEPC 76/15/Add.2.

IMO, 2022a. 2022 Guidelines for the development of a Ship Energy Efficiency Management Plan (SEEMP). Resolution MEPC.346(78). International Maritime Organization. MEPC 78/17/Add.1.

IMO, 2022b. 2022 Guidelines on survey and certification of the Energy Efficiency Design Index (EEDI). Resolution MEPC.365(79). International Maritime Organization. MEPC 79/15/Add.1.

IMO, 2022c. 2022 Guidelines on the method of calculation of the attained Energy Efficiency Design Index (EEDI) for new ships. Resolution MEPC.364(79). International Maritime Organization. MEPC 79/15/Add.1.

IMO, 2023. 2023 IMO Strategy on Reduction of GHG Emissions from Ships. Resolution MEPC.377(80). International Maritime Organization. MEPC 80/WP.12.

IMO, 2024. IMO's work to cut GHG emissions from ships. URL: `https://www.imo.org/en/MediaCentre/HotTopics/Pages/Cutting-GHG-emissions.aspx`.

Kanellos, F., 2013. Optimal power management with ghg emissions limitation in all-electric ship power systems comprising energy storage systems. IEEE Transactions on power systems 29, 330–339.

Kanellos, F.D., Tsekouras, G.J., Hatziargyriou, N.D., 2014. Optimal demand-side management and power generation scheduling in an all-electric ship. IEEE Transactions on Sustainable Energy 5, 1166–1175. doi:`10.1109/TSTE.2014.2336973`.

Maloberti, L., Adami, G., Figari, M., Zaccone, R., 2024. Evaluating alternative fuels and power systems for marine hybrid propulsion. Advances in Maritime Technology and Engineering: Volume 2 , 45doi:`10.1201/9781003508779-5`.

Maloberti, L., Zaccone, R., Gualeni, P., Mazzucchelli, P., 2022. A zero-emission ferry for inland waterways. Progress in Marine Science and Technology 6, 162 – 169. doi:`10.3233/PMST220021`.

Martelli, M., 2015. Marine Propulsion Simulation. De Gruyter Open Poland. doi:`10.2478/9783110401509`.

Martelli, M., Figari, M., 2022. A design framework for combined marine propulsion control systems: From conceptualisation to sea trials validation. Ocean Engineering 254, 111282. URL: `https://www.sciencedirect.com/science/article/pii/S002980182200676X`, doi:`10.1016/j.oceaneng.2022.111282`.

Zaccone, R., Campora, U., Martelli, M., 2021. Optimisation of a diesel-electric ship propulsion and power generation system using a genetic algorithm. Journal of Marine Science and Engineering 9. URL: `https://www.mdpi.com/2077-1312/9/6/587`, doi:`10.3390/jmse9060587`.

Real-time critical marine infrastructure multi-sensor surveillance via a constrained stochastic coverage algorithm

F Ponzini[a], C Fruzzetti[a,*], N Sabatino[a]

[a]*Department of Marine, Electrical, Electronic, Telecomunications Engineering and Naval Architecture (DITEN), Polytechnic School of Genoa University*
*Email: camilla.fruzzetti@edu.unige.it

Synopsis

In recent years, monitoring and protecting marine infrastructure have become increasingly critical. Surface marine vessels can provide valuable support in monitoring structures such as offshore wind farms, data cables, and pipelines. Employing surface vessels with ever-increasing autonomous capabilities allows for increased operation efficiency and strategic advantages. In critical infrastructure monitoring, the area of interest is known in advance, and the aim is to detect anomalies. This paper focuses on developing a guidance, navigation, and control framework suitable for a MASS and tailored for critical infrastructure monitoring missions. The primary goals are developing a stochastic-based coverage algorithm to ensure the surveillance of an area of interest and a real-time compliant shadow vessels monitoring system that provides situational awareness of the above-water surrounding environment, detecting threats and unexpected targets over time. The navigation in the operational environment is ensured by an appropriate proprioceptive sensing layer. The hypotheses and the methodologies are shown and explained in detail, together with the preliminary results reporting the first integration. The results are obtained via computer simulations applied to a wind farm critical infrastructure scenario; additional experimental tests are carried out in indoor and outdoor controlled environments to assess the proposed navigation and control systems capability, involving a marine autonomous surface ships test platform available in the university laboratory. The preliminary results demonstrate the ability of the systems to cooperate in the proposed architecture, monitor an Area Of Interest, detect threats, effectively manoeuvre the vessel in real-time, and estimate its state. Such a framework can be further enhanced by extending the perception capabilities for the underwater domain, integrating multiple control logic to allow for more efficient surveillance strategies, or extending the vessel capabilities beyond surveillance missions, adding capabilities like target chasing.

Keywords: GNC, MASS, critical infrastructure surveillance, dark ship detection, coverage algorithm, situational awareness

1 Introduction

Ocean-related economic activities have experienced exponential growth in the last decades in their outputs and relevance for the global economy. Since the 1960s, offshore oil and gas extraction activities have constantly increased their volume and revenue to the point that a relevant share of global fossil fuels come from the seabed (Jouffray et al., 2020; Jolly, 2016). From 1980 to 2022, the output of container ship trade has quadrupled (UNCTAD, 2022), making maritime trade activities account for 80% of the global trade volume and 70% (UNCTAD, 2017) of its value. Together with well-established seaborne economic activities like trading, ports, and oil and gas extraction, many emerging industrial sectors are participating in this economic boom. Among them, offshore wind farm building and data cable laying will be pivotal in the future economic exploitation of the ocean. The offshore wind farm sector is experiencing high investments as a consequence of the energy transition (Commission, 2023), while more than 95% of all the data that moves around the world goes through undersea data cables, totalling over 900,000 miles sit on the ocean floor (Chataut, 2024), which are bound to increase. This growth of both established and emerging ocean-related economic activities is increasing the reliance of industries and whole countries on maritime infrastructures up to the point that they can now be considered critical for ensuring proper energy and food security as land-based resources rapidly become more scarce (Jouffray et al., 2020).

Threats to critical marine infrastructures may come in various forms, from unintentional harms (Clare, 2021) to deliberate acts (Bueger, 2023; Knights, 2024), usually carried on by dark ships/shadow vessels (Kantchev, 2023), i.e. ships that cover their true intentions by implementing concealing techniques, such as turning off their Automatic Identification System (AIS) device, spoofing their AIS location or using a flag of convenience (Nguyen,

Authors' Biographies

Filippo Ponzini was born in Italy in 1996. He received his B.Sc. and M.Sc. in Naval Architecture and Marine Engineering from Genoa University (Italy) in 2019, 2021. Since November 2022, he is a PhD student in Marine Science and Technologies at the DITEN department of Genoa University. His research activity mainly concerns navigation systems for autonomous vessels and multi-sensor data fusion.

Camilla Fruzzetti was born in Italy in 1995. She received the BSc, the MSs, and the PhD in Naval Architecture and Marine Engineering from the University of Genoa in 2017, 2019, and 2024, respectively. Since November 2023, she is a research fellow at the University of Genoa. Her main research interests concern ship guidance and control logic for autonomous navigation.

Nicola Sabatino was born in Italy in 1999. He studied Naval Architecture and Marine Engineering at the University of Genoa (Italy), earning his B.Sc. and his M.Sc in 2021 and 2023 respectively. He currently is a PhD student at the University of Genoa. His main research interests revolve around the application of symbolic artificial intelligence methods to the problems of autonomous marine collision avoidance.

2023). Critical marine infrastructure vastly differs from land-based ones, mainly because of the challenges posed by conducting operations at sea, so their protection requires tailored solutions. One of the primary solutions to ensure adequate protection of critical marine infrastructure is surveillance and monitoring using Maritime Autonomous Surface Ships (MASS) and Unmanned Underwater Vehicles (UUV) (Bueger and Liebetrau, 2023). Several works have been done in this direction in recent years, mainly thanks to the recent progress in Artificial Intelligence (AI), computing and communication technologies. (Manzari, 2020) and (Ferri et al., 2017) present surveys on significant applications of autonomous vehicles for surveillance operations, the first focusing on both MASSs and UUVs, the second on cooperative networks of UUVs.

The key features that a MASS/UUV-based platform needs for surveillance operations are coverage-driven guidance, collision-free path planning capabilities, and obstacle and target detection. A survey on coverage path planning algorithms is presented by (Tan et al., 2021), which focuses on deterministic algorithms; (Duan and Bullo, 2021), instead, reviews stochastic coverage algorithms based on Markov Chains. (Zadeh et al., 2022) illustrates an optimal collision-free path planning algorithm for multi-surface vessel missions employing particle swarm optimisation, while (Song et al., 2019) adopts the well-known A* algorithm for the same issue. (Zaccone, 2024) presents the use of Dynamic Programming algorithm for collision-free path planning of autonomous ships. The work in (Molina-Molina et al., 2021) describes the adoption of a MASS equipped with cameras for tackling the obstacle and target detection problem; the proposed system adopts deep learning techniques for target detection, which were tested in a port facility. (Zhang et al., 2021b) presents a study on using LiDAR (Light Detection and Ranging) and image processing to achieve target and obstacle detection with a MASS. (Birk et al., 2012) shows an example of a simulated surveillance operation using MASSs: as part of the European project "Cooperative Cognitive Control for Autonomous Underwater Vehicle", they carried out a simulation involving the use of a MASS swarm for a cooperative patrolling operation with a human scuba diver.

This paper presents an integrated solution for the live surveillance of critical marine infrastructure adopting a MASS. The proposed platform, driven by a constrained stochastic coverage algorithm based on Markov Chains, is designed to survey a known domain and detect the presence of shadow vessel intruders using onboard LiDAR. Recent applications (Karaki et al., 2022) have demonstrated the capabilities of such sensors in detecting obstacles and targets, even undetectable by RADARs (Radio Detection and Ranging), in both coastal (Faggioni et al., 2022a,b), and blue-water scenarios (Martelli et al., 2022). This cutting-edge application of MASSs showcases the potential of autonomous maritime technologies in enhancing the security of critical marine infrastructures. This paper presents the overall proposed framework, the single subsystems, and the preliminary results for the final system statement and integration. A testing campaign is carried out on a simulated scenario to evaluate the performances of the high-level guidance algorithms and the perceptive system. Moreover, a series of tests in a real controlled environment is performed to validate the control and state estimation system and interaction with the vessel.

2 Autonomous surveillance platform architecture

The autonomous surveillance platform proposed in this paper follows the Guidance, Navigation, and Control (GNC) paradigm, already widely employed in the literature for defining a MASS (Fossen, 2011). A functional scheme of the developed architecture is shown in Figure 1.

In this application, the guidance system aims to compute the desired pose $\boldsymbol{\eta}_D$ and the desired speed array $\boldsymbol{\nu}_D$ needed to satisfy the critical infrastructure monitoring goal. Its hierarchical structure can be split into three subsystems: the coverage algorithm, which acts as the high-level path planner and defines a target location $\mathbf{WP}_{target}$ to be reached starting from the coverage mission goal, data from Geographic Information System (GIS), and an occupancy grid computed by the navigation system; the collision-free path planning, which computes a path as a series of waypoints $\mathbf{WP}_{list}$ to reach $\mathbf{WP}_{target}$ and updates such path if risk of collision arises; the track keeping, which computes the desired pose $\boldsymbol{\eta}_{TR}$ and speed array $\boldsymbol{\nu}_{TR}$ at each time step needed to follow the defined path.

The control system receives as inputs the desired pose and speed array with their feedback values. To satisfy the guidance aim, it computes the appropriate forces and moment $\boldsymbol{\tau}_C$ in the ship reference frame. This architecture aims to control three Degrees Of Freedom (DOF) and is composed of: the controller, which computes the needed $\boldsymbol{\tau}_C$ to nullify the difference between the desired setpoints and the feedback values as done in (Donnarumma et al., 2022); the force allocation logic, necessary to coordinate the thrusts T_i and the relative angles α_i to be asked to each different actuators to produce $\boldsymbol{\tau}_C$ globally, it is solved with optimisation techniques as in (Fruzzetti et al., 2022); and the thrust allocation logic to compute the relative setpoints for each actuator (the pump-jet angles α_i and revolution speed n_i) thanks to combinator curves.

The desired setpoints are then sent to the MASS. The Shallow Water Autonomous Multipurpose Platform (SWAMP) full-electric catamaran (Odetti et al., 2020) is selected as a test case for the tests in the controlled environment since it is available in the university infrastructure. It can also be adopted for the future integration of the whole architecture and its relative test in a controlled environment representing a scaled model of a critical infrastructure. It is equipped with an Inertial Measurement Unit (IMU), Global Positioning System (GPS) receivers,
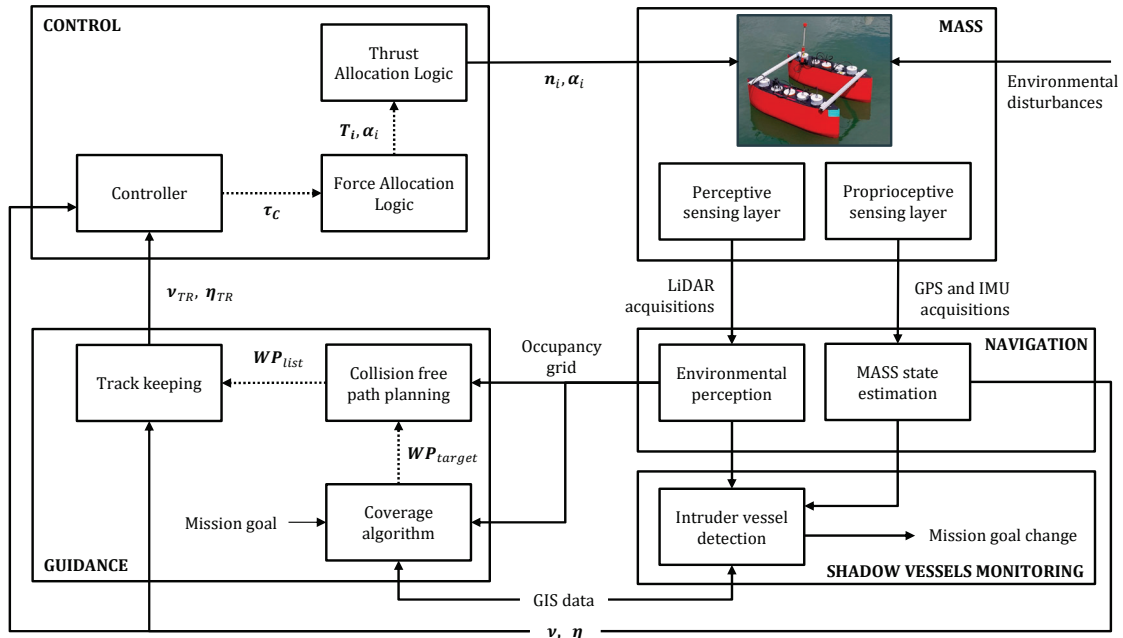
Figure 1: MASS architecture.

and a LiDAR, composing the proprioceptive and perceptive sensing layers of the Navigation system, while the communication is ensured by Wi-Fi.

The navigation system elaborates the information coming from the sensing layers. Two subsystems are present: the environmental perception and the MASS state estimation. The environmental perception module processes the acquisitions of the perceptive sensing layer and computes the obstacles occupancy grid of the operational domain; the MASS state estimation module processes the proprioceptive sensing layer outcome to estimate the vessel generalised pose ($\boldsymbol{\eta}$) and speed ($\boldsymbol{\nu}$).

The shadow vessels monitoring system is the core of the proposed architecture and monitors the operational domain. The inputs are the obstacle grid from the perceptive layer and the GIS data. The system continually analyses the acquisitions and compares them with the GIS data to detect shadow vessels. When the shadow vessel is detected, the surveillance mission can be concluded, and new logic can be triggered according to the operational scenario.

The communication middleware used among the previously described systems is implemented via the Message Queuing Telemetry Transport (MQTT) protocol (Yassein et al., 2017).

3 Reference frames and kinetics

This section presents the reference systems adopted within the paper and the transformations adopted between them. Figure 2 defines the reference frames that will be used throughout the paper:

- The n-frame $\{\boldsymbol{\Omega}, \underline{n}_i\}$ is an inertial Earth-fixed frame. The origin $\boldsymbol{\Omega}$ is located on the mean water-free surface at an appropriate location. The positive unit vector $\underline{n}_1$ points towards the North, $\underline{n}_2$ points towards the East, and $\underline{n}_3$ points downwards.

- The b-frame $\{\boldsymbol{\Omega}_I, \underline{b}_i\}$ is fixed to the vessel hull.The origin, $\boldsymbol{\Omega}_I = x_I \underline{n}_1 + y_I \underline{n}_2$, is located in the middle of the ship length taken along the symmetry axes, and on the waterline. The positive unit vector $\underline{b}_1$ points towards the bow, $\underline{b}_2$ points towards starboard, and $\underline{b}_3$ points downwards.

- The d-frame $\{\boldsymbol{\Omega}_{WP_1}, \underline{d}_i\}$ is fixed with the path defined by the two waypoints selected at each time step ($\boldsymbol{\Omega}_{WP_1}$ and $\boldsymbol{\Omega}_{WP_2}$) by the track keeping guidance. The origin is in $\boldsymbol{\Omega}_{WP_1} = x_{WP_1}\underline{n}_1 + y_{WP_1}\underline{n}_2$, the positive vector $\underline{d}_1$ points towards the vector $(\boldsymbol{\Omega}_{WP_2} - \boldsymbol{\Omega}_{WP_1})$, $\underline{d}_2$ points towards starboard, and $\underline{d}_3$ points downwards.

- The l-frame $\{\boldsymbol{\Omega}_L, \underline{l}_i\}$ is fixed with the on-board LiDAR sensor and is the system in which the point cloud is acquired. Its orientation with respect to system $\underline{b}$ frame depends on the installation and can be modelled as a heading bias δ_ψ.
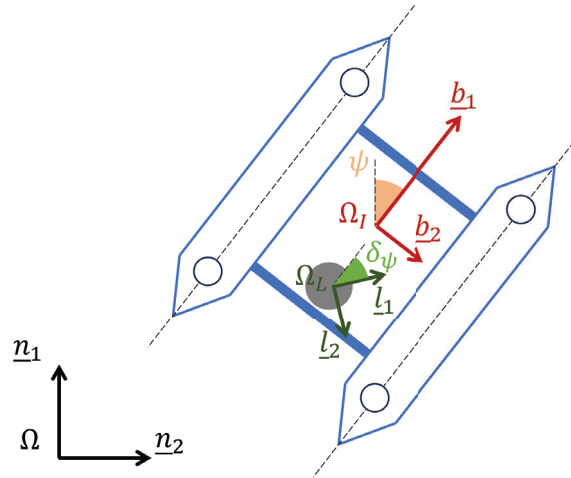
Figure 2: Reference frames.

The reference systems lie in the same plane and are related by the Euler angle and the relative rotations in (1). The generic rotation matrix is shown in (2).

$$\underline{n} = \boldsymbol{R}(\psi)\,\underline{b}, \quad \underline{n} = \boldsymbol{R}(\xi)\,\underline{d}, \quad \underline{n} = \boldsymbol{R}(\psi + \delta_\psi)\,\underline{l}, \tag{1}$$

$$\boldsymbol{R}(\star) = \begin{bmatrix} \cos\star & -\sin\star & 0 \\ \sin\star & \cos\star & 0 \\ 0 & 0 & 1 \end{bmatrix} \tag{2}$$

where ψ is the heading angle, ξ is the angle defined by the vector $(\boldsymbol{\Omega}_{WP_2} - \boldsymbol{\Omega}_{WP_1})$ and $\underline{n}_1$, δ_ψ is the installation heading bias of the LiDAR sensor, and $\star$ is the generic angle between the selected reference frames.

The adopted pose $\boldsymbol{\eta} = [x, y, \psi]$ and speed $\boldsymbol{\nu} = [u, v, r]$ arrays in this paper are, respectively, the positions with respect to the origin of the $\underline{n}$ frame and the heading angle, and the speed components in the $\underline{b}$ frame.

4 Coverage-based guidance strategy

The guidance system aims to compute proper paths and trajectories to guarantee the surveillance of a given Area Of Interest (AOI), i.e. the survey domain, with three subsystems as shown in Figure 1.

The coverage subsystem is the core of the proposed guidance strategies. It is responsible for implementing the high-level guidance, i.e. generating target locations $\mathbf{WP}_{target}$ to fulfil the surveillance mission. The target locations are generated to comply with two constraints: the randomness of the surveillance path and the coverage of the AOI.

To comply with these constraints a Markov Chain-based stochastic coverage algorithm is developed. A Markov Chain is a triple $(\mathcal{M}, \mathcal{G}, m)$ where $\mathcal{M}$ is a stochastic matrix, $\mathcal{G}$ is a connected graph representing the locations in the AOI, and m is the final state of the chain, that corresponds, in this application, to the probability of the MASS being in a specific location after an infinite number of jumps.

The developed stochastic algorithm proceeds as follows. Let $\mathcal{D}$ be a connected domain and $\mathcal{P}$ be a partition of it. The centroids of the elements of $\mathcal{P}$ are the states of the Markov Chain, i.e. the nodes of $\mathcal{G}$, and represent the target locations that the MASS will visit during the surveillance mission. At each iteration, the stochastic coverage algorithm removes from all available locations, i.e. the elements of $\mathcal{P}$, those within a distance d_{prox} from the MASS current location. The new $\mathbf{WP}_{target}$ is chosen randomly from the remaining cells according to a uniform probability distribution. This process is repeated each time the MASS reaches the previously generated target location. The distance d_{prox} is introduced to avoid that the $\mathbf{WP}_{target}$ is too close to the MASS current location. The random choice of $\mathbf{WP}_{target}$ ensures the randomness of the surveillance path, while the coverage of the AOI is ensured by the irreducibility of the Markov Chain, which is ensured by the connectedness of $\mathcal{D}$ (Duan and Bullo, 2021).

The collision-free path planning subsystem is responsible for implementing the guidance path planning and the reactive layer, i.e. it computes a collision-free path as a series of waypoints each time a new target location is computed by the coverage subsystem or each time the MASS faces the risk of collision. It takes as input the pose of the MASS $\boldsymbol{\eta}$, its speed $\boldsymbol{\nu}$, the occupancy grid of the domain, and a target location $\mathbf{WP}_{target}$. The algorithm adopted is described in (Zaccone and Martelli, 2018) and is based on a Rapidly exploring Random Tree (RRT*) path planning algorithm. Several cost functions can be adopted; in this paper, the choice is to penalise longer paths.

The first two subsystems of the guidance system can be coupled following the architecture in Figure 3. Here they act as a guidance system for a holonomic model of the MASS and this architecture can be used to test the performance of the coverage subsystem in a virtual scenario and its ability to interact with the collision-free path planning subsystem.
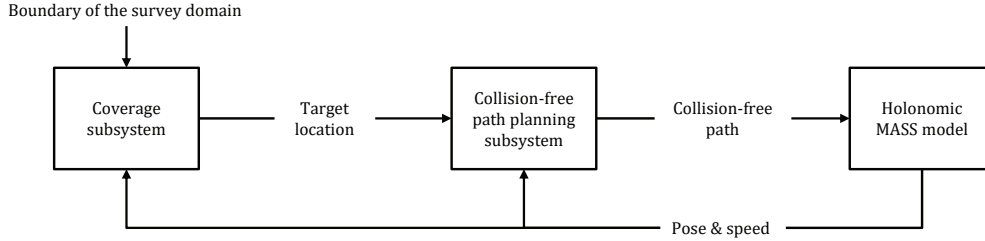
Figure 3: Coverage simulation architecture.

The track keeping subsystem follows the defined path controlling the 3-DOF of the horizontal plane as described in (Fruzzetti et al., 2024). At each time step, two consecutive waypoints are selected from $\mathbf{WP}_{list}$ and the switch at the following waypoints pair occurs when the along-track distance d_{sw} respect to $\mathbf{\Omega}_{WP_2}$ (see Figure 4a) is lower than a given distance. The speed law shown in Figure 4b is defined between each pair of waypoints. Four phases are highlighted to let an acceleration and deceleration phase between a maximum V_{max} and minimum V_{min} speed values in the proximity of the waypoints to increase the precision of the manoeuvre. The desired speed array trajectory results in (3). The desired instantaneous position x_d, the yellow point in Figure 4a, is defined following the kinematics outlined by the speed law and then rotated in $\underline{n}$ to obtain $\boldsymbol{\eta}_D^*$ (4). After each switch between the pairs of waypoints, the desired angle ξ is given with a ramp establishing a heading setpoint ϕ at each time step. The resulting pose array trajectory is reported in (5).

$$\boldsymbol{\nu}_{TR} = [V(t) \ 0 \ 0]^T \tag{3}$$

$$\boldsymbol{\eta}_D^* = \boldsymbol{R}(\xi)[x_d \ 0 \ 0]^T + \boldsymbol{\Omega}_{WP_1} \tag{4}$$

$$\boldsymbol{\eta}_{TR} = [\boldsymbol{\eta}_D^*(1:2) \ \phi]^T \tag{5}$$

5 MASS state estimation feedback

Effective vessel state estimation is crucial for the guidance and control systems and to enable the MASS to fulfil its tasks effectively. Thus, the navigation system must incorporate appropriate sensing layer processing to extract valuable information and construct the state vector, measuring and estimating the necessary quantities. The vessel state estimation vessel subsystems primarily rely on a Linear Kalman Filter (LKF) (Maybeck, 1990) with a fully kinematic constant velocity state transition model. Since the LKF state-space model is expressed in the inertial $\underline{n}$ frame, the speed component of the state x are rotated in the body frame $\underline{b}$ following the rotations in (1) to lead to the feedback state $x_{fbk} = [\boldsymbol{\eta}, \boldsymbol{\nu}]$.

Mainly, two use cases are planned: indoor preliminary tests and operational environment missions with the consequent use of a dedicated sensing layer for each setup, as shown in Figure 5. Both setups are based on the same LKF, which is adapted to receive a different measurement z by adjusting the observation matrix and the error models of the filter. Indeed, GPS cannot be used appropriately during indoor tests necessary for preliminary validations due
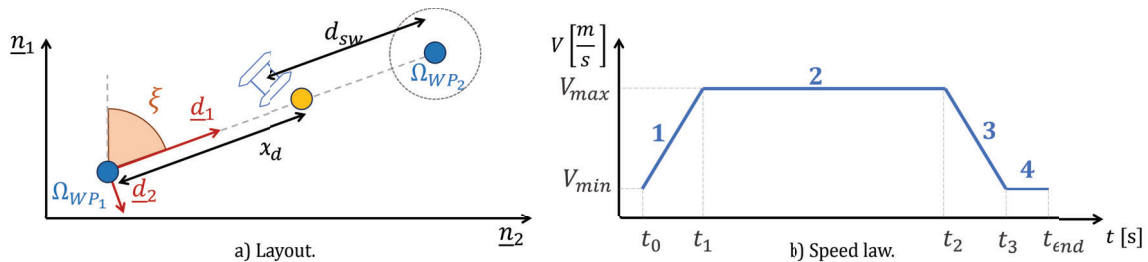
Figure 4: Track Keeping motion control scenario.
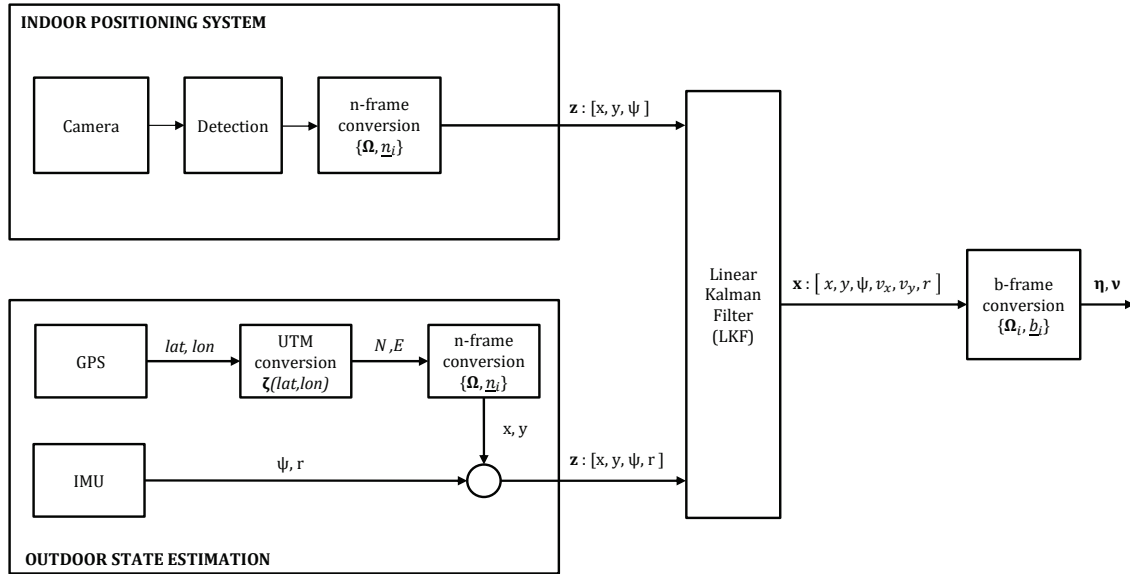
Figure 5: State estimation general pipeline.

to the lack of line-of-sight with satellites; hence, the Indoor Positioning System (IPS) presented in (Ponzini et al., 2023) is used. The resulting LKF measurement vector z is $[x, y, \psi]$, and the system can ensure the tests of development logic from the initial steps since the onboard mounted proprioceptive sensors are not involved. During the operating life, the vehicle state must be estimated based on the onboard GPS and IMU. The GPS provides the latitude and longitude measures, while the IMU provides the heading angle ψ and the rate of turn r via the embedded gyroscope and magnetometer. The general GPS position (lat_p, lon_p) is first reported in Universal Transverse Mercator (UTM) coordinates (Snyder, 1987), using local Easting and Northing coordinates. Then, considering the inertial $\underline{n}$ frame placed in the suitable location Ω of known coordinates (lat_Ω, lon_Ω), GPS position data can be expressed in the $\underline{n}$ frame according to (6). The resulting LKF measurement vector z is $[x, y, \psi, r]$.

$$z(1:2) = \zeta(lat_P, lon_P,) - \zeta(lat_\Omega, lon_\Omega) \tag{6}$$

where ζ refers to the UTM conversion function.

6 Environmental perception

Environmental perception aims to obtain information on the surrounding obstacles and targets and is crucial to safely and effectively fulfilling the mission goal. In this paper, environmental perception is entrusted to an onboard LiDAR and the obstacle detection is achieved using the occupancy grid method. Such an approach allows for fast and streamlined processing, bypassing time-consuming clustering methods, and can be effectively integrated with GIS data (Goodchild, 2009). The point cloud X^{LiDAR} is first projected onto the $\underline{l}_1, \underline{l}_2$ plane defined by the $\underline{l}$ frame and is sub-sampled to construct a list of obstacle-point Λ^{LiDAR}. The domain is divided into a grid of size ϵ, and each box occupied by at least one point of the LiDAR point cloud is considered full, leading to an obstacle point placed in its centroid. A large obstacle can be rendered with only a few obstacle points choosing the ϵ parameter compatibly with the collision-free path planner detailed in Section 4. This allows the rich information set of the point cloud X^{LiDAR} to be condensed into a lean list of obstacle-points Λ^{LiDAR}, obtaining the same result.

7 Shadow vessels monitoring

The obstacle-point set obtained from the environmental perception subsystem can be exploited to detect anomalies in the AOI, like dark ships/shadow vessels, and achieve the surveillance goal.

In this paper, the search is primarily oriented to AIS unequipped vessels or ones that intentionally keep it off and are not detectable by long-range RADARs. By cross-referencing GIS data, other prior information data such as AIS, and the obtained LiDAR point cloud, intruder vessels can be detected by subtraction. Figure 6 illustrates the entire shadow vessel detection pipeline. The MASS strategic operational environment is considered known; GIS morphology data are available, as well as other a priori information (AIS data, navigation information, etc.). The onboard LiDAR acquires the point cloud of the surrounding environment in $\underline{l}$ frame. A sub-sampled list of
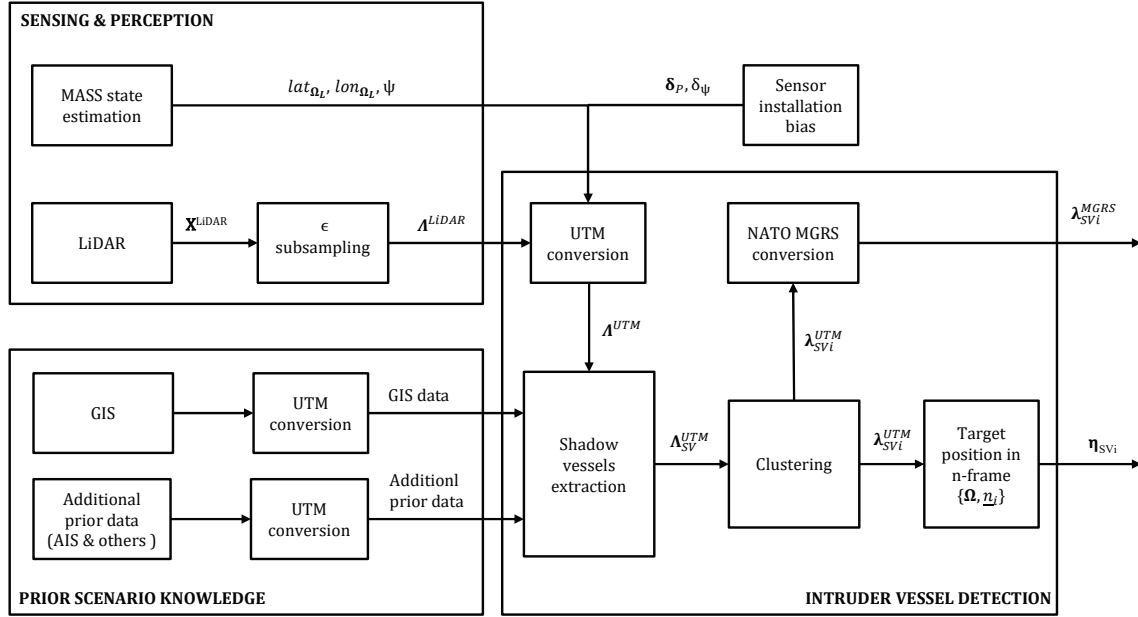
Figure 6: shadow vessels monitoring pipeline.

obstacle points $\mathbf{\Lambda}^{LiDAR}$ is derived from $\boldsymbol{X}^{LiDAR}$, according to Section 6, to reduce computational load. The obstacle points are then reported in UTM Easting-Northing coordinates ($\mathbf{\Lambda}^{UTM}$) according to (7), knowing the pose η of the supervising MASS by the state estimation feedback as given in Section 5. A likely bias $\boldsymbol{\delta}_P = \epsilon_x \underline{l}_1 + \epsilon_y \underline{l}_2$ on the position of LiDAR and GPS receiver is considered due to physical installation, in addition to the LiDAR installation bias δ_ψ.

$$\mathbf{\Lambda}^{UTM} = \boldsymbol{R}(\psi + \delta_\psi)\mathbf{\Lambda}^{LiDAR} + \boldsymbol{R}(\psi + \delta_\psi)\boldsymbol{\delta}_P + \boldsymbol{\zeta}(lat_{\mathbf{\Omega_L}}, lon_{\mathbf{\Omega_L}}) \tag{7}$$

All multi-source information is expressed in the same UTM reference frame, extracting on a geometrical basis the obstacle points that do not belong to any expected agent, i.e. spotting the shadow vessels. A buffer zone around known objects is carefully selected to mitigate sensor, positioning, and ego-motion errors. The $\mathbf{\Lambda}^{UTM}$ obstacle-points list is thus divided into environment-related obstacles $\mathbf{\Lambda}_{env}^{UTM}$, including information about objects known in advance, and shadow-vessel obstacle-points $\mathbf{\Lambda}_{SV}^{UTM}$.

Unsupervised learning clustering is used to separate individual shadow-vessels within the obstacle-points list $\mathbf{\Lambda}_{SV}^{UTM}$ providing a set of single vessel obstacle-points cluster $\boldsymbol{\lambda}_{SVi}^{UTM}$; by iterating through the list of clusters, the location of each can be easily calculated as the average (μ) of each cluster point cloud. The UTM locations can be easily converted to NATO Military Grid Reference System (MGRS) (Hager et al., 1992), as well as expressed in the $\underline{n}$ frame, constituting part of the shadow vessel pose vector $\boldsymbol{\eta}_{SV}$, according to (8).

$$\boldsymbol{\eta}_{SV_i}(1:2) = \mu(\boldsymbol{\lambda}_{SV_i}^{UTM}) - \boldsymbol{\zeta}(lat_{\mathbf{\Omega}}, lon_{\mathbf{\Omega}}) \quad for \quad \boldsymbol{\lambda}_{SV_i}^{UTM} \quad in \quad \mathbf{\Lambda}_{SV}^{UTM} \tag{8}$$

8   Results

This section reports the preliminary results obtained to validate the proper functioning of the architecture and the integrability of its components. The steps to reach the final aim of testing the proposed architecture in a real critical scenario are summarised in the following phases:

I. Architecture definition and requirements specification of each subsystem needed for the integration in the overall architecture. It is done in the previous sections of this paper.

II. Individual subsystem testing (computer simulation). Each subsystem is tested individually using computer simulation. This preliminary phase is essential for subsystem development.

III. Integration and testing in a virtual scenario. Tests in a virtual scenario representing a critical infrastructure using computer simulation are carried out. The results reported for this stage include the coverage-based guidance strategy, environmental perception, and shadow vessels monitoring systems in a wind farm scenario.

(a) Discretized AOI.

(b) Coverage algorithm final state estimate after 500 iterations.
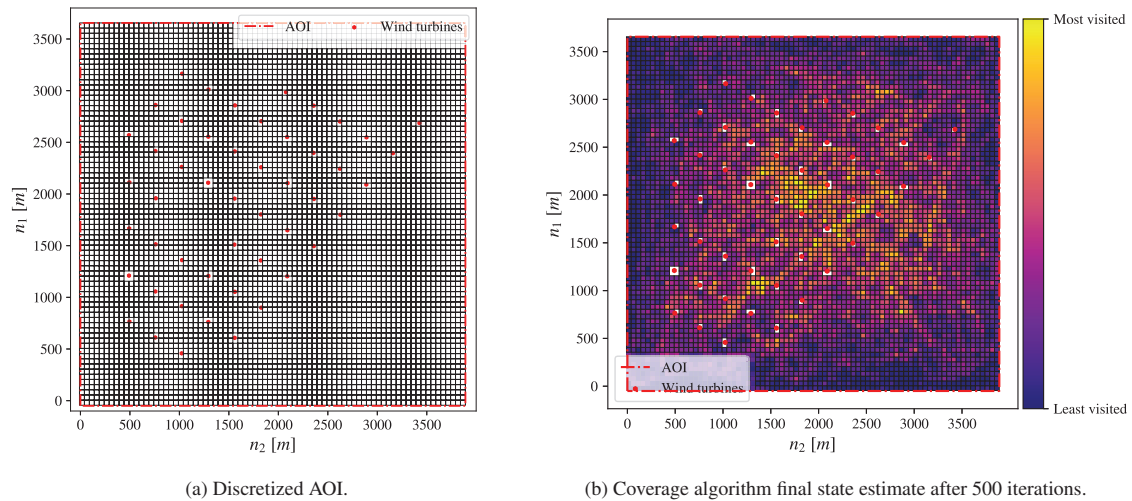
Figure 7: Surveillance simulation.

IV. Physical MASS testing in a controlled indoor scenario. The physical MASS (SWAMP vessel) available in the university infrastructure is selected as a test bed, and selected subsystem integrations in a controlled, indoor scenario are done to verify the potential use of SWAMP. Results for this stage are reported, regarding the control system and state estimation subsystem applied to SWAMP in the university test tank.

V. Outdoor test. The selected integrated systems are used in an outdoor environment to assess functionality that is not testable in the indoor test tank; results for this stage are reported and consist of state estimation subsystem results.

VI. Complete integration and model-scale testing. The proposed architecture with the physical MASS SWAMP can be fully integrated and tested in a real environment, representing a scaled model of the critical infrastructure. It will be the object of future studies.

VII. Operative environment test. The proposed architecture can be extended to a real surveying MASS in the operative AOI. It will be the object of future studies.

The first set of results is carried out in a virtual environment representing the Lillgrund Wind Farm (Sweden) through its GIS data gathered from the Global Offshore Wind Turbine dataset (Zhang et al., 2021a). It aims to test the coverage of the selected area from the coverage algorithm, the computation of a safe path from the collision-free path planner, the capacity of the environmental perception subsystem to perceive the surrounding environment, and the identification of a possible intruder from the shadow vessels monitoring system covering testing phase III. The virtual AOI is shown in Figure 7a. The discretisation has been performed using Shapely Python library (Gillies et al., 2024) producing square-like cells of $50\,m$ sides; cells overlapping with turbines have been removed. Then, the simulation layout described in Figure 3 is applied to assess the final state m of the stochastic coverage algorithm. The resulting heatmap representing m, however, how much a cell of the discretized AOI has been visited by the holonomic model, is shown in Figure 7b. The virtual scenario is then coupled with real acquired LiDAR scans to simulate a surveillance operation where the onboard LiDAR acquires the surrounding environment, the shadow vessels monitoring system compares the ϵ sub-sampled point cloud ($\epsilon = 1\,m$) with the available GIS data, and the vessel is moving in a subset of the path previous computed and shown in magenta in Figure 8 as a polyline between the WP_{target} marked with the orange triangles, and the WP_{list} marked with the blue circles. The shadow vessels monitoring system continues to compare the LiDAR sub-sampled scans with GIS data until the presence of an intruder vessel is reported. Figure 9a shows the point cloud acquired in the virtual scenario, while Figure 9b shows the shadow vessels monitoring comparison operation. The wind turbine obstacle points are shown in blue and are superimposed on the GIS shape (brown) with its $5\,m$ buffer zone shown in green; the detected shadow vessel, not overlaying any operational environment GIS data, is marked

in red and represents $\mathbf{\Lambda}_{SV}$. From the results, it is possible to see that the objectives set have been achieved.
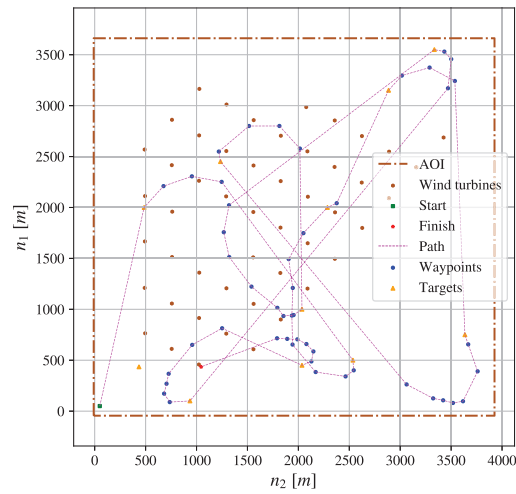
Figure 8: Slice of the surveillance path.

(a) LiDAR scan.

(b) Multi-source scenario.
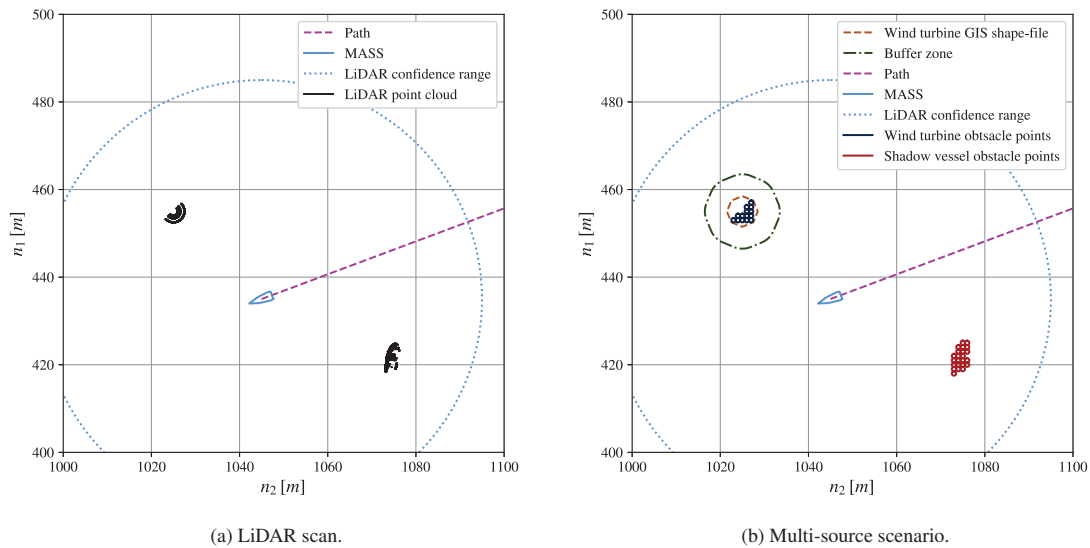
Figure 9: shadow vessels monitoring.

The second set of results is carried out in the indoor test tank to assess the estimation and the control capability of the MASS state estimation, the control, and the track keeping subsystems, corresponding to testing phase IV. The vessel moves between four waypoints with different heading angles. The trajectory acquired from the IPS and filtered through the LKF is marked in blue in Figure 10a, where the green waterline represents the starting point and the red one identifies the endpoint. The black intermediate waterlines are aligned with the estimated heading angle and are reported at a constant time interval in real dimensions. Figure 10b shows the two speed components in $\underline{n}$ at which MASS navigated during the manoeuvre. The speeds observed through the LKF are marked in red, while the speeds calculated as a time differential from the positions are marked in black; to compare the two results, the calculated speeds are filtered via a second-order Exponential Moving Average Filter (EMAF) with a weight factor of 0.6. The results show that SWAMP can be used as a test bed and that the state estimation subsystem can be used and transported to an outdoor environment.

The third set of results covers test phase V and is carried out in an artificial lake to validate the state estimation architecture using onboard sensors. The position is acquired using GPS, while the heading angle ψ and the rotation speed r are measured with the IMU. Figure 11 presents the results obtained using the same layout adopted for pre-

(a) Trajectory.

(b) Observed and calculated speeds.
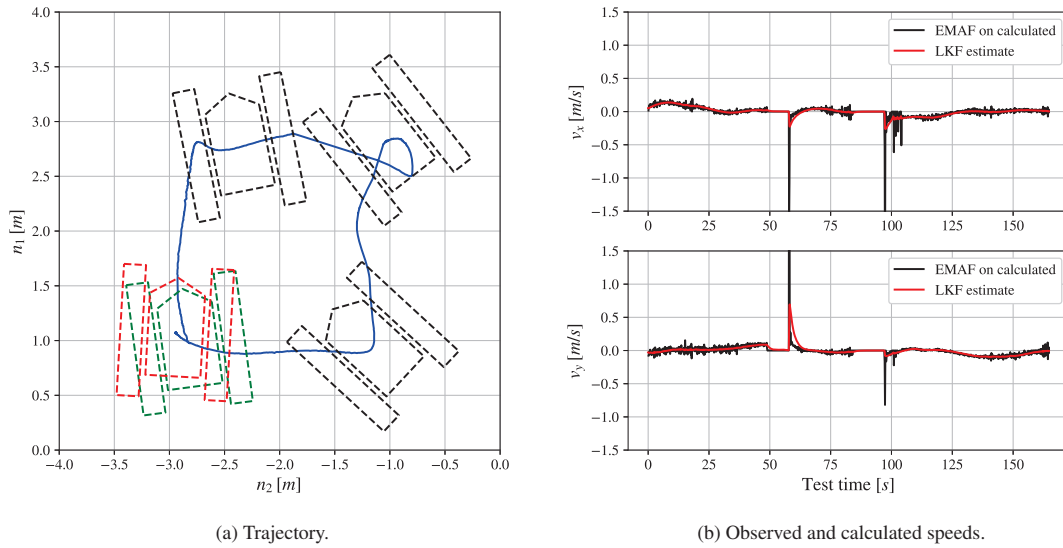
Figure 10: Indoor experimental test.

senting the results of Figure 10. The higher spikes observed are attributed to the greater measurement error of the GPS if compared to the indoor IPS and to the different acquisition frequencies. Despite the noisy measurement, the filter effectively estimates the velocities, mitigating sudden oscillations. The results show that the state estimation system can also be used successfully outdoors.

(a) Trajectory.

(b) Observed and calculated speeds.
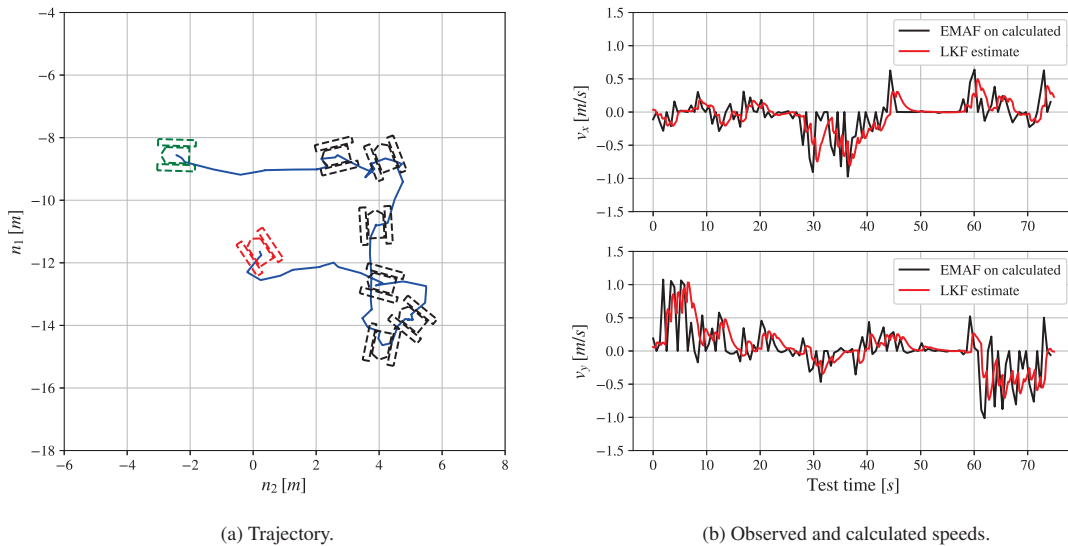
Figure 11: Outdoor experimental test.

9 Conclusions and further research

This paper presents a MASS architecture for critical infrastructure monitoring missions. The preliminary results obtained and presented demonstrate the ability of the proposed architecture to achieve its proper functioning and the integrability of its components. The real data-based simulation of the high-level guidance and perception coupled systems shows the ability of the proposed architecture to safely and effectively patrol an area of strategic

importance, detecting anomalies by cross-referencing LiDAR acquisitions with multi-source information. The tests in indoor and outdoor controlled environments demonstrate the architecture ability to control the MASS and estimate its state as well as the integrability of the proposed systems, capable of working synergically in real-time. The limitations currently encountered concern the triggering of the reactive guidance system and environmental perception based on a single sensor and integration of the entire architecture with the consequent test in the scaled and real test case. The perceptive layer needs further improvement by incorporating multi-sensor data fusion, considering both underwater and above-the-water situational awareness. Additional studies and tests can also be carried out by integrating different frameworks to take into account the mission change when the shadow vessel is detected. Hence, a bumpless function can be added to switch to control logic in 2-DOF and apply a law that allows, for example, to follow the shadow vessel or to track the shadow vessel with reactive logic.

Acknowledgement

References

Birk, A., Pascoal, A., Antonelli, G., Caiti, A., Casalino, G., Indiveri, G., Caffaz, A., 2012. Cooperative Cognitive Control for Autonomous Underwater Vehicles (CO3AUVs): overview and progresses in the 3rd project year. IFAC Proceedings Volumes 45, 361–366. doi:https://doi.org/10.3182/20120410-3-PT-4028.00060. 3rd IFAC Workshop on Navigation, Guidance and Control of Underwater Vehicles.

Bueger, C., 2023. Russian Spy Ship in North Sea raises concerns about the vulnerability of key maritime infrastructures. URL: https://theconversation.com/russian-spy-ship-in-north-sea-raises-concerns-about-the-vulnerability-of-key-maritime-infrastructure-204205. accessed on 13/05/2024.

Bueger, C., Liebetrau, T., 2023. Critical maritime infrastructure protection: What's the trouble? Marine Policy 155, 105772. doi:https://doi.org/10.1016/j.marpol.2023.105772.

Chataut, R., 2024. Undersea cables are the unseen backbone of the global internet. URL: https://theconversation.com/undersea-cables-are-the-unseen-backbone-of-the-global-internet-226300.

Clare, M., 2021. Submarine Clable Protection and the Environment. An Update from the ICPC. URL: https://www.iscpc.org/publications/submarine-cable-protection-and-the-environment/ICPC_Public_EU_March%202021.pdf.

Commission, E., 2023. Eu Wind Power Action Plan. URL: https://eur-lex.europa.eu/legal-content/EN/TXT/PDF/?uri=CELEX:52023DC0669.

Donnarumma, S., Fruzzetti, C., Martelli, M., Chiti, R., Pecoraro, A., Sebastiani, L., 2022. Rapid prototyping for enhanced dynamic positioning systems, p. 641 – 649. doi:10.3233/PMST220075.

Duan, X., Bullo, F., 2021. Markov chain–based stochastic strategies for robotic surveillance. Annual Review of Control, Robotics, and Autonomous Systems 4, 243–264. doi:https://doi.org/10.1146/annurev-control-071520-120123.

Faggioni, N., Leonardi, N., Ponzini, F., Sebastiani, L., Martelli, M., 2022a. Obstacle Detection in Real and Synthetic Harbour Scenarios, in: Modelling and Simulation for Autonomous Systems, Springer International Publishing, Cham. pp. 26–38. doi:https://doi.org/10.1007/978-3-030-98260-7_2.

Faggioni, N., Ponzini, F., Martelli, M., 2022b. Multi-obstacle detection and tracking algorithms for the marine environment based on unsupervised learning. Ocean Engineering 266, 113034. doi:https://doi.org/10.1016/j.oceaneng.2022.113034.

Ferri, G., Munafò, A., Tesei, A., Braca, P., Meyer, F., Pelekanakis, K., Petroccia, R., Alves, J., Strode, C., LePage, K., 2017. Cooperative robotic networks for underwater surveillance: an overview. IET Radar, Sonar & Navigation 11, 1740–1761. doi:https://doi.org/10.1049/iet-rsn.2017.0074.

Fossen, T.I., 2011. Handbook of marine craft hydrodynamics and motion control. John Wiley & Sons. doi:10.1002/9781119994138.

Fruzzetti, C., Donnarumma, S., Martelli, M., Maggiani, F., 2022. Dynamic positioning operability assessment by using thrust allocation optimization, in: Sustainable Development and Innovations in Marine Technologies. CRC Press, pp. 25–32.

Fruzzetti, C., Martelli, M., Lekkas, A., Skjetne, R., Breivik, M., 2024. Model-based motion control design for the

milliampere1 prototype ferry, in: 2024 European Control Conference (ECC), pp. 3636–3643. doi:`10.23919/ECC64448.2024.10591071`.

Gillies, S., van der Wel, C., Van den Bossche, J., Taves, M.W., Arnott, J., Ward, B.C., et al., 2024. Shapely. URL: `https://github.com/shapely/shapely`, doi:`10.5281/zenodo.5597138`.

Goodchild, M.F., 2009. Geographic information systems and science: today and tomorrow. Procedia Earth and Planetary Science 1, 1037–1043. doi:`https://doi.org/10.1016/j.proeps.2009.09.160`. special issue title: Proceedings of the International Conference on Mining Science & Technology (ICMST2009).

Hager, J.W., Fry, L.L., Jacks, S.S., Hill, D.R., 1992. Datums, Ellipsoids, Grids, and Grid Reference Systems. Defense Technical Information Center. doi:`10.21236/ada247651`.

Jolly, Claire, O., 2016. The ocean economy in 2030, in: Proceedings of the Workshop on Maritime Cluster and Global Challenges 50th Anniversary of the WP6, Paris, France. doi:`https://doi.org/10.1787/9789264251724-en`.

Jouffray, J.B., Blasiak, R., Norström, A.V., Österblom, H., Nyström, M., 2020. The Blue Acceleration: The Trajectory of Human Expansion into the Ocean. One Earth 2, 43–54. doi:`https://doi.org/10.1016/j.oneear.2019.12.016`.

Kantchev, G., 2023. Sweden Says Second Undersea Cable Damaged in Baltic Sea. URL: `https://www.wsj.com/world/europe/sweden-says-second-undersea-cable-damaged-in-baltic-sea-d9f21fea`.

Karaki, A.A., Bibuli, M., Caccia, M., Ferrando, I., Gagliolo, S., Odetti, A., Sguerso, D., 2022. Multi-Platforms and Multi-Sensors Integrated Survey for the Submerged and Emerged Areas. Journal of Marine Science and Engineering 10. doi:`10.3390/jmse10060753`.

Knights, M., 2024. Assessing the Houthi War Effort Since October 2023. URL: `https://www.washingtoninstitute.org/policy-analysis/assessing-houthi-war-effort-october-2023`.

Manzari, D.T.L.B.A.C.R.C.V., 2020. Marine Robots for Underwater Surveillance doi:`https://doi.org/10.1007/s43154-020-00028-z`.

Martelli, M., Faggioni, N., Ponzini, F., 2022. Detecting and Tracking Multi-Object in Real Marine Environment, in: Proceedings of the International Ship Control Systems Symposium. doi:`https://doi.org/10.24868/10707`.

Maybeck, P.S., 1990. The Kalman Filter: An Introduction to Concepts. Springer New York, New York, NY. pp. 194–204. doi:`10.1007/978-1-4613-8997-2_15`.

Molina-Molina, J.C., Salhaoui, M., Guerrero-González, A., Arioua, M., 2021. Autonomous marine robot based on ai recognition for permanent surveillance in marine protected areas. Sensors 21, 2664. doi:`https://doi.org/10.3390/s21082664`.

Nguyen, T., 2023. The challenges of dark ships to the safety and security of commercial shipping and the way forward. Asia-Pacific Journal of Ocean Law and Policy 8, 310 – 328. URL: `https://brill.com/view/journals/apoc/8/2/article-p310_007.xml`.

Odetti, A., Bruzzone, G., Altosole, M., Viviani, M., Caccia, M., 2020. SWAMP, an autonomous surface vehicle expressly designed for extremely shallow waters. Ocean Engineering 216, 108205. doi:`https://doi.org/10.1016/j.oceaneng.2020.108205`.

Ponzini, F., Zaccone, R., Martelli, M., 2023. A multi-sensor indoor tracking system for autonomous marine model-scale vehicles. Journal of Physics: Conference Series 2618, 012008. doi:`10.1088/1742-6596/2618/1/012008`.

Snyder, J.P., 1987. Map projections: A working manual, in: Professional Paper. U.S. Government Printing Office. volume 1395. doi:`https://doi.org/10.3133/pp1395`.

Song, R., Liu, Y., Bucknall, R., 2019. Smoothed A* algorithm for practical unmanned surface vehicle path planning. Applied Ocean Research 83, 9–20. doi:`https://doi.org/10.1016/j.apor.2018.12.001`.

Tan, C.S., Mohd-Mokhtar, R., Arshad, M.R., 2021. A Comprehensive Review of Coverage Path Planning in Robotics Using Classical and Heuristic Algorithms. IEEE Access 9, 119310–119342. doi:`10.1109/ACCESS.2021.3108177`.

UNCTAD, 2017. Review of Maritime Transport 2017. URL: `https://unctad.org/system/files/official-document/rmt2017_en.pdf`.

UNCTAD, 2022. Review of Maritime Transport 2022. URL: `https://unctad.org/system/files/official-document/rmt2022_en.pdf`.

Yassein, M.B., Shatnawi, M.Q., Aljwarneh, S., Al-Hatmi, R., 2017. Internet of Things: Survey and open issues of MQTT protocol, in: 2017 International Conference on Engineering & MIS (ICEMIS), pp. 1–6. doi:`10.1109/ICEMIS.2017.8273112`.

Zaccone, R., 2024. A dynamic programming approach to the collision avoidance of autonomous ships. Mathematics 12. doi:`10.3390/math12101546`.

Zaccone, R., Martelli, M., 2018. A random sampling based algorithm for ship path planning with obstacles, in: Conference Proceedings of iSCSS. doi:`https://doi.org/10.24868/issn.2631-8741.2018.018`.

Zadeh, S.M., Abbasi, A., Yazdani, A., Wang, H., Liu, Y., 2022. Uninterrupted path planning system for Multi-USV sampling mission in a cluttered ocean environment. Ocean Engineering 254, 111328. doi:`https://doi.org/10.1016/j.oceaneng.2022.111328`.

Zhang, T., Tian, B., Sengupta, D., Zhang, L., Si, Y., 2021a. Global offshore wind turbine dataset. Scientific Data 8, 191.

Zhang, W., Jiang, F., Yang, C.F., Wang, Z.P., Zhao, T.J., 2021b. Research on Unmanned Surface Vehicles Environment Perception Based on the Fusion of Vision and Lidar. IEEE Access 9, 63107–63121. doi:`10.1109/ACCESS.2021.3057863`.

MINION:
Modular and Independent Navigational Intelligent Orientable Nozzle-Thruster

A. Odetti, [a*], M. Caccia [a], G. Bruzzone [a]

[a]CNR-INM, National Research Council of Italy, Institute of Marine Engineering, Italy
*Corresponding author. Email: angelo.odetti@cnr.it

Synopsis

The MINION concept, standing for Modular Independent Navigational Intelligent Orientable Nozzle-Thruster, encapsulates a modular propulsion unit designed for Unmanned Marine Vehicles (UMVs) with power, communication, computing power, sensors (GNSS, IMU), and directional thrust within a compact, watertight module.
In other words the MINION concept posits that a modular directional thruster can work as a simple robotic vehicle, being equipped with all the sub-systems required to do it. Sets of MINION units can be suitably connected through mechanical frames and/or hulls to constitute different shape UMVs.
The propulsion system is designed for UMV applications requiring modularity, redundancy, and independence, enhancing portability, design flexibility, and cable elimination. MINION operates using a mixed-flow or centrifugal pump, achieving precise 360° thrust control through a steerable nozzle, thereby optimizing maneuverability in marine environments. When integrated into an Autonomous Surface Vehicle (ASV), MINION functions as a propulsion and steering unit, computing element, navigation sensor package, and energy source, offering protection during bottom collisions. Moreover, the MINION architecture is designed to facilitate automated adherence to FAIR (Findable, Accessible, Interoperable, Reusable) data principles. This includes the promotion of standardized variable naming conventions, thereby enhancing the interoperability and reusability of data generated by marine robotic systems.

Keywords: Thruster; Pump-Jet; ASV; USV; Modular; Dynamic Positioning

1 Introduction

Oceans, covering 71% of the Earth's surface, play a crucial role in regulating climate, supporting economies, and sustaining life. They act as carbon sinks, absorbing one-third of CO_2 emissions since the Industrial Revolution through marine processes such as *blue carbon* (Macreadie et al., 2019). Industries such as fisheries, shipping and energy depend on oceans, making sustainable management vital. Oceans influence climate patterns, generate half of the oxygen on Earth, and affect global weather systems. However, rising sea levels and extreme weather events due to climate change threaten coastal ecosystems and human settlements (Church et al., 2013; Antonioli et al., 2017).

Unmanned Surface Vehicles (USVs) offer a cost-effective solution to monitor ocean environments. Unlike traditional marine survey methods, USVs provide advantages in time efficiency, coverage, and resilience in extreme conditions (Bruzzone et al., 2020). They are deployed for environmental monitoring, hydrological exploration, search and rescue, and military applications such as antisubmarine operations. USVs also facilitate research in autonomous technologies such as navigation algorithms (Xing et al., 2023), collision avoidance (Zaccone and Martelli, 2020), and berthing (Wu et al., 2024).

This paper introduces a novel modular propulsion system for USVs, called MINION—Modular Independent Navigational Intelligent Orientable Nozzle-Thruster. MINION integrates power, communication, intelligence, Global navigation satellite system (GNSS) receiver, Inertial Measurement Unit (IMU) sensors, and thrust directionality into a single, watertight unit. Developed under the project (Odetti et al., 2020c), MINION enhances the capabilities of the SWAMP (Shallow Water Autonomous Multipurpose Platform) class of Autonomous Surface Vehicles (ASVs), initially designed for wetland monitoring. Beyond this, the system supports research in hydrodynamics (Pellegrini et al., 2023), propulsion (Odetti et al., 2019), and marine robotics (Odetti et al., 2020b). Its modular design offers flexibility and scalability, addressing various marine engineering challenges while contributing to the broader goal of improving marine technology.

2 Objectives

The primary scope of this paper is to introduce and validate the MINION propulsion system as a modular and autonomous solution for Unmanned Maritime Vehicles (UMV). The specific objectives and requiremetns we set out to achieve include the following:

- Enhanced Modularity and Flexibility: To design a propulsion unit that integrates key functions—power, communication, intelligence, and thrust—into a single compact, modular component, allowing for easy adaptation and integration with various UMV platforms.

- Improved Autonomy and reliability: To develop a system that supports advanced autonomous operations by incorporating onboard computing, navigation sensors, and wireless communication, thereby reducing the dependency on external systems and cables.

- Robust Performance also in Challenging Environments: To ensure that the propulsion system is capable of reliable operation in diverse and harsh marine environments, such as shallow waters, by utilizing a Pump-Jet principle for propulsion and thrust control.

- Integration and Data Management: To facilitate integration with existing marine robotics systems and adhere to FAIR data principles, enhancing data accessibility, interoperability, and usability across different research and operational contexts.

By fulfilling these requirements, the MINION system seeks to enhance the capabilities of UMVs, making them more adaptable, efficient, and applicable in various marine scenarios. The subsequent sections will illustrate how these goals are achieved through the design, implementation, and testing of the MINION propulsion unit.

3 State of the Art

MINION is a modular system that arises from the idea of creating a propulsion system engineered for various applications of unmanned Maritime Vehicle (UMV). The design principles of MINION are rooted in the imperative for modular, redundant, and independent systems, catering to exigencies such as robot portability, design flexibility, and cable removal. Functioning at a good level of autonomy, MINION establishes a paradigm in propulsion, integrating into UMV platforms.

Modularity (Chen and Liu, 2022) and interoperability are two critical keywords in the field of marine robotics. They ensure cost reduction, adaptability, and evolution throughout a system's life cycle. Modularity in marine robotics refers to the design and organization of systems into separate and interchangeable modules. According to Costanzi et al. (2020) this allows:

- Component Separation: Modularity involves breaking down a system into discrete components or modules. Each module performs a specific function and can be replaced or upgraded independently.

- Interchangeability: Modules are designed to be interchangeable. If one module fails or needs an upgrade, it can be swapped out without affecting the entire system.

- Cost Efficiency: Modularity reduces costs by allowing targeted maintenance and upgrades. It also facilitates adaptation to new technologies over the system's life cycle.

- Standardization: Open standards and architectures enhance modularity. Common interfaces and protocols enable seamless integration of different modules.

Modularity ensures flexibility, scalability, and efficient system management and for this reason "Modular" has become an important keyword in robotics as shown in fig. 1 where a research made in SCOPUS shows a clear trend in the presence of this keyword in robotics research. For this reason especially AUVs are designed in a modular way with middle section expandable by predefined payload sections. Examples are MARES AUV (Cruz and Matos, 2008) or the Starfish AUV (Sangekar et al., 2008). The hybrid vehicles like e-URoPe (Odetti et al., 2017a) and the Ecorobotics vehicle P2-ROV (Odetti et al., 2017b), are built from predefined modules while vehicles like TriMARES (Ferreira et al., 2012), are built from existing vehicles (Ferreira et al., 2010). The recently published MUM-vehicle (Ritz et al., 2019) is a large scale AUV, modularly configured of predefined and customized modules for deep-sea operations.

Also modular control strategies are design to be adaptable to various USVs (Müller et al., 2020).

The seek of modularity brought, in the recent years, to reduce the size of vehicles keeping modularity as a key point (Yang et al., 2024; Paraschos and Papadakis, 2021) and to develop various modules (Falcão Carneiro et al., 2022; Gutiérrez-Flores and Bachmayer, 2022) In particular, Tolstonogov et al. (2020) proposed a module that consists of a cylindrical housing, two endcups with wireless power transfer system (Martínez de Alegría et al., 2024) in each
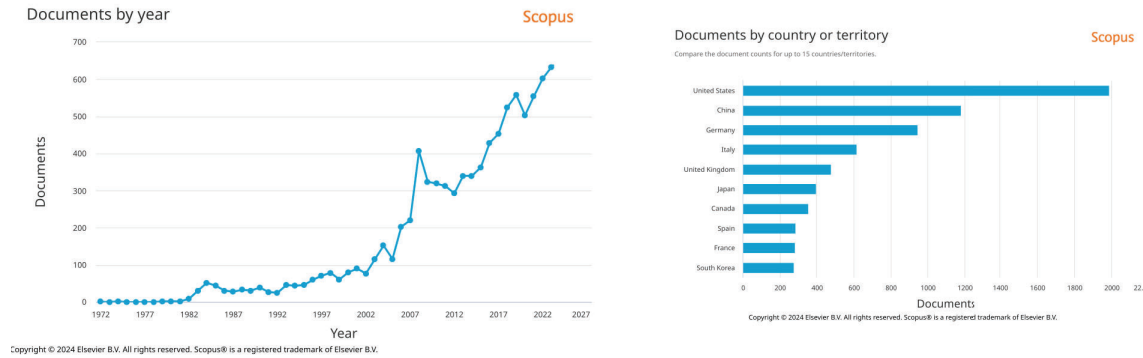
Figure 1: SCOPUS 2024 results of Advanced Search on *TITLE-ABS-KEY ("modular") AND TITLE-ABS-KEY ("robotics")*

of them, the battery pack with the single-board control computer inside. The authors used this module to create a vehicle that consists of various modules (Tolstonogov et al., 2021) and aims for long-term coastal monitoring.

Certainly! Here's the additional paragraph to include just after the introduction, addressing the specific requirements and objectives of the paper:

4 MINION description

MINION encapsulates a modular propulsion system that harmonizes Power, Communication, Intelligence, Sensoring (GNSS, IMU), Thrust, and Thrust Directionality within a singular compact and watertight element as shown in fig. 2 where it is shown that a MINION integrates a Pump-Jet thruster, motor controllers, 24V battery, Raspberry Pi 3b+, WiFi, GNSS, and IMU in a watertight enclosure. MINION is a full electric (24 V), small size
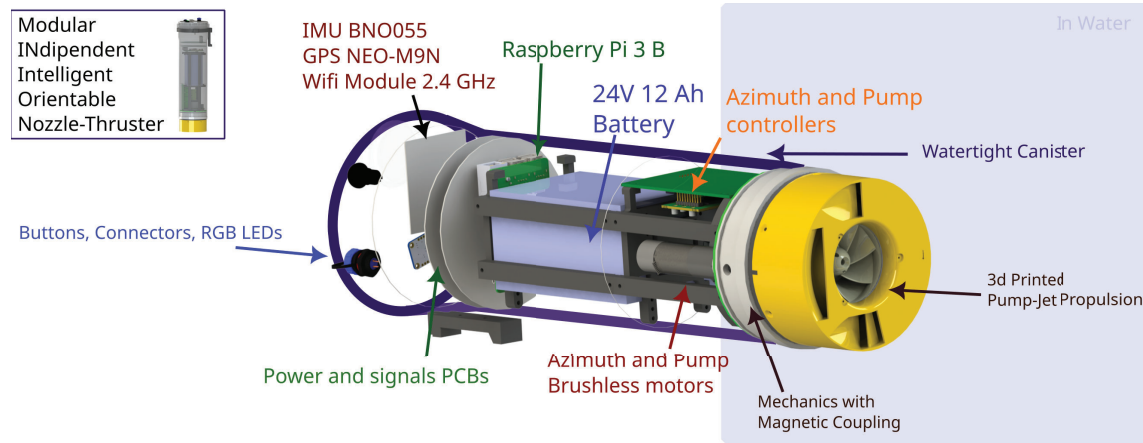
Figure 2: The MINION module overview

(Diameter = 145 mm, Height = 500 mm, Weight = 3.1 kg) and low power (Max consumption = 240 W) module. It incorporates in one single watertight enclosure (shown in fig. 3): Thruster and Thrust Vectoring via Pump-Jet concept exploitation Odetti et al. (2019), Pump and Azimuth motor controllers, a 24V - 12 Ah li-ion battery and Voltage converters, Raspberry Pi 3b+ with digital and analog signals board with signal converters, WiFi module for communication, GNSS for positioning and IMU for attitude.

The operational mechanism of MINION relies on the Pump-Jet principle, rooted in a mixed-flow or centrifugal pump, inducing static pressure to propel water through a steerable nozzle. Characterized by 360° steering for enhanced maneuverability, a Pump-Jet thruster leverages the centrifugal pumps impeller action to generate high-pressure water, and by directing this pressurized water through a steerable nozzle, it achieves thrust and control for effective maneuverable propulsion in shallow water marine environments. When assimilated onto an Autonomous Surface Vehicle (ASV), MINION serves as:

- Propulsion and steering unit safeguarding against damage during bottom collisions, allowing mitigating additional hydrodynamic resistance: By incorporating a Pump-Jet thruster, which is enclosed and steerable, the
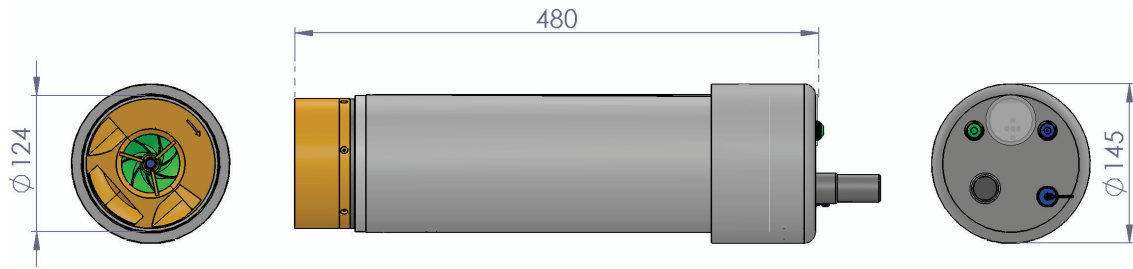
Figure 3: The MINION module overview size and encapsulation

MINION, minimizes the risk of entanglement or impact damage that traditional propellers might encounter in shallow environments.

- Onboard additional or principal computing element via Raspberry Pi 3b+: The MINION includes a Raspberry Pi 3b+ as its core computing unit. This versatile single-board computer can handle a range of processing tasks, from basic control functions of the Propulsion Unit to complex data analysis and decision-making algorithms. Its integration allows for onboard data processing, reducing the need for constant communication with external control systems and enhancing the vehicle's autonomous capabilities.

- Onboard additional or principal Navigation sensor-package element by integrating an IMU and a GNSS: The navigation capabilities of the MINION are bolstered by the inclusion of an Inertial Measurement Unit (IMU) that provides good attitude and orientation data by measuring acceleration and angular rates and a Global navigation satellite system (GNSS) module that delivers positioning information. Together, these sensors enable the MINION to navigate autonomously alone or installed on a vehicle, making it suitable for complex maritime environments requiring high degree of redundancy.

- Onboard additional or principal source of energy: The MINION is equipped with a 24V battery, serving as a power source for all its components. This battery not only powers the propulsion and control systems but can also ensure continuous operation to additional computing and sensor modules. By integrating the power supply within the module, the MINION enhances the vehicle's operational endurance and simplifies power management, eliminating the need for multiple external power sources and eliminating the cables.

- Wireless communication and removal of any cable from onboard: MINION incorporates wireless communication capabilities, enabling data transmission without the need for physical cables. This wireless connectivity simplifies the vehicle's operation, reducing potential points of failure and simplifying maintenance. By eliminating onboard cables, the MINION achieves a cleaner and more compact design, enhancing its maneuverability and reducing the risk of entanglement or damage during operation.

Conceived to create modular and independent systems, MINION is a watertight, detachable unit designed for easy transportation and adaptable deployment across diverse vehicles. The idea is that a MINION can be mounted on surface vehicles coupled with other independent modules as shown in fig. 4.

Additionally, the MINION architecture aims to incorporate automated FAIR (Findable, Accessible, Interoperable, Reusable) data compliance into marine robotics datasets Motta et al. (2023). This strategic initiative endeavors to establish standardized variable names, fostering domain interoperability and improving the findability, accessibility, and reusability of data collected by marine robotic systems.

5 Propulsion in MINION

Given the interest in ad-hoc solutions for wetlands monitoring, the authors defined a class of ASVs tailored to mission specifications. ASV design is based on guidelines from Odetti et al. (2018), inspired by Italian public and private organizations monitoring wetlands and shallow waters. Key design criteria for the Pump-Jet Module (PJM) include: (a) minimal draft for shallow waters; (b) survivability in grounding events; (c) high controllability; and (d) being lightweight and small. ASV propulsion systems often use commercial units, including free- or ducted propeller modules, water jet systems, and aerial systems (Figure 5).

In Odetti et al. (2019) the authors proposed a propulsion unit for an ASV design with an azimuth thruster, combining shallow water operation with satisfactory control. This thruster, named PJM, was developed for SWAMP ASV Odetti et al. (2020d,c).

Designed for shallow, confined waters and harsh environments, the PJM minimizes impact with waterway ground by using a flat bottom and specialized module. The PJM works in water depths as shallow as 50 mm
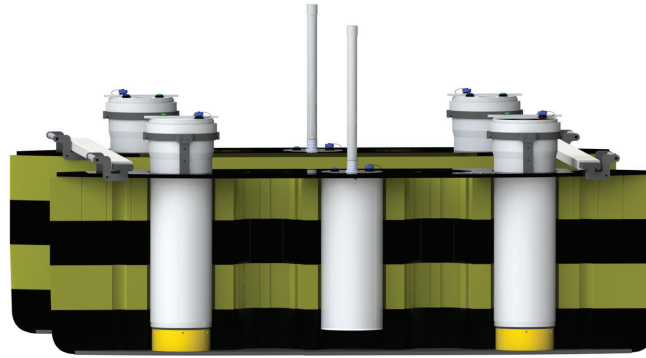
Figure 4: An example of four MINION mounted on SWAMP vehicle (Ferretti et al., 2023; Ferretti et al., 2023)
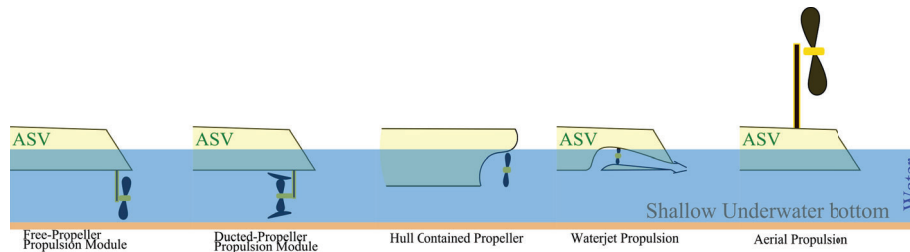
Figure 5: A schematic review of existing USV solutions

without risking damage, and its design minimizes damage from outcropping objects. ASVs need to access narrow areas and remain controllable in station keeping and path following, requiring an effective propulsion layout.

5.1 Pump-Jet System Description

As schematised in fig. 6, the Pump-Jet operates on the principle of vertical pump and is based on the application of the 3rd law of dynamics. Water is drawn into the thruster through a bottom-mounted intake on the vessel. Within the thruster, an impeller functions akin to a centrifugal pump: as it rotates, it accelerates the water, propelling it into a pump housing. The accelerated water is then expelled through a steerable nozzle positioned at the base of the thruster, generating a reaction force in the opposite direction and thus providing thrust to propel the vessel in the desired direction. This nozzle, integrated into the bottom plate, facilitates a flat-bottomed design and enables the installation of Pump-Jets in such hulls. By adjusting the nozzle's direction, precise control over thrust direction is achievable, facilitating vessel maneuvering. MINION boasts a 360-degree steerable nozzle, affording thrust capability in any direction around the vessel, thereby ensuring a good controllability.

The nozzle area at the bottom of the propulsion unit is about one third of the intake area, resulting in an outlet velocity four times higher than the intake velocity. This reduces the risk of sucking in unwanted objects in shallow waters.

The water is expelled at an angle of approximately 15 degrees from horizontal, converting almost all jet thrust into thrust. In shallow water, this minimizes disturbance to the bed, allowing for operations with limited impact as the expelled water rises toward the surface.

The high velocity of water exiting the nozzles enables the PJM to maneuver vessels at high speed, providing significant thrust due to the reliable intake performance of the mixed-flow pump.

The system is supported by a Housing made of PET and an Aluminum plate hosting two motors: the azimuth motor and the impeller motor. The azimuth motor provided with 59:1 gearbox and absolute encoder (2232X024BX4 with encoder AES-4096 and 22GPT 59:1 KS6 reduction by Faulhaber) shaft is connected to a driving spur gear made in PET that puts into rotation a driven spur gear (PET) connected to the Pump casing diffuser and nozzle providing thrust directionality. The controller (MCBL3002 P AES RS) is a Position Controller and it ensures that the motor maintains or reaches a specified position accurately with high precision. The homing
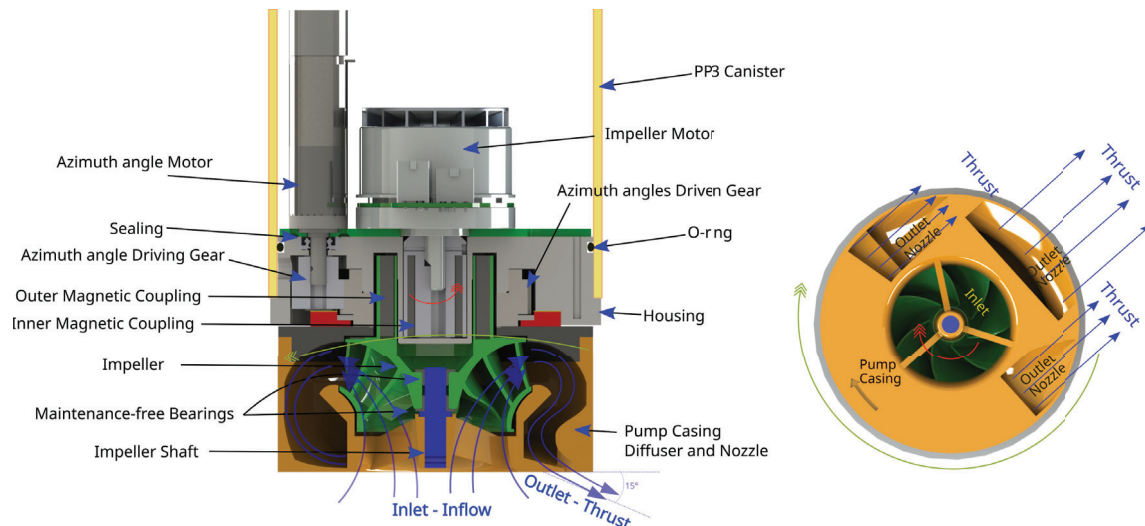
Figure 6: MINION's Pump-Jet functioning scheme.

for the system is provided by a reed switch and a magnet present on the Pump Casing. The impeller is moved by a second motor (EC 60 flat Ø60 mm, brushless, 200 W, with Hall sensors - ventilated by Maxon Motors) coaxial with the impeller that provides thrust with a speed controller (ESCON Module 50/8). The Coupling is achieved by using a magnetic coupling that ad-hoc designed that internally is connected directly to the motor shaft and externally is structurally contained on the impeller's structure. The impeller rotates on a Stainless steel shaft that is mounted on the Pump casing through two maintenance-free plain bearings (Igus). In terms of construction, the pump impeller, nozzle, and pump casing were all 3D printed in PA12. All the elements were made of lightweight inert plastics, so as not to compromise the environment where operates the ASV mounting the MINION.

The water-tightness of the mechanical system is ensured by a mechanical sealing on the azimuth side and by the presence of the magnetic coupling on the impeller side. A NBR o-ring sealing ensure water-tightness to the entire structure.

Inside the canister, the battery, the brushless motors, control electronics, Raspberry Pi and communication system are contained, making

5.2 Design Data

The design data for the Pump-Jet system included the project Thrust, project RPM, propulsor diameter' the dimensioning of the Magnetic Coupling

5.2.1 Pump Design

The Pump-Jet based on the SWAMP ASV's size and thrust needs, to calculate the pump the theory governing mixed-flow pumps was used to define the geometrical constraints underpinning the entire design.

The maximum diameter of the Pump-Jet Module (PJM) was defined based on the draught, payload, and dimensions of a small- to medium-sized ASV. Key geometric characteristics were identified to ensure the system could be scaled and matched to pump and vessel requirements. The casing height, and the inlet and outlet diameters of the impeller, were set proportionally to the main diameter. These dimensions, especially the outlet diameter, influenced the pump head and impeller RPM, crucial for motor selection. The water discharge angle was set at 15 degrees. The discharge nozzle was divided into three channels to achieve the required outlet area.

5.2.2 Propulsion Data

The design thrust of the MINION's pump-jet was identified as $T = 15$ N. The value was obtained from tests conducted on SWAMP (Odetti et al., 2020c) and on the functioning of pump-jet at speed as described in Odetti et al. (2020a) where the results identified the full advance speed of the SWAMP hull in both shallow and deep water. Additionally, self-propelling tests characterized the Pump-Jet Module's performance at various speeds and rotations. This enabled a thorough understanding of the module's characteristics essential for effective control of the Autonomous Surface Vehicle. The thrust roughly originates from water flow multiplied by outlet water velocity. For this reason, all these parameters must be calculated in order to model the thrust unit. The vessel's propulsion thrust is derived from the change in momentum when water enters and exits the jet thruster system (Altosole et al.,

2012). Therefore, the thrust produced by the Pump-Jet (PJ) system is expressed as follows:

$$T = \rho_w A_n V_o (V_o - V_i) \quad [\text{N}] \tag{1}$$

where A_n is the discharge area, V_o is the outlet flow speed, and V_i is the inlet flow speed. With respect to the output angle, the thrust is:

$$T_\alpha = \frac{T}{\cos \alpha_{out}} \quad [\text{N}] \tag{2}$$

Here α_{out} is supposed not to be grater than $\frac{\pi}{6}$.

Since the value to be extracted is the outlet water velocity V_o, the water flow must also be calculated. To do so, we can use the equation:

$$T_\alpha = \frac{\rho_w A_n V_o^2}{\cos \alpha_{out}} \tag{3}$$

where V_i is, in the first approximation, negligible. This assumption holds since this value does not substantially influence the value of H_p. During the impeller design, a small inflow velocity was assumed possible due to vehicle speed (SPJ, 2019). As mentioned above, case-by-case tests were performed to evaluate PJM thrust at various ASV velocities.

The flow rate at the outlet is therefore:

$$m_f = \rho_w A_n V_o \quad [\text{kg/s}] \tag{4}$$

$$Q_o = A_n V_o \quad [\text{m}^3/\text{s}] \tag{5}$$

The data calculated above allowed us to define the pump head necessary for designing the impeller. From the Bernoulli equation:

$$P_i + \frac{1}{2}\rho_w V_i^2 + \rho_w g H_p = P_o + \frac{1}{2}\rho_w V_o^2 + \rho_w g \Delta h + \rho_w g h_{loss} \tag{6}$$

where H_p is the head associated with the pump, and P_o and P_i are the outlet and inlet static pressures, which are equal because the atmospheric pressure added to the water column is constant. Δh is the static difference in the head between inlet and outlet, which in this case was null, and h_{loss} is the term associated with the loss of head due to the flow through the system and the pump. The h_{loss} value was added as a η_{loss} coefficient to the value of the pump head. This allowed to calculate the total head of the pump:

$$H_p = \left(\frac{V_o^2}{2g} - \frac{V_i^2}{2g} \right) / \eta_{loss} \tag{7}$$

In addition, the power associated:

$$P_{pump} = \rho_w g Q_o H_p \tag{8}$$

Using this value, it is possible to identify the pump type by calculating the pump specific speed:

$$N_s = \frac{n \sqrt{Q_o}}{H_p^{0.75}} \tag{9}$$

5.2.3 Calculation of Parameters for the Pump-Jet

Based on the above equations the design of the Pump-Jet propulsion system required the following methodology for calculating key parameters necessary for the Pump-Jet design. In order to determine the appropriate pump head (H_p) required to achieve the desired thrust, the Bolzano Theorem is employed. By iteratively varying the pump head within a specified range, an optimal value of H_{pj} is sought. This process involves computing the outlet velocity (V_{oj}) using the derived formula from the Bernoulli equation, where H_{pj} is incrementally adjusted.

$$V_{oj} = \sqrt{2gH_{pj} - \frac{2(p_o - p_i)}{\rho_w} + V_i^2} \tag{10}$$

The difference between the calculated thrust and the desired thrust is then evaluated to iteratively approach the optimal H_{pj} value. Finally, the index corresponding to the minimum difference is identified to obtain the most suitable $H_{pj} = H_{p0}$ value for the given thrust requirement. To obtain the actual pump head (H_p), a correction is applied to the theoretical pump head (H_{p0}) to account for pump efficiency (η_{pump}):

$$H_p = \frac{H_{p0}}{\eta_{pump}} \tag{11}$$

With the corrected pump head, the outlet velocity (V_o):

$$V_o = \sqrt{2gH_p - \frac{(p_o - p_i)}{\rho_w} + V_i^2} \tag{12}$$

and flow rates (Q_o) are computed.:

$$Q_o = A_n \cdot V_o \tag{13}$$

The inlet (V_{ii}) and outlet (V_{io}) velocities of the impeller are calculated based on the determined flow rates:

$$V_{ii} = \frac{Q_o}{A_i} \quad ; \quad V_{io} = \frac{Q_o}{A_{io}} \tag{14}$$

With this the Specific Pump Parameters are then computed. The pump specific speed (N_s) is derived from the corrected pump head and flow rates:

$$N_s = \frac{n_{prog} \cdot \sqrt{Q_o}}{H_p^{0.75}} \tag{15}$$

Additionally, an imperial unit equivalent of pump specific speed (N_{sgpm}) is computed for practical comparison and analysis. By following these calculations, it was possible to design the Pump-Jet propulsion system by defining parameters as diameter ratios, coefficients, and geometrical factors

From Stepanoff (Stepanoff, 1957) coefficients, derived from empirical data or equations to account for specific performance characteristics of the impeller design, are introduced. These coefficients serve as crucial factors in optimizing the impeller's performance. Inlet, Outlet, and Intermediate geometries are then calculated and defined, to calculate the various sections of the impeller. After this the velocity triangles, detailing velocity components and angles at different impeller stages, are computed. Blade height is determined from Stepanoff influencing fluid flow and pressure distribution. Angles at the inlet, outlet, and intermediate stages are then calculated to design the blades and the pump geometric in automatic.

After this phase a MATLAB Code was implemented to design the Pump-Jet fluid elements. The code includes constants and parameters for fluid properties, pump geometry, and efficiency, and it uses these inputs to calculate thrust, flow rates, and the performance characteristics of the pump-jet.

In fig. 7 it is reported the outcome of the code. The maximum torque provided by the coupling occurs when the magnets are shifted by 30 degrees. This is because the maximum attraction on one facing magnet coincides with the maximum repulsion from the adjacent magnet, which has reversed polarization.
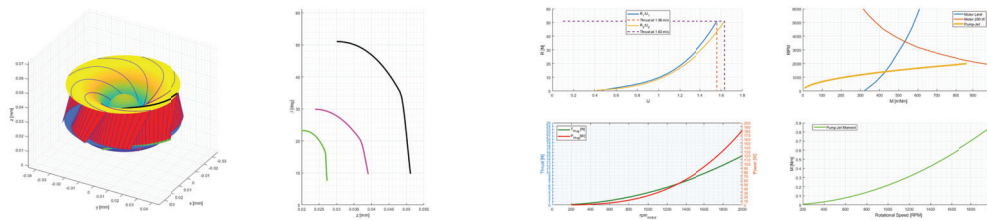
Figure 7: An example of the output of the MATLAB code used to calculate and design the pump-jet of the MINION

5.2.4 Permanent-Magnet Coaxial Synchronous Coupling

In this section, it is presented the analysis and optimization of the torque of the permanent-magnet coaxial synchronous coupling used to couple the Impeller motor to the Impeller itself. The advantage of magnetic coupling is that it eliminates the need for traditional shaft seals, reducing the risk of fluid leakage and environmental contamination. Furthermore by eliminating the need for dynamic seals, maintenance requirements are minimized, resulting in lower operating costs and increased uptime.

The optimization process focuses on the magnetic properties and geometrical parameters of the magnets involved and it is based on Charpentier and Lemarquand (1999) and Eliès and Lemarquand (1998). The process utilized MATLAB for the calculation and visualization of the force and torque interactions between the magnets, ensuring the optimal design parameters were identified.

In fig. 8 it is reported the outcome of the code. The magnets are faced with opposite poles facing in order to create an attractive force. Each magnet has the polarisation inverted in respect to the nearest magnet. When two magnets face each other, the exerted force becomes radial, resulting in a tangential component of zero. This configuration

is stable. As the internal magnet rotates, the tangential force on the external magnet initially increases rapidly, peaks at a maximum, then gradually decreases to a relative minimum before returning to zero (Eliès and Lemarquand, 1998). Deriving the analytical formula provides the rotation angle values corresponding to maximum or minimum points of the tangential force component was the outcome of this calculation. Since the number of facing magnets chosen was 6 (3 poles) in the code also the calculation of the repulsive force created when the internal magnets starts entering the repulsive field of the following external magnet had to be calculated. In the MINION, Neodymium magnets where used with a magnetic flux density of 1.23 Tesla.
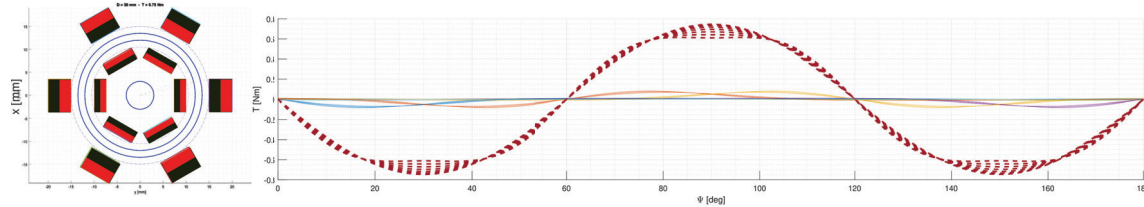
Figure 8: On the left the geometry of the Magnetic Coupling with Magnets faced with reversed poles. On the right the calculation output of the MATLAB code used to calculate the Magnetic Coupling of the pump-jet

5.3 Control System Hardware architecture

The MINION control system hardware architecture is based on the Raspberry Pi 3.0 model B SBC (Single Board Computer) running the Raspbian OS (Operating System). Raspberry Pi boards are inexpensive but very powerful computers based on ARM processors. The Raspbian OS (see https://www.raspbian.org/ for details) is a derived version for ARM processors of the Debian OS (a GNU/Linux-based OS). One of the main characteristics of the Raspberry Pi is the possibility to easily interact with a number of different hardware devices thanks to the presence of 4 USB 2.0 and of a 40-pin GPIO (General Purpose Input Output) header providing a number of interfaces options: digital I/O, PWM (Pulse Width Modulation), I2C (Inter-Integrated Circuit), SPI (Serial Perihperal Interface), serial. Additional digital, analog, serial, etc. I/O channels can be easily added to the SBC thanks to the expandability guaranteed by the presence of the USB, I2C, SPI and serial interfaces.

In particular, on the one hand, the SPI interface was used to communicate with additional A/D and D/A integrated circuits (i.e. MCP-4922 and MCP-3208) necessary for interact with sensors and actuators requiring analog signals.

Power on/off, enable/disable and faults signals are managed by means of the digital I/O channels (GPIOs) directly provided by the Raspberry Pi.

On the other hand, the I2C interface was used to communicate with a supplementary low-cost, extremely accurate RTC (Real Time Clock) based on the DS3231 integrated circuit. The time of the RTC is used for the synchronisation of the telemetry created by the system. The presence of a USB storage system onboard allows for the saving of this telemetry onboard the MINION itself.

On the Raspberry Pi is running a low level control system application called *minion* written in C++ that manages the various sensors and actuators communicating with the SBC by means of the above mentioned interfaces.

The schematic representation of the MINION's control system hardware architecture is reported in fig. 9.

As far as the sensors are concerned the following devices are managed by the control system:

- Adafruit BNO055 absolute orientation sensor: an IMU (Inertial Measurement Unit) providing absolute orientation (yaw, pitch and roll), angular velocities and linear accelerations - digital connection of type RS-TTL;

- U-blox ZED-F9P absolute position sensor: providing GNSS (Global Navigation Satellite System) positions - digital connection of type USB (virtual RS-232);

- temperature sensor providing internal temperature measurements - analog connection;

- voltage sensor providing battery voltage measurement - analog connection.

As far as the actuators are concerned the following devices are managed by the control system:

- Thruster motor: providing thrust - both digital and analog connections;

- Azimuthal motor: providing azimuthal control of the thrust - both digital and analog connections.

For further expansion of the control system plentiful analog and digital I/O channels are available.
Moreover the Raspberry Pi also provide a Wi-Fi interface that permits to communicate with the analogous hardware control systems located inside the other MINION modules.
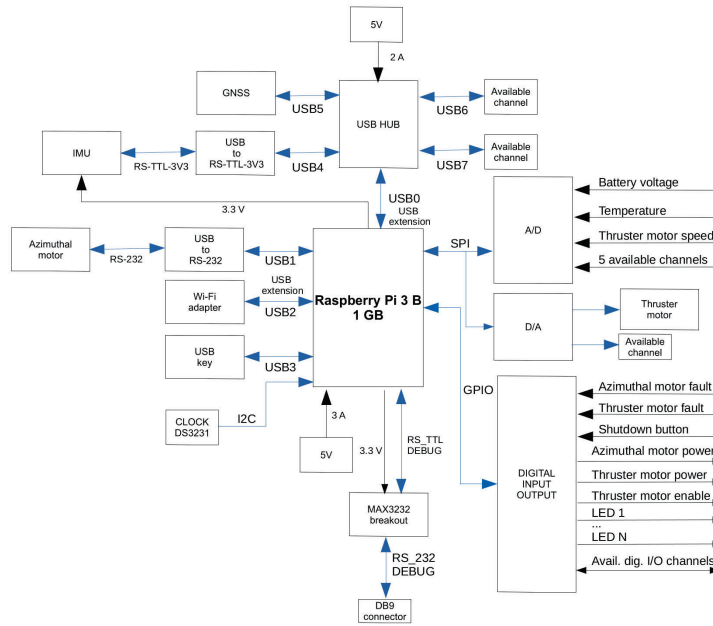
Figure 9: MINION's Control System Hardware Architecture

5.4 Powering

A Lithium-ion battery comprises seven cells in series and five sets of cells in parallel. Each cell has a nominal voltage of 3.7V and a capacity of 2600mAh. The total battery voltage is 25.9V, with a capacity of 13Ah. It offers a power capacity of 336.7Wh and 9.62Wh per cell. Li-ion batteries are prized for their energy density, lightweight and rechargeable properties, finding use in diverse applications from electronics to electric vehicles. The charging system provides 10 Ah thus giving the possibility of recharging the MINION in almost 1 h.

The MINION system is provided with possibility of battery bypass, enabling the integration of external power sources to supply energy to the system. This feature not only ensures continuous operation but also promotes the versatile utilization of onboard energy resources, enhancing the system's adaptability across various applications.

A system of solid state DC-DC converters are used to: stabilise the 24 V powering required by the motors, converting energy to various users, especially Raspberry Pi that requires 5 V for its operations.

6 Conclusions and further research

MINION (shown in fig. 10) serves as a propulsion and steering unit for ASVs. Only one MINION can be used as a single vehicle, being provided with all the features required for a marine robot, or to create a distributed robot. Its Pump-Jet thruster design reduces the risk of entanglement or impact damage in shallow water environments. From its inception, it was designed not just as a mere propulsion unit but as a comprehensive solution, integrating propulsion, navigation, computation, and sensing capabilities into a compact and adaptable package. Its integration with GNSS and IMU ensures precise navigation, allowing for accurate data collection and autonomous decision-making, essential for tasks ranging from maritime surveillance to underwater exploration. Being equipped with a Raspberry Pi 3b+ for onboard computing, this computing power enables real-time data processing, facilitating autonomous navigation and enhancing computational space onboard the vehicle. Coupled with wireless communication capabilities, MINION enables data transmission, enabling effective coordination between vehicles and human operators.

One of MINION's defining features is its modular design, which allows for easy integration with additional sensor modules. This modularity opens up a plethora of applications, from environmental monitoring to oceanographic research. Beyond its practical applications, MINION served in its early developments as an educational platform, providing students with hands-on experience in robotics, marine engineering, and autonomous systems.

6.1 MINION in Dynamic Positioning

The MINION concept, through its integration of propulsion, power, intelligence, sensors, and communication, offers a transformative approach to Dynamic Positioning systems. Its modularity, redundancy, and comprehensive functionality was intended to align with the requirements of various DP classes, thereby enhancing the reliability,
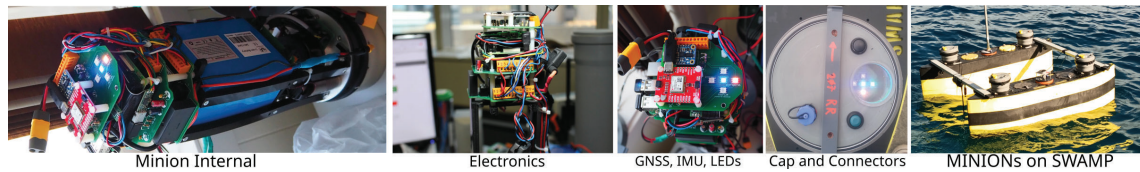
Figure 10: MINION Pictures. From Left: MINION internal construction (Electronics, Raspberry, Power Management, Battery, Motors, Mechanics); MINION electronics; Sensors and LED lights; Cap with connector for charging and buttons; MINIONs mounted on SWAMP

safety, and operational flexibility of maritime and offshore operations.

The initial idea of MINION concept was to meet and enhance the requirements of Dynamic Positioning (DP) systems.

6.1.1 Dynamic Positioning System Requirements

Dynamic Positioning (DP) (Sørensen, 2011; Alfheim et al., 2018) systems are critical in maritime and offshore operations, ensuring vessels and platforms maintain their position in challenging environments. Redundancy is essential to the reliability and safety of DP systems. The International Maritime Organization (IMO) classifies DP systems into four grades (DP Class 1 to DP Class 4) based on their redundancy and capabilities (DNV, 2016; MSC, 1994).

6.1.2 Benefits of the MINION Concept for DP Systems

The MINION concept offers numerous advantages for DP systems, enhancing their redundancy, capability, and flexibility in accordance to failure modes described in the rules (DNV, 2012). In terms of **redundancy**, the MINION units provide distributed thrusters across the vessel. This modularity ensures continuous position control even if some units fail. Each MINION unit contains its own power source, reducing dependence on a central power system and ensuring continuous operation. Additionally, the integrated sensors (GNSS, IMU) in each unit enhance the accuracy and reliability of position and heading data. The embedded computing capabilities in each unit allow for autonomous or collective control, ensuring functionality despite individual processor failures. The built-in communication systems in each MINION unit ensure continuous connectivity, providing multiple communication paths for reliability. The **capability and flexibility** of the MINION units are also significant. The steerable nozzles allow for 360° thrust control, improving maneuverability and position maintenance. The compact, watertight design of the MINION units facilitates easy installation, removal, and reconfiguration. Vessels can be equipped with varying numbers of MINION units to meet specific DP class requirements, from basic redundancy (DP Class 1) to high redundancy (DP Class 4). The robust design of the MINION units provides protection during bottom collisions, maintaining positioning capability even during impacts. Moreover, the MINION architecture adheres to **FAIR data principles** by supporting standardized variable naming conventions, ensuring that data generated is Findable, Accessible, Interoperable, and Reusable. In critical failures, the MINION units can switch to manual control or activate emergency disconnect systems, enhancing overall safety.

References

Martínez de Alegría, I., Rozas Holgado, I., Ibarra, E., Robles, E., Martín, J.L., 2024. Wireless power transfer for unmanned underwater vehicles: Technologies, challenges and applications. Energies 17. doi:`10.3390/en17102305`.

Alfheim, H.L., Muggerud, K., Breivik, M., Brekke, E.F., Eide, E., Øystein Engelhardtsen, 2018. Development of a dynamic positioning system for the revolt model ship. IFAC-PapersOnLine 51, 116–121. URL: https://www.sciencedirect.com/science/article/pii/S2405896318321682, doi:https://doi.org/10.1016/j.ifacol.2018.09.479. 11th IFAC Conference on Control Applications in Marine Systems, Robotics, and Vehicles CAMS 2018.

Altosole, M., Benvenuto, G., Figari, M., Campora, U., 2012. Dimensionless numerical approaches for the performance prediction of marine waterjet propulsion units. International Journal of Rotating Machinery Volume 2012. doi:10.1155/2012/321306.

Antonioli, F., Anzidei, M., Amorosi, A., Lo Presti, V., Mastronuzzi, G., Deiana, G., De Falco, G., Fontana, A., Fontolan, G., Lisco, S., Marsico, A., Moretti, M., Orrù, P., Sannino, G., Serpelloni, E., Vecchio, A., 2017. Sea-level rise and potential drowning of the italian coastal plains: Flooding risk scenarios for 2100. Quaternary Science Reviews 158, 29–43. doi:https://doi.org/10.1016/j.quascirev.2016.12.021.

Bruzzone, G., Odetti, A., Caccia, M., Ferretti, R., 2020. Monitoring of sea-ice-atmosphere interfacein the proximity of arctic tidewater glaciers: The contribution of marine robotics. Remote Sensing 12, 1707. doi:10.3390/rs12111707.

Charpentier, J.F., Lemarquand, G., 1999. Optimal design of cylindrical air-gap synchronous permanent magnet couplings. IEEE Transactions on Magnetics 35, 1037–1046. doi:10.1109/20.748851.

Chen, Y., Liu, K., 2022. Auv/rov/hov propulsion system, in: Encyclopedia of Ocean Engineering. Springer Nature Singapore, Singapore, pp. 102–112. doi:10.1007/978-981-10-6946-8_266.

Church, J.A., Clark, P.U., Cazenave, A., Gregory, J.M., Jevrejeva, S., Levermann, A., Merrifield, M.A., Milne, G.A., Nerem, R.S., Nunn, P.D., Payne, A.J., Pfeffer, W.T., Stammer, D., Unnikrishnan, A.S., 2013. Sea-level rise by 2100. Science 342, 1445–1445. doi:10.1126/science.342.6165.1445-a.

Costanzi, R., Fenucci, D., Manzari, V., Micheli, M., Morlando, L., Terracciano, D., Caiti, A., Stifani, M., Tesei, A., 2020. Interoperability among unmanned maritime vehicles: Review and first in-field experimentation. Frontiers in Robotics and AI 7, 91. doi:10.3389/frobt.2020.00091.

Cruz, N.A., Matos, A.C., 2008. The mares auv, a modular autonomous robot for environment sampling, in: OCEANS 2008, pp. 1–6. doi:10.1109/OCEANS.2008.5152096.

DNV, G., 2012. Failure mode and effect analysis (fmea) of redundant systems dnv-rp-d102. DET NORSKE VERITAS (DNV): Hamburg, Germany .

DNV, G., 2016. Assessment of station keeping capability of dynamic positioning vessels. DNV GL AS .

Eliès, P., Lemarquand, G., 1998. Analytical optimization of the torque of a permanent-magnet coaxial synchronous coupling. IEEE Transactions on Magnetics 34, 2267–2273. URL: https://api.semanticscholar.org/CorpusID:122377050.

Elsevier, 2024. Scopus. URL: https://www.scopus.com. accessed on: 2024-05-22.

Falcão Carneiro, J., Bravo Pinto, J., Gomes de Almeida, F., Cruz, N., 2022. Design and experimental tests of a buoyancy change module for autonomous underwater vehicles, in: Actuators, MDPI. p. 254. doi:doi.org/10.3390/act11090254.

Ferreira, B., Matos, A., Cruz, N., Pinto, M., 2010. Modeling and control of the mares autonomous underwater vehicle. Marine Technology Society Journal 44, 19–36. doi:10.4031/MTSJ.44.2.5.

Ferreira, B.M., Matos, A.C., Cruz, N.A., 2012. Modeling and control of trimares auv, in: 12th International Conference on Autonomous Robot Systems and Competitions, pp. 57–62.

Ferretti, R., Aracri, S., Bibuli, M., Bruzzone, G., Bruzzone, G., Caccia, M., Motta, C., Odetti, A., 2023. Application of a highly reconfigurable surface robotic platform for freshwater plume characterization and sampling near tidewater glacier front in Arctic critical environment., in: EGU General Assembly Conference Abstracts, pp. EGU–5514. doi:10.5194/egusphere-egu23-5514.

Ferretti, R., Bibuli, M., Bruzzone, G., Odetti, A., Aracri, S., Motta, C., Caccia, M., Rovere, M., Mercorella, A., Madricardo, F., Petrizzo, A., De Pascalis, F., 2023. Acoustic seafloor mapping using non-standard asv: technical challenges and innovative solutions, in: OCEANS 2023 - Limerick, pp. 1–6. doi:10.1109/OCEANSLimerick52467.2023.10244670.

Gutiérrez-Flores, P.A., Bachmayer, R., 2022. Concept development of a modular system for marine applications using ros2 and micro-ros, in: 2022 IEEE/OES Autonomous Underwater Vehicles Symposium (AUV), pp. 1–6. doi:10.1109/AUV53081.2022.9965867.

Macreadie, P.I., Anton, A., Raven, J.A., Beaumont, N., Connolly, R.M., Friess, D.A., Kelleway, J.J., Kennedy, H., Kuwae, T., Lavery, P.S., et al., 2019. The future of blue carbon science. Nature communications 10, 1–13. doi:https://doi.org/10.1038/s41467-019-11693-w.

Motta, C., Aracri, S., Ferretti, R., Bibuli, M., Bruzzone, G., Caccia, M., Odetti, A., Ferreira, F., de Pascalis, F., 2023. A framework for FAIR robotic datasets. Scientific Data 10, 620.

MSC, I., 1994. Circ. 645, guidelines for vessels with dynamic positioning systems. International Maritime Orga-

nization .

Müller, T., Pabst, J., Jeinsch, T., 2020. Designing a universal control module for unmanned underwater vehicles, in: Global Oceans 2020: Singapore – U.S. Gulf Coast, pp. 1–7. doi:`10.1109/IEEECONF38699.2020.9389161`.

Odetti, A., Altosole, M., Bibuli, M., Bruzzone, G., Caccia, M., Viviani, M., 2020a. Advance speed-hull-pump-jet interactions in small asv, in: Proceedings of 12th Symposium on High Speed Marine Vehicle (HSMV) Conference, Naples, Italy, IOS Press. pp. 197 –206.

Odetti, A., Altosole, M., Bruzzone, G., Caccia, M., Viviani, M., 2019. Design and construction of a modular pump-jet thruster for autonomous surface vehicle operations in extremely shallow water. Journal of Marine Science and Engineering 7, 222. doi:`doi10.3390/jmse7070222`.

Odetti, A., Altosole, M., Caccia, M., Viviani, M., Bruzzone, G., 2018. Wetlands monitoring: Hints for innovative autonomous surface vehicles design. Technology and Science for the Ships of the Future. Proceedings of NAV 2018: 19th International Conference on Ship and Maritime Research 1, 1014–1021. doi:`10.3233/978-1-61499-870-9-1014`.

Odetti, A., Bibuli, M., Bruzzone, G., Caccia, M., Spirandelli, E., Bruzzone, G., 2017a. e-urope: a reconfgurable auv/rov for man-robot underwater cooperation. IFAC-PapersOnLine 50, 11203–11208. doi:`https://doi.org/10.1016/j.ifacol.2017.08.2089`. 20th IFAC World Congress.

Odetti, A., Bibuli, M., Bruzzone, G., Cervellera, C., Ferretti, R., Gaggero, M., Zereik, E., Caccia, M., 2020b. A preliminary experiment combining marine robotics and citizenship engagement using imitation learning. IFAC-PapersOnLine 53, 14576–14581. doi:`https://doi.org/10.1016/j.ifacol.2020.12.1464`. 21st IFAC World Congress.

Odetti, A., Bruzzone, G., Altosole, M., Viviani, M., Caccia, M., 2020c. Swamp, an autonomous surface vehicle expressly designed for extremely shallow waters. Ocean Engineering 216, 108205. URL: `https://www.sciencedirect.com/science/article/pii/S0029801820311318`, doi:`10.1016/j.oceaneng.2020.108205`.

Odetti, A., Bruzzone, G., Bibuli, M., Ferretti, R., Zereik, E., Caccia, M., 2020d. An innovative asv for the monitoring of anthropogenic pressure on wetlands, in: EGU General Assembly Conference Abstracts, p. 11920. doi:`10.5194/egusphere-egu2020-11920`.

Odetti, A., Bruzzone, G., Caccia, M., Spirandelli, E., Bruzzone, G., 2017b. P2-rov a portable/polar rov, in: OCEANS 2017-Aberdeen, IEEE. pp. 1–6. doi:`10.1109/OCEANSE.2017.8084765`.

Paraschos, D., Papadakis, N.K., 2021. Autonomous underwater vehicle challenge: design and construction of a medium-sized, ai-enabled low-cost prototype. The Journal of Defense Modeling and Simulation 0, 15485129211027236. doi:`10.1177/15485129211027236`.

Pellegrini, R., Ficini, S., Odetti, A., Serani, A., Caccia, M., Diez, M., 2023. Multi-fidelity hydrodynamic analysis of an autonomous surface vehicle at surveying speed in deep water subject to variable payload. Ocean Engineering 271, 113529. doi:`https://doi.org/10.1016/j.oceaneng.2022.113529`.

Ritz, S., Golz, M., Boeck, F., Holbach, G., Rentzow, E., Kurowski, M., Jeinsch, T., Wehner, W.H., Richter, N., Voß, T., 2019. Large modifiable underwater mothership: A case study for ocean bottom nodes deployment and recovery, in: SPE Offshore Europe Conference and Exhibition, SPE. p. D031S013R001. doi:`10.2118/195776-MS`.

Sangekar, M., Chitre, M., Koay, T.B., 2008. Hardware architecture for a modular autonomous underwater vehicle starfish, in: OCEANS 2008, pp. 1–8. doi:`10.1109/OCEANS.2008.5152050`.

SPJ, S.G., 2019. Schottel spj15rd technical data.

Stepanoff, A., 1957. Centrifugal and axial flow pumps: theory, design, and application. Wiley New York.

Sørensen, A.J., 2011. A survey of dynamic positioning control systems. Annual Reviews in Control 35, 123–136. URL: `https://www.sciencedirect.com/science/article/pii/S1367578811000095`, doi:`https://doi.org/10.1016/j.arcontrol.2011.03.008`.

Tolstonogov, A.Y., Chemezov, I.A., Kolomeitsev, A.Y., Storozhenko, V.A., 2020. The modular approach for underwater vehicle design, in: Global Oceans 2020: Singapore – U.S. Gulf Coast, pp. 1–7. doi:`10.1109/IEEECONF38699.2020.9389134`.

Tolstonogov, A.Y., Fries, D., Storozhenko, V.A., Pryazhennikov, P.I., 2021. The dagon system: A modular auv for long-term monitoring and observation, in: OCEANS 2021: San Diego – Porto, pp. 1–9. doi:`10.23919/OCEANS44145.2021.9705978`.

Wu, X., Miao, X., Wang, W., He, D., 2024. Self-tuning iterative learning control for an usv: Application to an autonomous berthing operation with an avoidance obstacle mechanism. Ocean Engineering 301, 117548. doi:`https://doi.org/10.1016/j.oceaneng.2024.117548`.

Xing, B., Yu, M., Liu, Z., Tan, Y., Sun, Y., Li, B., 2023. A review of path planning for unmanned surface vehicles. Journal of Marine Science and Engineering 11. doi:`10.3390/jmse11081556`.

Yang, L., Xiang, X., Kong, D., Yang, S., 2024. Small modular auv based on 3d printing technology: Design, implementation and experimental validation. Brodogradnja: An International Journal of Naval Architecture and Ocean Engineering for Research and Development 75, 1–16. doi:`10.21278/brod75104`.

Zaccone, R., Martelli, M., 2020. A collision avoidance algorithm for ship guidance applications. Journal of Marine Engineering and Technology 19, 62–75. doi:`10.1080/20464177.2019.1685836`.

A structured metric approach to compare marine collision avoidance algorithms

R Zaccone[a*], S Donnarumma[a], M Martelli[a]

[a]Dept. of Electrical, Electronic, Telecommunications, Naval Architecture and Marine Engineering (DITEN), Polytechnic School, University of Genoa, Genova, Italy.
*Corresponding Author. Email: raphael.zaccone@unige.it

Synopsis

The rapid advancement of technologies enabling autonomous ship capabilities has outpaced the development of corresponding legislative and regulatory frameworks, creating a bottleneck in the global application of autonomous ships as defined by the four MASS degrees of autonomy. A significant issue is the absence of a well-defined process for certifying new algorithms and systems to be installed on board. Recently, a reliable, open-access structured set of scenarios, including several challenging COLREG encounter situations, has been published, intended for testing the numerous path-planning algorithms developed over the years. When connected to the testing framework, the modules must accomplish two primary tasks: determining the applicable COLREG rules (COLREG classification) and computing an evasive route. This paper focuses on defining an approach to evaluate the performance of collision avoidance algorithms through dedicated metrics. These metrics are formulated to quantitatively compare escape manoeuvres according to relevant performance indexes, helping a human-based compliance evaluation assess COLREG adherence. The operation of the comparison metrics is demonstrated by testing an existing collision avoidance algorithm developed by the authors. This demonstration underscores the effectiveness of the analyzed algorithms in efficiently managing the challenging scenarios proposed in the literature. Finally, the paper provides valuable suggestions for modifying and improving the testing scenarios to enhance the robustness of the comparison metrics.

Keywords: Autonomous Navigation, COLREG, Path Planning, MASS, Simulation

1 Introduction

The international shipping industry transports around 90% of world trade. Over the past decade, reported shipping losses have significantly dropped (up to 50%) due to technological advancements, improved ship design, and implementing regulations and risk management systems (Allianz, 2021). The post-pandemic consumption pattern is also bound to create surges in trade volumes, giving rise to vessel traffic, especially near coastal areas. As ships continue to increase in size and the amounts of cargo onboard, one single incident, such as a collision, can result in the loss of several precious human lives, and incidents like oil spills from tankers can have catastrophic and long-term consequences for marine ecosystems, the environment, and local economies. However, despite noteworthy improvements in shipping safety, navigational accidents remain frequent and almost daily occurrences (EMSA, 2023). The need to improve safety, reduce the environmental footprint, and upgrade the quality of the seafarer's welfare pushes the maritime community to start the journey towards autonomous navigation. At the heart of this endeavour lies the development of collision avoidance systems that can navigate the complexities of maritime environments with precision and reliability. As vessels increasingly transition towards autonomous operation, the importance of these systems cannot be overstated, as they serve as the linchpin for ensuring safe passage and mitigating collision risks in dynamic maritime scenarios.

Collision avoidance falls under the broader problem of path planning, i.e., the determination of an optimal path automatically based on information about the surrounding environment. In the robotics field, path planning is commonly divided into two levels (Choset et al., 2005; Filotheou et al., 2020), the off-line or global level, in which the path is determined based on a priori known information, such as fixed obstacles or weather forecasts

(weather routing), and the local or reactive level, in which subparts of the path are re-planned online in reaction to changes in the environment detected by sensors, such as moving or unexpected obstacles. The scientific literature proposed various approaches to reactive collision avoidance of marine vessels, including A* (Seo et al., 2023), Dijkstra's algorithm (Singh et al., 2017, 2018), visibility graphs (D'Amato et al., 2021), rapidly-exploring random trees (Chiang and Tapia, 2018; Zaccone and Martelli, 2020; Enevoldsen et al., 2021), Artificial Potential Field methods (Zhu et al., 2022; Li et al., 2021), Randomly-Exploring Random Trees (Zaccone and Martelli, 2020), Dynamic Programming (Zaccone, 2024), and various population-based heuristics (Ito et al., 1999; Kang et al., 2018; Ning et al., 2020; Gao et al., 2023).

However, the effectiveness of collision avoidance systems extends beyond their technical sophistication, as it encompasses their ability to adhere to international regulations, particularly the International Regulations for Preventing Collisions at Sea (COLREGs). With autonomous and human-crewed vessels navigating the same waters, seamless integration and compliance with established maritime regulations become essential for harmonious maritime operations.

Verifying and validating systems engineering projects is crucial for ensuring the designed systems meet their requirements and perform as intended. The international regulatory framework still needs more precise and comprehensive testing procedures and scenarios. To the author's best knowledge, only one paper in the scientific literature deals with this aspect (Pedersen et al., 2023). The paper suggests 55 scenarios for testing collision avoidance systems, which are used in this paper for verification purposes. Against this backdrop, rigorous verification and validation processes are necessary to assess collision avoidance system performance. However, evaluating the performance of these systems is a multifaceted endeavour, requiring the establishment of comprehensive comparison metrics that enable the quantitative assessment and comparison of different collision avoidance strategies.

These comparison metrics are the yardstick against which collision avoidance systems are measured, encompassing various performance aspects such as collision avoidance capability, manoeuvre characteristics, and responsiveness in dynamic environments, as reported by Filotheou et al. (2020). By defining and utilizing such metrics, researchers and practitioners can systematically evaluate the efficacy of different collision avoidance algorithms, thus facilitating informed decision-making in system selection and refinement.

To address the complexities inherent in evaluating collision avoidance systems, researchers have developed simulation frameworks that provide controlled environments for testing and validation. These frameworks are useful tools for assessing system performance under diverse maritime scenarios. Within these simulation frameworks, the integration of dedicated comparison metrics allows the researchers to quantitatively analyze and compare the performance of multiple collision avoidance algorithms.

This paper presents a comprehensive framework for evaluating collision avoidance systems in autonomous ships. By emphasizing the importance of comparison metrics, the paper demonstrates an approach for the systematic assessment and comparison of different collision avoidance algorithms.

2 Methodology

This paper proposes a methodological approach for the comparison of collision avoidance algorithms. The method requires comparing algorithms against a dataset of scenarios and evaluating their performance using synthetic indices or metrics. This section describes the proposed metrics, the logic scheme of the comparison, and some aspects of scenario definition.

In the proposed pipeline, the tested algorithms are fed a set of testing scenarios they try to solve. The resulting solutions consist, for example, of a set of waypoints and/or travel speeds or a set of machine, rudder, and telegraph commands. A motion control system that simulates the actions on a dynamic reference model can then take over these actions by providing the resulting kinematics. In this framework, it is helpful to identify a set of metrics to concisely evaluate the performance of the algorithms under test and make comparisons. Such metrics can be helpful to the human operator in addition to a qualitative assessment of the resulting kinematics of the solved scenario, whose COLREG compliance must be evaluated a posteriori.

2.1 Definitions

Describing a ship's route or manoeuvre through a sequence of waypoints is a common approach in the literature, not only at the global planning level but also at the reactive planning level. Such an approach features some relevant advantages for the application to large human-crewed ships, both in a fully automatic collision avoidance system and within a MASS Level 1 decision support framework, as the one Figure **??** illustrates. The representation of a manoeuvre by waypoints and legs is intelligible to seafarers, and the decision support system can propose it to the officer on the watch, who can understand it and decide whether to acknowledge it. Then, the new sequence of waypoints is then taken over by a motion control system, for example, based on Line of Sight **??**, which determines, based on GNSS localization, the necessary propulsion and steering actions to track the course according to the ship's dynamics with reasonably low track error.

Within this paper, a generic manoeuvre or route R is represented as a sequence of consecutive waypoints:

$$R = (\mathbf{x}_0, \mathbf{x}_1, \ldots, \mathbf{x}_N) = (\mathbf{x}_i)_{i=0}^N \tag{1}$$

A sequence of two consecutive waypoints $s = (\mathbf{x}, \mathbf{y})$ is called route leg. If $s_i = (\mathbf{x}_{i-1}, \mathbf{x}_i)$, and "$\oplus$" is the sequence concatenation operator such that $(\mathbf{x}, \mathbf{y}) \oplus (\mathbf{y}, \mathbf{z}) = (\mathbf{x}, \mathbf{y}, \mathbf{z})$, R can be represented as:

$$R = (\mathbf{x}_0, \mathbf{x}_1) \oplus (\mathbf{x}_1, \mathbf{x}_2) \oplus \ldots \oplus (\mathbf{x}_{N-1}, \mathbf{x}_N) = s_1 \oplus s_2 \oplus \ldots \oplus s_N \tag{2}$$

The notation $\vec{s} = \mathbf{y} - \mathbf{x}$ represents the vector connecting the start point of the leg to the endpoint. As a consequence, the course change between two consecutive legs s_i is expressed by the function θ defined as follows:

$$\theta(s_i, s_j) = \arccos\left(\frac{\vec{s}_i \cdot \vec{s}_j}{|\vec{s}_i||\vec{s}_j|}\right) \tag{3}$$

If there are M obstacles with known kinematics in the scenario, $\mathbf{a}_m(t)$ is the instantaneous position of the mth obstacle. For this study, the motion of the obstacles is approximated as a straight line, constant speed motion:

$$\mathbf{a}_m(t) = \mathbf{a}_m(t_0) + \mathbf{w}_m t \tag{4}$$

Where $\mathbf{w}_m$ represents the speed vector of the mth obstacle. The *CPA* is defined as the minimum distance between the centre points of the own ship $\mathbf{x}(t)$ and an obstacle, whose position over time is denoted by $\mathbf{a}_m(t)$, for $t \in [t_0, t_N]$. In particular, the $CPA_m(s_i)$ is a function defined as follows:

$$CPA_m(s_i) = \min_{t \in [t_i-1, t_i]} |\mathbf{a}_m(t) - \mathbf{x}(t)| \tag{5}$$

2.2 Performance metrics

The selection of a proper collision avoidance algorithm, among all the present in the literature, requires a comparative evaluation. Since algorithms return complex output that is difficult to compare, it is necessary to define quantitative synthetic metrics that can help make a selection. Various approaches have been proposed in the literature related to robotics (Filotheou et al., 2020) and, more specifically, to ship collision avoidance (Zaccone, 2024). In this paper, the following metrics have been considered:

- Path smoothness;

- The path elongation;

- The speed reduction;

- The minimum CPA;

- The maximum track error;

- The computation time.

The path smoothness $\sigma(R)$ expresses the mean heading changes squared, expressing how challenging a manoeuvre could be for a steering system. Manoeuvres involving smoother course changes can be implemented with lower track error and overshoots, ensuring that the actual path adheres more closely to the planned path. The smoothness σ can be defined as follows:

$$\sigma(R) = \frac{1}{N-2}\left(\sum_{i=1}^{N-1} \theta^2(s_i, s_{i+1})\right)^{\frac{1}{2}} \tag{6}$$

Notice that, if defined as above, σ is the lower the better.

The path elongation $L(R)$ is the non-dimensional length of the avoidance manoeuvre:

$$L(R) = \frac{\sum_{i=1}^N |\vec{s}_i|}{|\mathbf{x}_{end} - \mathbf{x}_{start}|} \tag{7}$$

Manoeuvres with shorter total lengths normally lead to smaller CPAs.

Speed reduction is a parameter for evaluating the algorithm, not the scenario. In other words, complicated scenarios may not admit solutions allowing the ship to maintain its initial speed. Given that it is not usually

appropriate to avoid a collision by increasing speed, in many cases, a reduction to a safe speed allows potential collisions to be avoided. It is, therefore, appropriate to monitor the speed reduction suggested by the algorithm to deal with the manoeuvre.

The minimum CPA during the manoeuvre $CPA_{min}(R)$ expresses the minimum distance at which the own ship avoids a target during the collision avoidance manoeuvre:

$$CPA_{min}(R) = \min_{i \in \{1,N\}} \left(\min_{m \in \{1,...,M\}} CPA_m(s_i) \right) \tag{8}$$

The value of CPA is expected to be above a minimum threshold, but different algorithms or parameterizations can generate more or less conservative manoeuvres.

The maximum track error $T_{max}(R)$ represents the non-dimensional maximum transversal deviation from the original track:

$$T_{max}(R) = \max_{i \in \{1,...,N\}} \frac{\vec{s_i} \cdot \mathbf{u}}{|\mathbf{u}|} \tag{9}$$

Where $\mathbf{u} = (\mathbf{x}_{end} - \mathbf{x}_{start}) \begin{bmatrix} 0 & 1 \\ -1 & 0 \end{bmatrix}$. In general, staying as close as possible to the original track is desirable whenever possible.

Lastly, the computation time to compute an evasive manoeuvre is crucial when real-time applications are required. Reduced computation time enables the deployment in real-time applications and on fast vessels.

The proposed metrics make it possible to compare different algorithms on the same scenario, whereas comparing an extensive set of scenarios can be difficult because the absolute value they take depends on the scenario setup. Defining a metric normalization approach to compare algorithms by aggregating or averaging data obtained in different scenarios is useful.

If $\mu(k,a)$ denotes a generic metric measuring the performance of algorithm a over the testing scenario k, the normalized metric $\mu_n(k)$ over a set A of algorithms is defined as follows:

$$\mu_n(k) = \frac{\mu(a,k) - \min_{a \in A} \mu(k,a)}{\max_{a \in A} \mu(k,a) - \min_{a \in A} \mu(k,a)} \tag{10}$$

It is worth noting that, using a normalized metric, the best algorithm over a scenario scores 1, and the worst scores 0. In the presence of a significant scenario dataset, normalized metrics allow one to understand how often one algorithm is better than the others on a per-scenario basis.

2.3 Scenario definition

Different approaches to defining scenarios for comparing collision avoidance algorithms exist in the literature. First, it is possible to differentiate between scenarios characterized by fixed obstacles, typical of robotic motion planning problems, in which the autonomous vehicle must find a collision-free path through a static map. In such cases, it is reasonable to refer to complex maps characterized by tortuous manoeuvres generated a priori or by more or less random placement of obstacles. In contrast, regarding marine vehicle collision avoidance, more attention is paid to moving obstacles, especially when considering COLREG compliance, a case in which scenarios must refer to typical navigational cases.

In the context of COLREG-compliant collision avoidance, many studies refer to so-called cornerstone scenarios, which represent the typical encounter conditions described by COLREG: head-on, crossing and overtaking. Some examples are proposed by Zaccone et al. (2019). Zaccone and Martelli (2020) presented navigation scenarios constructed a priori, characterized by dynamic obstacles with sudden course and speed changes. For testing and comparing a collision avoidance algorithm, Zaccone (2024) proposed an approach based on complete randomization of the positions of fixed and moving obstacles to assess the performance of the algorithms with a statistical metrics-based approach on a vast number of random scenarios. Eventually, Pedersen et al. (2023) systematized a methodology for generating navigation scenarios for testing collision avoidance algorithms, proposing an open source tool (DNV, 2023) and a dataset of 55 scenarios, built from cornerstone scenarios by combining them into more complex scenarios with two, three or more vessels.

3 Collision avoidance algorithms

The presented approach is applied to a set of algorithms to demonstrate its possible applications. Three algorithms, Dynamic Programming, Genetic Algorithm, and RRT*, are compared to this end.

Dynamic Programming (DP) is a practical approach for solving multi-stage optimization problems. From its introduction by Bellman Bellman (1954, 1966), DP has been successfully generalized and formulated to describe
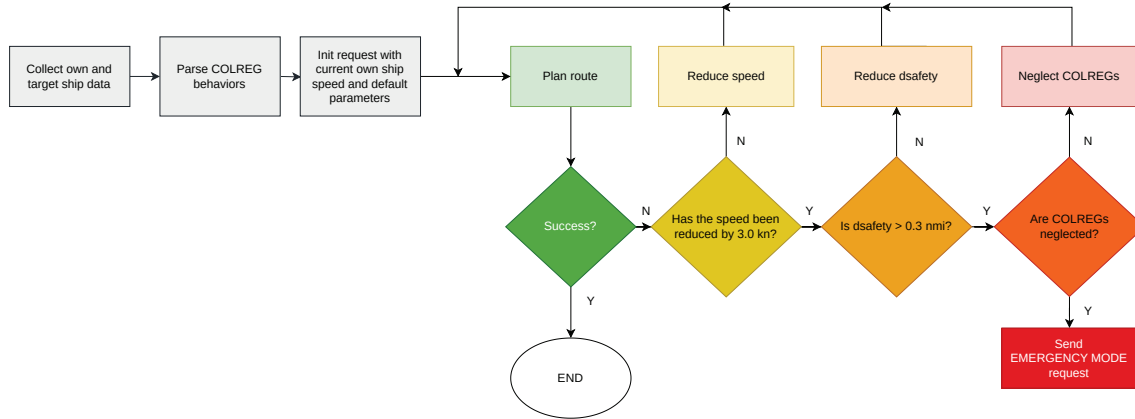
Figure 1: The proposed collision avoidance fallback strategy to deal with complex scenarios.

path planning problems Jones and Peet (2021). An application to marine collision avoidance was presented by Zaccone (2024), who also introduced a greedy-approximate solution scheme to reduce the computational complexity. The greedy-approximate DP is the first of the three algorithms featured in the present comparison.

Genetic Algorithm (GA) is a widely used Evolutionary algorithm that mimics the selection of genes in a population. Each candidate solution, referred to as a "phenotype" or "creature", is modelled as a sequence of parameters known as the "genotype" or "chromosomes". The first iteration generates a population of creatures with a random genotype. Then, the best creatures are selected according to a specific cost function. A new population for the next iteration is generated by quasi-randomly shuffling their chromosomes and introducing random mutations. This process is repeated until the population heuristically converges to one solution. GA allows for evaluating the minimum number of very complex functions and is generic enough to fit almost every optimization problem. In the proposed application, GA is used to find the best sequence of waypoints within the same gridded framework proposed by Zaccone (2024).

Eventually, the RRT* is a state-of-the-art algorithm in robotics and path planning: it is a random sampling algorithm designed to explore domains using tree structures and determine collision-free manoeuvres quickly. RRTs (LaValle, 1998) iteratively generate tree-like structures, initiating from a root node and terminating when a node is close enough to the desired goal. The "*" (star) variant, or Optimal RRT (Karaman and Frazzoli, 2011), includes local optimizations of the tree topology within a neighbourhood of each newly generated node, leveraging a cost function to generate heuristically optimal trajectories. The implementation of the RRT* used for this comparison has been presented by Zaccone and Martelli (2020).

The tree path planning algorithms can compute a collision-free path at a constant speed, keeping a minimum distance from the obstacles. The algorithms have been integrated into a collision avoidance strategy. The implemented strategy is represented in Figure 1 and operates based on the following steps:

1. The route is evaluated assuming that the own ship maintains its initial speed, meets a minimum CPA of 1 nautical mile and complies with COLREGs.

2. If no solution is found, the speed is reduced by up to 3 knots less than the initial speed. This speed reduction is small enough to occur in negligible time and be assumed instantaneous.

3. If no solution is available, the minimum allowable CPA is reduced to 0.3 nautical miles.

4. If no solution is found, the algorithm evaluates the possibility of violating COLREGs.

4   Results

Three collision avoidance algorithms are tested in this case study, specifically a greedy-approximate dynamic programming algorithm proposed by Zaccone (2024), an implementation of RRT* proposed by Zaccone and Martelli (2020) and a genetic algorithm. The three algorithms were used to minimize the same cost function (control energy) and with the same set-up of constraints, as described in Zaccone (2024).

The three algorithms were tested against the 55 scenarios proposed by Pedersen et al. (2023). These scenarios include cornerstone encounters, such as crossing, head-on, and overtaking, with only one target, as well as numerous seemingly dead-end situations characterized by multiple targets converging on the own ship. In such scenarios, compliance with COLREGs dictates that one's course should not vary from the give-way targets, leading to zero

(a) Scenario 2   (b) Scenario 29   (c) Scenario 43
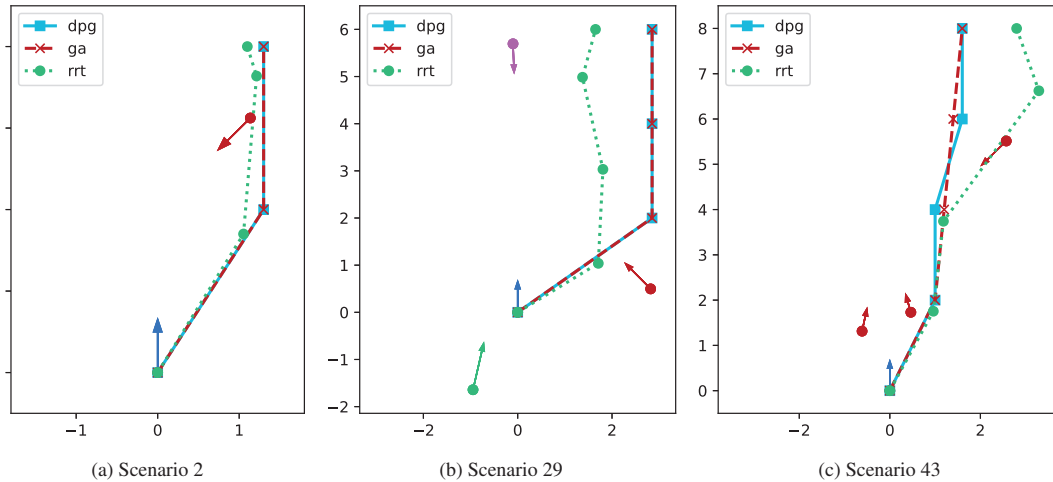
Figure 2: Three of the 55 scenarios proposed by Pedersen et al. (2023).

CPA. For this reason, give-way targets were not included in the minimum CPA analysis since evasive manoeuvring is expected from them.

Figure 2 presents some examples of the 55 scenarios proposed by Pedersen et al. (2023), specifically scenario 2, scenario 29 and scenario 43. The figure shows the solutions of the three tested algorithms. Given its scattered and random nature, RRT* always presents a more irregular trajectory. GA, on the other hand, presents a heuristically optimal solution that often coincides with dynamic programming.

Figures 3 to 8 present the aggregated performance parameters of the 55 scenarios. Violin plots have been used to evaluate and compare the algorithms: these plots (Hintze and Nelson, 1998) show how each quantity is distributed over the dataset by highlighting the average value.

Figure 3 presents the results related to smoothness: it is observed that both in a relative sense, DP and GA provide smoother trajectories than RRT*. Figure 4 shows the elongation of manoeuvres compared with the reference trajectory. It can be seen that although the values are similar in absolute terms, RRT* systematically provides longer manoeuvres than the other algorithms. From Figure 5, it is observed that all the algorithms succeed in most cases in solving the scenarios without reducing the speed. Figure 6 shows that all algorithms perform similarly in terms of CPA in an absolute sense, but by normalizing the values, it is observed that RRT* allows slightly higher CPAs to be maintained due to the greater freedom the algorithm has in placing waypoints. Looking at Figure 7, we observe that the DP algorithm is the best in moving away from the original track, while the RRT* is the worst, given its heuristic nature. Eventually, Figure 8 shows that the DP and RRT* perform significantly better than the GA in terms of computation time, the former in particular guaranteeing times of less than 100 milliseconds.

(a) Smoothness

(b) Norm. Smoothness
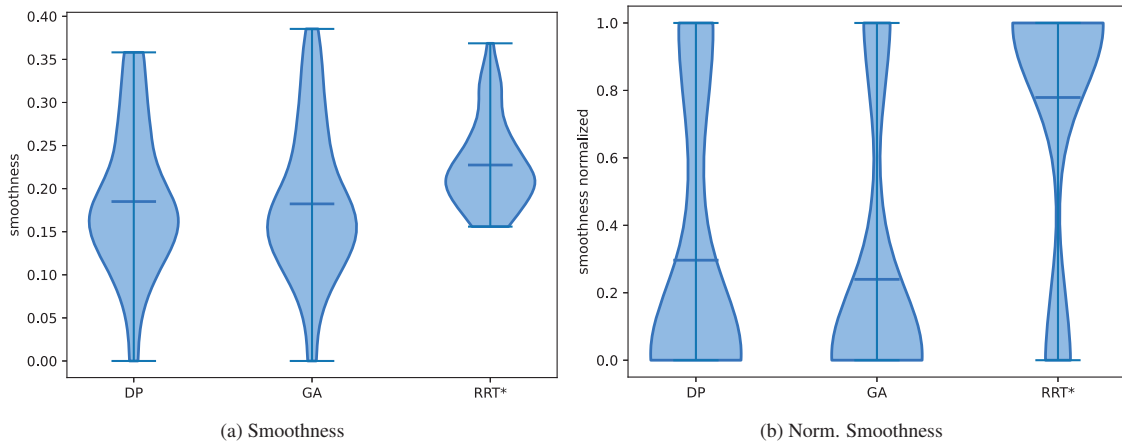
Figure 3: Smoothness violin plots on the 55 scenarios.

(a) Elongation

(b) Norm. elongation
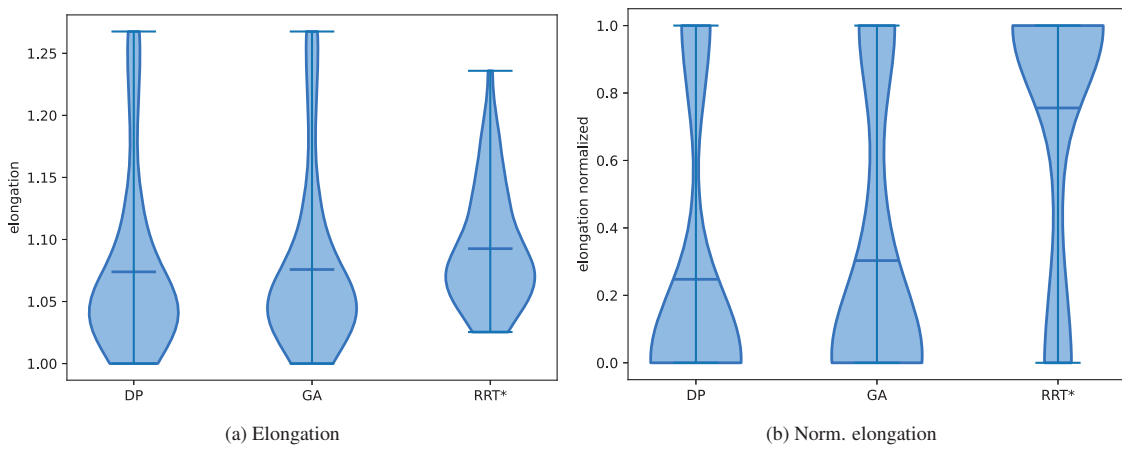
Figure 4: Percentage path elongation represented with violin plots on the 55 scenarios.
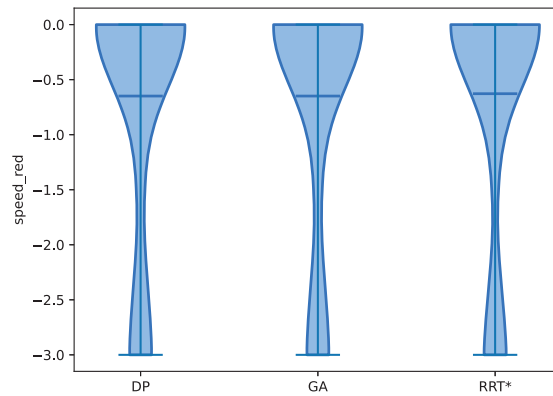
Figure 5: Speed reduction in Knots represented with violin plots on the 55 scenarios.

(a) CPA (nm)

(b) Norm. CPA
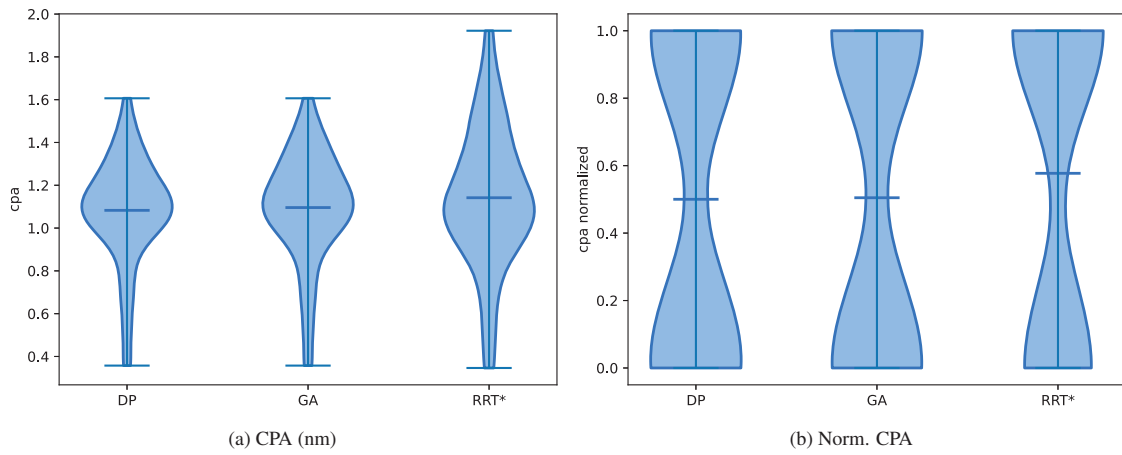
Figure 6: CPA in nautical miles represented with violin plots on the 55 scenarios.

(a) Track err.

(b) Norm. track err.
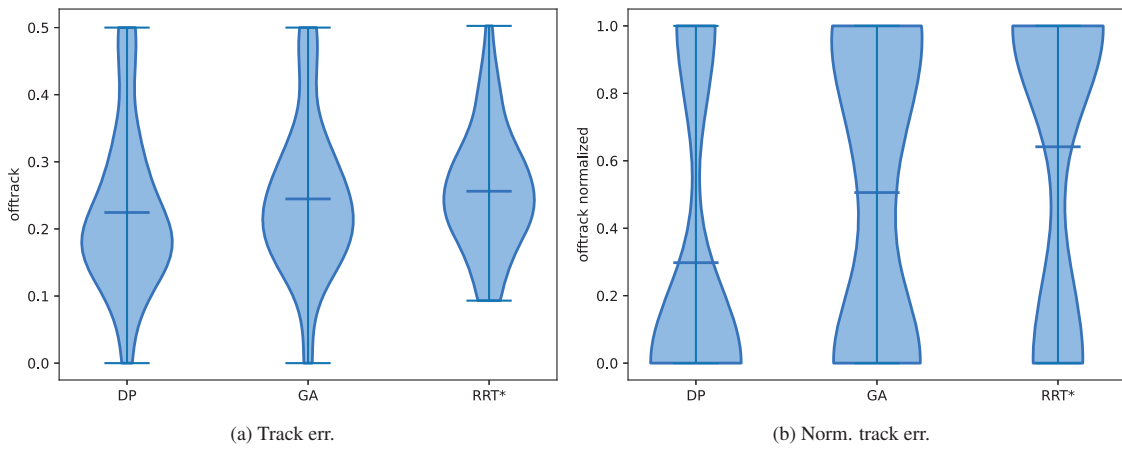
Figure 7: Track error violin plots on the 55 scenarios.

(a) Elapsed time (ms)
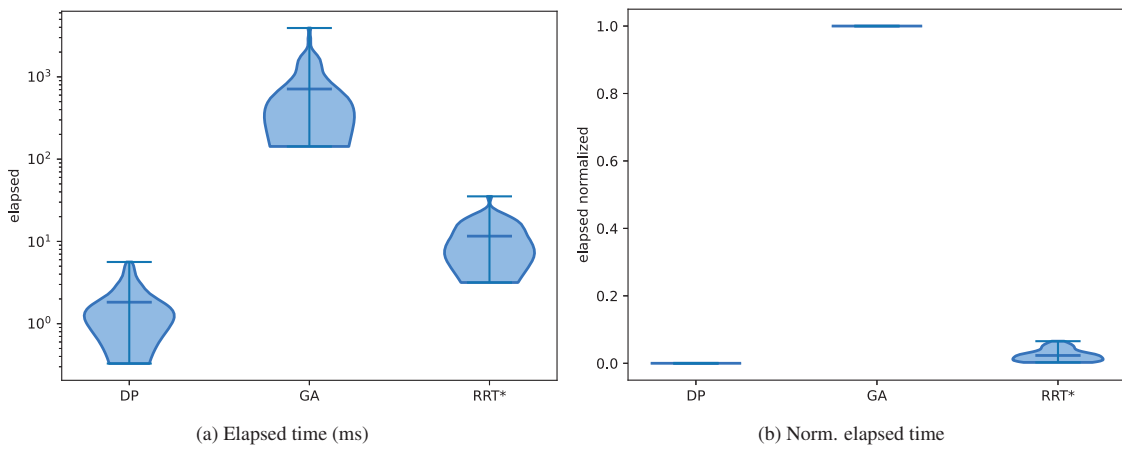
(b) Norm. elapsed time

Figure 8: Elapsed time in milliseconds represented using violin plots on the 55 scenarios.

5 Conclusions

Numerous algorithms for path planning, collision avoidance, and decision support have been presented in the autonomous navigation field. However, limited attention has been given to evaluating algorithms' performance for comparison purposes. This paper presented an approach for comparing collision avoidance algorithms based on appropriate performance metrics. The approach has been applied for demonstration purposes to three collision avoidance algorithms, comparing their performance on encounter scenarios proposed by third parties in the literature, showing how comparative evaluation of different algorithms on a defined set of scenarios can be performed.

However, the approach has some limitations. First, the performance metrics are constructed assuming the algorithms provide structured suggestions regarding waypoints. In principle, an algorithm can provide results in another form, which would require a different definition of some metrics. In addition, the viability of the proposed solutions was assumed in terms of the dynamic response of the ship, which could instead be verified and evaluated by an appropriate index. Finally, the automatic evaluation of COLREG compliance with a complex manoeuvre remains an open problem which cannot be released from expert judgment.

The scenarios used in this paper were proposed by third parties, and the analyses highlighted some critical issues. In particular, some particularly complex scenarios are of little practical and operational interest since, in navigational practice, they would be subordinate to the actions of target ships under COLREGs.

A potential future development could be to define scenarios in which the target ships have a plan of intended movement defined but not known a priori to the own ship. In this way, it could be assessed whether the own ship behaves according to the rules. Alternatively, the own ship could be called upon to interact with autonomous target ships commanded by a reference collision avoidance system for evaluation.

Acknowledgments

References

Allianz, 2021. Safety Shipping Review 2021. Technical Report. Allianz Global Corporate Specialty.

Bellman, R., 1954. The theory of dynamic programming. Bulletin of the American Mathematical Society 60, 503–515.

Bellman, R., 1966. Dynamic programming. Science 153, 34–37.

Chiang, H.T.L., Tapia, L., 2018. Colreg-rrt: An rrt-based colregs-compliant motion planner for surface vehicle navigation. IEEE Robotics and Automation Letters 3, 2024–2031.

Choset, H., Lynch, K.M., Hutchinson, S., Kantor, G.A., Burgard, W., 2005. Principles of robot motion: theory, algorithms, and implementations. MIT press.

DNV, 2023. Ship traffic generator. https://github.com/dnv-opensource/ship-traffic-generator. Accessed: 2024-05-19.

D'Amato, E., Nardi, V.A., Notaro, I., Scordamaglia, V., 2021. A visibility graph approach for path planning and real-time collision avoidance on maritime unmanned systems, in: 2021 International Workshop on Metrology for the Sea; Learning to Measure Sea Health Parameters (MetroSea), IEEE. pp. 400–405.

EMSA, 2023. Annual Overview of Marine Casualties and Incidents. European Maritime Safety Agency.

Enevoldsen, T.T., Reinartz, C., Galeazzi, R., 2021. Colregs-informed rrt* for collision avoidance of marine crafts, in: 2021 IEEE International Conference on Robotics and Automation (ICRA), IEEE. pp. 8083–8089.

Filotheou, A., Tsardoulias, E., Dimitriou, A., Symeonidis, A., Petrou, L., 2020. Quantitative and qualitative evaluation of ros-enabled local and global planners in 2d static environments. Journal of Intelligent & Robotic Systems 98, 567–601.

Gao, P., Zhou, L., Zhao, X., Shao, B., 2023. Research on ship collision avoidance path planning based on modified potential field ant colony algorithm. Ocean & Coastal Management 235, 106482.

Hintze, J.L., Nelson, R.D., 1998. Violin plots: a box plot-density trace synergism. The American Statistician 52, 181–184.

Ito, M., Zhnng, F., Yoshida, N., 1999. Collision avoidance control of ship with genetic algorithm, in: Proceedings of the 1999 IEEE International Conference on Control Applications (Cat. No. 99CH36328), IEEE. pp. 1791–1796.

Jones, M., Peet, M.M., 2021. A generalization of bellman's equation with application to path planning, obstacle avoidance and invariant set estimation. Automatica 127, 109510.

Kang, Y.T., Chen, W.J., Zhu, D.Q., Wang, J.H., Xie, Q.M., 2018. Collision avoidance path planning for ships by particle swarm optimization. Journal of Marine Science and Technology 26, 3.

Karaman, S., Frazzoli, E., 2011. Sampling-based algorithms for optimal motion planning. The international journal of robotics research 30, 846–894.

LaValle, S., 1998. Rapidly-exploring random trees: A new tool for path planning. Research Report 9811 .

Li, L., Wu, D., Huang, Y., Yuan, Z.M., 2021. A path planning strategy unified with a colregs collision avoidance function based on deep reinforcement learning and artificial potential field. Applied Ocean Research 113, 102759.

Ning, J., Chen, H., Li, T., Li, W., Li, C., 2020. Colregs-compliant unmanned surface vehicles collision avoidance based on multi-objective genetic algorithm. Ieee Access 8, 190367–190377.

Pedersen, T.A., Vasanthan, C., Karolius, K., Engelhardtsen, Ø., Houweling, K.P., Jørgensen, A., 2023. Generating structured set of encounters for verifying automated collision and grounding avoidance systems, in: Journal of Physics: Conference Series, IOP Publishing. p. 012013.

Seo, C., Noh, Y., Abebe, M., Kang, Y.J., Park, S., Kwon, C., 2023. Ship collision avoidance route planning using cri-based a* algorithm. International Journal of Naval Architecture and Ocean Engineering 15, 100551.

Singh, Y., Sharma, S., Sutton, R., Hatton, D., 2017. Optimal path planning of an unmanned surface vehicle in a real-time marine environment using a dijkstra algorithm, in: Marine Navigation. CRC Press, pp. 399–402.

Singh, Y., Sharma, S., Sutton, R., Hatton, D., Khan, A., 2018. Feasibility study of a constrained dijkstra approach for optimal path planning of an unmanned surface vehicle in a dynamic maritime environment, in: 2018 IEEE International Conference on Autonomous Robot Systems and Competitions (ICARSC), IEEE. pp. 117–122.

Zaccone, R., 2024. A dynamic programming approach to the collision avoidance of autonomous ships. Mathematics 12. URL: https://www.mdpi.com/2227-7390/12/10/1546, doi:10.3390/math12101546.

Zaccone, R., Martelli, M., 2020. A collision avoidance algorithm for ship guidance applications. Journal of Marine Engineering & Technology 19, 62–75.

Zaccone, R., Martelli, M., Figari, M., 2019. A colreg-compliant ship collision avoidance algorithm, in: 2019 18th European Control Conference (ECC), IEEE. pp. 2530–2535.

Zhu, Z., Lyu, H., Zhang, J., Yin, Y., 2022. An efficient ship automatic collision avoidance method based on modified artificial potential field. Journal of Marine Science and Engineering 10, 3.

Investigation on shipboard power quality on cruise ships under high penetration of power converters

Federico Graffione[a], Francesco Ghio[a], Marco Gallo[a], Fabio D'Agostino[a], Andrea Rudan[b], Federico Silvestro[a*]

[a]University of Genova, Italy; [b]Carnival Corporation, Italy

*Corresponding author. Email: federico.silvestro@unige.it

Synopsis

The maritime industry is undergoing a significant transformation with the integration of advanced power electronics and converter technologies onboard cruise ships. This work explores the effects of power converter integration on shipboard power quality, particularly in cruise vessels that depend heavily on these converters for efficient power conversion. The study proposes a preliminary investigation of the potential challenges arising from the complex interplay of power electronic devices, including variable frequency drives, rectifiers, and inverters, with the ship's power distribution grid. A comprehensive measurement campaign is conducted onboard representative cruise ships, utilizing advanced monitoring equipment to capture power quality indexes related to different power systems and conversion architecture. The primary objectives of this investigation are to assess power quality indexes and to develop models for analyzing and validating real measurement data. Two similar cruise ships, each equipped with different technologies for driving synchronous propulsion motors, were used as case studies. Through data analysis and ETAP modeling, the research compares the performance and power quality impacts of these technologies under various operational conditions. The findings reveal distinct total harmonic distortion of voltage behaviours for the two ships, highlighting the varying effects of synchro-converters and cyclo-converters on power quality during port and navigation conditions. The study emphasizes the importance of maintaining a stable and high-quality power supply in the maritime environment, and provides insights into the implications of power quality issues on the performance of onboard equipment.

Keywords: Power Quality, Shipboard Power System, Total Harmonic Distortion, All Electric Ship, Harmonic Load Flow.

1 Introduction

The electrification of ships has led to an increasingly widespread presence of power electronics and converters, particularly on All Electric Ship (AES). These technologies play a crucial role when there is a necessity to generate, distribute electrical power. Furthermore, to improve the energy efficiency of the ship, Direct Current (DC) energy sources such as Fuel Cell (FC) and Battery Energy Storage System (BESS) are progressively being implemented Gallo et al. (2023). These types of resources need to be interfaced to the ship's grid using converters. The presence of this power electronics equipment introduces power quality issues Barros and Diego (2016).

The definition of power quality is given by International Electrotechnical Commission (2024): *"characteristics of the electric current, voltage and frequency at a given point in an electric power system, evaluated against a set of reference technical parameters"*.

International standards, specifically related to shipboard power system applications, define both the typical operating conditions and the reference technical parameters. These deviations are considered within the power quality assessment and are measured using various indices and measurement methods IEEE (2009); International Association of Classification Societies (IACS) (2019); IEEE (2014).

Among the various metrics used to evaluate power quality, harmonic content is one of the key indicators. Harmonics, which are integer multiples of the power system frequency, are created by non-linear loads that distort

voltage waveforms and impact the entire power system. Harmonics are usually related to the presence of non-linear loads, such as propulsion motors and drives. The widespread use of power converters in marine applications, like propulsion and pumps, has led to non-linear loading constituting up to 80% of the generation capacity on modern vessels Kůs et al..

The limits defined by international organizations and marine classification societies, such as IEC, IEEE, DNV, ABS, and LRS, specify the allowable voltage harmonic distortion for shipboard electrical installations under all operating conditions. Standards refer to limits for Total Harmonic Distortion (THD), which measure the distortion caused by harmonics as a percentage of the fundamental frequency in voltage or current waveforms Milankov and Radić (2014). THD can be measured for both the voltage and the current. The THD voltage limit ranges from 5% to 8%, depending on the standard considered Barros and Diego (2016). The single harmonic limit ranges from 1.5% to 3%.

In the existing literature, authors have proposed different approaches to analyze and address power quality issues. In Tsvetanov et al. (2023b), an experimental setup is presented to evaluate the performance of an autonomous Shipboard Power System (SPS) in terms of THD. In Liu et al. (2018), an investigation on the power quality assessment onboard ship is suggested. The analysis shows that the effect of voltage unbalance and distortions in the SPS must be taken into account, particularly when differences on critical grid parameters under balanced and unbalanced are quite important. In Rigogiannis et al. (2023), power quality measurements on a ferry boat are presented. The analysis highlights the issue of high THD values associated with the power conditioning system. In Terriche et al. (2019), authors propose two open-loop algorithms to assess the harmonic distortion for short and long term preventive action stage on AES. In Mindykowski and Tarasiuk (2015), an analysis of the problem of electrical power quality and its impact in terms of safety is presented. The authors emphasize that ship classification societies should introduce requirements for the continuous monitoring of power quality in ship systems. In Crapse et al. (2007), a specific frequency-based power quality index is proposed to measure disturbances at different critical points within an electric ship power system.

Other studies investigate different solutions to manage the effects of power electronic devices on the electric grid. In Rahman et al. (2022), a distribution filtering solution is modelled and implemented, emphasizing the optimal placement of active filters primarily at higher voltage nodes. In Tsvetanov et al. (2023a), a static synchronous compensator is modelled to improve the power factor in autonomous SPS. In Semwal et al. (2022), an enhanced fractional least mean square is developed to improve the power quality in shipboard microgrids. In Li et al. (2017), a controllable inductive power filtering method is proposed. This method serves multiple purposes, including reducing the required installation space, suppressing harmonic currents, and damping harmonic resonance in the SPS. In Terriche et al. (2019), a combined structure of hybrid active power filter with parallel fixed capacitor-thyristor controlled reactor is proposed to compensate for the distortion and the sags of the voltage in SPS. In Liu et al. (2022), the authors introduce a shipboard power supply system that integrates transformers and filters. This setup ensures a harmonic-free power supply, benefiting stable operation and integrated optimization of compact, all-electric shipboard systems.

The proposed manuscript presents a methodology for analyzing and validating real measurement data collected from cruise ships under normal operating conditions. The primary goal is to analyse the power quality on the SPS. To verify the results derived from the data analysis, a model of the SPS is developed using the ETAP environment.

The paper is organized as follows: Section 2 introduces the analysis on the power quality measurements, Section 3 reports the development of the SPS model and non-linear loads behaviour, Section 4 presents model validation through the comparison with the real measurements, while conclusions are proposed in Section 5.

2 Power quality analysis in SPS

This study examines real power quality measurements taken from two cruise ships. The analysis is performed under specific assumptions using various correlation techniques. The primary metric for assessing power quality in this study is the voltage THD. This section describes the ships analyzed, the types of available data, and the analysis conducted. The two considered cruise ships are identified as Study Case 1 (SC1) and Study Case 2 (SC2). They fall into the category of mass-market cruises. The SPS of SC1 and SC2 is quite similar except for the type of propulsion drives, which are the main contributors to harmonic distortion.

2.1 Description of the SPS, for the SC1

Figure 1 presents the Medium Voltage (MV) single-line diagram of SC1. The generating resources of the ship are composed of six 14 MVA synchronous machines, driven by Diesel prime movers, connected to two main busbars at 11 kV.

Six 1720 kW asynchronous motors, used as manoeuvring thrusters, are directly connected (without intermediate speed control drive) to the main switchboard. These include three bow thrusters and three stern thrusters. Additionally, there are four Heat Ventilation and Air Conditioning (HVAC) compressors equipped with 1500 kW
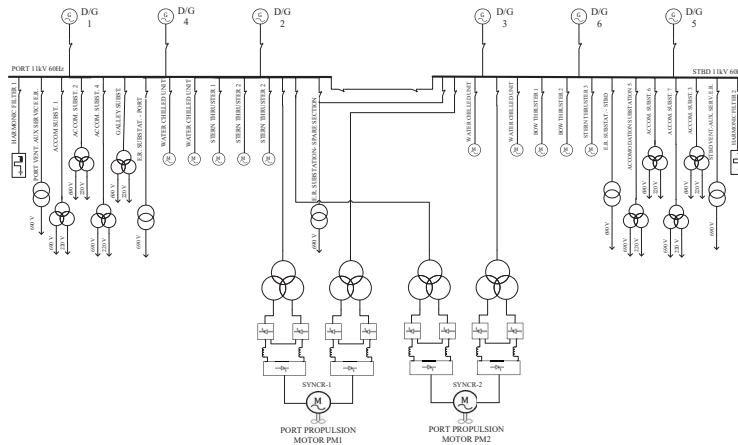
Figure 1: Shipboard Power System for SC1 cruise ship.

asynchronous motors. Transformers are used to supply Low Voltage (LV) busbars of hotel substations (on for each main vertical zones), the machinery auxiliary substations (divided into five substations), and the galley substation. In addition, the machinery auxiliary substations are further divided into two *Engine Room Ventilation Auxiliary Service*, two *Engine Room Substation* and one *Engine Room Substation - Spare Section*. There are two types of transformers: two-winding and three-winding. The three-winding transformer, composed of a primary winding and two secondary windings, allows supplying two different voltage levels. In this case, the two-winding transformers provide power to the machinery auxiliary substations, stepping down from 11 kV to 690 V. For the *Engine Room Ventilation Auxiliary Service*, these transformers have a rated apparent power of 2800 kVA, while for the *Engine Room Substation*, it is 3500 kVA. The hotel substations are powered by three-winding transformers with a rated apparent power of 1500 kVA, stepping down from 11 kV to 690 V and 220 V. Galley is supplied by a three-winding transformer with a rated apparent power of 2600 kVA, also stepping down from 11 kV to 690 V and 220 V.

The main propulsion service is provided by two Fixed Pitch Propeller (FPP) driven by two-windings synchronous machines, with a mechanical rated power of 21 MW. The electrical power system is provided through four 11/1.5/1.5 kV/kV/kV three-winding transformers, each rated at 13.4 MVA. The four transformers supply two synchroconverters, one for each propulsion motor. The synchroconverter is a power electronics component that realizes an Alternative Current (AC)-DC-AC conversion. It provides an output voltage with a variable frequency, so that the speed of the synchronous motor can be regulated

Finally, two double-tuned passive harmonic filters are connected to the MV busbar. These filters contain harmonic pollution, thus reducing the THD.

2.2 Description of the SPS, for the SC2

Figure 2 shows the single line diagram for the SC2. The generating resources of the ship are composed of four 16 MVA Diesel Generator (DG) and two 12 MVA DGs. These generators provide power at the MV busbar at 6.6 kV, 60 Hz. Similar to SC1, six manoeuvring thrusters with a power of 1720 kW are connected direct online to the main busbar. Additionally, there are four HVAC compressors with a power rating of 1570 kW.

The main propulsion system consists of two synchronous motors, each with a mechanical output power of 20 MW. Each motor drives a Controllable Pitch Propeller (CPP). Electrical power is supplied by four two-winding transformers that feed two cycloconverters. These devices are power electronics apparatuses that realize an AC-AC conversion, so that the synchronous motors' speed can be controlled through the regulation of the output voltage frequency.

2.3 Description of the available data

In the ships previously described, reported in Fig. 1 and in Fig. 2, active power data [kW] absorbed by the loads connected to the MV busbar are available. These measurements have been taken at the primary winding side on the transformers that separate the main switchboard from the secondary distribution grid. For installations not served by transformers, such as manoeuvring thrusters and HVAC compressors, measurements have been taken directly at the machine terminals. For the power plant, active and reactive power, current, voltage, and current and voltage THD are available. Finally, regarding propulsion motors, there are two types of data: active absorbed power
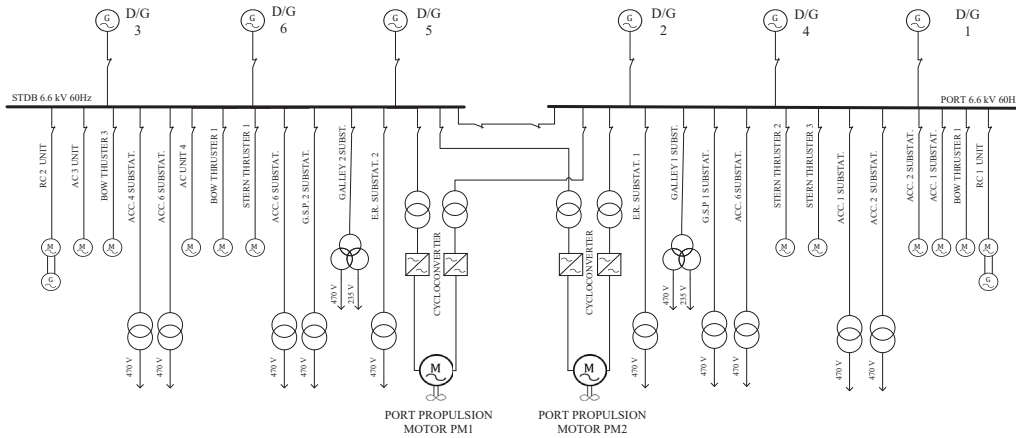
Figure 2: Shipboard Power System for SC2 cruise ship.

data from synchronous propulsion motors and active absorbed power from three-winding propulsion transformers. Figure 3 shows the location of the measurement units.
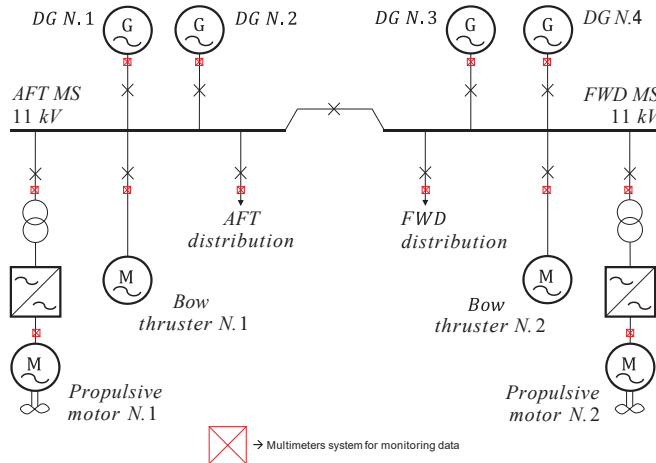
Figure 3: Notional arrangement diagram of multi-meters in the onboard electrical system.

The two ships operate on commercial cruise routes, typically spending the day in port, and sailing during the night.

Based on the power output from the onboard SPS, which varies with operational conditions and is primarily dependent on the sailing speed for SC1, we assume that:

- When it's in port (speed of 0 kn), the number of operating DGs is 1 to a maximum of 2, with a total active power output of approximately 8-10 MW, and peaks reaching 11 MW when 2 DG are active, with a mean cosphi = 0,87;

- During medium-speed navigation (between 8-13 kn), 2 DGs are required, collectively providing active power between 12-16,5 MW, with a mean cosphi = 0,80;

- For cruising speeds (18-21 kn), 3 DGs are needed, delivering a combined active power output of 27-37 MW, with a mean cosphi = 0,88. Peaks up to 46 MW are observed to achieve speeds around 23 knots, maybe in rough sea condition.

For SC2 it can be observed:

- When it's in port (speed of 0 kn), the number of operating DGs is 1, with a total active power output of approximately 6-7 MW, with a mean cosphi = 0,85, and peaks reaching 7,5 MW;

- During medium-speed navigation (between 8-13 kn), 2 DGs are required, collectively providing active power between 11-16 MW, with a mean cosphi = 0,61;

- For cruising speeds (18-22 kn), 4 DGs are needed, delivering a combined active power output of 25-35 MW, with a mean cosphi = 0,72. A peak of up to 41,5 MW is observed with 5 DGs active, presumably while navigating at a speed of approximately 20,4 kn, likely against adverse wind and current conditions or challenging marine weather.

The cubic relationships between the speed of the ship and the active power absorbed by the main propulsion, are shown in Fig. 4. These curves are obtained from measurements of active electrical power absorbed [MW] by the two synchronous propulsion motors, for both ships.
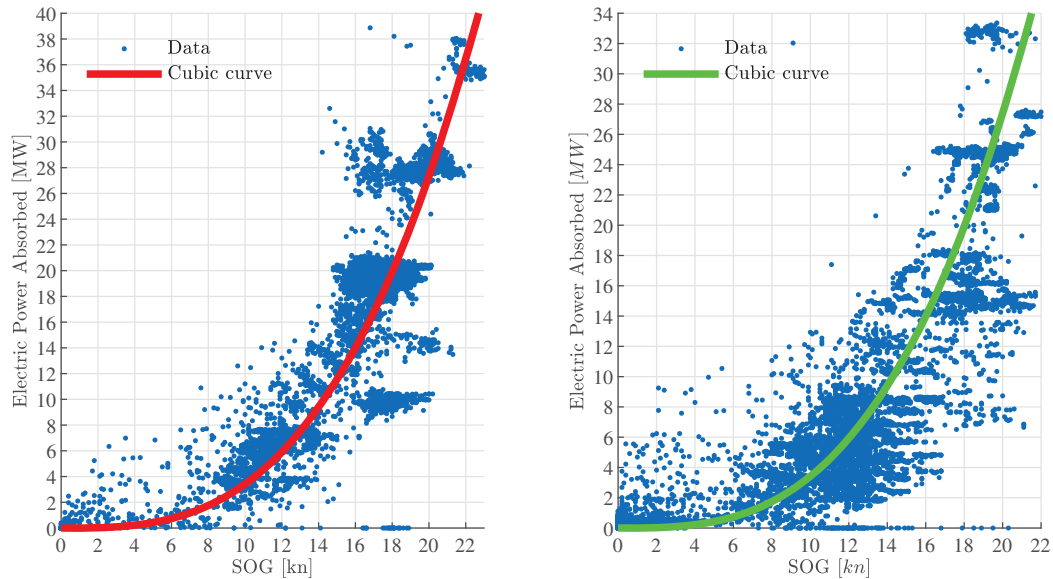
Figure 4: Cubic relationship fitting for SC1 (*left*), and for SC2 (*right*)

2.4 Analysis of Onboard Ship Measurement Data

The objective is to investigate the correlations between the active power absorbed from onboard electrical loads and the THD_V.

The initial step of the analysis involves categorizing the electrical load components divided into:

- Maneuvering thruster loads;

- HVAC compressors loads;

- Hotel substations loads;

- Engine auxiliary substations loads;

- Galley substations loads;

- Main propulsion loads.

Correlation analysis is performed. Pearson correlation coefficients are calculated for all pairs of input variables. A Pearson coefficient close to 1 indicates a tendency toward proportional and linear behavior in the data, while a coefficient near -1 suggests an inverse proportional relationship. Correlation is typically considered significant when greater than 70% Meghanathan (2016).

Measurements of the THD_V are taken by meters installed on the generator incoming cubicle, between the DG alternator and the MV busbar. Therefore, the number of meters corresponds to the number of DGs, as do the THD_V values. Simplifying by calculating an average value is appropriate since the observed values are relatively similar. Calculating an average value makes it easier to visualize and appreciate the behavior based on operational conditions, the number of DGs in operation, the electrical power generated by the plant, and the power absorbed by the onboard electrical loads.

Item 1	Item 2	SC1	SC2
HVAC compressor	THD_V	-0.15	-0.05
Maneuvering thruster	THD_V	0.23	-0.20
Hotel substation	THD_V	0.13	0.11
Galley	THD_V	0.14	0.02
Main propulsion	THD_V	-0.82	0.65
Engine auxiliary substation	THD_V	-0.65	0.52
Electric power supplied by DG	Main propulsion	0.97	0.97

Table I: Summary Table of Correlation Research

The Table I provides a summary of the correlation research between load categories for both case studies. The only load category strongly correlated with the variation in average THD is the main propulsion. Auxiliary machine substations also show a correlation because some loads support the main propulsion and therefore align with the load demand of the main synchronous motors. In Fig. 5, the correlation value between individual substations and the mean THD_V are represented, to identify which substation is most strongly correlated with the increase in load absorbed by the propulsion.

Figure 5 shows that for SC1 substations D, E, and F are most correlated with the variation of average THD_V, while for SC2 substations A and B exhibit this correlation.

Table I indicates a correlation between the power supplied by DGs and the electric power absorbed by the main propulsion, with a correlation coefficient of approximately 1, as these two quantities are of similar magnitude. Therefore, the primary variation in load supplied by the SPS is due to the load demand or reduction of absorption by the main propulsion.

Furthermore, in the correlation between synchronous propulsion motors power absorbed and the mean THD_V, there are different signs in the Pearson correlation coefficient between SC1 and SC2. For SC1, the correlation is negative, indicating that as the active power absorbed by the propulsion increases, the mean THD_V decreases. Conversely, for SC2, the correlation is positive, meaning that as the active power absorbed by the propulsion increases, the mean THD_V also increases.

In Fig. 6 and in Fig. 7, a typical daily profile in terms of active generated power, speed, and mean THD_V is shown. From the speed profile, it is possible to distinguish two main operational conditions, port and navigation.

For SC1, the mean THD_V decreases with increasing speed and, consequently, the active power absorbed by propulsion. In the other hand, for SC2, the opposite occurs. In SC1, there is a transition from a mean THD_V value ranging from approximately 4-4.5 (port condition) to 1.7-1.8 (navigation condition). Meanwhile, for SC2, there is
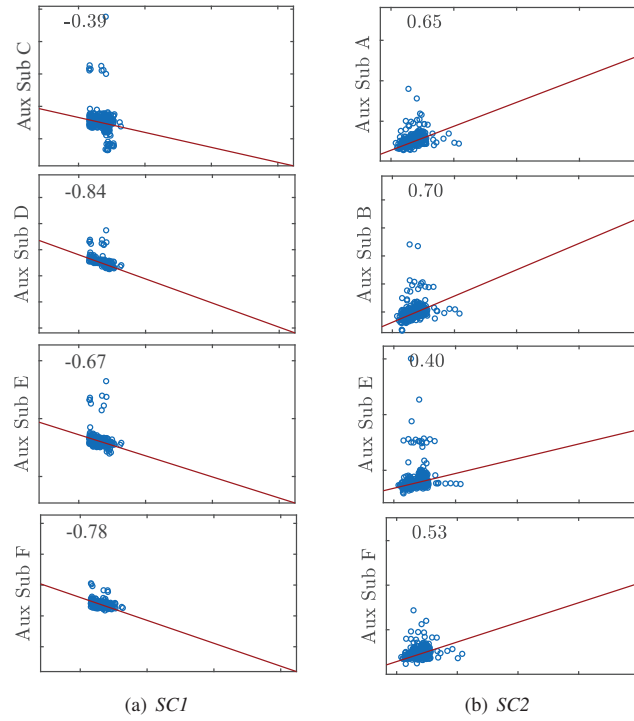
Figure 5: Correlation between Engine auxiliary and mean THD$_V$ for both study case

a transition from mean THD$_V$ around 2.9-3.2 (port condition) to 7.3-10.3 (navigation condition). The range within which THD$_V$ varies for SC2 depends on the navigation speed; as speed increases, the mean THD$_V$ also increases.
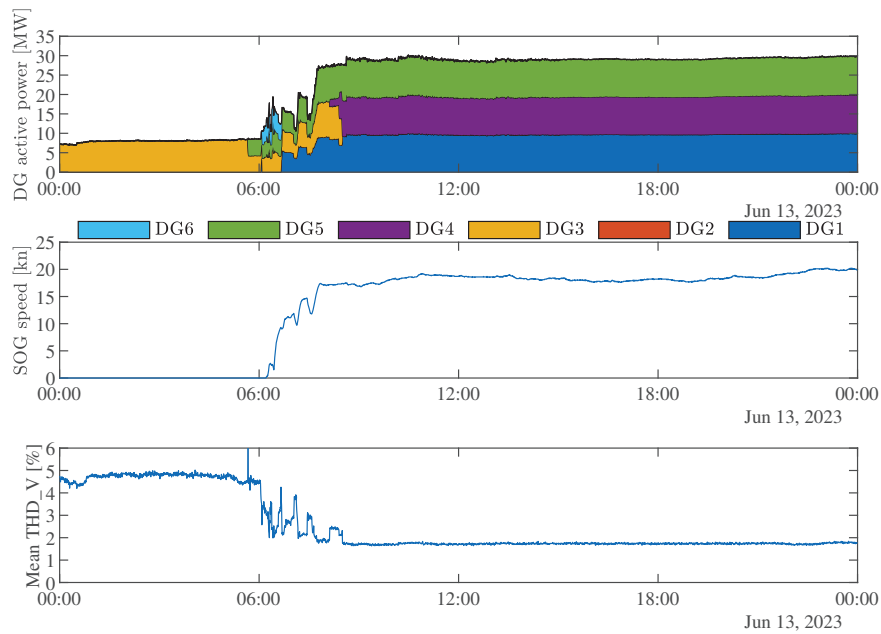
Figure 6: DG electrical power supplied, Speed Over Ground (SOG) and mean THD$_V$ for SC1.

As previously mentioned, the two units have different technologies for driving synchronous propulsion motors. SC1 is equipped with a synchroconverter, while SC2 has a cycloconverter. The main difference in terms of har-
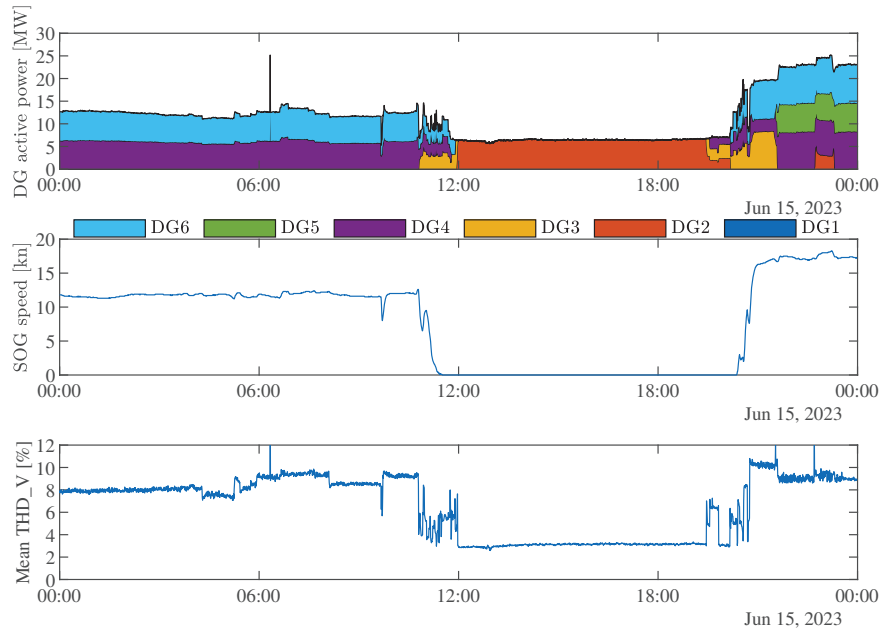
Figure 7: DG electrical power supplied, SOG and mean THD$_V$ for SC2.

monic pollution in the onboard grid is due to the fact that SC1 is equipped with two double-tuned passive harmonic filters (one for each busbar), whereas SC2 is not. As we will see in the following paragraphs, passive harmonic filters are connected to the grid when more than one DG is in operation. For SC1, this occurs during navigation, as typically only one DG is operational during port conditions.

3 Modeling of the integrated SPS

Starting from the data provided for the SPS of the SC1 and to validate the THD$_V$ measurements taken, a model is developed in ETAP environment. Specifically, the following assumptions are considered: the impedance of the cables is negligible compared to transformers and passive harmonic filters, the power factor of the substations is an input parameter, and the electrical loads of the substations are modelled as static loads. Part of the latter are considered as non-linear loads that inject harmonics according to the ideal current generator model with a certain injection profile. This was done by assuming the injection profile of the possible installed converters. Furthermore, synchronous generators and induction motors are modelled using the specific ETAP model component.

The model realization can be summarized in the following steps:

- Identification of operating conditions under steady-state conditions;

- Modeling the SPS in ETAP environment for the considered operating conditions;

- Performing Load Flow calculation;

- Performing recursive Harmonic Load Flow calculation to estimate the harmonic injection that match with real data measurements. Achieve convergence between the THD voltage value of the model and the real data measurements, by varying the percentage of loads under the converter until determining the amount of load injecting harmonics from the substations;

- Cross-validate the model results through the comparison with other operating condition related measurements.

3.1 Determining operating conditions

The load produced by the DG and the number of them in operation have been plotted, identifying conditions that can be defined as recursive over time regarding the THD$_V$ and the loads involved. It was noted:

- Case of ship in harbour $\rightarrow$ THD$_V \cong 4.30\%$;

• Case of ship in navigation → $THD_V \cong 1.7 - 1.8\%$.

Two points in time have been set under steady-state conditions, and the corresponding values of the electrical grid measurements have been assumed:

• Case of ship in harbour → 18/06/23 00:15 (UTC);

• Case of ship in navigation → 25/06/23 10:12 (UTC).
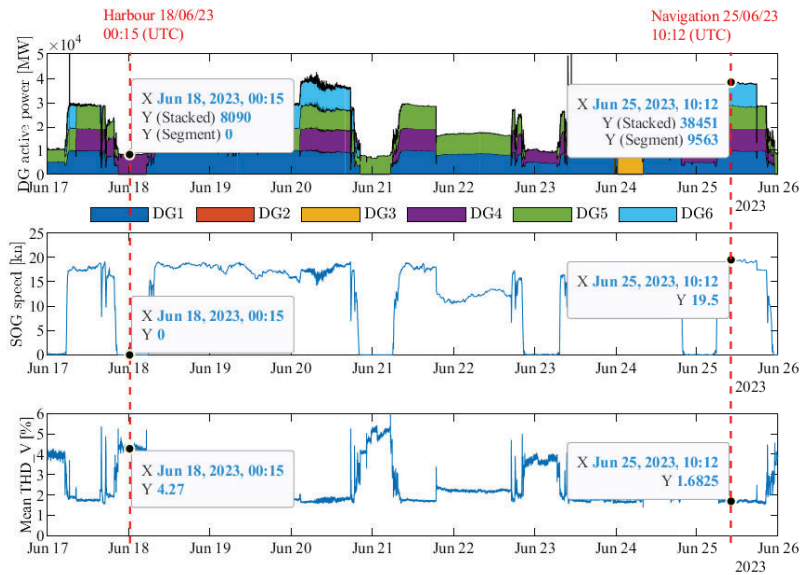
Figure 8: Temporal signal of active power generated by the onboard station, SOG speed, and average THD_V.

3.2 Modeling with ETAP Load Flow and Harmonic Load Flow

The SPS model is developed in the ETAP (Electrical Transient Analyzer Program) environment using the datasheets of the components. In this environment, it is possible to perform load flow analysis and harmonic load flow analysis. With ETAP, it is possible to perform a harmonic analysis of the grid and study the harmonic spectrum of voltage and current in the grid. This is done by modeling a load or a component as a 'harmonic source' and this is accomplished through a specific section in the settings of each load. Additionally, it is possible to perform a 'frequency scan' which returns the impedance magnitude and angle, as seen from the main switchboard.

3.3 Modeling the Electrical System of SC1 in ETAP

The ETAP model used for the load flow and harmonic load flow is presented in Figure 9.

In this model, the different modeling methods concerning linear and nonlinear loads are distinguished to perform a harmonic load flow analysis. An example of the different models is shown in Fig. 10, where:

• Load (1): this load represents the case of an electric motor controlled by a VFD (Variable Frequency Drive). For simplicity, it has been represented as a static load injecting harmonics according to the type of load and technology involved;

• Load (2): this load represents the case of substations, which we consider as aggregated loads of linear and non-linear loads. These are modeled as two static loads, one of which injects harmonics. The percentage of the load that injects harmonics is determined during the model calibration phase, and the injection profile is based on the present components;

• Load (3): This load represents the case of a load that can be considered linear, such as an induction motor, which is modeled according to the ETAP reference model.
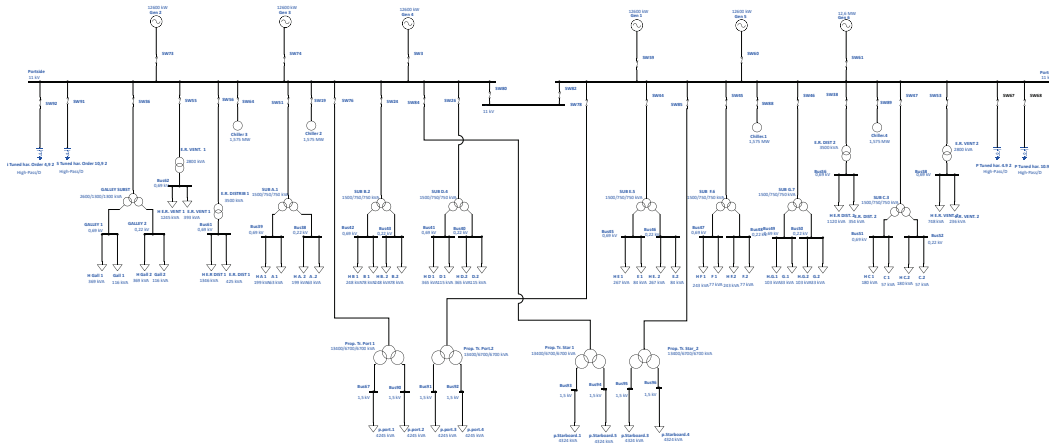
Figure 9: SPS ETAP model for harmonic analysis.
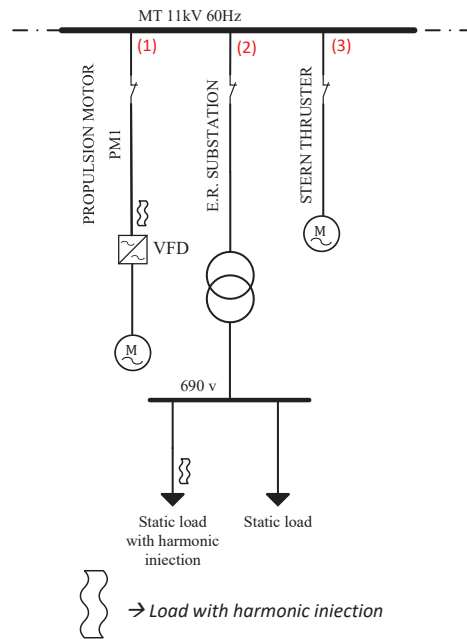
Figure 10: Example of modelling the different electric loads on ETAP.

The injection profiles assumed for the various electrical loads from the hotel substations, engine room substations, and propulsion are reported.

3.3.1 Propulsion Load

The harmonic injection profile for the propulsion loads is presented in the following figures and tables. This type of load is modelled as a (negative) current source with a defined harmonic spectrum, to represent a 24-pulse synchronous converter model, as shown in the following figures.

Harmonic Library	
Type:	Current Source
Manufacturer:	ABB
Model:	ACS600 6P
Phase Type:	Balanced

Table II: Harmonic injection model of the propulsive load

(a) *Current source injection waveform*

(b) *Current source injection spectrum*
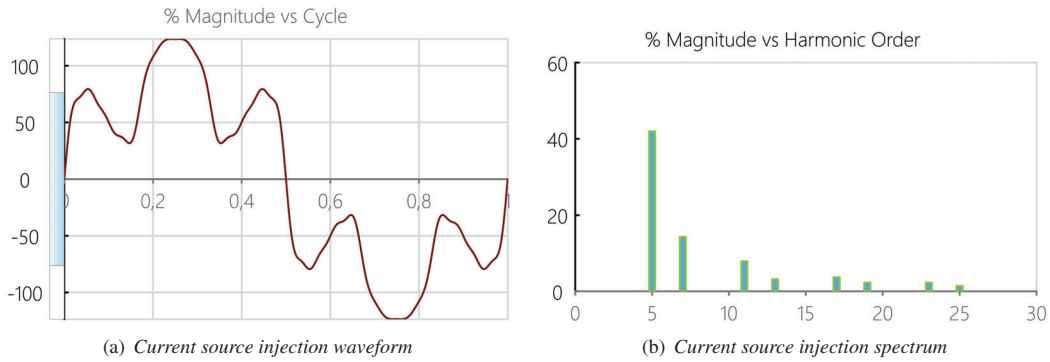
Figure 11: Injection form and spectrum ABB ACS600 6P
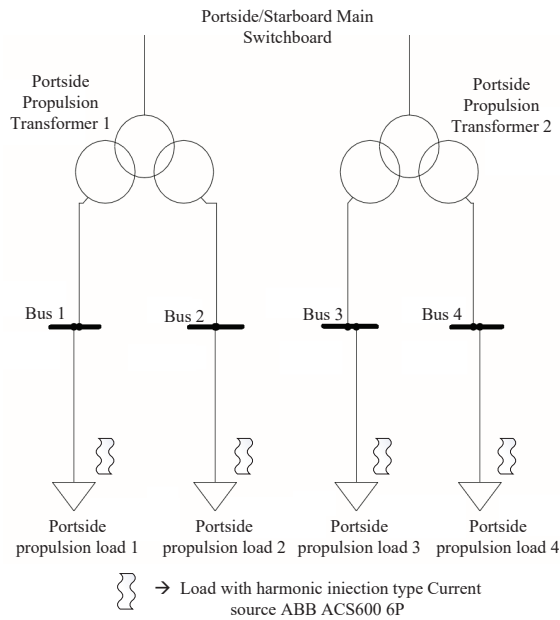
Figure 12: Model VFD 24 pulse in ETAP.

3.3.2 Engine auxiliary substations load

This type of load falls within the modeling of loads from the substations described earlier, so it is necessary to divide the load into two static loads. For the load injecting harmonics, it is considered that there are electrical components regulated by VFDs. The injection profile described in the following tables and figures is then assumed.

Harmonic Library	
Type:	Current Source
Manufacturer:	Rockwell
Model:	6-Pulse VFD
Phase Type:	Balanced

Table III: Harmonic injection model of the engine auxiliary substations load

3.3.3 Hotel substations loads

According to the real equipment information, a large part of each substation load (air conditioning) is supplied by a non-controllable 6-pulse rectifier. Therefore, an IEEE 6-pulse profile was used.

After several preliminary evaluations and calculations, the power factor of the electrical load from the substations has been assumed to be 0.92, while for the propulsion load, it was assumed to be 0.81.

(a) *Current source injection waveform*

(b) *Current source injection spectrum*
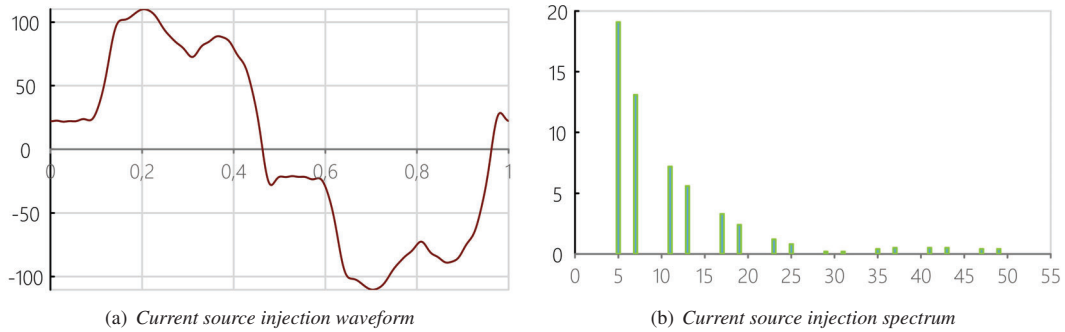
Figure 13: Injection form and spectrum 6-Pulse VFD

Harmonic Library	
Type:	Current Source
Manufacturer:	Typical IEEE
Model:	IEEE 6 Pulse
Phase Type:	Balanced

Table IV: Harmonic injection model of the hotel substations load

(a) *Current source injection waveform*

(b) *Current source injection spectrum*
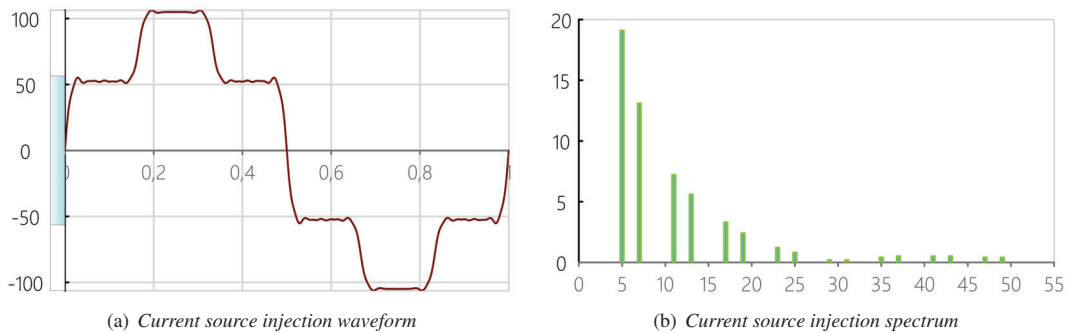
Figure 14: Injection form and spectrum IEEE 6 Pulse

4 Real data measurements validations

In this section, the results obtained from simulating the model using ETAP software are reported. Figure 15 shows the trend of THD_V on the main electrical panel as the percentage of harmonic load injection increases. It is noticeable how the trend is linear since, as the power under converters increases, it shows a linear correlation with the harmonic injection percentage.

These graphs provide the THD_V value obtained on the main panel as the portion of load subjected to converters increases. The results show that with approximately 76% of the load under converters and the assumed harmonic current injection profiles, the THD_V values match real measurements both when the ship is sailing and when it is in port.

4.1 Load flow results for harbour condition

In this section, Tables V and VI present the input data for the load flow related to the active and reactive power absorbed in the 'harbour' scenario. Another input is the voltage value on the main switchboard shown in Table VII, which is essential for achieving the adherence of the THD_V value of the harmonic load flow. Table VII also presents the load flow results in terms of current, active power, and reactive power supplied by the DG operating in the 'harbour' condition and the harmonic load flow results in terms of THD_V [%]. When data is absent in the table, it indicates components disconnected from the ship's power grid.

Figure16 presents the results, including the voltage waveform on the main switchboard, its spectrum, and the frequency scan, specifically the impedance angle and the impedance value related to the main switchboard.

| (a) *Case "Harbour":* | (b) *Case "Navigation"* |
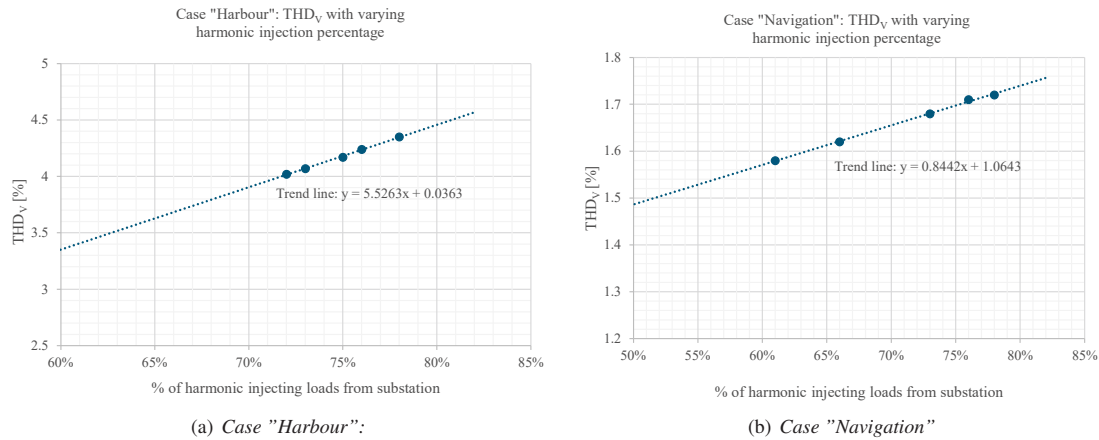
Figure 15: THD$_V$ with varying harmonic injection percentage

Substation	ACTIVE ELECTRIC POWER ABSORBED [kW]	REACTIVE ELECTRIC POWER ABSORBED [kVAR]
Acc. n°1	494.6	217.8
Acc. n°2	644.1	286.4
Acc. n°3	427.2	187.3
Acc. n°4	843.8	380.2
Acc. n°5	712.5	318.3
Acc. n°6	618.6	274.6
Acc. n°7	271.9	118.0
Galley	625.9	274.4
E.R.Dist.1	1534.0	708.0
E.R.Vent.1	601.0	266.3
E.R.Dist.2	1242.0	564.8
E.R.Vent.2	609.1	270.0

Table V: Load Flow Substations Transformers SC1 Case "Harbour"

Measure Chiller	AC 1	AC 2	AC 3	AC 4
ACTIVE ELECTRIC POWER ABSORBED [kW]	-	701.3	-	-
REACTIVE ELECTRIC POWER ABSORBED [kVAR]	-	573.7	-	-

Table VI: Load Flow Chiller HVAC SC1 Case "Harbour"

Measure D/G	n°1	n°2	n°3	n°4	n°5	n°6
DG ACTIVE POWER [kW]	-	-	-	9326	-	-
DG CURRENT AVG [A]	-	-	-	543	-	-
DG REACTIVE POWER [kVAR]	-	-	-	4440	-	-
DG THD$_V$ MAIN SWITCHBOARD [%]				4.21		
DG VOLTAGE AVG MAIN SWITCHBOARD [V]				10983		

Table VII: Load Flow Results DG SC1 Case "Harbour"

4.2 *Load flow results for navigation condition*

In this section, Tables VIII,IX,X andXI present the input data for the load flow related the active and reactive power absorbed in the 'navigation' scenario where, compared to the previous scenario, electrical loads from propulsion and harmonic filters in operation are added. The voltage value on the main switchboard is reported in Table XII. Table VII also presents the load flow results in terms of current, active power, and reactive power supplied by the DGs operating in the 'navigation' condition and the harmonic load flow results in terms of THD$_V$ [%]. When data is absent in the table it indicates components disconnected from the ship's power grid.
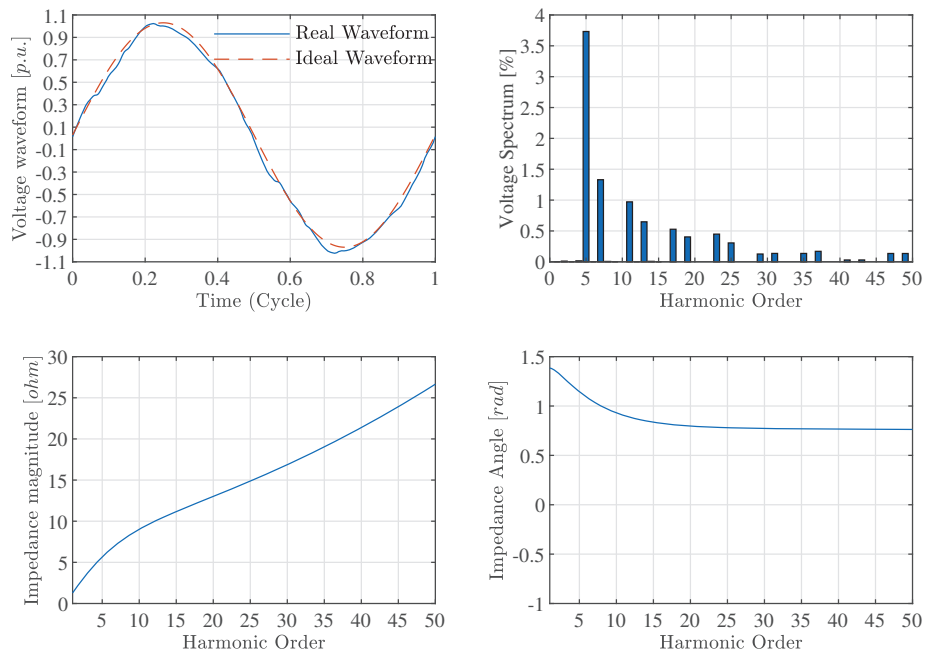
Figure 16: "Harbour" case

Substation	ACTIVE ELECTRIC POWER ABSORBED [kW]	REACTIVE ELECTRIC POWER ABSORBED [kVAR]
Acc. n°1	525.3	231.8
Acc. n°2	646.1	287.4
Acc. n°3	470.0	206.7
Acc. n°4	853.4	431.8
Acc. n°5	697.2	304.1
Acc. n°6	951.1	657.8
Acc. n°7	270.3	117.3
Galley	700.8	308.4
E.R.Dist.1	1782.0	797.2
E.R.Vent.1	1626.0	769.8
E.R.Dist.2	1481.0	304.1
E.R.Vent.2	993.2	451.5

Table VIII: Load Flow Substations Transformers SC1 Case "Navigation"

Measure Propulsion	PM 1	PM 2
ACTIVE ELECTRIC POWER ABSORBED [kW]	13050	13282
REACTIVE ELECTRIC POWER ABSORBED [kVAR]	8626	8790

Table IX: Load Flow Propulsion Transformers SC1 Case "Navigation"

Measure Chiller	AC 1	AC 2	AC 3	AC 4
ACTIVE ELECTRIC POWER ABSORBED [kW]	-	613.9	853.4	-
REACTIVE ELECTRIC POWER ABSORBED [kVAR]	-	518.4	658.0	-

Table X: Load Flow Chiller HVAC SC1 Case "Navigation"

Figure17 presents the results, including the voltage waveform on the main switchboard, its spectrum, and the

Measure Harmonic Filters	ACTIVE ELECTRIC POWER ABSORBED [kW]	REACTIVE ELECTRIC POWER ABSORBED [kVAR]
H.F. n°1 (4.9 th harmonic)	6.09	-2561
H.F. n°1 (10.9 th harmonic)	0.428	-2475
H.F. n°2 (4.9 th harmonic)	-	-
H.F. n°2 (10.9 th harmonic)	-	-

Table XI: Load Flow Harmonic Filters SC1 Case "Navigation"

Measure D/G	n°1	n°2	n°3	n°4	n°5	n°6
DG ACTIVE POWER [kW]	9604	-	-	9641	9643	9696
DG CURRENT AVG [A]	564.2	-	-	563.6	563.6	566.6
DG REACTIVE POWER [kVAR]	4720	-	-	4464	4610	4634
DG THD$_V$ MAIN SWITCHBOARD [%]	1.76					
DG VOLTAGE AVG MAIN SWITCHBOARD [V]	10950					

Table XII: Load Flow Results DG SC1 Case "Navigation"

frequency scan, specifically the impedance angle and the impedance value related to the main switchboard, where the operation of passive harmonic filters connected to the main switchboard can be observed.
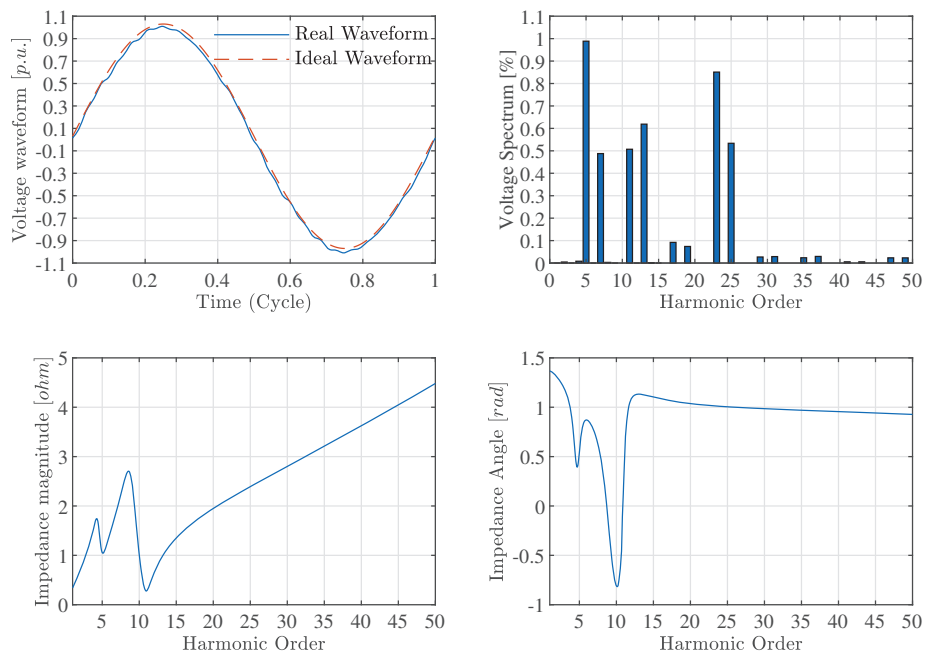
Figure 17: "Navigation" case

5 Conclusions and further research

This work has presented a methodology for analyzing and validating real measurement data collected from operating cruise ships, with the primary goal of studying power quality on the SPS. To verify the data analysis results, a model of the SPS is developed in the ETAP environment. Two similar cruise ships, equipped with different technologies for driving synchronous propulsion motors, were considered as case studies. SC1 is equipped with a synchro-converter, while SC2 uses a cyclo-converter. In port conditions, both units require only one DG to meet the electrical load. However, during navigation, at least two DGs are needed to meet the load demand, even at low speeds. The two units exhibit different THD_V behaviors under various operating conditions. In SC1, THD_V is higher during port operations and lower during navigation. Conversely, in SC2, THD_V is worse during navigation. The correlation between active power absorbed by the propulsion motors and THD_V shows a decreasing proportional correlation in SC1 and an increasing proportional correlation in SC2 (see Tab. I). An ETAP model was developed to compare and validate the data related to SC1, as more information was available regarding the SPS components. Following model calibration, load flow and harmonic load flow analyses were conducted. Comparing the frequency scans of 'harbour' and 'navigation' conditions revealed the impact of onboard passive harmonic filters on the power grid's impedance and power factor. In the 'navigation' condition, the filters operate at half their capacity, reducing system impedance at the tuning harmonics (4.9 and 10.9). This reduction aligns with the harmonic load flow results, showing decreased THD_V during navigation after the propulsion VFD operation. The ETAP model suggests that the lack of filtering action in port may cause THD_V values to approach the 8% threshold under steady-state conditions Mindykowski and Tarasiuk (2015). The ETAP model results, based on the active power values of electrical loads and voltage values at the main panel, show consistency between measured THD_V values and simulated results for the two steady-state conditions. This process verifies the data for SC1 and identifies the load magnitudes under converters and power electronics in various substations. Due to the complexity Future work will involve searching for harmonic injection profiles that yield specific THD_V values under various operating conditions, and filters configurations.

References

Barros, J., Diego, R.I., 2016. A review of measurement and analysis of electric power quality on shipboard power system networks. Renewable and Sustainable Energy Reviews 62, 665–672. doi:https://doi.org/10.1016/j.rser.2016.05.043.

Crapse, P., Wang, J., Abrams, J., Shin, Y.J., Dougal, R., 2007. Power quality assessment and management in an electric ship power system, in: IEEE Electric Ship Technologies Symposium, pp. 328–334. doi:10.1109/ESTS.2007.372106.

Gallo, M., Kaza, D., D'Agostino, F., Cavo, M., Zaccone, R., Silvestro, F., 2023. Power plant design for all-electric ships considering the assessment of carbon intensity indicator. Energy 283. doi:https://doi.org/10.1016/j.energy.2023.129091.

IEEE, 2009. IEEE Std 1159-2009. Recommended practice for monitoring electric power quality. IEEE Power and Energy Society .

IEEE, 2014. Ieee recommended practice and requirements for harmonic control in electric power systems. IEEE Std 519-2014 (Revision of IEEE Std 519-1992) doi:10.1109/IEEESTD.2014.6826459.

International Association of Classification Societies (IACS), 2019. Requirements concerning electrical and electronic installations.

International Electrotechnical Commission, 2024. Generation, transmission and distribution of electricity – operation (iec 614-01-01). URL: https://www.electropedia.org/iev/iev.nsf/display?openform&ievref=614-01-01. accessed: 2024-07-16.

Kůs, V., Peroutka, Z., Drábek, P., . Non-characteristic harmonics and interharmonics of power electronic converters, in: CIRED 2005 - 18th International Conference and Exhibition on Electricity Distribution. doi:10.1049/cp:20051030.

Li, Y., Peng, Y., Liu, F., Sidorov, D., Panasetsky, D., Liang, C., Luo, L., Cao, Y., 2017. A controllably inductive filtering method with transformer-integrated linear reactor for power quality improvement of shipboard power system. IEEE Transactions on Power Delivery 32, 1817–1827. doi:10.1109/TPWRD.2016.2574316.

Liu, Q., Liu, F., Zou, R., Wang, S., Tian, Y., Wang, Y., Yuan, L., Li, Y., 2022. A compact-design oriented shipboard power supply system with transformer integrated filtering method. IEEE Transactions on Power Electronics 37, 2089–2099. doi:10.1109/TPEL.2021.3102938.

Liu, W., Tarasiuk, T., Gorniak, M., Guerrero, J.M., Savaghebi, M., Vasquez, J.C., Su, C.L., 2018. Power quality assessment in real shipboard microgrid systems under unbalanced and harmonic ac bus voltage, in: IEEE Applied Power Electronics Conference and Exposition (APEC), pp. 521–527. doi:10.1109/APEC.2018.8341061.

Meghanathan, N., 2016. Assortativity analysis of real-world network graphs based on centrality metrics. Computer and Information Science 9, 7. doi:10.5539/cis.v9n3p7.

Milankov, R., Radić, M., 2014. Harmonics: Examples of negative impacts, in: 2014 16th International Conference on Harmonics and Quality of Power (ICHQP), pp. 435–438. doi:`10.1109/ICHQP.2014.6842817`.

Mindykowski, J., Tarasiuk, T., 2015. Problems of power quality in the wake of ship technology development. Ocean Engineering 107, 108–117. doi:`https://doi.org/10.1016/j.oceaneng.2015.07.036`.

Rahman, S., Ghering, J., Elizondo, N., Ahmad Khan, I., 2022. Intelligent filtering solutions for improving power quality in marine shipboard systems, in: IEEE Kansas Power and Energy Conference (KPEC). doi:`10.1109/KPEC54747.2022.9814803`.

Rigogiannis, N., Bogatsis, I., Pechlivanis, C., Terzopoulos, K., Kyritsis, A., Papanikolaou, N., Loupis, M., 2023. Power quality measurements in shipboard microgrids: A case study, in: International Conference on Electrical Drives and Power Electronics (EDPE). doi:`10.1109/EDPE58625.2023.10274026`.

Semwal, P., Narayanan, V., Singh, B., Panigrahi, B.K., 2022. Performance evaluation of power quality in shipboard microgrid under different working conditions, in: IEEE Global Conference on Computing, Power and Communication Technologies (GlobConPT). doi:`10.1109/GlobConPT57482.2022.9938368`.

Terriche, Y., Mutarraf, M.U., Mehrzadi, M., Su, C.L., Guerrero, J.M., Vasquez, J.C., Kerdoun, D., Alonso, A., 2019. Power quality and voltage stability improvement of shipboard power systems with non-linear loads, in: IEEE International Conference on Environment and Electrical Engineering and 2019 IEEE Industrial and Commercial Power Systems Europe (EEEIC / ICPS Europe). doi:`10.1109/EEEIC.2019.8783356`.

Tsvetanov, D., Djagarov, N., Grozdev, Z., 2023a. Improving power quality in shipboard power system using a static synchronous compensator: A simulation study, in: International Conference Automatics and Informatics (ICAI), pp. 124–132. doi:`10.1109/ICAI58806.2023.10339067`.

Tsvetanov, D., Milushev, H., Djagarov, N., Djagarova, J., 2023b. Investigation of power quality using a laboratory experimental setup of a shipboard power plant, in: International Conference Automatics and Informatics (ICAI), pp. 133–139. doi:`10.1109/ICAI58806.2023.10339035`.

Human Autonomy Teaming in Naval C2 – Insights from Dstl's Intelligent Ship Project

A J Tate, MSc, CMarEng FIMarEST[+]* & C J Cooke[+]

[+] Defence Science & Technology Laboratory (Dstl), UK
* Corresponding Author Email: *atate@dstl.gov.uk*

Synopsis

Future military forces and platforms will operate within increasingly complex operational environments, facing a more aggressive and diverse range of threats. This will continue to increase the volumes and speed of data, and hence information, that platforms and their human commanders will need to capture, process and respond to. This leads to a clear need to be able to effectively, and flexibly utilise the best of both human and Artificial Intelligence (AI) skill sets in future Command and Control (C2) and decision making more broadly.

The UK Defence Science and Technology Laboratory (Dstl - part of the UK Ministry of Defence (MOD)) has funded three phases of the Intelligent Ship project. The project explored Human-Machine, Machine-Machine Teaming (HM3T), considering relationships between team members, and the approaches needed to enable them, aiming to understand the challenges and opportunities this approach brings to future Naval C2 and defence more widely.

The project achieved this through the development of a range of intelligent machine agents and through the development, evaluation and demonstration of those agents, with human operators, within a systems level architectural 'sandpit' known as the Intelligent Ship AI Network (ISAIN). The project also started to consider underpinning design issues, such as: how to effectively design-in humans into a system; how to manage inevitable conflict between recommended Courses of Action (COA) and; how such a system should be configured and managed with varying Levels of Automation (LOA). This work was delivered by a multidisciplinary team of external suppliers and evaluated within Dstl's simulation facilities.

While there is current focus on removing humans from threat environments, automation and autonomy will continue to have limitations, which when coupled with UK policy, drives a continuing need, and a clear benefit from the use of human based analysis and decision making skills. The aim of this project was, therefore, to optimise military decision making rather than pursue solutions to full autonomy or crew reduction for their own sake.

This paper will build on a previous 2022 International Ship Control Systems Symposium (iSCSS) paper to provide an end of project perspective on the key insights and challenges identified. It will postulate what future research and development is required, and how the project lessons should be integrated into future C2 concepts and designs.

Keywords: AI; intelligent systems; automation; future command control; Human-Machine Teaming

1   Introduction

Future military forces and platforms will operate within, and against, an increasingly complex, diverse and technology focused set of threats. This will increase the volumes and rate of delivery of data, and hence information, that human commanders and their supporting systems need to capture, process and respond to. Decision making speed will also need to increase as threats themselves become faster, more numerous and less predictable, or identifiable.

These challenges are amplified when considering the application of future, and potentially more distributed, combat systems. Systems such as distributed high-powered sensors and Directed Energy Weapons (DEW) drive a need for better coordination across a force, or fleet, and also improved intra-platform connectivity between internal systems, for example, power system controllers, and navigation systems and the combat system itself.

Addressing these challenges inevitably leads Defence to consider the wider use of automation and autonomy, with an expectation of the wider implementation of Artificial Intelligence (AI) approaches within future Command and Control (C2) systems. While there is significant focus on autonomy in defence systems and platforms, this represents the focused use of AI within Decision making processes. The emergent paradigm of developing systems to handle decision making demands has been described as Decision Intelligence, defined by Gartner (Brethenoux, 2021) as a "practical discipline used to improve decision making by explicitly understanding and engineering how decisions are made, and outcomes evaluated, managed, and improved by feedback".

The benefit of combining machine and human based intelligence skills and strengths, coupled with the demands from policy, leads to a need to form effective and adaptable teaming relationships between intelligent machine agents, matching automation systems, and human operators – a Human-Autonomy-Team (HAT). The project has also used the term human-machine and machine-machine teaming (HM3T) to reflect the need to also enable multiple AI agents to work together within a team as collaborative AI.

Authors' Biographies

Andrew Tate is chartered senior principal engineer for Dstl (UK Ministry Of Defence (MOD)). He manages a range of naval focused Science & Technology research activities for UK MOD, focusing on power systems, sustainability and autonomy. He has an MSc in Marine engineering from Newcastle University and is a fellow of IMarEST.
Colin Cooke is senior principal scientist for Dstl (UK MOD). With 39 years of experience working on Science & Technology research activities for UK MOD, focusing on autonomous systems, and their underpinning technologies (e.g. autonomy, launch and recovery, system architectures, platform integration, C2, interoperability standards).

Defence needs to understand how to design, manage and integrate these systems in order to reduce the potential risks of complex HATs and to maximise the defence capability benefit they could bring. This requires a paradigm shift from designing systems and their interfaces with humans, to designing systems with human and machine teaming interaction as a fundamental element of the initial concept and design.

Dstl has previous briefed ISCSS of the outputs of the second phase of the Intelligent Ship project (Tate, 2022). This paper will take a wider retrospective view at the end of phase 3 activities to capture some of the key insights identified and to suggest key challenge areas and needs going forward, that could allow HAT and collaborative AI to be practically integrated into future C2 concepts. The research, while focused on Naval C2, has clear and transferable applicability and relevance to any future defence C2 system, network or platform where humans and AI agents need to work together in an effective HAT.

1.1. *Project aims & phases*

The Intelligent Ship project was initiated with an aim of starting to understand, develop and evaluate concepts that address the challenge of enabling, integrating and managing complex HM3Ts in generation after next platforms. It was funded under Chief Scientific Advisor's research funding under Dstl's Autonomy Programme.

The project was challenged to consider a clean sheet approach to avoid the constraints of current Naval C2 processes and system architectures. It attempted to understand and qualify the follow project vision:

Machine learning and AI will be more closely integrated and teamed with humans, leading to timely, more informed and trusted decision making and planning, within complex operating environments.

Each phase has had a specific focus which can be summarised as follows:

- Phase 1: **'develop enablers'** – This phase delivered a diverse range of AI agents across a range of naval functions via a Defence and Security Accelerator (DASA) industry call. It funded the underpinning development and experimentation 'sandpit', the Intelligent Ship AI Network (ISAIN)[1]. This phase also started the process of developing an underpinning tactical naval navigation agent (TACNAV), and delivered a study called Platform Design Risks & Opportunities (PeDRO)[2], which captured the context, impacts, risks & opportunities of wider use of machine intelligence & automation in naval platforms.
- Phase 2: **'Integrate & evaluate'** - this phase developed Phase 1 agents and a range of new agent concepts, before integrating them, with a number of agents from other programmes, into ISAIN. The whole system was then tested against a representative naval scenario using Dstl's Military Advisors as operators to qualitatively test issues such as Trust in Automation (TiA), usability and Situation Awareness (SA).
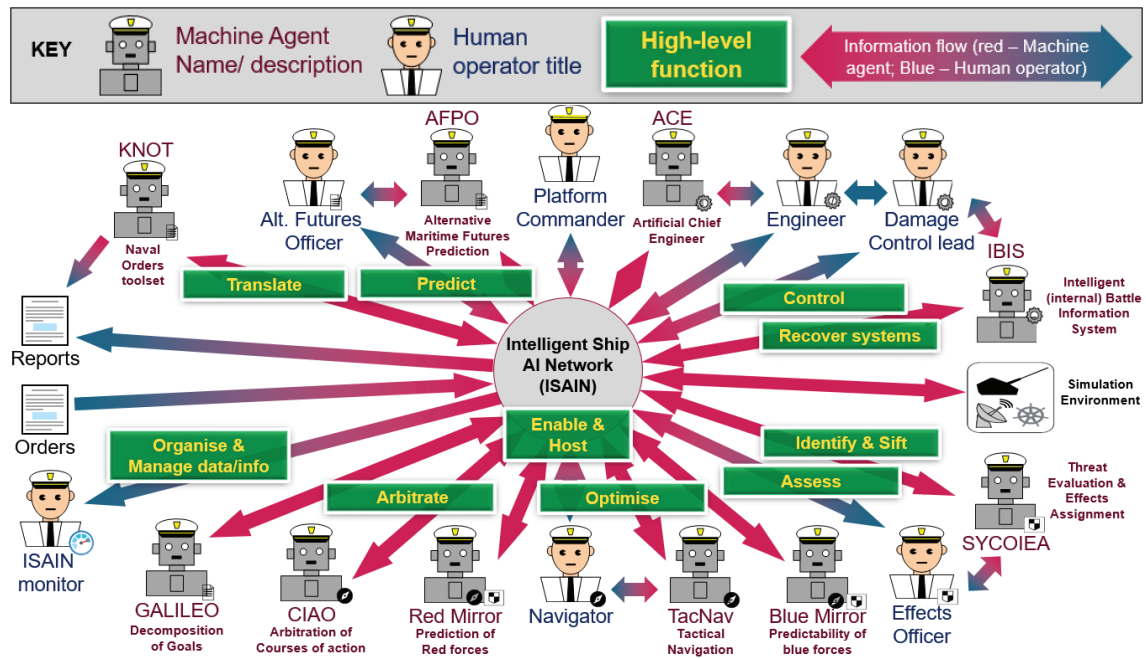
Figure 1: Phase 2 HAT system concept (humans and agents) & key functions

---

[1] ISAIN & TACNAV developed by CGI and owned by UK MOD/Dstl

[2] PeDRO informed further funding by BMT on their Highly Autonomous Warships Technologies (HAWT) project (BMT, 2021)

- Phase 3 '**Focus on the human in HAT**' – this phase aimed to use and adapt phase 2 agents and systems, but to design a system (both human and machine elements) from the ground up to meet future naval Anti-Air Warfare (AAW) capability needs. This resulted in greater focus on human-factors, roles and skill needs within the system; the requirements for human-machine interfaces and information management, and; the use of AI based arbitration approaches to manage potential conflict between proposed Courses of Action (CoA) from different agents.

It is important to note that the project purposely did not focus on, or aim to demonstrate, the potential to reduce crewing, rather to understand how a system could make best use of the strengths and skills of both machine and human intelligence working within a team. Inevitably, with greater technical maturity and trust in an Intelligent Ship type concept, crewing reductions should be possible.

2. End of project insights

The project previously presented a paper at INEC/ iSCSS 22 (Tate, 2022) which gave an insight into how the project was executed, details of some of the intelligent agents developed, and the evaluation approaches and key conclusions from the first two phases. The following discussion therefore, provides a retrospective discussion on some of the key insights at the project end. It is hoped that these provides general, and useful insights into the development, design, management and integration of complex HATs comprising of multiple agents and human operators (a HM3T) irrespective of the application or domain.

2.1. Designing-in humans early

The design of Naval C2 systems may start with assumptions around its human operators, their skills and needs, however, it is often the case that issues such as information management and HMI design, and corresponding training needs are considered later, perhaps too late, in any design process. The adoption of HAT, however, drives a demand to consider human operators early, and in parallel with the machine elements of a system, and has the potential to benefit from the best capabilities and skills of both the machines and humans.

The early adoption of intelligent systems has initially and is likely to continue to be focused on supporting existing operator roles and their core tasks. They have been typically designed to augment or directly replace a single operator and hence, have limited impacts on the overall roles, ranks and skills of the human team. An example of this would be a toolset/ agent that directly replaces an air picture compiler role.

The successful introduction of more sophisticated and broader capability intelligent agents offers both an opportunity and a risk that it drives changes within human organisations and hierarchical structures, changing the skills demand, the experience needed and ultimately roles. There is a clear potential impact on a range of Defence Lines of Development (DLODs) in areas such as training and people, as well as on more specific issues such as recruitment and retention.

An example of this is shown in Figure 2, showing a postulated conceptual AAW team structure and role descriptions developed under phase 3 of the project. These are based on a functional assessment of the AAW process, and the HAT system's design and policy needs, rather than existing Royal Navy (RN) team structures, roles or ranks

2.2. Decision making with varying Levels of Automation

Intelligent decision systems offer the opportunity to operate more dynamic Levels of Automation (LOA), where tasks could be allocated to humans and machines based on factors such as workload, threat level and the relative TiA in a given scenario or situation. An operator may need to take manual control of a system (potentially in, or on-the-loop) in peacetime operation to maintain SA and experience, and to build trust in (or understand the limitations of) the automation and autonomy. This creates a need to both understand how and when LOA should be changed, and how decision making is achieved at each LOA and is likely to change dependent on the situation.

A decision making framework was developed during phase 3 of the project as illustrated in Figure 3. It shows decision making across three LOA categories; fully automated, augmenting or decision support. It also shows how each category has a blend of human and machine interactions and how the best decision making approach depends on the characteristics of that decisions, e.g. Time available, level of risk or complexity. The project assessed an example complex AAW scenario to understand decision-making hot-spots. These are points of time when the complexity of a decision or the required speed of response places pressure on any C2 system, including its human operators. By using this framework an assessment of the balance between human and machine based decision making could be made. Examples of hot spots are shown in Figure 3, marked by the relative position of the green stars on each bar.

There are clear parallels to the current debates and experience with vehicle driver assistance systems, where operators need certainty over their responsibilities at any given point and need to maintain sufficient SA to take over control or intervene where and when necessary. For these reasons a clear policy is needed around how LOA

are managed and changed in a military context, based on balancing the desire to optimise decision-making, while ensuring sufficient operator understanding and visibility of both the LOA and their decision making role within it.
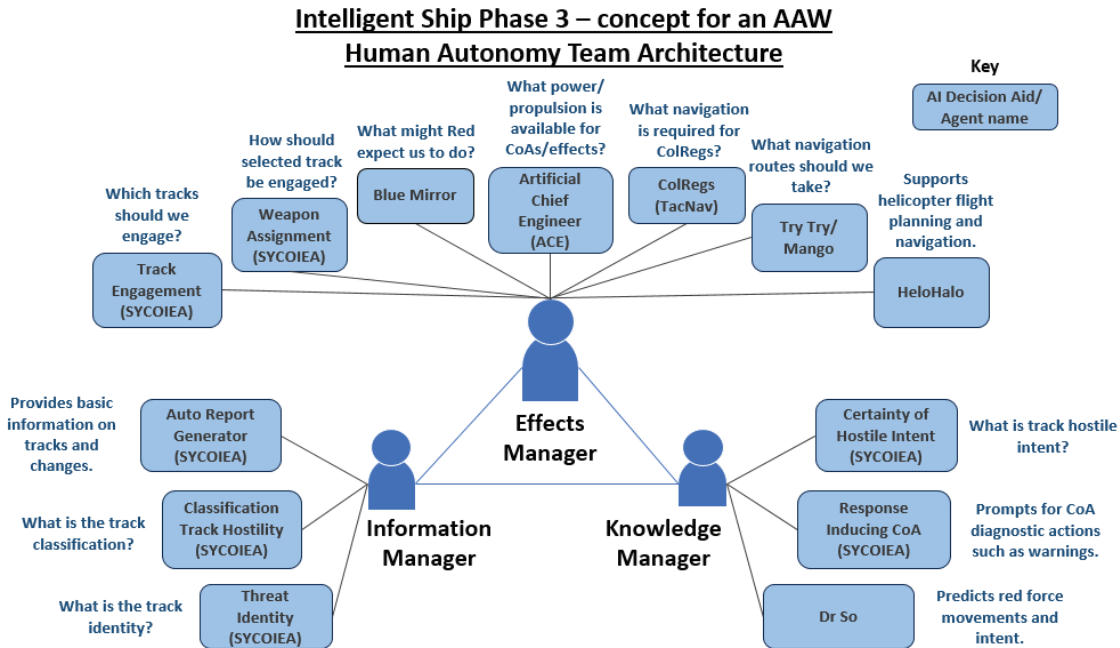
Figure 2: Proposed phase 3 AAW team structure & supporting Agents[3]
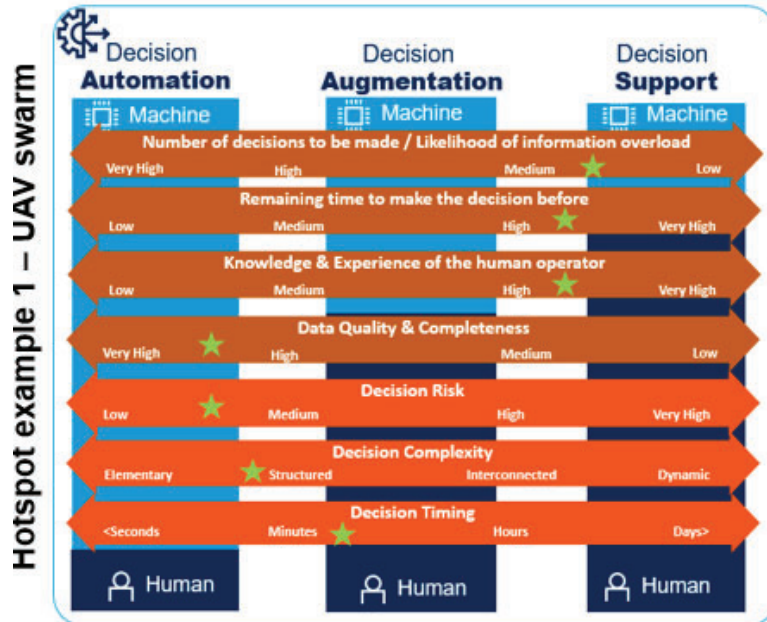
Figure 3: Phase 3 decision making framework with the characteristics of an example decision making hotspot (Developed by Decision Lab/ Diem)

2.3. *HAT Training aspects*

There is likely to be clear benefit in developing a combined approach to training and development of both operators and AI agents in parallel. For the human this allows them to build understanding, TiA and experience of AI agents' (or collaborative team of agents') limitations in a given scenario or context. For each agent there is a training demand for AI approaches (e.g. Reinforcement Learning (RL)) that would benefit from training

---

[3] More details on the individual agents can be found in the previous INEC/iSCSS paper (Tate, 2022)

scenarios involving humans, either to learn from their responses, or from the various training scenarios the operators train within. This would also help to inform development of HMIs.

While it is potentially dangerous to anthropomorphize machine agents within a HAT, human operators need to understand the limitations of, and develop trust in the same way as they would for new human team members. They will also need to train and develop as a team to become effective. Experience of non-intelligent systems show that user frustration can quickly result in limited trust, and hence reduced reliance upon it and in some cases not use it all.

Inevitably new agents based on machine learning or other AI training techniques will be 'inexperienced' in certain scenarios. Creating or capturing a desirable level of real world training data is a challenge, while naval platforms operate across a broad range of environments and tasks, resulting in large data-sets, they infrequently repeat the same tasks and experience certain environments and threats through-life, especially, and fortunately, high threat scenarios. This can limit the applicability of many big data based AI techniques and would make it valuable to able to integrate experience from other ships in a class, across the wider fleet, international partners or even from retired platforms, into currently deployed systems. This challenge places a demand on modelling and simulation capabilities as discussed in section 2.6.

2.4. *Enhancing Machine-Machine interactions*

While the Threat Evaluation and Weapons/Effects Allocation (TEW/EA) process offered the project significant and complex opportunities for multiple agents and operators to interact, the project also wanted to explore wider interactions with a platform's own systems. This drove the parallel development of TACNAV, platform control focused tools such as Rolls-Royce's Automated Chief Engineer (ACE – providing power and marine systems automated control) and Fraser Nash's Internal Battle Intelligent System (IBIS – optimising resilience and damage recoverability strategies).

By bringing these agents and their developers into a single integrated system and project, new links and opportunities were quickly identified, including new uses for tools, or for the data and information they produce. An example of this included using a real time analysis tool such as IBIS to generate predictions of future material state and residual capability after damage, and providing information or constraints to other agents proposed CoA. Another example was the ability to balance navigational options between the needs of safe passage (e.g. collision avoidance from TACNAV) and other directional demands, such as to provide line of sight for an effector (TEW/EA), all constrained by availability of power and propulsion (via ACE).

The concept of Tactical Energy Management (TEM) also becomes relevant, with better linkages between material state awareness, power management and navigation system potentially providing command or other agents with a better understanding of options and limitations with, for example, energy based systems such as Laser Directed Energy Weapons (LDEW).

2.5. *HAT System design & enablers*

The aims, development and key characteristics of ISAIN were discussed in a previous paper (Tate, 2022). ISAIN was configured to support HAT experimentation and was not optimised for deployment, but provided the project with the ability to configure, test, assess and monitor interactions between multiple AI agents and Human operators. In setting to work and then evaluating the HAT system developed in Phase 2, a number of lessons were learnt around the design, management and confirmation of a complex HM3T. These were investigated further in Phase 3 and reflected in the designs developed. This sections summarises some of the key enablers to facilitating a functional and effective HAT.

2.5.1. *HAT management*

Phase 2 of the project included a series of HAT evaluations events, allowing the system, and operator's experience of the system to be captured and assessed. This identified challenges around the management of the system and the information within it and hence a potential need for a HAT manager. It was envisaged that this could operate as a 'teammate' within the HAT, sensing and understanding the system environment, the processes within it and the capabilities and needs of the wider team members. Functions this HAT manager could provide include:

- **Functional Distribution** of functions and/or tasks between humans and AI agents within a HAT
- **Oversight and Control** of the ways and extent to which humans within a HAT are able to maintain SA and control over AI agent activity and understanding.
- **Coordination** of the ways in which humans and AI agents within a HAT are able to coordinate their actions and SA in response to constraints such as timing, resource allocation, prioritisation and conflict resolution.
- **Cognitive Enablement** i.e. the ways in which humans and AI agents within a HAT mutually co-facilitate complex cognitive activities such as sense- and decision-making.
- **Adaptation** of a HAT to new behaviours based on new circumstances and demands.

- **Ethics**   i.e. the ways in which humans and AI agents within a HAT apply/deploy ethical/ policy driven constraints.
- **Trust Calibration**   in which a HAT supports interactions that enable evidence-based calibration of appropriate and context specific trust

2.5.2. *Arbitration*

Decision arbitration was a core focus area for the project. A HAT is built around a set of AI agents that make observations, predictions and recommend a CoA. The term arbitration is, therefore, used to describe the process of resolving conflicting outputs or proposed CoAs from two or more agents in an explainable way. The concept was initially explored through the development and evaluation of an agent called Compounded Intelligent Agents for Optimisation (CIAO), which was based on Reinforcement Learning (RL) techniques and developed by Decision Lab.

Enacting the phase 2 HAT system's design suggested value in the use of a capability like CIAO in multiple locations within the system, potentially operating at different levels of decision making. An example could include a Navigation arbitrator agent, arbitrating between the outputs of two alternative navigation agents, before a higher level arbitrator ranked CoAs based on constraints, such as the availability of power.

This idea was developed further in phase 3 by considering which enabling AI or non-AI techniques would be best matched to each decision area and/or decision level. Techniques were assessed against decision making factors such as the level of explainability required, the decision speed needed and the overall complexity of decision making. Options considered included:

- Rules-Based algorithms: a set of explicit instructions or conditions that dictate system behaviour in all situations. These are typically pre-defined by domain experts and engineers. It is a deterministic approach, and there is no behaviour that is "learnt" in contrast to machine learning methods;
- Optimisation algorithms: a broad class of algorithms that are used to find the best possible solution to a problem by maximising or minimising a given objective function.
- Reinforcement Learning: RL is a machine learning approach where an agent learns how to act in response to either positive or negative reward signals received by interacting with its environment. The RL agent tries to maximise the expected cumulative reward received across an episode.
- Bayesian methods: statistical techniques based on Bayesian probability theory. For decision-making systems, Bayesian methods provide a framework for making decisions by combining prior beliefs with observed data, allowing for more informed and adaptive decision processes. Bayesian belief networks are a popular method well suited to decision-making under uncertainty.

The final design concept investigated was the potential need for the highest level arbitrator to have a management function in order to manage the complexity of multiple arbitration agents within any system. When combined with the concept of a HAT manager, the overall high-level structure of the system can now be summarised as shown in Figure 4.

2.5.3. *Information management and Human-Machine Interfaces*

Creating a collaborative AI system requires access to reliable, traceable and high quality data. This enables operational use of the agents, but also underpins agent training and testing during the development of both the agent and the system. This is a key challenge for any system, despite modern platforms generating significant levels of data, the sensors and data loggers were often not designed or optimised with these applications in mind. Real systems also come with significant levels of 'noise' making it essential to test collaborative AI and HAT systems against this realistic data to understand the impacts of data quality on system outcomes. This creates a demand to consider future platform's sensing and data processing capabilities, earlier and in greater detail, potentially with a greater emphasis on sensor quality, redundancy and reliability.

Assuming access to all the required data, a collaborative AI system will generate additional data and information itself, especially if AI agents actively interact and collaborate. This will augment the system's 'data-lake' further, requiring careful management to minimise data, processing and network system's scale and hence costs. If intelligent decision making is more disaggregated, then there will need to be a focus on network bandwidth, the better use of edge processing and local automation, and careful control of the amount of data required to perform certain functions.

Data and information management is also required at the Human-Machine Interface (HMI). Humans need to see the right information at the right time to make timely decisions, but will also need to understand machine proposed CoA to gain trust and insight into the systems limits and capabilities. This drives taught design of HMIs with potentially more information available and less operators, but also a need to enable 'drilling-down' into the system to provide explainability when required. The project showed, for example, the impact on operator TiA and SA of not knowing whether an agent was unable to provide a CoA or was simply still calculating options.
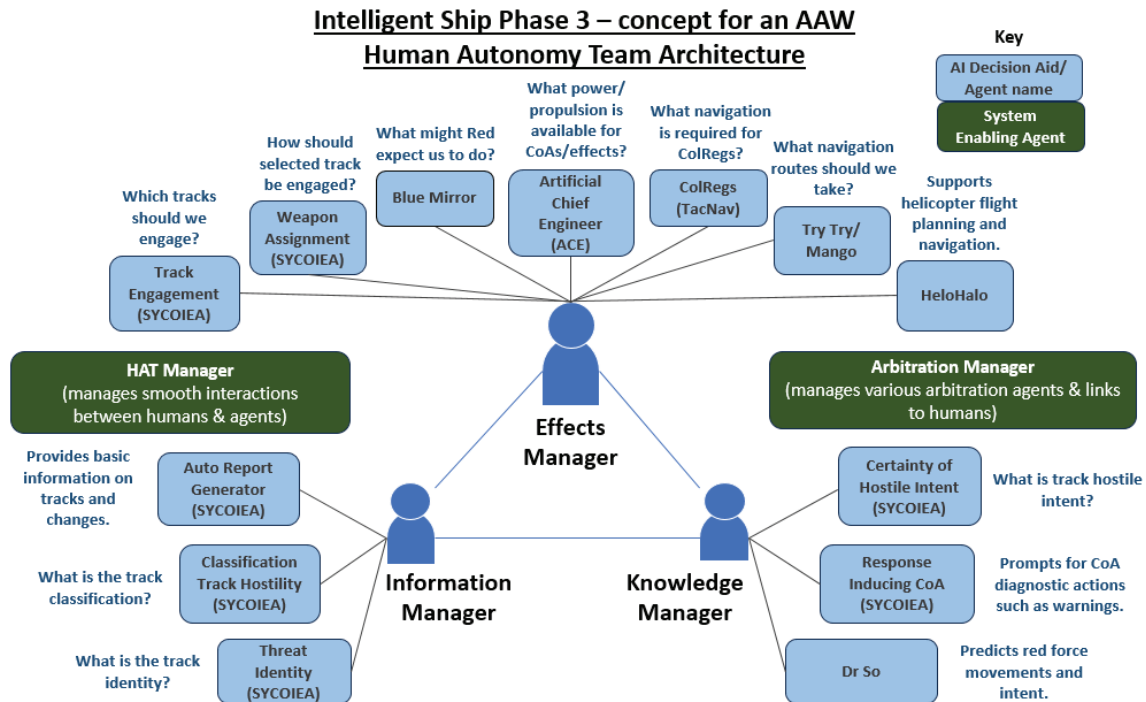
Figure 4: Intelligent Ship – proposed phase 3 AAW team structure with enabling agents added

2.6. *Modelling & simulation*

The project was underpinned by the ability to model and simulate the world in which the system operates, the data needed to operate it, and the impacts of its actions. Both cloud-based and site-based simulators were used, with cloud based solutions supporting initial remote development at each developer's site, and providing a level of high-level integration testing before installation within a physical test facility. For phase 2 this was Dstl's Command Lab, now in process of being upgraded to create the Maritime Experimentation Laboratory. This reduced demand on shared infrastructure from multiple projects, while benefiting from the higher powered computing environments available within a lab environment for final testing and evaluation. The use of open systems and standards throughout eased the complexity of integrating agents from different suppliers.

While the project found effective ways of managing its experimental needs, both through purposeful design of ISAIN and ownership of the labs and environments being used, it did not explore the wider, longer term enterprise challenges of developing, integrating and managing AI systems through-life. A range of modelling and simulation capabilities can be envisaged, from; high-level systems to undertake initial functional development and testing; real time semi-complex systems on which HAT systems can be tested and development and operational training can be undertaken, through to; high-speed, non-real-time, simulation systems to support rapid training of AI agents. This is further complicated by enabling access to data sources, linkages to other systems and potentially even to digital twins of certain systems.

Development and integration plans for an individual agent and the HAT system it is integrated into will also need to be developed. These need to define how and when it is tested, validated and assured, with what data and what level of interaction with humans, before road mapping how agents and systems are tested shore-side and when and how they are tested, and then deployed, on-board real platforms. Finally any links and opportunities to share capability with operational trainers and digital twins should be explored.

2.7. *Balancing investment, risk and maturity*

While the project focused on the design aspects on intelligent decision making systems, it also highlighted the clear need to undertake a balance of investment in which capabilities, tasks and functions would benefit from the integration of AI & HAT, considering their wider DLOD impacts.

It is unlikely that the highest level of automation and autonomy achievable in the future will be affordable, and there needs to be a pragmatic compromise between optimising designs and systems for leaner or zero crewing, making systems more robust or redundant, overall platform cost and the use of intelligent systems. Rules based control systems, or human based interventions may continue to be sufficient for many applications or tasks, be less costly and reduce the need to consider cyber-security and assurance.

Factors that will change the balance of investment with time will include:

- Relative maturity of AI and matching Automaton systems - automation, robotics and other systems will inevitably mature at different rates to AI control systems in different application areas, and in some cases the cost of matching automation could continue to be the main barrier to implementation.
- A need to balance capability with matching network and sensing needs – for agents to be 'aware' or able to learn from the environment and other constraints in their action space, they require connectivity to appropriate sensors and networks. The complexity and scale of these systems will impact platform design and cost, and also areas such as platform supportability, potentially adding workload onto human maintainers. Novel sensing approaches may help manage this challenge.
- Impacts on crewing – there is a need to prove the benefits of any automation or AI system against impacts to crew skills, roles and job engagement and satisfaction. While automation and autonomy could help to reduced crew sizes, care is needed to avoid adversely impacting recruitment and retention.
- System openness and flexibility – currently AI is good at specific tasks, it is less advanced in more general reasoning focused activities and in providing high levels of explainability critical to defence. This has led to early adoption in certain capability areas, but much longer development periods for the more sophisticated anticipated applications. This drives a need for open and flexible hosting, and modelling and simulation environments that allow future complex AI agents to be incrementally tested, trained and integrated into, and alongside, older systems.
- Managing reversionary operation – currently systems are generally designed to retain manual, human operated reversionary modes after failure or damage. This may not be ultimately possible in the future, due to the level of complexity needed to provide reversionary control, the cost and complexity of implementation, or due to the reduction or removal of crews from platforms. This will demand different approaches to safety, assurance, recovery and security of collaborative AI systems and ultimately change how the RN considers platform and systems survivability.

3. Summary & conclusions

As greater levels of intelligent decision making are integrated into platforms, it is inevitable that interactions between them will be required to maximise benefit. This requires C2 systems to consider this requirement early, and to reflect the expected needs, such as supporting simulation and modelling needs & the development of CoA Arbitration, that will enable such a transition well before the component AI capabilities mature and are incrementally deployed. This is both a technical, digitally based challenge (data, processing & networks) and a significant challenge to wider DLODs (e.g. to people, training and infrastructure).

Early consideration of human interactions, roles and skills in future HATs is also essential to ensure the best use of both human and machine skills-sets to maximise impact and capability. It is also necessary to realistically realise any practical crew reductions.

The Intelligent ship project has started to unpack some the opportunities and challenges of future naval C2 based on Collaborative AI and HAT, but can only be considered as the start of a longer journey. For example, experimentation to date has not used realistic data and hence there is limited understanding of data quality on system design, performance and human-machine interactions. Future work will be needed on how such a systems is managed and updated through-life, considering initial training, testing, validation and assurance, as well as developing systems' 'experience' through-life. There are significant HAT focused questions to explore around building trust, explainability and managing information effectively between human and machine elements of a systems, and around how and when a HAT system moves between different levels of automation.

At an enterprise level, defence ministries will need to consider and manage the wider DLOD risks of AI and autonomy, and understand modelling and simulation needs in the round, enabling initial testing of agents, systems and a HAT more generally, but also to allow through-life development and maintenance, and agent and operator training.

Finally, there is a clear need to have a high-level holistic assessment of where to focus development and investments in intelligent decision making, reflecting both capability demands, but also corresponding decision-making dynamics (speed, complexity & type), the maturity of AI techniques and realistic assessment of supporting sensing, data and automation systems required.

Acknowledgments

References

Tate, A., Purvis, E., Fromm, C., Jaya-Ratnam, D. (2022). 'The UK's Intelligent Ship project – exploring future human-machine and machine-machine teaming'. *INEC/iSCSS proceedings*.

Unnamed. BMT. (2023). 'Large Uncrewed Surface Vessel-LUSV – white paper'. *https://www.bmt.org/news/2023/charting-new-horizons-bmt-showcases-vision-for-lusv/*

Brethenoux, E. (2021). 'Decision Intelligence Is the Near Future of Decision Making'. www.Gartner.com

Automatic Maneuvering of Vessels with Power-Optimized Thrust Allocation

Dr. A Schubert *, N Eisenblätter, MSc, R Damerius, MSc, Prof. T Jeinsch

University of Rostock, Institute of Automation, Germany

*Corresponding author. Email: agnes.schubert@uni-rostock.de

Synopsis

Assisted and automated ship maneuvering can contribute to safer and cleaner port operations. Power consumption can be reduced by optimizing the thrust allocation to the available actuators. Within the established structure for guidance, navigation and control, thrust allocation belongs to the control module. Each controller mode requires an associated allocation that distributes the commanded forces at the controller output to the ship's actuators so that the desired motion is achieved. The allocation problem is formulated as a quadratic program. The paper focuses on a generic allocation approach for a vessel with a maximum of six actuator units. The method is explained using the specifications of the 52 *m* long research vessel *DENEB* and for the various phases of automatic port maneuvers in the area of German Naval Base Command Rostock-Warnemünde. The paper presents the results for dynamic positioning maneuvers with the real vessel under the influence of wind using the developed allocation approach.

Keywords: Consumption optimisation; Manoeuvring automation; Quadratic programming

1 Introduction

The introduction of assistance and automation functions in conventional shipping is motivated by a number of factors. These include saving fuel and emissions, avoiding collisions and the growing shortage of experienced nautical officers, which prompted Japan to launch the MEGURI project (Miyoshi and Ioki (2021)). At the same time, the challenges of navigating safely are increasing due to higher traffic volumes and ever-growing ship sizes (UNITED NATIONS (2019)). Assisted and automated ship maneuvering can also contribute to safer and cleaner port operations where combined precise and slow motions in three degrees of freedom are required, often using the full available propulsion power to compensate for the large influence of environmental forces on the ship (Schubert et al. (2024a)).

The presented approach follows the method of successive maneuver automation, which was explained in detail in Schubert et al. (2018). With the focus on conventional ships, full read access to all sensor and actuator data as well as the digital controllability of the actuators by the automation system is a basic requirement for automatic maneuvering (Schubert et al. (2023)). An assistance system is used to visualize both the planned and the actual trajectory of the automatic maneuver so that the captain can evaluate the functions of the automatic control system and fulfill his responsibilities. The automation system is based on a generic module structure for the tasks of guidance, navigation and control (GNC).

The topic of this contribution, the power-optimized thrust allocation, is part of the control module within the GNC structure, in which the forces commanded by the controller are optimally distributed to the available actuators. Each allocation must be ship-specific according to its actuator configuration and maneuver-specific according to the required motion behavior. However, the various ships are equipped with propulsion systems with similar functions, so that libraries can be created to describe the generated forces of a propulsion unit in order to establish a generic approach (Fossen and Johansen (2006)). The paper presents a generic allocation for a vessel with a maximum of six actuator units. These can be a rotatable thruster, a fixed thruster or a combination of main propulsion and rudder. The approach is applied to the research vessel *DENEB* with three such actuator units. This method is further explained in a subsequent section, which includes building the required matrices. These are deduced from geometric considerations and the constraints and power specifications of each actuator unit. The contribution is structured as follows. First, the vessel *DENEB* and the installed automation system with its components are described. The problem of power-optimized thrust allocation is solved by means of quadratic programming.

The next section presents the results of applying this allocation method to the research vessel in different operating modes.

Authors' Biographies

Dr.-Ing. Agnes U. Schubert works as a research assistant at the Institute of Automation at the University of Rostock in the field of marine control applications with a focus on modelling and the development of ergonomic assistance systems. The marine research is based on earlier experiences in chemical and medical automation.

Nick Eisenblätter MSc is a research assistant at the Institute of Automation at the University of Rostock. The focus of his research is on trajectory optimization for autonomous and cooperative agents.

Robert Damerius MSc is a research assistant at the Institute of Automation at the University of Rostock. The research focuses on the design of GNC systems for autonomous vehicles.

Prof. Dr.-Ing. Torsten Jeinsch is professor of Control Engineering and head of the Control Application Centre in the Institute of Automation at the University of Rostock. The research focus of institute lies in control applications in marine systems using fault tolerant algorithms.

2 Overview of the Automation System

The method is demonstrated with the 52 m long survey, wreck search and research vessel *DENEB* of German Federal Maritime and Hydrographic Agency (BSH), seen with the automation system in Fig. 1, in a marine area in the port of Rostock. She is equipped with propeller, rudder, stern thruster and pump-jet. That is a classic actuator configuration non-specialized on dynamic positioning (DP) operations. Due to its tasks as a survey vessel, the DENEB is equipped with high-performance sensor technology, including an Inertial Navigation System (INS) that fuses its data with other sensor inputs. Standard sensors include GNSS, GPS, DVL, AIS, Wind, Compass and an echo sounder. The vessel was built in 1994 and digitized in 2021 so that it can be used for the development of automatic maneuvering. More details of retrofitting can be found in Rethfeldt et al. (2021).

An overview of the automation system designed as an add-on solution is shown in Fig. 1. The maneuver assistance system (MAS) is installed directly above the bridge and can be used independently of the automation system for the purely assisted maneuvering by a nautical officer. The model-based MAS shows compactly all needed information for the motion and actuator states of the vessel as well as the planned, actual and predicted ship path in the electronic navigational chart (ENC). This system only reads the sensor data and bridge commands, but does not send any data to the ship's systems. More information on how the MAS works can be found in Schubert et al. (2024a).

For the automatic operation, the maneuver plan provided by the MAS is converted into a trajectory that is applied for position and heading control and within the feed-forward control module. In this case, the maneuver plan trajectory serves as a guidance functionality within the GNC structure. The automatically commanded actuator settings are sent to the vessel itself and to the MAS so that the nautical officer can supervise the automatic operations in comparison to the planned and predicted motion. In addition the onboard navigation solution, motion filters and a comprehensive sensor fusion are integrated in the navigation module. The solution is provided to the guidance and the control module. The controller development was started with the identification of the motion process to find a less complex dynamic motion model. Standard maneuvers such as coasting stops and an identification scheme for determining the added mass matrix were used for this purpose, in which only a few acceleration experiments have to be carried out with the vessel which was described in Hahn et al. (2021). In addition to the motion model, models were also developed for the wind influence (Schubert et al. (2024b)) and the energy consumption of the individual actuator units (Damerius et al. (2023)). Two controller modes are set up, the transit mode for higher speeds in the port and the DP mode for the maneuvering near the pier. The controller structures are described more in detail in Hahn et al. (2022). While the first allocation scheme was derived directly from the motion model without taking energy consumption into account, the optimal thrust allocation presented here is formulated as quadratic programming.
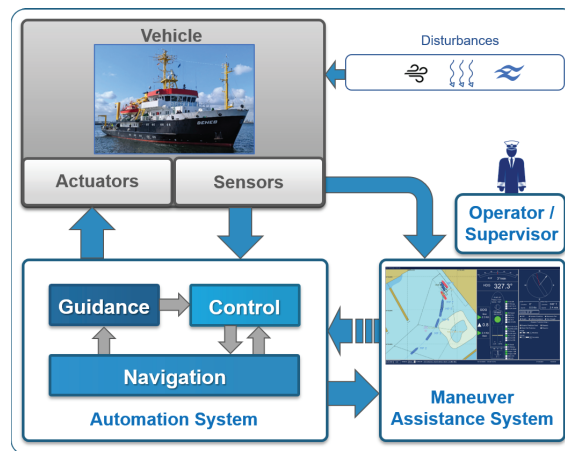
Figure 1: Overview of the automation system onboard research vessel *DENEB* based on assisted maneuvering

3 Generic Allocation

A generic approach was motivated by the repeated redevelopment of the GNC modules for the watercraft in different projects. The available propulsion systems are often similar or can at least be described with similar models and the functions based on them in feed-forward control, allocation and feedback control. The allocation converts the forces and torques commanded by the controller into manipulated variables of the actuators. How the

forces are distributed depends on the geometric position of the actuators in the hull and the thrust they can generate. Each actuator is defined by constraints on command values, rates of manipulated variables and construction specifications. The allocation can minimize power consumption with optimal distribution within the given actuator configuration.

The presented generic allocation is developed for a vessel with a maximum of six actuator units and three degrees of freedom (DoF) with surge, sway and yaw. The corresponding equation of motion is based on Newton's second law as referenced in Fossen (2011) with

$$M\dot{\nu} + C(\nu)\nu = D(\nu)\nu + \tau \tag{1}$$

where M is the inertia matrix, ν is the velocity vector, D and C are the damping and the Coriolis and centripedal matrices, and τ is the vector of external forces. It is calculated from the sum of the actuators thrust τ_{act} and additional external forces τ_{ext} such as wind or current for a motion model in three DoF to

$$\tau = \begin{pmatrix} X, & Y, & N \end{pmatrix}^T = \tau_{act} + \tau_{ext} \tag{2}$$

where X and Y are the forces in longitudinal and lateral direction and N is the yaw moment.

The optimization problem is solved using the MATLAB function *mpcActiveSetSolver* which finds an optimal solution x to a quadratic programming problem by minimizing the objective function J

$$\min_{x} \qquad \{J = \frac{1}{2}x^T H x + s^T Q s + f^T x\}$$
$$\text{subject to:} \quad A_{ineq}x <= b_{ineq} \qquad\qquad A_{eq}x = b_{eq}, \tag{3}$$

where H is the Hessian matrix, s are slack variables with their weight matrix Q introduced to simplify the optimization problem, f is a multiplier of the linear term, A_{ineq} and b_{ineq} specify the inequality constraints and A_{eq} and b_{eq} the equality constraints. The method is referenced in Schmid and Biegler (1994). The structure of the developed Simulink model is illustrated in Fig. 2. In the allocation input system, the standard actuator templates are provided and according to the vessel characteristics assigned. In addition, the current signals for the force and torque commands (X, Y, N) as well as the current settings of each actuator are involved. The actuator specifications are processed to prepare them as input to the solver. As the result, the optimum forces per actuator and the corresponding commands are provided to the vessel system.
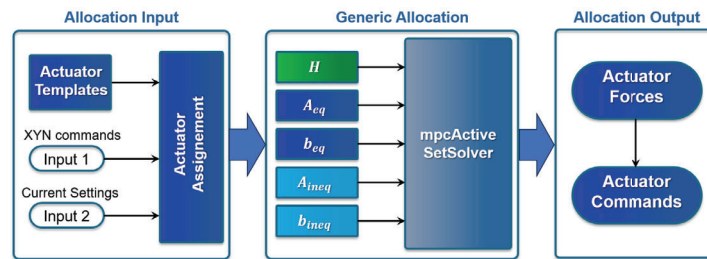
Figure 2: Structure of the model for the generic allocation

The vector x consists of the force components f_{xi} and f_{yi} in longitudinal and transversal direction that each actuator unit can supply. The torque generated by an actuator is based on the force components multiplied with the lever arm l in the corresponding direction to the center of gravity (CG) or geometric center of the vehicle. The three force components are considered in the matrix A_{eq}, which is a 3-by-12 matrix for a configuration of six actuator units with

$$A_{eq} = \begin{pmatrix} 1 & 0 & ... & 1 & 0 \\ 0 & 1 & ... & 0 & 1 \\ -l_{y1} & l_{x1} & ... & -l_{y6} & l_{x6} \end{pmatrix}. \tag{4}$$

The vector b_{eq} corresponds to the commanded forces of the controller in three DoF $b_{eq} = (X,Y,N)^T$. Three slack variables are introduced, so that Q is a 3-by-3 matrix as well as A_{eq} is extended to a 3-by-15 matrix.

The inequality specifications A_{ineq} and b_{ineq} outline the constraints for each actuator, detailing force limitations as linear inequalities based on the actuator's current setting, maximum values and changing rate, i.e. maximum possible change in one time step. These values are actuator and manufacturer-specific or can be defined by the captain or ship's engineer to ensure safe and gentle automatic allocation. Depending on the actuator type, there

are various complex model functions that reflect the relationship between the actuating variable and the resulting forces $[f_{xi}, f_{yi}]$. These functions are obtained from manufacturer specifications and identification maneuvers, which therefore include the interactions between the thruster and the hull. A major challenge is ensuring that the area, where the optimum forces lie, meets the requirement of convexity. In this generic allocation, the number of inequalities per actuator unit is limited to eight. This results in the matrix A_{ineq} having a size of 48-by-12 and with the extension for the slack variables having a size of 48-by-15. The vector b_{ineq} has a length of 48. So far, three actuator types have been realized: the rotatable thruster, the non-rotatable thruster and the combination of main propulsion and rudder. Setting up the inequalities depending on the actuator type is described in more detail in section 3.1.

Within the optimization problem, the Hessian matrix H contains the weights K_i for the force vector x. For the actuator configuration of six units, H is defined as a 12-by-12 matrix. To minimize power consumption, the coefficients of H represent the relationship between the required power and the quadratic force components for each actuator In Damerius et al. (2023), the power was approximated as a cubic function of the actuator throttle. Since the ratio between the weight factors is particularly important, the quotient of the maximum power and the maximum force in each direction and per each actuator is used for the weights K_i. The requirement for the weights q_j of the slack variables in Q is that they are significantly higher than K_i ($q_j >> K_i$), because slack variables are used to simplify the optimization problem or to always find a solution under each additional constraint. The linear term of the quadratic programming equation 3 is neglected in the generic approach.

The DP allocation in three DoF and the transit allocation in two DoF (X, N) are only distinguished by the numbers of rows in the matrix A_{eq} and vector b_{eq}.

3.1 Actuator Models and their constraints

3.1.1 Rotatable Thruster

The class of rotating thrusters includes azimuth thruster, pump-jets, pod-propellers or contra-rotating propellers Fossen and Johansen (2006). They produce a thrust in the direction of the rotation angle. The force components are calculated as follows

$$f_{RTx} = T_{RT} cos\alpha_{RT}$$
$$f_{RTy} = T_{RT} sin\alpha_{RT},$$
(5)

where T_{RT} is the thrust related to the throttle e_{RT} and α_{RT} is the rotation angle. This angle can be either unconstrained or constrained to a certain range. If two rotatable thrusters are mounted close together, it is possible that the actually free angle ranges must still be limited due to mutual interference. The thrust T_{RT} in longitudinal direction can be identified with several coast stop maneuvers and modeled by the following differential equation

$$m\dot{u} = -d_u u - d_{uuu} u^3 + X$$
(6)

where u is the longitudinal velocity, d_u and d_{uuu} are the coefficients for the first and third order terms. In the stationary case, $\dot{u} = 0$, the thrust X can be calculated from the commanded revolution speed e_{RT}. The possible values of e_{RT} for different types of rotatable thrusters can range from global, minimally negative to null. The maximum throttle is defined with 100 % engine order telegraph (EOT) or the scaled value of 1. To determine the range of the current available forces, the maximum throttle rates up $T_{RT,u}$ and down $T_{RT,d}$ are added to the current throttle $T_{RT,0}$ and the angle rates $\alpha_{RT,u}$ and $\alpha_{RT,d}$ are added to the current $\alpha_{RT,0}$ with

$$T_{RT,0} - |T_{RT,d}| \leq T_{RT} \leq T_{RT,0} + |T_{RT,u}|$$
$$\alpha_{RT,0} - \alpha_{RT,d} \leq \alpha_{RT} \leq \alpha_{RT,0} + \alpha_{RT,u}.$$
(7)

In the result, one or two non-convex circular segments characterize the available force range for the allocation optimization. Following Johansen et al. in the case of two segments for a positive and a negative throttle, non-convexity is avoided by optimizing the two segments in parallel whereby the result with the lower power consumption is subsequently selected. A single circle segment is converted into a convex polygon by approximating its boundaries with linear equations. A detailed description of secured converting can be found in Ruth (2008). The method is applied to the pump-jet allocation in section 3.2.

3.1.2 Non-Rotatable Thruster

Non-rotatable thrusters, installed within tunnels integrated into the ship's hull, are thus limited to producing force solely in the y-direction. Positioned either at the bow or stern, these thrusters are used at low maneuvering speeds to control transverse motion of the respective part of the vessel. A combination of lateral thrust at the bow and stern of a watercraft can be used for transversing close to structures. As no angle is varied, the description of the available force range resulting from the current actuating variable $e_{NRT,0}$ and the actuating rates $e_{NRT,d}$ and

$e_{NRT,u}$ for the throttle value is very simple. The valid force range is defined as a virtual rectangle with the following inequalities

$$
\begin{aligned}
fx &\leq 0 \\
-fx &\leq 0 \\
fy &\leq T_{NRT}(e_{NRT,0} + |e_{NRT,u}|) \\
-fy &\leq T_{NRT}(e_{NRT,0} - |e_{NRT,d}|),
\end{aligned}
\tag{8}
$$

where T_{NRT} denotes the thrust of the non-rotatable thruster at the given trottle constraints e_{NRT}. The structure of the thrust function calculated from the throttle is identical to that in 6. The coefficients d_u and d_{uuu} are of course different for each rotatable or non-rotatable thruster, identified by trials with force equilibrium in the respective direction.

3.1.3 Combination of Main Propulsion and Rudder

A non-rotating main propulsion is often the most powerful thrust generator on conventional ships and is usually combined with a rudder behind it. The combination is used for transit and in-port transit maneuvers, whereby setting the rudder angle generates a transverse force component and a yaw moment. At cruising speed, the rudder is the most effective steering instrument, and the course is changed quickly even with small changes in the rudder angle. The rudder's effectiveness decreases when the flow to it is low, primarily at low rotational speeds of the main propulsion. At reverse rotational speed, the effect of the rudder cannot be calculated, e.g. due to stalling. In general, the force models for f_x and f_y as functions of the throttle of the main propulsion e_{ME} and of the rudder angle α_{RUD} are strongly non-linear. To generate the convexity of the valid force range, the same principles are used as for rotating thrusters, which were presented in section 3.1.1 or in Johansen et al. (2008).

3.2 Allocation of the research vessel DENEB

The 52 m long research vessel *DENEB* has a diesel-electric propulsion system and three actuator units arranged along the longitudinal axis of the ship, the main propulsion with a flap rudder behind it and a non-rotatable thruster in the stern and a pump-jet as a fully rotatable truster in the bow. The geometric arrangement of the actuator units is presented in Fig. 3. The pump-jet and the main propulsion can produce thrust in the longitudinal direction, marked with the forces f_{x1} and f_{x3}. Transversal forces are generated by the pump-jet (f_{y1}), the stern thruster (f_{y2}) and the combination of main propulsion and rudder (f_{y3}). The three associated moments of the units are calculated using the product of the respective force component f_y and the distance l along the longitudinal axis to CG that lies in the origin of the body-fixed coordinate system. These geometric considerations directly result in the equality conditions in three DoF according to equation 4 with $l_{x1} = l_1$, $l_{x2} = l_2$ and $l_{x3} = l_3$ while the values of l_y are zero. While the main engine has the highest power, the pump-jet has 74% of it and the stern thruster only 8%.
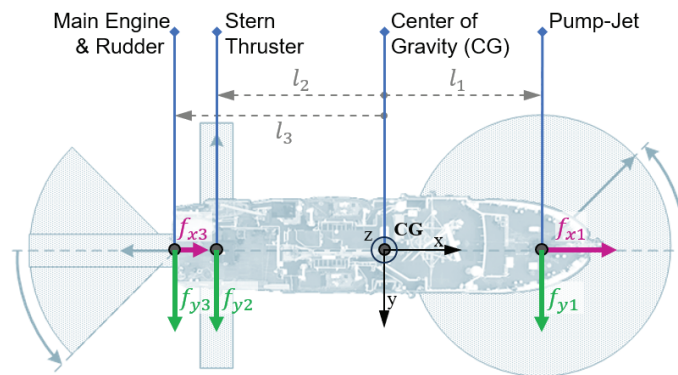
Figure 3: Geometric arrangement of the actuators on the *DENEB* and the generated forces in x- and y-direction

The throttle of the pump-jet is defined in a scaled range of $(0, 1)$ with a rate of change of 0.2 upwards and downwards from the current setting value. The angle can be varied within the unlimited range of $0..360deg$ with a changing rate of $20deg$ in both directions. This results in a single circle segment as a possible range for the forces fx and fy to be optimized. Figure 4 shows an example for such a segment (white area) and its linear constraints in the (f_y, f_x)-plane, which are inserted into the matrix A_{ineq}. The current setpoint $[0.6, 60deg]$ is marked with a blue cross. The blue circles show the lower and upper limits of the throttle value, while the gray lines limit the angle range. Five inequalities are provided for the outer limits and only one inequality for the inner limits. Following

Ruth (2008), the total of eight inequalities are

$$sin(\alpha_{min})f_x - cos(\alpha_{min})f_y \leq 0 \tag{9}$$

$$-sin(\alpha_{max})f_x + cos(\alpha_{max})f_y \leq 0 \tag{10}$$

$$-cos(\alpha_0)f_x - sin(\alpha_0)f_y \leq -T_{min} \tag{11}$$

$$cos(\alpha_{min} + (2i-1)\alpha_{seg})f_x + sin(\alpha_{min} + (2i-1)\alpha_{seg})f_y \leq cos(\alpha_{seg})T_{max} \tag{12}$$

with $\alpha_{min} = \alpha_0 - \alpha_d$, $\alpha_{max} = \alpha_0 + \alpha_u$, $\alpha_{seg} = (\alpha_d + \alpha_u)/5$, $i = 1:5$, $T_{min} = T_0 - |T_d|$, $T_{max} = T_0 + |T_u|$. (13)
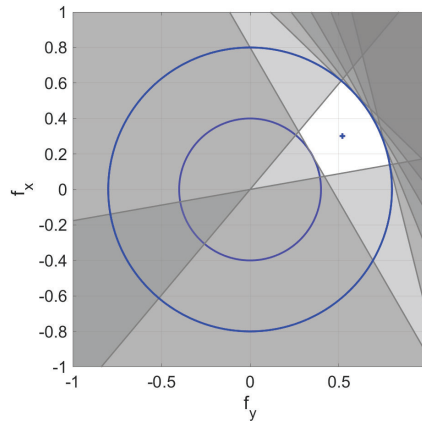
Figure 4: Linear inequalities to constrain the white circle segment of attainable thrust region of pump-jet

The throttle of the stern thruster can be changed within a range of $(-1,1)$ with a changing rate of 0.3. The inequalities of this thruster are constrained as it is defined in section 3.1.2.

The set values of the combination of main propulsion and rudder can be changed within the extreme limits of the throttle in the range $(-1,1)$ and the rudder angle in the range $(-40\ deg, 40\ deg)$. Due to the complex hydrodynamic phenomena at the rudder at negative rotational speed, the captain of the *DENEB* restricted the throttle range to positive values in automatic mode. As can be seen in Fig. 5, the values of f_y increase only slightly for angles greater than 12 *deg* on the starboard or port side. The displayed function values are calculated with

$$fx = ((k_1 e_{ME} + k_2 e_{ME}^3) * (1 + k_3 \exp(-k_4|\alpha_{RUD}|))) \tag{14}$$

$$fy = ((k_5 e_{ME} + k_6 e_{ME}^3). * tanh(-k_7 \alpha_{RUD})), \tag{15}$$

where the coefficients $k_1..k_7$ were approximated from measured values using the MATLAB curve fitting tool.
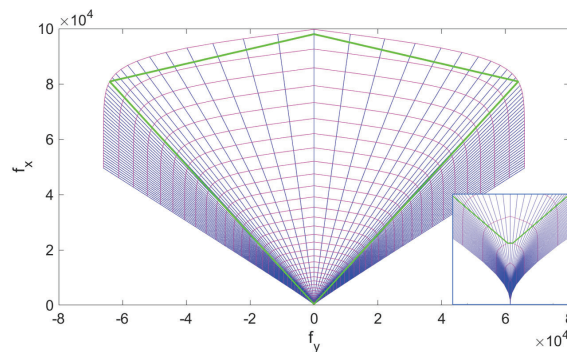
Figure 5: Function to describe the forces of the actuator combination with main engine and rudder as a function of the main engine throttle (magenta lines) and the rudder angle (blue lines) and the maximum of usable $[f_x, f_y]$ range (green outlined)

4 Results and Discussion

Figure 6 shows the results of DP control under the influence of wind using the developed generic allocation approach. The applied DP controller was already published in Hahn et al. (2022). The automatic tests were carried out in the harbor of the Hohe Düne naval base in Rostock/ Germany, which is closed to public traffic. In addition, this area is characterized by a low and therefore negligible current. The wind, on the other hand, has a major influence on the motion, as the ship has high superstructures, especially aft.

In DP mode, force balances are established in the x and y directions using all actuator units except the rudder. On the left side, the plots in figure 6 of various time series are presented. The upper plot shows the wind speed with a maximum value of more than 8 m/s. In the second plot, the position coordinates x and y are seen. The maximum deviation occurs at approximately 700 s with 0.6 m. The mean value of the position error lies beyond 0.2 m. The third plot on the left side shows the measured yaw angle. At approximately 300 s, a new heading angle with -45 deg was commanded. This implies that the mean angle of attack of the wind changes. While the wind used to come directly from the front and thus had a relatively small area of attack, it now comes from about 38 deg. Plot 4 and 5 show the actuator commands, in plot 4 the commanded throttle values for the pump-jet e_{PJ}, stern thruster e_{Thr} and main propulsion e_{ME} and in the lower plot the commanded angle of the pump-jet α_{PJ}. The rudder is not used during DP operation. Due to the changing of the heading angle, the pump-jet and the stern thruster are used at higher rotational speeds as well as the angle of the pump-jet is hold relatively stable to a value of 90 deg, that means in starboard direction. More force and more power is now used to minimize the y-deflection. Gusts of wind lead to major positioning errors. Overall, however, the result at such wind speeds is respectable and the allocation method has proven its worth.
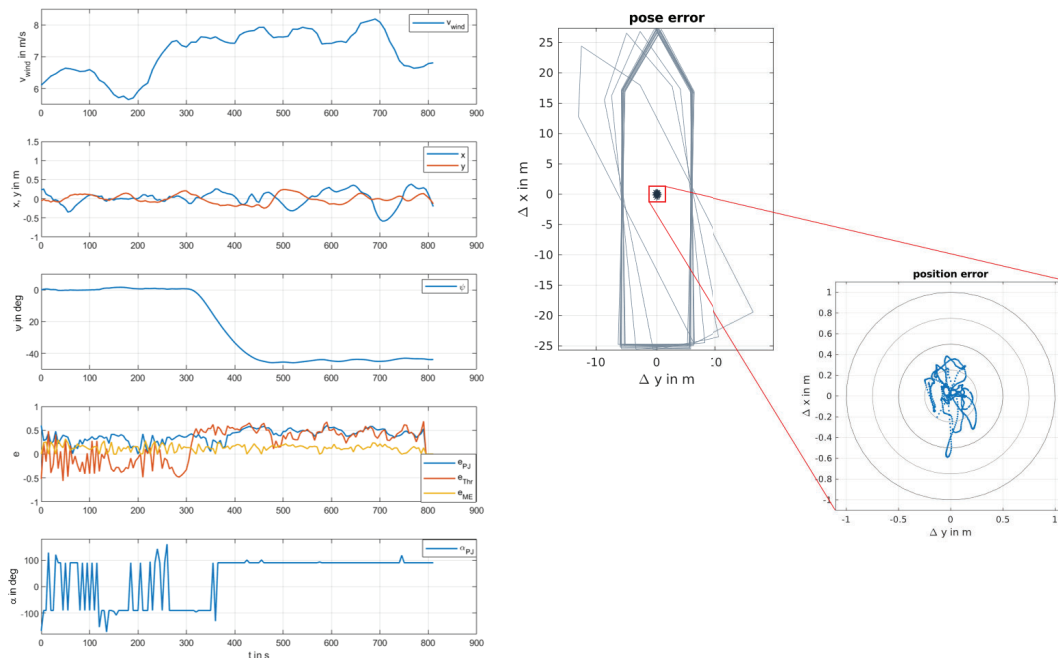
Figure 6: Results of DP control with the research vessel *DENEB* under the influence of wind with the plots of wind velocity v_{wind}, the position in (x,y) heading angle ψ, the commanded throttle settings for the pump-jet e_{PJ}, stern thruster e_{Thr} and main propulsion e_{ME}, and the commanded angle of the pump-jet α_{PJ} (left side) and the pose and position error $(\Delta x, \Delta y)$ (right side)

5 Conclusions and Outlook

The paper has presented the approach of a generic allocation using for watercraft with a maximum of six actuator units, three actuator types and control of motion behavior in three DoF. To minimize the power consumption, the quadratic programming method was chosen. For the three actuator types, templates are provided to fill the input matrices for equations and inequalities required for the optimization solver. The method is easy to apply to each watercraft in a new project. The description of the actuator types is further refined to meet the requirement of convexity and keep the approach as simple as possible. Additional types may need to be added as templates.

In the following stage, the allocation approach will be further checked during tests in the port of Rostock. There will also be investigations into whether speed over ground should be included in the allocation in order to map the speed-dependent effectiveness of the actuators. The upcoming autonomous cooperative scenario will include the DENEB and two autonomous surface vehicles from the University of Rostock. These three vehicles are connected through a central server, which is responsible for planning safe trajectories for each. For each of the vehicles, specific solutions are required for the basic models for dynamic motion, power consumption and environmental influences, as well as allocation and control based on these.

References

Damerius, R., Schubert, A.U., Rethfeldt, C., Finger, G., Fischer, S., Milbradt, G., Kurowski, M., Gluch, M., Jeinsch, T., 2023. Consumption-reduced manual and automatic manoeuvring with conventional vessels. Journal of Marine Engineering & Technology 22, 55–66. doi:`10.1080/20464177.2022.2154666`.

Fossen, T., 2011. Handbook of Marine Craft Hydrodynamics and Motion Control. John Wiley & Sons, Ltd. doi:`10.1002/9781119994138`.

Fossen, T.I., Johansen, T.A., 2006. A survey of control allocation methods for ships and underwater vehicles, in: 2006 14th Mediterranean Conference on Control and Automation, pp. 1–6. doi:`10.1109/MED.2006.328749`.

Hahn, T., Damerius, R., Jeinsch, T., 2021. An identification scheme to determine all off-diagonal elements of added-mass matrix for marine vessels, in: 13th IFAC Conference on Control Applications in Marine Systems, Robotics, and Vehicles CAMS 2021, Oldenburg/ Germany. pp. 175–180. doi:`10.1016/j.ifacol.2021.10.090`.

Hahn, T., Damerius, R., Rethfeldt, C., Schubert, A.U., Kurowski, M., Jeinsch, T., 2022. Automated maneuvering using model-based control as key to autonomous shipping. at - Automatisierungstechnik 70, 456–468. URL: `https://doi.org/10.1515/auto-2021-0146`, doi:`doi:10.1515/auto-2021-0146`.

Johansen, T.A., Fuglseth, T.P., Tøndel, P., Fossen, T.I., 2008. Optimal constrained control allocation in marine surface vessels with rudders. Control Engineering Practice 16, 457–464. doi:`https://doi.org/10.1016/j.conengprac.2007.01.012`. special Section on Manoeuvering and Control of Marine Craft.

Miyoshi, S., Ioki, T., 2021. Development of maneuvering system for realizing autonomous ships - preliminary report on approach maneuvering control and automatic berthing. ClassNK Technical Journal , 67–79.

Rethfeldt, C., Schubert, A.U., Damerius, R., Kurowski, M., Jeinsch, T., 2021. System approach for highly automated manoeuvring with research vessel deneb, pp. 153–160. 13th IFAC Conference on Control Applications in Marine Systems, Robotics, and Vehicles CAMS 2021.

Ruth, E., 2008. Propulsion control and thrust allocation on marine vessels. Ph.D. thesis. Trondheim, Norway.

Schmid, C., Biegler, L., 1994. Quadratic programming methods for reduced hessian sqp. Computers & Chemical Engineering 18, 817–832. doi:`10.1016/0098-1354(94)E0001-4`.

Schubert, A., Kurowski, M., Gluch, M., Simanski, O., Jeinsch, T., 2018. Manoeuvring Automation towards Autonomous Shipping, in: Proceedings of the 14th International Naval Engineering Conference INEC, International Ship Control Systems Symposium iSCSS, Glasgow, UK. pp. 1–8. doi:`DOI:10.24868/issn.2631-8741.2018.020`.

Schubert, A.U., Damerius, R., Fischer, S., Milbradt, G., Kirchhoff, M., Gluch, M., Jeinsch, T., 2024a. Comparison of performance in assisted and automatic berthing maneuvers with the research vessel deneb, in: Proceedings IEEE OCEANS 2024, Singapore. pp. 1–8.

Schubert, A.U., Damerius, R., Jeinsch, T., 2024b. Energy demand of vessels depending on current wind conditions, in: 2024 European Control Conference (ECC), pp. 1147–1152.

Schubert, A.U., Damerius, R., Rethfeldt, C., Kurowski, M., Jeinsch, T., Gluch, M., 2023. Concepts and system requirements for automatic ship operations, in: OCEANS 2023 - Limerick, pp. 1–8. doi:`10.1109/OCEANSLimerick52467.2023.10244661`.

UNITED NATIONS, 2019. UNCTAD - Review of Maritime Transport 2019. United Nations Publications, New York, USA.

Supplementing Experience-Based Platform System Robustness Requirements to Network Theory

E L Scheffers[a]*, dr. P de Vos[a]

[a]Delft University of Technology, The Netherlands
*Corresponding author. Email: E.L.Scheffers@TUDelft.nl

Synopsis

Reduced crewing concepts require a higher level of control and integration of platform systems. A clear reliability assessment of these systems in early design stages reduces the need for alternations in later design stages but remains challenging to perform. This paper addresses the design of reliable and integrated onboard systems such as cooling water, power distribution, and control systems. Current approaches to making platform systems more reliable, such as redundancy, modularity (independent subsystems) and reconfigurability, are analysed from a network theory perspective. Current graph measures do not align with experience-based requirements for improving system robustness. Our method combines the principles of network theory and experience- and rule-based system requirements to provide a comprehensive framework for a reliability comparison of integrated multilayer platform systems (distributing more than one type of flow). The robustness requirements are translated into network metrics to facilitate a quantitative trade-off typical to the early stages of the design process. The case study offers a preliminary view of the system topology of a notional naval vessel, consisting of power distribution, cooling water distribution and control systems. The network metrics facilitate an assessment of the system's reliability compared to alternative system topologies with differentiating numbers of nodes, edges and density. This study finds varying dependencies of the robustness metrics on the network properties, shining new light on whether and how one should compare distribution system robustness.

Keywords: Onboard Distribution Networks; Design-Support Systems; Design Heuristics; Robustness

1 Introduction

Despite its critical role, the maritime industry operates largely in the shadows, only gaining fleeting visibility when incidents like the Baltimore Bridge collision capture headlines. These and other situations arise from a significant list of challenges facing the maritime industry, such as higher-risk shipping routes, operations in hostile environments, reduced crewing concepts and a need to mitigate local and global environmental impact. The first two challenges directly influence the lives of men and women onboard commercial and naval vessels. Therefore, it is essential to improve the survivability of these ships. Most naval vessels can be approached as complex systems of systems (Rigterink (2014)); enhancing the robustness of vital onboard distribution systems will likely lead to lower vulnerability and higher overall survivability (Habben Jansen (2020)).

This vulnerability has been a topic of study in various maritime applications, such as offshore and naval vessels. In previous work, Scheffers and de Vos (2024) used the difference between Dynamic Positioning (DP) class 2 and class 3 redundancy regulations (American Bureau of Shipping (2021)) to capture system robustness for ships equipped with DP systems. This robustness is defined by de Vos and Stapersma (2018) as "The ability of energy distribution systems on board of ships to withstand perturbations in system operation". The comparison was performed by modelling the DP systems as integrated networks. The systems were solely analysed from a logical architecture as defined by Brefort et al. (2018), focusing on the physical relations between components. Moreover, no differentiation between node and edge type has been taken into account. The robustness was measured using network metrics based on three reliability aspects: independent subsystems, component redundancy and distribution redundancy. The research used a single class 2 DP system and a single class 3 DP system as a case study to validate the assumptions from Clavijo et al. (2022). The study concluded that the network robustness metric "modularity" could be applied as a proxy for "independent subsystems" for this specific case study. However, no conclusion could be drawn regarding the other network robustness metrics nor regarding the applicability of these metrics on other onboard distribution system architectures.

Amongst the vital distribution systems, we consider electric energy distribution systems, cooling water distribution systems and sensor data distribution systems. One of the three main recommendations of this previous work was to broaden the general validity and applicability of the study. It was suggested to study networks of varying dimensions: what is the influence on robustness of adding additional components to the network?

Authors' Biographies

Evelien SCHEFFERS is a PhD candidate at the Department of Maritime & Transport Technology, Delft University of Technology. In her research, she focuses on the application of network metrics to robust on-board distribution system design

dr Peter DE VOS is assistant professor in marine engineering and director of studies of TU Delft's Maritime Technology MSc programme. In his research, he focuses on the design of robust on-board Power, Propulsion and Energy systems, including robust alternative fuel applications in marine Internal Combustion Engines.

Therefore, the goal of this paper is to verify whether a system becomes more robust if a component or connection is added to the network, i.e. increasing redundancy, and, if this is the case, which components have a pivotal position in this robustness enhancement. This current work studies the same five network robustness metrics as were used in the previous study since these metrics and the corresponding reliability aspects are directly based on DP regulations. The five metrics are 1) modularity, 2) effective graph resistance, 3) maximum flow, 4) clustering coefficient and 5) circuit rank and are further explained in Table 2. It is assumed that the network robustness metrics are also applicable in a broader sense to the vital distribution systems onboard naval vessels.

The verification is performed using the aforementioned network robustness metrics, which will be explained later in more detail. With this research aim in mind, the study consists of the generation of networks representing integrated onboard distribution systems (the logical architecture by Brefort et al. (2018)) and is based on an existing benchmark architecture (de Vos and Stapersma (2018)). The integrated systems consist of different system components and the number of these components is varied for the generated networks. Next, the effect of the number of components and connections with regard to the selected network robustness metrics is studied. The contribution of this work lies in studying the effect of the variation of network size on the robustness of onboard distribution systems.

2 Network Generation

Modelling the onboard distribution systems as networks is performed using the mathematical concept of graphs $G(V,E)$. These graphs are comprised of a set of nodes/vertices V (components) (Newman (2010)). The components relate to each other through a set of links/arcs/edges E (connections). In this work, the nodes represent system components such as pumps, engines, switchboards and computers. The edges represent tangible connections like cables, pipes and tubes. The physical architecture, as defined by Brefort et al. (2018), is not considered in this study, so physical properties like the cable length or capacity are not included in the scope. This is in line with studying system diagrams and facilitates analysis in very early-stage design before layouts or arrangements are known.

The benchmark system model of vital distribution systems onboard a notional frigate developed by de Vos (2018) serves as a foundation for examining the impact of component count on network robustness. This model identifies twelve distinct function types of system components, each categorised into a specific "layer". Roughly half of these layers comprise converter nodes, also known as "converter layers," which transform one flow, such as electricity, into another, such as cooling water. The remaining layers consist of hub nodes, or "hub layers," which facilitate flow distribution across the vessel without altering the flow itself. A cooling water pump exemplifies a converter node, whilst a switchboard is a hub node. Figure 1 shows the benchmark system model with its five distinct flows and twelve distinct node types. Converter nodes cannot directly connect to other converter nodes; instead, they must connect via one or more hub nodes to enable flow distribution. The second and final network constraint is that hub nodes can connect directly to each other and together form the distribution system for a given flow.

2.1 Erdös-Rényi random network generation

A number of possible topologies are generated to compare different system architectures. This generation starts with only the nodes from the benchmark system and an empty edge set: $G_0 = (V_{\text{benchmark}}, E = \emptyset)$. The physical boundaries, as introduced in the benchmark system, are translated to mathematical boundaries using the Erdös-Rényi (E-R) random graph model Newman (2010). For computational simplification purposes, it is assumed that a converter component is only connected to the hub layer "above" and "below" a given component and no other interrelations exist. Future research will include adding the additional interrelations as present in Figure 1, e.g. the sensor components requiring electric power, next to cooling. The edges are included with probability p, independently from every other edge. Since the physical networks onboard are assumed to be relatively sparse, the edge probability is set on a constant value of $p = 0.15$. This value reflects a sparse network whilst still facilitating sufficient edges to generate a connected network. Figure 2 shows a close-up of the upper three layers of the network to visually explain these boundary conditions in edge generation. Zooming in on the edge generation within the first three layers (diesel generator components DG, main switchboard components MSWB and transformer components (TF)), edges are generated within the following conditions. First, a subgraph S of graph G is defined as:

$$S(V_S, E_S) \subseteq G(V_{\text{benchmark}}, E = \emptyset) \tag{1}$$

with:
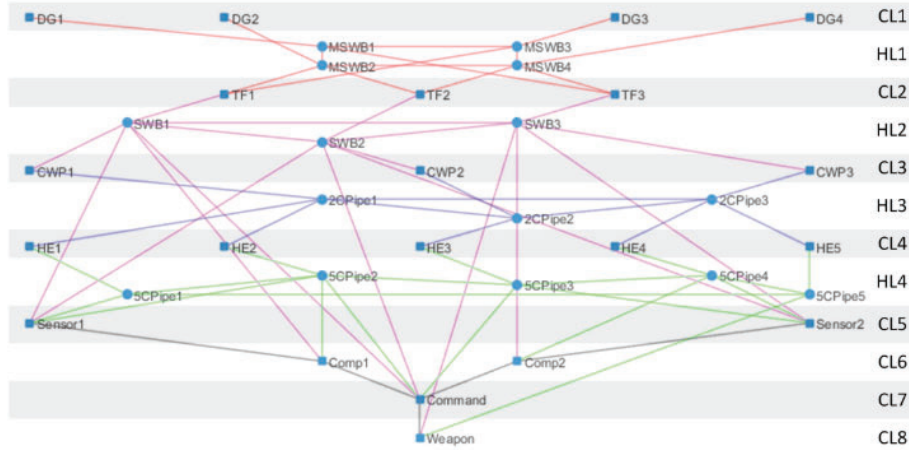
Figure 1: Benchmark energy and data distribution system model onboard a notional frigate (de Vos and Stapersma (2018)). The benchmark contains alternating converter layers (grey) and hub layers (white) and the five distribution flows 6600V AC (red), 400V AC (magenta), 2 °C cooling water (navy blue), 5 °C cooling water (green) and data (grey). The layers contain the following components: 1. diesel generator (DG), 2. main switchboard (MSWB), 3. transformer (TF), 4. switchboard (SWB), 5. cool water plant (CWP), 6. pipeline 2 °C (2Cpipe), 7. heat exchanger (HE), 8. pipeline 5 °C (5Cpipe), 9. Sensor, 10. Computer (Comp), 11. Command, 12. Weapon.

$$C_1 = \{v \in V \mid \text{layer}(v) = \text{DG}\}$$
$$H_1 = \{v \in V \mid \text{layer}(v) = \text{MSWB}\}$$
$$C_2 = \{v \in V \mid \text{layer}(v) = \text{TF}\} \tag{2}$$
$$V_S = C_1 \cup H_1 \cup C_2$$
$$E_S = \emptyset$$

where:

- C_i represents the node set of the i-th converter layer.
- H_i represents the node set of the i-th hub layer.

2.1.1 Edge generation

Now, edges are generated connecting the first (converter) layer to the first (hub) layer by means of an E-R random bipartite graph, i.e. no edges are generated within a layer, only between layers:

$$E_{C_1 \to H_1} = \{(c,h) \mid c \in C_1, h \in H_1, \text{ with } p = 0.15\} \tag{3}$$

To ensure that all converter components actively participate in the network, all converter nodes are "required" to be connected to at least one hub node within this E-R bipartite graph:

$$\forall c \in C_1, \exists h \in H_1 \text{ such that } (c,h) \in E_{C_1 \to H_1} \tag{4}$$

Contrary to converter layers, the hub nodes are connected within the layer. These edges are generated using an E-R random graph:

$$E_{H_1} = \{(h_1, h_2) \mid h_1, h_2 \in H_1, \text{ with } p = 0.15\} \tag{5}$$

where the edges form a path between all hub nodes within the layer so that the hub layer is a connected graph. This requirement stems from the engineering practice of making distribution between hub nodes possible and often controllable via e.g. switches and valves. The connectivity is affirmed by:

$$\forall h_1, h_2 \in H_i, \exists \text{ a path from } h_1 \text{ to } h_2 \tag{6}$$

The last edge set within subgraph S is the E-R bipartite graph from the hub layer to the converter layer, repeating the concept of Equation 3 and 4.

$$E_{H_1 \to C_2} = \{(h,c) \mid h \in H_1, c \in C_2, \text{ with } p = 0.15\} \tag{7}$$

$$\forall c \in C_2, \exists h \in H_1 \text{ such that } (c,h) \in E_{C_2 \to H_1} \tag{8}$$

The combined edge set E_S of the graph $S(V_S, E_S)$ is:

$$E_S = E_{C_1 \to H_1} \cup E_{H_1} \cup E_{H_1 \to C_2} \tag{9}$$

One should note that edges within this network have no flow type, direction or other physical properties (despite the obvious practical relevance and application of the connections); they simply represent an existing connection between two components. Physical properties make the network more realistic, however, unexpected and useful mathematical patterns might not be found.

2.1.2 Node addition

This study includes the influence of the number of components on robustness. Therefore, this network attribute should change for different generated graphs. To facilitate this, a random number $k \in 0, 1, 2$ nodes are added to each layer. This allows for a theoretical maximum of $n_{layers} \cdot k_{max} = 11 \cdot 2 = 22$ additional nodes in the graph. Since k is randomly determined for all graphs and layers, the likelihood of a generated network with $36 + 22$ nodes is slim. Figure 3 shows the upper three layers with the maximum number of nodes added to each layer ($k_1 = k_2 = k_3 = 2$). Visually, the added nodes are positioned in line with the existing nodes. Since the node addition is part of the input node-set V, the edge generation automatically includes the added nodes.
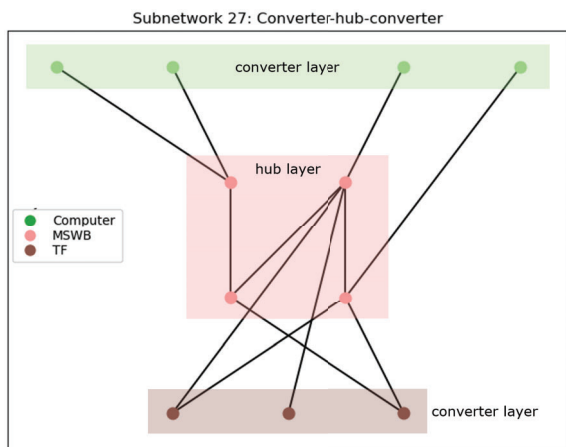
Figure 2: Upper three layers of the integrated system with the original number of nodes. The converter layers (green and brown) are both connected to the hub layer with an E-R random bipartite graph, connecting all converter nodes to at least one hub node. Within the hub layer (pink), an E-R connected graph is generated, which in its place connects the entire graph.
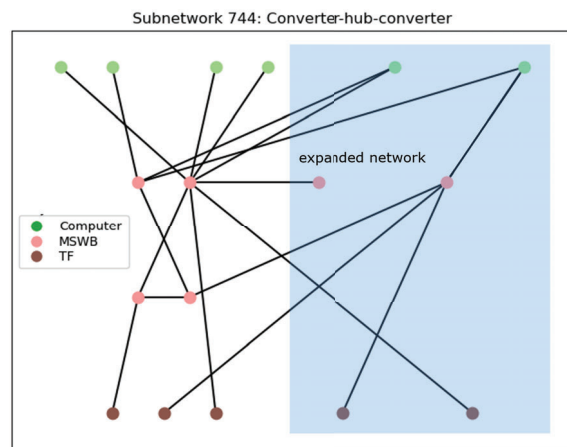
Figure 3: Upper three layers of the integrated system, each (randomly) expanded with two additional nodes highlighted with the blue box. For this generated network, all three layers have two additional nodes so $k_1 = k_2 = k_3 = 2$.

2.2 Generated network overview

Using the E-R random graph model, 2500 networks of the full 12 layers have been generated. The density (Equation 10) indicates the relation between the existing edges $|E|$ and the possible maximum number of edges. However, this does not take into account the limitations imposed by the network generation algorithm regarding the possible connections between nodes.

$$d(G(V,E)) = \frac{2|E|}{|V|(|V|-1)} \tag{10}$$

Table 1 shows the total number of nodes and edges, the network density of the undirected network, and the number of nodes per layer. The lower bound of the layer dimensions is equal to the network dimension of the

Table 1: Minimum and maximum number of nodes, edges, and network density with layer types. The network density is calculated as the ratio of existing edges divided to the total possible number of edges.

Name	Minimum [-]	Maximum [-]	Layer
Nodes	36	50	-
Edges	45	77	-
Density	0.055	0.094	-
Diesel Generator (DG)	4	6	Converter
Main Switchboard (MSWB)	4	6	Hub
Transformer (TF)	3	5	Converter
Switchboard (SWB)	3	5	Hub
Cool Water Pump (CWP)	3	5	Converter
$2°C$ Pipe (2CPipe)	3	5	Hub
Heat Exchanger (HE)	5	7	Converter
$5°C$ Pipe (5CPipe)	5	7	Hub
Sensor	2	4	Converter
Command	2	4	Hub
Computer	2	2	Data

original benchmark system de Vos and Stapersma (2018). The column "Layer" shows the alternating layer types. One should notice that the final layer, the data type computer layer, has a constant number of nodes ($|E|_{comp} = 2$). This is a simplified layer that includes both the command and weapon components from the original benchmark system in Figure 1. A constant number of nodes provides a consistent contribution to the network robustness, resulting in no changing influence on the robustness metrics. Figure 4 and Figure 5 display two extremes of generated networks; the minimum and the maximum number of nodes and edges, respectively. It is not a necessity that these generated networks contain both extremes in nodes and edges within one network.

2.3 Network Robustness Metrics

The applied network robustness metrics are a proxy for three reliability concepts: component redundancy, distribution redundancy and independent subsystems. First, the aspect independent subsystems refers to "two or more component groups, each of which is capable of individually and independently performing a specific function" (American Bureau of Shipping (2021)). The second reliability aspect, component redundancy, is achieved by the installation of multiple (functionally equal) components (American Bureau of Shipping (2021)). The last aspect, distribution redundancy, refers to the presence of "independent alternative paths between source and demand nodes which can be used to satisfy supply requirements during disruption or failure of the main paths" (Goulter (1987)). An overview of the applied network robustness metrics to estimate the system robustness of the generated networks is shown in Table 2.

3 Network database analysis

The generated network analysis is performed using the following steps. First, the relation between the metrics, number of nodes, edges and network density is visually inspected using a pairplot. This forms the initial step in understanding and getting familiar with the generated network database. Next, a Pearson correlation heatmap presents the linear relation between the metrics, network attributes and layer dimensions. This indicates the strength of positive and negative linear relations between the different studied network aspects. The third step is to study the influence of the number of nodes of each layer using a sensitivity analysis. Lastly, the use and applicability of the selected robustness metrics are evaluated using a second sensitivity analysis.

3.1 Pairplot and kernel density estimate

The pairplot in Figure 6 shows the five network robustness metrics, the number of edges, and the network density (Equation 10) on the *x*-axis and *y*-axis. What becomes clear from the colour gradient in the rows "Numedges" (number of edges) and "Density" is the direct relation between the edges and density, and the nodes: with an increase in nodes, the number of edges increases whilst the density decreases. Another apparent relation between the number of edges and the circuit rank in row "Numedges". Since both the number of nodes and the number of edges are directly and linearly present in the equation for circuit rank, this is a highly predictable relation.
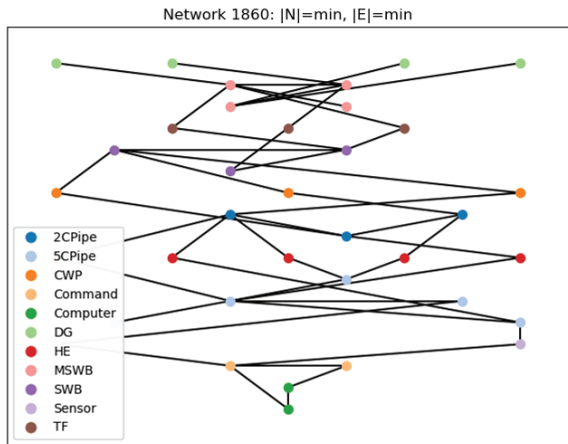
Figure 4: Generated network 1860 with the minimum number of nodes $|V|_{min} = 36$ and edges $|E|_{min} = 45$. The number of nodes corresponds to the number of nodes of the original benchmark system.
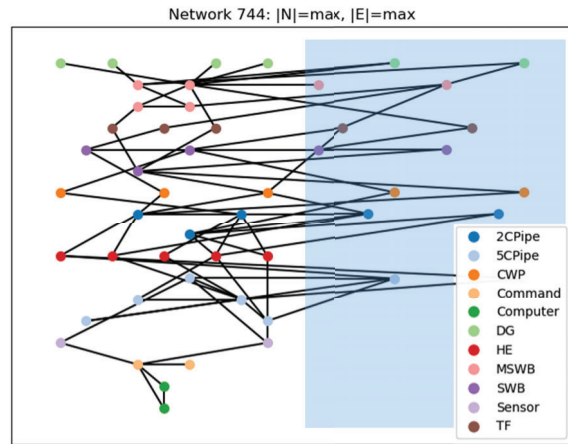
Figure 5: Generated network 744 (also shown in Figure 3) with the maximum number of nodes $|V|_{max} = 50$ and edges $|E|_{max} = 77$. With 14 additional nodes (highlighted in the blue box), the maximum of 20 additional nodes is not part of the generated network set.

Table 2: The calculation approach of the five selected network robustness metrics. The second column shows the three reliability aspects as defined based on the difference between the American Bureau of Shipping (2021) dynamic positioning class 1, 2 and 3 regulations.

Robustness metric	Reliability aspect	Calculation	Method notes
Modularity (Newman and Girvan (2004))	Independent subsystems	$Q_G = \frac{1}{2m} \sum_{ij} \left[A_{ij} - \frac{k_i k_j}{2m} \delta(c_i, c_j) \right]$	Partitioning using Leiden Algorithm (Traag et al. (2019))
Effective Graph Resistance (Ellens et al. (2011),Ellens and Kooij (2013))	Component redundancy	$R_G = \sum_{1 \le i \le j \le N} R_{ij} = N \sum_{i=2}^{N} \frac{1}{\lambda_i}$	λ_i is the i-th eigenvalue of the Laplacian matrix
Maximum Flow Newman (2010)	Component redundancy	Cut set algorithm: the removal of this number of nodes disconnects the source node from the sink node	A single artificial operational source and sink node are added, respectively connected to all source nodes (DG layer) and all sink nodes (Computer layer)
Clustering Coefficient Newman (2010)	Distribution redundancy	$c_G = \mathrm{Tr}(A^3) \left(\sum_{i=1}^{N} k_i(k_i - 1) \right)^{-1}$	k_i is the number of direct neighbours of node i
Circuit Rank	Distribution redundancy	$r_G = |E| - |V| + |C|$	$|C|$ is the number of connected components, which is 1 for all networks since they are generated as connected networks

The plots showing the interrelations between the five network robustness metrics (the upper five rows and the leftmost five columns) are scattered; there seems to be no direct and strong relation based on this figure. This statement also seems to be valid for the relation between the number of nodes and the robustness metrics after studying the diagonal KDE plots of these metrics. The peaks of the different-coloured plots appear somewhat in the same location which shows that the value distribution of robustness metrics is comparable for networks with the different numbers of nodes. This suggests that the number of nodes does not play a key role in network robustness, indicating a preliminary answer to the main research goal. The remaining part of the network database analysis is likely to shine more light on this relation.
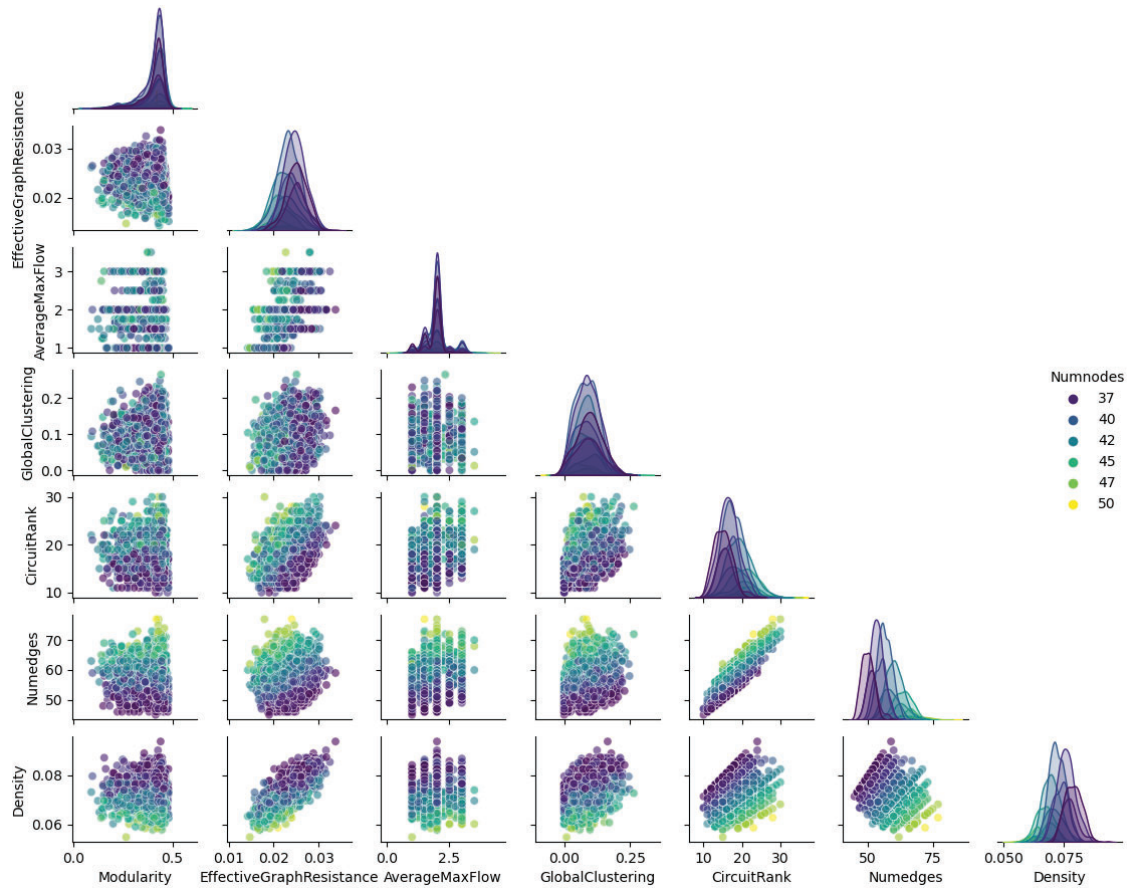
Figure 6: Pairplot showing the relation between robustness metrics and network dimensions. The diagonal plots show the kernel density estimate (KDE) of each metric. The colours represent the number of nodes (Numnodes) of each generated network, ranging from 36 (dark purple) to 50 (yellow).

3.2 *Pearson correlation coefficient*

The second analysis is a linear correlation analysis using the Pearson correlation coefficient $\rho_{X,Y}$. This coefficient indicates the strength of the linear positive or negative correlation between two variables and is calculated using

$$\rho_{X,Y} = \frac{\text{cov}(X,Y)}{\sigma_X \sigma_Y} = \frac{\mathbb{E}\left[(X - \mu_X)(Y - \mu_Y)\right]}{\sigma_X \sigma_Y} \tag{11}$$

where:

$$
\begin{aligned}
&\text{cov is the covariance} \\
&\sigma_X \text{ is the standard deviation of } X \tag{12}\\
&\mu_X \text{ is the expected value (the mean) of } X
\end{aligned}
$$

Figure 7 shows a heatmap representation of the Pearson correlation coefficient. In line with Figure 6, the *x*-axis and *y*-axis show the network robustness metrics, the number of nodes, edges, and density. Moreover, the number

of nodes per layer is added to this heatmap. One should note that the positive scale does not surpass a coefficient value of $\rho_{max} \simeq 0.3$ where the strongest possible positive correlation is $\rho_{max,theory} = 1$. Therefore, even the darker red squares indicate, at best, a moderate positive relation strength. The strongest negative correlation value is $\rho_{min} \simeq -0.7$ with a theoretical minimum value of $\rho_{min,theory} = -1$. Again, this relation is not fully linear but can be considered as a strong correlation.

By studying the heatmap from left to right, two things stand out: first, the column "modularity" shows barely any significant correlation with any of the other studied network aspects. Second, modularity does show a somewhat stronger negative correlation with the number of cool water plant (CWP) components (row "Layer_CWP"), a converter layer with 3 to 5 nodes in the middle of the network. This correlation suggests that a lower number of CWP nodes leads to higher modularity, which is the desired effect for this metric. Understanding the ground for this relation will be studied in future research. An initial assumption is that this layer plays a critical role in determining the number of partitions formed in the modularity algorithm.

Effective graph resistance, the second column, must decrease to indicate an improvement in network robustness (Ellens et al. (2011)). Therefore, the number of nodes and particularly the number of nodes within hub layers (MSWB, SWB, 2CPipe, 5CPipe) have a positive influence on the effective graph resistance. Since the addition of a node will in itself increase the effective graph resistance if nothing else changes, this decreasing influence is surprising. If resistance were the only used metric, one might suggest that removing, for example, a heat exchanger to add additional pipes in the hub layers does improve the overall system robustness. The causal relation between these components is grounds for future research.

Some minor remarks remain, starting with the columns "average max flow" and "global clustering coefficient", which both seem mainly influenced by edge presence and, to a lesser extent, by the varying numbers of nodes. Since the circuit rank does have a positive relation with the number of nodes within layers, this could point to the fact that most triangles (three fully connected nodes) are formed between layers whilst more general cyclic structures are more often (also) found in hub layers. The remaining columns show less remarkable trends, with only the very strong negative correlation between density and number of nodes standing out. Since the number of nodes is present almost quadratic as the denominator in the density definition in Equation 10, this is completely expected.

3.3 Network dimension and layer sensitivity analysis

In this study, a Sobol′ (2001) sensitivity analysis is performed using a Saltelli sample space (Saltelli (2002), Saltelli et al. (2010)). The goal of this analysis is to evaluate the influence certain variables have on other variables. The sample space is determined by the number of input variables D and an input size indicator N, which is $N = 2^{15}$ for the three performed analyses.

3.3.1 Input: 13 network aspects (incl. layers), Output: 5 robustness metrics

Table 3 shows the results of the first sensitivity analysis, which contains thirteen input variables $D = 13$ and five output variables (the network robustness metrics) and has a sample size $N = 2^{15}$. The first conclusion drawn from this table, supported by Figure 8, is that effective graph resistance, global clustering and circuit rank are not or very limited influenced by the number of nodes. The network density and number of edges, two network aspects that are inherently closely related, are dominant factors in the expected values for these three network robustness metrics. Figure 6 and Figure 7 show results in line with this conclusion, which supports this analysis. However, this relation was not predominant in the previous parts of this research. Appendix A shows a figure for all five analysed metrics within this first sensitivity analysis.

A second finding is that in line with the first column of Figure 7, the number of CWP converter nodes has the strongest influence on the modularity metric. Some higher-order interaction is found between the number of edges, the density and the CWP layer. However, these effects are small compared to the first-order sensitivity relations. The sensitivity analysis of the maximum flow metric (Figure 13) is further studied as part of the second sensitivity analysis.

3.3.2 Input: 10 network aspects (only layers), Output: 5 robustness metrics

The second and third sensitivity analyses separate the input of the general network attributes, the number of nodes, edges and density, from the layer-based input. For the second performed sensitivity analysis, the density, total number of nodes and the total number of edges are disregarded as input variables. This facilitates a study into the influence of different layers, their character (converter nodes or hub nodes) and number of nodes on the network robustness metrics. The sample size is $N = 2^{15}$. Appendix B shows the five analysed metrics with the number of nodes per layer as sensitivity indices.
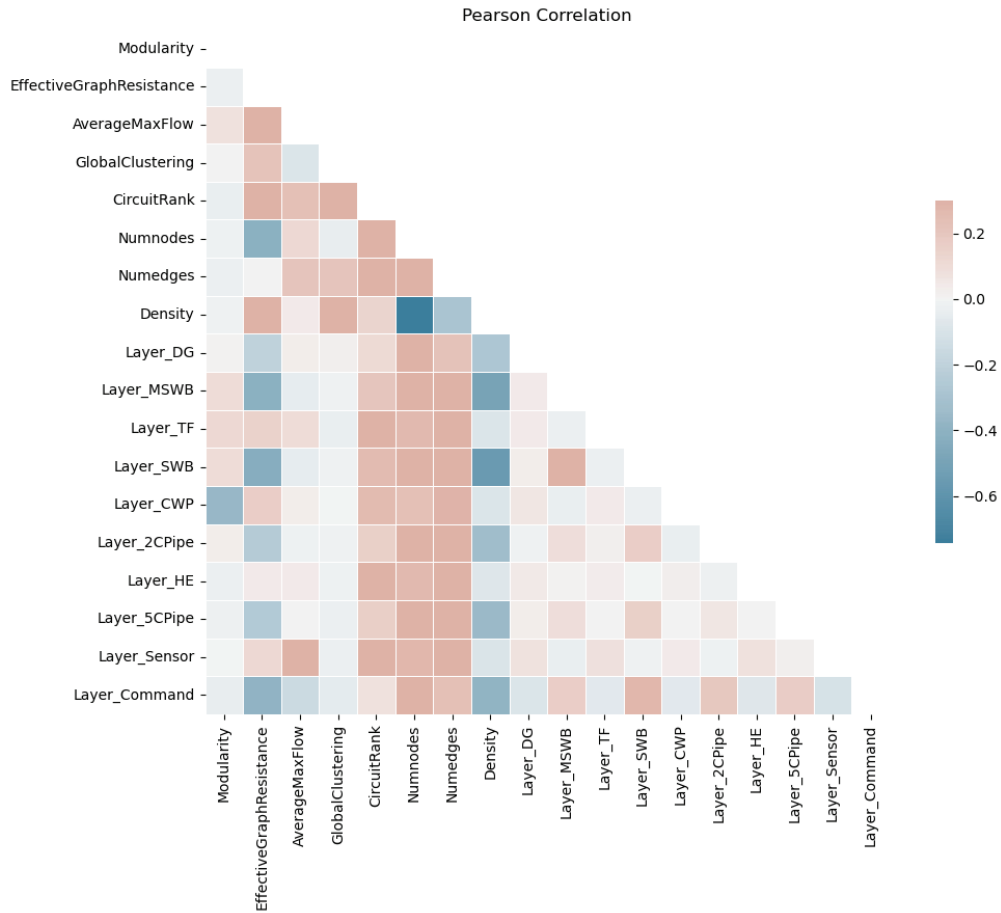
Figure 7: Pearson correlation heat map. The darker red squares indicate a positive linear relation, whereas the darker blue squares indicate a negative linear relation.

Maximum flow is almost fully determined by the sensor layer, which is in line with the first sensitivity analysis. The sensor layer is the smallest converter layer and is, therefore, a literal bottleneck in the flow from the operational source node ("above" the DG layer) to the operational sink node ("below" the Computer layer). Any additional component in the sensor layer facilitates a direct increase in flow through the system. Interestingly, the influence of the TF layer in the first sensitivity analysis (Figure 13) marginalises when the number of edges and density are not taken as input variables anymore. The plot "Second Order Sensitivity Indices for Average Max Flow" shows some weak second-order interaction between the TF layer and the density and sensor layer. However, the interaction seems to be predominantly part of the higher order.

Circuit rank is influenced by the number of nodes in all converter layers, whilst the number of nodes in hub layers plays a marginal role. This could be motivated by the boundary condition that all converter nodes must be connected to the previous and following hub layer. More nodes cause more edges, which is directly related to the number of circuits within the network.

3.3.3 *Input: 5 network robustness metric, output: 5 network robustness metrics*

The third sensitivity analysis focuses on the mutual influence of the network robustness metrics. For this analysis, the "input variables" and "output variables" change for each metric since the metric itself is considered input for the other metrics. Ideally, the five metrics have no influence on the other robustness metrics (Van Mieghem et al. (2010)). This orthogonality would indicate that the five metrics measure perfectly independent network properties and would, therefore, cover most of the character of the network when combined. However, the shared influence of density and number of edges on the metrics already suggests that the metrics are not fully independent. Appendix C contains five figures showing the first-order, second-order and total-order sensitivity analysis for each metric. As outlined earlier in 2, the five metrics correspond to three reliability aspects. For the sake of clarity and

Robustness metric	Main input variable (secondary input variable)	Value (significant secondary value)
Modularity	CWP Layer	$S_1 > 0.42$
Effective Graph Resistance	Density	$S_1 > 0.94$
Maximum Flow	Sensor Layer, (Transformer Layer)	$S_1 > 0.45, (S_1 > 0.14)$
Clustering Coefficient	Density, (Number of edges)	$S_1 > 0.72, (S_1 > 0.13)$
Circuit Rank	Number of edges, (Density)	$S_1 > 0.84, (S_1 > 0.14)$

Table 3: First order sensitivity analysis of network robustness metrics with 13 input variables. The second column shows the dominant variable and the second-most influencing variable with brackets; the corresponding values are given in the third column.
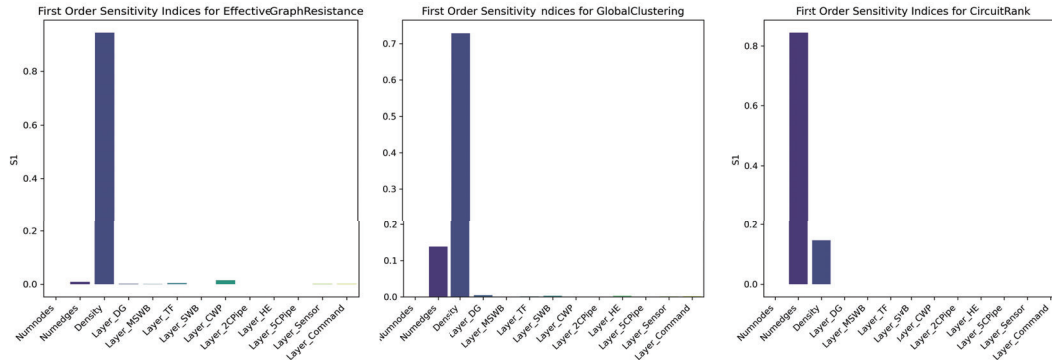
Figure 8: First order sensitivity analysis of the network robustness metrics Effective graph resistance, Global clustering and Circuit rank. The higher-order sensitivity analysis shows marginal values and is therefore not shown in this paper. The sample size of this analysis is set to $N = 2E15, D = 13$.

ease of reference, these aspects are reiterated here:

- **Independent subsystems** → Modularity
- **Component redundancy** → Effective graph resistance and Maximum flow
- **Distribution redundancy** → Clustering coefficient and circuit rank

It was initially expected that the number of nodes mainly influences the component redundancy and, to a lesser extent, the independent subsystems and distribution redundancy. However, Figure 12 shows limited influence of the number of nodes on the effective graph resistance. Therefore, this metric is possibly not the most suitable metric to measure component redundancy. The interesting part of the resistance metric is that it has the highest influence on modularity, maximum flow and circuit rank, respectively Figure 21, 23 and 25. The advantage of this metric is that it includes multiple aspects of other metrics, which is valuable if one metric is used as design or optimisation objective. However, a disadvantage is that the specific network properties that improve the value of the metric become less apparent. The global clustering coefficient and the circuit rank in Figure 24 and 25 are mutually influencing, which is in line with the expected behaviour as a proxy for distribution redundancy. The modularity sensitivity analysis in Figure 21 is in total order comparably equally influenced by the four other metrics. Together with the small influence of modularity on the other metrics, this is assumed to be an indication of the relative independence of this metric.

4 Conclusion and Discussion

The initial goal of this research was to determine the most robust integrated distribution system using network robustness metrics. The design space of these distribution systems showed variation in the number of nodes, edges, network density and network topology. In this research, 2500 connected networks have been generated using Erdös-Rényi random networks with boundary conditions mimicking common engineering practice. These networks are modelled based on the integrated distribution system on a notional frigate de Vos (2018). The physical boundary conditions have been translated to mathematical constraints, facilitating fast network generation and network analysis. The increase in case study size from two networks (Scheffers and de Vos (2024)) to 2500 has created a more thorough analysis and provided new insights with regard to what are "good, safe and robust" distribution systems.

This analysis is performed using five metrics, each presenting certain robustness aspects based on dynamic positioning (redundancy) regulations. First, modularity is determined by two main characteristics. The first and main influence is the number of nodes in the cool-water plant (CWP) converter layer. The secondary relation is with the number of edges and the density. Modularity is, however, relatively independent of the other measured network aspects. This makes this metric interesting in its own right and not easily simplified by just using the network density. Future research should be directed at the partitioning algorithm and linking the mathematical modularity to operationally independent subsystems. The effective graph resistance is, to some extent, positively influenced by the number of hub nodes (more nodes lead to a lower resistance) but is mainly determined by the system density. This metric includes a variety of network properties and even when different-sized systems are compared, a lower resistance network with equal or more nodes indicates a higher robustness. Despite its relation to the number of nodes in the hub layers, resistance might not be the perfect proxy for component redundancy due to its tight relation with network density. The maximum flow between the operational source and sink node is determined by the system's "bottleneck layer", which is the sensor layer in the used case study. In terms of robustness, including this metric is valuable to identify this layer. However, it does not indicate the robustness of the complete system. The global clustering coefficient mainly identifies triangles between layers and has a significant overlap with the circuit rank. The triangles between layers could prove interesting when certain nodes require additional components. Future research into the application of the local clustering coefficient is therefore recommended. The last metric, circuit rank, indicates that the number of nodes in the converter layers has more influence on the distribution redundancy than the hub layers. However, the number of edges is the main input variable to this metric since this number is also directly related to the number of nodes. Therefore, this metric should be disregarded as a valuable robustness metric.

The overall goal of this research was to study the influence of adding nodes to the network on robustness. Based on the three performed analyses, all five metrics show, at best, a weak relation with the total number of nodes. Therefore, the conclusion is that simply adding a component will not inherently make the network more robust. To conclude, one should be very critical of the specific network property a metric is indicative of. Figure 9 and Figure 10 show the most robust networks based on the effective graph resistance and modularity, respectively. With proper awareness of their limitations, the network robustness metrics can provide valuable support in the design process of onboard distribution systems, contributing to reduced system vulnerability and, ultimately, improved overall ship survivability.
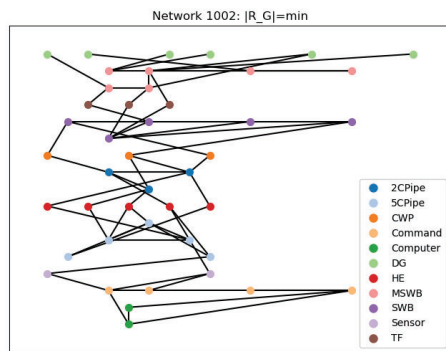
Figure 9: Generated network 1002 with minimum effective graph resistance, $R_G = 0.0143, Q = 0.433$.
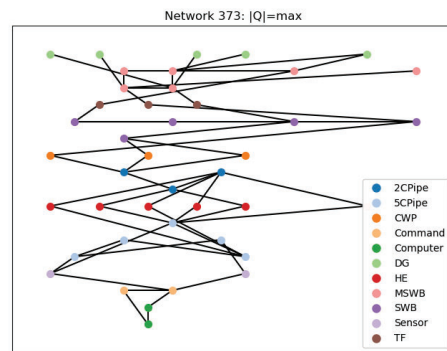
Figure 10: Generated network 373 with maximum modularity, $R_G = 0.0152, Q = 0.481$.

A   Appendix: sensitivity analysis 1
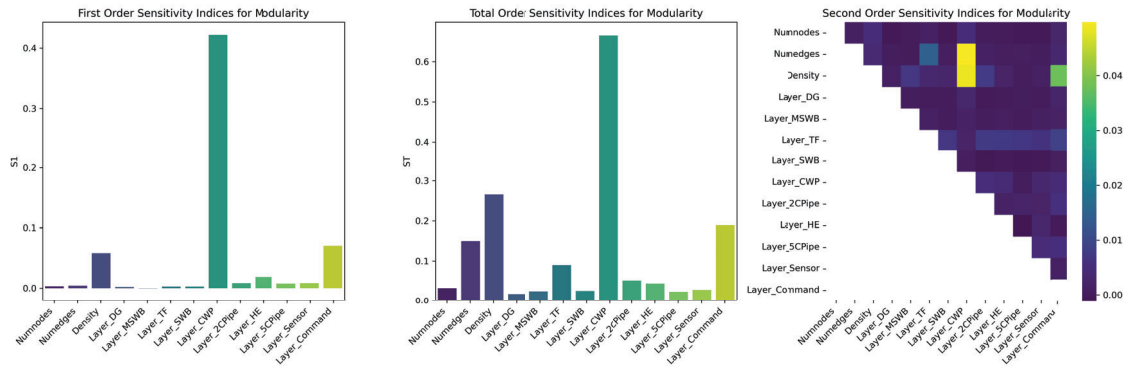
Figure 11: Modularity network robustness metric - sensitivity analysis: full sample space $N = 2E15, D = 13$.
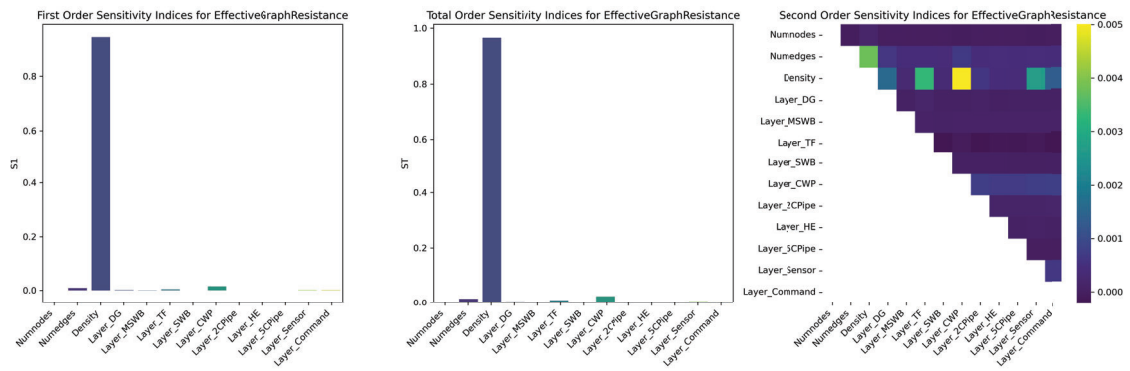
Figure 12: Resistance network robustness metric - sensitivity analysis: full sample space $N = 2E15, D = 13$.
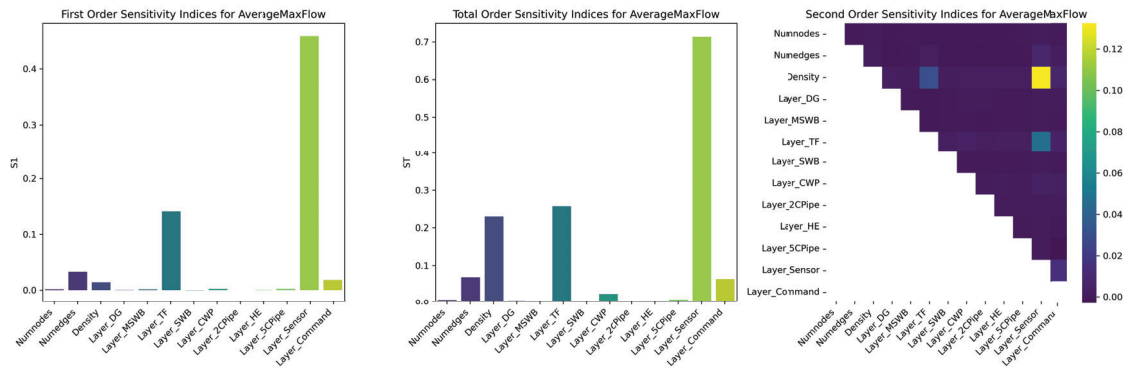
Figure 13: Max Flow network robustness metric - sensitivity analysis: full sample space $N = 2E15, D = 13$.
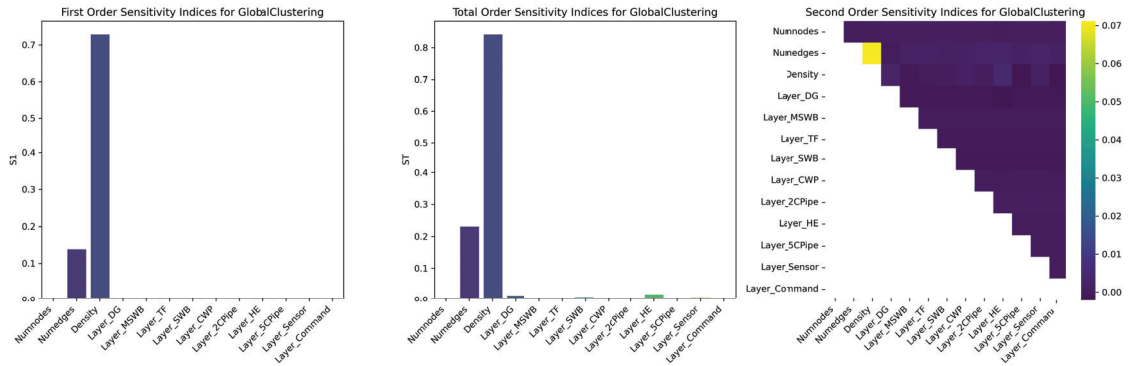
Figure 14: Clustering network robustness metric - sensitivity analysis: full sample space $N = 2E15, D = 13$.
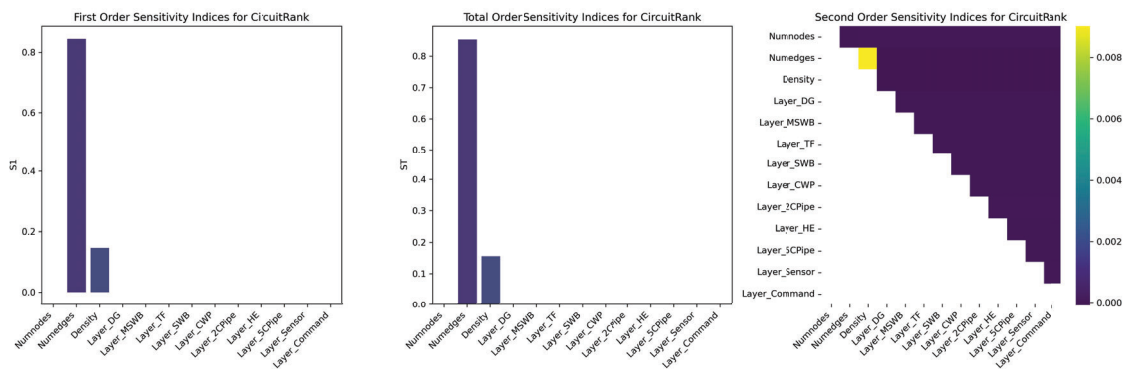
Figure 15: Circuit Rank network robustness metric - sensitivity analysis: full sample space $N = 2E15, D = 13$.

B   Appendix: sensitivity analysis 2
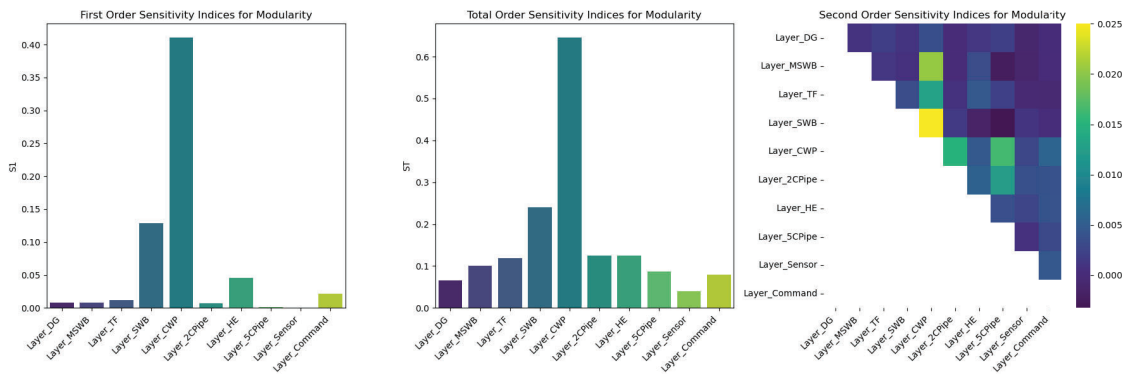
Figure 16: Modularity network robustness metric - layer sensitivity analysis: sample space $N = 2E15, D = 10$.
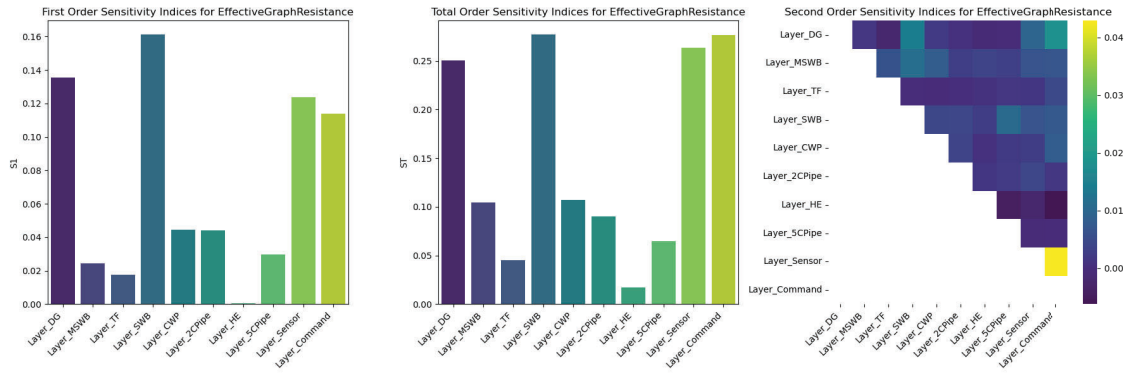
Figure 17: Resistance network robustness metric - layer sensitivity analysis: sample space $N = 2E15, D = 10$.
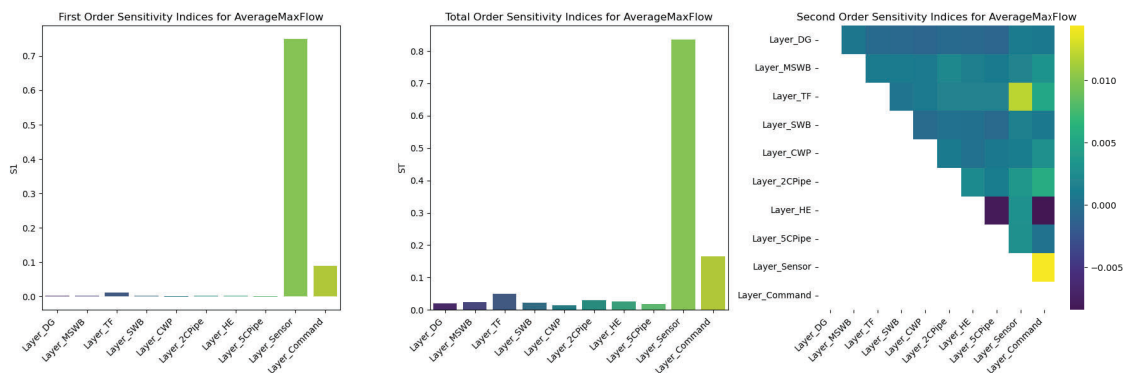
Figure 18: Max Flow network robustness metric - layer sensitivity analysis: sample space $N = 2E15, D = 10$.
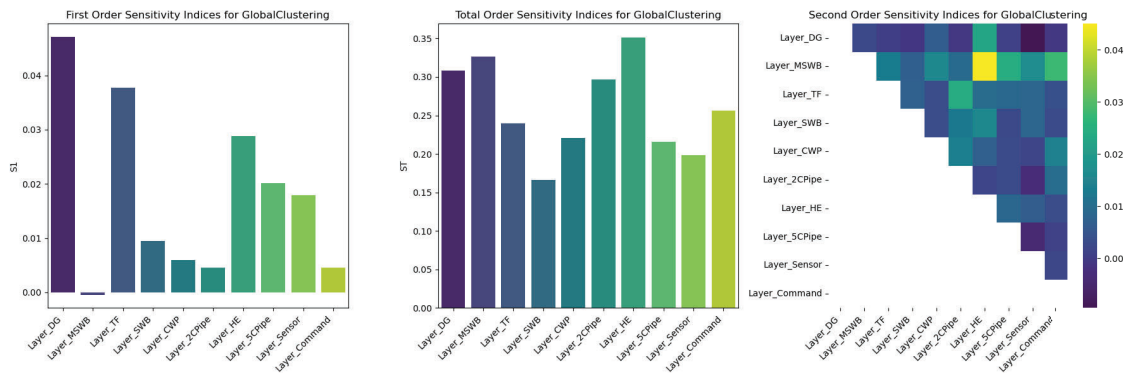
Figure 19: Clustering network robustness metric - layer sensitivity analysis: sample space $N = 2E15, D = 10$.
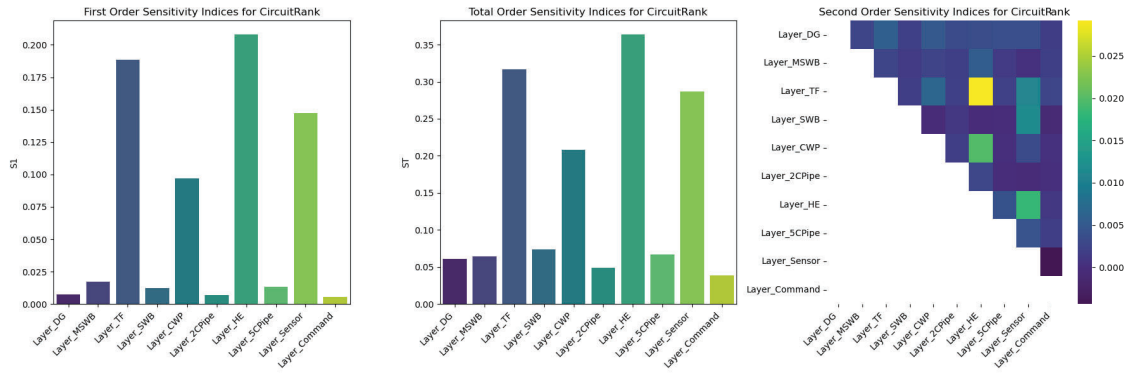
Figure 20: Circuit Rank network robustness metric - layer sensitivity analysis: sample space $N = 2E15, D = 10$.

C Appendix: sensitivity analysis 3
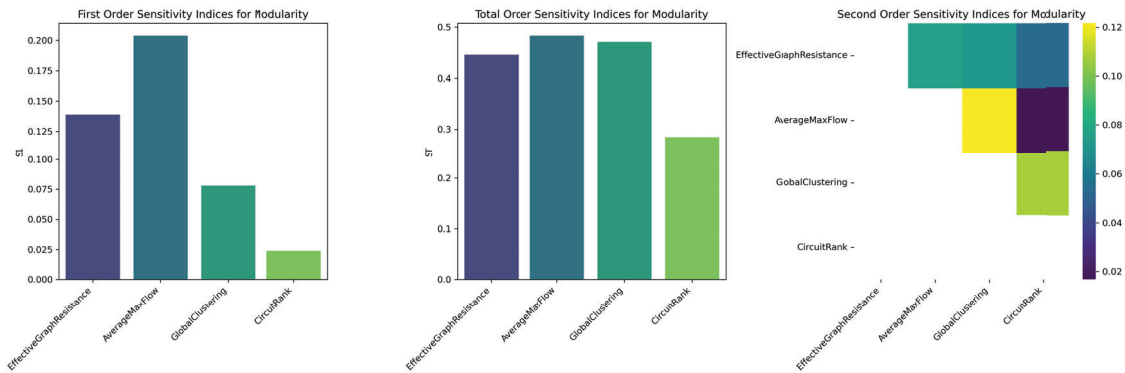
Figure 21: Modularity network robustness metric - mutual sensitivity analysis: sample space $N = 2E15, D = 4$.
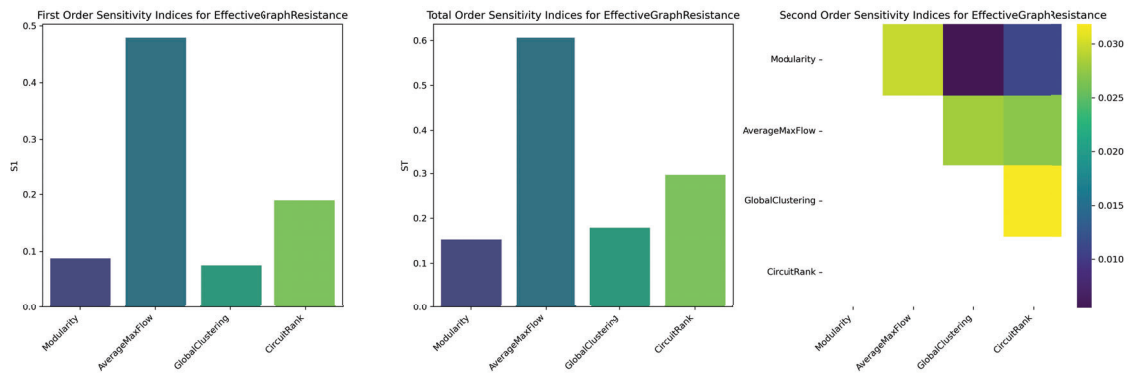
Figure 22: Resistance network robustness metric - mutual sensitivity analysis: sample space $N = 2E15, D = 4$.
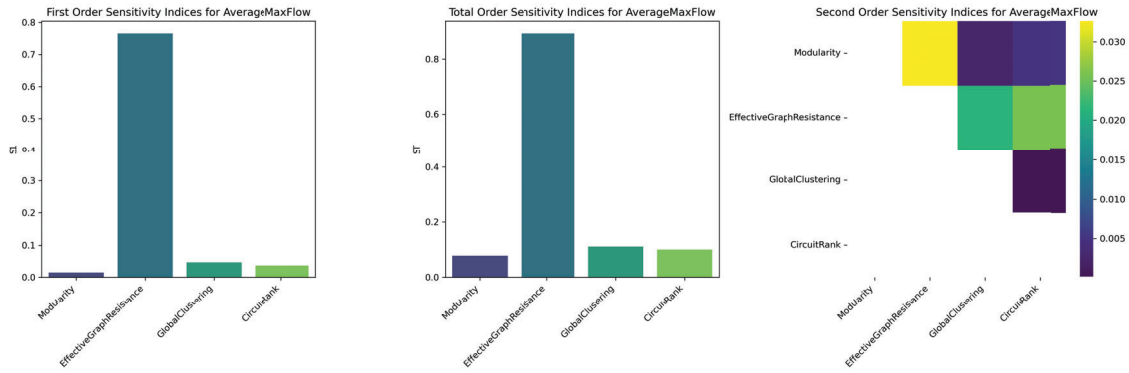
Figure 23: Max Flow network robustness metric - mutual sensitivity analysis: sample space $N = 2E15, D = 4$.
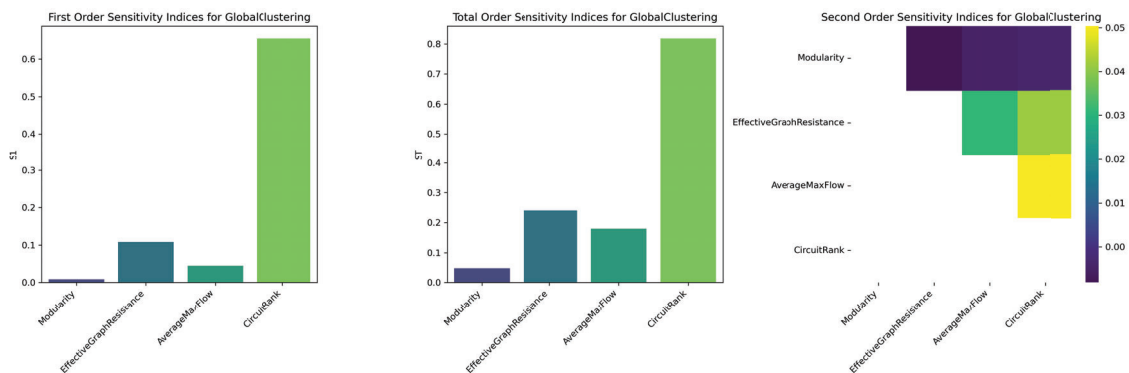
Figure 24: Clustering network robustness metric - mutual sensitivity analysis: sample space $N = 2E15, D = 4$.
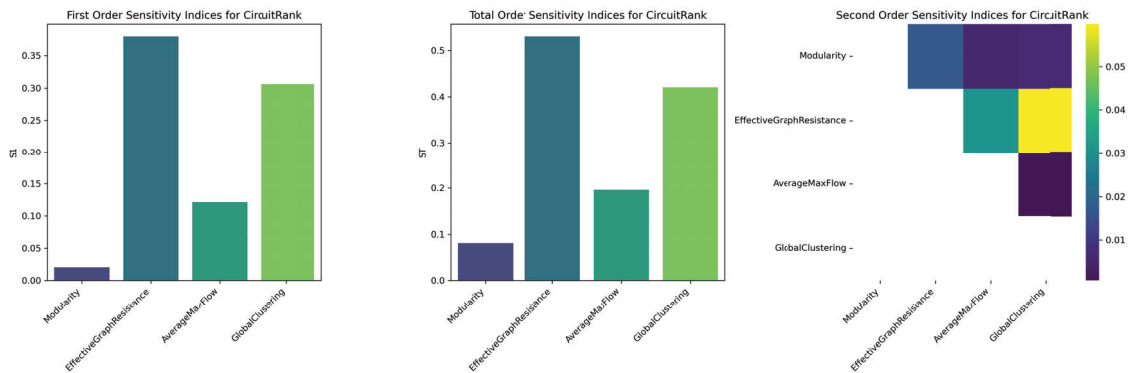
Figure 25: Circuit Rank network robustness metric - mutual sensitivity analysis: sample space $N = 2E15, D = 4$.

References

American Bureau of Shipping, 2021. Guide for Dynamic Positioning Systems 2021. Industry Guidelines. American Bureau of Shipping. Spring, USA.

Brefort, D., Shields, C., Habben Jansen, A., Duchateau, E., Pawling, R., Droste, K., Jasper, T., Sypniewski, M., Goodrum, C., Parsons, M.A., Kara, M.Y., Roth, M., Singer, D.J., Andrews, D., Hopman, H., Brown, A., Kana, A.A., 2018. An architectural framework for distributed naval ship systems. Ocean Engineering 147, 375–385. doi:10.1016/j.oceaneng.2017.10.028.

Clavijo, M.V., Schleder, A.M., Droguett, E.L., Martins, M.R., 2022. RAM analysis of dynamic positioning system: An approach taking into account uncertainties and criticality equipment ratings. Proceed-

ings of the Institution of Mechanical Engineers, Part O: Journal of Risk and Reliability 236, 1104–1134. doi:`10.1177/1748006X211051805`.

de Vos, P., 2018. On Early-Stage Design of Vital Distribution Systems on Board Ships. Ph.D. thesis. Delft University of technology. doi:`10.4233/UUID:EB604971-30B7-4668-ACE0-4C4B60CD61BD`.

de Vos, P., Stapersma, D., 2018. Automatic topology generation for early design of on-board energy distribution systems. Ocean Engineering 170, 55–73. doi:`10.1016/j.oceaneng.2018.09.023`.

Ellens, W., Kooij, R.E., 2013. Graph measures and network robustness. doi:`10.48550/arXiv.1311.5064`, arXiv:`1311.5064`.

Ellens, W., Spieksma, F., Van Mieghem, P., Jamakovic, A., Kooij, R., 2011. Effective graph resistance. Linear Algebra and its Applications 435, 2491–2506. doi:`10.1016/j.laa.2011.02.024`.

Goulter, I.C., 1987. Current and future use of systems analysis in water distribution network design. Civil Engineering Systems 4, 175–184. doi:`10.1080/02630258708970484`.

Habben Jansen, A., 2020. A Markov-based Vulnerability Assessment of Distributed Ship Systems in the Early Design Stage. Ph.D. thesis. Delft University of Technology. doi:`10.4233/UUID:F636539F-64A5-4985-B77F-4A0B8C3990F4`.

Newman, M.E.J., 2010. Networks: An Introduction. Oxford University Press, Oxford ; New York.

Newman, M.E.J., Girvan, M., 2004. Finding and evaluating community structure in networks. Physical Review E 69, 026113. doi:`10.1103/PhysRevE.69.026113`.

Rigterink, D.T., 2014. Methods for Analyzing Early Stage Naval Distributed Systems Designs, Employing Simplex, Multislice, and Multiplex Networks. Ph.D. thesis. University of Michigan. Michigan.

Saltelli, A., 2002. Making best use of model evaluations to compute sensitivity indices. Computer Physics Communications 145, 280–297. doi:`10.1016/S0010-4655(02)00280-1`.

Saltelli, A., Annoni, P., Azzini, I., Campolongo, F., Ratto, M., Tarantola, S., 2010. Variance based sensitivity analysis of model output. Design and estimator for the total sensitivity index. Computer Physics Communications 181, 259–270. doi:`10.1016/j.cpc.2009.09.018`.

Scheffers, E., de Vos, P., 2024. Supplementing Industry-Specific Dynamic Positioning Requirements to Network Theory. International Marine Design Conference doi:`10.59490/imdc.2024.820`.

Sobol′, I., 2001. Global sensitivity indices for nonlinear mathematical models and their Monte Carlo estimates. Mathematics and Computers in Simulation 55, 271–280. doi:`10.1016/S0378-4754(00)00270-6`.

Traag, V.A., Waltman, L., Van Eck, N.J., 2019. From Louvain to Leiden: Guaranteeing well-connected communities. Scientific Reports 9, 5233. doi:`10.1038/s41598-019-41695-z`.

Van Mieghem, P.V., Doerr, C., Wang, H., Hernandez, J.M., Hutchison, D., Karaliopoulos, M., Kooij, R.E., 2010. A Framework for Computing Topological Network Robustness .

Digital twin simulation model of hull-propeller-engine interactions for ship condition monitoring in irregular sea navigation

M. Acanfora*,**, M. Altosole*, F. Balsamo*, F. Scamardella*

* *University of Naples Federico II, Department of industrial engineering*
**Corresponding Author. Email: maria.acanfora@unina.it

Synopsis

Faults in the prime mover of a ship would lead to unpleasant consequences during navigation, especially in the event of bad weather. To avoid troublesome situations, any faults in the propulsive chain should be promptly recognized, by observing the initial degradation of sensitive mechanical components through condition monitoring techniques. However, the effects of such degradations need to be distinguished from the offset induced by the wave actions on a healthy system. This paper concerns the analysis of the consequences of several types of degradations on a ship sailing in rough weather. The study is carried out by means of a numerical simulation model that accounts for the hull, propeller and engine interactions in irregular head seas. The degradation levels of some relevant engine components (mechanical parts) are systematically modeled and simulated. The performances of hull dynamics, propeller actions, and engine performances are monitored (monitored variables) and compared with the healthy propulsion system, aiming at providing a correlation between cause and effect. To this end, a twin screw Ro-pax vessel, powered by two marine diesel engines, is considered.

Keywords: Ship dynamics, hull-propeller-engine interactions, marine systems, condition monitoring

1. Introduction

During navigation, it is of primary importance that the main engine of a ship operates healthy and efficiently, in order to avoid power loss and dangerous consequences. The degradation of main engine components should be identified in advance and appropriate replacements of deteriorated parts should be carried out together with an ad-hoc maintenance strategy (Zhao et al. 2022). This would increase the reliability of the prime mover, minimize the troublesome situations in open water navigation and thus increase the ship safety (Luo & Shin 2015).

The fault analysis of a system can: indicate that something is going wrong in the monitored system (fault detection), find the location of the fault (fault isolation) and quantify the magnitude of the fault (identification procedure) (Tleis 2019) (Frank & Seliger 1991). Among the available fault analysis, some of them were applied to marine diesel engines, which is the commonly adopted type of prime mover onboard ships. In (Laskowski 2015; Knežević et al. 2020), the failure of marine engines is studied by fault tree analysis, that uses logical relations for the assessment of possible faults in a system. In (Khelil et al. 2012; Bukovac et al. 2015; Campora et al. 2015; Zaccone et al. 2015), neural network methods are used at the scope of the fault analysis on different types of marine diesel engines. In (Altosole et al. 2022), the fault analysis is carried out by means of parameter estimation approach using a numerical simulation model of the marine engine, where the parameters resemble the magnitude of the faults. In (Orhan & Celik 2023), a literature review of the fault analysis methods for marine engines is carried out, covering a period on 20 years up to the 2022. Only a limited number of papers attempts to address in an explicit way the performances of the main engine operating in presence of rough weather i.e. connecting hull, propeller and engine behaviours in waves (Ghaemi & Zeraatgar 2021). It is immediately observable that a healthy engine operating in waves will have a different working status, resulting in a lower ship speed (depending on the additional wave resistance); moreover, this situation will have effects also on the propeller loading. A good simulator for a marine propulsion chain in rough sea is made up of several numerical sub-models representing the elements involved in the problem that are ship dynamic in waves model, propeller model, engine model. Usually, the dynamics of a ship is usually studied by 6DOF numerical models in the time domain based on the equations of the rigid body motions (Mortola et al. 2012; Matusiak 2021). However, these numerical approaches assume constant propeller revolutions, thus disregarding propeller interaction with the main engine.

The engine behaviour can be modelled with different levels of accuracy, according to the different purposes and, at the scope, there exist specific programming languages (Altosole et al. 2017; Mrzljak et al. 2017; Altosole et al. 2019) or commercial software (Theotokatos et al. 2016; Mocerino et al. 2021; Ceglie et al. 2023).

In the current paper, we adopt the numerical model for ship dynamics, based on the so-called hybrid or blended non-linear approach (Acanfora & Rizzuto 2019); whereas the engine model refers to a 0D model based on a filling and emptying approach (Benvenuto et al. 2017). The engine modelling choice, despite somewhat simplified compared to commercial software, has the advantage of being implemented in Matlab/Simulink environment, similarly to the numerical model of hull dynamics. Moreover, the sole engine model has been already used for condition monitoring analysis with degraded mechanical components in a previous research (Altosole et al. 2022). Besides, a preliminary coupling of these two numerical models has been presented in (Acanfora et al. 2022), in absence of any degradation of the engine and disregarding added resistance from hull fouling, where two irregular sea states were investigated.

Therefore, in this research, we further develop the numerical model including possible degradations in the propulsion chain. The hull under investigation is a Ro-pax ferry, powered by two four-stroke medium diesel engines. Given a reference irregular sea state, the effects on ship dynamics and on engine variables, when each degradation is set in the propulsion system, are simulated and analysed. Within the same framework, also hull fouling is treated as a source of degradation.

2. Hull, propeller, engine model

The time domain numerical simulation model is implemented in the MATLAB/Simulink environment, and it has a modular arrangement. The sub-models of ship dynamics in irregular seas includes all pertinent non-linearities regarding: the non-linear coupling terms of the rigid body dynamics; the non-linearities of hull geometry in the calculation of Froude–Krylov and restoring actions (subscript "FK" in (1)); the radiation forces and moments, implemented by means of the convolution integral (in (1), the terms a_{ij} and k_{ij}, with i and j from 1 to 6, are, respectively, the added mass coefficients corresponding to the infinite frequency, and elements of the memory function). Differently, diffraction forces and moments (subscript "diff" in (1)) were obtained by linear superposition of regular wave components by potential strip theory calculations. The term X_{res} in eq. 1 is the ship resistance in calm sea, function of the Froude number, while, the added wave resistance accounts only for ship inertia and for Froude–Krylov and restoring actions, that are predominant in case of long waves (i.e. prevailing on diffraction force in the advance direction). Therefore, in order to improve the accuracy of the numerical outcomes, it is recommended working with sea states characterized by wave lengths longer than ship length, thus with large characteristic periods.

The propeller characteristics in wave, i.e. thrust (T_{prop}) and torque (Q_{prop}), are corrected accounting for propeller emersion and propeller loading by means of the technique presented by (Smogeli 2006). The advance velocity at the propeller depends on the variable ship speed in wave (due to surge motions) and by the wake of the hull. For irregular sea problems, the implemented wake factor w, and the thrust deduction factor t_p, equal the values referred to calm sea state. The equation (1) is expressed in the body fixed reference frame centered at the ship center of gravity.

$$\begin{cases} (m + a_{11})\dot{u} + m(qw - rv) + a_{15}\dot{q} = -mgsin\theta + X_{FK} + X_{diff} - k_{11} - k_{15} + X_{prop} + X_{res} \\ (m + a_{22})\dot{v} + m(ru - pw) + a_{24}\dot{p} + a_{26}\dot{r} = mgcos\theta sin\phi + Y_{FK} + Y_{diff} - k_{22} - k_{24} - k_{26} \\ (m + a_{33})\dot{w} + m(pv - qu) + a_{35}\dot{q} = mgcos\theta cos\phi + Z_{FK} + Z_{diff} - k_{33} - k_{35} \\ (I_x + a_{44})\dot{p} + (I_z - I_y)qr + a_{42}\dot{v} + a_{46}\dot{r} = K_{FK} + K_{diff} - k_{44} - k_{42} - k_{46} \\ (I_y + a_{55})\dot{q} + (I_x - I_z)rp + a_{51}\dot{u} + a_{53}\dot{w} = M_{FK} + M_{diff} - k_{55} - k_{53} - k_{51} \\ (I_z + a_{66})\dot{r} + (I_y - I_x)pq + a_{62}\dot{v} + a_{64}\dot{p} = N_{FK} + N_{diff} - k_{66} - k_{62} - k_{64} \end{cases} \tag{1}$$

$$X_{prop} = (1 - t_p)T_{prop} \tag{2}$$

A PI (proportional integral) controller is used for modelling the engine governor. The function of the engine governor is to keep the rotation speed of the diesel engine constant despite variations of propeller load because of wave actions and fouling by allowing the engine to increase or decrease the torque generated.

The governor determines the torque supplied by the engine Q_e acting on the amount of fuel injected at each engine cycle. The engine revolutions N_e are the result of the solution of the dynamic equation of the shaft line

(Taskar et Al. 2016), depending on the rotating inertia of the whole propulsive chain J, where the shaft is assumed to be rigid.

$$\eta_m Q_e - Q_{prop} = J \frac{dN_e}{dt} \qquad (3)$$

In (3) the term η_m is a mechanical efficiency of the engine crank system and the propulsion shaft, that, in the current simulations, was assumed equal to 1.

The diesel engine model is based on a 0D filling and emptying approach, aiming at a compromise between obtaining a fairly accurate engine behaviour during transient stages and limiting the computational work of the simulator. All main engine components are arranged in blocks and modelled by algebraic and/or differential equations according to the principles of mass and energy conservation, whereas the fluid modelling is based on the assumption of ideal gas which composition varies through the engine components. The engine blocks are: cylinder, compressor, turbine, intercooler, turbocharger shaft (shaft TG). The 0D engine model consists in simplified modeling of the thermodynamic behavior of a single cylinder, and considers all cylinders working in phase.

At the scope of the application, a four-stroke turbocharger engine model is implemented, where the turbine and compressor are modelled using steady state maps. Engine and turbocharger speeds are calculated by dynamic equilibrium equations. A classical double zone Wiebe function is implemented for modelling the heat release during the combustion in each cylinder. The inlet valves timing can be varied to control the air flow at different engine speed and loads. Fresh air temperature, and fresh cooling water temperature are kept constant during the simulation.

For the sake of synthesis, the detailed description of the ship dynamics model and engine model are available in (Benvenuto et al. 2017; Acanfora & Rizzuto 2019), respectively.

3. Modelling of hull and engine degradations

The hull-propeller-engine model, implemented in the Simulink toolbox, allows for the possibility of introducing a degradation level in pertinent mechanical components, and in the hull surface smoothness, using degradation coefficients. All coefficients have unitary value when the engine works in a healthy state and there is no fouling on the hull. Each alteration in the coefficient values can reduce the efficiency or the working feature of a specific engine element (in the case of the hull fouling, increase the drag), with consequences on the whole propulsion chain. Among the numerous mechanical engine parts susceptible of failure, we selected the most representative, based on the experience of the co-authors and referring to the technical literature (Benvenuto & Campora 2007; Ceglie et al. 2023).

Table 1 reports the list of the degradations under investigation, i.e. the degradation coefficients, implemented in the pertinent engine simulation block; whereas the hull degradation coefficient is applied to the evaluation of Xres in the ship dynamics model. Once a degradation level is set in an engine part or in the hull, it is possible simulating within the numerical model the deviations between hull propeller engine interactions compared to the simulation outcomes referring to the health state of the engine.

Among the numerous state variables charactering the hull, propeller, engine behaviour a selection is made. At the scope, we focused our attention only on meaningful variables that can be reasonably monitored on board (Ceglie et al. 2023) (Altosole et al. 2022). These are listed in Table 2 and Table 3.

Table 1: List of hull and engine degradation coefficients

Simulation block	Degradation (Coefficient name)
Intercooler	Intercooler fouling (d_in_p)
Intercooler	Efficiency reduction (d_in_eff)
Compressor	Dirty air filter (d_co_eff)
Compressor	Efficiency reduction (d_co_re)
Compressor	Mass flow reduction (d_co_m)
Shaft TG	Bearing deterioration (d_tg_cu)
Turbine	Efficiency reduction (d_t_re)
Turbine	Fouling of the blades (d_t_pa)
Cylinder	Fuel flow reduction (d_c_co)
Ship dynamics	Hull fouling (d_h_f)

Table 2: List of monitored hull and propeller state variables

Hull	
Ship velocity	V
Heave	ζ
Pitch	θ
Propeller	
Torque	Q
Revolutions	N

Table 3: List of monitored engine state variables

Pressure (outlet)	
Compressor	p_c
Cylinder (outlet)	p_{cl}
Temperature (outlet)	
Compressor	t_c
Turbine	t_t
Cylinder	t_{cl}
Other	
Specific fuel consumption	sfc
Engine torque	Q_e
Engine Speed	N_e

4. Case study

The ship under investigation is a Ro-pax ferry named Seatech-D equipped with two diesel engines of 12MW each and a twin-screw propeller configuration. The hull has been used for previous researches concerning the applications and validations of the numerical model for ship dynamics in wave (Acanfora & Rizzuto 2019).

At the scope of the current study, the maximum speed is set as 24 knots. Two Wageningen B-series propellers are assumed, for which KT and KQ coefficients are available from (Barnitsas et al. 1981). The calibration and the validation of the engine model was carried out in (Altosole et al. 2022).

Table 2: Principal particulars of Seatech-D

Hull Seatech-D	
Length between perpendiculars, L (m)	158.00
Breadth, B (m)	25.00
Depth, D (m)	15.00
Draft forward, T_F (m)	6.10
Draft aft, T_A (m)	6.10
Displacement, Δ (tons)	13,766
Center of gravity above keel, KG (m)	11.834
Long. coordinate of the center of gravity from aft perpendicular, LCG (m)	74.77
Transv. radius of gyration in air, k_{XX} (m)	10.06
Long. radius of gyration in air, k_{YY} (m)	39.36
Propeller Wageningen B-series	
Number of blades Z	4
A_e/A_0	0.750
D_{prop} (m)	4.8
$P/_{Drop}$	1.2
Engine	
Number of cylinders	12
Bore (m)	0.51
Stroke (m)	0.60

Engine revolution N_{eng} (rpm)	514
Engine power P_B (MW)	12

Table 4 summarizes the main hull, engine and propeller features.

The applications are carried out for the same irregular sea realization (see Figure 1) obtained by the technique described in (Acanfora & Rizzuto 2019). The chosen sea state is described by the JONSWAP spectrum and it is characterized by a significant wave height Hs=5.5 m and a zero crossing period Tz=11 s. The ship sails in head sea. Prior to introduce any degradation in the numerical model, the state variables are simulated for the still water condition and for the irregular sea condition, given the unitary values of all degradation coefficients (i.e. engine healthy state) and a fixed propeller revolution Neng. Then, all degradations listed in Table 1, are induced, assuming a constant degradation level of 10 %, corresponding to a degradation coefficient value of 0.9, except for the hull fouling coefficient. In this case, the coefficient is meant to increase the drag of 5% and thus it is set equal to 1.05.

5. Results: no degradation

This section includes the still water and wave results for the engine working without any degradation. Each simulation lasts 10 minutes. Figure 1 shows a comparison between the hull state variables in absence and in presence of waves, whereas Figure 2 provides the same comparison but focusing on engine state variables.
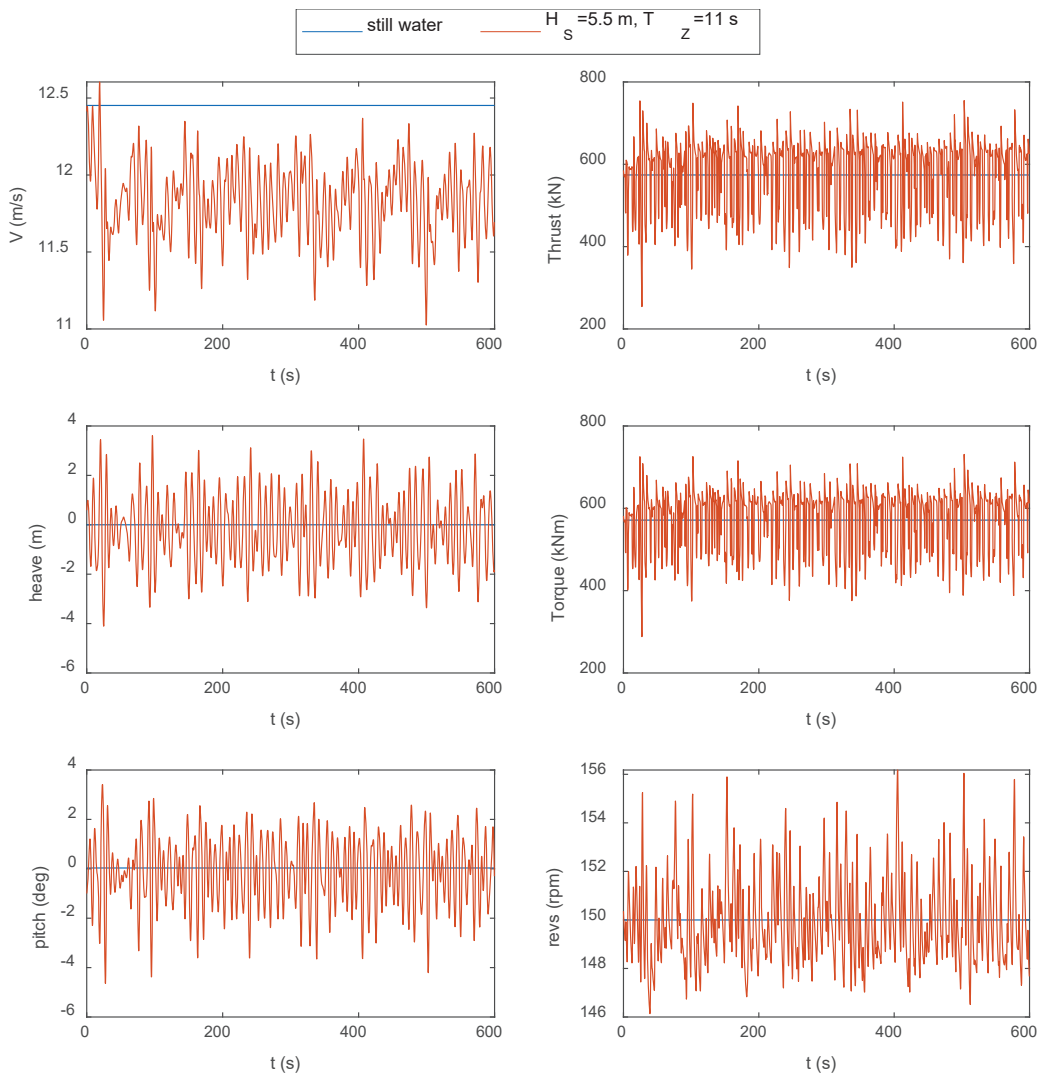
Figure 1: Hull and propeller behaviours in still water and in waves, no degradation

The steady behavior of the engine variable in still water condition presented in Figure 2, could be attributed to the 0D engine model assumptions.

Due to the added wave resistance, a speed reduction of almost 1.2 knots is observed in waves, compared to the still water case. However, the averaged propeller behaviour remains almost equal in the two cases, in terms of torque, thrust and revolutions (there is an increase of only 0.25% in thrust and torque), although in waves they show an irregular oscillatory trend. Although the propeller thrust is not a monitored variable, it is presented in Figure 1 for a more complete description of the simulated propeller behaviour. Regarding the monitored engine variables, it is possible observing that from the numerical simulation there are no significant oscillatory pressure variations in waves, that almost overlaps still water outcomes. Instead, for the remaining variables i.e. temperatures, engine torque, revolutions, and specific fuel consumption, the results exhibit an appreciable irregular oscillatory behavior in waves, but with average values almost equal to the corresponding still water outcomes.

This preliminary analysis suggests that for the chosen operational condition, there is no substantial change for irregular sea navigation in the mean values of the monitored engine and propeller variables. The only appreciable change is observed in the ship speed.
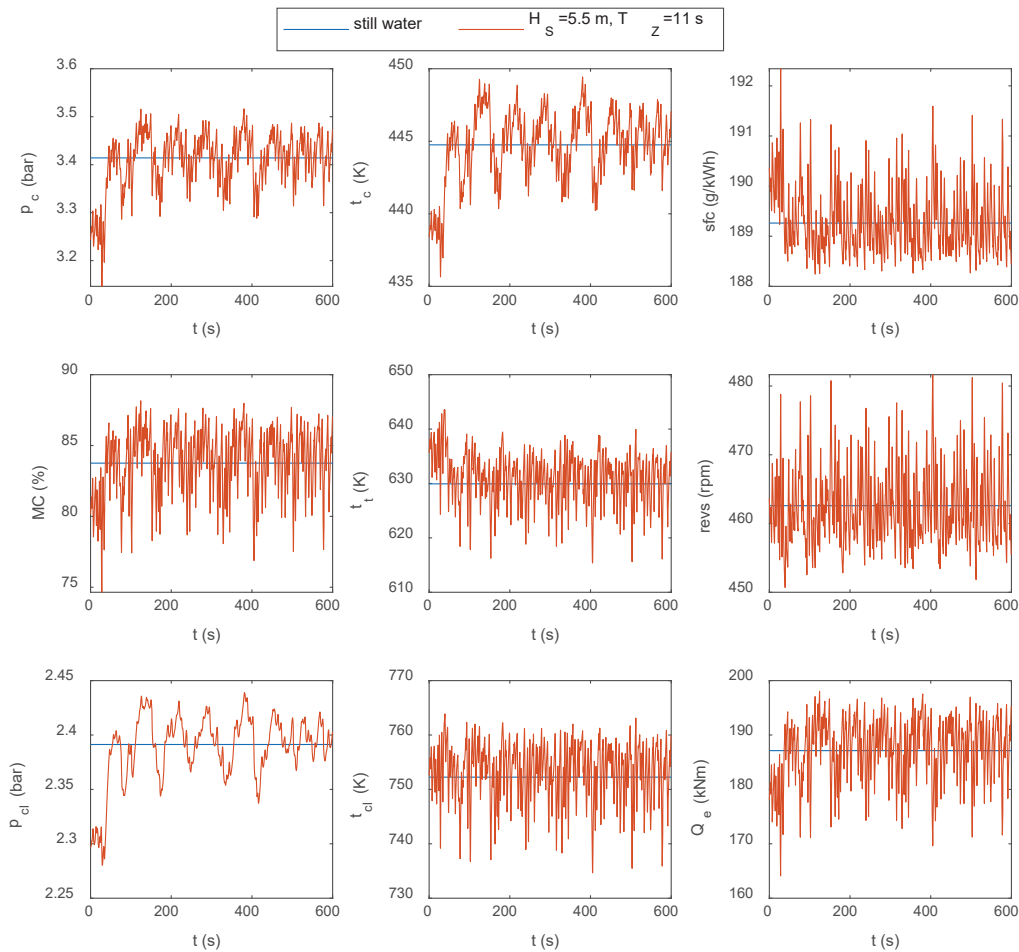
Figure 2: Engine behavior in still water and in waves, no degradation

Due to the absence of data from the field, validation of numerical simulation regarding the engine behavior in transient conditions was not possible. However, the obtained results appear reasonable, especially because they depend on the 0D engine model (i.e. neglecting the effective dynamics of the combustion).

Nevertheless, we can deduce that the ship sailing the chosen irregular sea experiences a greater fuel consumption than in calm sea navigation, mainly because of the speed reduction (increase in the navigation time), whereas the specific fuel consumption of the engine remains somewhat unaltered.

It is worth underlying that although the coupling between the presented hull dynamics model and engine model was not validated, the standalone models were properly calibrated and validated on the hull (Acanfora & Rizzuto 2019) and on the engine (Altosole et al. 2022) used at the scope of the case study.

6. Results: hull and engine degradations

This analysis aims at comparing the values of the monitored ship and engine variables between the nominal condition (i.e. no degradation) and the cases with an induced degradation. At the scope, ten numerical simulations are carried out, each of them corresponding to a specific altered degradation coefficient, in the starboard engine. Given the twin-screw arrangement of the ship, it was possible inducing degradation to the starboard engine and maintain the port engine operating at the nominal condition as a reference.

For each degradation case, the monitored variables of the degraded starboard engine (altered values) and the monitored variables of the non-degraded port engine (nominal values), were simulated and collected. Following, we analysed the offset between degraded vs non-degraded engine variables by calculating the root mean square of the error (rmse) between the monitored degraded vs non-degraded engine variables. The obtained results are arranged in Table 5, in order to investigate on the variations induced by the several degradation types. In Table 5, for each degradation scenario, the rmse between nominal and altered variables are shown as percentage of the nominal condition. As an example, setting in the simulation a fouling level of 10% in the intercooler (d_in_p) of the starboard engine, this degradation type causes an average variation in the cylinder temperature t_{cl} of 6% compared to the non-degraded engine (i,e, with no fouling at the intercooler).

In Table 5, it is possible observing how the degradation level of 10% in the engine components has a modest influence on ship speed compared to the hull fouling effects, for the sea state under investigation. The outlet pressure at the compressor has been resulted the most sensitive parameter, especially with degradation types belonging to the turbocharger system. Indeed, there are similar trends in the monitored variables given the mechanical element interested by the degradations, such as those referring to the intercooler (d_in_p e d_in_eff) or to the compressor (d_co_eff, d_co_re, d_co_m). The fouling on turbine blade degradation (d_t_pa) exhibits the largest observed deviation, in the outlet pressure at the cylinder, associated to a modest variation of the specific fuel consumption. Actually, this variable varies of almost 1% in all degradations associated to turbocharger and intercooler (that could be reasonable considering the modest degradation levels under investigation) and it remains unaltered for hull fouling degradation. Indeed, this is consistent with the fact that the engine is working with no degradation at its nominal condition, thus in case of hull fouling only a speed reduction of 1% is observed.

The specific fuel consumption increases of 11.13% for the degradation case involving the fuel flow reduction (d_c_co) i.e. associated to a valve leakage, that leaves somewhat unaltered the remaining engine monitored variables. The values in Table 5 cannot directly provide the state of the engine, especially dealing with small degradation levels and small alterations of the variables. However, this analysis suggests that each degradation scenario could have a peculiar set of sensitive variables to be used as an indicator of the healthy state of the system, using optimization techniques for condition monitoring (Altosole et al. 2022), (Ceglie et al. 2023).

Table 3: Offset of the engine monitored variables, with degradation vs no degradation

	t_{cl}	p_{cl}	t_c	p_c	t_t	sfc	N	Q_e	Q	V
d_in_p	6.02%	5.17%	0.11%	1.23%	7.33%	1.08%	0.03%	0.10%	0.10%	0.01%
d_in_eff	2.13%	0.69%	0.47%	2.02%	2.32%	0.32%	0.01%	0.05%	0.05%	0.00%
d_co_eff	6.78%	5.77%	0.17%	9.97%	8.26%	1.22%	0.03%	0.11%	0.11%	0.01%
d_co_re	6.66%	5.66%	0.28%	9.80%	8.10%	1.20%	0.03%	0.10%	0.10%	0.01%
d_co_m	6.49%	6.98%	3.67%	12.84%	7.93%	1.15%	0.03%	0.10%	0.10%	0.01%
d_tg_cu	6.30%	5.56%	3.32%	10.05%	7.71%	1.13%	0.03%	0.10%	0.10%	0.01%
d_t_re	6.36%	5.58%	3.33%	10.11%	9.68%	1.15%	0.03%	0.10%	0.10%	0.01%
d_t_pa	4.60%	19.55%	4.15%	13.15%	8.07%	0.51%	0.01%	0.06%	0.06%	0.01%
d_c_co	0.18%	1.03%	0.41%	0.99%	0.27%	11.13%	0.26%	0.87%	0.87%	0.11%
d_h_f	0.00%	0.00%	0.00%	0.00%	0.00%	0.00%	0.00%	0.00%	0.00%	1.03%

7. Conclusions

This work reported the development of a numerical model for the hull-propeller-engine interactions in rough sea conditions.

A brief description of ship dynamics in 6DOF was provided in the paper. The effects of manoeuvring on the propeller-engine matching were neglected. The case study accounted only for head sea navigation. The engine 0D model was implemented, including the possibility of simulating partial ineffectiveness of mechanical components by using degradation coefficients. Additionally, the hull degradation coefficient was introduced, regarding the effects of hull fouling on ship resistance.

A Ro-pax ferry, characterized by a twin-screw arrangement was chosen for the case study. Among all variables available within the numerical simulation, only a reduced number of engine and hull variables were presented in this study. Such variables were judged pertinent for monitoring the engine and hull state. A sample wave train realization was assumed and kept for all numerical simulations. It was observed that the sea state had influence on hull behaviour and that the average engine state depended only on the average engine power (no degradation case). Additionally, we observed that the mean value of specific engine consumption did not depend on hull dynamics in waves nor on hull fouling. Obviously, the total fuel consumption within a planned navigation would increase because of the increase in sailing time due to speed reduction.

The analysis of the monitored variables, induced by each degradation, disclosed that the most sensitive item for assessing turbocharger degradation was the outlet pressure at the compressor.

Based on the outcomes of the present study, although restricted to a limited case study, we could foresee that diagnostic techniques performed on the ship engine operating in rough sea navigation could still be successful by working on the mean values of the variables. Future studies are expected to address this topic.

In particular, in future studies, after a validation of the presented model (that will serve as a digital twin of the engine operating on a sailing ship), we will aim at employing techniques for condition monitoring of the engine state, by comparing the measured variables onboard with the simulated ones.

It is worth underlying that, although the presented outcomes refer only to the hull and engine under investigation, the proposed approach can be extended to different engine types and to different ships, given the availability of pertinent engine models and hull data.

References

Acanfora M, Altosole M, Balsamo F, Micoli L, Campora U. 2022. Simulation Modeling of a Ship Propulsion System in Waves for Control Purposes. J Mar Sci Eng, Vol. 10-1, Available from: https://doi.org/10.3390/jmse10010036

Acanfora M, Rizzuto E. 2019. Time domain predictions of inertial loads on a drifting ship in irregular beam waves. Ocean Eng; 174:135–147. Available from: https://www.sciencedirect.com/science/article/pii/S0029801818319917

Altosole M, Balsamo F, Acanfora M, Mocerino L, Campora U, Perra F. 2022. A Digital Twin Approach to the Diagnostic Analysis of a Marine Diesel Engine. In: Prog Mar Sci Technol. Vol. 6.; p. 198–206.

Altosole M, Benvenuto G, Campora U, Laviola M, Zaccone R. 2017. Simulation and performance comparison between diesel and natural gas engines for marine applications. Proc Inst Mech Eng Part M J Eng Marit Environ. 231:690–704.

Altosole M, Campora U, Figari M, Laviola M, Martelli M. 2019. A diesel engine modelling approach for ship propulsion real-time simulators. J Mar Sci Eng. Vol. 7.

Barnitsas MM, Ray D, Kinley P. 1981. Kt, Kq and Efficiency Curves for the Wageningen B-Series Propellers. Report N.237..

Benvenuto G, Campora U. 2007. Performance Prediction of a Faulty Marine Diesel Engine under Different Governor Settings. In Proc. International Conference on Marine Research and Transportation.

Benvenuto G, Campora U, Laviola M, Terlizzi G. 2017. Simulation model of a dual-fuel four stroke engine for low emission ship propulsion applications. Int Rev Mech Eng. 11:817–824.

Bukovac O, Medica V, Mrzljak V. 2015. Steady state performances analysis of modern marine two-stroke low speed diesel engine using mlp neural network model. Brodogradnja. 66:57–70.

Campora U, Capelli M, Cravero C, Zaccone R. 2015. Metamodels of a gas turbine powered marine propulsion system for simulation and diagnostic purposes. J Nav Archit Mar Eng. 12:1–14.

Ceglie M, Ferrante F, Giannino G. 2023. Employing Artificial Neural Network for Process Signal Estimation in the Monitoring of Smart Shipboard Diesel Engine Systems. In: Proc Symposium on High Speed Marine Vehicles.

Frank P, Seliger R. 1991. Fault Detection and Isolation in Automatic Processes. Editor(s): C.T. LEONDES, Control and Dynamic Systems, Academic Press, Volume 49, Part 5, Pages 241-287, https://doi.org/10.1016/B978-0-12-012749-8.50011-8.

Ghaemi MH, Zeraatgar H. 2021. Analysis of hull, propeller and engine interactions in regular waves by a combination of experiment and simulation. J Mar Sci Technol. 26:257–272. Available from: https://doi.org/10.1007/s00773-020-00734-5

Khelil Y, Graton G, Djeziri M, Ouladsine M, Outbib R. 2012. Fault detection and isolation in marine Diesel engines: A generic methodology. In: IFAC Proc Vol. Vol. 45. IFAC Secretariat; p. 964–969.

Knežević V, Orović J, Stazić L, Čulin J. 2020. Fault tree analysis and failure diagnosis of marine diesel engine turbocharger system. J Mar Sci Eng. 8:1–19. Available from: www.mdpi.com/journal/jmse

Laskowski R. 2015. Fault Tree Analysis as a tool for modelling the marine main engine reliability structure. Sci Journals Marit Univ Szczecin. 41:71–77.

Luo M, Shin SH. 2015. Half-century research developments in maritime accidents: Future directions. Accid Anal Prev. Available from: http://dx.doi.org/10.1016/j.aap.2016.04.010

Matusiak J. 2021. Dynamics of a Rigid Ship -with applications. Aalto University publication series SCIENCE + TECHNOLOGY, 4/2021. Available from: https://aaltodoc.aalto.fi/handle/123456789/24408

Mocerino L, Soares CG, Rizzuto E, Balsamo F, Quaranta F. 2021. Validation of an Emission Model for a Marine Diesel Engine with Data from Sea Operations. J Mar Sci Appl. 20:534–545.

Mortola G, Incecik A, Turan O, Hirdaris SE. 2012. A nonlinear approach to the calculation of large amplitude ship motions and wave loads. In: Sustain Marit Transp Exploit Sea Resour - Proc 14th Int Congr Int Marit Assoc Mediterr IMAM 2011. Vol. 1.; p. 249–255.

Mrzljak V, Medica V, Bukovac O. 2017. Quasi-dimensional diesel engine model with direct calculation of cylinder temperature and pressure Tehnicki vjesnik - Technical Gazette 24(3):681-686.

Orhan M, Celik M. 2023. A literature review and future research agenda on fault detection and diagnosis studies in marine machinery systems. Proc Inst Mech Eng Part M J Eng Marit Environ.

Smogeli ON. 2006. Control of Marine Propellers from Normal to Extreme Conditions. PhD-thesis 2006:187. Faculty of Engineering Science & Technology, NTNU.

Taskar B, Yum Kevin, Steen S, Pedersen E. 2016. The effect of waves on engine-propeller dynamics and propulsion performance of ships. Ocean Engineering. 122. pp. 262-277. 10.1016/j.oceaneng.2016.06.034.

Theotokatos G, Stoumpos S, Lazakis I, Livanos G. 2016. Numerical study of a marine dual-fuel four-stroke engine. In: Proc 3rd Int Conf Marit Technol Eng MARTECH 2016. Vol. 2.; p. 777–786.

Tleis N. 2019. Power Systems Modelling and Fault Analysis. In: Tleis N, editor. Power Syst Model Fault Anal (Second Edition). Academic Press. Available from: https://www.sciencedirect.com/science/article/pii/B9780128151174000229

Zaccone R, Altosole M, Figari M, Campora U. 2015. Diesel engine and propulsion diagnostics of a mini-cruise ship by using artificial neural networks. In: Toward Green Mar Technol Transp - Proc 16th Int Congr Int Marit Assoc Mediterr IMAM 2015; p. 593–602.

Zhao J, Gao C, Tang T. 2022. A Review of Sustainable Maintenance Strategies for Single Component and Multicomponent Equipment. Sustainability 14(5):2992. Available from: https://doi.org/10.3390/su14052992.

Enhancing Predictive Maintenance in the Maritime Industry with Unsupervised Learning

N. Faggioni[*+], A. Caviglia[*], N. Guarnera[#], E. Schininà[#], E. Sansebastiano[*] & R. Chiti[*]

[*] *Fincantieri NexTech, Viale Brigate Partigiane 92R, 16129, Genoa, Italy.*
[#] *Argo IT s.r.l., Via Caterina Rossi 2/1, 16154 Genoa, Italy.*

[+] Corresponding Author. Email: nicolo.faggioni@fincantierinxt.it

Synopsis

This paper introduces a novel approach centred on unsupervised learning, specifically leveraging state-of-the-art Recurrent Neural Networks (RNNs), particularly Long Short-Term Memory (LSTM). The study aligns with the domain of predictive maintenance (PdM) and time series analysis for evaluating the health status of devices.

The proposed methodology seeks to enhance current PdM practices by integrating machine learning (ML) into the conventional statistical framework. ML techniques are increasingly applied in the industrial sector, demonstrating their capacity to capture complex correlations that may elude human operators.

Indeed, the management of scheduled maintenance in the naval sector is a complex challenge, primarily due to the diversity of devices and systems on board ships. These systems vary in nature, complexity, and criticality, making it challenging to adopt a standardized maintenance strategy.

Solutions based on Condition-Based Maintenance (CBM) aim to perform maintenance based on the actual operational conditions of a system, rather than following fixed schedules. This approach relies on the use of sensors, continuous monitoring, and advanced diagnostics to assess the health status of components and predict failure times.

However, despite advancements in this direction, there are still significant challenges to address. One of the main challenges is the heterogeneity of systems on board ships.

Furthermore, approaching the predictive maintenance task for onboard ship equipment, a key challenge emerges when attempting to estimate the Remaining Useful Life (RUL) of a component given the scarcity of run-to-failure data. For such a reason, the developed model adopts a fully data-driven approach, where the failure characteristics (run-to-failure data) of the equipment are not pre-defined.

Moreover, the framework encompasses data acquisition, data preprocessing, Health Index (HI) construction, and the prediction of remaining useful life grounded in the examination of a documented failure case related to maritime equipment. Indeed, the framework has been tested on data corresponding to an actual equipment failure, enabling a direct comparison with its application to data from normally functioning equipment without anomalies.

The presented unsupervised approach serves a dual purpose: enabling real-time detection of potential failures and facilitating trend analysis of the device's health index. This dual functionality proves valuable in estimating the projected failure period.

Keywords: Condition-Based Maintenance (CBM), Predictive Maintenance (PdM), Long Short-Term Memory, Remaining Useful Life (RUL), Run-to-failure Data.

1. Introduction

Maintenance management in the naval sector poses unique challenges due to the diversity, complexity, and criticality of onboard systems (Coraddu et al., 2015). Conventional maintenance strategies often struggle to adapt to the dynamic operational conditions and varying maintenance requirements of maritime equipment. Condition-Based Maintenance (CBM) offers a more adaptive approach, relying on sensor data, continuous monitoring, and advanced diagnostics to assess the health status of components and predict maintenance needs based on actual operational conditions (Jardine et al., 2006).

Author's Biography

Nicolò Faggioni was born in Italy in 1991. He earned a Bachelor's degree in Nautical Engineering in 2014, followed by a Master's degree in Yacht Design in 2017, and a PhD in autonomous navigation in 2022, all from the University of Genoa. Currently, he is employed at Fincantieri NexTech, where he focuses on automation and control systems for the marine sector. His primary research interests include ship propulsion plants, mathematical modelling, data analysis, and numerical simulation.

Alessandro Caviglia was born in Italy in 1990. He earned a Bachelor's degree in Computer Engineering in 2019, followed by a Master's degree in Computer Engineering: Software and Computing Platforms in 2020 from the University of Genoa. Currently, he works at Fincantieri NexTech, specializing in automation and control systems for the marine sector. His primary areas of expertise are data science, cloud computing, and digitalization.

Nicola Guarnera was born in Italy in 1990. He earned a Master degree in Automation Engineering and control of complex systems in 2019, from the University of Catania. Currently, he is employed at Argo IT s.r.l., where he focuses on research and developing Machine Learning solutions and Data analysis on industrial problems. His primary research interests include modelling plants through mathematical, statistical and data driven approaches.

Emilio Schininà was born in Italy in 1992. He holds a bachelor's degree in Computer Science and Technology from the University of Ferrara in 2016 and a master's degree in Automation Engineering and Control of Complex Systems in 2020 from the University of Catania. He has previously worked under contract at the National Institute of Nuclear Physics (INFN). Currently, he collaborates with Fincantieri Nextech and ABB Limited, Italy.

Emanuele Sansebastiano was born in Italy in 1993. He earned a Bachelor's degree in Industrial Engineering in 2015, followed by a Master's degree in Robotics (European Master on Advanced Robotics) in 2017. Currently, he is employed at Fincantieri NexTech, where he is leading the development team of the Situational Awareness System (SAS) for maritime autonomous vehicles. His primary research interests include autonomous navigation, machine learning, fast computing data forecast.

Roberto Chiti was born in Italy in 1985. He earned a Master Degree in Naval Engineering in 2011 at University of Genoa. Currently he is employed at Fincantieri NexTech with the role of Project Leader for U212NFS submarines automation, for Italian Navy. His background and research interests refer to software control and dynamic simulation of ship propulsion systems, Dynamic Positioning System and Autopilot System.

However, despite advancements in CBM and predictive maintenance methodologies, significant challenges persist. One such challenge is the estimation of the Remaining Useful Life (RUL) of components, particularly in the absence of sufficient run-to-failure data (Zhang et al., 2021). Traditional approaches often rely on predefined models and assumptions, limiting their effectiveness in accurately predicting RUL. In this context, a data-driven approach becomes crucial, leveraging the available data to develop models that can adapt to the unique characteristics of maritime equipment.

The proposed methodology encompasses a comprehensive framework for predictive maintenance, including data acquisition, preprocessing, Health Index (HI) construction, and the prediction of remaining useful life (Xia et al., 2020). By adopting an unsupervised learning approach, the framework aims to overcome the limitations of traditional methodologies and provide more accurate and reliable predictions of equipment health and failure times (Liao et al., 2018).

In this context, the predictive maintenance (PdM) has emerged as a critical strategy in industrial sectors, aiming to enhance operational efficiency, minimize downtime, and reduce maintenance costs (Wu et al., 2020). In the domain of maritime equipment, particularly in the naval sector, the reliability and performance of devices are essential to ensure the completion of task without failures. Indeed, the adoption of advanced predictive maintenance methodologies becomes crucial.

This paper introduces a new approach focusing on unsupervised learning, leveraging Recurrent Neural Networks (RNNs), particularly short-term memory (LSTM), to address the challenges inherent in predictive maintenance of marine devices (Han et al., 2021). This approach advances beyond the supervised methods by offering a more flexible and adaptable solution for maritime applications where labelled failure data is often limited.

Conventional and most widespread predictive maintenance systems are based on statistical concepts, which often are based on linear models and predefined relationships between variables. The bottleneck of these approaches is their limitations to capture complex, non-linear interactions and hidden patterns within the multidimensional data typically generated by industrial equipment not well known at priori. For instance, traditional methods might struggle to detect interdependencies between multiple sensor readings that collectively indicate an impending failure, especially when these relationships change over time or under different operating conditions.

For such a reason, ML algorithms have proven to overcome this bottleneck by demonstrating the ability to capture complex correlations and patterns in the data, thus enabling more accurate predictions of equipment health and failure times (Zhao et al., 2023). The flexibility of ML models to adapt to evolving patterns in the data also makes them particularly well-suited for handling the dynamic nature of industrial processes and equipment behaviour.

This study seeks to augment current PdM practices by harnessing the power of ML, particularly by means of time series analysis for evaluating the health status of marine devices.

Furthermore, the effectiveness of the proposed approach is evaluated through real-world application to actual equipment failure data, enabling a direct comparison with traditional statistical methods.

A detailed description of the actual methodology is reported in section 2, while the potential development by means of LSTM is shown in section 3 and the results were discussed and shown in section 4. Eventually, the conclusion and recommendations are shown in Section 6 discussing the implications of what is shown for the field of predictive maintenance in maritime applications.

1.1. *Maritime scenario criticalities*

In the maritime domain, predicting potential failures holds critical importance for safeguarding both personnel and assets, as well as ensuring uninterrupted operational continuity (Lazakis et al., 2017).

Indeed, proactive failure prediction plays a pivotal role in ensuring the safety of crew members and passengers. By anticipating potential failures in critical systems such as propulsion engines can implement pre-emptive measures to mitigate risks of accidents at sea, thereby preventing potential loss of life and vessel operational capability (Ivankevich et al., 2019). Moreover, failure prediction methodologies are indispensable for preventing environmental catastrophes.

Maritime accidents, such as oil spills or collisions, can have devastating consequences on marine ecosystems (Duffey & Saull, 2009). From an operational point of view, predictive maintenance is essential to avoid costly downtime; in fact, unplanned equipment failures can result in significant financial losses for shipping companies due to interrupted operations and emergency repairs (Jimenez et al., 2020).

In addition, another key aspect is the reduction of operational capacity, which is very important for the military sector where the ship must guarantee the best performance even in adverse scenarios. By accurately predicting potential failures, operators can schedule maintenance activities during planned downtime, optimising operational efficiency and reducing financial burdens (Dalzochio et al., 2023). Furthermore, failure prediction methodologies contribute to enhancing operational efficiency by enabling proactive maintenance and replacement of components before they fail. This approach minimizes the likelihood of unexpected downtime and optimizes vessel uptime, allowing for smoother and more efficient maritime operations (Makridis et al., 2020).

Eventually, predicting potential failures in the maritime domain is essential for safeguarding lives and assets as well as optimizing operational efficiency. It represents a proactive approach to risk management that is critical for the sustainable and safe operation of maritime activities.

2. Statistical-based approach

Condition-based Maintenance (CBM) is an advanced maintenance strategy that monitors the actual condition of an asset based on data-driven logic. The actual condition of the asset is continuously monitored by on-line detection of significant working parameters. The aim of CBM system is supports maintenance personnel by providing indications of performance decay in certain indicators that could result in imminent failure.

Generally, the working principles is based on the comparison with average and base-line reference values in order to indicate that the equipment is deteriorating prematurely, thus increasing the probability of failure, or, conversely, that the equipment still has a good level of performance that may allow the maintenance personnel to assess whether to postpone a maintenance activity (Hart, 2011).

In addition to online monitoring, a predictive maintenance approach leverages historical data of equipment health indices to anticipate the need for preventive actions, enabling effective planning and optimal resource management in the medium and long term. Indeed, this makes it possible to anticipate when it will be necessary to intervene with preventive actions, allowing more effective planning and optimal management of resources (Tan et al., 2012). The analysis implements a similar approach to the Stochastic Process Control or SPC method used for the control and prediction of complex industrial processes in steady state (Hjartarson & Otal, 2006).

The analysis is based on periods of stationarity in the field data, discarding transient periods. In particular, the stationary flag is validated by means of stationary concepts such as the evaluation of kurtosis, skewness, and crest factor of the gathered sample data. If the evaluated statistical values are included within a certain threshold the sample is considered stationary and it is used for the condition-based monitoring task (Heywood & McGrail, 2015).

The approach is based on baseline maintenance that involves comparing the current performance of a piece of equipment to a known baseline performance. The baseline is established by measuring the performance of the equipment when it is in good condition and using this as a reference point for future performance analysis.

The goal of maintenance analysis based on baseline is to identify changes in equipment performance that may be indicative of potential failures or maintenance needs. By monitoring the performance of equipment over time and comparing it to the baseline, maintenance teams can identify deviations from normal performance and act before equipment failure occurs.

The system accesses the baselines of the various diagnostic parameters, the baseline of each diagnostic parameter "DP" ("Diagnostic Parameter") is defined in terms of an expected value "EV" ("Expected Value") and an expected range "ER" ("Expected Range", the standard deviation). Both values are expressed as a function of control parameter: primary parameter "PP" ("Primary Parameter").

Each DP diagnostic parameter is then associated with a dimensionless diagnostic index (DI), defined as:

$$DI = \frac{|AV - EV|}{ER} \tag{1}$$

where "AV" ("Actual Value") indicates the current value of the diagnostic parameter, understood as the average value over the sampling period T adopted for the diagnostic analysis.

The diagnostic index DI is therefore always positive and has a value of 0 when the current value of the diagnostic parameter coincides exactly with the expected value, while it takes on values greater than 1 when the current value of the parameter deviates from the expected value by more than the expected range of variation of the parameter itself.

Thus, values close to zero are interpreted as indicating a normal machine condition while values close to or greater than 1 are interpreted as an abnormal condition.

Detecting anomaly signals is an essential part of any maintenance predictive system. An anomaly signal is an indication that the performance of a piece of equipment is deviating from its expected or normal behaviour. It is important to note that anomaly detection is not a one-time activity, but rather an ongoing process.

Once the DI is known the trend analysis based on the DI time series could be performed. Significant divergence from this baseline indicates potential issues. For instance, an upward trend in vibration levels beyond the established threshold may signal mechanical wear or imbalance. Similarly, an increase in temperature readings might suggest overheating or lubrication failures. These deviations from normal behaviour, identified through trend analysis, enable maintenance personnel to proactively address emerging problems before they escalate into critical failures, ensuring sustained operational efficiency and reliability of the equipment (Mazidi et al., 2016).

Eventually, maintenance predictive systems should be continually monitored and adjusted based on new data and changing conditions to ensure that anomaly signals are detected in a timely and effective manner.

The proposed description of the statistics-based system is the workflow of the On-Condition Monitoring System (OCMS) developed by Fincantieri NexTech, Figure 1, one of the CBM tools available for industrial purposes, to summarize, the logical flow of information processing by the system, from the acquisition of field data at the lowest level to the trend analysis at the highest level, can therefore be described using the following diagram, to be interpreted with a bottom-up approach:
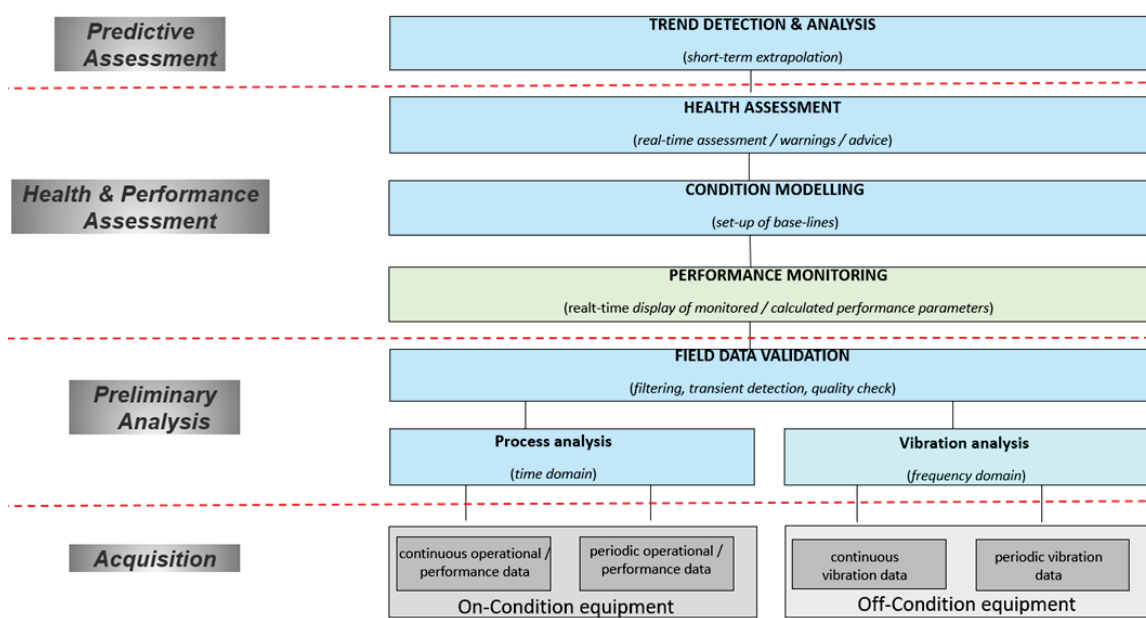
Figure 1. CBM system workflow

3. AI-based approach

In the realm of Artificial Intelligence (AI), the quest for efficient and robust anomaly detection methods remains pivotal, especially in the analysis of time series data across various industries, including finance, healthcare, and manufacturing (Pereira & Silveira, 2019). Various neural network architectures have been employed for time series analysis and anomaly detection. Convolutional Neural Networks (CNNs) excel at capturing spatial patterns, while Long Short-Term Memory (LSTM) networks are adept at modelling temporal dependencies. Autoencoders, another class of neural networks, provide a framework for unsupervised learning that can incorporate both these architectures.

This section shown the autoencoder technique, a sophisticated deep learning methodology, elucidating its role and effectiveness in identifying anomalies within time series datasets.

Autoencoders are particularly useful for anomaly detection due to their ability to learn compact representations of normal data. At their core, are a class of neural network models designed for unsupervised learning tasks. They learn to compress data (encoding) into a lower-dimensional representation and then reconstruct (decoding) the data back to its original form (Githinji & Maina, 2023). The intrinsic power of autoencoders lies in their ability to capture the most salient features of the data in the compressed representation. When applied to anomaly detection, this characteristic becomes particularly advantageous. By training exclusively on normal data, autoencoders develop a sense of 'normality' that is encapsulated in the lower-dimensional space. Anomalies, or deviations from this normality, are then detected based on the reconstruction error; a higher error indicates a data point that significantly diverges from the learned representation of normal data.

This section will further explore the intricacies of implementing autoencoders for anomaly detection in time series data, including the choice of architecture (e.g., LSTM autoencoders for handling temporal dependencies), the selection of appropriate loss functions, and the strategies for setting thresholds for anomaly detection. Practical considerations, such as handling variable-length sequences and ensuring model robustness, will also be addressed. Through this exploration, the autoencoder technique emerges not only as a powerful tool for anomaly detection but also as a testament to the versatility and adaptability of AI-based approaches in tackling complex data analysis challenges.

3.1. Data Preparation

The initial phase of proposed methodology focuses on the preparation of time series data for anomaly detection. This process encompasses fetching, preprocessing, normalizing, and structuring the data into a format suitable for ingestion by the LSTM-based autoencoder model.

3.1.1. Fetching and Initial Preprocessing:

The data is fetched from a designated database, comprising primary and secondary signals associated with specific equipment. In particular, the primary signal is the one that represent more the device behaviour. In detail, these signals represent two distinct features over the same time-period, essential for constructing a comprehensive view of the equipment's operational state. The fetched dataset spans a predefined interval, delimited by start and end dates, ensuring the relevance and timeliness of the data for anomaly detection tasks. The two features that represent the apparatus, one

representative of the load under which the systems are and the other the measure of vibration under analysis have been used.

Upon retrieval, the dataset undergoes initial preprocessing to ensure data integrity and usability. This step mitigates the influence of spurious data, enhancing the model's focus on meaningful patterns. In the train scenario it is crucial to choose a dataset representative of the good health of the apparatus under examination; this has been done because the model must learn how a good health scenario behaves to be capable, in the test phase, to recognize any anomaly by the increasing of the reconstruction error in magnitude.

Indeed, the model's ability to identify anomalies is based on deviations from the normal patterns it learned during training. This anomaly detection process does not require labelled data during the training phase but uses the learned representation of normal behaviour to flag deviations. Furthermore, the key difference between unsupervised and supervised approaches in this case lies in the use of the validation dataset. While the validation dataset is labelled, these labels are not used to train the model. Instead, the labels are only used to assess the model's performance in detecting anomalies.

Eventually, the chosen training dataset is concerning vibrational record of a bearing in the alternator apparatus of the couple "Diesel Engine – Alternator" related to the percentage of Electric Load output, for sake of clarity the data has been reported in dimensionless format.

Bearing vibration serves as a direct indicator of the mechanical health of the system, with increasing vibration often signalling developing faults or wear. However, vibration patterns can vary significantly under different operational conditions. This is where electrical load data become valuable.

The electric load data provides context for the operational state of the diesel engine-alternator couple. By correlating the bearing vibration with the electric load, the model can learn to distinguish between normal vibration changes due to varying load conditions and abnormal vibrations that may indicate a developing fault.

In Figure 2 was reported the entire dataset that has been used, the time series represent only the working day of devices, indeed, the entire dataset is composed of 95 day of recorder data.
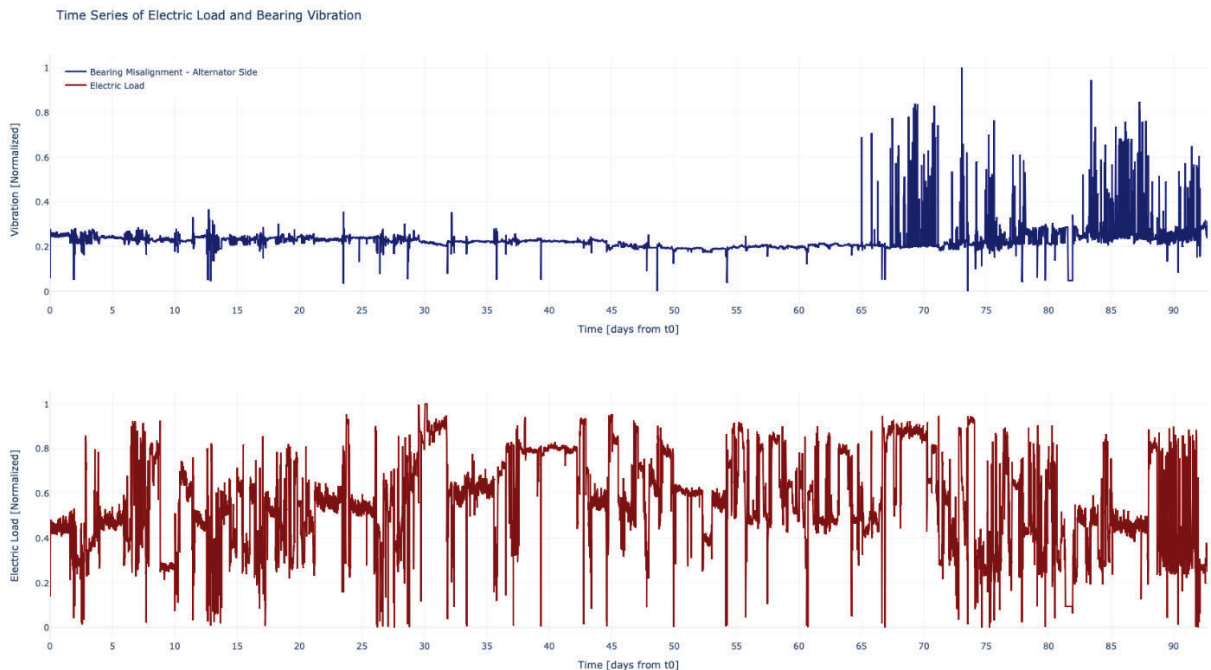
Figure 2. Bearing Vibration and Electric Load dataset.

The entire dataset was split into two parts, so that one part could be used for network training and the remainder for benchmarking. In particular, the division of the database was done knowing that the device broke down around the 95th working day the, by observing the timeseries data, the first fault symptoms started to appear around the 65th working day. The broke time was the only data available. Eventually, the time window used for the training dataset is between the beginning, the day zero, and the 46th day. The training dataset have been shown in Figure 3.
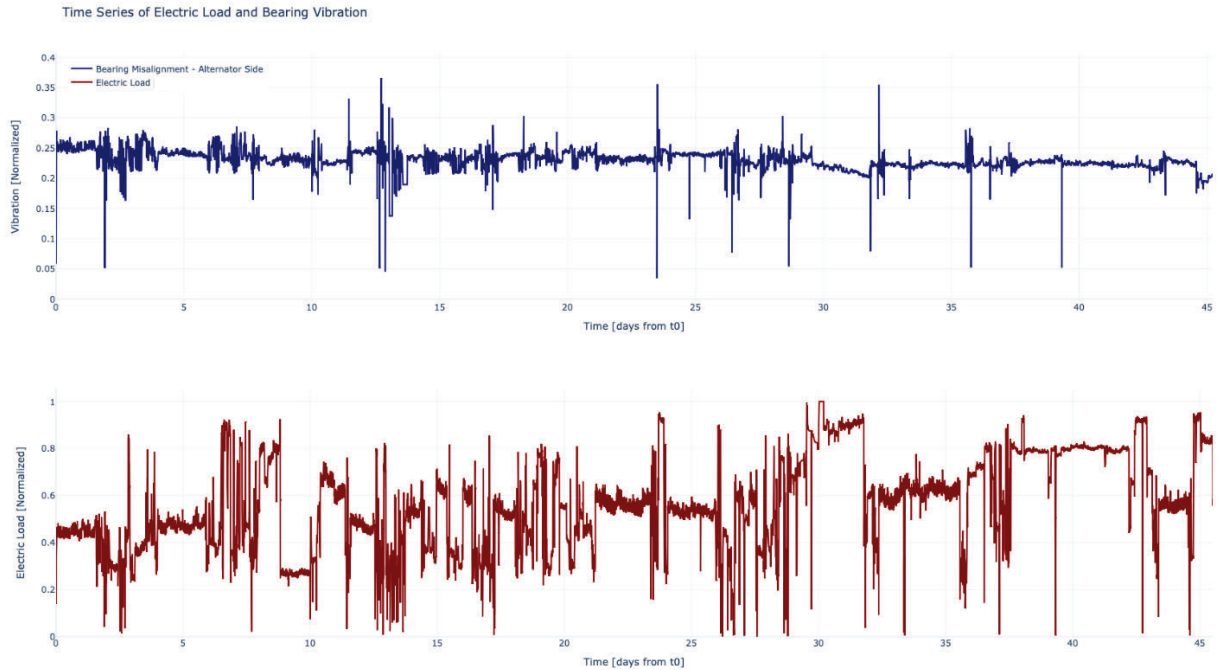
Figure 3. Bearing Vibration and Electric Load in good health status.

Those measurements represent the apparatus in a "good health" status, as no malfunctions were reported during this period. For such a reason this is have been used as data training set that will be fed to the autoencoder to learn how the bearing vibration behave in a good state of health. Instead, the benchmark is the data test represented in Figure 4 and it goes from 46th day and the day of failure, 95th day.
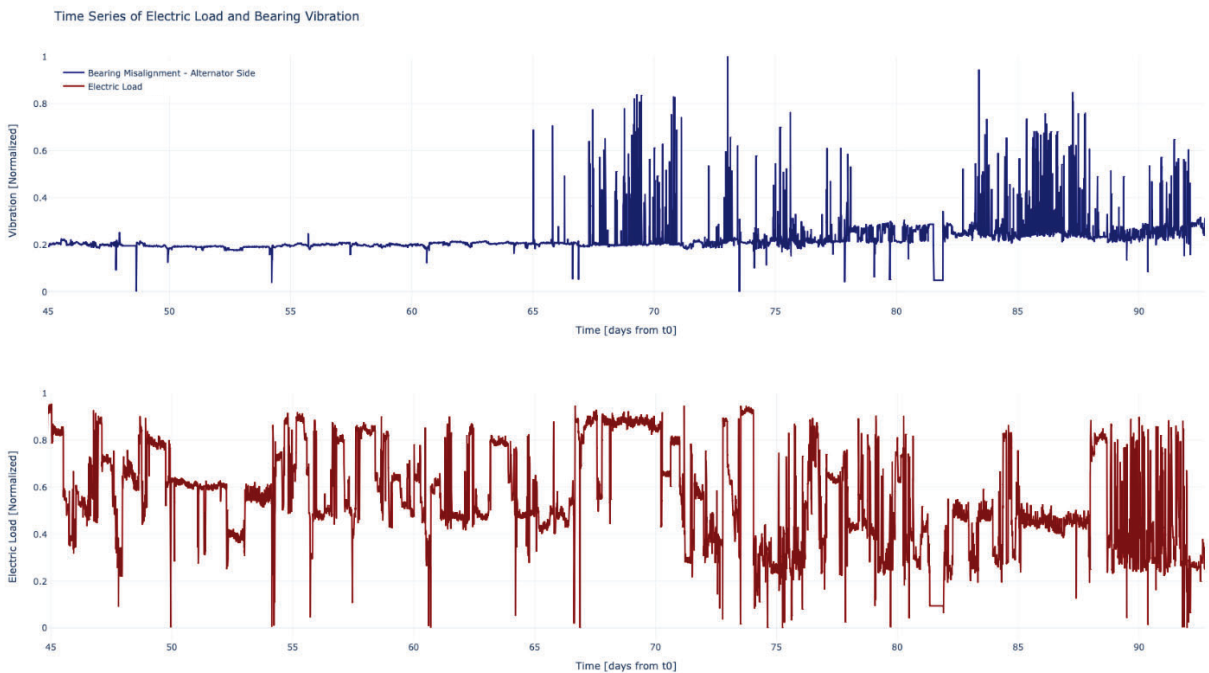
Figure 4. Bearing vibration and Electric Load anomaly.

It is notable the time representation of the anomaly as it is evolving in time; that the anomaly can be recognized, after approximately the 65th day, the bearing vibration begins to increase its peak activity (blue line).

3.1.2. Normalization

A critical component of data preparation involves scaling the features to a uniform range to transform each feature to the [0, 1] range. This normalization facilitates the model's learning by providing data in a consistent scale, crucial for the effective training of deep learning models.

3.1.3. Sequencing:

To accommodate the LSTM autoencoder's requirement for sequential data, the normalized data is structured into sequences. Each sequence, or "lookback" window, reflecting one day of data sampled at 5-minute intervals. This structuring into sequences allows the model to learn from the temporal dependencies within the data, a key aspect of its capability to detect anomalies. In this way the model must learn how the time relation subsists between all the shifted sequences.

3.2. Model Training

With the data prepared, the next phase involves training the LSTM-based autoencoder model. This training process is executed over a max of 2000 epochs with a batch size of 128, employing a validation split of 30% to monitor the model's performance on unseen data.

To enhance the model's learning efficiency and robustness, several strategies are employed:

- *ReduceLROnPlateau***:** This callback reduces the learning rate when a metric has stopped improving, enabling the model to fine-tune its weights more delicately as it approaches optimal performance.
- *ModelCheckpoint:* Ensures the preservation of the model that achieves the lowest validation loss, safeguarding the most effective version of the model for future anomaly detection tasks.
- *Early Stopping:* A custom callback checks for a stop condition after each epoch, allowing for dynamic termination of training based on specific criteria, ensuring resource efficiency, and preventing overfitting.

For reference, and to show the quality of the model, in Figure 5 the trend of the loss and validation loss represented as epochs increases has been shown.
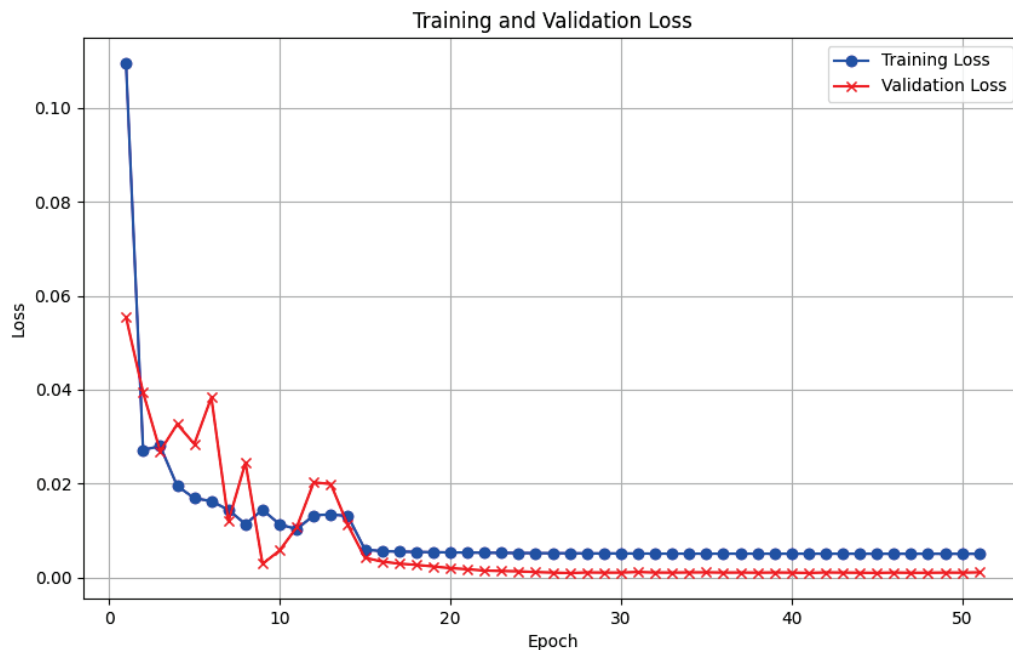
Figure 5. Train Loss and Validation Loss

It is possible to see, both training and validation loss decrease rapidly in the initial epochs, indicating that the model is learning effectively from the data. Moreover, the training loss (blue line with circle marker) continues to decrease steadily, showing the model's improving ability to reconstruct the training data. Indeed, the validation loss (red line with crossed marker) also decreases but starts to plateau earlier than the training loss. This is typical in deep learning models and suggests that the model is approaching its optimal performance on unseen data. The best performance, as indicated by the lowest validation loss, is achieved around the 30th epoch. This early convergence demonstrates the efficiency of our model architecture and training process. The early achievement of optimal performance (around the 30th epoch) highlights the effectiveness of training strategies, suggesting that further training may not yield significant improvements.
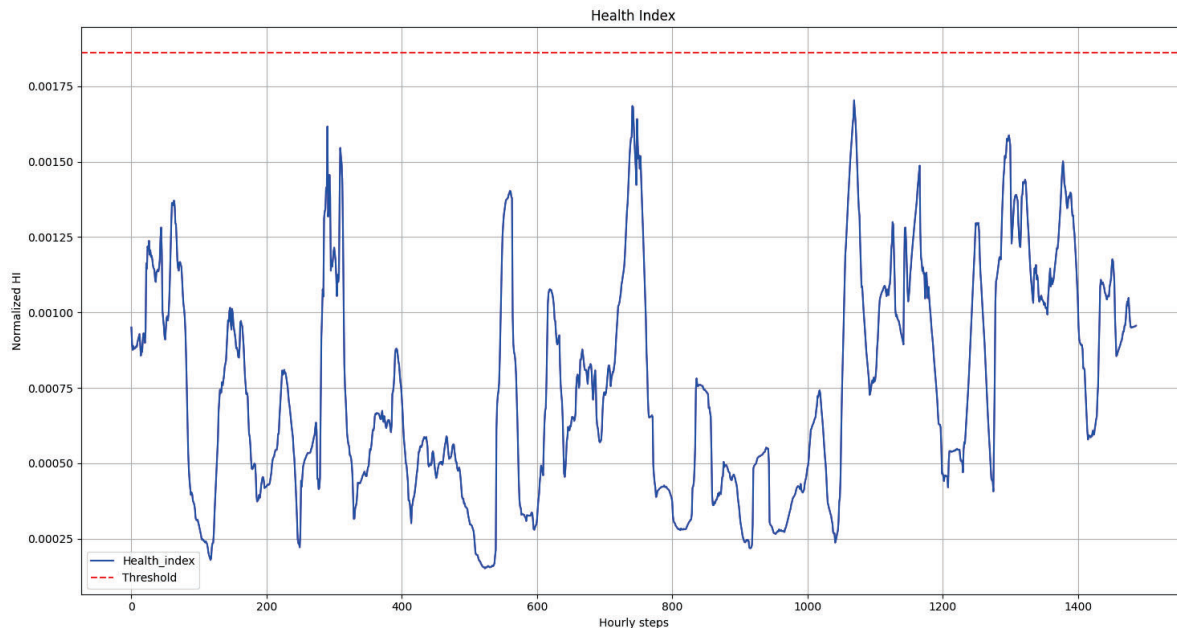
Figure 6. Health index of Trained Autoencoder

In Figure 6 the y-axis represents the Health Index, which is derived from the reconstruction error of the autoencoder. Lower values indicate better reconstruction, implying "healthier" or more normal behaviour of the system. While, the x-axis represents the time sequence of the training data, allowing us to visualize how the Health Index varies over time for known normal operating conditions. The red dashed line represents the anomaly threshold, set at the 99th percentile of the reconstruction errors observed in the training data. This threshold is crucial for distinguishing between normal operation and potential anomalies in future data. There are a few instances where the Health Index spikes above the general trend but remains below the threshold, these could represent natural variations in the system's behaviour that are still within normal operating parameters.

3.3. *Anomaly Threshold Determination*

The determination of an anomaly threshold is pivotal in distinguishing between normal and anomalous sequences. Following model training, the reconstruction error for each sequence is calculated by comparing the predicted output against the original input. This error reflects the model's ability to reconstruct the input data, with higher errors indicative of potential anomalies.

The threshold for classifying a sequence as anomalous is set at the 99th percentile of the reconstruction errors observed across the training dataset.

This threshold is chosen to identify the most significant deviations from the norm, capturing only the most pronounced anomalies. By focusing on these extreme discrepancies, the model effectively flags sequences that markedly diverge from the learned patterns of normal operational data, thus identifying potential issues or anomalies within the equipment's functioning.

4. Results; Identify an anomaly and the RUL line trend.

The proposed approach considers real-world application constraints. Indeed, for industrial applications, obtaining end-of-life (EOL) data is often challenging. This difficulty arises primarily because the complexity of an apparatus can varies significantly within the variables under observation. Consequently, the variables that must be monitored encompass a set of machinery that manufacturers typically do not provide with detailed EOL dynamic curves. Secondly, the aim is to develop a holistic approach applicable to every system without requiring a priori knowledge of threshold locations.

Moreover, as the system is used over time and more data are collected, thresholds can be adjusted based on empirical evidence.

Following these observations, Remaining Useful Life (RUL) analysis was initiated through examination of trend patterns in the data. The objective was to identify any trends or dynamic changes in the sequence under analysis, determining whether the system was entering a degradation regime or experiencing sudden, severe degradation. This analysis was conducted using linear interpolation of the Health Index (HI) over the last n days.

The purpose was to ascertain if anomalies could be detected before the HI effectively surpassed the established threshold, as shown in Figure 7. In particular, the figure shows the trend analysis assuming that the analysis was conducted the day before the first appearance of anomaly in the HI, i.e., the 64th day.

The RUL was interpolated for the last 11, 15, 19, and 21 days, and the intersection point of the trend line with the threshold was determined. Notably, each plot shows within the white box the number of days to reach the threshold value. Indeed, the mean RUL was assessed using these four RUL estimates. In this case, the estimated time to reach the danger zone is 212 days; this can be seen as a general indicator of the HI trend.

The first symptom of anomaly occurred on the 65th day when the magnitude of vibration became visible (Figure 4). Examining the four graphs individually as the observation period window varies, it becomes evident that shorter observation periods yield more sensitive but unstable forecasts. Conversely, longer windows produce more stable forecasts but are unable to capture sudden threshold exceedances. For this reason, as a first approximation, an average assessment of threshold exceedances was chosen.

On the 65th day, the system exhibited anomalous vibration magnitude, and the model detected this anomalous behaviour as the HI exceeded the HI threshold, as shown in Figure 8. A point of the HI crossed above the threshold, showing a value of 0.0041. Consequently, RUL interpolation showed a consistent drop in the time to intercept the threshold guard to 7.5 days, indicating that the system might be in a state of degrading performance.

Moving forward in time, the behaviour of the HI validates the advanced degradation state of the system. Figure 9 shows the prediction made at day 72, where the magnitude of the HI jumps to 0.07, with a clear upward trend indicating pronounced degradation in the apparatus's performance. Indeed, the prediction for the 11-day observation window is assessed as "already happened" for the intersection value between the HI threshold and the trend curve.

To obtain definitive confirmation of the apparatus's new degradation state, HI prediction was carried out until the end of the data, where the apparatus reached definitive failure on the 92nd day. This is represented in Figure 10, showing that the system remains above the threshold throughout the period until the apparatus's failure. It is worth emphasizing that once the threshold has been reached, the interpolation of the last days of the RUL loses its informative significance, as shown for the 11-day observation window.

In conclusion, this analysis demonstrates the effectiveness of the proposed approach in detecting and tracking system degradation over time. The method successfully identified the onset of anomalous behaviour and provided valuable insights into the progression of the system's health status, offering potential for early intervention and maintenance planning in industrial applications.

Figure 7 - RUL fitting for last 11, 15 19, 21 days at 64th day.
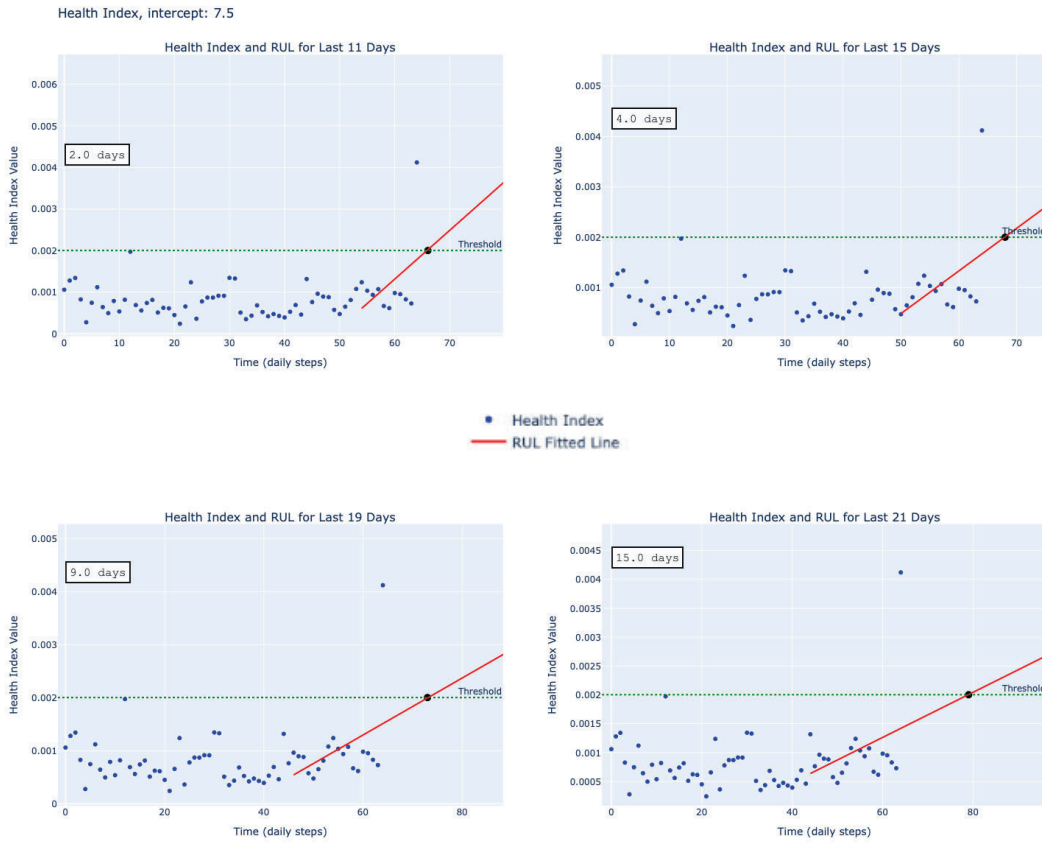
Figure 8 - RUL fitting for last 11, 15, 19, 21 days at 65th day
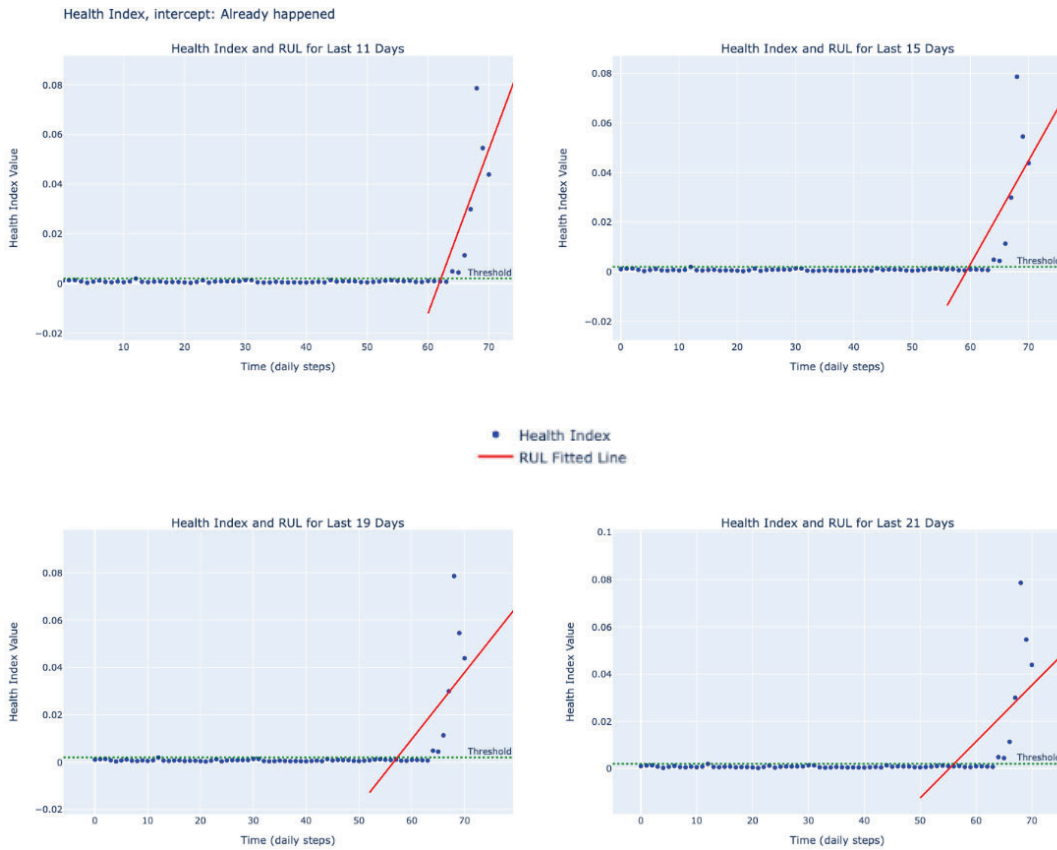
Figure 9 - RUL fitting for last 11, 15, 19, 21 days at 72nd day.
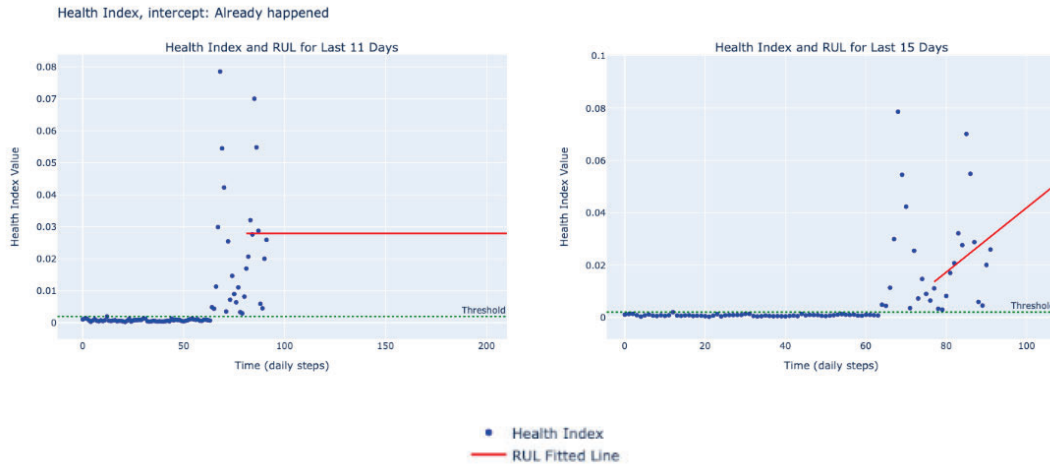
Figure 10 - RUL fitting for last 11, 15, 19, 21 days at near-end dataset.

5. Conclusions & developments

The research successfully implemented an LSTM-based autoencoder for anomaly detection in marine equipment sensor data. The model demonstrated the ability to identify developing faults in the bearing, as evidenced by changes in vibration patterns. The approach showed promise in handling data from different engine load profiles, suggesting potential adaptability to various operational conditions.

While not extensively discussed in this paper, preliminary observations suggest that the proposed method may offer improved fault tracking capabilities compared to traditional statistical approaches. However, a comprehensive comparative study will be carried out to quantify these potential advantages.

The results suggest that the proposed methodology has potential for enhancing predictive maintenance practices in maritime applications. By leveraging unsupervised learning techniques, this approach may be particularly valuable in scenarios where labelled failure data is scarce or unavailable.

However, it is important to note the limitations of this study. Detailed comparisons with conventional methods were not performed within the scope of this paper. Future work should focus on conducting comprehensive comparative studies with traditional statistical methods and other machine learning approaches to quantify potential improvements in predictive accuracy. Additionally, expanding the range of fault types and operational conditions tested would further validate the method's generalizability. Investigating the integration of this approach with existing maintenance systems in real-world maritime operations is also an important area for future research.

In conclusion, while this study demonstrates the feasibility and potential of the proposed unsupervised learning approach for marine equipment predictive maintenance, further research is needed to fully establish its comparative advantages and practical implementation challenges in real-world scenarios.

References

Coraddu, A., Oneto, L., Ghio, A., Savio, S., Figari, M., & Anguita, D. (2015). Machine learning for wear forecasting of naval assets for condition-based maintenance applications. 2015 International Conference on Electrical Systems for Aircraft, Railway, Ship Propulsion and Road Vehicles (ESARS), 1-5. https://doi.org/10.1109/ESARS.2015.7101499.

Dalzochio, J., Kunst, R., Barbosa, J., Neto, P., Pignaton, E., Caten, C., & Penha, A. (2023). Predictive Maintenance in the Military Domain: A Systematic Review of the Literature. ACM Computing Surveys, 55, 1 - 30. https://doi.org/10.1145/3586100.

Duffey, R., & Saull, J. (2009). Managing and Predicting Maritime and Off-shore Risk. TransNav: International Journal on Marine Navigation and Safety of Sea Transportation, 3, 589-596. https://doi.org/10.1201/9780203869345-112.

Githinji, S., & Maina, C. (2023). Anomaly Detection on Time Series Sensor Data Using Deep LSTM-Autoencoder. 2023 IEEE AFRICON, 1-6. https://doi.org/10.1109/AFRICON55910.2023.10293676.

Han, P., Ellefsen, A., Li, G., Æsøy, V., & Zhang, H. (2021). Fault Prognostics Using LSTM Networks: Application to Marine Diesel Engine. IEEE Sensors Journal, 21, 25986-25994. https://doi.org/10.1109/JSEN.2021.3119151.

Hart., P. (2011). Continuous asset monitoring on the smart grid. 2011 IEEE PES Innovative Smart Grid Technologies, 1-7. https://doi.org/10.1109/ISGT-ASIA.2011.6167132.

Heywood, R., & McGrail, T. (2015). Clarifying the link between data, diagnosis and Asset Health Indices. . https://doi.org/10.1049/CP.2015.1748.

Hjartarson, T., & Otal, S. (2006). Predicting Future Asset Condition Based on Current Health Index and Maintenance Level. ESMO 2006 - 2006 IEEE 11th International Conference on Transmission & Distribution Construction, Operation and Live-Line Maintenance, -. https://doi.org/10.1109/TDCLLM.2006.340747.

Ivankevich, A., Piterska, V., Shakhov, A., Shakhov, V., & Yarovenko, V. (2019). A Proactive Strategy of Ship Maintenance Operations. 2019 IEEE 14th International Conference on Computer Sciences and Information Technologies (CSIT), 3, 126-129. https://doi.org/10.1109/STC-CSIT.2019.8929741.

Jardine, A., Lin, D., & Banjevic, D. (2006). A review on machinery diagnostics and prognostics implementing condition-based maintenance. Mechanical Systems and Signal Processing, 20, 1483-1510. https://doi.org/10.1016/J.YMSSP.2005.09.012.

Jimenez, V., Bouhmala, N., & Gausdal, A. (2020). Developing a predictive maintenance model for vessel machinery. Journal of Ocean Engineering and Science, 5, 358-386. https://doi.org/10.1016/j.joes.2020.03.003.

Lazakis, I., Raptodimos, Y., & Varelas, T. (2017). Predicting ship machinery system condition through analytical reliability tools and artificial neural networks. Ocean Engineering, 152, 404-415. https://doi.org/10.1016/J.OCEANENG.2017.11.017.

Liao, Y., Zhang, L., & Liu, C. (2018). Uncertainty Prediction of Remaining Useful Life Using Long Short-Term Memory Network Based on Bootstrap Method. 2018 IEEE International Conference on Prognostics and Health Management (ICPHM), 1-8. https://doi.org/10.1109/ICPHM.2018.8448804.

Makridis, G., Kyriazis, D., & Plitsos, S. (2020). Predictive maintenance leveraging machine learning for time-series forecasting in the maritime industry. 2020 IEEE 23rd International Conference on Intelligent Transportation Systems (ITSC), 1-8. https://doi.org/10.1109/ITSC45102.2020.9294450.

Mazidi, P., Du, M., Tjernberg, L., & Bobi, M. (2016). A performance and maintenance evaluation framework for wind turbines. 2016 International Conference on Probabilistic Methods Applied to Power Systems (PMAPS), 1-8. https://doi.org/10.1109/PMAPS.2016.7763931.

Pereira, J., & Silveira, M. (2019). Learning Representations from Healthcare Time Series Data for Unsupervised Anomaly Detection. 2019 IEEE International Conference on Big Data and Smart Computing (BigComp), 1-7. https://doi.org/10.1109/BIGCOMP.2019.8679157.

Tan, A., Heng, A., & Mathew, J. (2012). Utilising Reliability and Condition Monitoring Data for Asset Health Prognosis. Science & Engineering Faculty, 89-103. https://doi.org/10.1007/978-1-4471-2924-0_4.

Wu, J., Hu, K., Cheng, Y., Zhu, H., Shao, X., & Wang, Y. (2020). Data-driven remaining useful life prediction via multiple sensor signals and deep long short-term memory neural network.. ISA transactions. https://doi.org/10.1016/j.isatra.2019.07.004.

Xia, M., Zheng, X., Imran, M., & Shoaib, M. (2020). Data-driven prognosis method using hybrid deep recurrent neural network. Appl. Soft Comput., 93, 106351. https://doi.org/10.1016/j.asoc.2020.106351.

Zhang, Z., Song, W., & Li, Q. (2021). Dual-Aspect Self-Attention Based on Transformer for Remaining Useful Life Prediction. IEEE Transactions on Instrumentation and Measurement, 71, 1-11. https://doi.org/10.1109/TIM.2022.3160561.

Zhao, K., Zhang, J., Chen, S., Wen, P., Ping, W., & Zhao, S. (2023). Remaining Useful Life Prediction Method Based on Convolutional Neural Network and Long Short-Term Memory Neural Network. 2023 Prognostics and Health Management Conference (PHM), 336-343. https://doi.org/10.1109/PHM58589.2023.00068.

Advancing Unmanned Surface Vessel Design: A Circular Economy Response to Global Conflict Evolution

D Brooks* BEng AMRINA, H Faria*[+] MEng AMRINA,

SubSea Craft, UK
[+]*Corresponding Author: Email: hfaria@subseacraft.com*

Synopsis

This paper explores the application of Circular Economy (CE) design principles to enhance the sustainability of Unmanned Surface Vessels (USVs) in the defence sector. It investigates the strategic benefits USVs can bring to maritime operations, particularly in conflict zones, due to their versatility. The integration of CE principles aims to improve sustainability, operational availability, and mission readiness by focusing on five key metrics: recyclability and repair, waste and emissions reduction, longevity optimisation, part count reduction, and design for disassembly.

Keywords: Circular Economy; Unmanned; Sustainability; Availability; Suitability

1. Introduction

The growing concern over global environmental issues is driving the implementation of a Circular Economy (CE) framework in the defence sector. Traditionally focused on operational and strategic goals, the sector now sees the potential of CE to help meet environmental targets and build supply chain resilience. This paper explores how the integration of CE principles within the design and operation of Unmanned Surface Vessels (USVs), can reduce resource consumption and enhance operational versatility.

USVs are crucial in current global maritime operations, they are capable of monitoring vast areas, gathering intelligence and tracking threats with no limitation on availability due to human welfare requirements. They are essential for tasks in conflict zones where there is a high risk to life, such as mine countermeasures, electronic warfare, and decoy purposes.

As the market shifts towards greater reliance on USVs, integrating CE principles becomes even more poignant. This analysis focuses on the environmental and economic benefits of adopting sustainable practices, particularly in hull construction, propulsion systems, and battery technologies. Through an examination of current practices and future possibilities, the paper aims to provide ideas for sustainable development in the defence sector.

2. Circular Economy

CE is an innovative economic framework that aims to transform the current global practices of creating, consuming, and disposing finite products. The objective instead is to create infinite solutions that generate economic, social, and environmental benefits.

The defence sector has already recognised CE has the potential to address environmental targets, the UK Ministry of Defence has stated in their Strategic Sustainability Action Plan to strive to build CE principles into defence designs by 2025 (MoD, 2021), through weighting acquisitions to products optimised to reduce emissions, largely to address the UK Defence's environmental target of net zero emissions by 2050. These targets are driven by the Paris Agreement, an international treaty adopted by the United Nations in 2015 to keep global temperatures rising more than 2°C between 1900 and 2100. Exceeding this limit would result in devastating economic and humanitarian impacts, including rising sea levels and extreme weather events. Predictions indicate that if the global temperature rises by 2.4°C by 2100, a 1.4 metre rise in sea levels would result in $460 billion in direct costs from land loss and forced migration, and up to 12% welfare losses in regions such as Southeast Asia (Pycroft, Abrell, & Ciscar, 2016).

While environmental impact has previously not been a driving factor for defence acquisitions, it is becoming an increasingly necessary consideration to ensure military operations and infrastructure are resilient to environmental disruptions. Introducing more sustainable initiatives in the defence market will also bring additional

Authors' Biography

Daisy Brooks is the Lead Naval Architect at Subsea Craft in Portsmouth, UK, working on the development of the diver delivery unit VICTA since 2022. Daisy has experience in the initial and concept design stages of surface and subsurface platforms having worked on defence design projects at both Steller Systems and QinetiQ. Daisy has a BEng in Mechanical Engineering and is working towards Chartered Status with RINA.

Henrique Faria is a Senior Naval Architect at Subsea Craft in Portsmouth, UK, working on the development of the diver delivery unit VICTA since 2020. During his time at Subsea Craft Henrique has been involved with the design and validation of surface and submerged crafts. Henrique holds a Meng in Ship Science with Naval Architecture from the University of Southampton.

advantages such as cost savings from reducing material waste, new revenue from circular product services, rapid technology innovation, increased collaboration with stakeholders, enhanced resource security, and the attraction of top talent that are environmentally conscious.

The impact sustainable changes in the defence sector could have, should not be underestimated, the US Department of Defence's CO2 emissions in 2017 was 1212 million tonnes, this is greater than the entire output of Sweden for the same year (Crawford, 2019). In 2023 the US Department of Defence accounted 80% of the federal government emissions and the defence sector in the UK accounts for 50% of government (Bowcott, Gatto, Hamilton, & Sullivan, 2021). Introductions of sustainability initiatives to address defence emissions could offer significant cost savings to the sector and environmental benefits globally.

The economic benefits of introducing sustainable initiatives in the defence sector have already been demonstrated. The Dutch Ministry of Defence used to incinerate uniforms costing the country €500,000 a year, in 2017 they collaborated with their uniform and equipment suppliers to repair and reuse uniforms and personal equipment, saving the Ministry approximately €8 million annually (Soufani, Tse, Esposito, & Kikiras, 2018).

3. The role of USV in current geopolitical conflicts

A study by the BlackRock Investment Institute detailed that three of the highest geopolitical risks globally are conflicts likely to involve significant marine operations: Russia's invasion of Ukraine affecting the Black Sea, US-China tensions impacting the South China Sea, and Gulf tensions involving the Strait of Hormuz (Donilon, Aldrich, & Lee, 2024).

The conflict between Russia and Ukraine at the Black Sea has shown a high increase on the use of USVs for reconnaissance and strike actions from both parties. Meanwhile, tensions in the Gulf have shifted to the crisis in the Red Sea, where in February 2024, three USVs prepared to be launched in a strike mission were detected and destroyed by US forces, indicating the need for heightened security measures to safeguard the Red Sea (U.S. Central Command, 2024). This presents an opportunity for US allied forces to deploy unmanned systems in the region for surveillance of international shipping lanes. Both conflicts in Ukraine and Red Sea are setting the scene for the use and development of USVs in the South China Sea for intelligence, surveillance, and strike operations near the disputed Spratley Islands. Future potential conflicts are driving the interest for Medium and Large USVs with greater payload capacity and endurance, this paper largely focusses on Small USVs that are most commonly used currently.

4. Current USV Market

As navies worldwide recognise the strategic advantages offered by USVs, driving requirements for their design and operations become well established. The pace for delivery of USVs must match the pace of the threats in the conflicts today, highlighting an important and well known requirement in the military world, modularity. A modular design approach delves into the functionality of the platform divided into specific, scalable, and reusable modules within a vessel. This design approach prioritises the development of common modules, akin to "Lego blocks", which constitute standardised sections of the craft. These modules can be seamlessly utilised across different mission profiles and adjusted in scale as required. Furthermore, the design facilitates quick installation of self-contained mission modules, enhancing flexibility and operational agility (Schank, et al., 2016). Modularity in USVs is currently focused on the types of payloads that can be carried and exchanged, including sensors, armament, and electronic warfare modules.USVs are also often required to operate at different sea conditions and mission profiles, demanding a, not only modular, but a robust craft that is also designed to operate covertly and strike when needed.

The Unmanned Systems Integrated Roadmap FY2011-2036 lists the main challenges that USVs face and, hence, the areas of which the US Department of Defence want to enhance in such vessels (Winnefeld, Jr. & Kendall, 2011). These are focused on the improvement of the autonomous systems within the craft, power and propulsion to achieve higher ranges, communication systems improvements and, more importantly for this paper, interoperability. Interoperability focuses on facilitating cross-domain service reuse through a centralised service repository, aiming to incorporate common interfaces, components, and systems from various platforms into USV production, with the goal of achieving a platform manufactured from 80% reusable components and systems.

The desire for interoperability improvement aligns with the proposed implementation of circular design principles to USV design. Such principles emphasise on creating platforms that prioritise ease of maintenance to enhance availability, facilitating quicker supply chain responses and suitability for different requirements. A CE approach will also promote sustainability on the manufacture, life cycle and operation of the USV.

5. Implementation of Circular Design Principles

When optimising USVs to reduce waste, performing Life Cycle Assessments (LCA) on existing and new designs is crucial for targeting sustainability initiatives to make impactful changes. AI can facilitate this, as demonstrated by Audi's use of AI to audit its supply chain, ensuring high environmental and ethical standards are met (Audi, 2019). The defence sector will faces challenges with using AI tools to perform LCAs as data security, integration with legacy systems, and regulatory compliance will likely prevent the effecitve use to generate detailed supply chain analysis.

An LCA of a typical maritime autonomous platform highlighted fuel consumption, hull construction and battery systems are the largest contributors to USVs environmental impact (Sanchez, Papaelias, Marini, Gjeci, & Marquez, 2021). The following CE principles will be considered in this section to reduce the environmental impact of the highlighted USV components; recyclability, waste reduction, longevity optimization, part count reduction, and design for disassembly (Charter, 2019).

5.1. Recyclability

The dominant material used to manufacture small USV hull forms is glass or carbon fibre. This is due to the low cost of glass fibre and the high strength to weight ratio of carbon fibre. However, recycling composite materials presents considerable challenges when compared to metals and plastics. The intricate structure of the composites makes the separation of matrix and fibre an arduous process (Shuaib & Mativenga, 2017).

Two techniques can be used for the recycling of composites, mechanical and thermo-chemical. The latter is split into fluidised bed processes, pyrolysis and solvolysis. Due to the low price of glass fibre and the degraded mechanical properties of the fibre when recycled through thermo-chemical processes, mechanical recycling is the most predominantly used method. Thermo-chemical processes are preferred for the recycling of carbon fibre composites, due to the high value of the material (Oliveux, Dandy, & Leeke, 2015). The energy consumption estimations of each of these processes can be seen in

Table 1.

Table 1 – Energy consumption estimations for each composite recycling process. The values are in range, as these vary depending on the speed that he machines operate (Wong, Rudd, Pickering, & Liu, 2017)

Recycling Process	Energy Consumption (MJ/kg)
Mechanical reduction	0.3 – 2
Fluidised bed process	6 - 40
Pyrolysis	30
Solvolysis	63 - 91

While mechanical reduction significantly reduces energy consumption, it fails to effectively separate fibre from resin, leading to material property degradation. Consequently, concerns regarding performance limitations restrict the market for the resulting material. On the other hand, pyrolysis and solvolysis are available for commercial exploitation and both techniques can output high quality recycled carbon fibres (Oliveux, Dandy, & Leeke, 2015) at the price of a high energy consumption.

Since the recycling of glass and carbon fibre structures is proven to be energy intensive to retrieve materials of sufficient quality for remanufacture, other options should be considered such as thermoplastic polymers commonly used to produce small crafts. High-density polyethylene (HDPE), which offers a simpler and less harmful solution to its recycling process and presents itself as a viable option for small USVs to fit within the UK Defence target of net zero emissions. HDPE recycling involves processes to reclaim and prepare the material for its reuse. It is then shredded to increase its surface area, helping the melting and extrusion of the material into pellets. The pellets can be sold for reuse in the manufacturing of new HDPE materials such as sheets and 3D printing filament. The simple recycling process reflects on its total energy consumption of only 1.6MJ/kg (Bataineh, 2020). In addition, recycled HDPE's mechanical properties remain similar (Chong, et al., 2017). Recycling HDPE into sheets preserves its integrity, and while 3D printing with recycled HDPE has been validated, minor issues may arise primarily from the printing technique rather than the material properties.

When assessing the recyclability of USVs, it is essential to consider not only the hull material but also the installed components, with batteries being a key component, required for providing hotel power and in some cases propulsion as well.

High density lithium ion batteries are the most common type of battery supplied to the defence sector, which contain cobalt, one of the EU's top 15 critical materials. Over 70% of the global cobalt supply comes from the Democratic Republic of Congo and 70% of the lithium ion battery market is manufactured in China. This concentration in the supply presents risks such as exclusive trade agreements and strategic supply constraints.

Additionally, the lithium ion battery demand is set to surge as electrical vehicles popularise, forecasts estimate demand shall exceed supply by 2030 (Bille, 2024). Investing in recycling could protect the national supply, but lithium-ion battery recycling is intricate, involving complex separation processes and handling of flammable electrolytes and reactive metals. Current recycling methods, hydrometallurgy and pyrometallurgy, use chemical and thermal treatments to recover batteries, which are energy intensive and rely on the use of additional raw materials, which isn't sustainable. Direct recycling is a simpler method where the cathode is extracted from the battery with minimal disassembly, re-energised with lithium, then reintroduced to the battery.

Studies suggest direct recycled cathodes can match the performance of new ones (Xu, et al., 2020) and the method is cost effective when recycling over 3000 tonnes annually (Lander, et al., 2021). As resources dwindle and battery designs evolve for easier disassembly, direct recycling is expected to become more profitable. Direct recycling emits 25% fewer greenhouse gases than pyrometallurgical and hydrometallurgical methods and producing a direct recycled cathode releases about half the greenhouse gases as producing a new cathode (Xu, et al., 2020). This data highlights the potential new battery recycling technology has to create a sustainable and economically viable endless battery supply for defence. Establishing a closed loop supply of batteries within country could enhance national security by ensuring a reliable source of essential equipment for USVs. Given the strategic importance of electrifying USV propulsion systems to achieve low acoustic signatures for critical missions, ensuring a steady supply of batteries is paramount. Closed loop battery recycling aligns with environmental sustainability goals set by multiple governments, which is increasingly prioritised in defence strategies. By minimising waste generation and reducing the carbon footprint associated with battery production, investing in direct recycling supports sustainability efforts while enhancing operational resilience.

HDPE recycling generates broader advantages by decreasing lead times and improving operational availability. Battery recycling technology has great potential to enhance national security; however, further research and development is required to enhance direct recycling profitability.

5.2. Minimise Waste and Emissions

When opting for HDPE for a USV hull, it is essential to consider its manufacturing advantages, especially regarding the potential utilisation of 3D printing technology. In the domain of small-scale 3D printing, addressing the recognised issues of shrinkage and adhesion inherent in the Fused Filament Fabrication (FFF) of HDPE, requires precise actions. This includes selecting suitable build plate materials and fine-tuning FFF printing parameters to mitigate void formation and counteract shrinkage caused by material crystallisation..

Adjusting these parameters, Schirmeister demonstrated the ability to 3D print a HDPE component with equivalent mechanical properties to injection-moulded HDPE, while minimising warping and void formation (Schirmeister, Hees, Licht, & Mulhaupt, 2019). This success holds promise for scaling up HDPE 3D printing and, potentially enabling the production of large HDPE components without the current challenges. It can then leverage the advantages of additive manufacturing over injection moulding for low-volume productions, particularly where lower initial costs and the flexibility for design changes are appealing for small unmanned vessels.

When compared with traditional lamination methods, 3D printing presents distinct advantages. Lamination techniques typically incur an estimated 25% waste of the total build, including fibre offcuts, resin waste, composite parts waste, vacuum bagging materials, and miscellaneous tools. A percentage of such waste can be recycled, but the remaining is discarded to landfill (Shuaib & Mativenga, 2017). With 3D printing, a contingency of 10% of the total filament material is allocated for initial setup mistakes and is fully recyclable and reusable. Large scale 3D printer companies process the waste back into usable HDPE and either feed back to their machines or sell it to other companies. This makes 3D printing attractive not only on the sustainability side but also for businesses to have minimal losses on production costs related to material wastage and reduced production and lead times.

Although waste in production is an important factor, typically, vessel usage contributes to 90% of a vessel's life cycle emissions, assuming a service life of approximately 20 years (Shuo Chen & Lam, 2022), (Burman, Kuttenkeuler, Stenius, Garme, & Rosen, 2016). This figure highlights the importance of fuel savings for economic and environmental reasons, optimising the propulsion system for specific operational profiles can help address this.

To facilitate propulsion modularity and adaptability across various mission profiles, outboard engines stand out as the optimal choice for small USVs. While these engines are typically fuelled by petrol, a limited selection are available for diesel use. By employing an interchangeable outboard approach, leveraging standardised fittings inherent to such engines, and incorporating an interface plate on the craft's transom, the USV's propulsion system can be easily assembled or disassembled with different outboard motors to suit the required mission profile. For instance, high-speed missions may necessitate a diesel-powered outboard to be fitted to the vessel, then easily exchanged for an electric alternative for low-speed, low acoustic operations, minimising propulsion system emissions. Although electric propulsion enhances platform sustainability by emitting zero emissions during operation, it introduces weight compromises due to battery requirements for power storage.

Outboard manufacturers are seeking to improve the efficiency of their engines and, subsequently, reducing the emissions of such modules. OXE Marine developed a Diesel-Electric Hybrid outboard engine, with a combination of a 300Hp diesel module attached with a 150Hp axial flux electric motor (OXE Marine, 2024). A diesel-electric outboard would enable the operator to widen the mission profile to include high speed transits and low speed covert movements, without a large impact on the equipment footprint inside the vessel. Looking at future options, Yamaha is releasing its first prototype of an outboard hydrogen engine, offering 425-450hp (Weiss, 2024), helping to reduce emissions from fuel cell manufacture and craft operation, whilst still maintaining high power outputs.

Reducing waste in platform production via additive manufacturing not only establishes a sustainable framework but also, coupled with outboard modularity, enhances the platform's suitability and flexibility for various missions.

5.3. Longevity and Repair

An important contributor to the longevity of a marine platform is the material and structural design of the craft. Hulls constructed from HDPE exhibit high strength and resistance to impact, offering protection against damage during slamming accelerations and collisions (Telak, Telak, & Niemczewski, 2023).

However, if a HDPE hull is damaged, its low melting temperature and robustness makes it ideal for conducting repairs on. Techniques like rotational welding, hot gas welding, and fusion welding can fix both small and large areas of damage. Sentinel, an Australian defence vessel manufacturer, already use rotational welding techniques to repair HDPE boats (Sentinel, 2024). These simple repair methodologies enable vessels to be quickly fixed and returned to operations, even when faced with limited resources in low infrastructure military environments.

The modular design of a USV can help facilitate prolong the usage of a vessel, by providing good access and utilising quick release fasteners, individual components and systems can be easily removed from vessels, enabling quick off craft repairs, expediting the restoration of vessels to operational status for missions.

Repairing components rather replacing them offers environmental benefits addressing defence sustainability targets. There are many electrical devices fitted on USVs such as motors, batteries, sonars, and lights which all have have high Green House Gas (GHG) embodiment levels, repairs of these items can extend product life, providing an opportunity to make substantial emission savings.

For example, a laptop with a life expectancy of 5 years has an embodiment carbon footprint of 304kgCO2, repairs that keep the laptop going beyond this life expectancy will prevent 60kgCO2 of emissions being released per year, minus any emissions associated with repairs, which for laptops is approixmately 5.9kgCO2 per repair (Privett, 2018).

Ensuring spare parts are accessible and technical support can be provided either physically or virtually, electrical device repairs can be conducted in the field, removing the need to wait on replacement devices to restore vessel funcitionality.

5.4. Decrease Part Count

To maximise the chance of mission success hull shapes should be optimised to the specific mission requirements which may include sea conditions, range, and speed. A novel approach to supplying USVs most suitable for their application is to set up a vessel supply service, a leasing scheme that would enable allied defence customers to share tailored assets, aligning with CE principles and defence strategies, of reducing resource consumption and emissions. Similar agreements like the Australia, United Kingdom, United States agreement (AUKUS) (Lejac & Rexha, 2022) demonstrate that the appetite for sharing capability internationally is growing and plausible to be implemented.

This service could provide a limited range of vessels designed for specific speeds, that could be supplied at varying readiness levels from bare boat to mission-ready platforms. The configuration options offered would use scalable standardised components and multipurpose parts, like multifunctional sensors would be implemented to reduce part count. Minimising component variation and count simplifies the supply chain, optimising procurement times and maintenance training, all helping optimise platform availability.

Operating within a restricted product range allows businesses to concentrate on minimising their environmental impact and enhancing manufacturing efficiency. As part of their service offerings, SMEs could provide fleet management solutions, creating opportunities for recurring revenue while simplifying vessel management for customers. This includes optimising vessel conditions through services like remote monitoring, diagnostics, and maintenance scheduling.

5.5. Design for Disassembly

For USVs to keep technically current and available, the ease to replace equipment is imperative. By having flexibility to change equipment, vessels can fit the most up to date technology and can easily adapt to a requirement changes from the end user. Such modularity and flexibility can be achieved through the implementation of a modular deck within the USV. The design of the deck in HDPE can be compared to a printed circuit board (PCB) design. Similar to a PCB, which functions based on the arrangement and interconnection of its components, the components within the modular deck design can be rearranged, swapped, or removed to alter the functionality of the deck as needed. Following a similar philosophy, the components within the modular deck design would be attached through the use of brackets, screws and heat-set threaded inserts. The process of attaching such inserts to the deck involves heating the insert and pressing it into a predrilled hole in the deck. The heat from the insert causes the HDPE to melt as it is pressed in place, once the plastic cools, it securely fixes insert in situ (Warren, 2021).

The USV deck would be structured in a grid pattern with inserts placed every 100mm, bespoke brackets would be made with the same pitch diameter to accommodate the fitting of modules within the vessel, allowing for easy reconfiguration. Figure 1 illustrates different arrangements plausible for the proposed modular deck design. Heat-set threaded inserts can also be utilised on the superstructure of the craft to fit equipment as desired.

The opportunity to quickly repurpose the entirety of the craft modules between roles and potentially users, improves the availability of the USV fleet and its suitability to different mission profiles. By enabling rapid adjustments to accommodate changing mission objectives or emerging operational needs, USVs can remain highly responsive and effective in dynamic environments. Furthermore, the ability to repurpose the craft without extensive upgrades or reconfigurations not only streamlines operational processes but also minimises downtime, ensuring that the USV fleet maintains a high level of readiness and operational capability at all times. This versatility ultimately enhances the overall effectiveness and value proposition of the proposed USV.
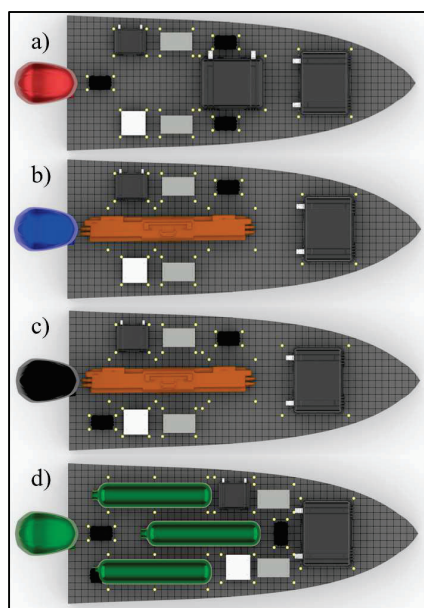
Figure 1 – Modular deck design representation. Highlighted points show which inserts would be used to accommodate decks for components in different USV's arrangements: a) Diesel version; b) Electric version; c) Diesel-electric version; d) Hydrogen version. Note: For the diesel and diesel-electric versions, the fuel tank is situated under the modular deck.

6. Conclusion

This paper highlights the importance of integrating CE principles into the design and production of USVs for the defence sector. By adopting CE principles, such as recyclability, waste minimisation, and design for disassembly, USVs can be more reliably supplied, cost-effective, less wasteful and adaptable to varying mission profiles. The focus on the recyclability of hull materials and components, along with the minimisation of waste and emissions during manufacturing and operation, contributes to environmental sustainability and national security. Additionally, the emphasis on modularity, longevity, and repairability enhances operational readiness and availability, crucial for addressing emerging threats and geopolitical tensions. Overall, the implementation of

CE principles offers a strategic advantage by optimising resource utilisation, reducing reliance on critical materials, whilst encouraging innovation and collaboration across the defence industry.

References

Audi. (2019, August 8th). *Supply chain monitoring: Audi uses artificial intelligence (AI) for sustainability.* MediaInfo, Audi. Retrieved from https://www.audi-mediacenter.com/en/press-releases/supply-chain-monitoringaudi-uses-artificial-intelligence-ai-for-sustainability-14037

Bataineh, K. M. (2020). Life-Cycle Assessment of Recycling Postconsumer High-Density Polyethylene and Polyethylene Terephthalate. *Advances in Civil Engineering*(Article ID 8905431).

Bille, B. (2024). *Increasing Lithium Ion Supply Security for Europe's Growing Batteru Industry: Recommnedations for a Secure Supply Chain.* The Hague: The Hague Centre for Strategic Studies.

Bowcott, H., Gatto, G., Hamilton, A., & Sullivan, E. (2021). *Decarbonizing defense: Imperative and Opportunity.* McKinsey and Company.

Burman, M., Kuttenkeuler, J., Stenius, I., Garme, K., & Rosen, A. (2016). Comparative Life Cycle Assessment of the hull of a high-speed craft. *Journal of Engineering for the Maritime Environment: Part M, 230*(2), 378 - 387.

Charter, M. (2019). Designing for the Circular Economy. In M. Charter, *Circular Economy innovation and design: setting the scene* (pp. 23-34). Routledge.

Chong, S., Pan, G.-T., Khalid, M., Yang, T. C., Hung, S.-T., & Huang, C.-M. (2017). Physical Characterization and Pre-assessment of Recycled High-Density Polyethylene as 3D Printing Material. *J Polym Environ, 25*(1), 136-145.

Crawford, N. C. (2019). *Pentagon Fuel Use, Climate Change and the Costs of War.* Boston: Boston University.

Donilon, T., Aldrich, J., & Lee, S. (2024). *Geopolitical risk dashboard.* U.S.A: BlackRock Investment Institute.

Gaustad, G., Krystofik, M., Bustamante, M., & Badami, K. (2018). Circular economy strategies for mitigating critical material supply issues. *Resources, Conservation & Recycling*(135), 24 -33.

Lander, L., Cleaver, T., Ali Rajaeifar, M., Kendrick, E., Edge, J. S., & Offer, G. (2021). Financial viability of electric vehicle lithium-ion battery recycling. *iScience, 24*(7).

Lee, N., & Clarke, S. (2019). Do low-skilled workers gain from high-tech employment growth? High technology multipliers, emplyoment and wages in Britian. *Research Policy, 48*.

Lejac, M., & Rexha, D. (2022). The AUKUS International Legal Agreement and its Impact on International Institutions and Security. *Corporate Governance and Organizational Behaviour Review, 6*(2).

Ministry of Defence. (2022). *The Defence Capability Framework.* UK Ministry of Defence.

MoD, U. (2021). *Climate Change and Sustainability Strategy, ADR009788, Version 1.* Creative Media Design.

National Ship Building Office. (2022). *National Ship Building Strategy.* City of London: London Open Government Licence.

Oliveux, G., Dandy, L. O., & Leeke, G. A. (2015). Current status of recycling of fibre reinforced polymers: Review of technologies, reuse and resulting properties. *Progress in Materials Science, 72*, 61-99.

OXE Marine. (2024). *OXE Hybrid 450.* Retrieved May 4, 2024, from https://www.oxemarine.com/outboards/oxe-diesel-outboards/oxe-hybrid-450/

Privett, S. (2018). *Potential impact of UK Repair Cafés on the mitigation of greenhouse gas emissions.* Guildford: Centre for Environment and Sustainability Faculty of Engineering and Physical Sciences University of Surrey.

Pycroft, J., Abrell, J., & Ciscar, J.-C. (2016). The Global Impacts of Extreme Sea-Level Rise: AComprehensive Economic Assessment. *Environ Resource Econ*, 225–253.

Sanchez, P. J., Papaelias, M., Marini, S., Gjeci, N., & Marquez, F. (2021). Life Cycle Assessment in Autonomous Marine Vehicles. *Lecture Notes in Data Engineering, Communications, and Technology, Volume 79*, 222-233.

Schank, J. F., Savitz, S., Munson, K., Perkinson, B., McGee, J., & Sollinger, J. M. (2016). *Designing Adaptable Ships: Modularity and Flexibility in Future Ship Designs.* RAND National Defense Research Institute.

Schirmeister, C. G., Hees, T., Licht, E. H., & Mulhaupt, R. (2019). 3D printing of high density polyethylene by fused filament fabrication. *Additive Manufacturing, 28*, 152-159.

Sentinel. (2024). *Sentinel Boats*. Retrieved May 2024, from www.sentinelboats.au

Shuaib, N. A., & Mativenga, P. T. (2017). Carbon Footprint Analysis of Fibre Reinforced Composite Recycling Processes. *International Conference on Sustainable Materials Processing and Manufacturing, 7*, 183-190.

Shuo Chen, Z., & Lam, J. (2022). Life cycle assessment of diesel and hydrogen power systems. *Transportation Research*(103), Part D.

Soufani, K., Tse, T., Esposito, M., & Kikiras, P. (2018). A roadmap to circular economy in EU defence inspired by the case of the Dutch Ministry of Defence. *The European Financial Review*.

Telak, O., Telak, J., & Niemczewski, T. (2023). Motor Boats in the Technology of HDPE with RIB Type Construction. *SFT, 61*(1), 166-178.

U.S. Central Command. (2024, February 26). *Feb. 26 Red Sea Update Press Release*. Retrieved from U.S. Central Command: https://www.centcom.mil/MEDIA/PRESS-RELEASES/Press-Release-View/Article/3687554/feb-26-red-sea-update/

US Army. (2023). *Army Climate Strategy Implementation Plan 2023 - 2027.*

Veal, R. (2023). *Janes Unmanned Maritime Vessels* (2023-2024 ed.). Janes.

Warren, M. (2021). *Installation Press for Heat Set Inserts.* University of Mississippi.

Weiss, C. (2024, February 14). *New Atlast: Yamaha's world-first hydrogen outboard unveiled on prototype boat.* Retrieved May 4, 2024, from https://newatlas.com/marine/yamahas-hydrogen-outboard-boat-prototype/

Winnefeld, Jr., J. A., & Kendall, F. (2011). *The Unmanned Systems Integrated Roadmap FY 2011-2036.* United States of America Department of Defense.

Wong, K., Rudd, C., Pickering, S., & Liu, X. (2017). Composites recycling solutions for the aviation industry. *Sci China Tech Sci, 60*, 1291-1300.

Xu, et al. (2020). Efficient Direct Recycling of Lithium-Ion Battery Cathodes by Targeted Healing. *Joule, 4*(12).

Hybrid Turbocharging for Alternatively Fueled Internal Combustion Engines in Naval Applications

Ir. J Vollbrandt[a,b*], Dr. A Coraddu, MSc, CEng, MIMarEST[a], Dr. ir. R D Geertsma, CEng, FIMarEST[a,b]

[a]Delft University of Technology, The Netherlands; [b]Netherlands Defence Academy, The Netherlands

*Corresponding author. Email: j.vollbrandt@tudelft.nl

Synopsis

The global shipping industry is at a crucial juncture, facing an urgent need to reduce greenhouse gas emissions in the short to medium term to mitigate climate change. A shift towards alternative fuels is imminent, necessitated by the limitations in current fuel cell and battery technology in terms of power density. Addressing this, navies worldwide are not only exploring the use of alternative fuels to diminish environmental impact but also seeking solutions to reduce emissions signatures and decrease reliance on fossil fuels. In this paper, we investigate the use of hybrid turbocharging to improve the dynamic performance of alternatively fueled combustion engines. We extended an existing and validated Mean Value First Principle (MVFP) engine model of a spark-ignited (SI) throttle-controlled Caterpillar 3508*A* gas engine with a hybrid turbocharger. The study investigates the impact of electrical power Power-Take-In/Off from the turbocharger shaft on the engine's air path dynamics for different use cases, considering transient and steady state phases. We demonstrate that a generator set can benefit from hybrid turbocharger by significantly reducing the engine speed drop and settling time after a load step. While accelerating from 0 to cruise speed, propulsion engines benefit less from hybrid turbocharger, due to risk of compressor surge during low engine speeds. The overall results show that simply adding electric power to the turbocharger shaft during transient phases does not unlock the full potential of hybrid turbocharging for alternatively fueled combustion engines. The implementation of hybrid turbocharging requires careful integration, reconsideration of sizing and matching of turbine and compressor, and the combination with blow-off, blow-by, and waste gate valves to prevent compressor surge. However, the capability for electrical power take-off/in within a larger propulsion and electrical power generation plant context suggests a reduction in spinning reserves and an increase in overall system efficiency during steady state. Thus, implementing hybrid turbocharging can play an important role in the transition to alternative fuels and the reduction of greenhouse gas emissions.

Keywords: Modeling and simulation; Mean value first principle model; Transient performance; Alternative fuels; Hybrid Turbocharging

1 Introduction

Current fuel-cell and battery technology cannot provide sufficient energy and power density for naval vessels in the short and medium term [38, 29, 32]. Therefore, navies worldwide investigate the use of alternative fuels in combustion engines to reduce greenhouse gas emissions, reduce signatures, and lessen their reliance on fossil fuels. While gas turbines are still considered for providing boost power to naval combatants due to its high power density, the majority of naval vessels rely on fuel-efficient turbocharged diesel engines to sail at cruise speed [9, 12, 57, 49]. Alternative fuels that can replace F76 in these conventional propulsion systems are consequently favoured.

Since its introduction more than a century ago, turbocharging is probably the most important driver of increasing fuel efficiency and power density of the diesel engine [56, 27]. The majority of modern marine four stroke engines adopt a single-stage charging concept due to its reliability and cost-efficiency. In these engines, the turbocharger delivers maximum charge pressure close to the point of nominal power for the highest power output and engine efficiency. However, in part-load operation of the engine, the turbocharger cannot maintain the maximum charge air pressure due to the reduced exhaust mass and energy flow. Consequently, the maximum engine torque and efficiency decrease accordingly [27, 4]. Various charging concepts, such as sequential and 2-stage turbocharging, have been developed to cope with deteriorating part-load performance [26, 28, 45, 34, 36], varying in complexity, maintainability, costs, and dynamic performance. However, so far, these concepts have only been adopted in niche applications, such as naval vessels, fast ferries and yachts [25, 60, 59, 5]. An alternative method of improving part load performance of single-staged turbocharged marine diesel engines is by

implementing hybrid turbocharging [58, 39]. Hybrid turbocharging has been researched extensively for automotive applications [30, 14, 43, 19] and is also referred to as e-turbocharging, next to possible configurations of electrical turbo-compounding and e-boosting [23, 31, 1]. E-turbocharging and electrical turbo-compounding have been applied first in high-performance engines, for example, in F1 racing [51, 6, 44], but can be found in road-going automotive engines by now [24, 17, 50]. Diesel engines for heavy-duty road transport have been developed with mechanical turbo-compounding [37, 55], but e-turbocharging will likely make its introduction in the next generation of heavy-duty CI engines [35, 8]. Investigating hybrid turbocharging for naval applications can combine two advantages: it can decrease fuel consumption [10, 46] and increase dynamic performance [62, 33].

For marine diesel engines, hybrid turbocharging has been examined to improve part-load efficiency and decrease engine fouling [52, 10, 11] or increase the efficiency of Selective Catalytic Reduction (SCR)-systems [42] on low loads during extensive phases of slow steaming. More interestingly is the implementation of hybrid turbocharging on marine internal combustion engines running on alternative fuels, for example, for large dual-fuel gas engines [20, 3, 40, 2]). By investigating steady-state operating conditions, the authors concluded that hybrid turbocharging systems can increase engine efficiency over the complete engine envelope, especially during gas-mode and under part-load conditions. During steady-state operations, two different cases need to be distinguished: withdrawal of electrical power from the turbocharger shaft, which we refer to as PTO, or Power-Take-Off, and addition of electrical power to the turbocharger shaft, which we refer to as PTI, or Power-Take-In.

With PTO, electrical power withdrawn from the turbocharger shaft is fed into the ship's electrical grid, ideally reducing the necessary amount of running auxiliary generators or the electrical power taken off via a shaft generator. In this case, the total system efficiency increases and might offset a decreasing main engine's efficiency due to a lower charge air pressure and resulting trapped mass, as discussed in [10, 20] A special case arises when the turbocharger is not matched to deliver maximum charge air pressure close to nominal power but at lower power output. Running at nominal power, a part of the charge air mass flow is discharged via a blow-off valve to prevent excessive charge air pressures. This would allow for electrical power withdrawn from the turbocharger shaft without penalizing the engine's efficiency [3, 2, 11].

With PTI, the additional energy fed to the turbocharger results in the engine's higher charge air pressure, thus increasing its efficiency. The necessary electric power is withdrawn from the ship's grid and must be included in the total fuel consumption. Nevertheless, PTI is favourable when the increase in engine efficiency offsets the electrical power requirements, which might be the case during low engine load [52, 40]. While improving the fuel efficiency is an important achievement in reducing global greenhouse gas emissions, limited research has been conducted on improving the dynamic performance of marine internal combustion engines using hybrid turbocharging.

By investigating a typical naval acceleration manoeuvre, Rusman [47] concluded that hybrid turbocharging could improve the dynamic performance of the investigated diesel engine and decrease the time required for the manoeuvre. Westhoeve [58] investigated several load steps and load ramps with different settings of a hybrid turbocharger. He concluded that increasing the charge-air pressure before the load increase can achieve the largest performance gain. However, this might result in very high air-excess ratios and significant gas-mode misfire. Mestemaker et al.[39] propose hybrid turbocharging for large four-stroke diesel engines used on dredging vessels to reduce turbo-lag during highly fluctuating dredging operations. By implementing hybrid turbocharging, the recovery time of the engine subjected to load steps can be reduced, but the maximum loading capacity is not increased. Additionally, the control system has to be set up carefully to prevent thermal overloading of the engine. Although current research is limited to compression ignition engines, either on diesel or dual-fuel, the benefits of hybrid turbocharging for marine internal combustion engines are revealed.

The aim of this paper is to investigate hybrid turbocharging for marine spark-ignited combustion engines running on alternative fuels. Spark-ignited engines are currently the only available engines suited to run on 100% methanol and might, therefore, play an important role in the transition to alternative fuels. As discussed in [54], the dynamic performance of marine spark-ignited combustion engines can be limited by the inertia of the turbocharger and might benefit from hybrid turbocharging. For this reason, this work considers a naval combatant as a use case, equipped with two 5 MW gas engines with hybrid turbocharging. We investigate a typical acceleration manoeuvre of the vessel and PTO/PTI options during steady state operation.

2 Theoretical Framework

The engine simulation model used to generate the results presented in this paper is a generic model of a marine high-speed, 4-stroke, spark-ignited gas engine with a single point of injection. The proposed mean value first principle engine model relies on the filling and emptying approach for the air and exhaust path dynamics and the 6-point Seiliger cycle for the closed in-cylinder process. The model has been derived from the model as presented in [54], and the gas path has been further simplified to reduce calibration efforts and computational costs. The current model uses just one volume element for the inlet receiver since the volumes of the air cooler and exhaust receivers are very small compared to the volume of the inlet receiver, see Figure 1. The air cooler and exhaust

receiver are implemented by a simple pressure- and temperature loss. Hybrid turbocharging is represented by an additional torque, as shown in Figure 1, and the load is represented by a simple propeller model for mechanical propulsion and by a lumped load for an electrical power system.
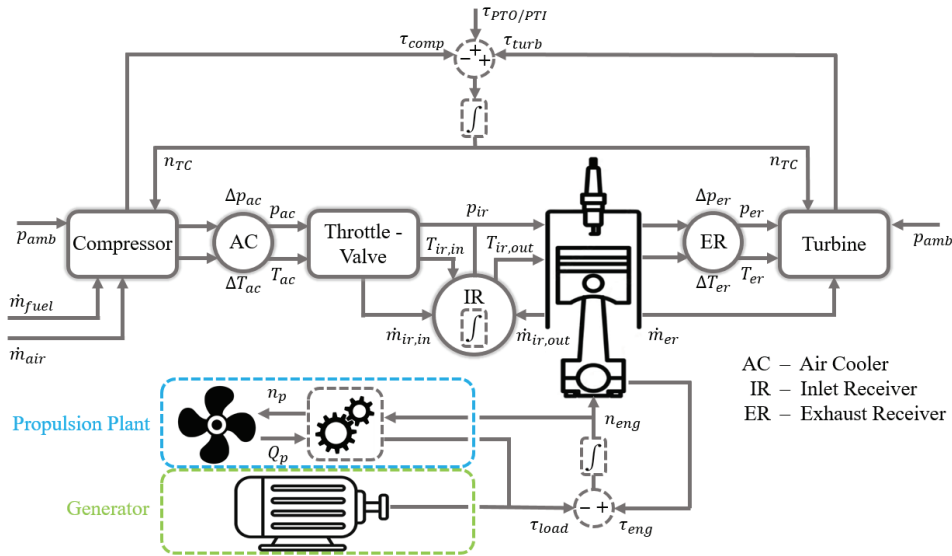
Figure 1: Block diagram of the proposed simulation model showing the reduction in volume elements involved in the gas exchange process and the investigated use cases with propulsion plant and generator.

2.1 Power take-off / Power take-in

With a hybrid turbocharger, PTO and PTI are realized by withdrawing and feeding electrical power with an electric motor/generator directly from the turbocharger shaft. For this research, the electric motor/generator is not modelled, but the corresponding torque is simply added or subtracted to the shaft. The turbocharger shaft speed is thus determined considering the following equation of motion:

$$\dot{n}_{TC} = \frac{1}{2\pi J_{TC}} \left(\eta_{m,TC} \tau_{turb} - \tau_{comp} + \tau_{PTO/PTI} \right), \tag{1}$$

with n_{TC} the rotational speed of the turbocharger shaft, $\eta_{m,TC}$ the mechanical efficiency of the turbocharger, τ_{turb} the torque delivered by the turbine, τ_{comp} the torque requested by the compressor, $\tau_{PTO/PTI}$ the torque withdrawn or fed by the electric motor/generator and J_{TC} the turbochargers mass moment of inertia.

2.2 Propeller and Hull Model

A propeller model is necessary to predict the delivered thrust force and the required torque from the engine based on the rotational speed of the shaft. Fast naval combatants with combined diesel $\vee$ gas (CODOG) / with combined diesel $\wedge$ gas (CODAG) propulsion plants are typically equipped with a controllable-pitch propeller (CPP). To predict propeller thrust, torque and efficiency, the open water test results of the Wageningen C-series [16, 15] have been implemented in the propeller model. To read out the four quadrant diagram, the hydrodynamic pitch angle β is determined by:

$$\beta = \arctan\left(\frac{v_a}{0.7\pi n_p D_p} \right), \tag{2}$$

with n_p the shaft speed, D_p the propeller diameter, and v_a the propeller advance speed, which is determined by:

$$v_a = v_s(1 - f_w), \tag{3}$$

with v_s the ship speed, and f_w the wake fraction. The four quadrant diagram provides the thrust coefficient C_T torque coefficient C_Q for the desired propeller pitch setting and are used to calculate propeller thrust T_P and torque Q_P via:

$$T_P = C_T \frac{1}{2} \rho v_h^2 \frac{\pi}{4} D_p^2 \tag{4}$$

$$Q_P = C_Q \frac{1}{2} \rho v_h^2 \frac{\pi}{4} D_p^3, \tag{5}$$

where v_h is the hydrodynamic velocity and can be calculated via:

$$v_h = \sqrt{v_a^2 + (0.7\pi n_p D_p)^2} \tag{6}$$

Due to the propeller's interaction with the hull, the requested torque of the propeller installed after the ship slightly deviates from the torque of an open-water propeller. Therefore, the relative rotative efficiency η_r is introduced [61]:

$$\eta_r = \frac{Q_P}{M_P}, \tag{7}$$

where M_P is the torque requested by the propeller behind the vessel. To account for the time delay between changing the propeller pitch set point and the actual movement of the propeller blades, Geertsma [21] proposes the following first-order linear equation:

$$\dot{PD} = \frac{1}{\tau_{PD}} (PD_{set} - PD), \tag{8}$$

with $PD(t)$ the actual pitch of the propeller, $PD_{set}(t)$ the pitch set point, and τ_{PD} representing the actuation delay. The hull model relates the thrust generated by the propellers to speed of the ship via the following equation of motion:

$$\dot{v}_s = \frac{1}{m_{ship}} \left[k_p T_P - \frac{R_{ship}(v_s)}{1 - f_t} \right], \tag{9}$$

with k_p the number of propellers, R_{ship} the ship resistance as a function of the ship speed, f_t the thrust deduction factor, and m_{ship} the mass of the ship. The equation of motion limits the ship's dynamics to just one degree of freedom, in surge direction, which is considered to be sufficient for the analysis of acceleration manoeuvres.

2.3 Controller Model

The engine control model has been introduced in [54], see Figure 2. The engine speed is controlled by the throttle valve, forming a controllable restriction on the mass flow of gas from the compressor to the the inlet receiver. A PID controller generates setpoints for the throttle valve. A TecJet gas valve adjusts the fuel flow, controlling the amount of fuel added to the inlet air before the compressor. The TecJet's PID controller uses tabular values for the desired air-to-fuel ratio and the actual air-to-fuel ratio received from the inlet receiver conditions.

3 Case Study

The Caterpillar 3508A high-speed, 4-stroke, spark-ignited gas engine is used for the case study. This engine is currently running on natural gas from the grid but has run on methanol and different blends of NG with hydrogen in the past [48, 7] and is, therefore, a suitable representative for a marine spark-ignited engine able to run on alternative fuels. The engine is presently used in the engine research facilities of the Netherlands Defense Academy in Den Helder. The test set-up and data acquisition are described in [54], and engine parameters are given in Table 1.
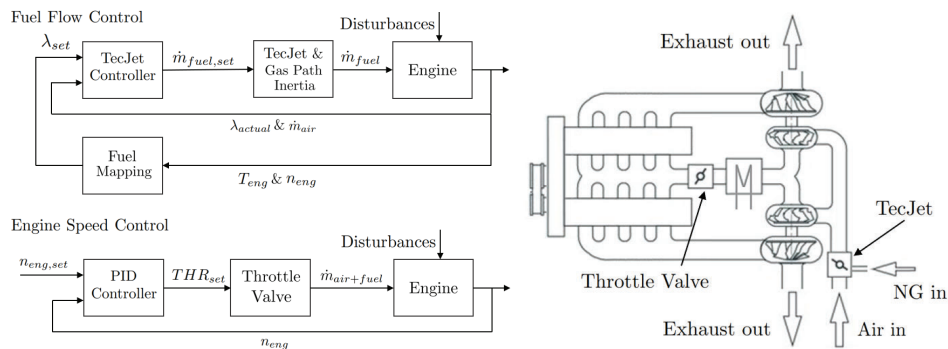
Figure 2: Schematic layout of the engine and controller from [54]

Table 1: Engine parameters Caterpillar 3508B

Feature	Value
Number of cylinders	8
Rated speed	1500 rpm
Cylinder arrangement	60° V
Rated power	500 kWe
Bore	170 mm
Turbocharger type	Garrett TW6146
Stroke	190 mm
TC quantity	2
Displacement	34.5 L
TC configuration	Parallel
Compression ratio	12:1
Max boost pressure	2.25 bar absolute
Fuel type	Low-calorific natural gas
Injection method	Single point injection before TC
Ignition method	Spark ignited (SI)

3.1 Validation Engine Model

For validation of the derived engine model, a measurement run on the experimental set up has been executed on constant engine speed with load steps increasing from 16% to 30%, 60%, and 80% and decreasing from 80% to 50% and 20% of the Maximum Continuous Rating (MCR) load. The validation run has been divided into segments with steady state operating points and dynamic segments with the transition between steady state operating points, as reported in Figure 3. To determine the error between the measurements and the simulation results, three different
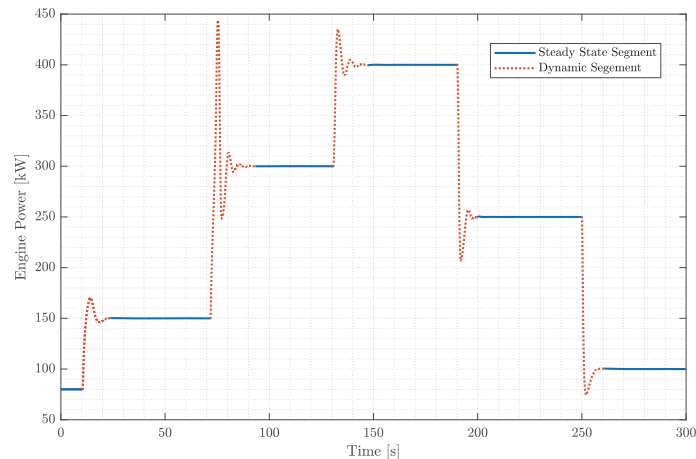
Figure 3: Engine power time trace showing the steady state and dynamic segments

indexes of performance [22, 13] have been evaluated for the complete validation run (Table 2), all steady state segments (Table 3) and all dynamic segments (Table 4). These indexes are defined as follows:

1. The mean absolute error (MAE):

$$\text{MAE}(h) = \frac{1}{m} \sum_{i=1}^{m} \left[h(x_i^t) - y_i^t \right], \tag{10}$$

with m the sample size, $h(x_i^t)$ the predicted model outcome for any given variable and for every sample point, and y_i^t the measurement of the given variable;

2. The Mean Absolute Percentage Error (MAPE):

$$\text{MAPE}(h) = \frac{100}{m} \sum_{i=1}^{m} \left[\frac{h(x_i^t) - y_i^t}{y_i^t} \right]; \tag{11}$$

3. The Pearson Product-Moment Correlation Coefficient (PPMCC):

$$\text{PPMCC}(h) = \frac{\sum_{i=1}^{m}(y_i^t - \bar{y})[h(x_i^t) - \hat{\bar{y}}]}{\sqrt{\sum_{i=1}^{m}(y_i^t - \bar{y})^2}\sqrt{\sum_{i=1}^{m}[h(x_i^t) - \hat{\bar{y}}]^2}}, \tag{12}$$

with $\bar{y} = \frac{1}{m}\sum_{i=1}^{m} y_i^t$ and $\hat{\bar{y}} = \frac{1}{m}\sum_{i=1}^{m} h(x_i^t)$.

The simulation was executed for validation using the Runge-Kutta method and a fixed step-size of 0.1 ms. This increased the computational costs significantly (execution time of 240 s), but the fixed step size ensured the correct ratio of sample points taken during the steady state and dynamic segments. For optimal performance, the simulation can be executed using a solver with a variable step size, which will increase the step size during steady-state segments. Using the Dormand-Prince method and a variable step size with a maximum step size of 0.1 s resulted in an execution time of 7 s. The simulation results of the validation have been obtained with MATLAB Simulink $R2023b$ running on an Intel Core $i7-1365U$ processor and 16 GB RAM.

Table 2: Performance measures complete simulation

Variable	MAE	MAPE	PPMCC
Engine Power P_b	5.55 [kW]	2.41 [%]	0.9873
Engine Speed n_{eng}	3.77 [rpm]	0.25 [%]	0.7370
Throttle valve set point THR_{set}	2.93[%]	10.76 [%]	0.9127
Turbocharger Speed n_{TC}	2277 [rpm]	4.68 [%]	0.9880
Pressure air cooler p_{ac}	3.44 [kPa]	2.38 [%]	0.9882
Pressure inlet receiver p_{ir}	3.07 [kPa]	2.84 [%]	0.9902
Pressure outlet receiver p_{or}	4.27 [kPa]	2.76 [%]	0.9880
Total engine efficiency η_{eng}	1.99[%]	6.97 [%]	0.8915

Table 3: Performance measures steady state segments

Variable	MAE	MAPE	PPMCC
Engine Power P_b	1.06 [kW]	0.62 [%]	0.9999
Engine Speed n_{eng}	0.77 [rpm]	0.05 [%]	0.0639
Throttle valve set point THR_{set}	2.01[%]	4.43 [%]	0.9748
Turbocharger Speed n_{TC}	1893 [rpm]	4.21 [%]	0.9965
Pressure air cooler p_{ac}	2.54 [kPa]	1.88 [%]	0.9993
Pressure inlet receiver p_{ir}	1.85 [kPa]	1.96 [%]	0.9988
Pressure outlet receiver p_{or}	3.44 [kPa]	2.24 [%]	0.9990
Total engine efficiency η_{eng}	1.69[%]	6.21 [%]	0.9977

Table 4: Performance measures dynamic segments

Variable	MAE	MAPE	PPMCC
Engine Power P_b	19.40 [kW]	7.77 [%]	0.9487
Engine Speed n_{eng}	12.99 [rpm]	0.87 [%]	0.7401
Throttle valve set point THR_{set}	5.83[%]	30.59 [%]	0.8385
Turbocharger Speed n_{TC}	3573 [rpm]	6.48 [%]	0.9592
Pressure air cooler p_{ac}	6.33 [kPa]	4.05 [%]	0.9547
Pressure inlet receiver p_{ir}	6.75 [kPa]	5.57 [%]	0.9642
Pressure outlet receiver p_{or}	6.83 [kPa]	4.35 [%]	0.9549
Total engine efficiency η_{eng}	2.89[%]	9.24 [%]	0.6163

3.2 Generator Step Load

The first use case examined represents the switching on of a large electrical consumer on the vessel's grid. For this use case, the engine model of the Caterpillar 3508A gas engine is considered to be driving an electric generator

at a constant speed of 1500 rpm. Due to the switching, the generator load is increased instantaneously from 200 kW to 385 kW (40% to 77% of MCR). Consequently, the engine speed drops to 1415 rpm and fails the NATO STANAG 1008 for Quality Power Supply (QPS) by exceeding the worst case excursion for the grid frequency, see Table 5 and Figure 4.

The hybrid turbocharger's PTI function adds electric energy to the turbocharger shaft to improve the engine's step load response. Electric energy is added from the moment the generator load is increased and is held constant until the engine speed has stabilized (about 15 s after the load step). Different power settings for the PTI have been investigated, and the results for the inlet receiver pressure and the resulting engine speed are presented in Figure 4. With higher PTI power settings, the turbocharger shaft achieves higher acceleration rates and a faster compressor outlet pressure rise is realized, thus affecting the inlet receiver pressure. Due to the higher inlet receiver pressure, more air and fuel are forced into the cylinder and the engine develops more torque faster. This results in a quicker recovery of the engine speed and a smaller deviation from the speed set point. By providing 5 kW of electric power (or 2.5 kW per TC), the engine can pass the STANAG 1008 worst case excursion criterion. Increasing the PTI setting to 20 kW (or 10 kW per TC), the engine is even able to pass the STANAG 1008 transient tolerance criterion. Since the engine speeds deviate less from the set point, the overshoot during the recovery is also significantly reduced. The results show that hybrid turbocharging can significantly improve the engine's response to a step load and improve the stability of the electrical grid as well.

Table 5: QPS Frequency characteristics according to STANAG 1008 [41]

Characteristics	Tolerance	Transient Tolerance	Worst Case Excursion
Frequency $60Hz$	$\pm3\%$	$\pm4\%$	$\pm5.5\%$
Recovery time	-	2 s	2 s
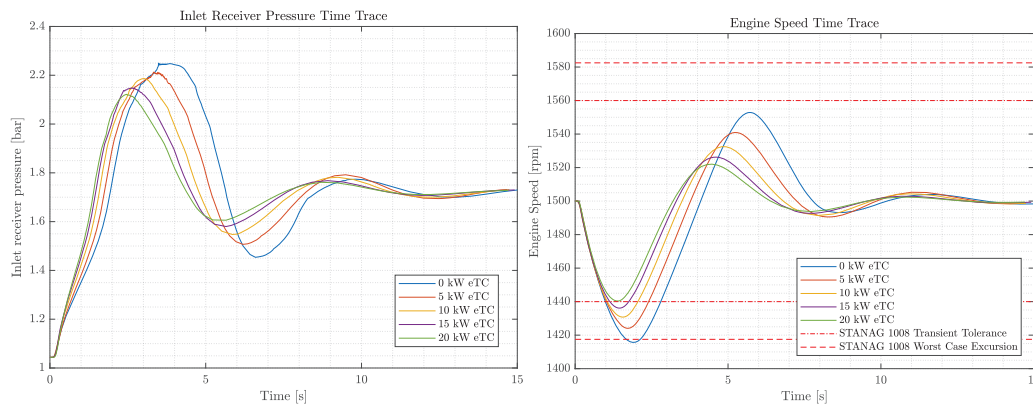
Figure 4: Simulation results of inlet receiver pressure(left) and engine speed (right) for a step load 200 kW-385 kW and different PTI power settings

3.3 Case Vessel

For the second case study a typical CODOG propulsion plant of a fast naval combatant is considered, see Figure 5. Due to redundancy requirements, these propulsion plants consist of two independent shaft lines and at least one prime mover per shaft line. CODOG propulsion plants are always combined with controllable pitch propellers to facilitate easy reversing and improve the vessel's maneuverability. With this layout, the vessel can sail at cruise speed using reciprocating engines, and higher speeds are achieved by switching to the gas turbine. Since this paper focuses on the performance of reciprocating engines, gas turbines are not included in this research, and only ship speeds up to cruise speed are considered. Currently, no marine spark-ignited internal combustion engines are available, delivering sufficient power for this case study. Therefore, the Caterpillar 3508A gas engine, as presented in Table 1, is implemented. To match the requested torque at cruise speed, the engine's torque delivery is scaled by a factor 10 while all other engine parameters are held constant. The parameters of the case vessel are presented in Table 6.
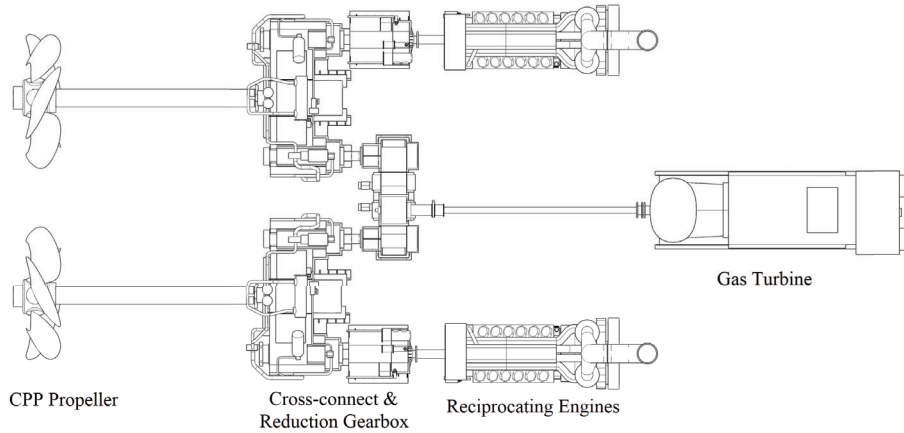
Figure 5: CODOG Propulsion System Layout

Table 6: Case vessel parameters, according to[53]

Feature	Value
Ship mass m_{ship}	6000×10^3 [kg]
Design speed $v_{ship,d}$	28.7 [kn]
Total resistance at design speed $R_{ship,d}$	1309 [kN]
Number of propellers k_p	2
Thrust deduction factor f_t	0.068
Wake fraction f_w	0.05
Propeller diameter D_p	4.8 [m]
Propeller pitch at design speed PD_d	1.8
Gearbox reduction ratio cruise speed i_{GB}	14.563

3.4 Vessel Acceleration Manoeuvre

Due to the controllable pitch propellers, the vessel's achievable acceleration rate depends on the combination of propeller pitch and engine speed set points. The resulting combinator curve and the corresponding propeller pitch and engine speed increase rates are determined during the vessel's detailed design phase. They are often a trade-off between engine characteristics, propeller characteristics (mainly cavitation) and operational experiences.

Within this paper, two different approaches are implemented and investigated, presented in Figure 6. The first approach resembles the combinator curve typically implemented in the Royal Netherlands Navy (RNLN) frigates. With this approach, the propeller pitch is increased faster than the engine speed, resulting in a higher engine load and lower acceleration rate, see Figure 7. The second approach resembles the combinator curve implemented in the Royal Danish Navy's (RDN) air-defence (Iver Huitfeldt class) frigate. This frigate is propelled by four MTU $20V8000$ engines in a CODAD propulsion plant arrangement. By increasing the engine speed early and faster than the propeller pitch, a higher acceleration rate is achieved by reducing the engine loading at the same time, see Figure 8. In combination with an adaptive pitch control strategy, propeller blade loading and resulting cavitation can be reduced while improving manoeuvrability [18].

To improve acceleration performance, the hybrid turbocharger's PTI function adds electric energy to the turbocharger shaft during the acceleration manoeuvre. For the acceleration manoeuvre, two cases are investigated: PTI with 200 kW per engine (or 100 kW per turbocharger) and PTI with 400 kW per engine (or 200 kW per turbocharger). With this additional power, the turbocharger's rotational speed increases, resulting in increased compressor outlet pressure. Depending on the throttle valve position, the increased compressor outlet pressure raises the inlet receiver pressure as well, resulting in a higher trapped mass of air in the cylinder. Ultimately, this results in an increased engine power limit, as shown in Figure 7 and Figure 8. For low compressor mass flows, corresponding with low engine speeds and low engine loads, the additional power provided via PTI has to be limited to prevent compressor surge, as discussed by Mestemaker et al. [39]. An excessive increase in the turbocharger speed due to high PTI settings will result in a quick rise in the compressor outlet pressure since the compressor mass flow is determined by the engine's swallow capacity, and flow separation in the compressor may occur. Higher compressor mass flows correspond with higher engine speeds and higher engine loads, reducing the risk of compressor

surge due to the greater margin between the compressor working point and the surge limit. Unfortunately, with high compressor mass flows, the effect of providing additional power via PTI on the compressor outlet pressure is diminished due to the high compressor power requested. As a result, the engine can only fully benefit from hybrid turbocharging if the engine is highly loaded while accelerating from medium to high engine speeds.

Results for the acceleration manoeuvre with the RNLN combinator approach, Figure 7, show that the propulsion engines benefit from the PTI and can deliver more power during the second half of the acceleration manoeuvre. The time needed to accelerate from 0 kn to 19 kn is reduced by 15 s (or about 10%) for a PTI setting of 200 kW per engine. Since the compressor outlet pressure does not linearly increase with the addition of electrical power via PTI, doubling of the PTI setting to 400 kW per engine results in just a slight increase in available engine power. The time needed to accelerate from 0 to 19 knots is reduced by an additional 5 s.

Results for the RDN combinator approach, Figure 8, show that in this situation, the propulsion engines only marginally benefit from hybrid turbocharging. By quickly ramping up the engine's speed with reduced propeller pitch, the requested power is limited, and the PTI's addition of energy is bound by the compressor surge limit. During the second half of the acceleration manoeuvre, the engine is running at maximum engine speed and providing additional power via PTI results in just a slight increase of the compressor outlet pressure. By implementing hybrid turbocharging, just a few seconds can be gained during the acceleration from 0 kn to 19 kn. Nevertheless, the RDN combinator approach without PTI results in a quicker acceleration manoeuvre than the RNLN combinator approach with the assistance of the hybrid turbocharger.

The results show that, depending on the design of the combinator curve, the propulsion engines can benefit from hybrid turbocharging during an acceleration manoeuvre. However, careful design of the combinator curve with respect to the engine envelope or adaptive pitch control strategies can facilitate higher acceleration rates than implementing hybrid turbocharging alone.
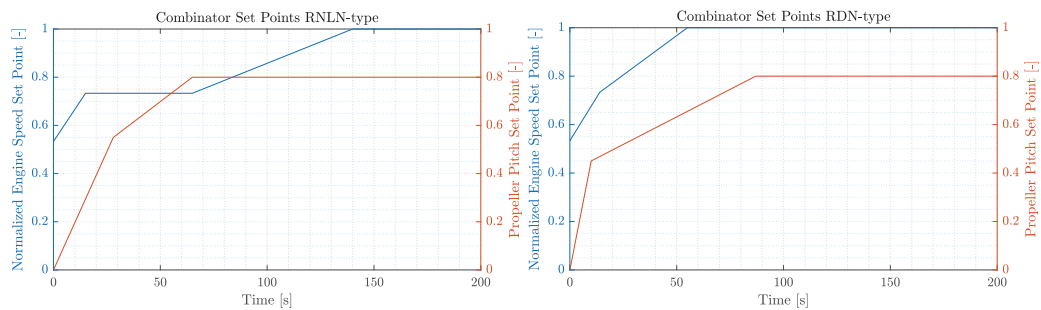
Figure 6: Combinator Set Points for Engine Speed and Propeller Pitch as used by the Royal Netherlands Navy (RNLN,left) and the Royal Danish Navy (RDN,right)
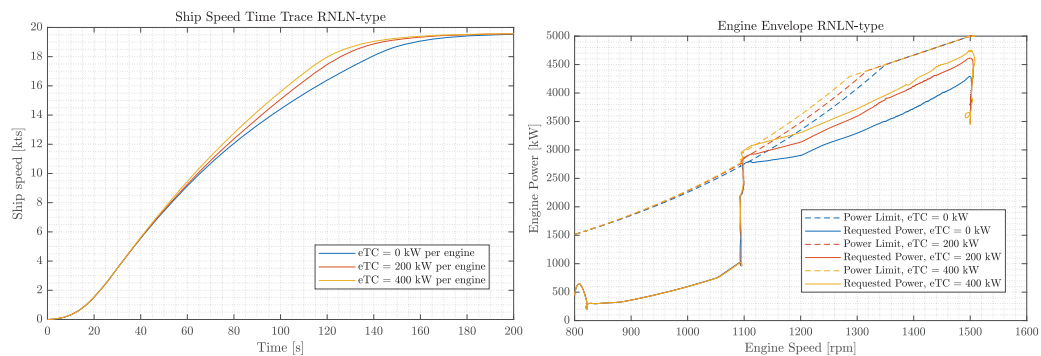
Figure 7: Results for the acceleration manoeuvre with the RNLN approach, showing the ship speed (left) and the requested power plotted in the engine envelope (right) for different PTI settings

3.5 Efficiency Considerations

The previous sections show that hybrid turbocharging can be beneficial for transient performances if additional electrical energy is fed to the turbocharger shafts. This electric energy has to be produced on board the vessel and is not freely available. Increasing the charge air pressure of the engine, either during a load step on the generator or
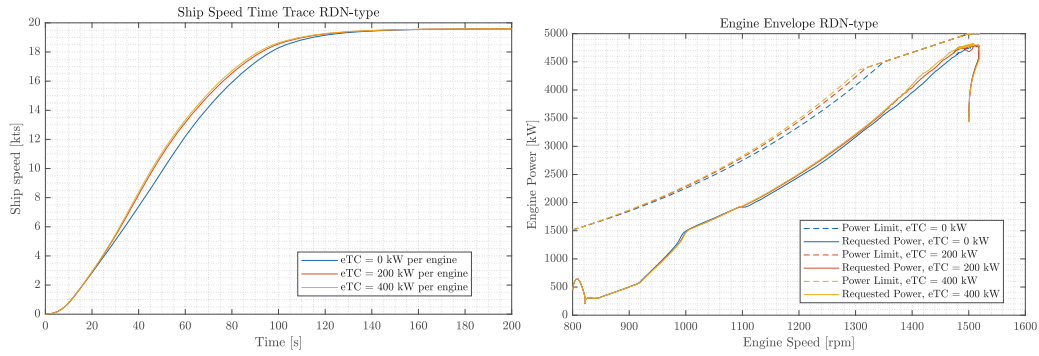
Figure 8: Results for the acceleration manoeuvre with the RDN approach, showing the ship speed (left) and the requested power plotted in the engine envelope (right) for different PTI settings

during an acceleration manoeuvre, can increase the engine's power output, supplying more fuel at the same time. Since the electric energy fed to the hybrid turbocharger cannot be recovered, total system efficiency decreases. Fortunately, transient phases, such as maneuvering, switching large electrical consumers, or starting up another generator set, represent a negligible part of a naval vessel's operational profile.

Considering the total system efficiency, it is thus more interesting to investigate steady state performance of the vessel. Using the PTO functionality of the hybrid turbocharger, electric energy can be subtracted from the shaft. Consequently, the compressor speed and resulting compressor outlet pressure are reduced. Unless the engine is running at maximum power and the throttle is fully opened, the charge air pressure (pressure in the inlet receiver) is held constant by the throttle valve by varying the throttle position and the resulting pressure difference across the throttle. Increasing the amount of electric energy subtracted with the hybrid turbocharger increases the throttle valve position. Essentially, the pumping losses of the engine are decreased while keeping the break power and thus the mechanical efficiency of the engine constant, see also Table 7 for the a ship speed of 20 kn. With this engine load, a maximum of 500 kW of electric power could be subtracted from the hybrid turbocharger, representing 10% of the nominal engine power.

Table 7: Throttle position and pressure values for different PTO settings on the propulsion engines at a ship speed of 20 kn

PTO set point	0 kW	100 kW	200 kW	300 kW	400 kW	500 kW
Throttle position	52.3°	57.5°	59.4°	60.6°	61.6°	62.0°
Turbocharger speed	77 600 rpm	77 100 rpm	76 200 rpm	75 500 rpm	75 200 rpm	75 100 rpm
Pressure compressor out	1.873 bar	1.859 bar	1.833 bar	1.815 bar	1.804 bar	1.798 bar
Pressure inlet receiver	1.640 bar					
Engine Power	3650 kW					

Since the PTO function of these propulsion engines is insufficient to cover the typical hotel load and provide backup capability for a naval combatant, additional generator sets are required. For the case vessel a hotel load of 2000 kW is considered and electric power is provided by two MTU 16V4000 diesel generator sets. With this configuration, four different scenarios are investigated, and the resulting system efficiency breakdown is presented in Table 8. The propulsion engines without PTO function and two running generator sets for electric power are considered in scenario 1. In the second scenario, the PTO function is designated as emergency power generation, and just one generator set is running to cover the hotel load. Since a maximum of 500 kW can be subtracted per propulsion engine, not the complete hotel load can be covered in case the generator set fails. However, 1000 kW should be sufficient to provide energy to all critical consumers and prevent a black-out. In scenarios 3 and 4, the PTO provides electric power, reducing the load on the two running generator sets. While subtracting a maximum of 500 kW per engine is possible, this results in increased sensitivity to external disturbances like wave loading and possible thermal overloading.

The results show that throttle-valve-controlled spark-ignited marine internal combustion engines achieve lower efficiencies compared to modern diesel engines due to significant throttling losses, especially in part load. However, these engines profit notably from hybrid turbocharging with the PTO function reducing throttling losses, resulting in an increase of the engine efficiency of up to 4% during cruise speed of 20 kn. The gain in engine efficiency of the propulsion engines even offsets the declining engine efficiency of the diesel generators, thus resulting in an

Table 8: System efficiency breakdown, ship speed 20 kn, hotel load 2000 kW

	Without PTO	**PTO standby**	**PTO** 250 kW	**PTO** 500 kW
Propulsion engine load	3650 kW	3650 kW	3650 kW	3650 kW
PTO	0 kW	0 kW	250 kW	500 kW
Propulsion engine efficiency	0.297	0.297	0.318	0.338
Number of gensets running	2	1	2	2
Genset load	1000 kW	2000 kW	750 kW	500 kW
Genset efficiency	0.38	0.41	0.34	0.32
System efficiency	0.311	0.316	0.321	0.335

increase in the propulsion system's total efficiency.

4   Conclusions and Future Work

This paper has explained how hybrid turbocharging can benefit marine spark-ignited combustion engines running on alternative fuel. An existing Mean Value First Principle (MVFP) model has been extended and validated to investigate hybrid turbocharging. For validation, we introduced three different performance indexes and presented their results for the steady state and dynamic segments of the simulation run. We can conclude from the validation that a mean value simulation model can perform with reasonable accuracy and predict the gas path dynamics well enough to investigate the effects of hybrid turbocharging on transient performance.

By investigating different use cases, the effect of hybrid turbocharging during transient phases and steady state has been evaluated. We have shown how the response of a marine generator set running on alternative fuel to a load change can be improved by using the hybrid turbocharger's PTI function. A hybrid turbocharger can significantly reduce the engine speed drop after a load step, thus increasing the grid's stability. This allows for larger load steps while complying with NATO STANAG 1008. For spark-ignited propulsion engines running on alternative fuels, we can conclude that the advantages of a hybrid turbocharger are limited during an acceleration manoeuvre. Although the time required to accelerate from 0 to cruising speed can be reduced slightly using the hybrid turbocharger's PTI function, larger performance gains can be achieved with propeller pitch and engine speed set points that match the engine's envelope. This stresses again the importance of a well designed combinator curve to improve maneuverability and reduce time. However, implementing hybrid turbocharger on the propulsion engines can improve the system efficiency with 2.5% during steady state phases. Using the PTO function reduces throttling losses, and the additional electric power is fed to the vessel's grid.

Special attention was paid to preventing compressor surging while simulating the acceleration manoeuvre with PTI on the hybrid turbocharger. At low to medium engine speeds, the margin between the normal operating point and compressor surge is very small. Future work should include blow-off, blow-by, and waste gate valves as well as considering alternative compressor and turbine sizing to increase the charge air pressure at low engine speeds without exceeding the surge limit. With these extensions in mind, different maneuvering operations should be investigated, including acceleration with varying initial ship speeds and sea margins. Furthermore, additional steady state cases should be investigated, including the effects of PTO and PTI with varying engine load and external disturbances. Although the current model can predict the performance and efficiency of the investigated gas engine within reasonable accuracy, extending the gas path might require a more sophisticated simulation approach since not all aspects of blow-off, blow-by and waste gate control can be captured well with a mean value model.

Acknowledgement

References

[1] Aghaali, H., Angström, H.E., 2015. A review of turbocompounding as a waste heat recovery system for internal combustion engines. Renewable and sustainable energy reviews 49, 813–824.

[2] Altosole, M., Balsamo, F., Campora, U., Mocerino, L., 2021. Marine dual-fuel engines power smart management by hybrid turbocharging systems. Journal of Marine Science and Engineering 9, 663.

[3] Altosole, M., Benvenuto, G., Campora, U., Silvestro, F., Terlizzi, G., 2018. Efficiency improvement of a natural gas marine engine using a hybrid turbocharger. Energies 11, 1924.

[4] Baines, N., 2005. Fundamentals of Turbocharging. Concepts NREC.

[5] Bilousov, I., Bulgakov, M., Savchuk, V., 2020. Modern Marine Internal Combustion Engines. Springer.

[6] Boretti, A., 2018. Changes of e-kers rules to make f1 more relevant to road cars. Advances in Technology Innovation 3, 26.

[7] Bosklopper, J., Sapra, H., van de Ketterij, R., van Sluijs, W., Bekdemir, C., de Vos, P., Visser, K., 2020. Experimental study on a retrofitted marine size spark-ignition engine running on port-injected 100% methanol. INEC 2020, Delft .

[8] Breitbach, H., Christmann, R., Gabriel, H., Metz, D., 2020. Die zweite generation des ebooster von borgwarner. MTZ-Motortechnische Zeitschrift 81, 46–49.

[9] Bricknell, D.J., Partridge, R., 2006. Power and propulsion for the modern global combatant. Horizon 124, F100.

[10] Bucknall, R., Suarez De La Fuente, S., Szymko, S., Bowers, W., Sim, A., 2018. Evaluation of electric-turbo-charging applied to marine diesel-engines, in: Conference Proceedings of INEC, pp. 1–12.

[11] Campora, U., Coppola, T., Micoli, L., Mocerino, L., Ruggiero, V., 2023. Techno-economic comparison of dual-fuel marine engine waste energy recovery systems. Journal of Marine Science and Application 22, 809–822.

[12] Casson, C.P., Wood, C.J., Bricknell, D.J., Daffey, K., Partridge, R., 2006. Power and propulsion for the new global combatant. Brycheins Ltd. .

[13] Coraddu, A., Oneto, L., Cipollini, F., Kalikatzarakis, M., Meijn, G.J., Geertsma, R., 2022. Physical, data-driven and hybrid approaches to model engine exhaust gas temperatures in operational conditions. Ships and Offshore Structures 17, 1360–1381.

[14] Cross, D., Brockbank, C., 2009. Mechanical hybrid system comprising a flywheel and CVT for motorsport and mainstream automotive applications. Technical Report. SAE Technical Paper.

[15] Dang, J., Van den Boom, H., Ligtelijn, J.T., 2013. The wageningen c-and d-series propellers, in: 12th International Conference on Fast Sea Transportation FAST, Citeseer. pp. 1–10.

[16] Dang, J., Brouwer, J., Bosman, R., Pouw, C., 2012. Quasi-steady two-quadrant open water tests for the wageningen propeller c-and d-series, in: Proceedings of the Twenty-Ninth Symposium on Naval Hydrodynamics, Gothenburg, Sweden, pp. 1–19.

[17] Davies, P., Bontemps, N., Tietze, T., Faulseit, E.T., 2019. Elektrisch unterstützte turboaufladung-schlüsseltechnologie für hybridisierte antriebssstränge. MTZ-Motortechnische Zeitschrift 80, 30–39.

[18] Drakoulas, M., Reurings, J., Meijn, G., Wittingen, M., 2022. Adaptive pitch control: Simulation performance evaluation against conventional propulsion control, in: Conference Proceedings of INEC, pp. 1–13.

[19] Ekberg, K., Eriksson, L., 2017. Improving fuel economy and acceleration by electric turbocharger control for heavy duty long haulage. IFAC-PapersOnLine 50, 11052–11057.

[20] Figari, M., Theotokatos, G., Coraddu, A., Stoumpos, S., Mondella, T., 2022. Parametric investigation and optimal selection of the hybrid turbocharger system for a large marine four-stroke dual-fuel engine. Applied Thermal Engineering 208, 117991.

[21] Geertsma, R., Negenborn, R., Visser, K., Loonstijn, M., Hopman, J., 2017. Pitch control for ships with diesel mechanical and hybrid propulsion: Modelling, validation and performance quantification. Applied energy 206, 1609–1631.

[22] Ghelardoni, L., Ghio, A., Anguita, D., 2013. Energy load forecasting using empirical mode decomposition and support vector regression. IEEE Transactions on Smart Grid 4, 549–556.

[23] Golloch, R., Merker, G.P., 2005. Downsizing bei verbrennungsmotoren. MTZ-Motortechnische Zeitschrift 66, 126–131.

[24] Heiduk, T., Weiß, U., Fröhlich, A., Helbig, J., 2016. Der neue v8-tdi-motor von audi teil 1: Aggregatearchitektur und aufladekonzept mit elektrischem verdichter. MTZ-Motortechnische Zeitschrift 77, 24–31.

[25] Heim, K., 2002. Existing and future demands on the turbocharging of modern large two-stroke diesel engines, in: 8-th Supercharging Conference, Dresden, pp. 1–2.

[26] Herring, P., 1987. Sequential turbocharging of the mtu 1163 engine. Transactions 100.

[27] Heywood, J.B., 1988. Internal combustion engine fundamentals. Mcgraw-hill.

[28] Hiereth, H., Prenninger, P., 2007. Charging the internal combustion engine. Springer Science & Business Media.

[29] Hoang, A.T., Foley, A.M., Nižetić, S., Huang, Z., Ong, H.C., Ölçer, A.I., Nguyen, X.P., et al., 2022. Energy-related approach for reduction of co2 emissions: A critical strategy on the port-to-ship pathway. Journal of Cleaner Production 355, 131772.

[30] Hopmann, U., Algrain, M.C., 2003. Diesel engine electric turbo compound technology. Technical Report. SAE Technical Paper.

[31] Hountalas, D., Katsanos, C., Lamaris, V., 2007. Recovering energy from the diesel engine exhaust using mechanical and electrical turbocompounding. Technical Report. SAE Technical Paper.

[32] Inal, O.B., Charpentier, J.F., Deniz, C., 2022. Hybrid power and propulsion systems for ships: Current status and future challenges. Renewable and Sustainable Energy Reviews 156, 111965.

[33] Katrašnik, T., Trenc, F., Medica, V., Markič, S., 2005. An analysis of turbocharged diesel engine dynamic response improvement by electric assisting systems. Journal of Engineering for Gas Turbines and Power .

[34] Kech, J., Hegner, R., Mannle, T., 2014. Turbocharging: Key technology for high-performance engines. MTU Engine Technology White Paper .

[35] Kech, J., Rappsilber, R., Thiesemann, J., 2019. Elektrisch unterstützte aufladung für off-highway-hochleistungsmotoren. MTZ-Motortechnische Zeitschrift 80, 52–61.

[36] Kisbenedek, E., Andersson, N., 2018. Review on Recent Advances for Marine Turbocharger Technologies. B.S. thesis. CHALMERS UNIVERSITY OF TECHNOLOGY.

[37] Mack Trucks, 2020. Mack announces updated mp8he engine with turbocompounding. https://dieselnet.com/news/2020/10mack.php. Accessed: 2024-04-29.

[38] McKinlay, C.J., Turnock, S.R., Hudson, D.A., 2021. Route to zero emission shipping: Hydrogen, ammonia or methanol? International journal of hydrogen energy 46, 28282–28297.

[39] Mestemaker, B., Westhoeve, J., Visser, K., 2019. Evaluation of hybrid electric turbocharging for medium speed engines. Technical Report. SAE Technical Paper.

[40] Montal Almirall, D., 2019. Electric power generation from the hybrid turbocharger of a marine propulsion diesel engine. B.S. thesis. Universitat Politècnica de Catalunya.

[41] NATO, 2021. NATO - STANAG 1008: CHARACTERISTICS OF SHIPBOARD 440V/230V/115V 60Hz, 440V/115V 400Hz and 24/28VDC ELECTRICAL POWER SYSTEMS IN WARSHIPS OF THE NATO NAVIES. Technical Report. North Atlantic Treaty Organization (NATO).

[42] Nielsen, J.B., Yum, K.K., Pedersen, E., 2020. Improving pre-turbine selective catalytic reduction systems in marine two-stroke diesel engines using hybrid turbocharging: A numerical study of selective catalytic reduction operation range and system fuel efficiency. Proceedings of the Institution of Mechanical Engineers, Part M: Journal of Engineering for the Maritime Environment 234, 463–474.

[43] Pasini, G., Lutzemberger, G., Frigo, S., Marelli, S., Ceraolo, M., Gentili, R., Capobianco, M., 2016. Evaluation of an electric turbo compound system for si engines: A numerical approach. Applied Energy 162, 527–540.

[44] Piancastelli, L., Peli, F., Pezzuti, E., et al., 2018. The advantage of the "split" turbocharger in formula 1 engines. Tecnica Italiana 61, 36–41.

[45] Pucher, H., Zinner, K., 2012. Aufladung von Verbrennungsmotoren: Grundlagen, Berechnungen, Ausführungen. Springer-Verlag.

[46] Rusman, J., 2018a. Charge air configurations for propulsion diesel engines aboard fast naval combatants, in: Conference Proceedings of INEC, pp. 1–11.

[47] Rusman, J., 2018b. Charge air configurations for propulsion diesel engines aboard fast naval combatants. Msc thesis. Delft UNIVERSITY OF TECHNOLOGY.

[48] Sapra, H., Linden, Y., van Sluijs, W., Godjevac, M., Visser, K., 2019. Experimental investigations of performance variations in marine hydrogen-natural gas engines, in: Cimac Congress, pp. 1–17.

[49] Saunders, S., 2015. Jane's Fighting Ships 2015-2016. Janes.

[50] Scheub, J., Zecchetti, D., Habermann, J., Maniar, M., 2021. Mehr effizienz und leistung mittels elektrischem turbolader. MTZ-Motortechnische Zeitschrift 82, 78–84.

[51] Schmalzl, H.P., 2014. Zurück in die zukunft wege der aufladung. MTZ-Motortechnische Zeitschrift 75, 90–95.

[52] Shiraishi, K., Krishnan, V., 2014. Electro-assist turbo for marine turbocharged diesel engines, in: Turbo Expo: Power for Land, Sea, and Air, American Society of Mechanical Engineers. p. V01BT23A003.

[53] Vollbrandt, J., 2016. Improving the maneuvering performance of diesel hybrid propulsion plants for fast naval combatant. Msc thesis. Delft UNIVERSITY OF TECHNOLOGY.

[54] Vollbrandt, J., Coraddu, A., Geertsma, R., 2023. Transient performance of alternatively fueled internal combustion engines for naval applications, in: Conference Proceedings of EAAW, pp. 1–11.

[55] Volvo Group, 2021. With continued north american success, volvo truck's d13 turbo compound engine now standard on all vnl models. https://www.volvogroup.com. Accessed: 2024-04-29.

[56] Watson, N., Janota, M.S., 1982. Turbocharging the internal combustion engine. Macmillan Education UK.

[57] Webster, J.S., Fireman, H., Allen, D.A., Mackenna, A.J., Hootman, J.C., 2007. Us navy studies on alternative fuel sources and power and propulsion methods for surface combatants and amphibious warfare ships. Naval engineers journal 119, 35–48.

[58] Westhoeve, J., 2018. Hybrid Electric Turbocharging: Improving the loading capability and efficiency of a dual fuel engine. Msc thesis. Delft UNIVERSITY OF TECHNOLOGY.

[59] Wilbur, C.T., Wight, D., 2016. Pounder's marine diesel engines. Elsevier.

[60] Woodyard, D., 2009. Pounder's marine diesel engines and gas turbines. Butterworth-Heinemann.

[61] Woud, J.K., Stapersma, D., 2002. Design of propulsion and electric power generation systems. IMarEST.

[62] Zellbeck, H., Friedrich, J., Berger, C., 1999. Die elektrisch unterstützte abgasturboaufladung als neues aufladekonzept. MTZ-Motortechnische Zeitschrift 60, 386–391.

Validation of Power System Control Methodologies using a Microgrid Testbed Employing Low and Medium Voltage AC and DC Sources

C. Tschritter*, A.N. Johnston*, L. Vu[ſ], T. Nguyen[ſ], D.A. Wetz*, T.V. Vu[ſ], K. Schoder[‡], J. Langston[‡], H. Ravindra[‡], M. Stanovich[‡], C.M. Schegan[+], and J.M. Heinzel[+]

* *Univ. of Texas at Arlington (UTA), Arlington, TX USA*
[ſ] *Clarkson University, Potsdam, NY USA*
[‡] *Florida State University, Center for Advanced Power Systems, Tallahassee, FL USA*
[+] *Naval Surface Warfare Center - Philadelphia, Philadelphia, PA USA*
* Corresponding Author. Email: wetz@uta.edu

Synopsis

Future shipboard power systems are likely to look and operate much differently than they do today. The changes stem from the need to operate a much wider array of loads, many of which will demand high power in a transient manner. Architectures employing distributed power generation sources and energy storage are attractive, especially when the hooks are built in to rapidly control as many facets of the sources and loads as possible. This however is not always possible as more flexibility comes with increased complexity and costs that are not always easy to implement. As control strategies are developed, testbeds are needed to validate simulations and performance when real hardware is involved. Here a low and medium voltage (MV) AC and MV DC testbed at the University of Texas at Arlington (UTA) is being used to study robust control algorithms that are being developed and modeled by Clarkson University (CU). The testbed emulates one zone of a multi-zone power system and CU has developed algorithms intended for optimized shedding of loads and the ramp-rate support of a generator supplying transient loads. Multiple levels of control have been introduced to study the impact each has on maintaining power system operability. The testbed and its integration with these control strategies will be presented along with experimental results collected to date.

Keywords: Power System Control, Energy Storage, Load Shed, Ramp-rate, Pulsed Loads

1. Introduction

In 1903, the first diesel electric ship, the Vandal, was launched into the water. At the same time, another ship utilizing diesel electric propulsion, the Petite-Pierre, was launched as well. By the 1920s ships using diesel electric propulsion were being mass constructed. These ships generally employed steam-based turbine generators to drive the propeller motors and the speed of the motor is adjusted through the speed of the generator (Hansen 2015). This

class of shipboard power systems started to fall to the wayside however with the introduction of diesel engines. The all-electric concept did stage a resurgence in the 1980s due to the advancement of power electronic devices and the concept accelerated with the increased viability of variable speed drives in the 1990s (Ortiz 2010). An abundance of studies covering shipboard power system architectures employing medium voltage (MV) AC, MV DC, or some mixture, have been conducted with progress gradually being made suggesting expanded usage soon. Many cruise vessels liquefied natural gas (LNG) tankers, and icebreakers, currently employ electric propulsion, as well as AC and DC loads in constant or transient operation (Office of Naval Research 2021). These ships and studies have highlighted the benefits of a microgrid architecture; however, considerable work and study is still necessary for these architectures to reach their full potential. The work presented here is a stride to reach the full potential of this architecture.

Among the advantages a microgrid architecture offers are improved operability and reduced susceptibility to power quality issues that occur when transient loads are deployed. The ability to actively control multiple sources and shed lower priority loads significantly improves the operability. Load shedding should occur quickly when there is not enough power to source all the loads, ensuring that critical loads remain powered (Doerry 2010, Tschritter 2023a, Johnston 2022). Without real-time control and monitoring, load shed events could happen randomly and with zero consideration of priority or operability. When monitoring and controls are available, loads may be shed in a controlled manner, offering the ability to prioritize and maximize operability of the system. When transient loads are ramp-rate buffered using energy storage, the voltage and frequency sags and surges are significantly reduced, greatly improving power quality. Without active ramp-rate buffering, the heavy loading and unloading of traditional generation sources occurs uncontrollably with detrimental impact on the generator efficiency.

Here, the University of Texas at Arlington (UTA), will demonstrate the deployment of transient loads on a low and MV AC and DC testbed known as the Intelligent Distributed Energy Analysis Laboratory (IDEAL) (C. Tschritter, 2022, C. Tschritter, 2023, C. Tschritter, 2024, A.N. Johnston, 2020, A.N. Johnston, 2020, A.N. Johnston, 2021, A.N. Johnston, 2022). Recently a 37-kW diesel generator was integrated into the testbed and it is able to be operated alone and in synchronization with the other generators in the testbed using a Woodward ATLAS-II™ generator controller. This work will be presented. A demonstration of Clarkson University's (CU's) Advanced Load Shed (ALS) and Predictive High Ramp-Rate (PHRR) controls, which have been previously documented in (C. Tschritter, 2023 and C. Tschritter, 2024) will also be made.

IDEAL Experimental Testbed

The IDEAL testbed has been documented extensively in previous work, as referenced above, but it is always changing and growing. To reduce the repeat of previously published work, the readers are referred to those articles for a more thorough understanding. The purpose of the IDEAL testbed is to emulate a single zone of a distributed shipboard zonal power system architecture. Zonal architectures for shipboard power systems have been previously proposed as seen in Doerry's one-line diagram in Figure 1 (Doerry 2010). The IDEAL testbed employs multiple sources and loads that are monitored and controlled to demonstrate the benefits these features afford towards improving operability and power quality, among other metrics.
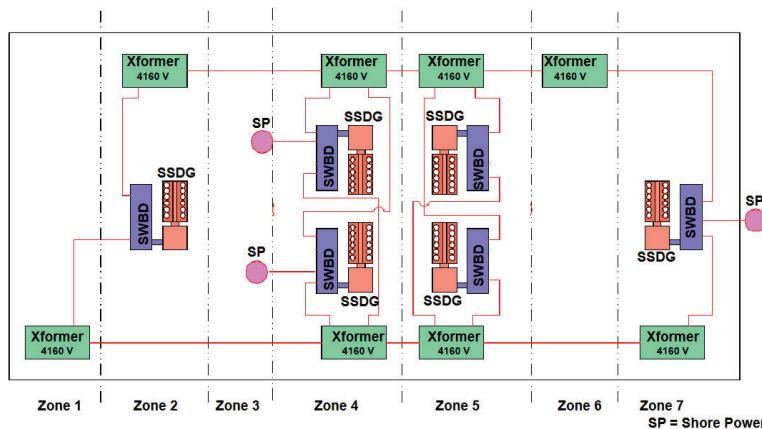
Figure 1. One line diagram depicting a potential zonal organization of shipboard power systems.

A one-line diagram of the IDEAL testbed is seen in Figure 2. In the upper left-hand side of the diagram, two generators are seen. The first is the 37 kW diesel generator previously mentioned. The second is a 150-kW electric motor generator that is controlled by a variable frequency drive. The two generators can be operated independently, or they can by synchronized using a Woodward ATLAS-II™ engine controller. Off the 480 VAC bus, there are

multiple continuous and transient loads employed. The first is ~200 kW MV power electronic drive that produces a three phase, 4160 VAC output. Its output is split two ways. In the first, it is transformed back down to 480 VAC and fed into a 350-kW resistive load bank that is digitally broken up into multiple smaller loads, referred to as Non-Vital Load L1-1 and Non-Vital Load L2-2. The second is into a multipulse rectifier that produces a 6 kVDC output that is connected to a three step, 50 kW each, resistive load bank. That load is broken up into Vital Load L2-1 and Non-Vital Load L2-2. Next the 480 VAC bus is loaded by a power supply that creates 0 – 12 kVDC at 0 – 8 A. Its output current is adjusted using an analog reference voltage from the controller to emulate continuous or transient load(s) using another resistive load. Here that load is broken up into Vital Transient Load L3-1 and Vital Transient Load L3-2. Next, there are two power electronic converters that interface the 480 VAC bus to a DC bus operating between 750 VDC and 1000 VDC. Here, only one of the converters is used, the 150 kW AC/DC converter, that is unidirectional from AC to DC. It creates 0 – 1200 VDC at 0 – 125 A. It output current is adjusted using analog controls to force power from the generator(s) onto the DC bus. The second converter is a bi-directional supply that allows power to be transferred from the battery on the DC bus back up to the L1, L2, and L3 group loads but again it is not employed in the work presented here.

On the DC bus, there are multiple devices connected. On the left side there is a 40-kW electric motor-generator set that produces a nine-phase, 711 VAC output that is rectified using an actively controlled AC/DC rectifier onto the DC bus. That generator set is not employed in the work presented here. There is also a 500-kW bi-directional power converter between the main building grid and the DC bus that can be used to emulate sources or loads as needed but that is also not used here. On the right side, there is a resistive Mission Load 1 (ML1) that is sourced by a DC/DC converter that creates 0 – 6 kVDC at 0 – 12.5 A. The supply's output current is regulated using an analog reference signal from the controller. Finally, there is a lithium-iron-phosphate (LFP) battery that is floated on the DC bus to buffer the generator when the transient ML1 is operated as described later.
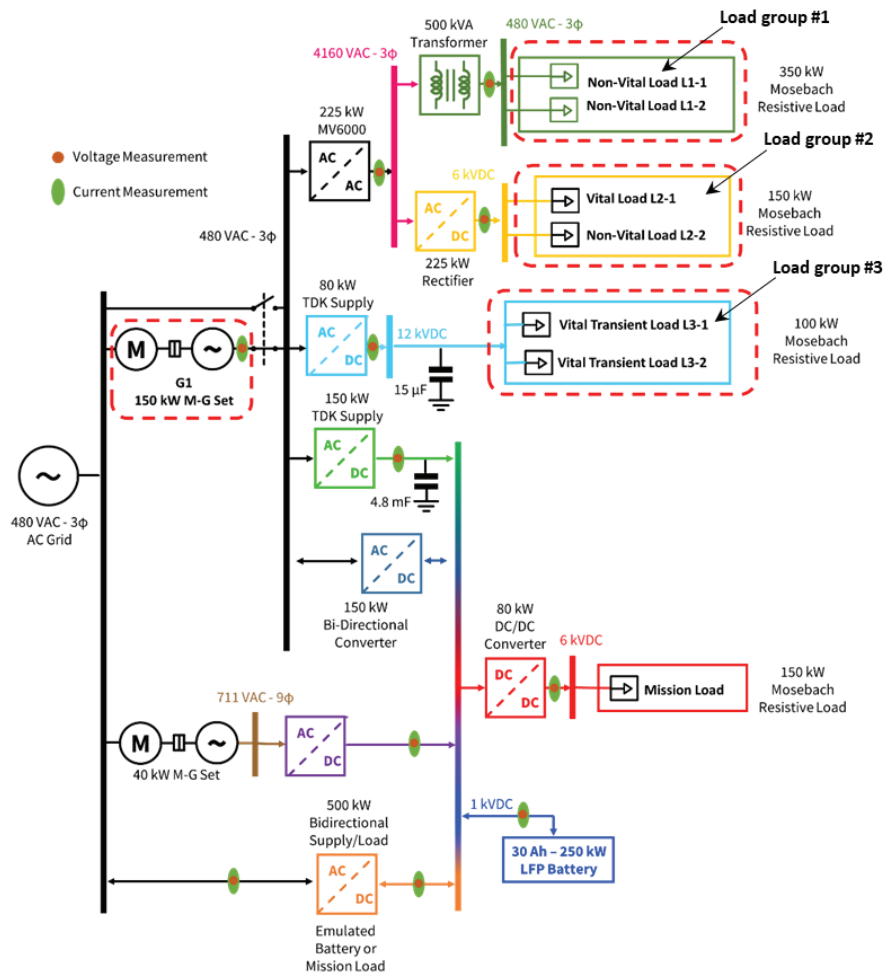
Figure 2. One Line diagram of the Intelligent Distributed Energy Analysis Laboratory (IDEAL) hardware.

A critical addition to the testbed is the 37-kW diesel generator (DG). The importance of the DG is highlighted as it more effectively represents a shipboard diesel generation as compared to the 150-kW electric motor generator (MG) set. The diesel allows for a more realistic measure of power quality when transient loads are supported and the impact adjusting its ramp-rate while buffered by energy storage can improve it. Ramping of the generation source through buffering by energy storage along with the impact transient loads have on power quality are more accurately represented when using the diesel generator. Because this generator is sized for 37 kW, all the loads have been scaled to create similar impact as compared to using the MG set. In this scenario, the loads L2-1 and L2-2 are unable to be used since they require a minimum of ~45 kW each. Instead, they are emulated by splitting the resistive load bank that represents L1-1 and L1-2 into four loads. This change makes no noticeable difference to the power architecture.

When multiple generator sets are employed in a shipboard power system, they must be synchronized such that their voltage waveforms and frequencies are aligned before they can be tied onto the same bus. This is achieved using an engine-generator controller, in this case a Woodward ATLAS-II™. On its own the ATLAS-II™ can synchronize and close the breakers on two generators but when a third generator is added, additional hardware is needed. Here Woodward LS5 breaker controllers are installed on each of the three 480 VAC generators. The ATLAS-II™ brings the generators into synchronization and works with the LS5s to physically connect the generators onto the bus when the time is right. The dual wound generator was only recently installed, after the work discussed here was performed, so synchronization of only the DG and MG will be discussed here. Together, they bring the total power capability of the testbed up to 187 kW. A one-line diagram showing the ATLAS-II™'s integration with the LS5's in the testbed is shown in Figure 3.
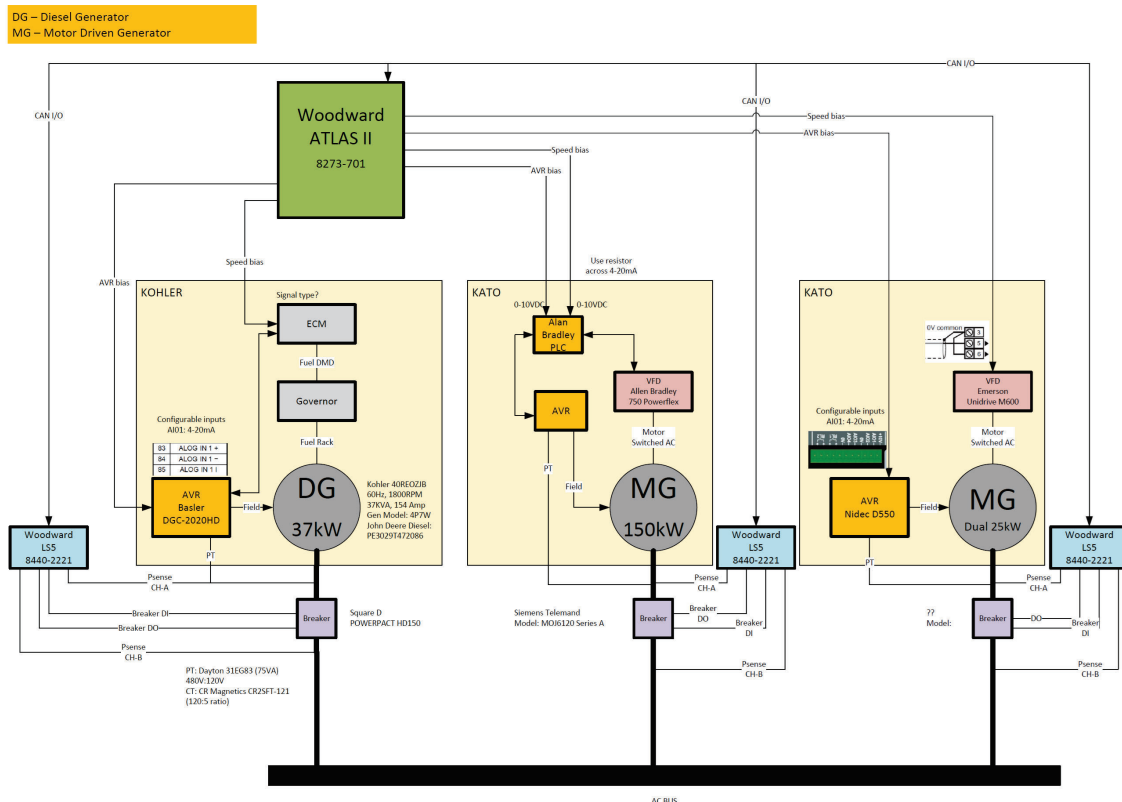
Figure 3. One Line diagram of ATLAS II connecting the 150 kW MG and 37 kW DG.

2. ALS and PHRR Control Methodology

Two software controllers, known as the ALS and PHRR controllers, have been developed by CU and deployed to the IDEAL testbed. In 2023, a series of experiments were performed using only the MG set as a source and it was demonstrated how successful the ALS and PHRR controls were at improving operability and ramp-rate support of the MG set (Tschritter 2023a, Tschritter 2023b). The ALS and PHRR were described in detail in those prior publications and the reader is referred to those for more in depth understanding. In summary, the ALS controller keeps the load demand below the generation capacity shedding the lowest priority loads when necessary

to ensure maximum operability. The PHRR controller's primary purpose is to improve and maintain power quality during the operation of transient loads. The PHRR controller achieves this by regulating the current, and therefore the power, supplied by the 1 kV converter. By doing this, it forces the battery to buffer the ML and allows the generator to be ramped on and off as transient loads come on and off the bus. This decreases the deviations on the voltage and frequency of the generator's 480 V bus when operating transient loads. Figure 4 presents a diagram showing how the IDEAL testbed interfaces with CU's ALS and PHRR controls that run on a Simulink Real-Time computer. The two systems communicate via User Datagram Protocol (UDP) messaging with delay times on the order of 100 ms.
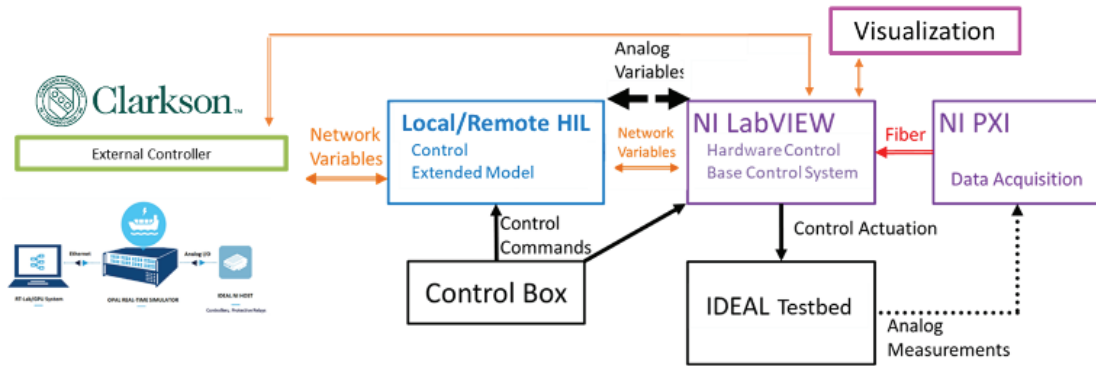
Figure 4. Flow diagram of Clarkson's controller integrating with the NI controller and IDEAL.

3. Experimental Results

3.1. Transient unbuffered loading

Multiple experiments have been conducted here to assess the power quality of the 480 V bus when transient loads are deployed. Military Standard (MIL-STD) 1399 specifies the power quality limits for a 440 V 60 Hz generator. Figure 6 and Figure 7 plots the voltage and frequency envelope limits defined in MIL-STD 1399. These specifications do not specify standards for a 480 V system, but to provide an appropriate measure for the scenarios tested here by scaling the 440 V standard to 480 V, making the line-to-line root-mean-square (RMS) voltage bounds used for this demonstration 446 V and 504 V.
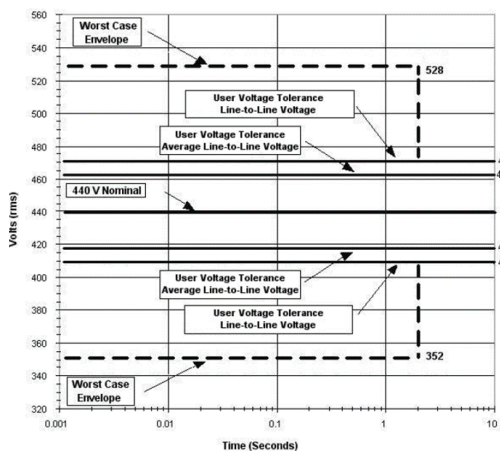
Figure 5. Voltage power quality standard from MIL-STD 1399.
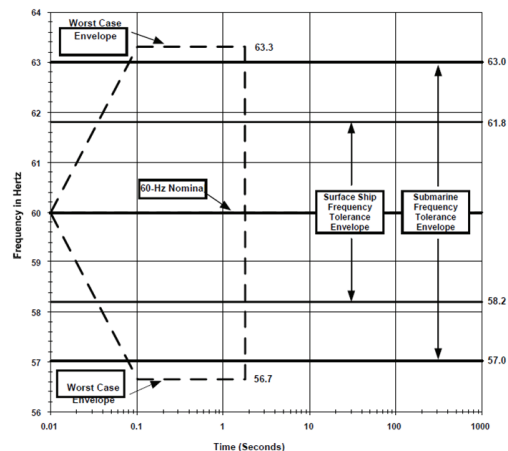
Figure 6. Frequency power quality standard from MIL-STD 1399.

To characterize when the DG's voltage and frequency deviations exceed the power quality standards, a 10 second step load was engaged and disengaged, incrementing the load by 10 kW on each subsequent engagement until it reaches 40 kW. Figure 7 and Figure 8 present voltage and frequency measurements collected from the DG during the four respective transient load events. As seen in the figures, the frequency deviation exceeded the worst case bound of 56.7 Hz when the step load power reached 30-kW step load. The 20-kW load is also outside MIL-

STD 1399 due to the recovery from the worst case bound on the frequency to the standard bound taking longer than 2 seconds to recover.
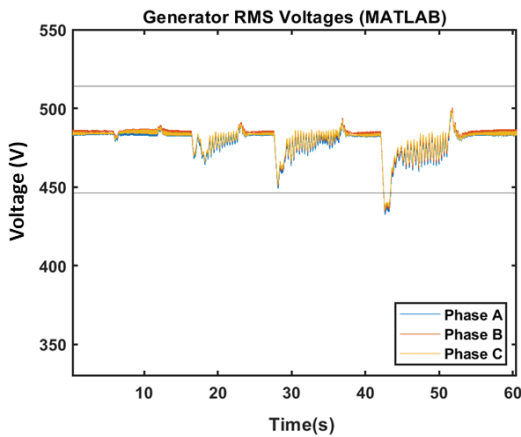
Figure 7. Voltage deviation as transient load increases.
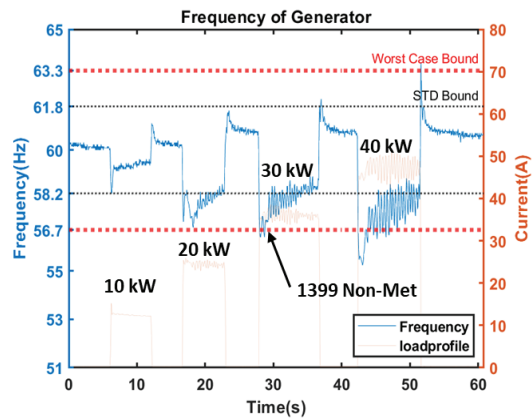
Figure 8. Frequency deviation as transient load increases.

3.2. Ramp-rate and power quality improvement

Since the MIL-STD 1399 frequency bounds were exceeded when it was transiently loaded with a 30-kW step, that power level is used in subsequent load scenarios to identify how the PHRR improves the power quality metric. Because the voltage of the DG set was maintained within the standard bounds during the 30-kW load while the frequency failed, improving frequency is the primary focus. Figure 9 presents data collected when the generator was ramped through the 1 kV DC power converter at rates of 2 kW/s, 4 kW/s, and 8 kW/s up to 30 kW. As shown, only the 2 kW/s ramp-rate kept the generator fully within the bounds of MIL-STD 1399. In the 4 kW/s and 8 kW/s plots, the cyan lines indicate the 2-second recovery window specified by the MIL-STD 1399. In those cases, the frequency does not recover to within the standard bounds within the 2 second envelope. This means that 2 kW/s is a safe ramp-rate as high as 4 kW/s can be used in extreme conditions where power quality is less paramount.
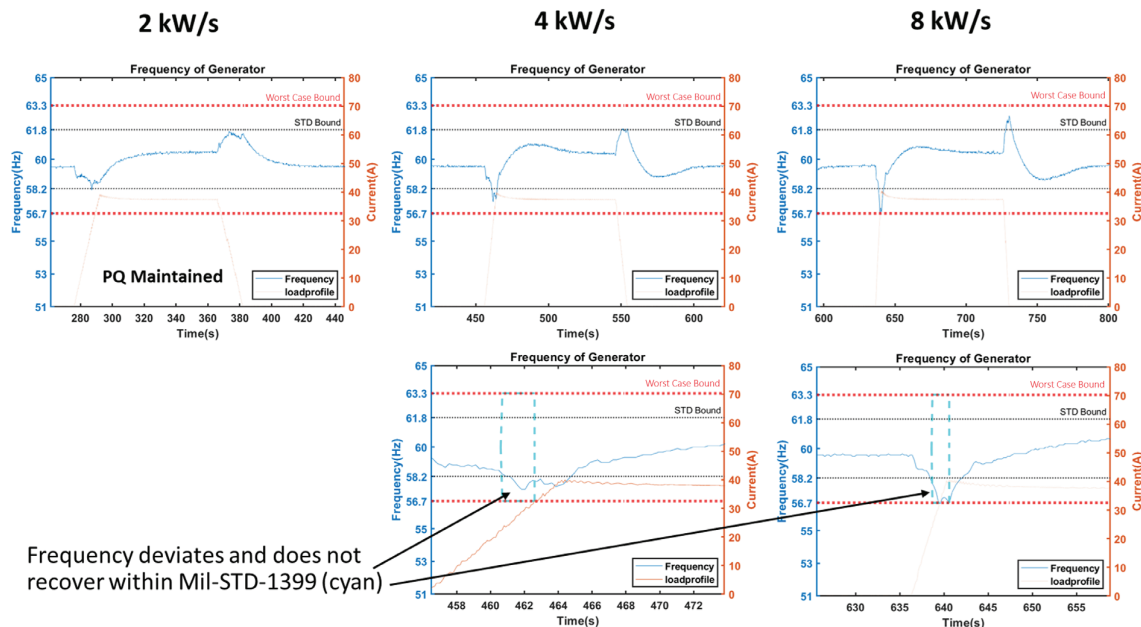
Figure 9. 4 kW/s constant ramp of a 30-kW load.

3.3. PHRR results

The ramp-rate values above were provided to CU for consideration in their development of their PHRR algorithm. The PHRR controller uses the 4.4 kW/s ramp-rate as an upper bound, meaning the ramp-rate will typically be lower, but can be pushed to the upper bound. To demonstrate the PHRR controller, a repeated load profile of 32 kW was engaged and disengaged in a 5 second on, 1 second off profile. This repeated program is stressful on the DG and provides several opportunities for the power quality to falter. At the start of each pulse, the transient load is initially buffered entirely by the battery, and then the generator is ramped up at a rate of 4 kW/s. This is repeated for 10 engagements, with the generator current being maintained through the off periods while it recharges the battery. Upon completion of the tenth load cycle, the current continues to recharge the battery until its state of charge (SoC) reaches 60%. A graph plotting the power sourced by the battery, the load power through the 6 kV AC/DC power converter, and the power supplied by the generator through the 1 kV AC/DC converter converter, is seen in Figure 10. Additionally, a graph of the frequency deviation is included in Figure 11, which demonstrates full compliance with MIL-STD 1399.
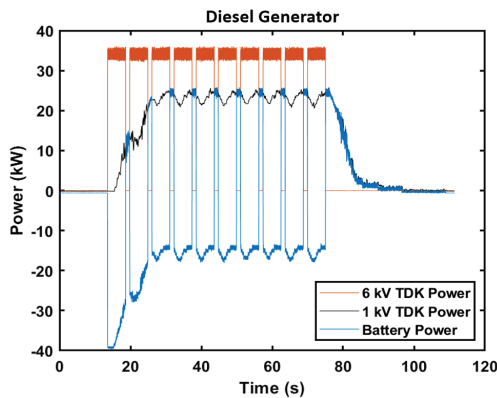
Figure 10. PHRR controller with a 4 kW/s max ramp-rate.
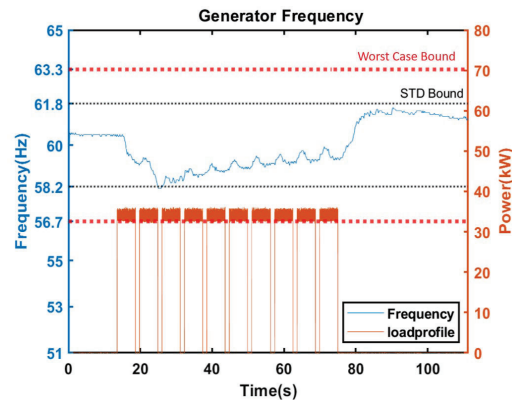
Figure 11. Frequency deviation during the PHRR controller scenario.

3.4. Generator Failure

To emphasize the importance of load shed algorithms, a scenario utilizing synchronized generators is shown. In this scenario, a generator failure is emulated by opening a breaker on one of the generators, causing the load demand to exceed the generation capacity of the system with no load shed intervention. Figure 12 shows the power and frequency behaviour of each generator across the test time. The two generators in the system are synchronized together with a 60-kW base load between them at approximately the 30 second mark. The dashed blue line represents the power sourced from the MG set with a maximum rating of 150 kW. The power sourced by the DG set is represented by the solid blue line and is has a maximum rating of 37 kW. After about 2.5 minutes, the MG set breaker is opened, causing the DG to become the only generation source. The power output is unable to be maintained by the DG alone, resulting in the bus voltage and frequency sagging. The sagged output of the generator continues for approximately 5 seconds, after which the LS5 breaker controller opens the DG breaker to protect it, ultimately resulting in all 60 kW of load failing to be supplied. This is one of the worst possible outcomes for the power system, with a silver lining of the DG being protected due to the LS5's intervention.
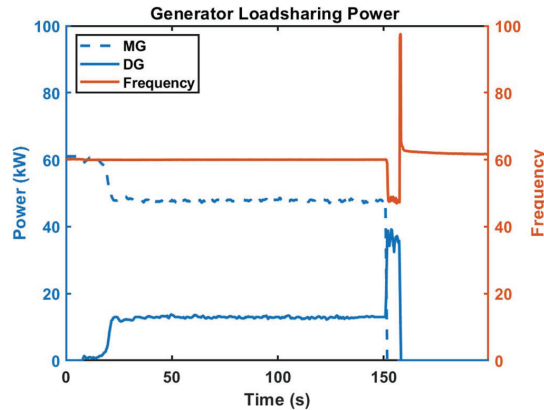
Figure 12. Scenario where loss of generator causes unintentional load shed.

3.5. ALS Controls on the Disel generator

In an effort to prevent the situation in the previous scenario, the ALS controller is deployed. A sample scenario showing the effectiveness of the controller is described here. After load is put onto the bus, the allowable power generation of the DG is manually reduced in the controller, causing the power being supplied to exceed that allowed by the controller. The breaker on the MG is not opened here, but the scenario effectively replicates generation loss, as well as other cases where a generator may become derated below nominal power. Table 1 presents each load's power ratings and weights. Figure 13 plots data collected during the generator derating scenario. Loads L1-1, L1-2, L2-1, L3-1, and L3-2 are engaged. At the 49 second mark, the generator is derated from its original 37 kW to 32 kW. This causes the ALS controller to shed L1-1 to bring the load demand below the power generation capacity. This maximizes the operability of the system, protects the generator, and prevents any uncontrolled load shed events from occurring.

Table 1. Load ratings and weights used for the DG

Load	DG Source	
	Rating (kW)	Weight
L1-1	4	0.2
L1-2	4	0.2
L2-1	8	1
L2-2	8	0.2
L3-1	8.5	0.5
L3-2	8.5	0.5
Gen	37	NaN
Reserved power	5%	NaN
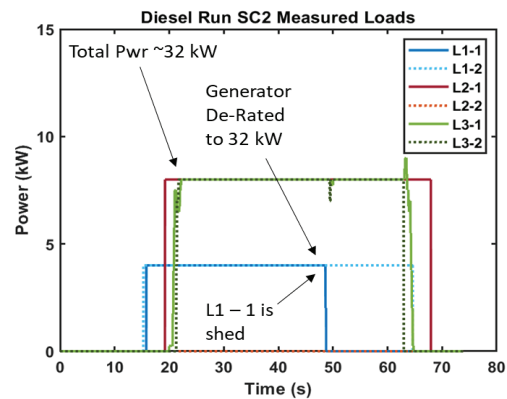
Figure 13. ALS scenario 2.

4. Conclusions

Future shipboard power systems are likely to employ a much wider array of loads, many of which will demand high power in a transient manner. The sudden high-power demands can have a detrimental effect on the entire power system. To mitigate these effects, new shipboard power system architectures propose the use and deployment of well monitored and controlled microgrid or zonal topology. UTA has setup a low and medium voltage AC/DC testbed on which to study these architectures along with the required monitoring and control strategies. In this work, a DG installed on the IDEAL testbed was used to demonstrate the power quality challenges that transient loads can introduce. ALS and PHRR controls developed by CU were implemented to improve operability when load shed events become necessary and maintain power quality when transient loads are employed.

Acknowledgements

References

J.F. Hansen and F. Wendt, 'History and State of the Art in Commercial Electric Ship Propulsion, Integrated Power Systems, and Future Trends,' Proceedings of the IEEE | Vol. 103, No. 12, December 2015.

G. Ortiz, J. Biela, D. Bortis, J.W. Kolar, "1 Megawatt, 20 kHz, Isolated, Bidirectional 12 kV to 1.2 kV DC-DC Converter for Renewable Energy Applications," The 2010 International Power Electronics Conference – ECCE ASIA, IEEE, 2010.

ONR Electric Ship Research Development Consortium, https://www.esrdc.com/, Online August 19, 2021.

N. Doerry, 'Shipboard Distribution Systems: Present and Future,' CAPS 10th Anniversary Celebration & NGIPS Workshop, October 14-15, 2010, Tallahassee, Florida, http://doerry.org/norbert/papers/20101014CAPS-DistributionSystems-final.pdf

C. Tschritter, A.N. Johnston, T. Nguyen, D.A. Wetz, T.V. Vu, J. Langston, H. Ravindra, M. Stanovich, K. Schoder, C.M. Schegan, and J.M. Heinzel, 'Robust Control of a Medium Voltage AC/DC Testbed,' 2022 International Ship Control Systems Symposium (iSCSS), November 7 – 10, 2022, Delft Netherlands.

C. Tschritter, A.N. Johnston, L. Vu, T. Nguyen, D.A. Wetz, T.V. Vu, J. Langston, H. Ravindra, M. Stanovich, K. Schoder, M. Steurer, C.M. Schegan, and J.M. Heinzel, 'Advanced Load Shed and Predictive Ramp Rate Control of a Medium Voltage AC/DC Testbed,' 2023 IEEE Electric Ship Technologies Symposium (ESTS), August 1 – 4, 2023, Alexandria, Virginia

C. Tschritter, A.N. Johnston, L. Vu, T. Nguyen, D.A. Wetz, T.V. Vu, J. Langston, H. Ravindra, M. Stanovich, K. Schoder, M. Steurer, C.M. Schegan, and J.M. Heinzel, 'A Prediction and Load Shed Based Approach of Controlling a Medium Voltage AC/DC Testbed,' Journal of Marine Engineering Technology (JMET), https://doi.org/10.1080/20464177.2024.2340897, April 2024.

A.N. Johnston, Z.R. Bailey, D.A. Wetz, G.K. Turner, and J.M. Heinzel, 'Design and Commissioning of a Medium Voltage Testbed with Emulated Pulsed Loads,' Naval Engineers Journal, Volume 134, Number 3, 1 September 2022, pp. 129-144(16).

A.N. Johnston, G.K. Turner, D.A. Wetz, Z.R. Bailey, C. Schegan, J.M. Heinzel, and M. Giuliano, 'Emulation of a Single Zone of an Integrated Power System,' American Society of Naval Engineers (ASNE) Intelligent Ships Symposium (ISS), April 28 – 29, 2021, VIRTUAL.

A.N. Johnston, D.A. Wetz, R. Madani, A. Davoudi, G.K. Turner, D.A. Dodson, B.J. McRee, Z. Bailey, D. Pullaguram, J.M. Heinzel, M. Giuliano, and C.M. Schegan, 'Mitigating Transient Loads in Medium-Voltage Direct Current Microgrids,' Proceedings of the 2020 American Society of Naval Engineers (ASNE) Advanced Machinery Technology Symposium (AMTS), October 7-8, 2020, Philadelphia, Pennsylvania.

A.N. Johnston, D.A. Wetz, Z. Bailey, D.A. Dodson, B.J. McRee, and J.M. Heinzel, 'A Medium Voltage, Distributed Power Generation Testbed Deploying Transient Loads,' Proceedings of the International Ship Control Systems Symposium (iSCSS), October 6 – 8, 2020, Delft, Netherlands.

Energy profiling and planning and multi-objective optimization algorithms comparison performance

D Mitropoulou, MSc[a]*, D *Dembinskas, MSc[a] ,Dr T. Miao, PhD[a]*

[a]*RH Marine Netherlands BV, The Netherlands;*

*Corresponding author. Email: despoina.mitropoulou@rhmarine.com

Synopsis

The modernization of naval ships requires continuous advancements in technology to ensure adaptability, sustainability, extended range, and reliability. In response to these challenges, the naval shipbuilding sector has adopted key technology trends, particularly in the fields of automation and the design of integrated, smart cyber-physical systems. As part of this development a research in the performance evaluation of a previously developed novel Energy Management and Control System (EMS) is performed, to ensure the smooth operational capabilities of naval vessels, addressing the necessity of designing high-performance ships for all operating conditions.

This paper aims to build upon the developments by exploring the potential benefits of integrating different multi-objective optimization algorithms into the EMS of naval ships. The traditional focus on fuel cost savings in current energy management systems may not fully handle the versatility of naval vessels, as each mission entails distinct operational requirements. The ability to adapt to a wide variety of missions in a continuous changing world underscores the importance of developing more sophisticated integrated control algorithms with multiple optimization goals. Yet, complexity can have an impact in terms of performance, and simplicity can be of great importance when choosing the most optimal optimization algorithm.

The proposed review is focusing on the performance comparison between four optimization algorithms: Lagrange-multiplier, Nelder Mead, interior point and active set and analyses the performance in terms of cost and computing time when optimizing shipboard energy production in a hybrid propulsion plant with a hybrid power supply. It considers the trade-off between multiple and conflicting operating goals, including fuel savings, maintenance costs, noise, and IR of on-board assets. To ensure equitable comparisons, a previously developed model of an Offshore Patrol Vessel, as published in INEC 2020 with title "Multi-objective optimization and Energy Management: adapt your ship to every mission" has been employed for testing and benchmarking purposes. Simulation results under varying operational profiles highlight the applicability, validity, and advantages of different EMS algorithms compared to conventional rule-based strategies currently in use.

Keywords: Energy Management; Hybrid propulsion; Multi-objective optimization; Algorithms performance

1. Introduction

The introduction of increasingly smart automation systems and advanced user interfaces has facilitated more precise operational information onboard, enabling integrated system configuration management advice. Using data from interconnected management systems such as the Integrated Mission Management System (IMMS), Signature Management System, and Integrated Platform Management System (IPMS), ships can achieve optimized behaviour and performance tailored to their holistic operational demands.

For instance, selecting the optimal propulsion plant configuration across various operational conditions can lead to reductions in signatures (including noise and Infra-Red (IR)), Life Cycle Costs (LCC) (including maintenance and fuel consumption), and exhaust emissions. Additionally, new objectives with respect to the ship's operational mode, like optimized route planning or just-in-time arrival can be implemented, considering the most efficient route.

Optimization is particularly applicable to systems where operational choices exist regarding power generation, distribution, and/or consumption with more than one type of source like combination of a diesel generator with a battery device, e.g. hybrid power generation and propulsion plants. In such systems, power can be generated from different sources/storage devices and can be used to propel the vessel through various means, allowing for flexibility in energy generation, distribution, and consumption. Each mission's specific optimization goals and priorities and load profile influence these choices, determining the vessel's optimal operating point.

Authors' Biographies

D. Mitropoulou obtained a master's degree in electrical engineering at the National Technical University of Athens and a master degree in Sustainable Energy Technology from Delft University of Technology. She is the manager of Power Systems department at RH Marine.

D. Dembinskas obtained a bachelor's degree in electrical and Electronics engineering at the Siauliai University of Lithuania, a master degree in Electrical engineering at Delft University of Technology and a master degree in Wind energy at Norwegian University of Science and Technology. He is a Consultant of Power Systems department at RH Marine.

T. Miao obtained his PhD in Engineering Technology from the KU Leuven, with the topic of autonomous sailing, a master degree in Maritime Engineering from the Norwegian University of Science and a master degree in Maritime Engineering from the Royal Institute of Technology. He is a consultant at RH Marine.

As previously mentioned (Mitropoulou, et al., 2020) , current technology enables momentary automated optimization of electric power generation, primarily focused on fuel savings (Breijs & Amam, 2016) (Geertsma, Negenborn, Visser, & Hopman, 2017) (Kalikatzarakis, Geertsma, Boonen, Visser, & Negenborn, 2018). The significant value of such optimization algorithms has been demonstrated through various project results, indicating the potential for further gains by incorporating multiple optimization goals. Building upon this, efforts have been made to optimize ship operation towards minimal total cost of ownership (TCO) by accounting for battery lifetime in the control system (Mitropoulou & Elling, 2018).

For this paper in order to conduct the performance comparison between the four different optimization algorithms: Lagrange-multiplier, Nelder Mead, interior point (Lagrange-based), and active set (Lagrange-based), and analyse the performance in terms of cost and computing time, tests were conducted on all four aforementioned algorithms. These tests were applied across three sailing scenarios, entailing differing power demands and limitations, as well as diverse weight factor configurations. Notably, the Lagrange multiplier algorithm is currently employed in our existing Rhodium Energy Management System (EMS). Our objective is to distinguish and analyse the differences between the Lagrange method and the newly tested approaches, thereby informing and directing our future research and development efforts. It is important to acknowledge a minor deviation in this analysis: we incorporated nonlinear models in the constraints (specifically pertaining to the battery and electrical motor). Consequently, we employed numerical implementation to approximate the optimal solution point, as opposed to traditional analytical resolution techniques involving matrix calculations.

Section 2 provides a description of the studied system, focusing on a single system to illustrate the proposed EMS and demonstrate its feasibility.

Section 3 outlines the optimization objectives and constraints considered.

Section 4 discusses how to integrate multiple conflicting objectives into a single optimization goal, with different solution methods described.

Section 5 presents case studies comparing the proposed solution method to a baseline, demonstrating its validity.

Finally, conclusions, discussions, and results on dynamic profiles are provided in subsequent sections.

2. Description of the system

The research work puts emphasis on several optimisation strategies for the Energy Management System. The optimisation strategies are selected in the way that they can be adapted to every configuration of the power plant and propulsion plant. This research case focuses on previously adapted single line model (Mitropoulou, et al., 2020) which is presented in Figure 1.

The single line consists of the following objects:

- Main engines (ME) 2x each 9.1 MW nominal power and connected to its own shaft and propeller
- Diesel generators (DG) 4x each have rated power of 2.45 MW
- Battery banks (BB) 2x each with a capacity of 1 MWh with a maximum discharge/charge rate of 5C, resulting in 5 MW.
- Electric motors (EM) 2x each with a rated power of 3 MW with power take in (PTI) and power take off (PTO) capability.

Figure 1 represents the single line divided into three segments: propulsion, DC distribution and AC distribution. Going from the top of the diagram, which is the propulsion section consists of the main engines, gearboxes with the clutches, electric motors, with a capability of the power take in and power take out, and controllable pitch propellers. The middle position of the single line consists of the DC distribution network, which includes diesel generators connected to rectifiers and then to the DC switchboards. These switchboards supply power to several rectified auxiliary loads. The efficiency of all converters are taken into account including a factor of the power flow direction, which means that power is delivered or absorbed. The bottom section illustrates the low-voltage AC distribution and corresponding AC auxiliary loads.

For the fare comparison and following aforementioned developments the control diagram is kept as well the same aboard the vessel, which is depicted in Figure 2. This study centers on the energy management system (EMS), represented as the tertiary control loop. Information is transmitted from the EMS to both the primary control layers, namely the converters, governors, and active voltage regulators (AVRs), and the secondary control layers, including the power management system (PMS), propulsion control system (PCS), and battery management system (BMS). The PCS provides inputs to the main propulsion system, such as power and speed set points for the ME and PTI, as well as pitch control for the propeller. In instances where the motor operates as a shaft generator (i.e., PTO), it receives its power and speed set points from the PMS. Inputs for the PCS are derived from lever position, autopilot data, and dynamic position (DP) information, culminating in a virtual shaft speed set point. This set point, along with actual shaft power feedback from the PCS, is provided to the EMS.

The EMS provides power setpoints to the batteries and PTOs, diesel generators receive power and speed setpoints. Positioned one control level below the EMS, the PMS is tasked with distributing power setpoints based on load demand. In its turn, the PMS provides the auxiliary power feedback to the EMS. One level above the EMS, the integrated mission management system (IMMS), which consist of the mission planning and signature management systems. These systems translate operational modes into weight factors, as well as constraints and provides them to the EMS. In addition, supplementary information, including load prediction profiles, is supplied by various third-party applications through a high-level control system like integrated platform management system (IPMS) to the EMS.
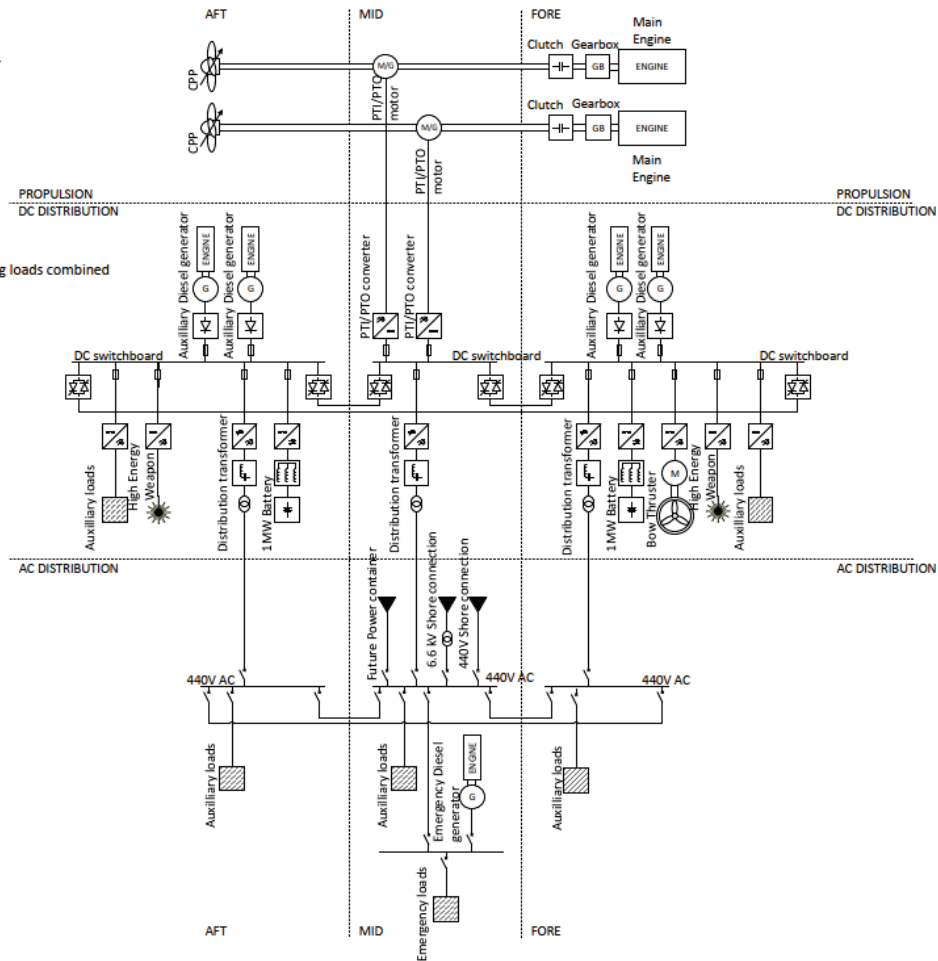
Figure 1: Single line diagram
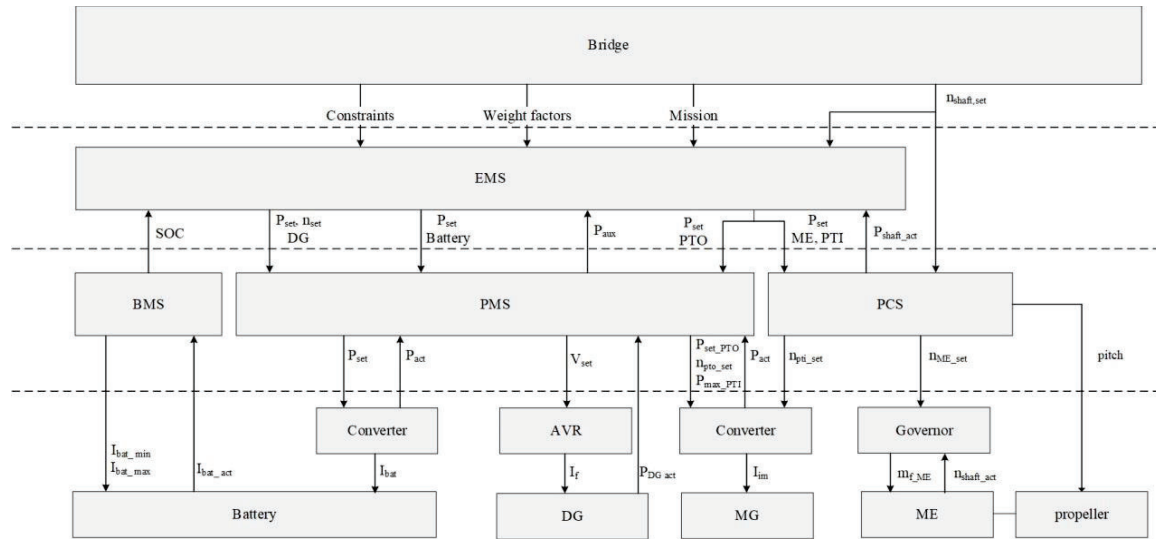
Figure 2: Control diagram

3. Definition of the optimization problem

This section describes the optimisation goals that are implemented in the different algorithms. As mentioned in the research (Mitropoulou, et al., 2020), this continuation of the previous work utilises the same operational constrains, goals for the optimisation and total objective function. In the further subsections, the operational constrains, the goals for the optimisation and the objective function will be briefly explained.

One thing must be kept in mind, sometimes different or even conflicting goals are defined. They consist of the following: Fuel consumption, life cycle cost (LCC), Noise and Infra-red signature (IR). The importance of the goals is defined by the weight factors. These weight factors are an input to the system from the user or the IMMS system and closely depend on the mission and operational requirements.

3.1. Model set-up and constraints

3.1.1. Fuel Consumption

In order to optimize the system with respect to fuel consumption, we consider the fuel consumed by the main engines (MEs) and diesel generators (DGs). Additionally, we represent the batteries with a virtual fuel consumption. This approach is focusing on optimizing the equipment's set points for the current moment, without considering past or future states. Batteries, however, inherently manage energy storage over time, meaning the energy they store must have required fuel used for charging in the past. Moreover, charging the battery now incurs a fuel cost, but it can save fuel in the future by discharging instead of using the DGs or MEs for power generation. Therefore, we account for a virtual fuel cost when using the batteries.
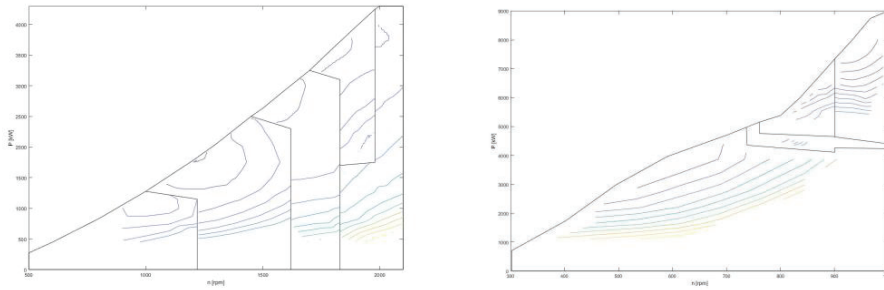
a. Auxiliary DG   b. ME

Figure 3: Auxiliary DG (left) and Main engine (right) fuel maps (in g/s)

Fuel consumption for the DGs and MEs is determined by using fuel maps, illustrated in Figures 3(a) and 3(b), respectively. The DG fuel map is divided into five regions, and the ME map into four, each delineated by black bounding boxes. These maps feature isolines representing fuel consumption rates (in grams per second). To estimate consumption from these maps, we fitted polynomial functions to each region. This process yielded a function,

$$f_{fuel,com,reg} = \sum_{j=0}^{J} \sum_{k=0}^{K} a_{,com,reg,j,k} n^j P^k, \tag{1}$$

where $a_{,com,reg,j,k}$ are the coefficients for the polynomial for component com operating in region reg. Furthermore n is the speed of the component and P its power output. Also, J and K are the degrees of the polynomial in the speed and power respectively. To integrate the battery's fuel cost, we use two equivalence factors, Eq_{char} and , Eq_{disc} which represent the expected future fuel savings per unit of energy charged into the battery now, while estimates the fuel previously consumed to charge each unit of energy. Different use cases were simulated with different equivalent factors and from these cases the better battery utilization was at lower Eq factors.
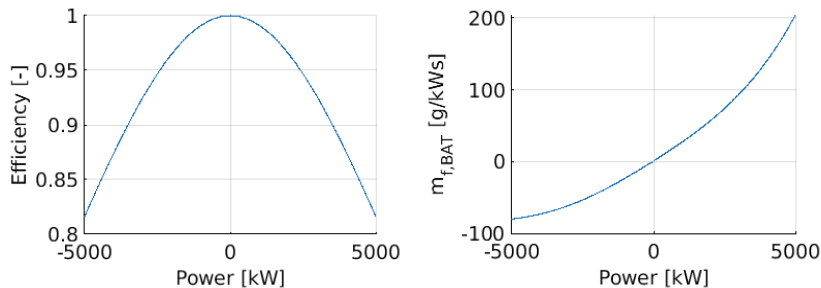
a) Efficiency   b) Equivalent fuel consumption

Figure 4: Battery efficiency and equivalent fuel consumption.

The battery's fuel cost is determined by multiplying the energy charged or discharged by the respective equivalence factor, depending on whether the battery is charging or discharging. Figures 4(a) and 4(b) show the battery efficiency and the resulting equivalent fuel consumption using $Eq_{char} = Eq_{disc} = 0.025$, which because of simulations proved to be optimal value for the best battery utilisation.
To determine the total fuel consumption of the system, we sum the fuel consumption of each individual component.

3.1.2. LCC

Regarding the LCC goal of the optimization, the focus was primarily on the main engines (MEs), diesel generators (DGs), and batteries, as these components were identified as the most critical contributors to the overall cost. The LCC for the MEs and DGs was modelled by incorporating a fixed operational cost, along with a cost

component that varies linearly with the speed of the respective ME or DG. This relationship can be expressed as follows for any given ME or DG.

$$f_{LCC,i} = a_{fixed} + a_{speed}n \; if \; P > 0, \tag{2}$$

where the coefficients are given by a_{fixed} and a_{speed} .

The Life Cycle Cost (LCC) of the battery was modelled with higher complexity due to the several factors that affect its lifetime. Battery degradation is influenced by the amount of power drawn from it and its current State of Charge (SoC). Additionally, discharging the battery when its SoC is low leads to greater damage. This relationship is depicted in Figure 5, which illustrates the LCC model for the battery. It is important to highlight that, for the purposes of this model, we assumed that charging does not significantly contribute to battery damage. The LCC of battery i were modelled using:

$$f_{LCC,i} = \frac{\Delta \text{Damage}_i a_{rpl} 3600}{\Delta t} + a_{fixed} \; if \; P_i \neq 0, \tag{3}$$

here ΔDamage_i is the damage incurred by the discharging of the battery, a_{rpl} is a coefficient representing the replacement costs of the battery and a_{fixed} is a fixed cost for operating the battery. Furthermore, Δt is the aforementioned time at which the system is expected to operate with the given operational values. To calculate the damage incurred by the discharging the battery at certain SoC levels, the following model is used.

$$CTF(DoD) = \sum_{i=0}^{4} a_i DoD^{-i}, \tag{4}$$

Figure 5: Battery lifecycle cost

where $CTF(DoD))$ are the current number of cycles to failure depending on the depth of discharge DoD and a_i are model coefficients. The EMS keeps track of the current DoD and calculates the new expected DoD using the currently calculated settings. The damage to the battery, is calculated using:

$$Damage = \frac{1}{CTF(DoD)\varepsilon}, \tag{5}$$

where ε is a factor based on the current charge rate or current discharge rate of the battery (Li, et al., 2017) . The previous level of degradation of the battery is continuously monitored, and the expected new degradation is calculated based on the current operating conditions of the battery. The degradation difference (ΔDamage) is then determined by subtracting the old degradation value from the new degradation estimate.

3.1.3. Noise

The noise optimisation goal was modelled for both the main engines and the diesel generators. Due to the lack of availability of maps on the engine noise relative to speed and power, an assumption of the maps was generated, and they were based on expert inputs as shown in Figure 6(a) and Figure 6(b) for the ME and DG noise, respectively. The main assumption is that the MEs contain resonance frequencies and thus produce the highest noise levels at 500 and 900 rpm at 95 dB. The noise generation at the lowest and highest speed (400 and 1000 rpm) are the lowest, which is about 20 dB lower. Furthermore, there is another dip in noise output at 750 rpm, with a reduction of about 10 dB compared to the peak value. These values are then further scaled based on power output, which means more power relates to higher noise output. The same assumptions were made for the diesel generators, where the values were scaled for the different speed envelopes of the DGs.
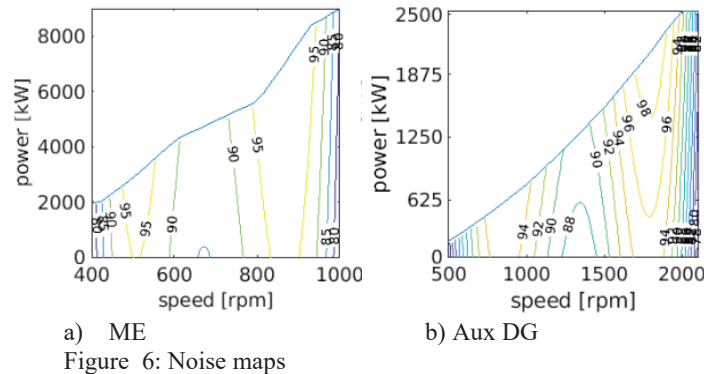
a) ME   b) Aux DG
Figure 6: Noise maps

As with the fuel consumption, the produced noise was approximated by component com using a polynomial as presented:

$$f_{noise,com} = \sum_{j=0}^{J} \sum_{k=0}^{K} a_{com,j,k}\, n^j P^k, \tag{6}$$

here n and P are the speed and power of the component and $a_{com,j,k}$ are the coefficients for the polynomial utilised to model the component's noise. These results were obtained with approximations similarly as for the fuel maps.

The overall system noise was obtained by taking the maximum of the modelled noise output on all main engines and diesel generators in this system. So that, the resulting noise of the system is the noise output of the loudest component.

3.1.4. IR

As previously mentioned in the previous paper (Mitropoulou, et al., 2020) the infrared goal is considered being produced by the main engines only. The model map of the IR output for a ME is based on speed and power and was generated using a high fidelity model (Kalikatzarakis, Geertsma, Boonen, Visser, & Negenborn, 2018). The resulting model map was approximated using a polynomial function and was separated into two regions, which is given in Figure 7. This resulted in a modelled IR output of ME i operating in region reg given by function:

$$f_{IR,i,reg} = \sum_{j=0}^{J} \sum_{k=0}^{K} a_{j,k,reg}\, n^j P^k, \tag{7}$$

here n and P are the speed and power output of the main engine, respectively. Furthermore, $a_{j,k,reg}$ are the coefficients of the polynomial in region reg.
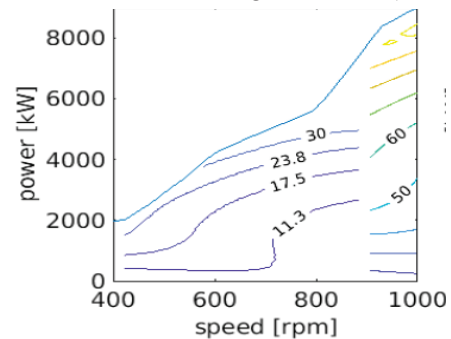
Figure 7: Main engine IR map

3.1.5. Total objective function

To incorporate these goals of fuel, LCC, noise and IR together the following approach is utilised. This is because calculated goals output values in different domains. As an example, fuel consumption is calculated in grams per second, where noise levels are outputted in decibels. Therefore, for the better comparison of the different objectives, these are normalised. The normalisation is followed by multiplication of each objective by a weight factor. The weight factors can take a value within [0-1] and sum up to 1. Resulting in a total objective function which is obtained by summing each normalised and weighted goal. As it can be observed below, the total objective function is given by:

$$f_{obj}(x) = w_{fuel} \frac{f_{fuel}}{f_{fuel}^{norm}} + w_{LCC} \frac{f_{LCC}}{f_{LCC}^{norm}} + w_{noise} \frac{f_{noise}}{f_{noise}^{norm}} + w_{IR} \frac{f_{IR}}{f_{IR}^{norm}}, \tag{8}$$

here, $f_{fuel}, f_{LCC}, f_{noise}$ and f_{IR} are calculated as described above and depend on the decided control values P_{ME}, P_{DG}, n_{DG}, P_{EM}, and P_{bat}). The normalization factors $f_{fuel}^{norm}, f_{LCC}^{norm}, f_{noise}^{norm}$ and f_{IR}^{norm} are computed as follows. A baseline is calculated for a given set of inputs. This set is the control inputs, when the battery is not used, and the propulsive power is generated as much as it can be possible by the MEs. The DGs generate power to support the electric loads and a minimum number of DGs is utilised. The electric motors are used in motoring mode when the main engine, which shares a shaft with the electric motor, is unable to provide sufficient propulsive load on its own. In situations where any of the electric motors demand additional power, the diesel generators would increase their output to supply the load. This baseline configuration establishes the initial values for various optimization goals. These baseline values are then used as normalization factors, allowing each objective to be measured as a relative increase or decrease from the baseline. This normalization ensures that different objectives are comparable on a common scale.

4. Optimisation algorithms

Four algorithms were investigated in this paper. The main purpose of the investigation was performance and total cost. The optimisation algorithms are listed below with a brief introduction.

4.1. Lagrange multiplier

The Lagrange multiplier algorithm is a method used for solving constrained optimization problems. It works by creating a Lagrangian function, which combines the original objective function with the constraints, each multiplied by a Lagrange multiplier. This function is then analyzed by taking its derivatives and setting them to zero to find critical points. Solving these resulting equations provides values that meet both the gradient of the original function and the constraints simultaneously. By evaluating the original objective function at these critical points, one can determine the maximum or minimum values within the given constraints. This algorithm is extensively used across various scientific fields due to its efficiency in addressing optimization problems that involve constraints.

4.2. Interior-Point Algorithm

Interior-point algorithms are advanced optimization techniques grounded in principles of convex optimization and numerical analysis. These methods solve constrained optimization problems by iteratively refining solutions within the feasible region's interior. They use barrier functions to ensure constraints are fulfilled throughout the process. Using sophisticated numerical methods and linear algebra, interior-point algorithms navigate complex, high-dimensional solution spaces. Their robustness and efficiency make them invaluable for optimizing complex systems under constraints, applicable in several fields such as engineering, economics, and finance.

4.3. Active-Set Algorithm

The active-set algorithm is a specialized numerical optimization method designed for solving nonlinear constrained problems, particularly those with a few active constraints compared to the total set. It iteratively converges on solutions by concentrating computational resources on the active constraints that are binding or nearly binding. This approach aims to minimize a quadratic approximation of the objective function. During the process, the algorithm updates the active set based on any newly identified constraints that are violated. Convergence is achieved when criteria like optimal conditions or specific tolerances are met. The strength of this algorithm lies in its ability to exploit the sparsity of active constraints, making it well-suited for problems with a limited number of such constraints. However, it may struggle with large-scale problems or dynamically changing constraint sets, often necessitating the use of alternative methods like interior-point algorithms or sequential quadratic programming.

4.4. Nelder-Mead Algorithm

The Nelder-Mead algorithm, also known as the simplex or downhill simplex method, is a technique for nonlinear optimization, particularly effective for smooth but potentially non-convex objective functions. It starts by forming a simplex in the parameter space, typically centered around an initial guess of the optimal solution. The algorithm iteratively evaluates the objective function at each vertex of the simplex and adjusts the simplex through operations like reflection, expansion, contraction, or shrinkage to explore the parameter space and improve the solution. Convergence is achieved when the objective function meets a predefined tolerance level or when the simplex's size sufficiently decreases. While the Nelder-Mead algorithm is appreciated for its simplicity and independence from gradient information, it can converge slowly, especially in high-dimensional or poorly conditioned scenarios, and it does not guarantee finding a global optimum. Despite these limitations, its flexibility and effectiveness across a wide range of optimization problems have led to its widespread use.

5. Simulation & Evaluation

5.1. Simulation

Simulations were conducted in Matlab to compare the energy-saving performance and computing time of the aforementioned four algorithms. All simulations were performed on a Windows 10 system running on a laptop equipped with an Intel i9 processor. The ship model used in the simulation is based on a previously developed model of an Offshore Patrol Vessel. We defined three scenarios, representing different missions from low to high energy requirements in order to test the algorithms. These settings are derived from previous work and correspond with those presented in the paper published by RH Marine, Damen, and TNO (Mitropoulou, et al., 2020). The normalization factors of the cost function are used to obtain the equivalent cost for different aspects and remain consistent across all scenarios and have been defined based on the parameters provided in the table.

The specifications of each scenario are listed in Table 1, including the ship's current state (initial state for optimization, such as ship speed, shaft speed, and State of Charge (SoC) of the battery bank), power demands and certain properties (e.g., the battery's equivalent charge and discharge factors).

Table 1: Current ship states and demands for three scenarios

Parameters	unit	Scenario		
		1	2	3
Ship speed	knot	20	20	20
Shaft speed - portside	rpm	75	97	129
Shaft speed - starboard	rpm	75	97	129
Shaft power demand - ps	kW	1710	3650	8640
Shaft power demand - stb	kW	1710	3650	8640
Auxiliary loads	kW	1650	1650	1650
State of charge of battery 1	-	0.7	0.7	0.7
State of charge of battery 2	-	0.7	0.7	0.7
Equivalent charge factor	-	0.035	0.035	0.035
Equivalent discharge factor	-	0.035	0.035	0.035
Safety margin	-	0.99	0.99	0.99
Normalization factor - fuel	-	293.8110		
Normalization factor - LCC	-	146.3675		
Normalization factor - noise	-	94.4147		
Normalization factor - IR	-	44.3437		

A notable feature of our testing methodology is that the on/off statuses of the main engines (MEs) and diesel generators (DGs) are not directly modified within the algorithms. Instead, these statuses are pre-configured in a comprehensive list or table that includes all possible component combinations. Initially, we assess whether each configuration meets the demand requirements. Among the feasible configurations, we then select the one that minimizes operational costs. This approach enables us to explore more efficient combinations of operational states (e.g., all MEs and DG1 are on, while the other DGs are off) for each algorithm.

A benchmark solution is used for the performance comparison, which is not optimal but meets the power demands, based on the experience and knowledge from previous projects and sailings. In this benchmark, the battery power is always set to 0, which means batteries are manually turned off when we do not use EMS. The results of all algorithms are compared to the benchmark and the difference percentages are calculated. The total power of all main engines is, theoretically, the sum of the demand for shaft power and losses.

Table 2: Benchmark outputs for three scenarios

Parameters	unit	Scenarios		
		1	2	3
Power output, port side main engine	kW	1823.227	3856.582	9100.000
Power output, starboard side main engine	kW	1823.227	3856.582	9100.000
Speed of the 1st diesel generator	rpm	2099.000	2099.000	2099.000
Speed of the 2nd diesel generator	Rpm	2099.000	0	0
Speed of the 3rd diesel generator	Rpm	2099.000	0	0
Speed of the 4th diesel generator	Rpm	0	0	0
Power output, 1st diesel generator	kW	550.768	1650	1677.627
Power output, 2nd diesel generator	kW	550.768	0	0
Power output, 3rd diesel generator	kW	550.768	0	0
Power output, 4th diesel generator	kW	0	0	0
Power output/input, 1st battery	kW	0	0	0
Power output/input, 2nd battery	kW	0	0	0

Due to the possibility of applying weight factors, tests are conducted not only with multiple scenarios but also with various combinations of weight factors. For the two-objective cases, the weight factor combinations range from 0.1 for fuel and 0.9 for LCC to 0.9 for fuel and 0.1 for LCC. A detailed example is provided for a weight factor combination of 0.5(50%) on fuel cost and 0.5(50%) on LCC, which is also defined as the OPEX mode. For the four-objective case, the weight factor combinations change in two patterns. In one pattern, fuel and LCC are paired and share the same values, while IR and noise are also paired and vary in the same manner. The other pattern involves a fixed weight factor set (0.1, 0.2, 0.3, and 0.4). One detailed example is given below for the balance mode (25% weight on each aspect).

It is noted that for the four-objective case, simulations were conducted using only the interior-point, active-set, and Nelder-Mead methods. The Lagrange method was not employed because it requires manual calculation of the derivatives of both the cost function and constraints. This process can be particularly challenging with nonlinear objective functions.

Table 3: Output of power sources using three algorithms in the OPEX weight-factor setting (50% on fuel, and 50% on LCC) of the two-objective case in scenario 1

Parameters	Unit	Lagrange	Interior point	Active set	Nelder Mead
Main Enginer power ps	kW	0.000	0.000	0.000	0.000
Main Enginer power stb	kw	3560.378	0.000	0.000	3288.803
Battery bank 1 power	kW	187.411	339.683	0.000	0.000
Battery bank 2 power	kW	187.411	339.683	0.000	0.000
Diesel generator 1 power	kW	1572.699	2317.982	1771.777	2176.790
Diesel generator 2 power	kW	0.000	2317.982	1771.777	0.000
Diesel generator 3 power	kW	0.000	0.000	1771.777	0.000
Diesel generator 4 power	kW	0.000	0.000	0.000	0.000
Diesel generator 1 speed	rpm	1724.230	2043.398	1894.506	1932.576
Diesel generator 2 speed	rpm	0.000	2043.398	1894.506	0.000
Diesel generator 3 speed	rpm	0.000	0.000	1894.506	0.000
Diesel generator 4 speed	rpm	0.000	0.000	0.000	0.000

Scenario 1
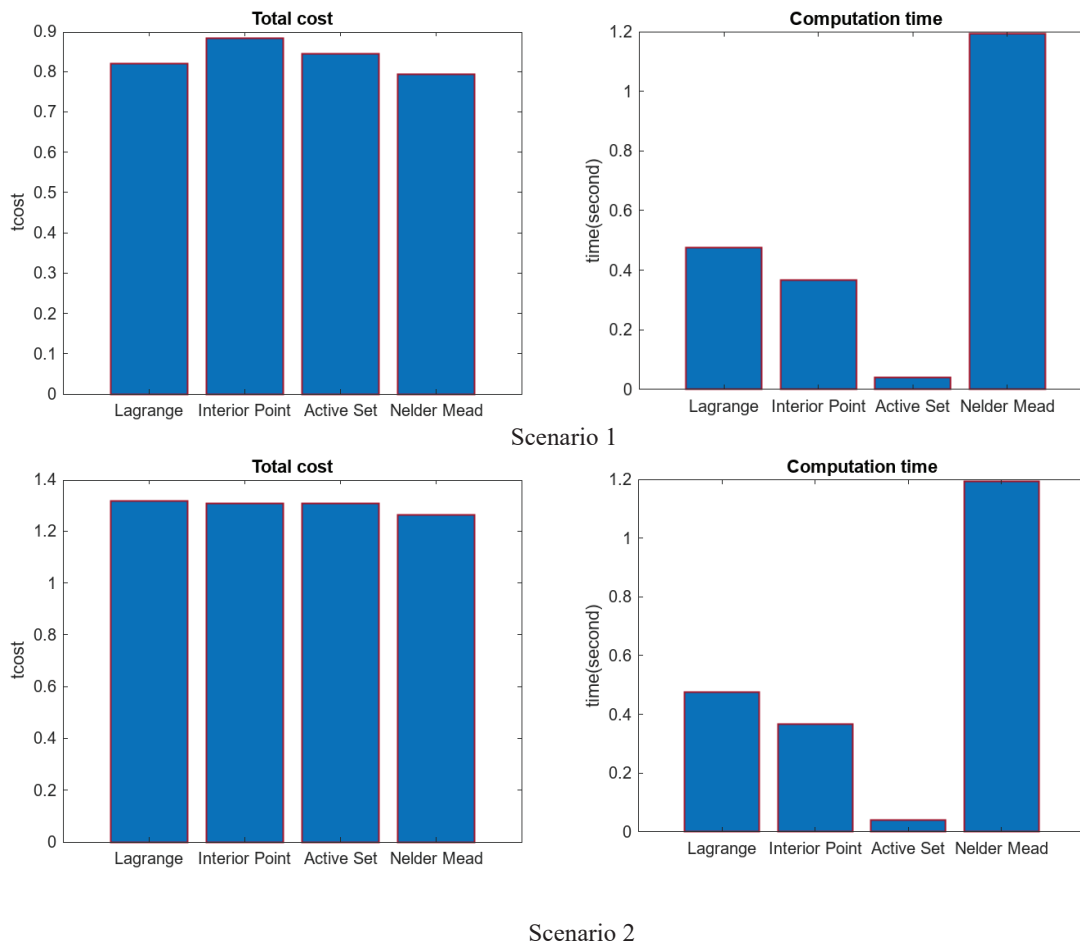
Scenario 2

Figure 8: One example of two-objective case - OPEX (weight factor 50% fuel 50% LCC)

Table 4: Output of power sources using three algorithms in the balance weight-factor setting (25% on fuel, 25% on LCC, 25% on IR, 25% on noise) of the four-objective case in scenario 1

Parameters	Unit	Interior point	Active set	Nelder Mead
Main Enginer power ps	kW	0.000	0.000	0.000
Main Enginer power stb	Kw	0.000	0.000	0.000
Battery bank 1 power	kW	339.683	339.683	316.273
Battery bank 2 power	kW	339.683	339.683	316.273
Diesel generator 1 power	kW	2317.982	2317.982	2341.394
Diesel generator 2 power	kW	2317.982	2317.982	2341.390
Diesel generator 3 power	kW	0.000	0.000	0.000
Diesel generator 4 power	kW	0.000	0.000	0.000
Diesel generator 1 speed	rpm	2043.398	2043.398	2099.928
Diesel generator 2 speed	rpm	2043.398	2043.398	2099.928
Diesel generator 3 speed	rpm	0.000	0.000	0.000
Diesel generator 4 speed	rpm	0.000	0.000	0.000
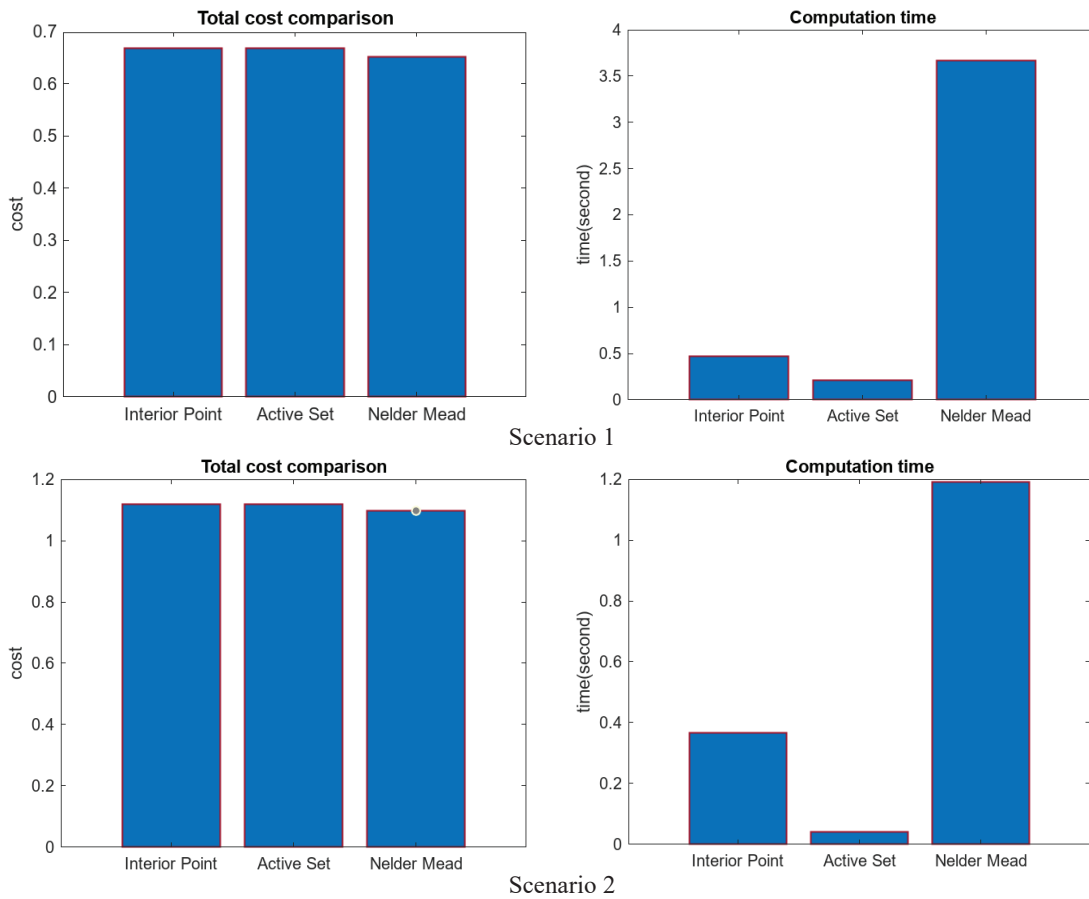
Figure 9: One example in four-objective – balance (weight factor 25% fuel 25% LCC 25% IR 25% noise)

5.2. Evaluation

The simulation results indicate that the Nelder-Mead method outperforms the Lagrange and two other methods in terms of cost in most cases. However, in certain scenarios, such as the two-objective case in scenario 1 with weight factors of 0.1 for fuel and 0.9 for LCC, the Nelder-Mead solution is not the most cost-effective (with interior-point and/or active-set methods performing better). Nevertheless, it seems that consistently performs better than the Lagrange method in all other cases. The improvement in cost efficiency between the Lagrange and Nelder-Mead methods ranges from approximately 1% to 8% across the tested cases.

The average computational time of the Nelder-Mead method is the longest in most cases. Occasionally, the interior-point method has the longest computational time (e.g., in scenario 5 with only the fuel objective), but this is not common. Although the Nelder-Mead method takes longer than the Lagrange method, the computation time remains within the acceptable limits for the EMS system's maximum desired calculation period of 60 seconds.

One limitation of the Lagrange method during this test is its case/model specificity. Particularly, when the cost function, equation, or constraints change, the derivatives must be updated accordingly. This becomes difficult with nonlinear models, as significant additional work is required due to its limitations in handling nonlinear cases. The fuel map used in this test comprises different regions, each with distinct coefficients or even different polynomials of varying orders. The Lagrange method cannot automatically switch among these regions, necessitating additional effort to specify the settings. In contrast, the Nelder-Mead method does not rely on derivatives, thereby reducing the need for additional work when introducing new cases, factors, or models. This makes it more adaptable for future changes.

Table 5: Total cost and computation time of the four algorithms with different weight factor combinations in two-objective optimization case of scenario 1

W_fuel	W_LCC	Reference cost	Lagrange		Interior point		Active set		Nelder Mead	
			Total cost	Comp. time	Total cost	Comp. time	Total cost	Comp. time	Total cost	Comp. time
0.1	0.9	1.1495	0.6689 (58.19%)	1.6742	**0.5790 (50.37%)**	0.4412	**0.5790 (50.37%)**	0.3847	0.5817 (50.61%)	4.4976
0.2	0.8	1.1682	0.7066 (60.48%)	1.7004	0.6451 (55.23%)	0.4108	0.6451 (55.23%)	0.3882	**0.6327 (54.16%)**	5.4334
0.3	0.7	1.1869	0.7443 (62.70%)	1.7053	0.7113 (59.93%)	0.4260	0.7113 (59.93%)	0.3743	**0.6836 (57.59%)**	3.9637
0.4	0.6	1.2057	0.7820 (64.86%)	1.7338	0.7774 (64.48%)	0.4863	0.7774 (64.48%)	0.3784	**0.7346 (60.93%)**	3.6676
0.5	0.5	1.2244	0.8197 (66.94%)	1.7153	0.8834 (72.15%)	0.6068	0.8436 (68.90%)	0.3802	**0.7940 (64.85%)**	4.7439
0.6	0.4	1.2431	0.8574 (68.97%)	1.7134	0.9263 (74.52%)	0.5075	0.9097 (73.18%)	0.3779	**0.8397 (67.55%)**	4.6157
0.7	0.3	1.2619	0.8951 (70.93%)	1.7068	0.9565 (75.80%)	0.5917	0.9565 (75.80%)	0.3848	**0.8918 (70.67%)**	4.0779
0.8	0.2	1.2806	0.9328 (72.84%)	1.7198	0.9358 (73.08%)	0.5969	0.9358 (73.08%)	0.3737	**0.9021 (70.44%)**	4.8002
0.9	0.1	1.2994	0.8333 (64.14%)	1.7208	0.9085 (69.92%)	0.8679	0.9085 (69.92%)	0.3273	**0.8240 (63.42%)**	6.6095

Table 6: Total cost and computation time of the four algorithms with different weight factor combinations in two-objective optimization case of scenario 2

W_fuel	W_LCC	Reference cost	Lagrange		Interior point		Active set		Nelder Mead	
			Total cost	Comp. time	Total cost	Comp. time	Total cost	Comp. time	Total cost	Comp. time
0.1	0.9	0.9258	0.9048 (97.73%)	0.3456	0.9090 (98.18%)	0.2671	0.9090 (98.18%)	0.1468	**0.8640 (93.33%)**	1.6474
0.2	0.8	1.0272	1.0076 (98.09%)	0.3492	1.0088 (98.21%)	0.2493	1.0088 (98.21%)	0.1404	**0.9881 (96.19%)**	1.4357
0.3	0.7	1.1286	1.1104 (98.39%)	0.3412	1.1086 (98.23%)	0.2969	1.1086 (98.23%)	0.1406	**1.0685 (94.67%)**	1.2300
0.4	0.6	1.2300	1.2132 (98.63%)	0.3443	1.2085 (98.25%)	0.2857	1.2085 (98.25%)	0.1434	**1.1606 (94.36%)**	1.2948
0.5	0.5	1.3314	1.3160 (98.84%)	0.3362	1.3083 (98.27%)	0.2633	1.3083 (98.27%)	0.1393	**1.2621 (94.80%)**	1.6161
0.6	0.4	1.4327	1.4188 (99.02%)	0.3530	1.4081 (98.28%)	0.2636	1.4081 (98.28%)	0.1437	**1.3507 (94.27%)**	1.2748
0.7	0.3	1.5341	1.5215 (99.18%)	0.3449	1.5080 (98.30%)	0.2726	1.5080 (98.30%)	0.1391	**1.4835 (96.70%)**	1.3350
0.8	0.2	1.6355	1.6243 (99.32%)	0.3464	1.6078 (98.31%)	0.2815	1.6078 (98.31%)	0.1400	**1.5439 (94.40%)**	1.1766
0.9	0.1	1.7369	1.7232 (99.21%)	0.3473	1.7076 (98.32%)	0.5049	1.7076 (98.32%)	0.1375	**1.6088 (92.63%)**	1.7600

Table 7: Total cost and computation time of the four algorithms with different weight factor combinations in two-objective optimization case of scenario 3

W_fuel	W_LCC	Reference cost	Lagrange		Interior point		Active set		Nelder Mead	
			Total cost	Comp. time	Total cost	Comp. time	Total cost	Comp. time	Total cost	Comp. time
0.1	0.9	1.1611	1.1532 (99.32%)	0.1509	1.1529 (99.29%)	0.3986	1.1552 (99.49%)	0.2217	**1.1489 (98.95%)**	1.2543
0.2	0.8	1.4341	1.4239 (99.29%)	0.1459	1.4226 (99.20%)	0.3728	1.4270 (99.50%)	0.2270	**1.4191 (98.95%)**	1.4445
0.3	0.7	1.7071	1.6946 (99.26%)	0.1654	1.6923 (99.13%)	0.4438	1.6986 (99.50%)	0.2144	**1.6920 (99.11%)**	1.1543
0.4	0.6	1.9802	1.9653 (99.25%)	0.1477	1.9620 (99.08%)	0.3877	1.9667 (99.32%)	0.2111	**1.9519 (98.57%)**	1.0586
0.5	0.5	2.2532	2.2359 (99.23%)	0.1522	2.2317 (99.05%)	0.3690	2.2354 (99.21%)	0.2198	**2.2266 (98.82%)**	1.3616
0.6	0.4	2.5262	2.5066 (99.22%)	0.1466	2.5015 (99.02%)	0.3580	2.5057 (99.19%)	0.2133	**2.4977 (98.87%)**	1.5435
0.7	0.3	2.7993	2.7773 (99.22%)	0.1507	2.7712 (99.00%)	0.3176	2.7748 (99.13%)	0.2211	**2.7700 (98.96%)**	1.3979
0.8	0.2	3.0723	3.0480 (99.21%)	0.1473	3.0409 (98.98%)	0.2859	3.0447 (99.10%)	0.2214	**3.0314 (98.67%)**	1.9626
0.9	0.1	3.3453	3.3186 (99.20%)	0.1459	3.3106 (98.96%)	0.3073	3.3145 (99.08%)	0.2216	**3.2139 (96.07%)**	2.2189

Table 8: Total cost and computation time of the four algorithms with different weight factor combinations in four-objective optimization case of scenario 1

Weight factor				Interior point		Active set		Nelder Mead	
W_fuel	W_LCC	W_noise	W_IR	Total cost	Time (s)	Total cost	Time (s)	Total cost	Time (s)
0.45	0.45	0.05	0.05	0.8402	0.5132	0.8093	0.2115	**0.7907**	3.3387
0.40	0.40	0.10	0.10	0.7969	2.3007	**0.7750**	0.4882	0.7865	3.7023
0.35	0.35	0.15	0.15	0.7537	0.4334	**0.7407**	0.1991	0.7510	4.0846
0.30	0.30	0.20	0.20	0.7015	0.4351	0.7064	0.1975	**0.6988**	3.2590
0.25	0.25	0.25	0.25	0.6673	0.5924	0.6673	0.1867	**0.6507**	3.4811
0.20	0.20	0.30	0.30	0.6240	0.4665	0.6240	0.1899	**0.6030**	3.3847
0.15	0.15	0.35	0.35	0.5808	0.4885	0.5808	0.1927	**0.5551**	2.6862
0.10	0.10	0.40	0.40	0.5376	0.4344	0.5376	0.1991	**0.5082**	3.6932
0.05	0.05	0.45	0.45	0.4944	0.9328	0.4944	0.2062	**0.4596**	2.7352
0.40	0.30	0.20	0.10	0.8203	0.4816	0.8203	0.2046	**0.8105**	3.9088
0.10	0.20	0.30	0.40	0.5142	0.3920	0.5142	0.1900	**0.4910**	2.8459

Table 9: Total cost and computation time of the four algorithms with different weight factor combinations in four-objective optimization case of scenario 2

Weight factor				Interior point		Active set		Nelder Mead	
W_fuel	W_LCC	W_noise	W_IR	Total cost	Time (s)	Total cost	Time (s)	Total cost	Time (s)
0.45	0.45	0.05	0.05	1.2703	0.2067	1.2703	0.0396	**1.2305**	1.2104
0.40	0.40	0.10	0.10	1.2324	0.2046	1.2324	0.0409	**1.2140**	1.1614
0.35	0.35	0.15	0.15	1.1944	0.2191	1.1944	0.0398	**1.1746**	1.1896
0.3	0.30	0.20	0.20	1.1565	0.2192	1.1565	0.0418	**1.1479**	1.1852
0.25	0.25	0.25	0.25	1.1185	0.2107	1.1185	0.0409	**1.0975**	0.9684
0.20	0.20	0.30	0.30	1.0806	0.2272	1.0806	0.0396	**1.0502**	1.3762
0.15	0.15	0.35	0.35	1.0426	0.2060	1.0426	0.0401	**1.0059**	1.4648
0.10	0.10	0.40	0.40	0.9563	0.3456	1.0047	0.0414	**0.9405**	0.9165
0.05	0.05	0.45	0.45	**0.8306**	1.4590	0.9581	0.0392	0.8410	1.2540

Table 10: Total cost and computation time of the four algorithms with different weight factor combinations in four-objective optimization case of scenario 3

Weight factor				Interior point		Active set		Nelder Mead	
W_fuel	W_LCC	W_noise	W_IR	Total cost	Time (s)	Total cost	Time (s)	Total cost	Time (s)
0.45	0.45	0.05	0.05	2.2149	0.3393	2.2185	0.1332	**2.2067**	1.1457
0.40	0.40	0.10	0.10	2.1981	0.3022	2.2015	0.0973	**2.1816**	1.0650
0.35	0.35	0.15	0.15	2.1813	0.3160	2.1845	0.0802	**2.1481**	1.1828
0.30	0.30	0.20	0.20	2.1320	0.9050	2.1674	0.0765	**2.1100**	1.0269
0.25	0.25	0.25	0.25	**1.9339**	1.6661	2.1502	0.0809	1.9897	1.4031
0.20	0.20	0.30	0.30	1.9247	0.8518	2.1330	0.0767	**1.8488**	1.4996
0.15	0.15	0.35	0.35	**1.6018**	1.6396	2.1156	0.0751	1.6499	1.5007
0.10	0.10	0.40	0.40	2.0973	0.2426	2.0983	0.0736	**1.4883**	1.2462
0.05	0.05	0.45	0.45	**1.2992**	1.5984	2.0810	0.0757	1.3108	1.3184

6. Conclusions & Recommendations

Based on our findings, overall, Nelder Mead has the best performance in terms of the total cost optimization in the majority of cases, compared to the Lagrange multiplier and other two variants. Though in some cases, e.g. the two-objective case with weight factors of fuel and LCC as 0.1 and 0.9 combination, the solution of Nelder Mead is not the best cost wisely (interior-point and/or active-set is better), it is always better than the Lagrange. The improvement percentage between Lagrange and Nelder Mead is around 1-8% according to the cases tested.

The average computational time of Nelder Mead is longest in the most cases. Sometimes interior-point is the longest (only fuel objective, scenario 3) but this is not common. Though the time is longer than the Lagrange, this duration still remains within the acceptable bounds for the EMS system's maximum desired calculation period (60 seconds).

One limitation of the Lagrange that became apparent during this test is that it is case/model specific. Especially, when the cost function or the constraints change, the derivatives need to be re-formulated. And when there are nonlinear models, more work needs to be performed additionally, such as linearization of non-linear models since Lagrange is limited in non-linear cases. The fuel map used in this test has different regions. In each region, different coefficients or even different polynomials with different orders are used. The Lagrange multiplier method cannot switch automatically among these regions and additional work needs to be done to specify the settings. On the

contrary, Nelder Mead does not use derivatives and thus does not require for much additional work when new cases or models need to be used, which makes it more general for future changes.

Considering the current results, our conclusion is adopting a hybrid approach: executing multiple algorithms simultaneously, either across separate cores in a centralized system or on distinct computers in a distributed setup, would be optimal. This would utilize the strengths of each method, aiming for the best outcome. Given the computational power we would have, this strategy is feasible.

As an alternative methodology, when one algorithm is used, in order to minimize the risk, one could consider enhancing the Lagrange or the other two methods with a high-level pre-configuration layer. This layer would determine specific operational regions and the on/off status of the MEs and DGs. Such an approach could align closely with the expectations of on board crew who have predefined requirements. This would allow to perform optimizations within these set parameters, potentially fulfilling stakeholder's needs more effectively.

Acknowledgements

References

Mitropoulou, D., Kalikatzarakis, M., Van Der Klauw, T., Blockland, A. Geertsma, R., Bucurenciu, A., Dembinskas, D. 2020. Multi-objective optimization and Energy Management: adapt your ship to every mission, in: Proceedings of the 16th international naval engineering conference, pp. 1–12.

Barton, R.R., Ivey Jr, J.S., 1996. Nelder-mead simplex modifications for simulation optimization. Management Science 42, 954–973.

Breijs, A., Amam, E., 2016. Energy management–adapt your engine to every mission, in: Proceedings of the 13th international naval engineering conference, pp. 1–8.

Geertsma, R., Negenborn, R., Visser, K., Hopman, J., 2017. Design and control of hybrid power and propulsion systems for smart ships: A review of developments. Applied Energy 194, 30–54.

Kalikatzarakis, M., Geertsma, R., Boonen, E., Visser, K., Negenborn, R., 2018. Ship energy management for hybrid propulsion and power supply with shore charging. Control Engineering Practice 76, 133–154.

Li, J., Xiong, R., Yang, Q., Liang, F., Zhang, M., Yuan, W., 2017. Design/test of a hybrid energy storage system for primary frequency control using a dynamic droop method in an isolated microgrid power system. Applied Energy 201, 257–269.

Mitropoulou, D., Elling, L., 2018. New developments in energy management-battery lifetime incorporation and power consumption forecasting, in: Proceedings of the 14th international naval engineering conference, pp. 1–12.

Sciarretta, A., Serrao, L., Dewangan, P., Tona, P., Bergshoeff, E., Bordons, C., Charmpa, L., Elbert, P., Eriksson, L., Hofman, T., et al., 2014. A control benchmark on the energy management of a plug-in hybrid electric vehicle. Control engineering practice 29, 287–298.

Sundstrom, O., Guzzella, L., 2009. A generic dynamic programming matlab function, in: 2009 IEEE control applications,(CCA) & intelligent control,(ISIC), IEEE. pp. 1625–1630.

van Vugt, H., Sciberras, E., de Vries, L., Heslop, J., Roskilly, A.P., 2016. Ship power system modelling for the control and optimisation of multiple alternative energy sources on-board a ship, in: Proc. 15th Int. Conf. Comput. IT Appl. Martime Ind. (COMPIT), pp. 240–254.

Comprehensive Approaches to Enhance Maritime Wireless Networks: A Survey

D J Powell, MEng, PhD[a1]

[a]*Global Maritime Services, London, UK.*
Corresponding author. Email: jas.powell@globalmaritimeservices.com

Synopsis

In this review paper we explore the advancements and challenges in maritime communication systems. Traditional maritime communication methods, such as high-frequency (HF), very-high-frequency (VHF), and satellite communications, are increasingly insufficient due to their limited bandwidth and high costs. These limitations necessitate the adoption of advanced communication technologies like Mobile Ad Hoc Networks (MANETs), Vehicular Ad Hoc Networks (VANETs), Wireless Mesh Networks (WMNs), and Software-Defined Radios (SDRs). We highlight the potential of cognitive radio technology and cooperative networking to dynamically utilize underutilized frequency bands and enhance network performance through node collaboration. These technologies aim to provide robust, scalable communication solutions adaptable to the challenging maritime environment. Despite advancements, challenges such as network scalability, latency management, data security, and the dynamic nature of maritime environments persist. Here we review recent developments in maritime communication, focusing on the implementation and performance of ad hoc wireless networks, SDRs, and integrated network architectures. The paper emphasizes the importance of adaptive routing protocols, efficient network formation, robust hardware integration, and continuous monitoring. In conclusion, the integration of cognitive and cooperative technologies offers promising solutions for enhancing maritime communication, but ongoing research and development are essential to address remaining challenges and optimize these systems for real-world applications.

Keywords: Marine systems; Wireless networks; Routing protocols; Ship interaction; Ship communication

1. Introduction

The maritime industry, a cornerstone of global trade and security, is undergoing a significant transformation driven by the need for advanced communication technologies. Traditional maritime communication systems, which primarily rely on high-frequency (HF), very-high-frequency (VHF), and satellite communications, are increasingly becoming inadequate to meet the modern demands of high-speed data transmission and real-time applications. HF and VHF systems offer limited bandwidth and low data rates, which are suitable for basic voice communications but fall short in supporting data-intensive operations like video surveillance and comprehensive situational awareness. Although satellite communications can provide broader coverage and higher data rates, their high costs and latency issues make them less viable for routine and widespread use in maritime operations, especially at higher latitudes.

Reliable communication links are essential for navigation, coordination, safety, and emergency response. However, the expansive and often remote nature of maritime domains poses significant challenges to traditional communication methods. Mobile Ad Hoc Networks (MANETs) and their specialized variants, such as Vehicular Ad Hoc Networks (VANETs), and Wireless Mesh Networks (WMNs), and software-defined radios (SDRs) have emerged as promising alternatives, offering dynamic, self-organizing capabilities that can form resilient, high-bandwidth networks without the need for fixed infrastructure. Cognitive radio technology allows for the opportunistic use of underutilized frequency bands, known as white spaces (WS), which can significantly improve the efficiency and cost-effectiveness of maritime communication systems. Cooperative networking, on the other hand, leverages the collaboration between network nodes to enhance overall network performance and reliability. These network technologies aim to provide robust and scalable communication solutions by integrating cognitive and cooperative technologies. Such networks can dynamically adapt to the maritime environment, ensuring seamless communication even in remote, harsh and challenging conditions.

Despite these advancements, significant challenges remain, including network scalability, latency management, data security, and the dynamic nature of maritime environments. Addressing these issues is critical for the successful deployment of next-generation maritime communication systems. This paper provides a comprehensive review of recent developments in maritime communication technologies, focusing on the implementation and performance of ad hoc wireless networks, SDRs, and integrated network architectures. By examining these innovations, we aim to highlight their potential to revolutionize maritime operations and outline the future directions for research and development in this field.

This review aims to synthesize the methodologies, technologies, and innovations presented in these studies, offering a holistic perspective on the advancements in communication protocols and systems. By exploring the

---

[1] Author Biography

Dr Jas Powell works as the Head of Engineering for Global Maritime Services and is currently exploring the use of AI enhanced sensors to work towards autonomous shipping.

complementary benefits of these solutions, this paper seeks to provide valuable insights for researchers, engineers, and stakeholders in the maritime and ad hoc networking domains.

In the subsequent sections, we will delve into the methodologies and technologies employed in the reviewed studies, compare their key findings and innovations, and discuss the practical implementations and future directions for research. This comprehensive analysis will guide the development of robust, scalable, and efficient communication systems, ultimately enhancing the connectivity and operational capabilities in maritime and wireless ad hoc networks.

2. Background

The maritime industry has long relied on traditional communication systems, primarily satellite links, for ensuring connectivity over vast oceanic expanses. However, these systems are often plagued by high costs and limited bandwidth, necessitating the exploration of alternative communication frameworks. The advent of cognitive and cooperative communication technologies offers promising solutions to these challenges.

Effective communication systems are essential for the operation and safety of maritime vessels. The maritime industry, which includes commercial shipping, ocean fishery, and naval operations, relies on robust communication links for navigation, coordination, and emergency response. Similarly, ad hoc networks, often used in military, emergency response, and remote sensing applications, require dynamic, decentralized communication solutions due to their lack of fixed infrastructure and mobile node configurations.

Maritime communication systems are integral to ensuring the safety, security, and efficiency of maritime operations. Traditionally, these systems have relied on high-frequency (HF), very-high-frequency (VHF), and satellite communication technologies. HF and VHF systems provide basic communication services but are limited by narrow bandwidth and low data transmission rates, making them insufficient for modern applications that require high-speed data transfer, such as real-time video monitoring and large-scale data exchange. Satellite communication systems, while capable of supporting higher data rates and broader coverage, are often associated with high costs and latency issues, limiting their feasibility for widespread use in routine operations.

The integration of advanced communication technologies in the maritime domain has become increasingly critical due to the growing demand for reliable, high-speed, and secure data exchange across various maritime platforms. This need has driven extensive research into MANETs, VANETs, WMNs, and blockchain-based security enhancements.

Given the increasing frequency and complexity of maritime activities, there is a pressing need for alternative communication technologies that offer higher data rates, lower latency, and cost-effective solutions. This need has driven research into the deployment of wireless ad hoc networks and the utilization of software-defined radios (SDRs) to form robust, flexible, and scalable maritime communication networks
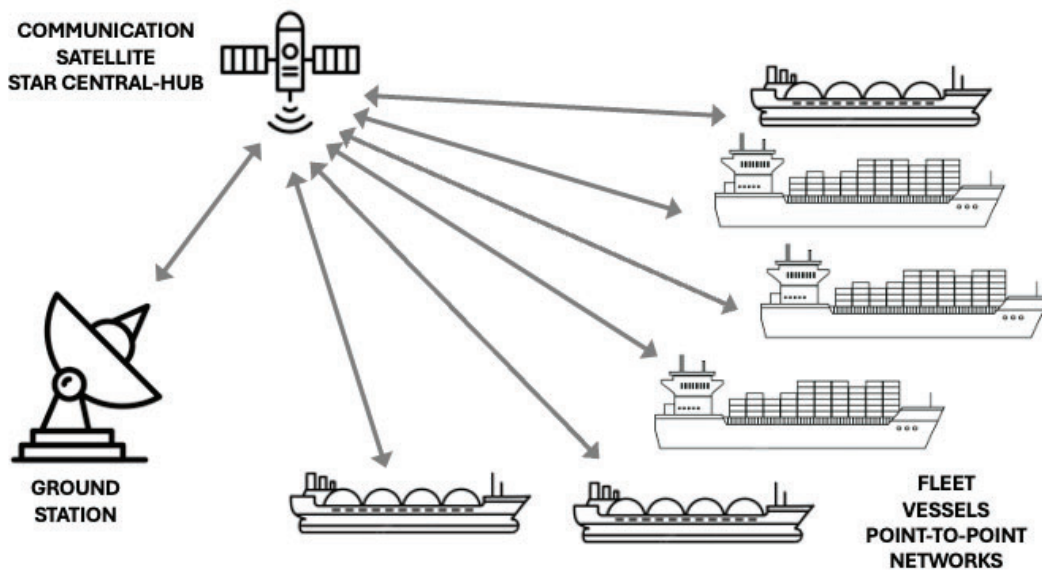
Figure 1: Example Star network topology showing a Ground Station (Command and Control) connected via Communication Satellite to all individual Fleet Vessels via Point-to-Point Network links.
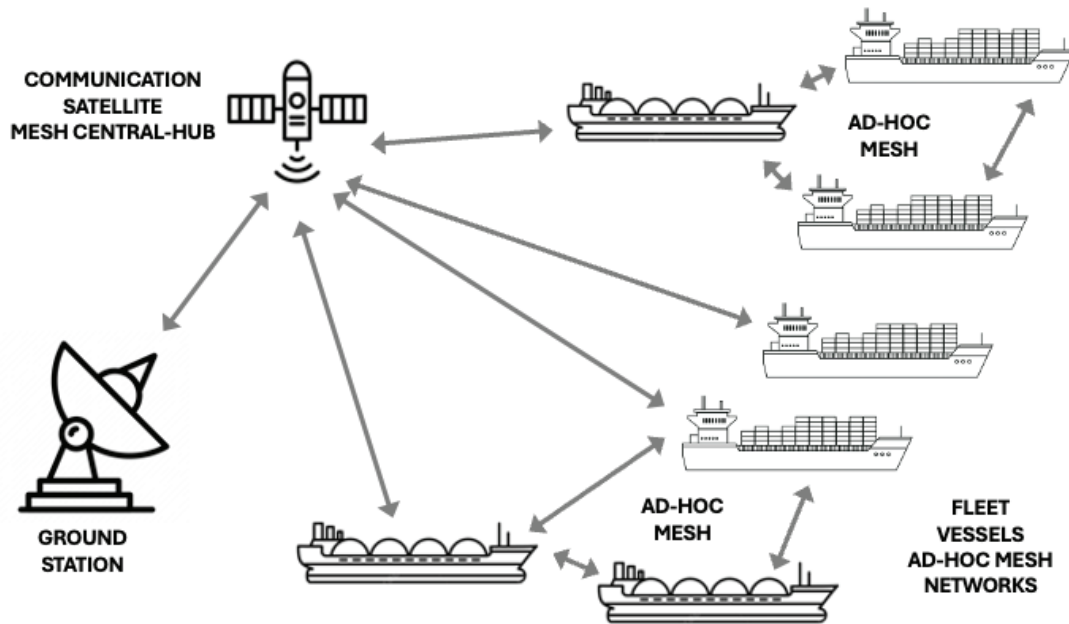
Figure 2: Example Ad-Hoc Mesh Network topology showing a Ground Station (Command and Control) connected via Communication Satellite to Fleet Vessels via Ad-Hoc Mesh Network links, in this topology the Fleet Vessels that do not have connectivity to the satellite use neighbouring vessels to share communications links and exchange valuable information.

3. Literature Review

3.1 Wireless Mesh Networks and Ad Hoc Networks

Akyildiz et al. (2005) provided an extensive survey of WMNs, discussing their architecture, characteristics, applications, and the key factors influencing protocol design. WMNs consist of mesh routers and clients, offering advantages such as low costs, easy maintenance, robustness, and reliable service coverage. The paper highlighted the potential of WMNs to integrate with various networks (e.g., Internet, cellular, IEEE 802.11) and their applicability in numerous areas, including home networking, community networks, and metropolitan area networks. The survey underscored the importance of scalability, Quality of Service (QoS), and security in protocol design, identifying the need for cross-layer designs and the integration of advanced technologies like multiple input/multiple output (MIMO) and cognitive radios to enhance WMN performance.

Boukerche et al. (2011) provided a comprehensive review of routing protocols for ad hoc wireless networks, emphasizing the absence of fixed infrastructure and the need for efficient, dynamic routing solutions. The paper categorized routing protocols into source-initiated (reactive), table-driven (proactive), hybrid, location-aware, multipath, hierarchical, multicast, geographical multicast, and power-aware protocols. A comparative analysis based on metrics such as throughput, packet delivery ratio, control overhead, and energy efficiency revealed that each protocol has specific strengths and weaknesses suited to different applications and network conditions. The study emphasized the need for scalable, energy-efficient, and robust routing solutions to handle high mobility and dynamic topologies in ad hoc networks.

Ad hoc networks, which enable direct communication between devices without the need for fixed infrastructure, are particularly suitable for maritime applications where traditional network setups are impractical. Agrawal et al. (2023) provide an exhaustive review of ad hoc networks, including MANETs, VANETs, WMNs, and wireless sensor networks (WSNs). They discuss various routing protocols such as proactive, reactive, and hybrid protocols, highlighting their impact on network performance in terms of speed, efficiency, and reliability. The study also addresses the unique challenges of ad hoc networks, including node mobility, bandwidth constraints, and error-prone channels, emphasizing the need for robust and efficient routing solutions tailored to dynamic environments like maritime settings.

3.2 Maritime Communication Networks

Ad hoc networks, characterized by their self-forming and self-healing capabilities, have emerged as a promising solution for enhancing maritime communication. These networks can dynamically organize mobile nodes (e.g., ships, buoys) into multi-hop networks, eliminating the need for fixed infrastructure. Various studies have explored the implementation of ad hoc networks in maritime contexts, highlighting their potential to support broadband data transmission over the sea.

For example, Vann (2010) examined the use of SDRs to create ad hoc meshed networks aimed at improving Maritime Interception Operations (MIO). The study demonstrated the feasibility of using SDRs to create robust, high-bandwidth communication networks capable of supporting voice, video, and data transmissions between Visit, Board, Search, and Seizure (VBSS) teams and command centres.

Laarhuis (2010) introduces MaritimeManet, a mobile ad hoc network specifically designed for maritime environments. Unlike traditional MANETs that rely on omni-directional antennas, MaritimeManet uses multiple directional antennas arranged in a circular pattern to achieve extended transmission ranges. This design enhances signal-to-noise ratios and mitigates the power problem associated with long-distance communication. MaritimeManet supports distributed applications like Sensors in Concert (SinC), which provides continuous and comprehensive maritime surveillance. The system's ability to self-organize and self-heal, coupled with its scalability, makes it a robust solution for various maritime applications.

Bai et al. (2012) investigated the feasibility of integrating various wireless communication technologies to provide efficient and cost-effective communication solutions for mobile users on ocean fishery vessels. Their study focused on analysing existing wireless technologies, understanding their propagation characteristics over the sea, and proposing an integrated wireless networking system. This system combines a MANET, cellular mobile network, and satellite mobile network to leverage the strengths of each. The proposed system architecture and the development of a prototype validated the feasibility and effectiveness of this integrated approach for enhancing communication capabilities in maritime environments.

Maritime environments present unique communication challenges, including signal reflections off the sea surface and fluctuating connectivity due to ship movements. Ejaz et al. (2013) address these challenges with the Maritime Two-State (MTS) routing protocol, specifically designed for maritime multi-hop wireless networks. The MTS protocol operates in two states: beaconing, where ships broadcast routing tables to nearby vessels, and predicting, where ships use historical data to predict future positions and reduce communication overhead. Simulation results indicate that the MTS protocol significantly outperforms existing protocols by reducing periodic updates, bandwidth utilization, jitter, and end-to-end delay, making it a highly effective solution for maritime communication.

WiMAX and LTE technologies have also been explored for enhancing maritime communications. Manoufali et al. (2014) discussed the potential of WiMAX-based maritime wireless mesh networks, which extend terrestrial broadband networks to coastal waters. These networks form multi-hop connections involving shore stations, ships, and other maritime structures. Such systems support high-speed data transmission, essential for applications like maritime safety and surveillance.

Sumić et al. (2015) investigated the optimization of data traffic routes for maritime vessels to address the high costs associated with satellite communication. Their research proposed a hybrid communication approach that integrates satellite and terrestrial links. By utilizing a mathematical model, they demonstrated how switching between satellite links on the high seas and terrestrial links near ports could significantly reduce costs and increase link capacity. The case study in the Netherlands highlighted the practical benefits, showing that the ship could save costs by spending 27.8% of its voyage within terrestrial link range. This approach underscores the potential of integrating terrestrial communication technologies to enhance the cost-efficiency and capacity of maritime data communications.

Xiao et al. (2020) focused on implementing video transmission over maritime ad hoc networks. The study developed video transmission software integrated with maritime broadband wireless ad hoc network systems. Utilizing MANET routers equipped with SDR platforms, the research demonstrated the capability to support multi-hop video transmission. This addresses the critical need for real-time video communication in maritime safety monitoring and accident investigation.

Seferagic et al. (2021) proposed a multimodal network architecture to enhance situational awareness among maritime vessels. The architecture integrates various network interfaces and employs an abstraction layer to manage multimodal communication, traffic, and QoS improvements. This approach ensures seamless and robust communication across different network technologies, supporting the growing demands for high data-rate applications in maritime environments.

In the context of extending network reach and flexibility, Berto et al. (2021) present a novel (long-range) LoRa-based mesh network that operates without traditional gateways. This gateway-free approach is particularly advantageous in maritime and remote applications, where infrastructure is sparse. The network leverages low-cost ESP32 Heltec WiFi LoRa V2 boards equipped with Semtech SX1276 LoRa transceivers, facilitating peer-to-peer communication and multi-hop networking. Their experimental results demonstrate significant improvements in communication efficiency and reliability, showcasing the potential of LoRa technology to support robust and scalable maritime communication systems.

Mishra et al. (2022) evaluated the feasibility of Sea Ad-Hoc Network (SANET) for maritime communications, comparing three routing protocols (Epidemic Routing Protocol, Randomized Rumor Spreading, and Spray and Wait) and three connecting technologies (WiMax, VHF, and Long-Range WiFi). The study demonstrated that SANET could effectively address the limitations of traditional communication systems

by providing infrastructure-less, flexible, and cost-effective communication solutions, particularly in regions with poor satellite coverage or during emergencies.

Wang et al. (2023) explored the application of MANETs for improving ship-to-ship communication and interaction. Their research focused on developing a network architecture that adapts dynamically to different navigation scenarios, such as open seas and congested coastal areas. By designing both intercommunication and cluster modes, the study provided a robust framework for managing communication in varying maritime environments.

The intercommunication mode, suitable for open seas with fewer ships, ensures stable and high-quality communication paths necessary for collision avoidance. Conversely, the cluster mode, ideal for congested areas, uses a hierarchical topology to efficiently manage communication among numerous ships.

3.3 Cognitive and Cooperative Technologies

The concept of maritime wireless mesh and ad hoc networks has gained traction as a viable alternative to satellite communication. These networks aim to provide high-speed, cost-effective communication by leveraging cognitive radio technology to exploit underutilized frequency bands, known as white spaces (WS).

In 2012, Zhou and Harada proposed a cognitive maritime wireless mesh/ad hoc network designed to opportunistically utilize available WS in the maritime spectrum. Their work laid the foundation for subsequent research by demonstrating the feasibility of cognitive radios in maritime settings to improve communication efficiency and reduce costs.

Building on the foundational work of Zhou and Harada, Yang et al. (2015) introduced the Cooperative Cognitive Maritime Wireless Mesh/Ad Hoc Networks (CCMWMAN) framework. This framework integrates cognitive and cooperative communication technologies to enhance network performance. The study emphasized the importance of game theory in managing resource allocation among network nodes, proposing a symmetrical system model and a price game based on payoff functions to achieve Nash equilibrium in cooperative communication scenarios.

In a follow-up study in 2016, Yang et al. expanded on their earlier work by developing a bi-level game theory model for resource allocation in cognitive maritime networks. This model addressed the interactions between primary users (PUs) and secondary users (SUs), employing a Stackelberg game to manage resource distribution efficiently. The proposed model demonstrated significant improvements in network throughput and overall system performance, highlighting the potential of game theory in optimizing maritime communication networks.

Peng et al. (2020) proposed an enhanced Ad-hoc On-Demand Distance Vector (AODV) routing protocol, termed AIS-aided AODV (A-AODV), tailored for MANET. This protocol leverages the Automatic Identification System (AIS) to reduce flooding during route discovery by utilizing ship location information. A-AODV maintains a ship-location table to store and use AIS data for efficient routing decisions, significantly lowering routing overhead. Experimental validation on a MANET testbed demonstrated that A-AODV supports multi-hop data transmission with lower routing overhead compared to standard AODV, highlighting the potential of integrating AIS data to improve routing efficiency and network performance in maritime environments.

Accurate classification of maritime vessels is essential for effective maritime surveillance and operational management. Krüger (2018) evaluates several ad hoc classification methods using real-life AIS data, including Decision Tree, Fuzzy Rule, k Nearest Neighbor (kNN), Neural Networks, and Naïve Bayes. The study finds that Decision Tree and Fuzzy Rule classifiers achieve the highest accuracy, providing reliable classification results. This research underscores the importance of robust data-driven methods in enhancing maritime situational awareness and improving operational efficiency in surveillance systems.

3.4 Secure Routing in Decentralized Networks

Neumann et al. (2018) addressed the challenges of secure routing in community mesh networks, which share characteristics with maritime networks due to their decentralized and open nature. They introduced the Securely Entrusted Multi-Topology Routing (SEMTOR) protocol, designed to establish cryptographically secure and individually trusted routing topologies without central management. SEMTOR allows each node to define its trusted nodes, ensuring secure and autonomous routing. The protocol's integration with the BMX7 routing protocol and extensive benchmarking demonstrated its scalability and efficiency in networks with hundreds of nodes. SEMTOR's robustness against various attacks and its ability to maintain secure communication paths in dynamic and diverse network environments highlight its relevance for maritime and other ad hoc applications.

Blockchain technology has emerged as a promising solution to enhance security and efficiency in ad hoc networks. Juarez et al. (2023) propose a dual layer blockchain architecture for VANETs, comprising an event chain and a reputation chain. This architecture employs Bayesian inference to dynamically update the reputation scores of nodes based on their behaviour, effectively identifying and mitigating malicious nodes. The study reports an 86% success rate in countering malicious behaviours through extensive simulations, highlighting the potential of blockchain technology to secure communication networks against various cyber threats in both terrestrial and maritime environments.

4. Practical Implementation

The practical implementation of advanced maritime communication systems involves several key considerations, ranging from the integration of new technologies into existing infrastructures to addressing the unique challenges posed by the maritime environment. The studies reviewed provide a comprehensive foundation for understanding these aspects and offer valuable insights into effective deployment strategies.

4.1 Network Planning, Configuration and Topology Design

Deploying ad hoc networks in maritime environments requires careful planning of network topology to ensure robust and reliable connectivity. Configuring SDRs for maritime operations requires careful planning of network parameters, such as frequency bands, modulation schemes, and power settings. The configuration should optimize coverage and data throughput while minimizing interference. Dynamic configuration capabilities allow SDRs to adapt to changing conditions and optimize performance in real-time, a feature crucial for maritime environments with varying signal propagation characteristics. Key considerations include node placement, transmission range, and network density.

4.2 Adaptive Routing Protocols

Implementing adaptive routing protocols is crucial for maintaining network performance in the dynamic maritime environment. Protocols like Ad-hoc On-Demand Distance Vector (AODV) and Optimized Link State Routing (OLSR) are suitable for dynamic and scalable networks. Protocols like the Maritime Two-State (MTS) routing protocol proposed by Ejaz et al. (2013) should be adapted and tested in real-world conditions to ensure they can handle the frequent topology changes and long transmission distances typical of maritime networks. Boukerche et al. (2011) reviewed various routing protocols suitable for ad hoc and practical protocol selection involves choosing the most suitable routing protocol (e.g., reactive, proactive, hybrid) based on specific application requirements and network conditions. Implementing multi-hop communication extends the network's reach and enhances its resilience. This requires developing efficient routing algorithms that can dynamically manage the network's topology and ensure data packets are delivered reliably across multiple hops.

4.3 Integration of Hardware

The deployment of Software-Defined Radios (SDRs) in maritime environments, as demonstrated by Vann (2010), involves equipping vessels with SDR units capable of forming ad hoc meshed networks. Peng et al. (2020) leveraged AIS data for efficient route discovery in maritime ad hoc networks. For practical implementation, ensure all vessels are equipped with AIS transponders and receivers to provide accurate real-time location data. Implementing data-driven vessel classification systems requires continuous collection and processing of AIS data. Krüger (2018) demonstrates the effectiveness of using real-life AIS data for vessel classification, highlighting the need for robust data preprocessing and feature extraction techniques to ensure accurate classification. These units must be ruggedized to withstand harsh maritime conditions, including exposure to saltwater, humidity, and temperature extremes. The installation process should ensure secure mounting and protection from physical damage while maintaining accessibility for maintenance and upgrades.

4.4 Network Formation

Establishing a MANET involves deploying network nodes on ships, buoys, and shore stations. The study by Xiao et al. (2020) illustrates the importance of a robust network management protocol that can handle the dynamic topology of maritime operations. MANETs should support self-forming and self-healing capabilities to ensure continuous communication links, even when individual nodes move or fail. Akyildiz et al. (2005) highlighted the potential of WMNs for providing robust communication in maritime and terrestrial applications including deployment of mesh routers and clients on vessels and coastal stations to create a multi-hop network, and implementing network management software to oversee mesh topology, optimize routes, and ensure load balancing.

4.5 Machine Learning Models

Deploying machine learning models, such as Decision Trees and Fuzzy Rule classifiers, involves training these models on historical AIS data and continuously updating them with new data to maintain accuracy. Real-time classification systems can be integrated into maritime surveillance platforms to provide operators with timely and accurate vessel identification.

4.6 Quality of Service (QoS) Management

Ensuring Quality of Service (QoS) is essential for applications that require high data rates and low latency, such as video surveillance and real-time monitoring. The multimodal architecture should include mechanisms for prioritizing traffic, managing bandwidth allocation, and minimizing latency. Techniques like traffic shaping and adaptive bandwidth management can help maintain QoS under varying network conditions.

4.7 Security Management

Implement robust security measures to protect data integrity and privacy, including encryption, authentication, and intrusion detection systems. Setting up a blockchain infrastructure involves deploying nodes capable of handling blockchain operations, such as verifying transactions and maintaining the ledger. The dual layer blockchain architecture proposed by Juarez et al. (2023) can be implemented using lightweight blockchain clients to minimize resource consumption while ensuring robust security and trust management. Developing and

deploying smart contracts on the blockchain can automate various network management tasks, such as reputation scoring and malicious node detection.

4.8 End-User Devices

Deploying video transmission systems requires equipping end-user devices, such as PCs and tablets, with appropriate software and hardware interfaces. These devices should connect seamlessly to MANET routers via Ethernet or wireless connections. User-friendly interfaces are crucial for ease of operation, allowing crew members to initiate and manage video communications with minimal technical expertise. Bai et al. (2012) proposed an integrated system combining MANET, cellular, and satellite networks. The practical network implementation included establishing a MANET among vessels for ship-to-ship communication and integration of this network with cellular gateways (for nearshore communication) and satellite gateways (for deep-sea communication).

4.9 Field Trials

Conducting extensive field trials is vital for validating the performance of the implemented systems. Trials should simulate various maritime scenarios, including open sea, coastal areas, and congested shipping lanes. Performance metrics such as data throughput, latency, packet loss, and network stability should be rigorously tested and analysed. The feedback from these trials can guide further optimizations and refinements.

4.10 Continuous Monitoring and Maintenance

Post-deployment, continuous monitoring of network performance and regular maintenance of hardware are essential to ensure long-term reliability. Implementing remote monitoring tools can help detect issues promptly and facilitate timely interventions. Regular updates to software and firmware can enhance functionality and security, adapting to evolving operational requirements.

In conclusion, the practical implementation of advanced maritime communication systems involves a comprehensive approach that integrates robust hardware, adaptive network configurations, multimodal architectures, and efficient software solutions. By addressing the specific challenges of the maritime environment and conducting thorough testing and validation, these systems can significantly enhance the operational capabilities and safety of maritime operations.

5. Key Performance Indicators

In the maritime domain, reliable and resilient communication networks are essential for ensuring safety, operational efficiency, and coordination between vessels, offshore platforms, and control centres. Network topologies, particularly in wireless environments, must address challenges posed by vast oceanic distances, dynamic node mobility (such as moving ships), and environmental factors like weather and interference. This paper addresses the comparison of traditional network topologies in maritime applications e.g. the wireless point-to-point (or star) topology and the wireless ad-hoc mesh topology, each requiring distinct Key Performance Indicators (KPIs) to measure their effectiveness and ensure optimal performance.

5.1 Wireless Point-to-Point (or Star) Network Topology

In a wireless star topology, all communication is centralized through a hub, which is typically a satellite, shore-based control center, or a dedicated base station on a large vessel. This centralized structure offers simplicity and predictability, but it also presents unique challenges due to the single point of failure at the hub. KPIs in this topology focus on monitoring the central node's performance and the links between it and the surrounding nodes.

5.1.1 Latency

Measuring the round-trip time (RTT) between vessels or offshore platforms and the central hub is critical, especially when supporting real-time applications like voice, navigation data transfer, or collision avoidance systems. High latency can cause delays in critical decision-making, especially in mission-critical maritime operations.

5.1.2 Throughput

This KPI tracks the rate of successful data transmission between nodes and the central hub. In maritime environments, where data-intensive applications such as remote monitoring, sensor data transmission, and video feeds are common, ensuring adequate throughput is essential. It is vital to assess the hub's ability to handle concurrent data streams from multiple nodes without becoming a bottleneck.

5.1.3 Packet Loss

Packet loss is particularly significant in maritime communications due to long distances and potential interference from the environment. High packet loss in a star topology can indicate signal degradation, congestion at the central hub, or issues with individual vessel connections. Continuous monitoring of packet loss is essential to maintain service reliability.

5.1.4 Hub Availability

The hub represents a single point of failure in the network. Therefore, ensuring its uptime and reliability is paramount. Any downtime at the hub could result in total communication breakdown, which is particularly detrimental in the maritime domain, where safety and real-time coordination are crucial.

5.1.5 Signal-to-Noise Ratio (SNR)

In maritime wireless communications, maintaining a strong SNR is essential. Long transmission distances and environmental factors like weather conditions or interference from other maritime communication systems can degrade the signal quality. A low SNR can lead to errors in data transmission, reduced throughput, and increased latency.

5.2 Wireless Ad-Hoc Mesh Network Topology

A wireless ad-hoc mesh network is decentralized, with nodes (vessels or platforms) forming direct connections with each other, allowing for dynamic routing and multiple communication paths. This topology provides greater redundancy and resilience but introduces challenges in network management, as there is no central point controlling the entire network. The KPIs for measuring the performance of a wireless ad-hoc mesh topology differ significantly from those in a star topology.

5.2.1 Hop Count

In a mesh topology, data packets may travel through multiple nodes before reaching their destination. The number of hops directly impacts network performance. Minimizing hop count reduces latency and increases the overall efficiency of the network. A lower hop count is particularly important for real-time communication services, such as voice over IP (VoIP) or emergency alerts.

5.2.2 Link Quality Indicator (LQI)

The LQI measures the quality and strength of links between nodes, which can vary dynamically in a maritime setting due to vessel movement, weather conditions, and distance. Monitoring LQI ensures that data is transmitted over the best possible links, improving the overall network reliability and performance.

5.2.3 Route Diversity

One of the key advantages of a mesh network is the ability to reroute data through multiple paths if one link fails. Route diversity measures the availability of alternative communication paths, providing insight into the network's resilience. High route diversity indicates that the network can withstand failures or disruptions without significant degradation in performance.

5.2.4 Mobility Support and Handoff

Given the highly dynamic nature of the maritime environment, where vessels are constantly moving, tracking the network's ability to support seamless mobility is critical. KPIs such as handoff times and the success rate of handoffs between nodes are crucial for maintaining uninterrupted communication as vessels move in and out of range.

5.2.5 Jitter

Jitter refers to the variation in packet arrival times. In an ad-hoc mesh network, where data may travel through several nodes and over changing paths, jitter can become a significant issue, especially for real-time services like voice and video. Monitoring jitter helps ensure that the network remains stable and that time-sensitive data is delivered reliably.

6. Conclusion

The transformation of maritime communication systems is critical to advancing the operational efficiency, safety, and security of maritime activities. Traditional communication technologies, including HF, VHF, and satellite systems, are increasingly inadequate to meet the modern requirements for high-speed, real-time data transmission essential for contemporary maritime operations. The exploration of wireless ad hoc networks, software-defined radios, and integrated multimodal network architectures presents promising solutions to these challenges.

The collective insights from these studies reveal the necessity of integrating terrestrial communication technologies, secure routing protocols, and AIS data to improve maritime communications. The hybrid approach of using both satellite and terrestrial links can be complemented by secure, decentralized routing mechanisms and efficient route discovery protocols. Future research should focus on further integrating these technologies to develop robust, cost-effective, and high-capacity communication systems for maritime and ad hoc networks. This integrated approach promises to address the unique challenges of these environments, providing reliable and efficient communication solutions for their growing demands.

The reviewed studies provide a wealth of insights and advancements in the field of communication solutions for maritime and ad hoc networks. The unique challenges posed by the vast and dynamic maritime environments, along with the decentralized nature of ad hoc networks, necessitate innovative and robust communication protocols. The key contributions from these studies underscore the importance of integrating diverse technologies and optimizing routing protocols to achieve reliable, cost-effective, and efficient communication.

Despite these advancements, several challenges persist, including network scalability, latency, data security, and the dynamic nature of maritime environments. Addressing these challenges requires ongoing research and development to optimize routing protocols, enhance the robustness of ad hoc networks, and integrate emerging

technologies such as 5G. Additionally, future research should focus on the practical deployment of these technologies in diverse maritime scenarios, ensuring their reliability and effectiveness in real-world conditions.

The exploration of cognitive and cooperative technologies within maritime wireless mesh/ad hoc networks mark a significant leap forward in the quest to enhance maritime communication. The integration of cognitive radio technologies with mesh networking has the potential to transform the maritime communication landscape, providing high-speed, cost-effective, and reliable connectivity that traditional satellite systems fail to offer.

Despite these advancements, several challenges remain. The dynamic and often harsh maritime environment poses significant obstacles to maintaining stable and reliable communication links. Fluctuating sea states, interference from maritime activities, and regulatory constraints on frequency use are critical issues that future research must address. Furthermore, the integration of emerging technologies, such as machine learning and artificial intelligence, offers promising avenues for optimizing resource allocation and network management.

The integration of advanced communication technologies in maritime operations is essential to meet the growing demand for reliable, high-speed, and secure data exchange. This technical review has examined several key studies that contribute to this evolving field, highlighting significant advancements and identifying areas for future research and development.

In conclusion, the development of cognitive and cooperative maritime wireless mesh/ad hoc networks represent a promising frontier in maritime communication. By leveraging the capabilities of cognitive radio and cooperative networking, these systems offer a path towards more efficient, cost-effective, and reliable maritime communication solutions. Continued research and development in this field are essential to overcoming existing challenges and fully realizing the potential of these innovative technologies. The future of maritime communication is bright, with cognitive and cooperative technologies poised to play a central role in driving this transformation.

7. Challenges

Despite significant advancements, several challenges remain in developing robust maritime communication networks. The dynamic and harsh maritime environment poses unique challenges such as fluctuating sea states and interference from maritime activities. Future research must address these issues by refining cognitive radio technologies and enhancing the resilience of communication protocols.

Moreover, the integration of advanced technologies like machine learning and artificial intelligence could further optimize resource allocation and network management. Ensuring the security and reliability of these networks is also crucial, given the increasing reliance on digital communication for maritime safety and navigation.

The development of cognitive and cooperative maritime wireless mesh/ad hoc networks represent a significant step towards achieving high-speed, cost-effective maritime communication. The integration of game theory into resource allocation strategies offers a promising approach to enhancing network performance and ensuring reliable communication in the dynamic maritime environment.

7.1 Scalability and Network Management

One of the primary challenges in both maritime and ad hoc networks is scalability. As the number of nodes increases, maintaining efficient and reliable communication becomes increasingly complex. Protocols must be designed to handle large-scale networks without compromising performance. Future research should focus on developing scalable routing protocols that can dynamically adjust to network size and topology changes, ensuring consistent performance.

7.2 Security and Trust Management

Security is a critical concern in decentralized networks. Neumann et al. (2018) addressed secure routing through the SEMTOR protocol, but the ever-evolving nature of security threats requires continuous improvement. Ensuring data integrity, preventing unauthorized access, and protecting against various attack vectors remain paramount. Future studies should explore advanced cryptographic techniques, distributed trust management systems, and real-time threat detection mechanisms to enhance network security. Maritime communication systems are vulnerable to various security threats, including spoofing, jamming, and cyber-attacks. The integration of blockchain technology, as explored by Juarez et al. (2023), offers promising solutions for enhancing security, but practical implementations and scalability remain challenges. Ensuring robust security while maintaining system performance is a critical area for further research

7.3 Integration of Emerging Technologies

The integration of emerging technologies such as cognitive radios, machine learning, and blockchain can potentially revolutionize maritime and ad hoc network communications. Cognitive radios can dynamically adjust frequencies to avoid interference, while machine learning algorithms can optimize routing decisions based on real-time data. Blockchain technology could provide a decentralized and secure method for managing trust and authentication. Research should focus on integrating these technologies into existing frameworks to enhance adaptability, efficiency, and security.

7.4 Energy Efficiency

Energy consumption is a critical factor, particularly for nodes in ad hoc networks and maritime vessels operating on limited power supplies. Boukerche et al. (2011) highlighted the importance of power-aware routing protocols. Future research should aim to develop energy-efficient communication protocols that minimize power consumption without sacrificing performance. Techniques such as energy-harvesting, sleep-mode operations, and optimized transmission scheduling can be explored to extend the operational life of network nodes. Energy efficiency is a significant concern for maritime communication systems, particularly for nodes deployed on buoys or autonomous vessels with limited power supplies. Efficient energy management strategies are needed to prolong the operational lifespan of these nodes without compromising communication quality.

7.5 Environmental and Physical Constraints

The highly dynamic nature of maritime environments presents a significant challenge for ad hoc networks. The movement of ships, variable weather conditions, and the vastness of the ocean can cause frequent changes in network topology, making it difficult to maintain stable and reliable communication links. Traditional routing protocols may not be adequate in such conditions, necessitating the development of more adaptive and resilient protocols. Maritime environments present unique physical and environmental challenges, including signal attenuation due to water, interference from weather conditions, and the curvature of the Earth affecting long-range communication. Bai et al. (2012) analyzed over-the-sea radio propagation effects, but further studies are needed to develop robust models that can predict and mitigate these challenges. Experimental validation in diverse maritime conditions is essential to refine these models.

7.6 Cost-Effectiveness

While integrating multiple communication technologies can enhance performance, it also increases complexity and cost. Sumić et al. (2015) and Bai et al. (2012) proposed hybrid approaches to balance cost and efficiency, but the economic feasibility of large-scale deployment remains a concern. Future research should focus on optimizing cost-effectiveness, exploring low-cost hardware solutions, and developing economic models to justify investments in advanced communication infrastructures.

7.7 Interoperability

Ensuring seamless interoperability between different communication technologies and protocols is vital for the success of integrated systems. Akyildiz et al. (2005) discussed the potential of WMNs to integrate with various networks, but practical implementation requires standardization and compatibility. Future work should aim at developing universal standards and protocols that facilitate seamless communication across different platforms and technologies. Maritime communication networks often face limitations in bandwidth and suffer from high latency due to the large distances involved. These constraints can hinder the performance of data-intensive applications and affect real-time communication. Innovative solutions that optimize bandwidth usage and reduce latency are crucial for improving the efficiency of maritime networks. The integration of various communication technologies, such as AIS, LoRa, MANETs, and blockchain, poses interoperability challenges. Ensuring seamless communication and data exchange between different systems and technologies requires standardized protocols and interfaces.

8. Future Directions

The advancement of cognitive and cooperative maritime wireless mesh/ad hoc networks mark a significant progression in maritime communication. However, the implementation and optimization of these technologies face several formidable challenges that require further research and innovative solutions.

8.1 Optimization of Routing Protocols:

Further research is needed to develop and optimize routing protocols tailored to maritime environments. Protocols must be adaptive to the dynamic nature of maritime operations, providing reliable and efficient routing under varying conditions. Studies should focus on reducing overhead, improving route discovery processes, and enhancing fault tolerance.

8.2 Network Scalability and Management:

One of the primary challenges in implementing maritime wireless communication systems is network scalability. As the number of nodes (ships, buoys, etc.) increases, the network must efficiently manage and maintain robust communication links. Ensuring consistent performance across a wide area, especially in dense maritime environments, requires sophisticated network management and optimization strategies. The dynamic nature of maritime operations, with constantly moving nodes, further complicates this task.

8.3 Latency and Data Transmission Rates:

Although significant progress has been made in enhancing data transmission rates, achieving low latency remains a critical challenge. Real-time applications, such as video surveillance and emergency response, demand minimal delays in data transmission. Wireless ad hoc networks and SDRs need to be optimized to reduce latency while maintaining high data rates, ensuring seamless and timely communication across maritime networks.

8.4 Interoperability with Existing Systems:

Integrating new communication technologies with existing maritime systems (HF, VHF, and satellite) is another challenge. Ensuring interoperability and seamless transition between different communication platforms

is necessary to provide continuous and reliable communication. This requires standardization efforts and the development of compatible interfaces and protocols.

8.5 Integration of Emerging Technologies:

Exploring the integration of emerging technologies, such as 5G and beyond, with maritime communication systems holds great potential. 5G technology promises ultra-low latency, high data rates, and enhanced connectivity, which can significantly benefit maritime operations. Research should focus on the practical implementation of 5G in maritime contexts, addressing coverage, deployment, and interoperability challenges.

8.6 Spectrum Management and Regulatory Constraints

Efficient utilization of white spaces is central to cognitive maritime networks, but it is accompanied by regulatory challenges. Different countries have varying regulations regarding the use of licensed but unused frequency bands. Harmonizing these regulations to allow seamless cognitive radio operations across international waters remains a critical issue. Additionally, ensuring that secondary users do not interfere with primary users is essential to comply with regulatory requirements and protect vital maritime communication channels. Future studies should focus on developing standardized regulatory frameworks and advanced spectrum sensing technologies to detect and avoid PU transmissions reliably.

8.7 Interference and Coexistence

The coexistence of multiple cognitive and non-cognitive communication systems in the maritime environment can lead to interference, affecting overall network performance. As maritime communication networks grow in complexity and density, managing this interference becomes increasingly challenging. Research into sophisticated interference mitigation techniques and cooperative communication protocols is necessary to ensure harmonious operation of diverse communication systems.

8.8 Development of Robust Security Measures

To address the data security challenges, further study is required to develop advanced encryption techniques, secure communication protocols, and intrusion detection systems specifically designed for maritime networks. Ensuring data integrity and confidentiality while maintaining high performance is a key area for future research. Maritime communication systems must handle sensitive information, including navigation data, surveillance footage, and emergency communications. Ensuring the security and privacy of this data is paramount. Ad hoc networks, due to their decentralized nature, are particularly vulnerable to security breaches. Robust encryption, secure routing protocols, and intrusion detection systems are essential to protect data integrity and prevent unauthorized access.

8.9 Environmental Adaptation Strategies

Developing communication technologies that can adapt to and mitigate the effects of harsh maritime environments is crucial. Research should explore advanced signal processing techniques, adaptive modulation schemes, and robust hardware designs that can operate reliably under challenging conditions. Maritime environments pose unique challenges, including harsh weather conditions, multipath propagation, and interference from physical obstacles such as waves and ships. These factors can significantly impact the performance and reliability of wireless communication systems. Developing resilient communication technologies that can withstand and adapt to these environmental conditions is crucial.

8.10 Large-Scale Field Trials

Conducting large-scale field trials and real-world experiments is essential to validate the performance and reliability of proposed communication technologies. These trials should involve various maritime scenarios, including open sea, coastal areas, and busy shipping lanes, to comprehensively assess the effectiveness of the technologies under different conditions.

In conclusion, while significant advancements have been made in maritime communication technologies, addressing the challenges of scalability, latency, security, environmental adaptation, and interoperability requires ongoing research and development. By focusing on these areas, future studies can further enhance the capabilities of maritime communication systems, ensuring they meet the evolving demands of modern maritime operations.

References

Agrawal, R., Faujdar, N., Tavera Romero, C.A., Sharma, O., Muttashar Abdulsahib, G., Khalaf, O.I., Mansoor, R.F., Ghoneim, O.A. (2023) Classification and comparison of ad hoc networks: A review, Egyptian Informatics Journal, Vol 24, 1, pp1-25, doi.org/10.1016/j.eij.2022.10.004

Akyildiz, I. F., Wang, X., & Wang, W. (2005). Wireless mesh networks: A survey. Computer Networks 47, pp445–487, doi.org/10.1016/j.comnet.2004.12.001

Bai, Y., Du, W., Shen, C. (2012). Over-the-Sea Radio Propagation and Integrated Wireless Networking for Ocean Fishery Vessels. In: Sénac, P., Ott, M., Seneviratne, A. (eds) Wireless Communications and Applications. ICWCA 2011. Lecture Notes of the Institute for Computer Sciences, Social Informatics and Telecommunications Engineering, vol 72. pp 180–190, doi.org/10.1007/978-3-642-29157-9_17

Berto, R.; Napoletano, P.; Savi, M. (2021) A LoRa-Based Mesh Network for Peer-to-Peer Long-Range Communication. Sensors, 21, 4314. doi.org/10.3390/s21134314

Boukerche, A., Turgut, B., Aydin, N., Ahmad, M. Z., Bölöni, L., & Turgut, D. (2011). Routing protocols in ad hoc networks: A survey. Computer Networks, 55(13), 3032-3080. doi.org/10.1016/j.comnet.2011.05.010

Ejaz, W., Manzoor, K., Kim, H.J., Jang, B.T., Jin, G.J., Kim, H.S., (2013) Two-state routing protocol for maritime multi-hop wireless networks, Computers & Electrical Engineering, Vol 39, 6, pp1854-1866, doi.org/10.1016/j.compeleceng.2013.03.011

Juárez R., Bordel B., (2023) Augmenting Vehicular Ad Hoc Network Security and Efficiency with Blockchain: A Probabilistic Identification and Malicious Node Mitigation Strategy, Electronics, 12(23), pp4794, doi.org/10.3390/electronics12234794

Krüger, M., (2018) Experimental Comparison of Ad Hoc Methods for Classification of Maritime Vessels Based on Real-Life AIS Data, 21st International Conference on Information Fusion (FUSION), Cambridge, UK, 2018, pp. 1-7, doi.org/10.23919/ICIF.2018.8455362

Laarhuis, J.H., "MaritimeManet: Mobile ad-hoc networking at sea," (2010) International WaterSide Security Conference, Carrara, Italy, pp. 1-6, doi.org/10.1109/WSSC.2010.5730256

Manoufali, M., Alshaer, H., Kong, P., & Jimaa, S. (2014). An Overview of Maritime Wireless Mesh Communication Technologies and Protocols. International Journal of Business Data Communications and Networking (IJBDCN), 10(1), 1-29. doi.org/10.4018/ijbdcn.2014010101

Mishra, N.; Kastner, M.; Jahn, C., (2022) : Marine communication for shipping: Using ad-hoc networks at sea, International Conference of Logistics (HICL), Vol. 33, pp. 523-557, doi.org/10.15480/882.4715

Neumann, A., Navarro, L., Cerdà-Alabern, L. (2018). Enabling individually entrusted routing security for open and decentralized community networks. Ad Hoc Networks 79 20–42, doi.org/10.1016/j.adhoc.2018.06.014

Peng, S., Wang, Y., Xiao, H., Lin, B. (2020). Implementation of an improved AODV routing protocol for maritime ad-hoc networks. 13th International Congress on Image and Signal Processing, BioMedical Engineering and Informatics (CISP-BMEI), 7-11. doi.org/10.1109/CISP-BMEI51763.2020.9263519

Seferagić, A., Haxhibeqiri, J., Pilozzi, P., Hoebeke, J. (2021) Multimodal Network Architecture for Shared Situational Awareness amongst Vessels. Sensors, 21, 6556. doi.org/10.3390/s21196556

Sumić, D., Peraković, D., Jurcević, M. (2015). Optimizing data traffic route for maritime vessels communications. Ocean Engineering, 175, 127-137. doi.org/10.1016/j.proeng.2015.01.495

Vann, C. (2010). Implementation of Software Programmable Radios to Form Ad-Hoc Meshed Networks to Enhance Maritime Interception Operations. Thesis, Naval Postgraduate School Monterey CA, pp59.

Wang, X., Zhang, Y., Liu, Z., Wang, S., Zou, Y. (2023) Design of Multi-Modal Ship Mobile Ad Hoc Network under the Guidance of an Autonomous Ship. J. Mar. Sci. Eng., 11, 962. doi.org/10.3390/jmse11050962

Xiao, H., Wang, Y., Peng, S., Lin, B. (2020). Implementation of Video Transmission over Maritime Ad Hoc Network. WASA 2020. LNCS, vol 12384, doi.org/10.1007/978-3-030-59016-1_43

Yang, T. et al. (2015). Resource Allocation in Cooperative Cognitive Maritime Wireless Mesh/Ad Hoc Networks: An Game Theory View. WASA 2015. LNCS, vol 9204 doi.org/10.1007/978-3-319-21837-3_66

Yang T, Feng H, Yang C, et al. (2016) Cooperative Networking towards Maritime Cyber Physical Systems. International Journal of Distributed Sensor Networks. 12(3). doi:10.1155/2016/3906549

Zhou, M.T., Harada, H., (2012) Cognitive maritime wireless mesh/ad hoc networks, Journal of Network and Computer Applications, Vol 35, 2, pp518-526, doi.org/10.1016/j.jnca.2010.12.018

Continuous integration for the development of a COLREG-compliant decision support system

Quentin Ageneau[a], Guillaume Nulac[a]

[a] *SIREHNA, 5 rue de l'Halbrane, 44340 Bouguenais, France*
 * Corresponding Author. Email: quentin.ageneau@sirehna.com

Synopsis

The recent development in the field of autonomous navigation at sea is moving the focus from theoretical work and lab experiments to industrial solutions for the market. The move from the lab to the industry raises the question of the ability to deliver a consistent, dependable autonomous navigation capability to shipowners. One aspect is the hardware architecture, the dependability of which is traditionally ensured by applying long-standing, mature norms and guidelines (IEC61508, class regulations and guidelines). Another is the confidence that can be placed in software. The three questions are:
- how do the algorithms perform in terms of computational time, relevance of the proposed routes, repeatability, accuracy? This question is addressed with quantitative performance evaluations (see paper by Martelli et al 2024, Safenav session).
- have the algorithms been implemented correctly in the embedded software that will be deployed onboard? The answer is more of a Boolean type, and the related industry standard is software tests and Continuous Integration (CI).
- how does the system perform as a whole, once the software has been deployed and integrated with other soft- and hard-ware? This is addressed with Hardware-In-the-Loop (HIL) testing and the well-known industrial processes of Factory Acceptance Tests (FAT), Harbour Acceptance Tests (HAT) and Sea Acceptance Tests (SAT).
We have focused on the second aspect of software dependability, applied to a Decision Support System (DSS) whose role is to raise alerts and issue COLREG-based recommendations whenever a hazardous situation is identified at sea. We have implemented a Software-In-the-Loop (SIL) environment that can be used with CI tools to validate automatically that the recommendations and alerts issued by the DSS are consistent with the COLREG.
A major difference with simulations used for assessing the overall performance of algorithms (e.g., with Monte Carlo methods), is the need for exact repeatability: in a software-test context, developers need to be able to replay test scenarios exactly, to investigate why tests pass or fail. In this paper we present the test environment and discuss the constraints in terms of configuration management induced by the use of simulation in a CI context, including for the multi-agent simulator and the parameterization of test scenarios.

Keywords: COLREG, CI, continuous integration, test

1. Introduction: Developing industrial-grade collision avoidance decision support systems

Preventing ship collisions at sea has been a long-standing concern. The international rule for preventing accidents is the Collision Regulations (COLREGs) issued by the International Maritime Organization (IMO, 1972). However, COLREGs application is largely dependent on their application by human operators and their interpretation of maritime situations, vessels' manoeuvring capability, or other vessels' behaviour. In the recent record of maritime accidents, "human action" still accounts for sixty percent of all accidents (Martelli, 2023). Many attempts at improving navigation safety with the help of technology have been undertaken, but the interaction between man and safety systems sometimes had unexpected, disastrous consequences (see, e.g. Perrow, 1999). One of the main challenges lies in the difficulty for humans to have a clear understanding of the maritime situation around them; adding more sensors only adds to the difficulty.

In this context, the recent progress of computer vision and data fusion has opened new opportunities for maritime safety. Computers are now able to build a maritime situation with the help of the data provided by radars, but also cameras fitted onboard ship – relieving or complementing the human brain in this task. It is also very easy for a computer to infer an evasive route from a list of rules such as, for instance, the COLREGs.

Quentin Ageneau is a Software Architect in embedded systems specialized in unmanned surface vehicle at SIREHNA
Guillaume Nulac is a Systems Architect with years of experience in the domain of embedded maritime software and systems at SIREHNA.

The Safenav project intends to leverage these new opportunities to provide ship captains with a decision-support system (DSS) able to detect hazardous situations and make COLREGs-compliant recommendations. A major difficulty is to demonstrate that the system is able to provide relevant and reliable recommendations in all situations. Any flaw in the following aspects of system design could have catastrophic consequences in operation:

- Algorithms: ineffective, irrelevant or unreliable algorithms could mean that the maritime situation provided by the system is wrong, or the evasive manoeuvre recommended by the system is irrelevant. The system shall have firmly established algorithmic grounds, mathematically demonstrated and thoroughly tested in a wide number of cases.
- Software implementation: the implementation of the algorithms in the form of industrial software is a potential source of errors in itself. "Industrial software" has a lot more features than just the evasive manoeuvre algorithm, including authentication and cybersecurity, real-time calculation capability, log and memory management, obsolescence management, etc. Developing such software is an incremental, continuing process where each increment is a source of risk and regressions that shall be addressed with the greatest care. This paper explores this topic in further detail.
- System integration: eventually, software is deployed and integrated onboard. Conventional processes such as the well-known tryptic Factory / Harbour / Sea acceptance tests, are the typical way to demonstrate, step by step, that the system as a whole performs as expected.

Continuous Integration (CI) is the state-of-the-art approach to ensure that software is compliant with its requirements at all times during the development process - thus addressing the second bullet point. In this approach, software applications are *built and tested* as often as possible within the CI pipeline – not only at each release or new feature, but virtually every time a software developer has changed a line of code – in order to provide instantaneous feedback on any error in the code. Continuous Integration is made possible by *automated* testing. An automated test is a scenario that can be run automatically on the freshly built software application, the outputs of which can be automatically evaluated with respect to a pre-defined reference. In order for the developers to make the most of a CI pipeline, the tests shall be reasonably fast and repeatable (to enable debugging whenever a test fails).

In the context of a COLREGs-compliant DSS, each test involves a maritime situation with all its complexity: the ship that is fitted with the DSS (referred to as "Own ship") navigates in the vicinity of other ships that may have their own decision capability (see, e.g., Pedersen et al, 2023). The Own ship navigates either by following strictly the path recommended by the DSS, or with a delay (if the captain waits to apply recommendations), or without any consideration for the recommendation. Any action taken by the Own ship potentially results in a different end situation, depending on the reactions of the other ships in the simulation: the complexity of the simulation is driven not only by the DSS of the Own ship, but also by feedback loops involving the other ships.

The paper describes how to validate a COLREGs-compliant DSS implementation in a CI. The software in the loop simulator used to test the DSS will be described in section 2. Section 3 provides a description of a Continuous Integration pipeline that uses the simulator described in section 2 to run and validate the test scenarios also described in section 2. The advantages and limitations of the approach are discussed in section 4.

2. Software in the loop simulation of a Decision Support System
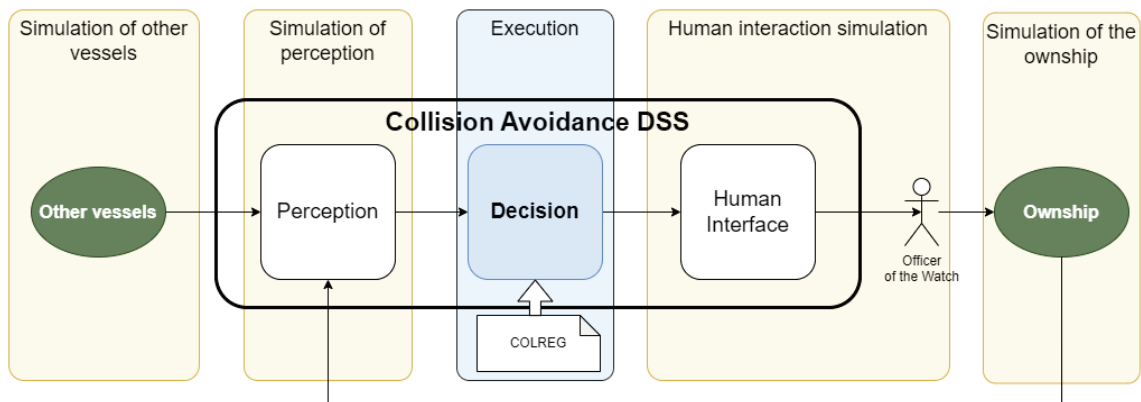
Figure 1 – Overall simulation context

Figure 1 illustrates the simulation environment used to validate a collision avoidance decision support system, and more specifically the Decision support module wherein.

The collision avoidance decision support system is made of three main modules:
- Perception: this part of the system includes the sensors and algorithm that works together in order to build a consistent and relevant knowledge of the maritime situation and its environment,
- Decision: based on the perception of the ship situation and the ships' objectives, this component elaborates recommendations including path planning and avoidance manoeuvres,
- Human interface: unlike fully automated navigation systems, the quality of interactions between machines and human is essential to guarantee the effectiveness of the decision support system. If the interface is liable to misinterpretations, delayed or flawed recommendation display, the evasive manoeuvres may not be implemented as recommended by the Decision module.

In order to test a DSS (and more generally a complex software) in a CI, a specific "wrapper" need to be developed. The Safenav's SIL platform was developed to do so. It is composed of two main components:
- Maritime situation simulator: Runs the simulation and provides updated inputs to the DSS
- Validation Module: Validate the behavior of the DSS
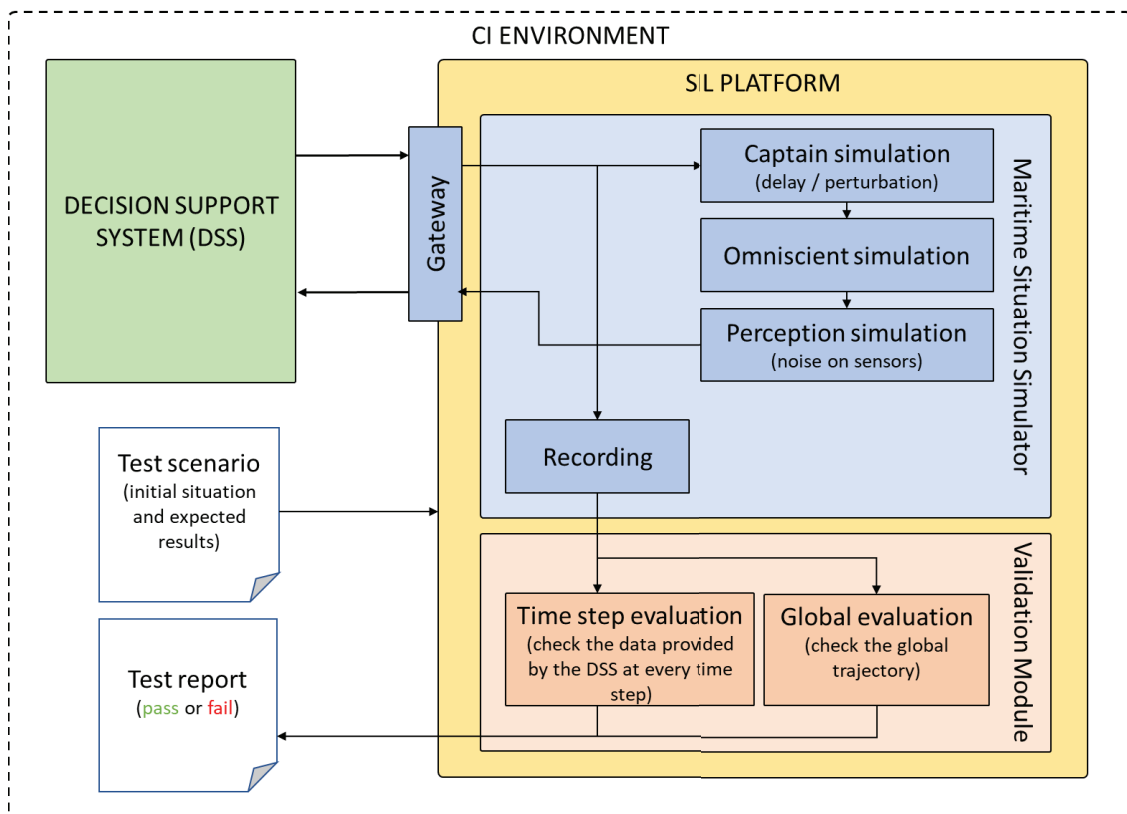
Figure 2 Functional block diagram of the simulator of the Safenav DSS

2.1. Test scenarios

In the context described in this paper, the CI is used to ensure that changes in the source code do not induce functional regressions. The absence of a regression is verified by running a Test case, defined as:
- An initial Maritime situation,
- A behavioural model of the Own ship and of the surrounding ships (including the reaction time of the Officer of the Watch to be considered in this particular Test case),
- A time limit for the simulation,
- A validation criterion to be evaluated with respect to the simulated Maritime situation record.

For the sake of simplicity, environmental conditions have been neglected and the vessels are assumed to evolve in a perfect, open sea environment devoid of navigation channels or signals and mapped with Cartesian coordinates.

The Test cases shall be representative of actual hazardous situations encountered at sea and they shall cover as wide a spectrum of maritime situations as possible. The 55 "situations" proposed by Pedersen et al, 2023, complemented with a set of 12 scenarios devised by the University of Rijeka for the Safenav project, have been used to generate a basic set of Test cases. How to extend this set, especially by including limit cases unforeseen a priori, will be discussed in section 4.

In what follows, the surrounding ships have been assigned a trivial behavioural model – each vessel follows a straight route at constant speed regardless of the surrounding ships, including the Own ship.

As a general rule for devising the set of test scenarios, only those scenarios for which a COLREG-compliant route is known to exist have been selected: scenarios where the collision risk is detected when the Own ship is already within the CPA of the approaching vessel, for instance, have been discarded.

The total number of scenarios is on the order of a few dozens to a few hundred. With the simulator described in this section, it takes in the order of seconds to run each scenario on a standard computer, with a total testing phase in the CI pipeline that takes in the order of a few minutes. This is a reasonable time for a developer to receive a relevant feedback.

2.2. Maritime situation simulator

In this paper, a Maritime situation is defined by the positions, speeds and headings of several ships sailing in an area of interest. It is the role of the Maritime situation simulator to infer the Maritime situation record based on the initial situation and the characteristics of the ships (behaviour depending on their environment, manoeuvring capability, etc.).

The position and speed of the vessels including the Own ship are evaluated with time simulation. A perfect Perception assumption has been taken: the Decision module knows the Maritime situation exactly and with no time delay. In a further stage, sensors may be simulated to be more representative of the actual system.

The Human interface has been modelled by introducing a delay in the application of the recommended manoeuvres. Similarly, this first approach can be extended and enriched in further work, as mentioned in section 4.

The recommended route issued by the Decision module is sent to the Maritime simulation simulator that converts it into a new route increment for the Own ship – adding a time delay accounting for the reaction time of the Officer of the Watch if need be. This is done at every time step: the Own ship's route is the result of the consecutive updates received from the DSS, and does not necessarily coincides with any of the individual routes recommended by the Decision module.

After the position and speed of the Own ship have been updated, the position and speed of all the other ships is computed. This is done by taking into account the manoeuvring and behavioural characteristics of every ship, including their autonomous decisional capability. The position and speed of all the ships, including the Own ship and the other vessels, is then fed back into the Decision module for the next time step.

At the end of the simulation (specified as a predefined time limit), the entire Maritime situation record is stored for further use by the validation module (see section 2.3).

2.3. Validation module: COLREGs considered here and automated criteria

The goal of this paper is to verify that the navigation pattern followed by the Own ship is consistent with COLREGs. This is done by analysing the Maritime situation record. The simulator infers the Maritime situation record from:

- The initial Maritime situation
- The actions of the Officer of the Watch, based on the recommendations from the DSS,
- The manoeuvring characteristics of the Own ship,
- The behavioural and manoeuvring characteristics of the other vessels.
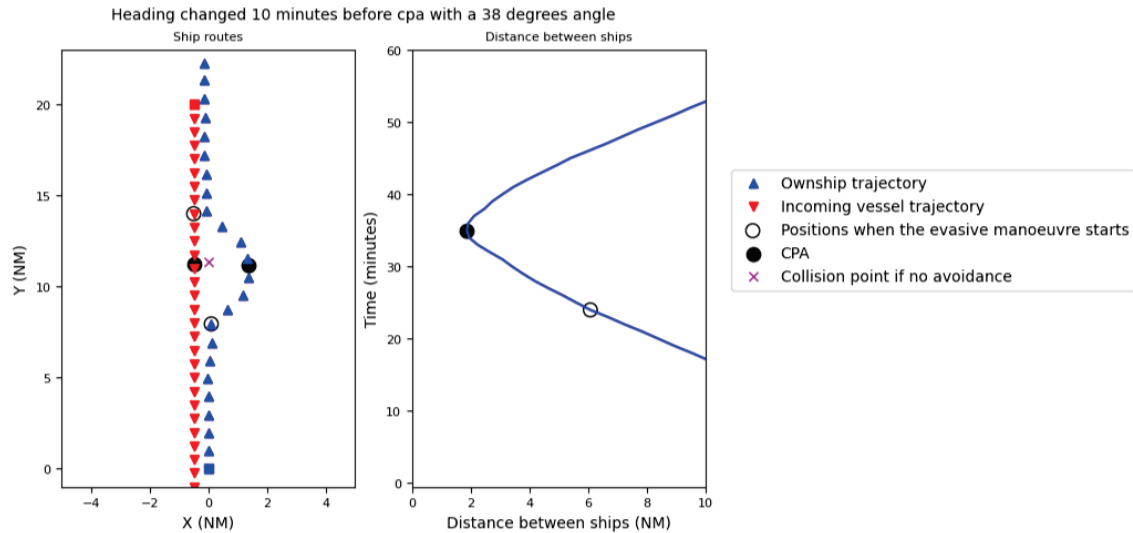
Figure 3 – Maritime situation record, as generated by the Maritime situation simulator.

The spirit of the COLREGs is not to simply prevent collisions, but to anticipate on potential collisions to come. Thus, it is not enough to check for the absence of a collision to declare an evasive manoeuvre COLREG-compliant.

"Rule 14 - Head-on situation" is one such navigation rule, and it will be used to explain the automation process in the sections that follow – together with Rule 8, that provides requirements on how the evasive manoeuvre shall be implemented.

Figure 4 to 7 illustrates how COLREGs are validated against several Maritime situation records corresponding to a "head-on" encounter between the Own ship and an incoming vessel. Each case displayed corresponds to a different behaviour of the Own ship. The following COLREG requirements (and the violation thereof) are captured:
- The route lies in the half-plane located starboard from the initial route of the ship: this criterion validates rule 14, that states that the vessel shall alter her course to starboard
- The route deviates from the original one more than 10 minutes before tCPA. This criterion validates Rule 8(a), according to which the ship shall alter her course "ample time" before collision
- after the Own ship has altered her course, the heading is 30 degrees starboard from the original route. This criterion validates Rule 8(b), according to which the evasive manoeuvre shall be sharp.
- The distance between the recommended route and the approaching vessel is above CPA at all times. Here we have chosen CPA = 0.6 nautical miles.
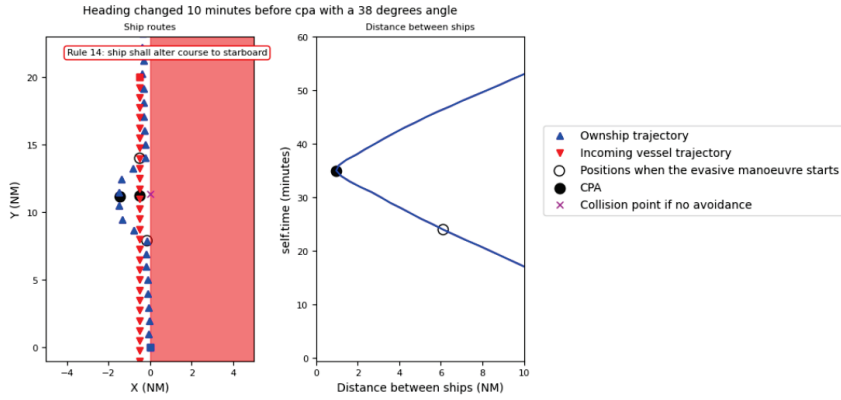
Figure 4 – Maritime situation records: The collision is avoided, but the Own ship crosses the route of the incoming vessel then leaves her on starboard.
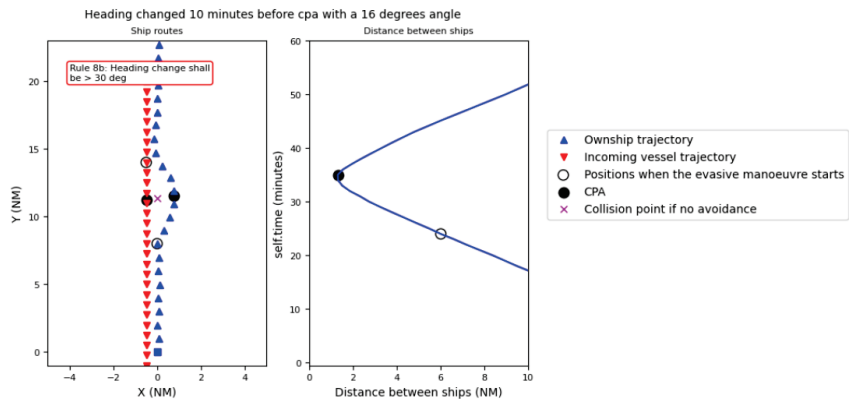
Figure 5 – Maritime situation records: The evasive manoeuvre is not sharp enough.
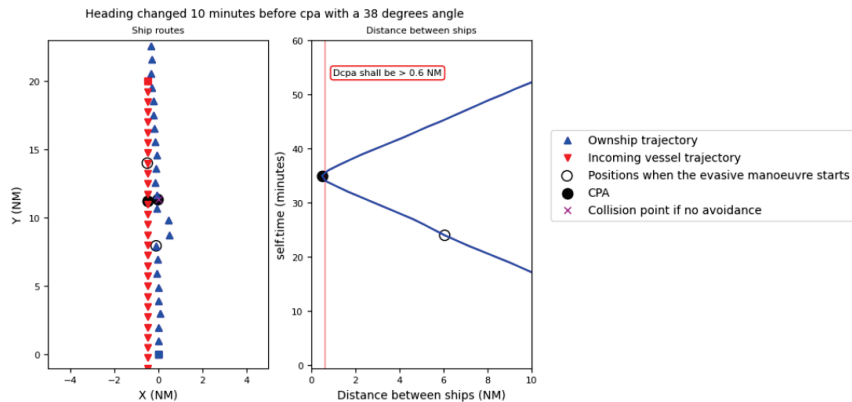
Figure 6 – Maritime situation records: The evasive manoeuvre fails to keep the vessels at a safe distance.
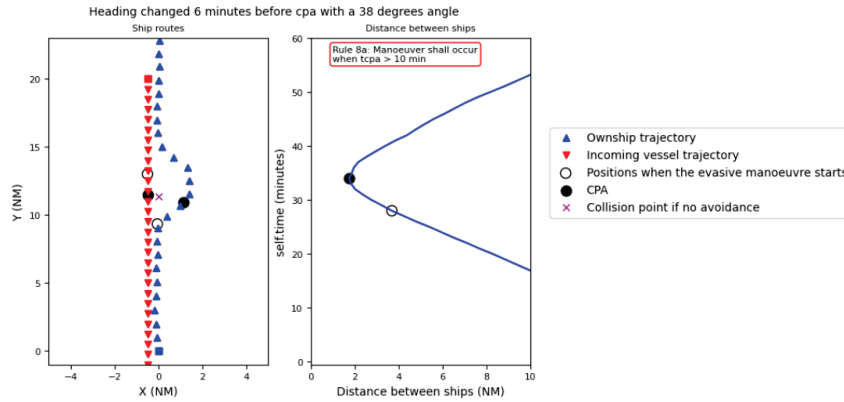
Figure 7 – Maritime situation records: The evasive manoeuvre was initiated too late.

The validation procedure implemented here has two important properties:
- It is entirely automated: there is no need of a human eye to assess the compliance of the routes to Rule 14,
- Any kind of route followed by the Own ship can be assessed, including routes that are the result of incremental updates (as would be the case if the Officer of the Watch had adjusted to several recommendations sent to her at different times).

3. Implementation of a continuous integration environment

3.1. CI methodology applied to a collision avoidance DSS

Continuous Integration (CI) is a method of software development, where code changes are continuously built and tested: the delay between the writing of the code and its validation with tests is reduced to a minimum (on the order of a few seconds to a few minutes). CI is commonly paired with Continuous Deployment (CD) to automatically deploy, and monitor changes (outside the scope of this paper). The aim of CI is to identify bugs or regressions early in the development cycle and reduce the chance that new code was developed on a buggy previous version.

In the context of the DSS development in the Safenav project, the CI is designed for all the lifecycle phases of the DSS system and not only during the initial development period. This includes:
- The initial development phase: this is especially useful during this early development phase because the software code changes a lot. However, tests must be written sparingly because requirements and specifications may also change a lot during this period, which would render many tests obsolete. A good balance between tests quantity and tests durability must be found.
- The validation phases and integration with other systems: during this period, slight adjustments may be required and fast delivered due to interfaces issues with other systems. This is very important to avoid regression during this period that may involve a lot of resources (human and hardware platforms).
- The production phase: if a bug is detected on board a ship during the effective use of DSS, it is critical to avoid any regression in the modified software that may be deployed on many platforms. At this stage of the project, the amount of tests shall cover the whole DSS functions and the maximum possible situation that may be encounter by the system in real life
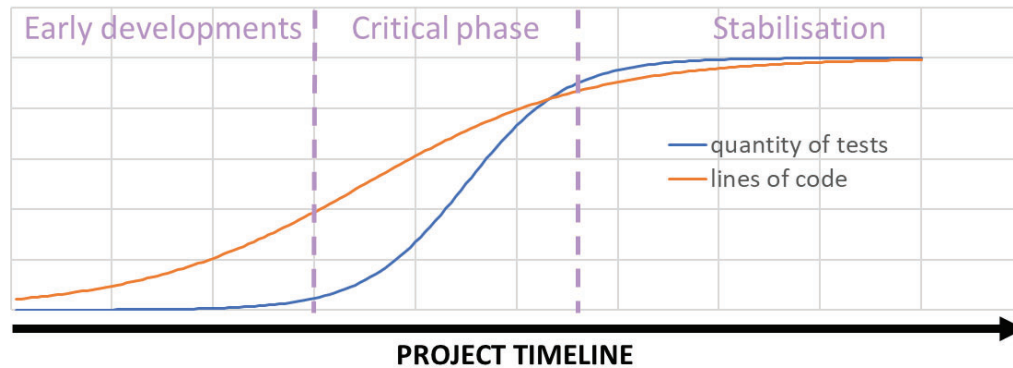
Figure 8 – Evolution of lines of code and quantity of CI tests over time in a typical software project

The first step before configuring a CI environment is to think about what is expected from the CI and what are the important requirements that shall be addressed by the CI. This will depend on:
- Organisation of the software code management
- Identification of the feared events that we must mitigate through the CI process
- Transverse requirements about the performance of tests and their hierarchy

The Gitlab SCM host at least 3 repositories for the development of the DSS:
- The DSS itself, including each submodule that may be provided by third parties
- The SIL platform simulator and associated files
- A repository containing configuration files, including the scenario used for the tests

During the DSS lifecycle, many events may require a code modification:
- New features requested by customer (or any people involved in the project)
- Refactoring of code required for engineering reason
- Bug or incident detected, during any phase of the DSS lifecycle

Every code modification can lead to regression of the existing functions of the DSS and this can lead to more or less critical consequences for the projects:
- loss of time during development phase
- critical injury of people using DSS on board a ship
- any other intermediate consequences

Evaluation of a DSS using complex simulations in the context of a Continuous Integration process is challenging with respect to the three qualities of an efficient CI:
- Automated evaluation: COLREGs have been devised to guide ship captains, yet leave them some freedom of action to prevent collisions in the best ways they see fit. COLREGs leave some room for interpretation, which is not easy to consider in automated tests (see, e.g. Pedersen et al, 2023).
- Reasonably fast tests: a subset of maritime scenarios, simulated in a reasonably coarse fashion, shall be established to ensure a good testing coverage within a controlled run time.
- Repeatability: in order for the developers to be able to debug the DSS efficiently, not only the source code of the DSS, but also the entire test environment, testing parameters and test outputs shall be versioned. This places a constraint on the development and execution environments of the simulator.

3.2. Implementation of the CI pipeline

The implementation of a CI pipeline using a Gitlab environment is chosen for this paper. This choice is motivated by the extensive capacities of the Gitlab open source version (Community Edition, under MIT licence).

A pipeline is a sequential list of tasks that can be triggered by various events, like source code increments (commits or merges), or on a predefined schedule. The tasks defined for the SafeNav DSS are the following:

Stage	Task	Description
1 - Check format		Use Linters and Code Formatters that analyse source code to detect potential errors, security vulnerabilities, or coding style issues.
2 - Build		Clone project, fetch dependencies, compile and link
3 - Tests	Unit tests	Execution of the unit tests of the DSS
	External interfaces tests	Each external interface is tested using a predefined dataset ensuring that each field of the tested interfaces is consistent with the content of the scenario. This step ensures an easy integration phase afterwards
	Functional scenarios tests	The aim of this step is to validate the main functionalities of the DSS, in particular the relevance of the DSS recommendations and the correctness of the indicators sent to the GUI. Those tests are carried out using the DSS as a black-box. The SIL platform is used to emulate a complete maritime situation that will serve as a playground for the DSS. The simulation is initialized using a test scenario and evolves as the DSS provides recommendations. The success or failure of each scenario is evaluated directly after the simulation.
4 - Deploy		Package and store on a repository

The CI pipeline is completely automated, is automatically triggered, and it can run in the background, on a separate machine: it makes software testing extremely easy and harmless to the software developer, who can proceed with the development and have his code tested along the way. Rather than scheduling a few tedious, a posteriori testing phases – inevitably followed by debugging work on code that has been implemented a few days or a few weeks before – developers have numerous, instantaneous feedbacks on code they just wrote and can fix while everything is still fresh in their minds.

3.3. *Output of a pipeline and debugging*

The Test stage of the CI is configured to generate a test report composed for each test case of:
-   a Boolean output "Pass or Fail",
-   in case of failure, a job artifact with all necessary elements to replay the job.

Suite	Test Case	Status	Time (s)	Error Message
test_maritime_scenarios.py	test_ID100_gui_indicators[11_responsibilities_between_vessels.yaml]	PASS	0.0	
test_maritime_scenarios.py	test_ID100_gui_indicators[12_heavy_marine_traffic.yaml]	PASS	0.0	
test_maritime_scenarios.py	test_ID200_colreg_detection[01_head-on.yaml]	FAIL	41.92	AssertionError: Colregs [7, 14] not cle (...)
test_maritime_scenarios.py	test_ID200_colreg_detection[02_crossing_from_starboard_side.yaml]	FAIL	48.09	AssertionError: Colregs [7, 15, 16, 17] (...)
test_maritime_scenarios.py	test_ID200_colreg_detection[03_crossing_from_port_side.yaml]	PASS	1.86	
test_maritime_scenarios.py	test_ID200_colreg_detection[04_overtaking.yaml]	PASS	1.88	
test_maritime_scenarios.py	test_ID200_colreg_detection[05_head-on_or_crossing_dilemma.yaml]	PASS	2.15	
test_maritime_scenarios.py	test_ID200_colreg_detection[06_stand_on_or_appropriate_action_dilemma.yaml]	PASS	2.22	
test_maritime_scenarios.py	test_ID200_colreg_detection[07_crossing_from_starboard_or_overtaking_action.yaml]	FAIL	61.3	AssertionError: Colregs [7, 15, 16, 17] (...)
test_maritime_scenarios.py	test_ID200_colreg_detection[08_crossing_from_port_side_and_overtaking_action.yaml]	PASS	2.41	
Showing 11 to 20 of 36 entries			Previous 1 2 3 4 Next	

Figure 9 - HTML test report: Summary of the test campaign results with a pass/fail status
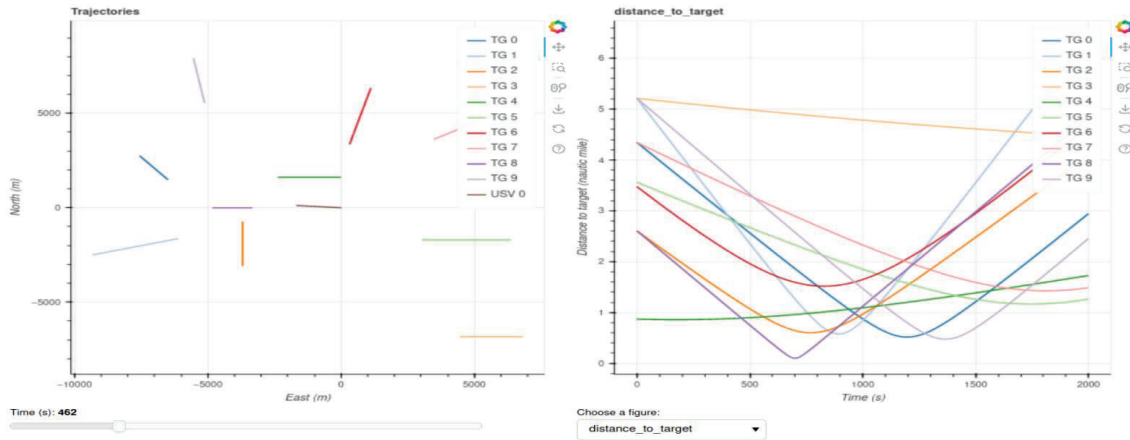
Figure 10 - HTML test report: Indicators and graphs available for each test

The interactive HTML test report makes understanding KOs much simpler. Analysis of indicators coupled with the ability to replay a scenario under the same conditions allows fails to be solve in a short loop by the developer.
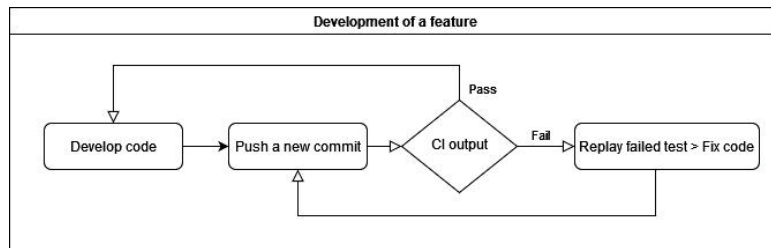
Figure 11 – Development workflow using Continuous Integration. As long as the code passes the tests, development can proceed. Whenever a new code increment fails, the developer is invited to investigate the failed test immediately, based on the artefacts logged by the CI.

4. Discussion

A fully automated validation of a COLREG-compliant DSS has been shown to enable the use of Continuous Integration to improve the robustness of software development. The CI pipeline runs a set of predefined Test cases that are intended to cover the entire range of Maritime situations that may be encountered at sea.

A common issue with complex systems is the vast diversity of situations that can be encountered. A slight deviation in the initial conditions (e.g., speed of encounter vessel) may generate widely different outputs. Another source of diversity is when the Maritime situation representativeness will be increased, either by including external elements such as environmental conditions, coastlines or navigation channels, or by enriching the model of the Own ship (taking into account sensors accuracy, human factor, etc.). By definition, the CI environment we have set up addresses only a limited number of scenarios.

This first set of scenarios could be complemented with scenarios generated at random or extracted from AIS traffic databases. Every time a failed scenario has been found, if the scenario is relevant, a new Test case shall be added to the existing set run by the CI.
It is expected that the number of failed scenarios among those generated at random should decrease over time, while test coverage naturally increases in the process.

Being able to easily visualize the output of the DSS is another challenge that need to be addressed. Generating 3D views of the simulation will be beneficial for debugging and it also brings the opportunity to add a perception

module into the testing loop. We even can imagine simulating a view of the ownship's bridge as it was during the simulation to make a sea captain challenge the DSS decisions.

A drawback of the discussed improvements is the increasing computational time that may render the CI pipeline ineffective for non-regression verification purposes. One option is to have a two-stage CI:
- During daytime and for non-regression validation purposes: test a limited number of predefined scenarios,
- Nightly: generate multiple scenarios and whenever one of them fails the validation criteria, log the results of the simulation for further analysis

Acknowledgements

References

Martelli M., Žuškin S., Zaccone R. & Rudan I. A COLREGs-Compliant Decision Support Tool to Prevent Collisions at Sea, in TransNav Volume 17, Number 2, June 2023

Huang, Y., Chen, L., Chen, P., Negenborn, R. R., & van Gelder, P. H. A. J. M. (2020): Ship collision avoidance methods: State-of-the-art. Safety Science, 121, 451-473.

International Maritime Organization, 1972. International Regulations for Preventing Collisions at Sea (Consolidated edition, 2018). Archived on 03-March-2023. Retrieved from https://www.samgongustofa.is/media/log-og-reglur/COLREG-Consolidated-2018.pdf

PERROW, C. Normal Accidents: Living with High Risk Technologies - Updated Edition (REV-Revised). Princeton University Press, 1999.

Tom Arne Pedersen et al 2023 J. Phys.: Conf. Ser. 2618 012013

Autonomous Machinery Control Systems for Naval Unmanned Surface Vessels

M J Roa* B.S. Electrical Engineering, M.S. Information Systems

* *Naval Sea Systems Command (NAVSEA), USA*
* Corresponding Author. Email: michael.j.roa.civ@us.navy.mil

Synopsis

Advancements in automation, artificial-intelligence, robotics, motion-control, satellite based communications, geo-spatial positioning systems, and real-time machinery control systems have enabled ship designers to consider the implementation of totally automated autonomous or semi-autonomous remotely controlled unmanned surface vessels to operate in a variety of marine and naval applications. The possibility of being able to operate unmanned naval vessels poses several operational benefits and cost savings for naval vessel operators while at the same time introduces inherent risks that must be mitigated through robust system safety and redundancy requirements. Unlike manned vessels, on unmanned vessels machinery control systems will need to act autonomously to replicate functions that are normally performed by human operators. This paper will (a) provide a list of machinery control functions normally done by humans that will need to become autonomous, (b) identify key requirement areas that will need to be developed for totally autonomous unmanned naval surface vessel machinery control systems, and (c) provide an update on ongoing efforts to develop standards and requirements for autonomous machinery control systems on unmanned naval surface vessels.

Keywords: Autonomous; Unmanned; Machinery Control systems

1. Background

The U.S. Navy has been increasingly pursuing the development of unmanned surface vessels to support for a variety of missions including surveillance, intelligence gathering, anti-surface warfare, anti-submarine warfare, anti-air warfare, mine warfare, search and rescue, maritime security operations, and expeditionary warfare. Unmanned surface vessels (USVs) are being developed to operate in fully autonomously modes where a mission is pre-programmed into the USV which then carries out the mission with no human intervention (CRS 2019). USVs are also being developed to be operated in a semi-autonomous mode where a land or ship based remote control center remains in communication with the USV and send commands to the USV to carry out the required mission. In the case of shipborne remote control centers, one concept calls for a single manned warship to operate with a group of USVs which operate similar to a battle group to carry out specified missions (Fuentes 2024). For all these variations, operating the machinery plant without any human intervention for long durations of time (i.e., 30 or more days unmanned) is a considerable challenge for systems designers of USV machinery control systems. Multiple essential control systems including propulsion, steering, electrical plant, auxiliaries, and damage control must be designed to function with no assistance from human operators for extended periods of time. In this regard, system designers must anticipate every conceivable function normally performed by humans to be performed autonomously without any support from a human operator. These functions include everything from routine daily maintenance to recovery from major casualties and damage events deemed recoverable. This paper will focus on three topics that unmanned surface vessel control system developers should be aware of when considering the Machinery Control System (MCS) design on a fully-autonomous or semi-autonomous unmanned surface vessel as follows:

1. Key Machinery Control System functions to Support Autonomous Unmanned Operation
2. Key MCS Characteristics and Essential Features required for Autonomous Operation
3. Development of Specifications and Standards for USV Machinery Control Systems

Author's Biography

Michael J. Roa earned a B.S. degree in Electrical Engineering from The Citadel (1986) and later earned a M.S. degree in Information Systems at the University of Maryland Baltimore County (2009). He has 38 years of experience in naval and commercial marine machinery control, electrical power, navigation and interior communication systems. He is currently assigned as Engineering Manager for Unmanned Surface Vessel Machinery Control Systems at Naval Sea Systems Command (NAVSEA) Headquarters, Washington, D.C.

2. Discussion

For an unmanned vessel, one of the biggest challenges is to automate all the machinery control and monitoring functions that are normally performed by watch standers during normal machinery plant operations as well as special situations such as recovery from casualties and damage events such as fire and flooding. USVs will likely be manned during initial plant startup dockside, leaving and entering port, fueling at sea (UNREP), and during plant shutdown after returning to the pier. Once the vessel has completed restricted maneuvering and has entered open ocean, the machinery plant will need be placed into either semi-autonomous mode with a remote operator in the loop or full autonomous mode and all functions required to keep the plant safely operating will need to be fully automated (Gain, 2020). In many cases, there will be an insufficient level of automation specified or the required level of monitoring is not provided to automate a particular function because they are typically performed by watch standers. For example, the basic USCG regulations (46 CFR, 2024) and classification society rules for periodically unattended engine-room (i.e., ABS ACCU, DNV-GL E0, and LR UMS notations) are all based on the capability to leave the machinery plant unattended for up to 24 hours. Things like automatic standby pump changeover, propulsion machinery automatic safety slowdowns and shutdowns, automatic fuel oil transfer, and automatic power management are all standard features for periodically unattended engine-room. However, human intervention is still required for many functions such as performing routine maintenance, responding to alarms and taking corrective action, resetting machinery controllers after a shutdown, restarting machinery to recover from casualties, aligning piping systems for proper operation, operating ballast pumps to maintain vessel stability, activating fire-fighting systems upon detection of a fire, and performing dewatering to mitigate flooding. In order to successfully operate in an unmanned fully autonomous mode, the MCS will need to have a sufficient level of automation, control, and monitoring to autonomously perform these additional types of functions with no human intervention.

3. Differences between Manned and Unmanned Surface Vessel Operations

Similar to manned vessels USVs can be equipped with sensors, weapons, or other payloads with the added capabilities to be operated remotely, semi-autonomously, or (with technological advancements) autonomously (CRS 2019). USVs can be individually less expensive to procure than manned ships because their designs do not need to incorporate spaces and support equipment for extended operations with onboard human operators. USVs can be particularly suitable for long-duration missions that might tax the physical endurance of onboard human operators, or missions that pose a high risk of injury, death, or capture of onboard human operators. Consequently, USVs are sometimes said to be particularly suitable for so-called "three D" missions, meaning missions that are "dull, dirty, or dangerous." (Diab 2014, Robinson, 2015, Marr, 2017).

From a controls perspective, while a manned vessel relies on human operators at various shipboard control stations to make all critical decisions and respond to system malfunctions or damage control events, on an unmanned vessel all of the logic to execute these functions must be performed by an Autonomous Control System (ACS) which has been preprogrammed to execute a specified operational mission for a prolonged period of time. In order to facilitate autonomous operations, the ACS will need to be provided with enhanced monitoring capabilities in order to be able to sense the state of the machinery plant via the Machinery Control System (MCS) and make fully automated decisions which would normally be made by a human operator. Even routine watch-stander actions such as shifting fuel oil service tanks, periodically cycling equipment, or shifting strainers will somehow need to be automated. When responding to machinery casualties or damage events (i.e., fire, flooding), the ACS will need to assess the condition of the machinery, take corrective action, reconfigure the machinery plant to recover from the casualty, and where possible continue on with the specified mission. Consequence analysers, similar to those found on Dynamic Positioning (DP) Vessels to determine if it is safe to continue DP operations after a casualty, may need to be employed to ultimately decide whether or not the vessel can safely continue with an unmanned mission in a degraded state following a machinery casualty or damage control event. Lastly, as there are no maintenance or repair personnel onboard, machinery will need to have a high level of reliability in order to support prolonged unmanned missions without failure. Table 1 outlines the main differences between manned and unmanned surface vessel control system key functions.

Table 1: Differences Between Manned and Unmanned Surface Vessel Control System Key Functions

Key Functions	Manned Vessels	Unmanned Vessels
Routine maintenance	Performed by crewmembers manually	Must be fully automated to be done by MCS or equipment must be designed to be maintenance free for the specified duration of the mission
Equipment monitoring	Roving watch-standers can check on equipment status by visual/audible observations	Requires enhanced system monitoring, more sensors, camera systems, acoustic/vibration monitoring systems
System alignment	Performed by crewmembers manually operating valves and starting equipment	Must be fully automated such that all the equipment and valves are placed in the correct state by MCS to meet all equipment start permissives
Cycling of key rotating machinery to balance running hours	Performed by crewmembers manually, usually once a day	Must be automated such that equipment is shifted by MCS on a daily basis or may be based on running hours
Recovery from machinery casualties	Typically manually done by crewmembers who troubleshoot the problem, reset safety devices, and restart equipment manually	Must be automated such that the MCS can assess if the problem has been resolved and automatically reset safeties and restart equipment once all permissives have been satisfied. Will likely require enhanced monitoring and additional sensors.
Damage control functions	Performed by crewmembers who manually respond to damage events. An operator at Damage Control Central or repair lockers will take manual actions such as activating fire suppression systems, shutting down key equipment such as fuel pumps and vent fans, closing valves, dampers, hatches, and watertight/firetight doors to isolate spaces, and starting dewatering and ballasting equipment	Must be fully automated such that ACS directs MCS to take automatic action in response to detection of damage event such as fire or flooding

4. Key Machinery Control System functions to Support Autonomous Unmanned Operation

The following is a list of key machinery functions that will need to be performed autonomously by the MCS in order to support prolonged unmanned operation.

1. Routine maintenance and monitoring
   a. Strainers and filters - All strainers and filters for machinery systems may be fitted with a means of automated change out or cleaning such that when the system detects a clogged strainer or filter due to high differential pressure alarm, the system is arranged to take automated action clean, change, or shift the strainer or filter. Such action will prevent casualties such as a clogged seawater strainer from causing Main Propulsion Diesel Engines (MPDEs) or Ship Service Diesel Generators (SSDGs) to overheat and shutdown.

    b.   Lube oil analysis – Where lube oil quality must be monitored, the system may be arranged to automatically sample and analyze lube oil and where required shutdown machinery and changeout lube oil.

    c.   Motor insulation resistance monitoring – Online megger reading for key electrical motors may be incorporated to warn that motor insulation breakdown is imminent and initiate automated changeover to standby motor/pump.

    d.   Vibration monitoring – Built-in accelerometers may be installed on key rotating machinery to provide an early indication of high vibration which would enable automated changeover to standby machinery before the equipment suffers a bearing failure or other damage due to high vibration.

    e.   Machinery Condition Based Monitoring (CBM) and Trend Analysis – Enhanced system performance monitoring of key parameters (i.e., temperatures, pressures, flow) may be provided to enable an onboard Condition Based Monitoring (CBM) system to perform trend analysis, diagnostics, and prognostics to predict when equipment is prone to failure and take automated action to prevent failures.

    f.   Provide overall health status of HM&E systems – Data can be recorded and analyzed to enhance system performance and efficiency.

    g.   A means of automatically lubricating or greasing the propulsion shaft seal may be required where the ability to periodically provide the propulsion shaft seal with lubricant or grease is needed to meet the manufacturers recommended maintenance requirements.

2.   Alignment of machinery systems for startup, shutdown, and routine operations – The following functions may need to be fully automated to support unmanned operations.

    a.   Prime-mover Startup to ensure that propulsion prime-movers are safely brought online in time to meet speed demand changes or to recover from a casualty.

    b.   Drivetrain Alignment may be automated to ensure that the drivetrain (i.e., main engine, reduction gear clutch, shafting, waterjet bucket) is properly aligned before main engine startup and after main engine shutdown to enable trail shaft mode.

    c.   Shutdown of online propulsion prime-movers/drivetrains and transition to trail shaft mode based on the current speed/power demand in order to reduce fuel/power consumption and maximize efficiency.

    d.   Stopping and locking the shaft when a drive train is required to be shutdown in order to prevent prolonged duration at high speeds from causing damage to gears/bearings in system (MPDE, Gear, Shaft, or Waterjet) due to loss of lubrication.

    e.   Automated start, stop and E-Stop for all propulsion and auxiliary equipment.

    f.   Opening of key valves in auxiliary systems (fuel oil, lube oil, cooling water) to align them for propulsion machinery startup/shutdown.

    g.   Isolation of systems to prevent a single failure from affecting multiple systems/equipment. For example, alignment of fuel oil service system valves serving main propulsion diesel engines such that a fuel leak on one engine does not require shutting down all MPDEs.

    h.   Closure of key fittings and valves when equipment is secured. For example, automated closure of air intake and exhaust gas dampers upon diesel engine shutdown to prevent engine damage due to prolonged seawater intrusion when diesel engines are secured.

    i.   Fuel oil transfer – The fuel oil transfer system may need to be fully automated to refill fuel oil service tanks by automatically transferring fuel from fuel oil storage tanks.

    j.   Pumps may be arranged to automatically shutdown when a low fluid level is detected to avoid damage to the pump.

    k.   Lube oil sump level monitoring may be provided for key machinery such as MPDEs, SSDGs, and reduction gear in order to prevent a low sump level from causing damage to engines or gears.

    l.   Line shaft bearing temperature monitoring system may perform automatic engine slowdowns/shutdowns when a high line shaft bearing temperature is detected in order to prevent drive shaft damage from occurring.

    m.   Fueling at-sea – The fuel oil transfer system may be arranged to automatically align fuel oil system valving to allow refueling at-sea.

    n. Ballast/Deballast –The ballast/deballast and tank level monitoring systems may be arranged to automatically start/stop ballast/deballast pumps, align ballast system valves, and transfer ballast water in order to maintain the vessel within stability limits.

    o. Machinery Space Ventilation System – may be capable of automatically maintaining proper engine room and generator room ventilation pressure based on engine operation and compartment pressure.

3. Electrical Plant functions – The electrical plant may utilize the following features to enable prolonged unmanned operation.

    a. Power management – full automatic power management to automatically start and parallel SSDGs when the load is increasing to prevent overloading of SSDGs and automatically disconnect and stop SSDGs when the electrical load decreases to prevent low loading effects on engines and maximize fuel efficiency.

    b. Automatic standby SSDG startup to recover from a loss of an SSDG.

    c. Propulsion power limiting – On electric propulsion ships, the system may automatically reduce propulsion power or delay startup of a propulsion motor to prevent overloading of SSDGs upon a generator failure.

    d. Load shedding – automatic tripping of non-essential loads to prevent SSDG overload upon loss of an SSDG.

    e. Recovery from load shedding – automated recovery after a load shed event may be required to restore the electrical plant configuration. The system will need to be able to automatically reengage tripped breakers after sufficient electric plant generating capacity is regained.

    f. Heavy consumer blocking – Automatic start blocking, time delay, or soft starting of heavy power consumers to prevent large inrush motor current from overloading/tripping SSDGs.

    g. Sequential startup – Upon recovery from a blackout, automated sequential startup of essential motors and other loads to prevent simultaneous starting of too many motors from overloading of SSDGs

    h. Blackout recovery – Automated standby SSDG startup and dead bus pickup to recover from a blackout condition.

    i. Automatic Bus Transfer (ABT) switches may be provided for all essential loads to ensure continuity of power to essential systems.

4. Climate control systems – In spaces housing heat sensitive equipment (such as electronic equipment, computers, network switches, and servers) climate control systems maybe fully automated to maintain the required heat and humidity levels to prevent overheating of sensitive electronic equipment. Additionally, automated changeover to a backup climate control system may be provided. For spaces where crewmembers are normally stationed during manned modes of operation (i.e., the bridge), provisions will need to be made to automatically adjust climate control system for prevailing weather conditions.

5. Pollution abatement systems

    a. Bilge housekeeping – The machinery bilge water system may be fully automated to maintain machinery space bilge well levels.

    b. Oily waste water processing – The oily water separator may be arranged to automatically process oily water waste and maintain overboard discharge to within 15 ppm per MARPOL Annex VI (IMO, 2024).

    c. Black and Gray water processing may be fully automated to support manned modes of operation.

    d. Air emissions - where required by MARPOL, automatic changeover between fuel types may need to be accomplished when entering/leaving Emission Control Areas (ECAs) designated under regulation 13 of MARPOL Annex VI.

    e. Sewage treatment – Operation of the Marine Sanitation Device (MSD) and Vacuum Collection, Holding, and Transfer (VCHT) System may be fully automated to support manned modes of operation.

6. Cycling of key rotating machinery to balance running hours – in order to prevent unbalanced wear and tear leading to premature machinery failure, the MCS shall autonomously monitor running hours and wherever

possible cycle between online and standby machinery to keep running hours balanced. The logic sequence will be designed to equalize hours on a periodic basis on duplicated machinery. Examples include:
a.   Propulsion engines (when operating in a trail shaft mode)
b.   SSDGs
c.   Auxiliary pumps (fuel oil, lube oil, cooling water)
d.   Firemain pumps (when continuously running on a wet firemain)
e.   Steering gear HPUs

7.   Recovery from machinery casualties – The MCS will need to be capable of performing the following functions automatically in order to recover from machinery failures.
a.   Start/restart of propulsion machinery to restore propulsion
b.   Start/restart of standby auxiliary pumps
c.   Start/restart of standby SSDGs
d.   Reducing speed command upon loss of a propulsion train
e.   Resetting engine/turbine/motor controllers after a safety system shutdown
f.   Resetting motor controllers after a motor overload shutdown
g.   General troubleshooting and analysis of diagnostics

8.   Damage control functions – the following damage control features/functions may need to be fully automated in order to support isolation of a fire/flooding event and subsequent recovery/restoration of propulsion and electrical power during unmanned autonomous operation.
a.   Activation of fire-fighting systems in affected spaces upon detection of fire
b.   Intelligent fire detection sensors with polling (heat/optical/smoke) to minimize false alarms
c.   Pump startup and system valving alignment for sprinkling and watermist systems to release sprinkling water or watermist in the affected space
d.   Shutdown of rotating machinery in affected spaces to prevent machinery damage from fire/flooding
e.   Shutdown of flammable liquid system pumps and closure of tank suction valves and bulkhead stop valves (i.e., fuel oil, lube oil) to isolate compartments where a fire has been detected
f.   Shutdown of ventilation of affected spaces to isolate compartments where a fire has been detected
g.   Closure of key fittings such as fire dampers to isolate compartments where a fire/flood has been detected
h.   Closure of watertight/firetight doors to isolate compartments where a fire/flood has been detected
i.   Startup and alignment of dewatering systems upon detection of flooding
j.   Ballast system operation to maintain vessel stability
k.   Recovery from a fire or flooding event
l.   Isolation of firemain ruptures (i.e., by use of smart valves)

5.   Key MCS Characteristics and Essential Features required for Autonomous Operation

An area of concern for MCS system designers is defining the key characteristics needed for a machinery control system to support autonomous operations. The following is a list of essential MCS design features needed to support autonomous unmanned operation.

1.   System Architecture -
a.   Autonomous Control System (ACS) Interface – The MCS will have redundant interfaces via an autonomy bus to the ACS at the network layer where higher level decision functions may be implemented (NAVSEA, 2019). The ACS may incorporate logic such as a Mission Consequence Analyzer (aka Decision Support System) that monitors the state of MCS machinery to determine if the vessel can continue to carry out the specified mission autonomously upon detection of a machinery plant system or equipment failure. The Mission Consequence Analyzer is to be able to perform calculations to verify that in the event of a single fault there will be sufficient thrust, electrical power, and steering capability available to maintain the required speed and heading to carry out the specified mission.

b. MCS Layer - a robust fault tolerant and redundant MCS architecture should be selected to maximize system performance and fault tolerance. MCS functions should be implemented at the control layer to ensure deterministic system behavior and prevent processing delays associated with the network layer from occurring due to jitter, latency, and insufficient bandwidth. MCS will need to report ship speed, heading, and machinery plant conditions to the higher level ACS and concurrently accept and execute directions in return.

2. Autonomy Level – The appropriate vessel autonomy levels will need to be to be specified and defined in the ship specifications in order to support the required unmanned missions. The level of autonomy required will drive requirements for both the ACS and MCS. For example, the American Bureau of Shipping (ABS) Requirements for Autonomous and Remote Control Functions (ABS, 2022) specifies the following autonomy levels:
    a. Smart: System augmentation of human functions. The system provides passive decision support, such as in the form of health or performance anomaly detection, diagnostics, prognostics, decision/action alternatives, and/or recommendations.
    b. Semi-Autonomy: Human augmentation of system functions. System operation builds upon a smart foundation and is governed by a combination of system and human decisions and actions.
    c. Full Autonomy: No human involvement in system functions. The system makes decisions and takes actions autonomously. Humans perform a supervisory function solely, and have capability to intervene and override actions made by the system.

3. Redundancy and Fault Tolerance – The MCS will need to be fully redundant in all aspects to be able to sustain unmanned operations after a single failure. In this regard, the MCS will be provided with features such as redundant control consoles, network data processing equipment, network data communication cabling, and power supplies. Data Acquisition Units (DAUs) and Input/Output mapping will need to be arranged such that a loss of a single DAU does not result in a loss of all propulsion, electrical power, or steering capability.

4. Remote Operation and Autonomous Operation – MCS will need to be able to perform all required functions to support both Remote Vessel Operation where the USV is being controlled by a remote operator on an off-ship location such as another manned vessel or a shoreside control center (i.e., Unmanned Operations Center (UOC) and full Autonomous Operation where the vessel is autonomously carrying out a pre-programmed mission and the ACS is in full autonomous control and is not being controlled by an off-ship operator (DNV 2021). A means of changing modes should be incorporated to enable placing MCS into an autonomous mode where the MCS is being controlled by ACS.

5. Recovery from Machinery Plant Casualties – In the event of a single machinery casualty, it should in general be possible to restore all key vessel functions without assistance by personnel on board. The MCS will need to ensure that any serious malfunctions of machinery systems providing control, alarm or safety functions will automatically initiate corrective actions to put the system into a safe state to minimize the risk to the vessel and crew (LR, 2017). Depending on the failure or incident causing stop of the function, the restored function may have reduced capacity. Restoration of the function may be assisted by a decision support system (such as the ACS) or performed automatically by the automation system (MCS).

6. Recovery from Damage events (Fire, Flooding) – To the maximum extent practicable, the MCS may support recovery from a damage event such as fire or flooding. In this regard an automated means such as a Damage Decision and Assessment (DDA) system may constantly review a comprehensive set of ship parametric data, assess, and make recommendations to the MCS for actions to be taken to mitigate shipboard fire, flooding, equipment, and structural damage, or CBR contamination. The DDA system function may be part of the ACS.

7. Cybersecurity – The vessel design may incorporate cybersecurity measures to ensure development of all autonomous control and communications systems adhere to secure software coding best practices, and that control systems are configured and physically protected in accordance with applicable cybersecurity guidelines.

6. Development of Specifications and Standards for USV Machinery Control Systems

There are a number of ongoing efforts to develop specifications and standards with detailed MCS requirements for USVs including efforts by the U.S. Navy, International Maritime Organization (IMO), governmental organizations, and classification societies. Some examples of publications that have been developed or are being developed for use on Unmanned Autonomous Surface Vessels include:

1. U.S. Navy
   a. Unmanned Maritime Autonomy Architecture (UMAA) / Architecture Design Description (ADD), U.S. Navy, PMS 406
2. IMO
   a. IMO MASS Code - refers to a goal-based code for Maritime Autonomous Surface Ships (MASS)123. The code is being developed by the International Maritime Organization (IMO) to regulate the operation of MASS123. The code is currently non-mandatory, but it is expected to become mandatory through SOLAS and other IMO instruments, as relevant, upon experience with its application1. The mandatory code is expected to enter into force on 1 January 2028.
3. Governmental Organizations
   a. UK Industry Code of Practice for Maritime Autonomous Systems Ships (MASS)
   b. Norwegian Forum for Autonomous Ships (NFAS) - Definitions for Autonomous Merchant Ships
4. Classification Societies
   a. ABS Requirements for Autonomous and Remote Control Functions
   b. Lloyd's Register Unmanned Marine Systems Code
   c. DNV-GL Class Guideline - Autonomous and remotely operated ships

7. Analysis of Industry Requirements for USV Machinery Control Systems

One of the main challenges for industry in development of USV machinery control systems with autonomous capabilities to support naval/military applications is that there is a gap between what requirements are available from commercial industry and what additional requirements are needed for USVs engaged in military missions with prolonged durations (i.e. 30 days or more). Appendix 1 provides a high-level comparison matrix of commercial industry standards that have been published for autonomous and remotely operated unmanned vessels mainly for commercial applications. From a quick survey/comparison of the guidance provided for commercial USVs from IMO, governmental organizations, and classification societies the main focus of these requirements is on vessel safety, crew safety, and protection of the environment. These are all design aspects that would also be suitable for a naval USV, however, these requirements (in general, existing industry guidance in Appendix 1) fall short of defining key MCS functions that will be needed on an unmanned vessel executing a prolonged military/naval mission. For example, further detailed requirements need to be developed for MCS key functions outlined in Table 1. Until more detailed industry guidance is developed, these MCS aspects will need to be defined in the shipbuilding specification as they are not typically included on commercial off the shelf (COTS) machinery control system designs. Note that NAVSEA is in the process of developing a USV MCS Design, Practices, and Criteria (DPC) Manual to address this gap in the requirements. Until these requirements are made available, based on the survey of existing industry requirements, it is recommended that the following tiers of requirements be invoked for MCS designs on naval USVs:

Tier 1 – Classification Society Rules for Commercial Ships (i.e., ABS Marine Vessel Rules) with notation for unattended engine-room (i.e., ABS ACCU Notation; ACCU = Automated Control System Certified for Unattended Engine-room) – Classification society rules cover the base minimum level of redundancy and safety required for commercial vessels and specify what automation is needed to support unmanned engine-room operation for up to a duration of up to 24 hours. ACCU indicates that a self-propelled vessel is fitted with various degrees of automation and with remote monitoring and control systems to enable the propulsion machinery space to be periodically unattended and the propulsion control to be affected primarily from the navigation bridge by human operators. These requirements are well developed having been in existence for decades and form the foundation for what MCS functions are required to support minimally manned or unmanned machinery room operations.

Tier 2 – Classification Society Guidance for Unmanned Autonomous/Remotely Controlled Vessels (i.e., ABS Requirements for Autonomous and Remote Control Functions) – These requirements will supplement the Tier 1

requirements and will provide additional requirements needed to support unmanned and autonomous operation. As outlined in Appendix 1, these guidance documents provide detailed design criteria for key functions such as: Autonomy Levels, Internal sensors (platform monitoring), External sensors and sources of data, Data interpretation, Remote (Off-Ship) Steering and Propulsion Control, Autonomous Steering and Propulsion Control, Emergency Stop, Sense and Avoid System (COLREGS) (Autonomous/Remote Navigation), and Cybersecurity.

Tier 3 – Additional Key MCS Design Criteria needed to support semi/full autonomous unmanned vessel operation (i.e., NAVSEA USV MCS Design, Practices, and Criteria (DPC) Manual (in development)) – Such a manual would close the gap in what is needed between a COTS MCS and an MCS capable of supporting autonomous unmanned operation for prolonged military missions. For example, topics outlined in Section 4 and 5 of this paper (not covered by Tier 1 or 2) as well as key functions listed in Table 1 would be addressed in detail. In the interim, these are topics that should be addressed in the shipbuilding specification until industry guidance becomes available.

Furthermore, in order to operate in a military environment and carryout military missions, additional design aspects may need to be considered that are beyond the scope of this technical paper. This could be a fourth tier of design criteria outlined in the shipbuilding specification or captured in a future naval/military standard, specification or DPC manual. For example, while the U.S. Navy is planning for USVs to be low-cost, high-endurance, reconfigurable ships based on commercial ship designs, with ample capacity for carrying various modular payloads (CRS, 2019), in order operate in a military environment and support weapons systems, exterior communication systems, and military sensors (i.e., air search radar, electronic warfare, sonar systems) design aspects such as electromagnetic compatibility (EMC) hardening, vibration dampening, acoustic signature mitigation, heat signature mitigation, radar cross section minimization, and survivability are all examples of things that a designer may need to consider in order to successfully carry out the military mission.

8. Conclusions

While a great deal of progress has been made in the development of standards and specifications for unmanned vessels capable of semi-autonomous (remotely controlled) or fully autonomous operation, further work is needed to identify and automate machinery control system functions necessary to support these modes of operation. Current industry guidance does not adequately cover all of the key MCS functions needed for unmanned autonomous operation. The U.S. Navy is working to develop an Unmanned Surface Vessel Control Systems Design, Practices, and Criteria Manual. Further refinement of standards and specifications for unmanned vessel machinery control systems will be essential to support the increasing demands from industry as unmanned vessels are likely going to fulfill an expanding list of mission roles and responsibilities for both naval and commercial applications.

9. Recommendations

The commercial and naval shipping industries, classification societies such as ABS, DNV/GL, and Lloyd's Register, international authorities such as IMO and IACS, and regulatory bodies such as USCG should continue to refine and publish updated standards and specifications for machinery control systems on unmanned vessels capable of being remotely or autonomously operated.

10. References

Congressional Research Service (CRS): Navy Large Unmanned Surface and Undersea Vehicles: Background and Issues for Congress, July 2019.

Gidget Fuentes, USNI News: Navy 'Hell Hounds' Squadron Crafting Missions for Small, Lethal Drone Fleet, May 20, 2024

United States Code of Federal Regulations (CFR): "Title 46 Shipping, Subchapter F Marine Engineering, Part 62 Vital System Automation", 2024 Edition

Nathan Gain, Naval News: "US Navy Issues Request For LUSV/MUSV CONOPS Development", January 6, 2020

Ann Diab: "Drones Perform the Dull, Dirty, or Dangerous Work," Tech.co, November 12, 2014

Bonnie Robinson: "Dull, Dirty, Dangerous Mission? Send in the Robot Vehicle," U.S. Army, August 20, 2015

Bernard Marr: "The 4 Ds Of Robotization: Dull, Dirty, Dangerous And Dear," Forbes, October 16, 2017.

International Maritime Organization (IMO), MARPOL Annex VI - Prevention of Air Pollution from Ships, 2024

Naval Sea Systems Command (NAVSEA), Unmanned Maritime Systems (PMS 406): Unmanned Maritime Autonomy Architecture (UMAA) Architecture Design Description (ADD), Version 1.1a, December 2019.

American Bureau of Shipping (ABS): "Requirements for Autonomous and Remote Control Functions", Library of ABS Rules and Guides, August 2022.

Det Norske Veritas (DNV): Class Guideline, "Autonomous and remotely operated ships", DNV-CG-0264, September 2021.

Lloyd's Register (LR): LR Code for Unmanned Marine Systems (UMS), June 2017

Appendix 1 - Unmanned Vessel – Autonomous and Remote Machinery Control Systems Requirements Survey

Requirements to Support Unmanned Remotely Controlled / Autonomous Vessel Operation	Autonomy Degree (See Note 1)	ABS Requirements for Autonomous and Remote Control Functions	UK Industry Code of Practice for Maritime Autonomous Systems Ships (MASS)	Lloyd's Register Unmanned Marine Systems Code	DNV-GL Class Guideline - Autonomous and remotely operated ships	Norwegian Forum for Autonomous Ships (NFAS) - Definitions for Autonomous Merchant Ships
Cybersecurity	1-4	2.9 Cyber Security 2.9.3(c) High Risk Level The vessel is to comply with the CS-1 or CS-2 notation requirements in the ABS Guide for CyberSecurity Implementation for the Marine & Offshore Industries (ABS CyberSafety® Vol. 2).	10.6 Cyber security - A Cyber Security Analysis shall be conducted.....	Section 9 - Level of Integrity (Software) Lloyd's Register Cyber Enabled Ships – Draft ShipRight Procedure ISO 27032 cyber security certification	SECTION 2 MAIN PRINCIPLES – [11] Cyber security - The design of both the overall auto remote infrastructure and the individual systems should explicitly take cyber security aspects into account. DNVGLCP- 0231 Type approval programme – Cyber security capabilities of control system components	Refers to Cyber-enabled ships, ShipRight procedure – autonomous ships. First edition, July 2016, A Lloyd's Register guidance document.
Autonomy Levels Defined	1-4	4 Smart-to-Autonomy Levels i) Smart: System augmentation of human functions. The system provides passive decision support, such as in the form of health or performance anomaly detection, diagnostics, prognostics, decision/action alternatives, and/or recommendations. ii) Semi-Autonomy: Human augmentation of system functions. System operation builds upon a smart foundation and is governed by a combination of system and human decisions and actions. iii) Full Autonomy: No human involvement in system functions. The system makes decisions and takes actions autonomously, Humans perform a supervisory function solely, and have capability to intervene and override actions made by the system.	Table 2.3: Level of Control Definitions – 6 levels: 0- Manned 1- Operated 2- Directed 3- Delegated 4- Monitored 5- Autonomous	4.1.2 Autonomy 7 Levels (AL): 0- Manual 1- On-board Decision Support 2- On &Off-board Decision Support 3- 'Active' Human in the loop 4- Human on the loop, Operator/ Supervisory 5- Fully autonomous: Rarely supervised operation 6- Fully autonomous: Unsupervised operation	Section 4, Table 1 Levels of autonomy functions (5 levels) M - Manually operated function. DS - System decision supported function. DSE - System decision supported function with conditional system execution capabilities (human in the Loop) SC - Self controlled function (the system will execute the operation, but the human is able to override the action. Sometimes referred to as 'human on the loop'. A - Autonomous function (the system will execute the function, normally without the possibility for a human to intervene on the functional level).	4.2 Operational autonomy levels – proposes four operational autonomy levels: Decision support: This corresponds to today's and tomorrow's advanced ship types with relatively advanced anti-collision radars (ARPA), electronic chart systems and common automation systems like autopilot or track pilots. The crew is still in direct command of ship operations and continuously supervises all operations. This level normally corresponds to "no autonomy". Automatic: Automatic: The ship has more advanced automation systems that can complete certain demanding operations without human interaction, e.g. dynamic positioning or automatic berthing. Constrained autonomous: The ship can operate fully automatic in most situations and has a predefined selection of options for solving commonly encountered problems, e.g. collision avoidance. Fully autonomous: The ship handles all situations by itself. This implies that one will not have an SCC or any bridge personnel at all. This may be a realistic alternative for operations over short distances and in very controlled environments. However, and in a shorter time perspective, this is an unlikely scenario as it implies very high complexity in ship systems and correspondingly high risks for malfunctions and loss of system.

252

Proceedings of the International Ship Control Systems Symposium (iSCSS)

Requirements to Support Unmanned Remotely Controlled / Autonomous Vessel Operation	Autonomy Degree (See Note 1)	ABS Requirements for Autonomous and Remote Control Functions	UK Industry Code of Practice for Maritime Autonomous Systems Ships (MASS)	Lloyd's Register Unmanned Marine Systems Code	DNV-GL Class Guideline - Autonomous and remotely operated ships	Norwegian Forum for Autonomous Ships (NFAS) - Definitions for Autonomous Merchant Ships
Internal sensors (platform monitoring)	2,3	3.4 Monitoring and Alarm System(s) 3.4.1 Goal - This subsection establishes minimum requirements for monitoring and alarm system(s). 3.4.2 Functional Requirements - In order to achieve the goal, the following functional requirements are embodied in the provisions of this chapter: ● Monitoring and alarm system(s) is/are to be provided. ● The Operator is to be provided with the necessary information and awareness of the operation of the function. 3.4.3 Requirements - In order to comply with 5/3.4.2, the following apply. 3.4.3(a) Monitoring and alarm system(s) - The monitoring and alarm system(s) is/are to comply with 4-9-2/7 of the Marine Vessel Rules. Displays for the monitoring and alarm system(s) is/are to be provided at the operator control station(s). 3.4.3(b) Control awareness - Means are to be provided at all operator stations to identify the system which is having present control over the Function.	Section 7.6 - Internal sensors (platform monitoring)- Internal sensors may be fitted for monitoring the platforms' vital functions and safety. This may include a monitoring capability which would normally be provided by crew onboard.	Chapter 4 Control System, 4.1.2 - The control system shall record the sensor output for all sensors on which the control system is dependent and all propulsion and manoeuvring system activities at appropriate intervals over the duration of the mission. This data shall be protected from loss or damage and readily recoverable in all Reasonably Foreseeable Operating Conditions.	SECTION 5 VESSEL ENGINEERING FUNCTIONS [6.4.1] Status and situational awareness - It should be possible to observe real-time operational status, readiness and capacity of the vessel function or system from RCC. [6.4.2] Alerts 6.4.2 - Abnormal conditions and situations should generate alerts that in general are categorised and prioritized.....	Table 2 – MUNIN Main function groups and sub-groups Propulsion Main energy Electric Auxiliary
External sensors and sources of data	2,3	APPENDIX 1 - High Level Goals (Autonomous Vessel) 2.4 Safety of Navigation = The vessel is to navigate based on the principles in COLREG. This includes: ● Maintaining steering capability (refer to A1/2.1 above) ● Communicating with surrounding vessels in accordance with the requirements of the current regulatory regime ● Communicating distress to surrounding vessels ● Weather monitoring and routing ● Notice to Mariners and Navigation reference ● Law of the Seas compliance	Section 7.7 - External sensors and sources of data - External sensors may be fitted to sense and/or measure the environment, surroundings, navigational data, and other platforms and systems,......	Chapter 6 Navigation Systems. 4.1.2 - The UMS shall be fitted with sensors, systems and equipment to provide feedback to the Operator or autonomous control system of the operating state and potential hazards. The feedback should be appropriate for the Autonomy Level, and operating state and environment of the UMS.	SECTION 4 NAVIGATION FUNCTIONS, [3] Condition detection....Facilities supporting the principles in COLREG rule 5 of maintaining a proper lookout and the subsequent design criteria from SOLAS V/22 shall be a part of the vessel design. These facilities shall serve the purpose of: — Maintaining a continuous state of vigilance by sight and hearing, as well as detection of significant change in the operating environment. — Fully appraising the situation and the risk of collision, grounding and other dangers to navigation. — Detecting ships or aircraft in distress, shipwrecked persons, wrecks, debris and other hazards to safe navigation.	5 Operating design domain- The Automatic DNT will be the set of tasks assigned to the automation system, on shore or on board. This defines the requirements for sensor systems, object detection and classification, anti-collision systems etc.

Proceedings of the International Ship Control Systems Symposium (iSCSS)

Requirements to Support Unmanned Remotely Controlled / Autonomous Vessel Operation	Autonomy Degree (See Note 1)	ABS Requirements for Autonomous and Remote Control Functions	UK Industry Code of Practice for Maritime Autonomous Systems Ships (MASS)	Lloyd's Register Unmanned Marine Systems Code	DNV-GL Class Guideline - Autonomous and remotely operated ships	Norwegian Forum for Autonomous Ships (NFAS) - Definitions for Autonomous Merchant Ships
Data interpretation	2,3	3.5 Data Analytics 3.5.1 Goal This subsection establishes minimum requirements for constituent systems using data analytics techniques. Data analytics techniques include machine learning, artificial intelligence, data mining and statistics.	Section 7.8 - Data interpretation - - The ability to interpret sensor data on board in a timely manner with regard to its impact on MASS safety and performance and to execute its responsibilities in accordance with COLREG and international law; The ability to transmit sensor data in a timely manner to an off-board system or human operator.....	Chapter 6 Navigation Systems, 4.1.4	SECTION 4 NAVIGATION FUNCTIONS [4] Condition analysis - Facilities supporting the classification of objects detected should be provided. Classification of other vessels should include the ability to distinguish between the following vessel classes - see COLREG Rule 18:	5 Operating design domain - The Dynamic Navigation Task (DNT) – adapted from the "dynamic driving task" defined in [3], will be the sum of all tasks that need to be executed by the ship automation system and/or the human operators to handle all foreseeable operational requirements in the ODD.
Remote (Off-Ship) Steering and Propulsion Control	2,3	SECTION 6 Remote Control Functions 2.1 Criteria - The function is to be clearly identified. The function may reside within a single system or it may be performed by a combination of multiple constituent systems working in concert to deliver the function. The remote control function is to comply with the following criteria: i) The Remote Control Station is to be constantly manned ii) The Remote Operator is to be designated and will have responsibility over the Function being controlled in a remote location. iii) The Remote Operator is to be able to monitor the system and operations under remote control at all times. iv) The Remote Operator is to be able to control the function in real-time from the remote location.	Section 7.9 Control – off-board human operator The MASS shall have the ability to be controlled by a Control System which may be an on-board, off-board system or human operator, or a distributed system involving one or more of these elements.	Chapter 4 Control System, Section 4.2, Remotely controlled control system 4.2.1 The control panel shall be designed using human factors methodology. The controls are to be easily identifiable and are to be arranged in a logical way to reflect their function, means of operation and hierarchy of importance. 4.2.2 The Operator is to be alerted if the UMS is approaching operating range limit. If the UMS exceeds the operating range limit, it shall automatically return into a safe state alerting the Operator.	SECTION 5 VESSEL ENGINEERING FUNCTIONS, [4.2.3.2] Propulsion and steering machinery - The main command location for control of propulsion and steering machinery should be at the location of the responsible engineering watch in RCC.	4.4 Ship autonomy types - Remote control. Same as direct control, however here the SCC is in control of the ship. One can also here argue that this is not really a type of autonomy. However, as communication links normally cannot be made 100% reliable, the ship will in most cases need fallback procedures that can be activated autonomously when communication fails.
Autonomous Steering and Propulsion Control	4	APPENDIX 1 - High Level Goals (Autonomous Vessel) 2 Goals 2.1 Maintain Steering & Propulsion The propulsion system and supporting auxiliaries are to be designed and constructed to provide • Continuity of propulsion power, • Continuity of electrical power, and • Continuity of position/course	Section 7.9 Control - on-board The MASS shall have the ability to be controlled by a Control System which may be an on-board, off-board system or human operator, or a distributed system involving one or more of these elements. 7.11 - Propulsion control - MASS shall have propulsion control as far as necessary to be capable of ensuring that safe operating speeds appropriate to its situation are not exceeded. 7.12 - The MASS shall have steering control as may be necessary to maintain a safe heading.	Chapter 4 Control System, Section 4.3, Autonomous control system 4.3.1 The autonomous control system shall carry out the programmed mission in an accurate and timely manner with an appropriate level of integrity. 4.3.2 The autonomous control system shall react to changes in its environment including other vessels and moving objects. 4.3.3 It shall be possible within a timeframe appropriate for the operational profile of the UMS to override the autonomous control system to initiate a corrective action or activate a safe state. 4.3.4 The UMS shall fail to a safe state in the event of deviation from normal operation and initiate a system to facilitate location and recovery. 4.3.5 The link between the autonomous control system and the Operator is to be as far as reasonably practicable maintained at all times.	SECTION 5 VESSEL ENGINEERING FUNCTIONS, [4.2.6] Automatic operation (AO) - If the propulsion or steering function is arranged to be automatically operated (AO): The automation system should fully control propulsion/steering machinery and supporting auxiliary systems in all defined operational modes. The engineering watch in RCC will supervise the operation and may intervene if deemed necessary. The automation system may be arranged such that the responsible personnel is given a notification or warning in due time before it carries out an order. The operator may then choose abort or modify the order.	4.4 Ship autonomy types - Fully autonomous. Not supervised by SCC. This type of autonomy is generally complicated to implement and will also mean that the owner of the ship has less control of its operation. Generally, approval of this type of ship will require major changes in regulations, mainly because there is no longer any equivalence to the master or other officers on board.

Requirements to Support Unmanned Remotely Controlled / Autonomous Vessel Operation	Autonomy Degree (See Note 1)	ABS Requirements for Autonomous and Remote Control Functions	UK Industry Code of Practice for Maritime Autonomous Systems Ships (MASS)	Lloyd's Register Unmanned Marine Systems Code	DNV-GL Class Guideline - Autonomous and remotely operated ships	Norwegian Forum for Autonomous Ships (NFAS) - Definitions for Autonomous Merchant Ships
Emergency Stop	4	2.1.2 Operator and Operations Supervision Level An operator is to be designated and will have responsibility over the Autonomous Function. The operator may be physically located onboard the vessel or in a remote location. The operator station is to be constantly manned. i) The operator is to supervise the function executions either continuously, periodically or as needed ii) The operator is to be able to intervene, override, and take over the operation when deemed necessary by the operator	7.10 Emergency Stop - The MASS shall have a defined condition of Emergency Stop, which must be fail safe under conditions where normal control of the MASS is lost. Under Emergency Stop, propulsion is reduced to a safe level in a timely manner.	Chapter 4 Control System, Section 4.1.11 - An emergency manual control enacted through a high integrity independent system is to be provided in a prominent position on all primary and secondary Operator consoles to activate a safe state.	SECTION 5 VESSEL ENGINEERING FUNCTIONS, [4.2.6] Automatic operation (AO) -...It should be possible to manually intervene and control the propulsion/steering system from the RCC....The engineering watch in RCC should be provided with sufficient monitoring, alerts, diagnostic functions and controls to intervene in case of unexpected events and failures which are not safely handled by the automatic control functions.	5 Operating design domain...It is generally not possible to guarantee that the conditions the ship operates under, always are within the ODD limits. Exceptions can occur, e.g., in cases of major technical failures or sudden changes in weather conditions. To handle such cases, a DNT Fallback [3] must be defined and implemented. The DNT Fallback should take the ship to as safe a situation as is possible under the given circumstances ("Minimal risk condition" [3]). This will consist of different strategies, dependent on the operational condition. Normally, one can assume that the DNT Fallback will be updated from the SCC before the ship's operational context changes significantly.
Sense and Avoid System (COLREGS) (Autonomous/Remote Navigation)	4	APPENDIX 1 - High Level Goals (Autonomous Vessel) 2.4 Safety of Navigation - The vessel is to navigate based on the principles in COLREG. This includes: • Maintaining steering capability (refer to A1/2.1 above) • Communicating with surrounding vessels in accordance with the requirements of the current regulatory regime • Communicating distress to surrounding vessels • Weather monitoring and routing • Notice to Mariners and Navigation reference • Law of the Seas compliance	Section 7.13 COLREG- compliant behaviors and fail-safes - The Control System shall be capable of operating in accordance with the requirements of Chapter 5 and Chapter 10 to a level of compliance with COLREGS appropriate to the MASS class.	Chapter 6 Navigation Systems, 4.1.13 1.1.1 This Chapter covers the systems required for safe navigation of the UMS. This includes systems on board and off-board for the identification and avoidance of navigational hazards and the communication between these, and systems for communication with other vessels to relay intentions. It does not include control of the navigation system itself or the control of systems to carry out avoidance of navigational hazards.	Appendix D - 3.7 Navigation Decision Support system for Collision- and Grounding Avoidance – NDSS CA-GA - To cover unmanned vessels and based on input from the above navigation sensors, a total system for determining the risk of collision and grounding and aiding in execution of a safe voyage plan should be provided. This system should use and process all available information from navigational sensors and systems in a robust manner in order to avoid single failures.	4.4 Ship autonomy types - Automatic bridge. The bridge system controls the ship while crew on the bridge continuously monitors the situation and can intervene at any time. The level of automation may be arbitrarily high, but crew is always ready to intervene. Table 2 – MUNIN Main function groups and sub-groups 2.4 Anti-collision – Detect and avoid other objects in the vicinity that may be a danger to the ship. Use COLREGS where applicable. 2.5 Anti-grounding - Avoid groundings by keeping to safe channels with

Note 1: IMO degrees of Autonomy

Degree one: Ship with automated processes and decision support. Seafarers are on board to operate and control shipboard systems and functions. Some operations may be automated and at times be unsupervised, but with seafarers on board ready to take control.

Degree two: Remotely controlled ship with seafarers on board. The ship is controlled and operated from another location. Seafarers are available on board to take control and to operate the shipboard systems and functions.

Degree three: Remotely controlled ship without seafarers on board. The ship is controlled and operated from another location.

Degree four: Fully autonomous ship. The operating system of the ship is able to make decisions and determine actions by itself.

Stability and control of a ship electric grid emulator

G Tsourakis* PhD   J Prousalidis* PhD, Prof. NTUA

NTUA, GR
* Corresponding Author. Email: tsouraki@power.ece.ntua.gr

Synopsis

This paper presents an analysis of the frequency control and stability of the ship electric power system emulator of the School of Naval Architecture and Marine Engineering of NTUA. The emulator is an AC three-phase microgrid, comprising Generation, Distribution, Consumption, Protection and Supervising Monitoring-Control sub-systems. The generation system consists of (three) small AC synchronous generators (5 to 6 kVA each), while its loads are a passive RL load and a three-phase induction motor. The system is an electric island as its frequency and voltage are defined by its synchronous generators. The use of converter-driven three-phase induction motors as prime movers of the synchronous generators results to a particular power system, with some special characteristics in its stability and control.

Keywords: Stability; ship grid emulator; educational

1. Introduction

The mandate for reduced environmental footprint of all ships according to the resolutions of the International Maritime Organization (IMO) and the European Union, as well as other governmental bodies, has led worldwide to the development of a series of measures, all under the umbrella of the sustainable decarbonisation of the maritime sector.

The improvement of the efficiency of the entire powertrain of the ship energy systems has been under investigation during the last two decades and within this context it has been shown that the extensive electrification of ship systems, including propulsion can be one good way to reach the ultimate green target at least for certain ship types.

Within this framework of ship electrification several issues during operation need to be investigated and further clarified, such as power quality problems, stability problems and short circuit faults. To this end, a ship electric grid emulator system has been materialized at NTUA. The system is actually an AC three-phase one, comprising Generation, Distribution, Consumption, Protection and Supervising Monitoring-Control sub-systems.

The aim of this paper is to present the concept of operation of this ship electric grid emulator, but also the analysis of important operating conditions of all the aforementioned sub-systems focusing on designing more efficient and environmentally friendly ships.

Authors' Biography
Georgios Tsourakis is a post-doc researcher at the National Technical University of Athens.
John Prousalidis is Professor at the School of Naval Architecture and Marine Engineering of the National Technical University of Athens.

2. Description of physical system and implemented model

A simplified one-line diagram (SLD) of the system is shown in Figure 1. Dashed lines indicate future installations.
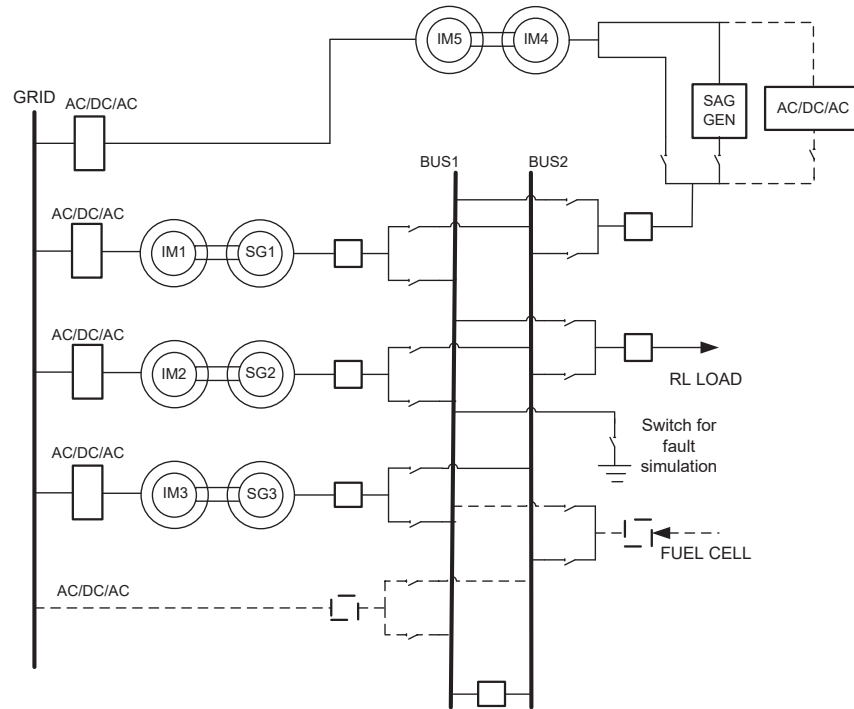

Figure 1: Single-Line Diagram of the grid emulator

The power generation sub-system comprises three synchronous generators (two of 5.9 kVA/400V/50Hz/pf=0.8 and one of 5 kVA/400V/50Hz/pf=0.8). As the generators are of low power, they produce Low Voltage (400 V), so no transformers are used in the system. Due to the difficulties of finding and installing small diesel engines, an induction motor fed by the local grid via an AC/DC/AC converter plays the role of the prime mover for each generator, while the governor operation is emulated via the power electronic inverter rotating the prime mover - electric motor. As it will be shown, this results to an adequate emulation of the droop frequency control. Also, the converter-driven AC induction motor can potentially be controlled in a way to emulate a prime mover like a diesel engine.

On the other hand, the generator output voltage is regulated via installed Automatic Voltage Regulators (AVRs). It is noted that the system is essentially electrically isolated with respect to the local grid, with the exception of auxiliary circuits (e.g. the AVRs of the synchronous generators and protection relays). This allows the emulation of the electric grid of a ship, with its protection and control systems, which is the first priority of the grid emulator.

The system loads are a passive RL load and a three-phase induction motor. Similarly to the synchronous generators (but with opposite power flow), the mechanical load of the motor is another induction motor connected to an AC/DC/AC converter and acting as a regenerative brake. The ensemble of the motor and AC/DC/AC converter can be used to simulate various mechanical loads, e.g. a propeller.

The system has been modelled in MATLAB/Simulink. Induction motor and synchronous generator models have been developed in Simulink, implementing the corresponding well-known rotating electric machine equations from (Krause, 2000). The rotating shaft of each generator set is common for the induction motor and the synchronous generator. Assuming all rotating masses can be lumped as a single one, a single equation of motion has been used for each generator set, i.e. the rotor speed is common for the induction motor and the synchronous generator. The electromagnetic torque of the induction motor (resp. synchronous generator) tends to accelerate (resp. decelerate) the rotor.

3. Frequency control

The use of induction motors as prime movers results to a particular system with respect to Frequency Control. To demonstrate the operation principle of the grid emulator, a single generator set is analysed first, as shown in Figure 2. This can refer to either a single generator set being in operation, or an equivalent for two or three generator sets.
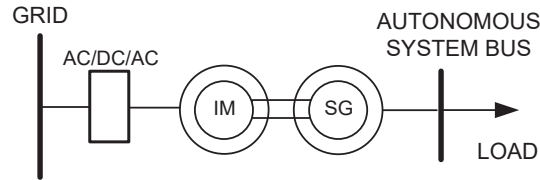

Figure 2: Single-Line Diagram of one generator set

The well-known characteristic curve of the induction motor power as a function of its rotor speed is shown in Figure 3. The induction motor is supplied with terminal voltage of nominal amplitude and frequency (50 Hz). Normal operation of the induction motor is within a narrow range close to 1 per unit (pu) rotor speed, i.e. the speed that corresponds to electrical frequency of 50 Hz, while the motor power is zero at exactly 50 Hz. For example, to supply 50% of its nominal mechanical power, the rotor speed is approximately 0.98 pu. Since the rotors of the induction motor and the synchronous generators are coupled on the same axis, the electric frequency of the autonomous system is 98% of the induction motor stator frequency, i.e. 49 Hz. The frequency of the voltage supplied to the induction motor can be adjusted, in order to have 50 Hz at the autonomous system.
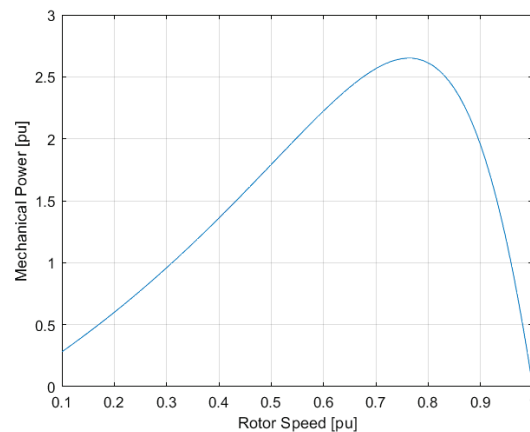
Figure 3: Power – Rotor Speed characteristic curve of induction motor

3.1. *Primary Frequency Control: Step Increase of Load*

To demonstrate the primary frequency control of the grid emulator, we simulate a step increase of the load, starting from an operating point with the two 5.9 kVA generators in operation (SG1 and SG2), initially supplying an RL load of 4.17 kW. At t=2 s, a 10% step increase of the load is simulated. Figure 4(a) shows that the two generators equally share the load increase, as expected since they are identical. Figure 4(b) shows the stator frequency of the two induction motors that drive the two generators (constant at 50 Hz), as well as the electric frequency that corresponds to the rotor speeds of the two generators. The common frequency of the two synchronous generators is the autonomous system frequency. After the load increase, the autonomous system frequency drops, which is the expected result of primary frequency control (Kundur, 1994). On a 5.9 kVA base, the droop of each generator can be calculated at approximately 3.2%. Therefore, the induction motor of each generator operates as an equivalent turbine with its governor and droop control. Approximating the characteristic curve of Figure 3 to be linear at the normal operating region, its slope defines the droop of the equivalent governor, defined as:

$$R = \frac{\Delta f}{\Delta P}$$

, where Δf is the steady-state change of the frequency in pu and ΔP is the steady-state change of active power in pu. On a 5.9 kVA base, the droop of each generator can be calculated at approximately 3.2%.
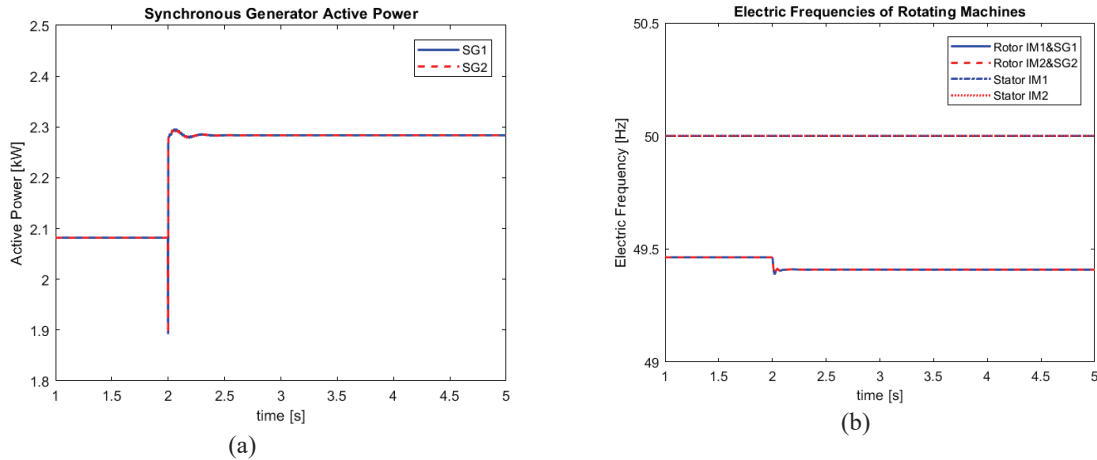
Figure 4: Response to a load step change: (a) Active power of synchronous generators and (b) rotating machines' frequencies

3.2. *Secondary Frequency Control: Step change of induction motor frequency*

Next, the system response to a step change of the electric frequency of the voltage applied to one of the induction motors (IM2) is examined. This results to a shift of the corresponding power-speed curve of Figure 3 to the right, so that zero power corresponds to 51 Hz. Figure 5 shows the original curve (blue, continuous), together with the shifted curve (red, dashed).
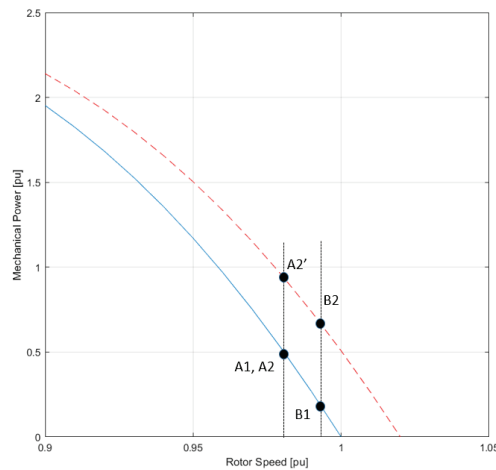
Figure 5: Power – Rotor Speed characteristic curves of induction motors

If the two motors initially operate at the same operating point (A1, A2) and at equilibrium (i.e. their output power matches the load), they provided equal mechanical power. Given that their rotors are synchronised via the autonomous system, they have the same rotor speed at equilibrium. Assuming that after the step change of its stator electrical frequency, IM2 maintains the same rotor speed, it would operate at point A2', while IM1 remains at A1. However, there is no equilibrium under these conditions, since the total sum of power from IM1 and IM2 exceeds the load power. Therefore, the motors will accelerate, i.e. their operating points will move to the right. An equilibrium is possible at operating points B1 and B2, where the total power sum is the same with the initial equilibrium point.

The dynamic response of the system is shown in Figure 6. Figure 6(a) shows the active power of each synchronous generator, while Figure 6(b) shows the frequencies of the rotating machines. In the latter, the applied step change can be seen in stator frequency of IM2.
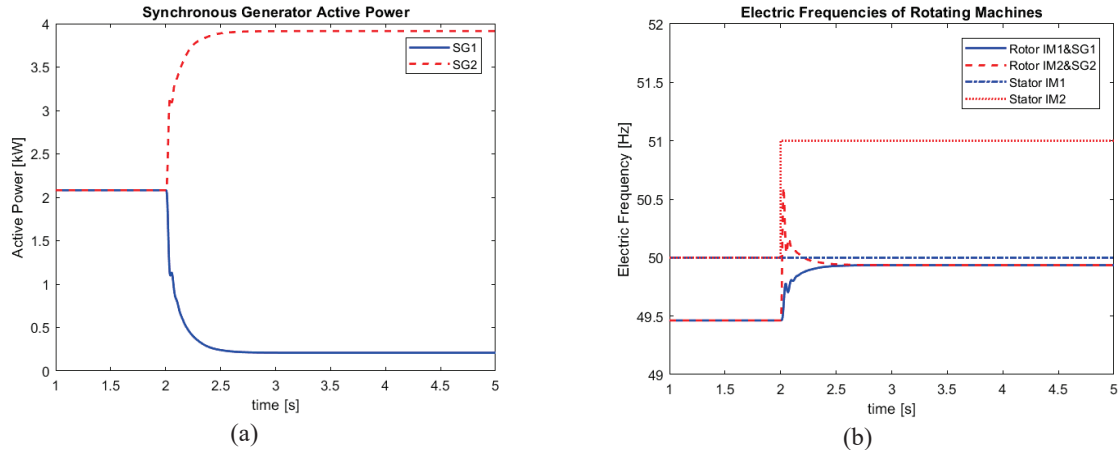
Figure 6: Response to a step change in the frequency of the voltage applied to IM2: (a) Active power of synchronous generators and (b) rotating machines' frequencies

As expected, the results of Figure 6 show that SG2, which is driven by IM2, takes now a higher share of the load power, while the autonomous system settles at a higher frequency. Therefore, adjustment of the difference of stator frequency of IM1 and IM2 provides a means for regulating power sharing and system frequency.

4. Large-disturbance stability

In this section, the response of the autonomous system to three-phase faults is examined from the stability point of view. A three-phase fault is simulated at the AC bus of the autonomous system by decreasing temporarily the load inductance to a very small value at t = 2 s. The terminal voltages of the two synchronous generators, shown in Figure 7(a), are identical as they are connected at the same AC bus, without transformer. Figure 7(b) shows the rotor speeds (frequencies) of the two machines. It can be seen that the system reaches a steady-state equilibrium during the fault at a higher rotor speed.
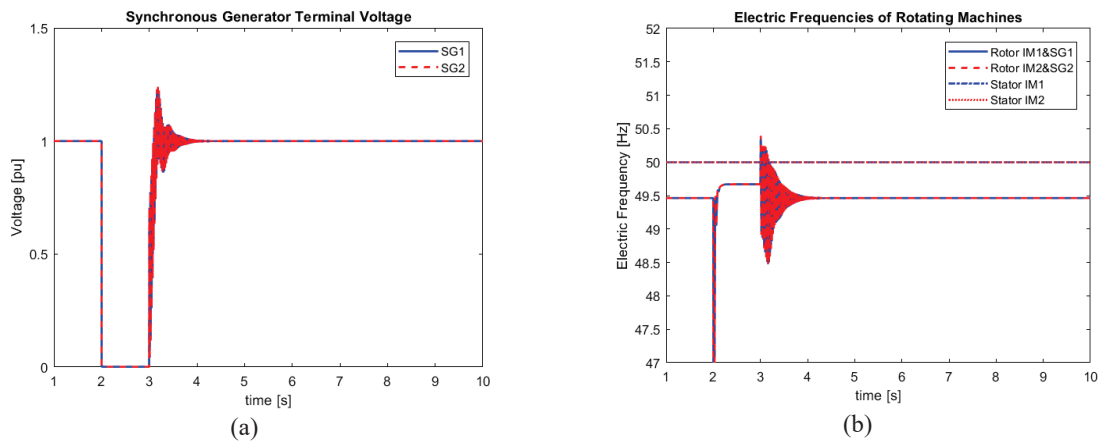
Figure 7: Three-phase fault response: (a) Synchronous generators' terminal voltage (a) and rotating machines' frequencies

Figure 8(a) shows the active power of the rotating machines. During the fault, the power into the induction motors reaches a new steady-state value. As the active power of the synchronous machines is zero during the fault, all the power of induction motors is consumed in losses. Figure 8(b) shows that during the fault the excitation voltage of the synchronous generators is limited to its maximum value.

As in common autonomous systems, the risk of loss of synchronism is very small, since the generators accelerate together. However, in the specific system, overfrequency also appears not to be of concern. Indeed, as the power in an out of the induction motors is reduced, their speed is increased, however it is limited at their stator frequency which corresponds to zero mechanical power.
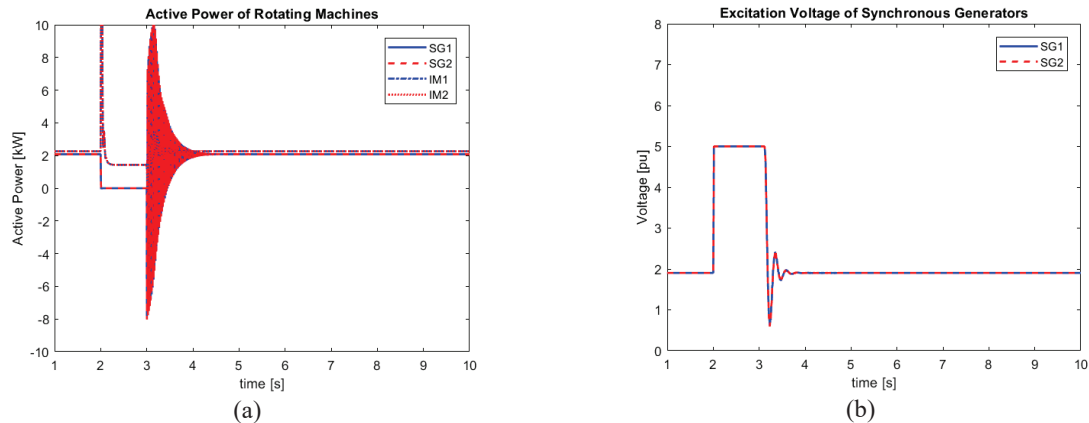
Figure 8: Three-phase fault response: Synchronous generators' (a) active power (a) and excitation voltage

5. Conclusions

This paper presented an analysis of the frequency control and stability of the ship electric power system emulator of the School of Naval Architecture and Marine Engineering of NTUA. The emulator is an AC three-phase islanded microgrid, comprising Generation, Distribution, Consumption, Protection and Supervising Monitoring-Control sub-systems.

It was shown that the use of converter-driven induction motors as prime movers for the synchronous generators results to a peculiar system with special characteristics. The slope of the induction motor power-speed curve defines the droop of the equivalent prime mover (primary frequency control), while modifying the stator frequency of the induction motors can be an effective way for power sharing and secondary frequency control.

Finally, the autonomous system response to three-phase faults has been analyzed and it has been shown that it reaches a steady-state equilibrium if the fault duration is high enough. Therefore, no risk of either losing synchronism or overfrequency occurs.

References

2023/1804/EU Regulation on the deployment of alternative fuels infrastructure, and repealing Directive 2014/94/EU, 13 September 2023, Official Journal of the European Union (22 Sep 2023).

2023/1805/EU Regulation on the use of Renewable and low-carbon fuels in maritime transport, and amending Directive 2009/16/EU, 13 September 2023, Official Journal of the European Union (22 Sep 2023)

Krause P.C., Wasyncczuk O. & Sudhoff S.D.: "Analysis of Electric Machinery", IEEE Press, New York, 2000.

Kundur P.: "Power System Stability and Control", McGraw-Hill, 1994.

Lee, K.L., Ong, L.K., Leow, K.S., "Making green ship a reality", Proceedings of 2004 International Naval Conference (INEC 2004), Amsterdam (The Netherlands), 14-16 March 2004, pp. 180-190.

MARPOL 73/78 Annex VI: "Prevention of Air Pollution from Ships, International Maritime Organization", August 2004.

MEPC 61/inf.18, "Reduction Of GHG Emissions From Ships - Marginal abatement costs and costeffectiveness of energy-efficiency measures", October 2010.

MEPC.1-Circ.681-2: "Interim Guidelines On The Method Of Calculation Of The Energy Efficiency Design Index For New Ships", August 2009.

MEPC.1-Circ.684: "Guidelines for Voluntary Use Of The Ship Energy Efficiency Operational Indicator (EEOI)", August 2009.

MEPC.1-Circ.683: "Guidance for The Development of A Ship Energy Efficiency Management Plan (SEEMP)", August 2009.

Prousalidis J., Patsios C., Tsourakis G., Dallas S., Antonopoulos G., Katsikas P, Karlovits N, Georgiou V., Bucknall R. Greig A. : "Comparison of DC vs AC via ship electric grid emulators", Proceedings of 12th INEC (2014), paper No 63, Amsterdam (The Netherlands), May 2014.

Optimizing Fuel Management for Halifax Class Frigates: Leveraging Sensor Data for Enhanced Efficiency

Igor Lapin*

* *L3Harris MAPPS Inc., Canada*
* Corresponding Author. Email: igor.lapin@l3harris.com

Synopsis

This article explores how operational data from sensors integrated with Royal Canadian Navy (RCN) Halifax Class Frigates onboard Integrated Platform Management System (IPMS) can be leveraged to minimize fuel consumption. The idea is to use IPMS data logged by the Equipment Health Monitoring (EHM) software tool. This, along with data collected from temporary fuel meters installed on several Halifax Class Frigates, aids in the development of fuel consumption models for onboard power generating and propulsion equipment. The study aims to identify the most fuel-efficient driving mode among the options available for specific operational conditions, leveraging the Combined Diesel or Gas (Turbine) Propulsion System (CODOG) and twin shaft arrangement of the Halifax Class Frigates. Building upon this, the developed fuel consumption models are employed to implement various fuel optimization methods on a specific ship platform. This entails the adaptation and integration of these methods into dashboards for enhanced accessibility, with the fuel consumption models providing essential input data.

In the course of the study, several fuel optimization techniques were examined, revealing valuable information about their applicability in specific cases, taking into account factors such as data availability and reliability. The development process of equipment fuel consumption models showcased how sensors designed for operational support could enhance fuel consumption optimization efforts.

Fuel Management Dashboard (FMD) application prototype was developed to facilitate user access to current operational data, fuel consumption-related information as well as fuel consumption optimization tools.

Enhanced value could be realized with the installation of high-quality fuel flow meters during ship construction or the prolonged use of temporary fuel flow meters to capture data across the ship's speed and load ranges.

The IPMS emerged as a valuable information source supporting fuel optimization initiatives.

Validation of the FMD performance in the field and its value to end-users is pending; however, the progress achieved thus far shows promising potential.

Keywords: Navy; Fuel Consumption; Fuel Efficiency; Data Analysis; Simulation and Modelling.

1. Introduction

While in naval operations, mission success takes precedence over fuel consumption concerns, there are still many opportunities to optimize fuel usage, improve endurance, and reduce associated costs (Brown, 2007). Fuel cost constitutes a significant portion of overall ship operating expenses (Schreiner, 2021). Continuous monitoring of fuel usage efficiency, based on reliable equipment fuel consumption models, is essential to ensure efficient operation, enhance endurance, and enable prompt corrective action when deviations occur. (Mandler, 2000, Schreiner, 2021)

The Halifax-class propulsion system operates in a CODOG configuration. Main propulsion is provided by two General Electric LM2500 Gas Turbines (GTs), each rated 17.7MW, one SEMPT Pielstick Propulsion Diesel Engine (PDE) rated to deliver 6.47MW at rated speed, the main reduction gear is Royal Schelde cross connect gear box, that connects the gas turbines and diesel engine to port and starboard shaft lines driving two Escher Wyss controllable, reversible-pitch propellers (see Figure 1). This propulsion system configuration offers various driving modes. Refer to Table 1. These different modes influence propulsion fuel consumption, with multiple options often available for achieving the same speed (Schreiner, 2021).

The potential sources of data required to build fuel consumption models include engine shop trials, ship sea trials, and historical data collected by the onboard Integrated Platform Management System (IPMS) also known as Supervisory Control and Data Acquisition (SCADA) System (Brown, 2007, Mandler, 2000).

The shop trial data, carried out by the Original Equipment Manufacturer (OEM) may not perfectly reflect the fuel efficiency of the engine when operated on a specific ship in real-world circumstances. This discrepancy can

Author's Biography

Igor Lapin is a Software Lead at Marine Systems Simulation and Data Analytics Group of L3Harris MAPPS Inc., Canada. He holds a BSc in Marine Engineering from State Marine Academy in Odessa, Ukraine and a certificate in Machine Learning and Data Science from McGill University in Montreal, Quebec, Canada. His career includes 18 years onboard as a marine engineer, 8 years as a ship technical superintendent and a senior power plant engineer, and 6 years as a data scientist. He is a holder of a first-class marine engineer certificate. Author's current research interests include modelling and simulation of ship equipment processes using System Control and Data Acquisition (SCADA) generated sensors time series data and data analytic tools, focusing on application of machine learning in equipment maintenance optimization, fuel and energy efficiency improvement, development of marine and power generation equipment digital twins, and digitalization of marine operations.

arise due to differences in operating conditions, ship-specific factors, and limited representation inherent in the testing program.
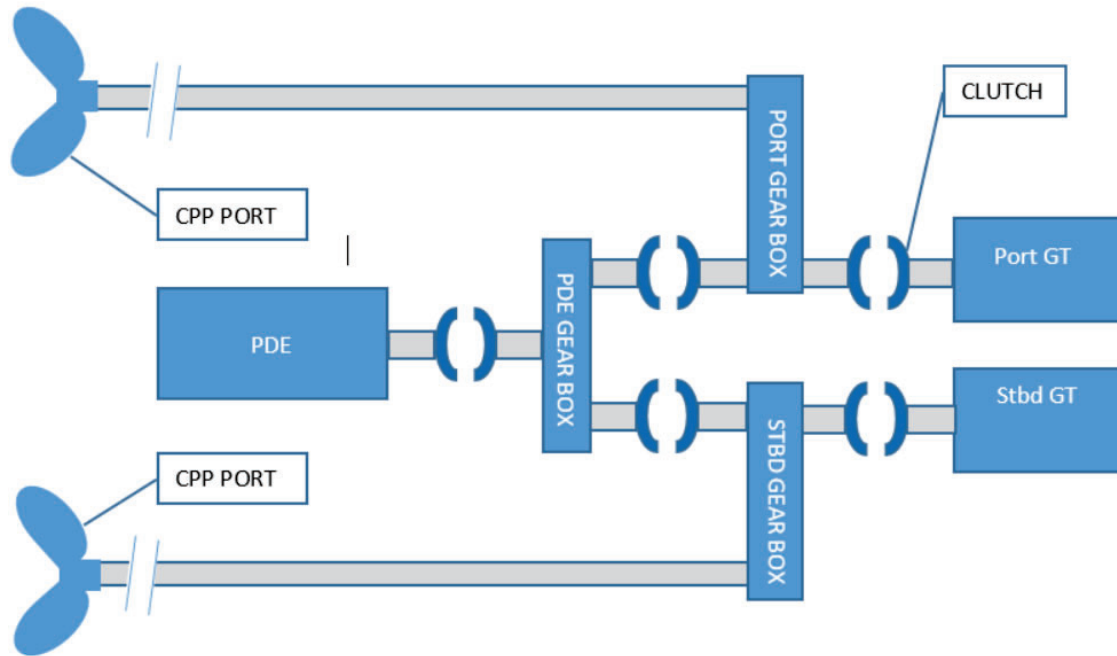

Figure 1 Halifax Class Frigate principal drivetrain diagram

Table 1 Halifax Class Frigates CODOG driving modes

Driving mode	Name	Description
PDE XCON	Propulsion diesel engine cross connected	PDE connected to both propeller shafts
PDE PORT	Propulsion diesel engine unitized (Port side)	PDE connected to Port side propeller shaft, Stbd propeller shaft either locked or trailing
PDE STBD	Propulsion diesel engine unitized (Stbd side)	PDE connected to Stbd side propeller shaft, Port propeller shaft either locked or trailing
PGT UNI	Ports Gas Turbine unitized (Port side)	PGT connected to Port side propeller shaft, Stbd propeller shaft either locked or trailing
SGT UNI	Stbd Gas Turbine unitized (Stbd side)	SGT connected to Stbd side propeller shaft, Port propeller shaft either locked or trailing
PGT XCON	Ports Gas Turbine cross connected	PGT connected to both propeller shafts
SGT XCON	Stbd Gas Turbine cross connected	SGT connected to both propeller shafts
TWO GT XCON	Two gas turbines cross connected	Both gas turbines connected to both propeller shafts. Both drive both shafts
TWO GT UNI	Two gas turbines cross connected	Both gas turbines connected to both propeller shafts. Each drives its shaft

While sea trial data can provide a rough estimate of fuel consumption, the actual fuel usage of a ship may deviate from predictions based on such data. Normal wear and tear on the ship and its equipment, which sometimes cannot be fully restored to "as new" condition through repair and maintenance, can affect actual fuel consumption, making sea trial data less reliable for estimating actual fuel usage.

More up to date fuel consumption models for each driving mode can be developed using data collected by IPMS integrated sensors while the ship is sailing. Ideally, data collection should commence immediately after the ship leaves dry-dock, where hull cleaning, painting, propeller blade repair, and propulsion equipment overhaul typically occur. These models reflect the optimal fuel efficiency achievable under ideal conditions and serve as benchmarks for comparing actual fuel efficiency in the future.

This paper pertains to a study initiated in 2020 with the objective of assessing the feasibility of utilizing the equipment operational data generated by the IPMS to construct fuel consumption models for power generating and propulsion equipment. The study also incorporates data from temporary fuel flow meters installed on the related equipment on board of several Halifax Class frigates. The aim was to develop fuel efficiency models for selected equipment, which will subsequently be utilized in FMD.

For this purpose, the data from both sources was consolidated, cleaned and analyzed using Machine Learning (ML) methods.

Fuel consumption models were built for diesel generators and all driving modes that were represented in consolidated data. For driving modes that were not adequately represented in the available flow meter data, the models were generated using the IPMS Onboard Training System (OBTS) simulator.

Based on the fuel consumption models, it was possible to pinpoint the most fuel-efficient driving mode depending on the ship speed order. Related recommendations along with supporting information were shown in the FMD. Along with displaying actual fuel consumption information, obtained from IPMS integrated sensors, several fuel consumption optimization features and techniques that analyze fuel consumption reduction from various perspectives have been designed.

The FMD with fuel consumption models at their core will be deployed on board of one of the Halifax Class Frigates in the year 2024. Upon completion of the trial period, FMD generated data will be analyzed and the performance of fuel consumption models will be accessed against recognized quality metrics.

2. Problem analysis

Fuel cost and ship's endurance are critical factors in naval ship operations. Efficient fuel management is essential not only to minimize operational expenses but also to enhance endurance, which directly translates into a strategic military advantage. Optimizing fuel efficiency can extend a ship's operational range and duration, providing greater tactical flexibility and effectiveness during missions.

However, achieving optimal fuel efficiency presents several challenges. Diverse mission requirements often restrict flexibility in adjusting factors such as ship speed. Monitoring tools for fuel efficiency are typically basic and lack comprehensive consideration of all influencing factors. Additionally, fuel usage data is often fragmented and requires integration from disparate sources, such as fuel flow meters and IPMS systems.

3. Objectives

The long-term goal is to facilitate an effective continuous ship fuel efficiency monitoring.
The main objectives of the study were to:
1. Examine the factors affecting ship fuel consumption, such as speed, driving mode, weather, draft, trim, hull, and propeller condition, and assess their availability within Halifax Class frigates' IPMS data.
2. Develop fuel consumption models for onboard power generating and propulsion equipment for each driving mode.
3. Identify the most fuel-efficient driving mode among the options available for specific operational conditions.
4. Develop tools for continuous fuel efficiency monitoring, implemented through interactive dashboards
5. Develop fuel consumption optimization algorithms that account for multifaceted factors influencing fuel consumption.

A derived objective was to provide various stakeholders, ashore and onboard, information about the fuel efficiency via adapted fuel management dashboards.

4. Hypotheses

Integration of fuel flow meter data with IPMS data enables the development of accurate fuel consumption prediction models for various ship driving modes. Furthermore, implementing fuel consumption optimization techniques based on these models can lead to significant improvements in fuel efficiency, increased endurance and cost savings for navy operations.

5. Limitations

Given that the permanent fuel flow sensors are unavailable, the fuel consumption models will need to utilize data from temporarily installed isolated fuel flow meters. The flow meter data (collected from four frigates) may not necessarily correspond to occasions when the selected ships had just left dry-dock. Consequently, the resulting models may not accurately represent the best achievable performance in terms of fuel efficiency.

It was noted that some equipment was not used during the data collection period. Furthermore, only one of the ships that participated in the study was equipped with the newer diesel generators at the time of data collection. Other ships in the study were still operating with the original engines. Diesel generator flow meter data was mostly limited to loads ranging from 300-650 kilowatts (kW) in spite of a 950 kW rating (see Figure 2).

The analysis of power plant load structure and methods to reduce it is beyond the scope of this study. The total DG load is used to calculate the related fuel consumption, which is then added to the total ship fuel consumption for endurance and range calculations.

Additionally, certain driving modes (PGT UNI, TWO GT UNI, and PDE UNI) were not adequately represented, which means that related models may lack accuracy.

Sufficient data representing PDE is available for only one ship. It is worth noting a phenomenon of lower-than-OEM-declared specific fuel consumption that was observed at partial PDE loads across all PDE data.

To standardize models across the fleet, navigational sensor data reflecting weather conditions was excluded from the analysis. Instead, indirect indicators reflecting sea state were used as substitutes during this phase.

6. Methods

6.1. Data collection and processing methods.

In this work, the following equipment was selected for fuel efficiency study: Diesel Generators (DG), Propulsion Diesel Engine (PDE) and Gas Turbines (GT).

There are two major sources of data utilized in the study. The data related to above equipment produced by IPMS integrated instrumentation and recorded by its EHM module is the first major source. The on-board EHM monitors and records any data or processed information pertaining to the on-board machinery equipment monitored/controlled by the IPMS. EHM data contains the following information: time stamp, sensor Identification Number (ID), sensor status, sensor value.

The second large source of data came from fuel flow meters that were temporarily installed onboard selected ships to gather fuel flow information from the equipment identified above. The fuel flow meter data consists of the fuel flow history recorded on the local sensors and collected at periodic intervals. Depending on the ship, the dataset covers the data from several months to several years of ship operations.

The fuel flow meter data contains the following fields: time stamp, fuel temperature, fuel supply and fuel return flow meter values. The data update frequency is equal to one minute.

The data from both sources was merged based on time stamp and resampled by one minute.

The operational modes that were underrepresented in the dataset were appended to ensure they are not mistakenly treated as outliers during the outliers' removal process.

The resulted data was cleaned from outliers using One Class SVM (Support Vector Machine) method, which is a ML technique for detecting outliers by learning the normal behavior of a dataset and identifying instances that deviate significantly.

The following filters were used for process transients' removal: limiting the difference between targeted and achieved values of the propellers pitch, propeller shafts speed, gas turbine load (PLA) level of fluctuations, change of driving mode and ship speed order.

6.2. Diesel generators (DG)

The following ML algorithms were used to build DG fuel consumption models: Least Absolute Shrinkage and Selection Operator (LASSO), k-Nearest Neighbors (kNN), Random Forest and Linear Regression as initial approach to the problem. The following model features were selected for preliminary analysis:
1. Engine power, (kW)
2. Sea water temperature
3. Intake Manifold Temperature
4. Engine Speed
5. Power Factor
6. Engine Running Hours
7. Exhaust Manifolds Temperature
8. Crankcase Pressure
9. Ambient Air Temperature
10. Engine power, kW.
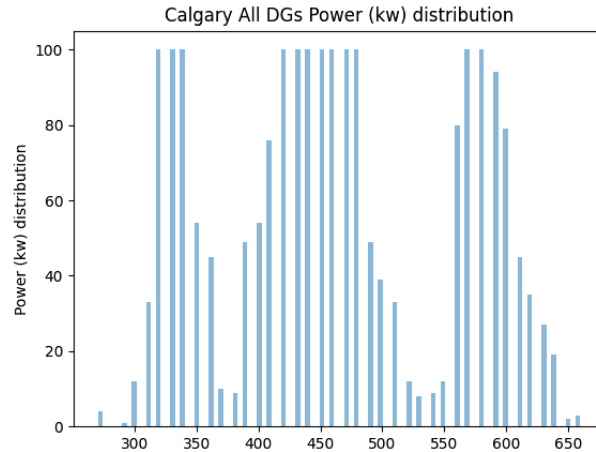
Figure 2 DG load distribution

To estimate the accuracy of the model, its R^2 (R- Squared) measure was used. R^2 is a statistical measure that represents the proportion of the variance of the dependent variable that is predictable from the independent variables.

The model R^2 results under testing are as follows:
1. LASSO: 0.9
2. kNN: 0.98
3. Random Forest: 0.97
4. Linear regression based solely on kW power input: 0.94

A simplified Linear Regression model based solely on kW power as the input was explored. This simpler approach maintained a high R-squared value (0.94), indicating only a minimal unexplained variance when compared to the best but more complex model utilizing multiple inputs (kNN: 0.98). The robust R-squared test results validate the accuracy of the model, justifying its selection as the final choice.

6.3 Gas Turbines (GT)

Flow meter data was available for the following driving modes: SGT XCON, PGT XCON, and TWO XCON. For TWO UNI driving mode the data set is sparse and noisy, especially when the ship speed is above 20 knots and as a result, the prediction may have a low accuracy. The SGT/PGT UNI dataset covers a narrow span of speeds.

Figure 3 SGT XCON speed distribution

Figure 4 PGT XCON speed distribution

Figure 5 TWO UNI speed distribution
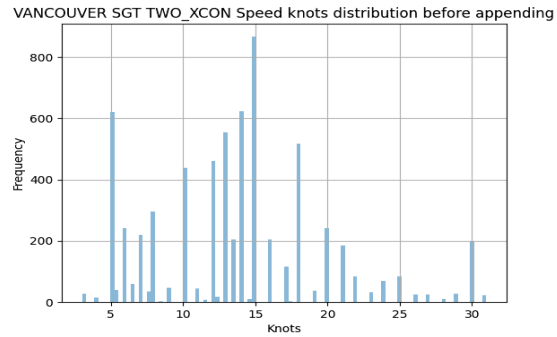
Figure 6 TWO XCON speed distribution
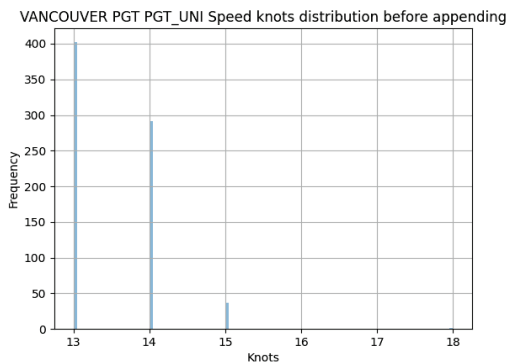
Figure 7 PGT UNI speed distribution
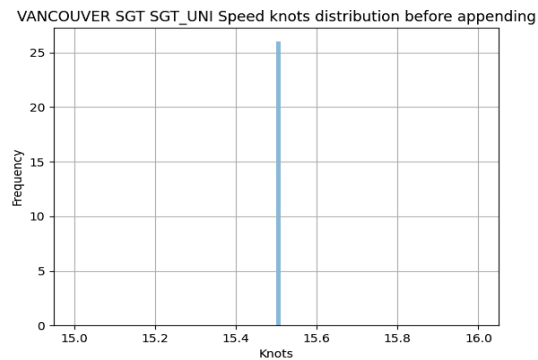
Figure 8 SGT UNI speed distribution

Figures 3 to 8 show the distribution of GT data depending on the driving mode and selected speed and provide an insight for the most frequently used speeds.
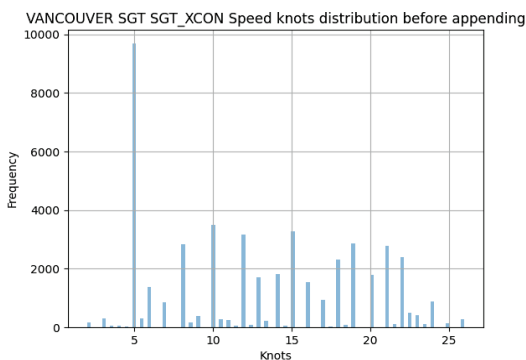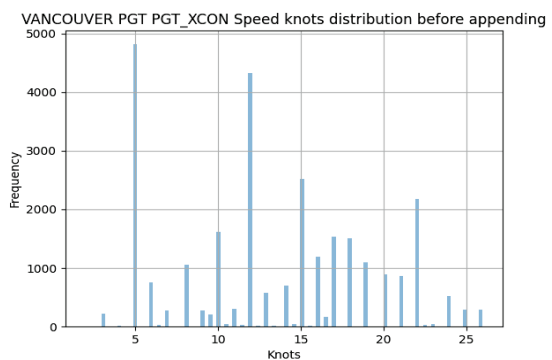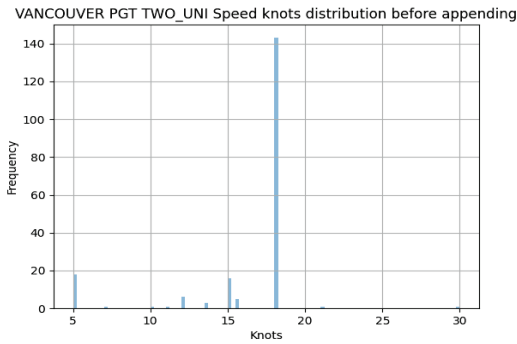
The following model features were selected for preliminary analysis:

1. Ship speed
2. Sea water temperature
3. Sea state (engineered feature, combining steering gear rudder angle dynamics and propeller shaft speed fluctuations)

The analysis highlighted inconsistencies of the impact of sea state feature and sea temperature on fuel consumption across different GT and operational modes. Consequently, the final model opts for ship speed as the independent variable, ensuring greater reliability and consistency in predictions. Polynomial Regression was used to build GTs fuel consumption models due to its easier interpretability for the engineers onboard.

PGT UNI and SGT UNI driving modes are represented just by three and one unique speed values accordingly. The method using adjustment of outliers' removal filter and following OBTS simulation was used to generate the model for these modes.

6.4 PDE (Propulsion Diesel Engine)

Flow meter data is available for PDE XCON driving mode (see Figure 9). EHM and flow meter data covering PDE UNI (Port or Stbd) driving mode is not available. SVM and Polynomial regression ML algorithms were initially used for this study. Similarly to GTs, there was no clear evidence confirming a strong correlation between sea states (indirectly derived), sea temperature and fuel consumption in the observed data. Consequently, these features were discarded.

Since both SVM and Polynomial Regression algorithms demonstrated relatively similar performance, Polynomial Regression was chosen for further study and ship speed was selected as the only input model parameter. Upon analyzing the fuel consumption predictions at lower ship speed settings, it was observed that for two out of three ships that participated in the study, the predicted Specific Fuel Consumption (SFC) values

were significantly lower than that documented by OEM in the engine shop trial report. This discrepancy is highly improbable, as the fuel efficiency typically peaks when the engine is new and gradually diminishes when accumulating running hours.

Considering the lower-than-expected predicted PDE fuel consumption at lower ship speeds for the majority of participating ships, an OEM-based fuel consumption model with ship speed as the input signal was selected as the final model.

Due to the lack of available data for the PDE unitized driving modes, the model was generated by combining capabilities of the IPMS OBTS simulation module and PDE XCON fuel consumption model.
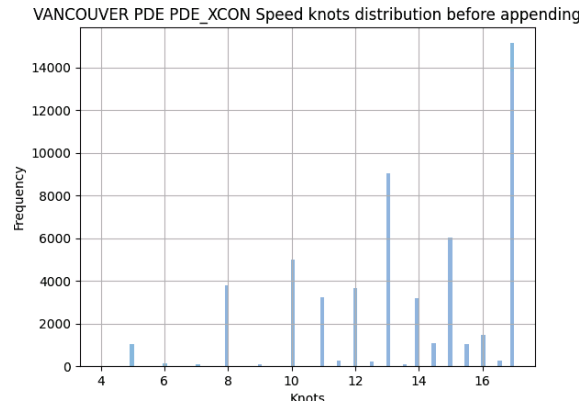
Figure 9 PDE XCON speed distribution

7. Results

Using the methods described above, it was found that the information provided by the IPMS sensors and temporary fuel flow meters was sufficient for building the fuel consumption models for the most frequently used driving modes.

Less frequent driving modes such as unitized modes were not appropriately represented in the data. In order to build their fuel consumption models, the capabilities of OBTS and its physics-based models were utilized.

The most fuel-efficient mode depends on the selected equipment and speed.

TWO UNI and TWO XCON GT modes are similar. The differences may be attributed to different losses in the main gearboxes. The difference between PGT XCON and SGT XCON modes may reflect the actual state of GTs onboard of a selected ship and different losses in the gearbox. In addition, the noise in the data could be a contributing factor. PGT UNI and SGT UNI models are identical since they were both built based on data produced by HMCS Vancouver with help of OBTS. PDE PORT and PDE STBD models are identical as well, as they were also based on the OBTS simulator.

Using the fuel consumption models described above, the following methods of ship fuel efficiency monitoring and optimization have been developed and integrated into Fuel Management Dashboards.

7.1. Ship Endurance and Range

The endurance estimation feature allows calculating the maximum time at sea given the sequence of driving modes, corresponding speeds and fuel safety margin as well as the estimated diesel generators load defined by the user. A ship's range value is derived from the endurance calculations (see Figure 10).

7.2. Voyage Planning

This feature enables the calculation of the Fuel Remaining Onboard (ROB) upon arrival from a specific voyage. Users can define the ports of departure and arrival, precise ship route, expected speed at different route segments, as well as specifying different modes of operation. This feature assists in estimating when the ship needs to be refueled (see Figure 11).

Fuel Management
Main

Last Observed Weather

Wind Speed	9.9	kt
Sea Temp	9.9	°C
Air Temp	9.9	°C
Atm Pressure	9.9	Bar

Speed

SOG (kt)	STW (kt)	Port Order (kt)	Stbd Order (kt)
99.99	99.99	99.99	99.99

Current Position

Current Date	xx/xx/xx
Current Time	23.59.59
Latitude	00.00.00
Longitude	00.00.00

DG1	DG2	DG3	DG4	GT (Port)	GT (Stbd)	PDE
READY	ONLINE	STOPPING	No Signal	STOPPED	STOPPED	STARTER ON

Power Generation
Source: SHIP

System Load (kW)

Generating Capacity (kW)

Fuel Status

Fuel Remaining (m³)

Fuel Consumption (m³/h)

Endurance (days)	Endurance (nm)	Generator Consumption (m³/h)	Propulsion Consumption (m³/h)
99.99	99.99	99.99	99.99

Shaft Output
Drive Mode: PDE XCON

Port Shaft Speed (RPM)

Stbd Shaft Speed (RPM)
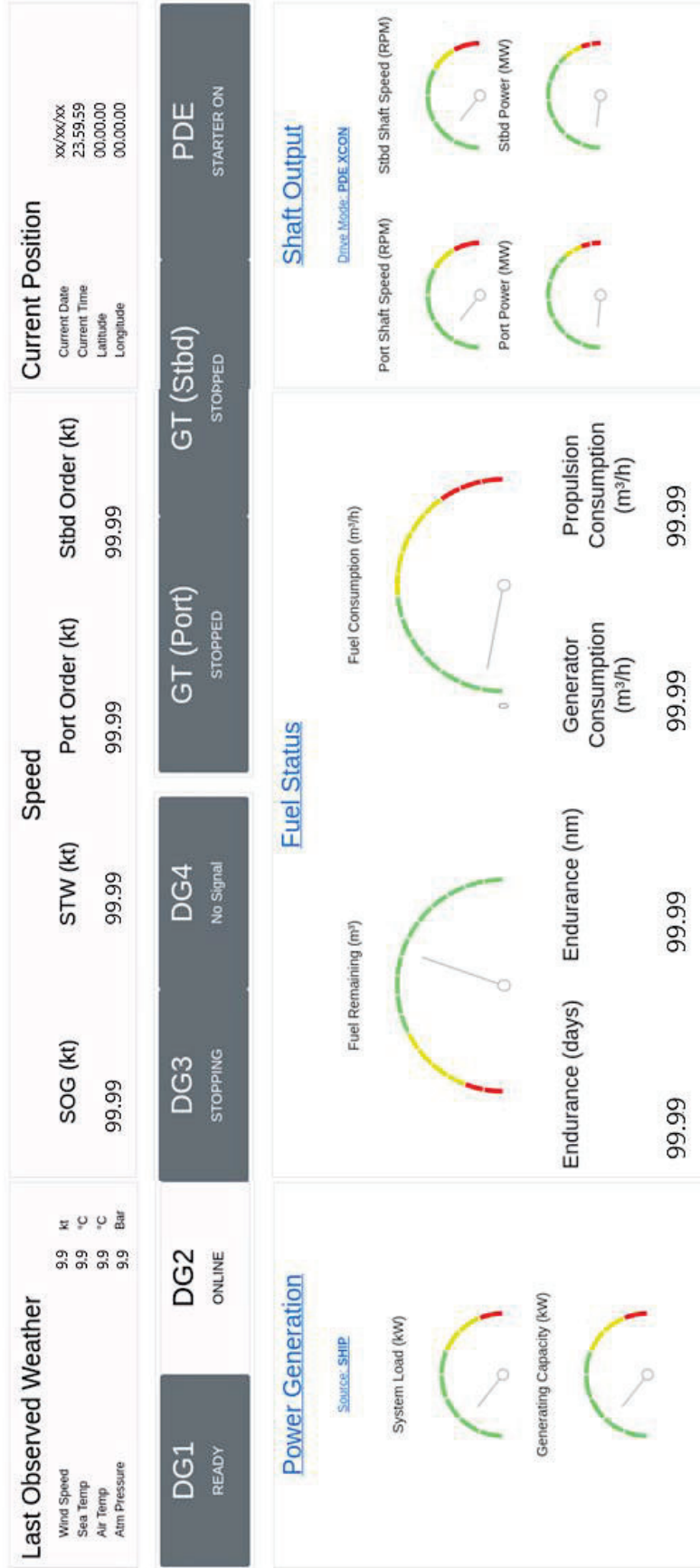
Port Power (MW)

Stbd Power (MW)

Figure 10 Fuel Management Dashboard Endurance
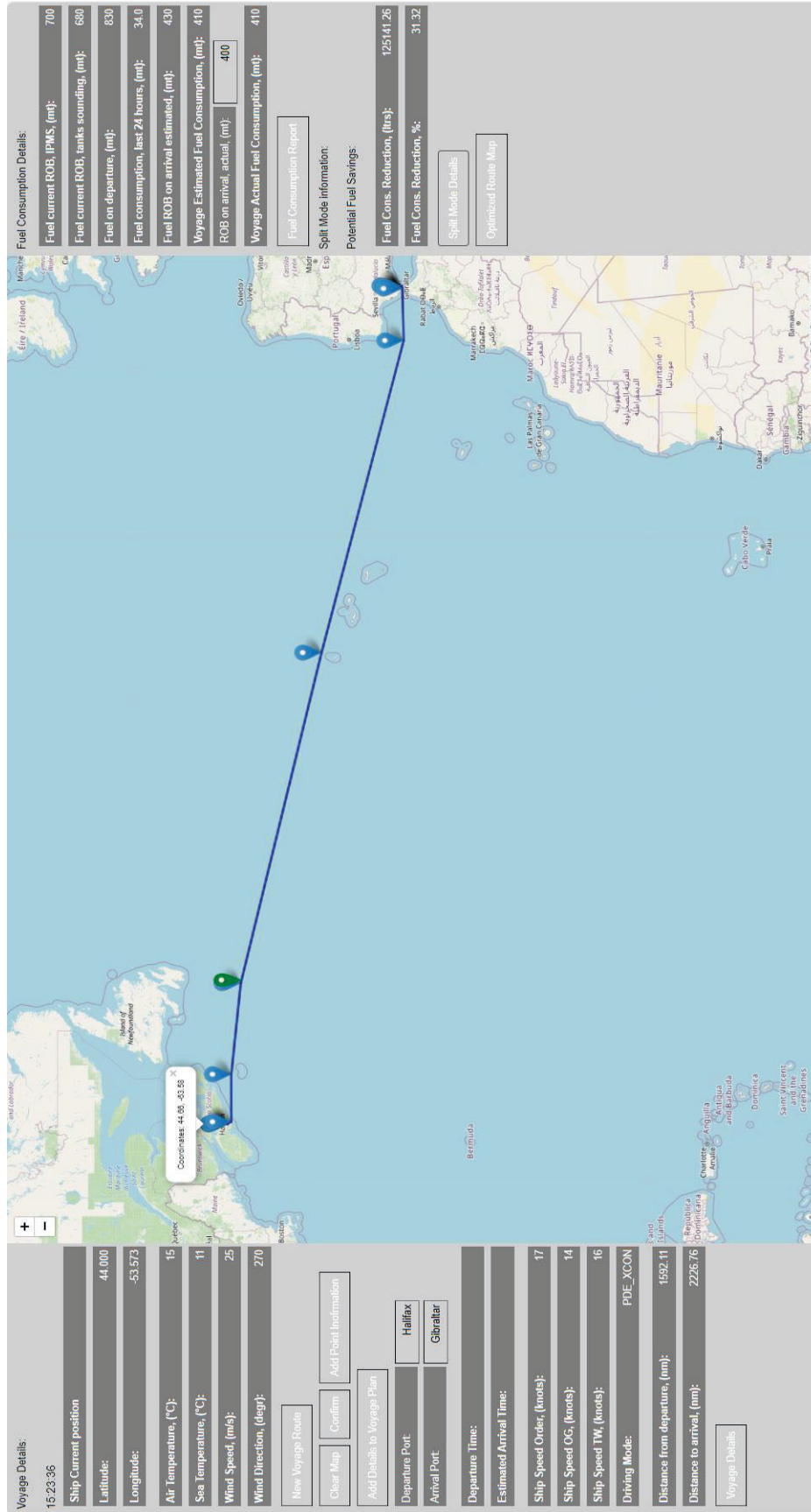
Figure 11 Voyage Planning page view

7.3. *Sea Passage Time optimization*

This technique allows minimizing the overall operating costs of the ship by optimizing its speed while underway, with fuel consumption models developed in this study at its core. This adjustment effectively manages the time taken to reach the port of destination. This optimization method can use various inputs, including selected driving mode and initial speed, fuel cost, crew cost underway and in port, port charges, etc.

Sea Passage Time Optimization Case

Conditions

- Ship is underway to port of destination with PDE driving @ **17 knots** on PDE XCON

- Distance to destination - 400 nautical miles

- Dock availability window - 7 days

- Fuel Cost - 940 $/metric ton

- Crew details: 180 persons is on board.

- Average annual salary - 75 k$.

- Time required to complete planned port tasks - 4 days

- The latest time of arrival is 24 hour after initial ETA.

Cost of ship underway is defined in this calculation by the following factors:

- Fuel cost

- Crew cost (head count, salary, load factor)

- Maintenance – 2 k$/day

Cost of ship in port is defined by the following factors:

- Fuel cost

- Crew cost (head count, salary, load factor)

- Port charges – 50 k$/day

- Maintenance – 1.5 k$/day

Optimization results:

- Recommended Speed: **16 knots**

- Recommended driving mode: PDE XCON

- The new Estimated Time of Arrival (ETA) is **1.47** hours later than the initial.

- Potential savings: **5.2 k$**

Figure 12 Sea Passage Time Optimization

The outputs of this algorithm are the new recommended speed underway, the driving mode, and the updated Estimated Time of Arrival (ETA), which correspond to the minimal ship running cost and potential cost savings if these recommendations are followed.
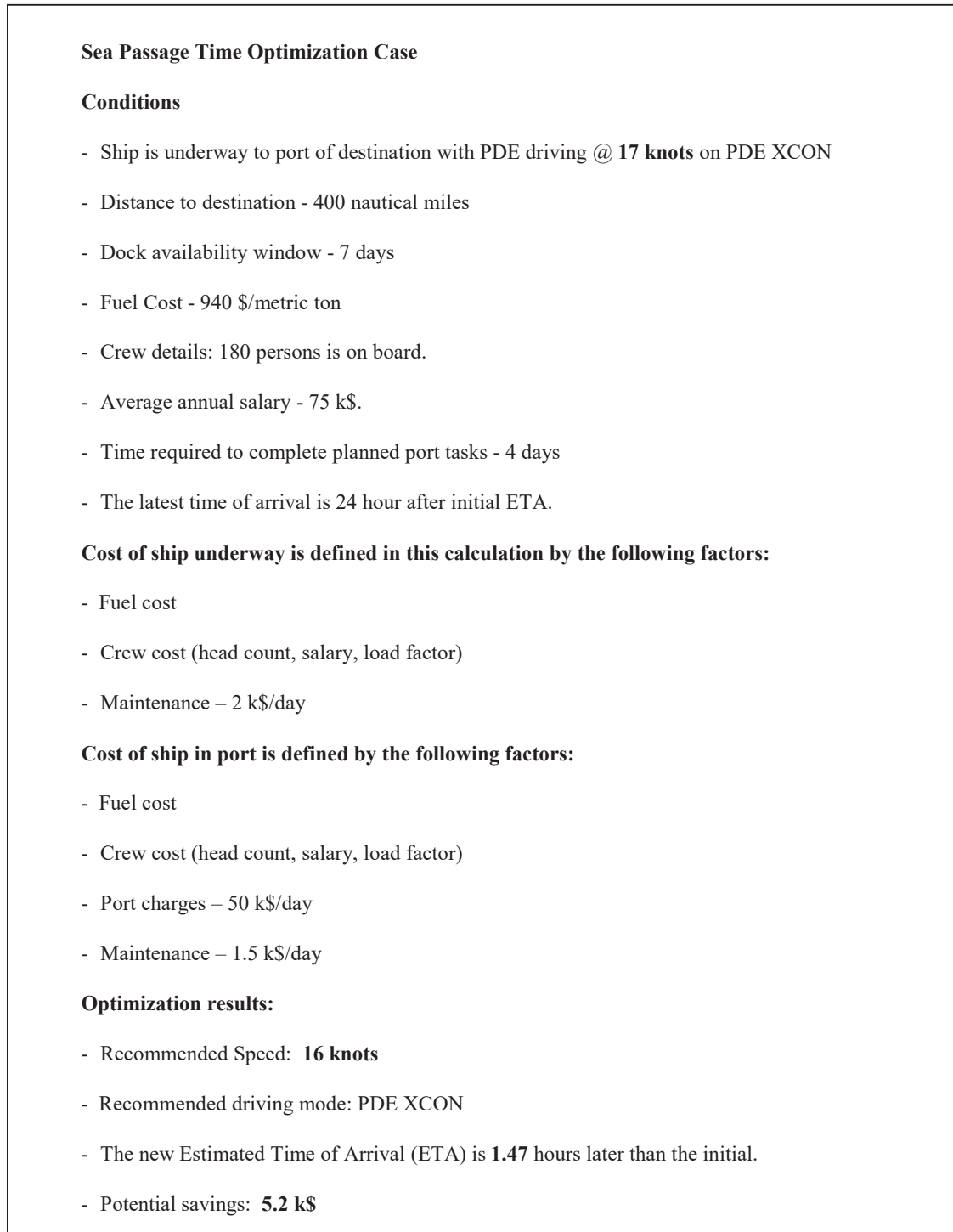
Figure 12 shows the application of this method using a representation with hypothetical ship technical details and cost data. The optimization task is to find the best balance between the time underway and the duration of stay in port, which is affected by the difference in hourly ship costs underway and in port. As can be seen, the optimization algorithm recommended reducing sea passage speed to 16 knots. The amount of potential savings depends on the input variables, such as the number of crew onboard. The list of input variables can be further refined, and actual data will be used once this dashboard function is deployed.

7.4. *Mixed Mode Plant Operation*

The objective of this feature is to reduce the fuel consumption by selecting an optimal sequence of driving modes and speeds. Mixed Mode Plant Operation optimizes fuel consumption by blending different driving modes and speeds while maintaining the scheduled arrival time (Brown, 2007). It leverages varying fuel consumption rates across different driving modes. The output of this method is the sequence of driving modes and speeds that guarantee a minimum fuel consumption during the sea passage. Figure 13 (not based on actual data) illustrates the concept of Mixed Mode Plant.

Figure 14 displays the results of Mixed Mode Plant Operation optimization for a ship trip from Halifax to Gibraltar. Time of arrival dictates a sea passage speed of 19 knots. Preliminary selected drive mode is PGT XCON.

As the result, the algorithm recommended splitting the sea passage between two driving modes:
1. PDE XCON with speed of 17 knots and
2. PGT XCON with speed of 23.35 knots.

In this case, resulting fuel consumption reduction would correspond to a 13.3% of fuel economy. Time underway and estimated time of arrival (ETA) remain unaffected.

The software automatically adds the new waypoint, indicating the location where the transition from the first driving mode to the second one should occur (see Figure 15).
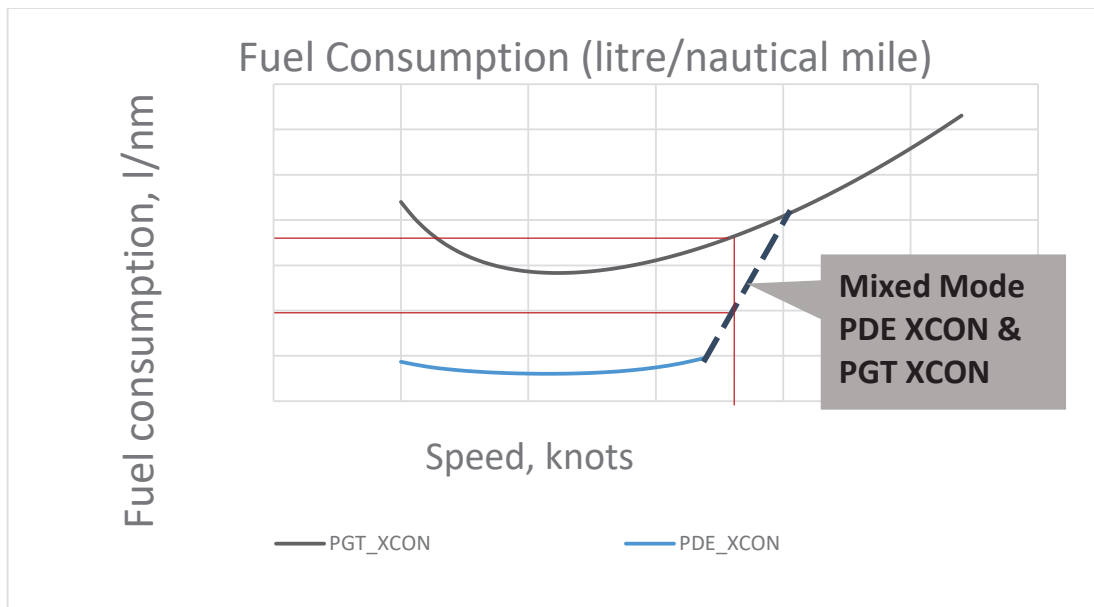
Figure 13 Mixed Mode Plant
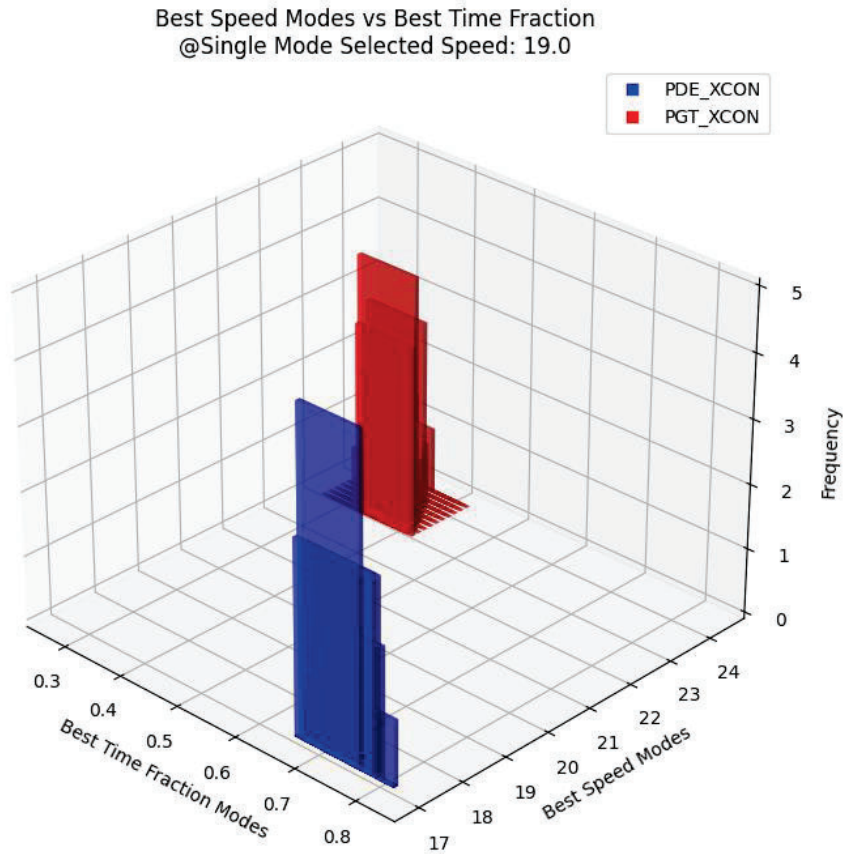
Figure 14 Recommended Mixed Mode Plant configuration

Selected Type: Enroute
Operational Mode: In Transit
Driving Mode: PGT_XCON
Selected Speed: 23.35
# of DGs In Operation: 3
DG Average Load: 800
Boilers Status: Yes

Segment 2
PGT_XCON@23.35kn

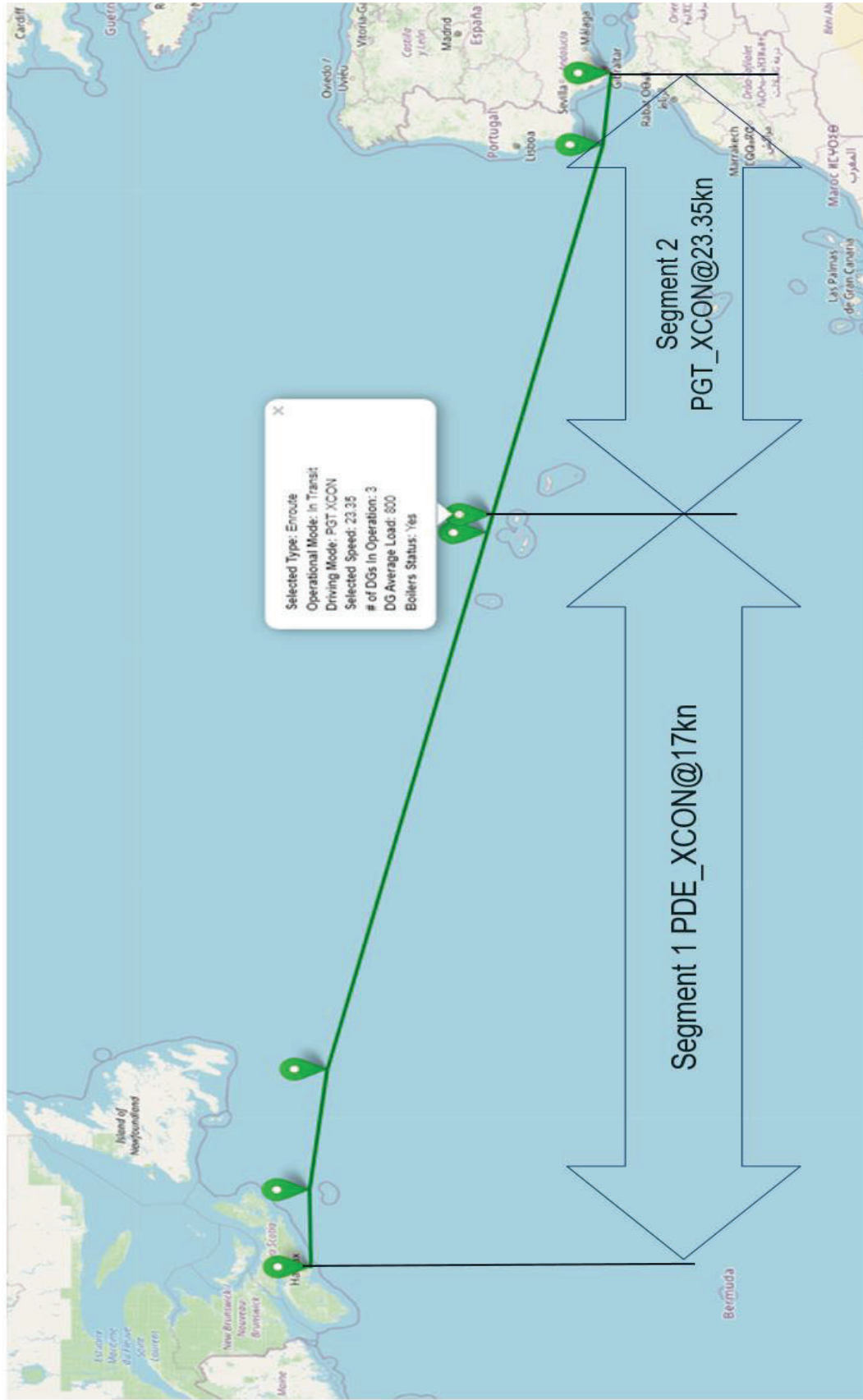Segment 1 PDE_XCON@17kn

Figure 15 Mixed Mode Plant page view

7.5. Propeller Slip Monitoring Feature

The Propeller Slip Monitoring dashboard feature provides frequent automatic propeller slip measurements and compares them with the slip baseline model built using historical data collected by IPMS/EHM versus traditional propeller slip calculations based on the ship and propeller design data. Figure 16 illustrates the propeller slip concept.

A large amount of historical data captured by EHM allows building propeller slip baselines based on the actual data rather than the design data. A baseline of propeller slip can be built by analyzing related EHM data obtained immediately after the ship left dry-dock, or following underwater hull clean up, or propeller repair or blades polishing.

High propeller slip suggests deterioration of hull or propeller conditions, which can impact fuel consumption, and decrease propulsion efficiency (Schreiner, 2021). This feature offers advantages such as reduced fuel costs due to propeller condition monitoring, fewer diving inspections, and enhanced timing for underwater propeller/hull cleaning. Figure 17 visualizes ship speed with respect to propeller shaft speed and propeller pitch.
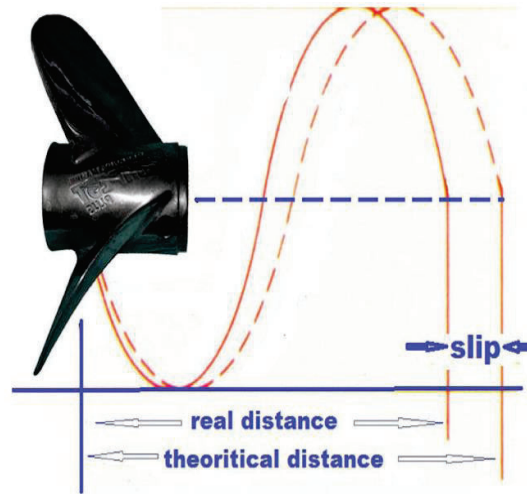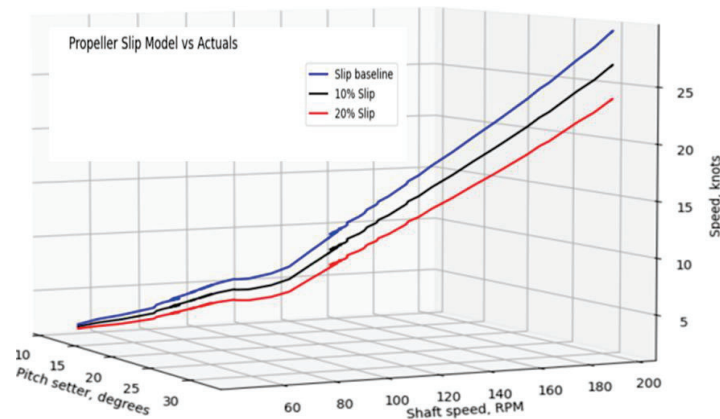

Figure 16 Propeller Slip concept

Figure 17 Speed as a function of Propeller Shaft Speed and Propeller Pitch

8. Discussion

The result of this study indicates that IPMS and fuel flow meter data contain the necessary information to construct models for the most commonly used driving modes for targeted power generation and propulsion equipment. The most fuel-efficient mode for every speed was determined.

As expected PDE in cross-connected mode facilitates the most fuel-efficient operation when the ship speed is in the range of 8 to 18 knots, whereas as observed in the simulations, PDE in unitized mode provides the best fuel efficiency when the speed is below 8 knots (although this needs to be substantiated with data, when it becomes available). If the speed exceeds 18 knots, using mixed modes (Refer to **Error! Reference source not found.**) over the transit, meaning different speeds at different time involving PDE XCON and either turbine in cross-connected mode or two turbines will facilitate an optimal fuel consumption. For the speeds in the range of 26-31 knots, the combination of single cross-connected GT and double gas turbines running in unitized or cross-connected mode may be the best scenario.

PDE fuel flow meter data related to mid to high PDE loads demonstrates similarity with OEM provided sea trial report. At the same time, fuel flow meter data related to partial loads was lower than declared by OEM for the same load. Therefore, the model based on flow meters was substituted by an OEM-based model.

The fuel consumption models developed in this project enabled the creation of features for estimating and optimizing fuel consumption from various perspectives. They also support voyage planning, refueling scheduling, and maintenance and inspection planning. Paired with live operational data, and a user-friendly interface of the fuel dashboard, these features enhance situational awareness and provide valuable assistance to the crew onboard.

9. Conclusion

In general, the objectives of this study were achieved. During the course of this study, the data was analyzed and fuel prediction models for all driving modes were developed. As a result, the most efficient driving modes and corresponding speeds were identified. This information is presented in the Fuel Management Dashboards and can be used to help selecting the best driving mode while taking into consideration operational requirements and constraints. It also helps to estimate the potential fuel savings when comparing the actual and optimal driving modes. From the data science point of view, this study has helped to streamline the process of consolidating data from diverse sources such as IPMS and isolated fuel flow meters. It has also facilitated research work aimed to apply various fuel optimization techniques to a specific ship platform.

Fuel Management Dashboards developed in this phase of the project provide a clear and informative snapshot of the ship's operational status with just a single glance. They lay the foundation for developing additional dashboard pages that can target specific aspects of fuel management and efficiency, both onboard and ashore.

To further develop and refine researchers' efforts, focus should be directed towards analyzing additional fuel flow meter data and enhancing existing fuel consumption models, particularly targeting modes that are underrepresented in the data available in this study.

Analyzing the power plant load structure and exploring methods to reduce it will be a valuable focus for the next phase of the research, offering potential improvements in overall fuel efficiency and operational effectiveness.

Following the deployment of the Halifax Class Fuel Management Dashboards, the subsequent step involves assessing the effectiveness and user-friendliness of the dashboards for the intended users. Potential enhancements of the fuel consumption models include incorporating environmental factors such as sea state and water temperature. As the indirect method employed to account for weather conditions proved unsatisfactory, exploring alternative methods could improve the accuracy of the consumption models.

Acknowledgement

References

Brown, G., et al: "Steaming on Convex Hulls", Research Gate Publication, August 2007.

Cumming, D., et al: "Overview of Hydrodynamic Research Effort to Derive a New Stern Design for the Halifax Class Frigates", 8th Canadian Marine Hydromechanics and Structures Conference, 16-17 October 2007

Schreiner, E.: "Halifax-Class Efficiency Improvement Strategy", Canadian Forces College, 2021

Mandler, M.: "Summary of Cutter Energy Management Audit Results and Recommendations", U.S. Coast Guard Research and Development Center, May 2000.

RESILIENT: Advance a Ship's HM&E resiliency through contextual information models and innovative ML/AI analytics At-The-Edge

W A Johnson, BSE Chem Eng, *University of Michigan, United States*
Corresponding author, Email: wajohnson@ra.rockwell.com

J G Walker, BS Computer Science, *University of Oklahoma, United States*
Corresponding author, Email: johnnywalker@thorsolutions.us

Synopsis

Maritime supply chain disruptions over recent years stemming from causes such as piracy, the COVID-19 pandemic, blockage of the Suez Canal and the ongoing Red Sea crisis, underscore the pressures on navies and commercial ships for higher ship operational availability. Ships are sailing longer distances, at higher speeds and in more challenging environmental conditions. These settings are consequentially increasing demands for more effective ship machinery monitoring. However, although shipboard systems generate more data than ever, using that information to improve operational availability remains elusive; data from a ship's electrical auxiliary and main propulsion systems are often disorganized, undefined, and not timely. Further, data is sometimes undiscoverable and frequently unusable by the ship's information system to prevent or mitigate equipment failures. Moreover, increasing demands for more sophisticated analytics to improve machine reliability, with likely thousands of data points per system without any relationship model to help interpret this data continues to make machinery monitoring efforts more complex and costly. Creating the datasets is just one piece of the puzzle. These data points take on different meanings dependent on grouping. The lack of consistent data requirements definitions and context from one information system to another introduces other challenges to integrating machinery room operational data into the ship's higher-level information system and further up into an organization's fleet maintenance center. To this end, this paper explores two evolving areas of technology: 1) Machine learning schema for common hull, mechanical, and electrical system machinery equipment to improve contextualizing performance anomalies and that equipment's baseline operations and 2) an AI Information model for machinery equipment that could advance the ability of crews to reduce unplanned failures, increase availability, and obtain an accurate representation of the ship's readiness state. These activities will drive improved reliability, maintainability, and supportability of these systems and a higher readiness for a propulsion plant, electrical plant, damage control system, and ship's auxiliaries.

Key Words: Edge Analytics; Reliability Analysis; MCSA; CbM+ Maintenance; AI/ML Diagnostics

1   Introduction

It's often said that the workhorse of manufacturing and industrial control systems is the ubiquitous 3-phase, induction motor. A globally pervasive converter of electrical energy into mechanical energy, electric motors, not just induction, but also synchronous AC, field DC, wound, and more, transform electrical power into a cyclical mechanical activity with a typical robust, long operational life. Moreover, Machine Learning and AI algorithms applied within the technology of variable frequency drives and similar controllers are derived by the foundational principles that operate an electric motor. The current signature, voltage signature, and instantaneous power signature between the motor's stator and rotor are the essential forces that create the initial and continuous torque produced by a motor. Each of these forces can be analyzed to determine motor performance, health and the operational conditions of the equipment driven by the motor with predictive results. This predictive analysis, often termed Condition Based Maintenance Plus (CbM+), is a significantly beneficial result. Accordingly, this paper presents how a spectral analysis of the electric current is a valuable method to separate components of the current sine wave and to associate these components with useful mechanical properties of the motor. For example, a gradual degradation in one of the mechanical features within the motor can be detected by an analysis of the electric field interactions between the rotor and stator. This discovery is determined by comparing healthy, normal operation of the motor (defined as baseline performance characteristics), and deviation from this baseline. Different types of deviation from baseline operations represent different mechanical

problems developing inside the motor. The mechanical properties of electric motor failure types are revealed in different current signatures within the motor. Research shows that we can use motor current signatures to identify ball bearing wear, rotor rub, outer/inner race bearing faults, motor unbalance, shaft misalignment, and more. Coupling these earlier efforts with today's computer processing advances, we can begin to train an automation system, i.e. machine learning, and define other AI basis tools to describe equipment condition predictively.

Authors' Biographies

Warren Johnson is the Marine Industry Manager for Rockwell Automation. He received a Bachelor of Science degree in Chemical Engineering from the University of Michigan. Mr. Johnson served as a naval officer in the U.S. Navy then transitioned to a career in controls engineering. He has automation systems design, development, and integration experience of over 24 years across various industries including marine and power generation. He has worked in industrial control and automation solutions from Rockwell Automation for a significant portion of that time.

Johnny Walker, CEO/ President of Thor Solutions LLC, is a retired U.S. Navy officer. Afloat, CAPT Walker commanded USS CHAMPION (MCM 4) and USS GUNSTON HALL (LSD 44). Ashore, CAPT Walker served as a Navy Staff, OPNAV N85/95 Requirements Officer / Resource Sponsor, PEO Ships LCAC & SSC (LCAC 100 Class Craft) Acquisition Program Manager—and as the PEO Ships MAAC Ships Program Manager, (PMS 470). He is a University of Oklahoma computer science graduate & completed an MMAS in Middle Eastern Studies at the U.S. Army CGSC.

2   Motor Current Signature Analysis

With the rapid advances in computer processing for capturing high speed minutiae events and their interactions, electric motor performance trends can now be reasoned from the motor's electrical current events (sic. trend analysis). An alternating current (AC) motor's current sine wave is a cyclic event that occurs across a typical frequency range
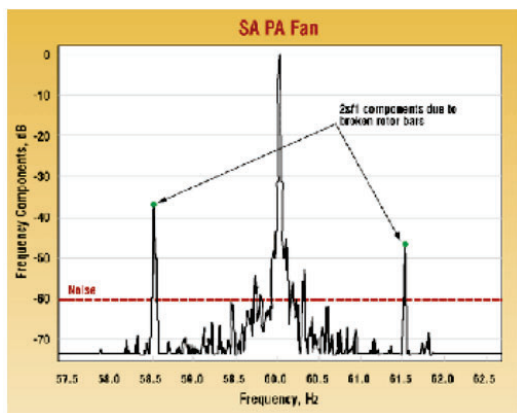

Figure 1: Frequency spectrum from motor with broken rotor bars (Miljković, 2015).

from 1 - 60hz and even higher frequencies depending on application. Whereby the amplitude and waveform vary as the motor poles are passed by each revolution of the motor's rotor. Variable frequency drives are power supply devices to motors which have the electronics to capture a buffer of the motor's 3-phase current waveform. Motor waveform characteristics are critical for today's Motor Current Signature Analysis (MCSA) techniques—establishing a motor's operational baseline and assessing deviations from this baseline. Earlier studies established correlations (or signature analysis), between the motor's current waveforms and known mechanical problems in that motor. For example, each motor type has a general set of correlations established for equivalent mechanical problems like bearing wear, rotor static and dynamic eccentricity, broken bar and shorted windings. To establish these correlations, Fast Fourier Transformations are used to decompose the motor current waveform's components from the time domain into the frequency domain. This analysis reveals the amplitudes (dB) of those different component frequencies (within the output resultant current supplied to the motor stator), whereby those frequencies are derived from effects between the magnetic fields of the rotor and stator. These effects are caused by hardware parts degradation which can cascade into mechanical failure. For a 50Hz motor, the MCSA primary frequency peak is 50Hz and correspondingly 60Hz for a 60Hz motor. Figure 1's MCSA frequency spectrum shows 60Hz motor with a rotor asymmetry condition indicative of a broken bar condition within its rotor cage; the MCSA's two sideband peak frequencies have occurred at those frequencies defined as the motor's "twice slip frequency" as calculated from the motor's 60Hz supplied frequency (Miljkovic, 2015). The magnitude (dB) of the two MCSA sidebands indicates the severity of the rotor's asymmetry which, because those sidebands are more proportionally near the primary frequency dB, indicates a broken bar condition, i.e. a First Principle. The "slip frequency" sidebands for a healthy motor will be at much smaller magnitudes (dB) compared to the primary peak frequency.

Similar effects of sideband frequencies occur when there are air gap differences between a motor's rotor and stator. This anomaly, which leads to increased vibration, lower output peformance, and even motor failure, is called rotor static eccentricity and rotor dynamic eccentricity. Rotor static eccentricity is when the air gap deviation remains stationary during the rotor's rotation while dynamic eccentricity occurs when the air gap deviation transits around 360

degrees of rotor rotation. This is detected because the rotor's magnetic field will influence the AC current within the stator windings due to the air gap proximity between the rotor and stator at the closest point around the circumference, causing an Unplanned Magnetic Pull force that creates other sideband current peak frequencies (Thompson and Gilmore, 2003). Those sideband frequencies are calculated by equation (1) for the static eccentricity of an induction motor.

$$f_{ec} = f_g \left\{ (R \pm n_d) \left(\frac{1-s}{p} \right) \pm n_{ws} \right\} \tag{1}$$

Of which, the f_{ec} is the eccentricity frequency, f_g is the grid or supply frequency, R is the number of rotor bars, n_d is plus/minus 1, s is slip, p is pole pairs, and n_{ws} is 1, 3, 5, 7…. The f_{ec} is seen on a spectral analyzer at multiples of the f_g and is the anticipated motor current frequency signature for this type of motor fault condition (Miljković, 2015).

a) Concentric   b) Static eccentricity   c) Dynamic eccentricity
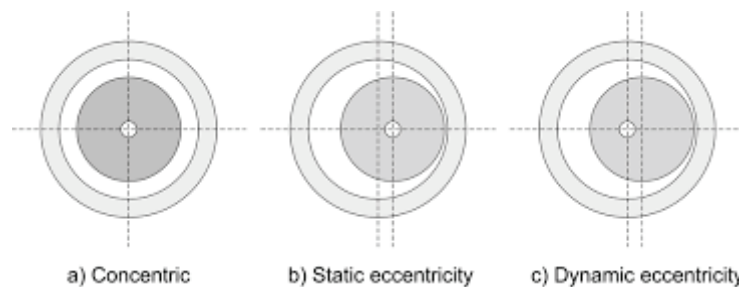
Figure 2: Air Gap Eccentricity (Miljkovic, 2015).
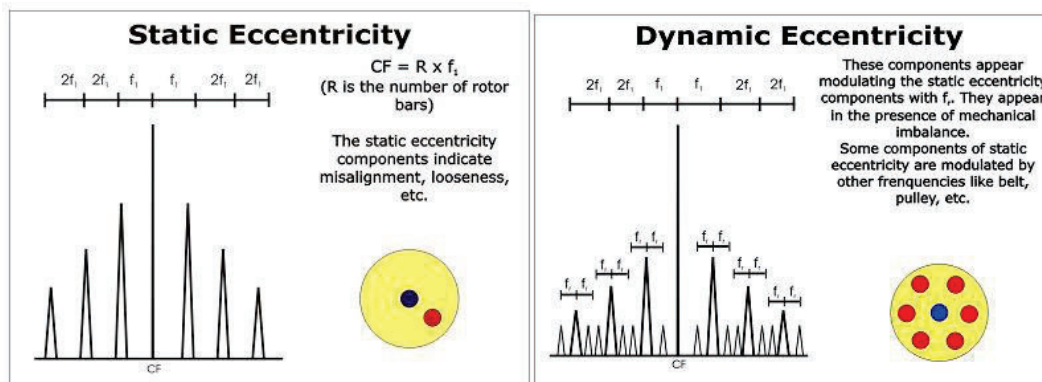
Figure 3: Current Signatures of Static & Dynamic Eccentricity (Lambert-Torres, 2009).

Voltage and Instantaneous Power signatures are used similarly to discern even more motor (and mechanical load) diagnostic conditions. Applying these earlier MCSA principles with today's AI and Machine Learning At-The-Edge technology advances condition-based maintenance plus CbM+ programs to the next level of resilient ship performance: optimal operating levels of the vessel's machinery equipment and determining hardware remaining useful life. Opportunely, new methods can capture these signature data without added spectral analyzers and separate

current and/or voltage sensing equipment. This no longer needed additional hardware is replaced by intelligent control devices like soft starters and variable frequency drives—which, while operating motors, simultaneously cache the motor current data into their memory and that data is pulled forward to a Machine Learning application.

3   AI & MACHINE LEARNING At-The-Edge

Industry continues to collect voluminous machinery data into Cloud-Based systems to perform data analysis. Using significant computing resources and data scientists, firms pursue process correlations leading to new capacity and optimization. This analytical loop continues refinement with less and less data analysis latency coming near real time to production events on the factory floor. Artificial Intelligence (AI) and Machine Learning have made this possible. Further, the closer AI and Machine Learning get to the data source, the more these processing techniques reach the "Edge." Inasmuch, near/ real-time analytics at sea requires AI and/or Machine Learning to function at the vessel's equipment level. The existing motor soft starters and variable frequency drives in the ship's machinery plant equipment become those data sources, feeding their operational parameters not into a huge data server cluster and up to the Cloud, but rather to immediate local applications within the ship's machinery rooms. For example, integrating a Dockers Container OCI based machine learning app into a ship's PLC-chassis slot processor and connecting it via the ship's network to every soft starter and VFD in the machinery room.

Machine Learning (ML) apps can be straightforward—i.e., don't require significant engineering expertise to determine what data needs to be captured. The operator simply follows a user guide to identify each VFD type for data capture, select its IP address, and then add the particular load device, asset, or motor's nameplate information. Each asset's configured input fields may include bearing information (inner/ outer/ race multiplier, rolling element multiplier, cage multiplier, etc.), for an induction motor as well as the number of blades for a pump or fan. The embedded intelligence within an ML app uses this pump/fan and motor bearing configuration as inputs into its First Principles derived failure modes. When power is applied to the motor and it becomes operational from the vessel's activity, a ML app can begin training itself on motor performance to establish a baseline. If the motor load runs at a single speed/frequency, the app trains on that frequency in minutes. If the motor has operational modes at different frequencies, an ML app can adapt to monitor the change and automatically begin the training process for the new frequency. Or a frequency range can be specified in advance and that guidance sets the range of frequencies which will be trained for that asset within the ML app. This is "no code" machine learning done through the following process steps.

Operational Steps	Process Steps
1 • Establish baseline asset behavior under normal conditions	Process raw sensor signal with AI driven feature extraction
2 • AI automatically monitors deviation from baseline behavior	Analyze deviation / drift from baseline (unsupervised learning)
3 • Flag and notify user when an anomaly is detected	Contextualize anomaly / deviation
4 • Leverage embedded expertise or label the detected anomaly	Share the insights to the bridge and engineering stations

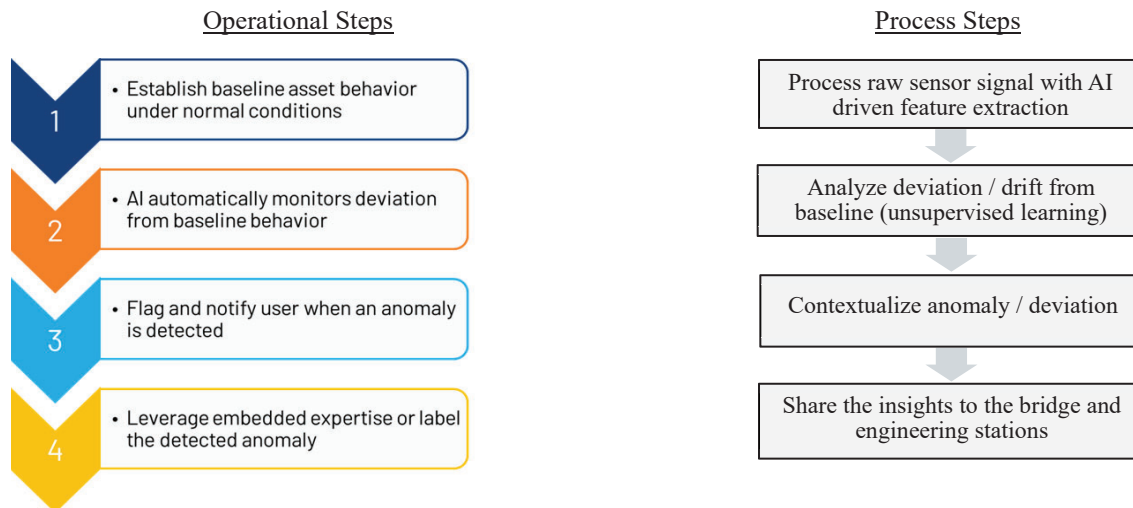Figure 4: Embedded ML Expertise alignment of the operation to process steps.

The motor's baseline is established by training for each 1/2hz frequencies throughout the user defined operating frequency range. The commanded frequency of the VFD is automatically communicated to the ML app through the ship's network; onwards the ML app accomplishes the training and monitoring simultaneously. Once sufficient data

is acquired from the asset, the training switches to automatic monitoring. Figure 5 presents an example architecture. Of significance: this design adds no additional equipment that's not already installed in the ship's machinery room other than a single edge analytics processor.
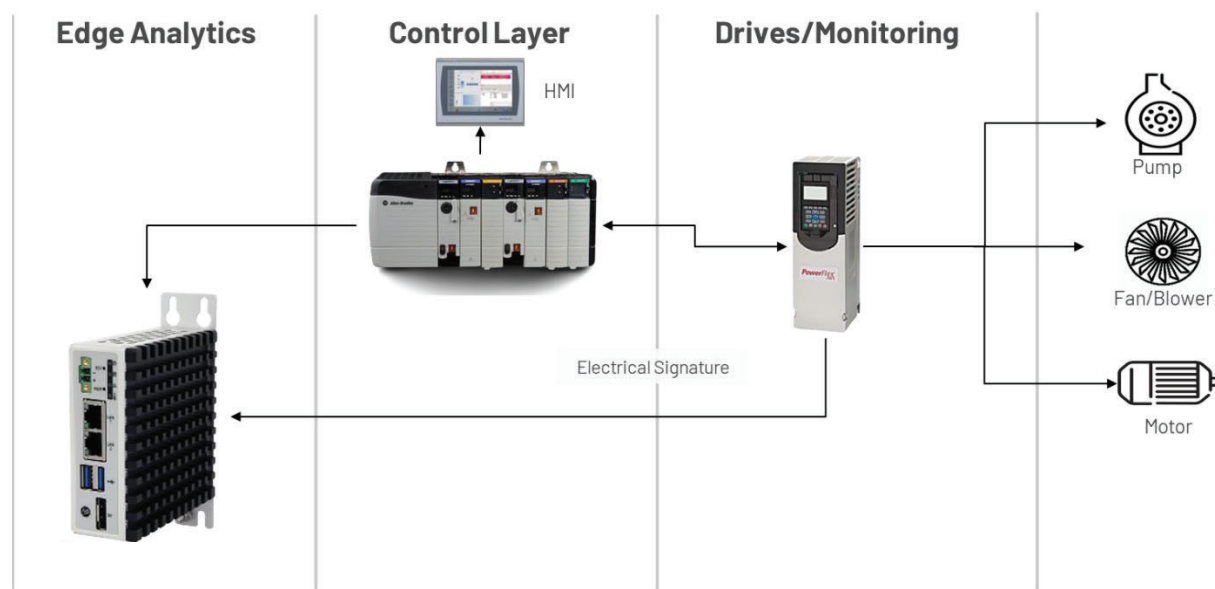

Figure 5: Example ML-At-The-Edge Architecture

Deviations from the asset's established baseline are anomalies which will be evaluated against the embedded expertise of First Principles derived failure modes and effects within the ML app—categorized as a particular failure anomaly. If the deviation is outside of embedded knowledge cases, then the user has the option to flag it as either normal behavior or identify it as a new anomaly issue. This new anomaly becomes a new failure risk for the asset and it is tracked onward.

Rather than being an anecdotal set of concepts, the ML app directly applies those embedded expertise First Principles of MCSA which alleviates the need for those higher-level skills or unique expertise of vibration engineers and data scientists. The ML app addresses the two categories of anomalies: the first anomalies which align to recognized problems like bearing failure, identified through prior industry knowledge and the second category, anomalies unique to the user's application. Beyond the First Principles' recognized anomalies, an ML At-The-Edge app can be applied to those second category of anomalies to reclassify them per the user's definition and accumulate that continuous learning through user training that identifies more unique anomalies at that single asset or from multiple assets. As anomalies are labelled by crewmembers, ML At-The-Edge becomes a critical tool operating around the clock 24 hours, 7 days a week and advancing the crew awareness of machinery plant condition. This is significant because organizations today simply don't have the depth of CbM analysis experts to accomplish round the clock analyses across the breadth of their plant's motors and other assets (Bernet, 2022).

3.1 AI/ML First Order Readiness Improvement

This description of configuration steps annotates an example of an actual, deployable MCSA ML At-The-Edge architecture and shares the extent of how little added capital expenditure is necessary to begin to gain ML predictive analytics of the conditional readiness for a ship's machinery assets. When this ML At-The-Edge is incorporated into an existing Condition Based Maintenance (CbM) system, the result is more than the preventative CbM time-based maintenance and becomes predictive CbM+ maintenance with maintenance activities occurring only when needed. The readiness of the vessel is more predictable and achieved with direct, first order improvements in operational savings, maintenance cost reduction, and failure costs' lead time delays dramatically reduced.

3.2   *AI/ML Second Order Readiness Improvement*

We take this another step further to realize there is a second order of improvement to a ship's readiness and resiliency. Couple this onboard MCSA ML At-The-Edge analysis of all electrical assets within a ship's electric and propulsion plants together with the operational parameters already captured by the PLC-controlled system for these same assets' duty cycles and operational modes, leads to an increased knowledge about how certain operational processes effect the asset's optimal performance and captures historical causes of advanced deterioration of that asset. Blade wear, shaft imbalance, bearing failures, etc. are now interconnected with that asset's historical data of its operations and can benefit the ship's engineering officer and engineering department in determining the remaining useful life of components and subsystems thereby gaining a higher understanding about the readiness state of the vessel. For the world's navies and commercial shipowners of large vessel fleets, they could advance their understanding of how different kinds of auxiliary subsystems serving the same purposes, i.e. compressors, pumps, ballast management, blowers, etc., have the longest service life and reliability/robustness factors across their multiple vessel types. These quantifiable results can be inputs into a derivation of the earlier proposed Value Driven Power Management Philosophy (VDPMP) value function to ascertain which assets or subsystems within the electric plant have the greatest improvement to robustness/reliability and therefore return on expense for accomplishing future retrofit upgrades to that ship's electric plant (Ditaranto, Samimi, Walker, Withee, and Woodward, 2014). This further promotes one of the original principles of VDPMP which is achieving those resiliency requirement tenets of a sound, reliable, and robust electrical power generation and distribution system that is composed from a best practice applied standard configuration architecture (Ditaranto, Samimi, Walker, Withee, and Woodward, 2014).

$$F_s(N, O, P, Q, R, S, T, U, V) = A_1 N + A_2 O + A_3 P + A_4 Q + A_5 R + A_6 S + A_7 T + A_8 U + A_9 V \qquad (2)$$

The derivation here from the original VDPMP value function F is that the variables *N, O, P,…V* now represent the value metrics associated of a single asset or subsystem F_s within the electric plant with specific outcome requirements such as remaining useful life, degradation rate, robustness, maintenance cost, and acquisition costs; and the Constants A_n represent their relative weighting factors. By combining MCSA ML At-The-Edge analysis with the existing operational modes/duty cycles of that same asset into a database of metrics, establishes those quantifiable inputs that contribute to a formal method, and an AI information model, to provide the selection of improvements based upon optimal outcomes at the lowest cost. The result of each sub-system's robustness value F_s can then be pulled up into the individual Redundancy/Robustness/Reliability (RRR) variable $F(A_n)$ within the overarching, original VDPMP level analysis of the entire electric plant's VDPMP for resiliency and adaptive capacity. In their paper, Walker et al, state that this is the principal purpose for VDPMP's importance.

4   Information Model toward Remaining Useful Life Metric

A dataset that contains the MCSA analytics, the operational modes, duty cycles, and individual operational parameter values, i.e. pressure, temperature, flow etc. can be applied into a gradient boost decision tree model. Gradient boosting is a machine learning ensemble technique of adding the predictions of weak learners, each a Decision Tree, sequentially. In each iteration, the goal is to optimize the model's predictive weighting of data points based on the previous errors of the last Decision Tree until the predicted output error of the model is minimized. To create this gradient boost model, one begins by establishing a base model from a set of operational parameters that have a relationship to a particular failure mode of the asset and create an initial set of error residuals through the first Decision Tree by using the Gradient boosting regressor function because our target, the predicted remaining useful life, is a continuous function. That base model's error residuals are then plugged into a second Decision Tree and a new data point in the data set is plugged through the first and second Decision Trees to produce another set of error residuals, and this is done iteratively until the model's prediction errors from that collected data point parameter becomes sufficiently close to the observed correlated value (Saini, 2024). If the error of the model becomes greater from one iteration to the next, that particular error residual is weighted higher in the model's next successive decision tree

against the other correct predictions giving it precedence in improving the model until these combined weak learners are now a strong model that accurately predicts the future operational correlation. This strong model has the outcome of more reliably predicting the remaining useful life of that asset. The overall iterative process of sequentially adding weak learners is shown in Figure 6 and is the gradient boost principle.
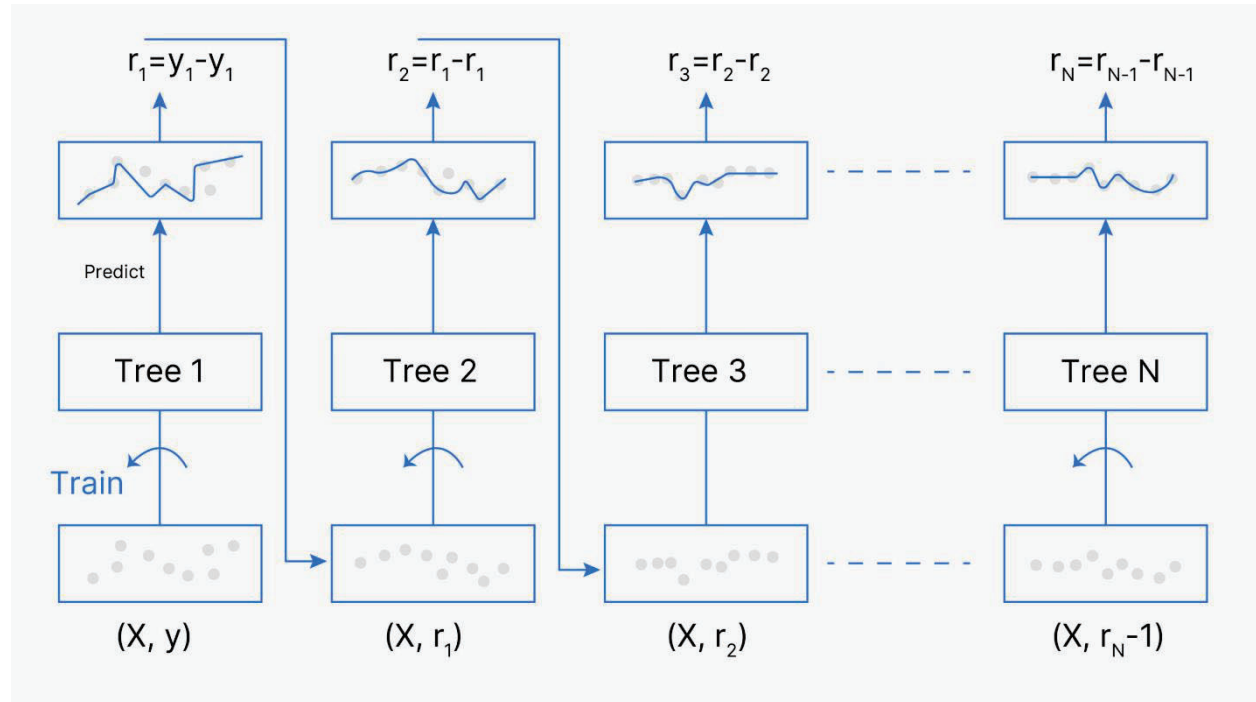

Figure 6: Gradient Boosting Tree regression (Saini, 2024).

In Gradient boosting regression, the loss function used to calculate error residuals from the Base model prediction and then from each Decision Tree iterative prediction is the following equation:

$$L = \frac{1}{n} \sum_{i=0}^{n} \left(y_i - \gamma_i \right)^2$$

(3)

Where n is the number of stumps in the decision tree, y_i is the observed value, γ_i is the predicted value. To find the minimum value of the error, i.e. difference between observed and predicted values, an individual takes the derivative of that loss function and sets it equal to zero. This calculates the minimum error residual for each of the decision tree's leaves. A learning rate, typically a value between 0 and 1, is selected and multiplied to that decision tree prediction to reduce the model's inherent bias. For a learning rate of 0.1, the gradient boosting model can be represented like Figure 7 which in this case the decision trees are for the height data parameter.

$$F_2(x) = 73.3 + 0.1 \ * \ \boxed{\text{Height} <1.55} \ + \ 0.1 \ * \ \boxed{\text{Height} <1.55}$$

| -17.3 | 14.7,2.7 | -15.6 | 13.8,1.8 |

$\gamma_{1,1} = -17.3 \qquad \gamma_{2,1} = 8.7 \qquad\qquad \gamma_{1,2} = -15.6 \qquad \gamma_{2,2} = 7.8$
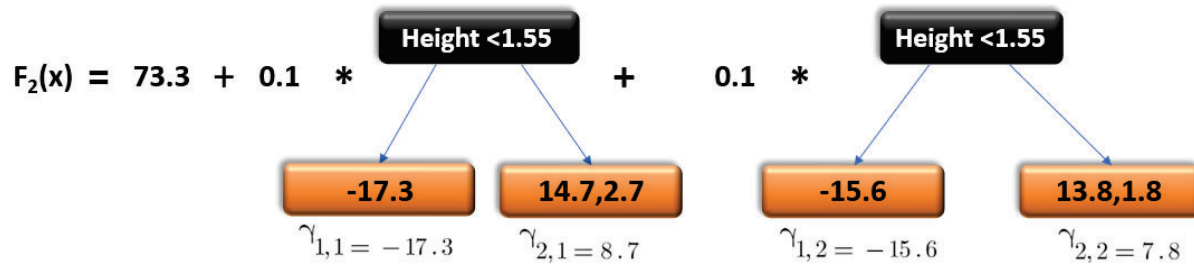
Figure 7: Gradient boost model (Saini, 2024)

This method of creating a gradient boosted tree predictive AI model was applied to a U.S. Air Force facility's compressor system which led to an AI information model result that successfully predicted the remaining useful life of that compressor with a prediction of failure within 40 minutes of that event (Reis and Resseguie, 2023). This result underscores the value of ML At-The-Edge for ships when combined with an AI information model to determine those numerous assets' health and readiness throughout the ship's machinery plant and its auxiliary systems before the vessel deploys and while underway.

5   Conclusions

This paper surveyed the significant benefits of using ML At-The-Edge in shipboard applications to advance crewmembers' efforts to keep the ship's conditional readiness and reliability to meet requirements. Years ago, Motor Current Signature Analysis (MCSA) was performed by contracted CbM/vibration analysts or motor experts on a defined cadence; this and similar traditional CbM monitoring techniques were left to the dedicated few experts to perform. Alternatively, reams of data have been collected into the Cloud for data scientists to comb through to discover possible insights and correlations between operational activities. All at higher costs that came along with delays to transform that data into root causes and preemptive insights needed of real-time operations. These hurdles are even greater to maritime operations of vessels at sea. However, these obstacles can be overcome through embedded expertise ML apps deployed within OCI containers at the deck plates. The embedded knowledge of earlier classified MCSA anomalies of shipboard motor and machinery assets can be trained into the ML app without a CbM analyst's expertise and, even in the unique shipboard environment, can be continuously monitored all the time without pulling voluminous data into the Cloud. Combining this MCSA ML embedded expertise with those assets' operational events and duty cycles into lower density datasets at the ship can lead to greater readiness capabilities from leveraging AI information model algorithms like gradient boosted decision trees. Gaining metrics such as remaining useful life means even greater shipboard readiness is achievable.

Acknowledgements

References

Miljković, D. (2015). Brief Review of Motor Current Signature Analysis. *CrSNDT Journal*. 5. 14-26.

Thomson, W. T. & Gilmore R. J. (2003, September). *Motor Current Signature Analysis to Detect Faults in Induction Motor Drives – Fundamentals, Data Interpretation, and Industrial Case Histories*. Proceeding of the Thirty-Second Turbomachinery Symposium, Houston, TX.

Ditaranto, Samimi, Walker, Withee, & Woodward (2014, September 9 – 10). *An Electric Power Management Program via a Value Driven Engineering Philosophy for Navy Surface Ships*. ASNE Fleet Maintenance & Modernization Symposium. Virginia Beach, VA.

Saini, A. (2024, January 10). *Gradient Boosting Algorithm: A Complete Guide for Beginners*. Analyticsvidhya. https://www.analyticsvidhya.com/blog/2021/09/gradient-boosting-algorithm-a-complete-guide-for-beginners/

Chow, M. (2000, October). Guest Editorial Special Section on Motor Fault Detection and Diagnosis. *IEEE Transactions on Industrial Electronics*, Vol. 47, No. 5.

Reis, G. & Resseguie, R. (2023, August). *AI/ML Innovation for Condition-Based Maintenance (CbM+) to address the DoD mandate*. Department of the Air Force Information Technology and Cyberpower. Montgomery, AL.

Lambert-Torres, G. (2009, May). *Reducing the Downtime Cost in the Brazilian Refineries through the Remote Induction Motor Health Monitoring and Induction Motor Management*. NPRA Reliability & Maintenance Conference and Exhibition.

Bernet, J. (2022, April 11). *Remote condition monitoring can alleviate worker shortages*. Plant Engineering. https://www.plantengineering.com/articles/remote-condition-monitoring-can-alleviate-worker-shortages/

State-of-the-art Full-Scale Simulator for a Ship Hybrid Power System in a Shuttle Tanker

Pramod Ghimire[a*], Christian Høyem Andersen[a], Jarle Thorstensen[a], Krishna Kumar Nagalingam[b], and Mehdi Zadeh[c]

[a]*Kongsberg Digital, Horten, Norway;* [b]*Kongsberg Maritime, Kongsberg, Norway;* [c]*Norwegian University of Science and Technology, Trondheim, Norway*

*Corresponding author. Email: pramod.ghimire@kongsbergdigital.com

Synopsis

To maximize efficiency and minimize emissions, ship power systems are transforming from a conventional to more sophisticated power systems, such as battery hybrid-, fuel cell hybrid-, onboard DC-, and fully battery electric power systems. Such sophisticated power systems also raise the complexity due to different power system configurations and utilization philosophies. On the other hand, a realistic simulator system enhances the research and development, engineering, and training of such complex systems. Firstly, simulator can be used to simulate the what-if scenarios onboard a vessel. The ship operators can simulate a scenario which they are encountering or going to encounter soon. From the simulator results, they can observe, understand, and analyze the outcome of such scenario. It helps them make an informed decision for safe and efficient operation. Secondly, the full-scale simulators including the control system can also be used in virtual prototyping of the ship system. During the ship design phase, simulator can be used to evaluate the choice of right producers to meet power system requirements in both intact and worst-case failure (WCF) conditions. Further, power and energy management system (PEMS) needs to ensure effective use of energy carriers (engine generator sets and battery systems) and energy consumers (propulsion system and heavy loads) for the safe, stable, and efficient operation. This work develops and demonstrates a full-scale simulator for a battery-based hybrid power system in a shuttle tanker. The simulator is developed integrating the dynamic component models and control system models. The dynamic component models are developed based on the first principles with varying fidelity. Majority of the required models are previously developed and are available in the in-house model library. However, in this work, physics-based battery systems, DC grid, grid converters and their control counterparts such as battery management-, energy management systems are newly developed. The simulator is used to study the impact of battery in sudden load change and fluctuating loading conditions, where battery systems proved to effectively manage the situations and stabilize the generator output power. Further, the third simulation scenario also showed that the control system ensures sufficient propulsion power even if the worst-case failure occurs.

Keywords: Battery Hybrid Power System; Onboard DC and AC Power System; Power and Energy Management System; Worst Case Single Failure

1 Introduction

Although maritime industry is a backbone of global trade and economy, it is also responsible for significant global emissions, accounting for almost 3% of global greenhouse gas (GHG) emissions (Ghimire, 2022). To reduce or limit emission footprints, collective efforts towards implementing sustainable solutions in each step can be an effective way (IMO, 2021). Both academic institutions and the industries are working hand-on-hand to innovate cleaner, efficient and effective solutions, which can be grouped into greener fuels, and greener technologies

(Ghimire, 2022). In a conventional ship power system, generator sets are driven by engines running on fossil fuels, which have been the primary energy source till date. However, due to stricter emissions and efficiency regulations, alternative energy sources are being explored. The green and renewable energy sources include hydro power, wind, and solar energy. The energy produced by the alternative energy sources can be stored in energy storage systems (ESSs) like batteries, super-capacitors, and flywheels, or used to artificially produce greener fuels such as bio fuels or synthetic fuels (e-fuels).

Various greener fuels (green hydrogen, methanol, and ammonia) are being studied and discussed in the maritime industry (ABS, 2020). The challenges of these new greener fuels lie in the economic feasibility, supply infrastructure, and onboard space requirement. Similarly, greener technologies, such as battery-electric, fuel cell-electric, solar and wind energy-based, and hybrid concepts, are also being explored for the implementation in both new ship builds and retrofitting of the existing ships (ABS, 2020; Arief and Fathalah, 2022; Shakeri et al., 2020). These technologies are well-accepted; however, they have some limitations. For instance, these technologies may fit only for a particular ship type or a mission. However, battery-hybrid technology is one of the technically and economically feasible options for the majority of ship types (Ghimire et al., 2024).

Rapid advancement in battery technologies, especially improved energy and power density and reduced cost of lithium-ion battery, is enabling the implementation of hybrid and pure battery-based power system in various industries such as automobile, maritime, offshore, and so on (Othman et al., 2019). Further, lithium-ion batteries outperform the conventional ones because of higher specific energy, open circuit voltage, charging and discharging rate, and cycle life; lower self-discharging rate; and relatively flat discharge curve (Ghimire et al., 2019). The battery hybrid power system in a ship is characterized by the integration of battery system(s) into the conventional ship power systems Ghimire et al. (2019). Battery systems operate in DC power system architecture and can serve both as a power producer and a consumer. For instance, battery can be charged to store the surplus energy when load power suddenly drops, whereas it can be discharged to supply the energy deficit when load power suddenly increases. In other words, battery systems help in stabilizing the onboard power system. It can be also used to charge or discharge in such a way that the fuel consumption of the fossil-fueled engine reduces, and the overall efficiency improves (Miyazaki et al., 2016).

Although integrating the battery or energy storage systems onboard a ship has the potential to improve power system stability, reduce emissions and fuel consumption, it also increases the complexity of overall power system with respect to architecture, control, operation, and maintenance philosophies. For instance, battery systems require the operation within the defined parameters like charging and discharging rate, current, voltage, and temperature to acquire better performance and safety (ABS, 2017). Besides, it also requires sophisticated monitoring and protection systems to enhance both battery life and safety (Ghimire et al., 2019, 2022).

As the ship systems are getting more complex, interactions between the subsystems also increases. Therefore, it is necessary to study and analyze the interactions of these subsystems not only during the operation but also in the research, design, engineering, and development phases. Similarly, to operate and maintain newly integrated components and technologies onboard a ship, requires the proper training of the crew such that they become familiar about the new components and technologies. A realistic simulator system can be a promising solution to the discussed problems (Skjong et al., 2018; Ghimire et al., 2021a,b). The simulation of ship systems in a real ship scenario incorporating the interactions between subsystems serves as an effective tool that can be used during the research, design, engineering, development, operation, training, and maintenance phases (Skjong et al., 2018). However, in some scenarios when a system of interest is defined as a particular system or subsystem, it may not require simulating a whole complex system. Therefore, the simulator needs to be modular enhancing the use of flexible interconnections between different subsystems.

With a full-scale simulator (see Fig. 1), ship owners and operators can benefit from the ship design to operation and maintenance phases. The full-scale simulators including a control system can be used in virtual prototyping of the ship systems. For instance, during the ship design phase, simulator can be used to evaluate the choice of right producers to meet power system requirements in both intact and worst-case failure (WCF) conditions. This helps in effective ship designing and reducing the CAPEX. Similarly, simulator can also be used to simulate the what-if scenarios onboard a vessel. The ship operators can simulate scenarios which they are encountering or going to encounter soon. From the simulator results, they can observe, understand, and analyze the outcome of their actions in such scenarios. It helps them make the informed decisions for ensuring safe and efficient operations.

In the recent decades, as the computational capacity has significantly improved, data-based methods and tools, such as artificial intelligence and machine learning, are increasingly implemented to solve the problems in an effective manner. These methods and tools require sufficient data to train their algorithms in all possible scenarios, which may not always be possible to collect at once in the real world. Therefore, a realistic simulator can also serve as a synthetic data generator to train the algorithms of the modern problem-solving tools.

This work develops and demonstrates a modular full-scale simulator for a battery-based hybrid power system in a shuttle tanker. The simulator is developed integrating the dynamic component and control system models.

Figure 1: A full-scale shuttle tanker simulator. (Source: K-Sim® Navigation simulator.)

The dynamic component models are developed based on the first principles with varying fidelity. Majority of the required models were previously developed and available in the in-house model library in maritime simulation, Kongsberg Digital (Kongsberg Digital, 2023). However, in this work, physics-based battery systems, DC grid, grid converters, and their control counterparts such as battery management-, energy management systems are newly developed. Simulation scenarios are developed to study the impact of battery systems under sudden load change and fluctuating loads. Another scenario included the testing of worst-case failure-based load dependent start of the generator engines. The simulation results show that the battery systems effectively stabilize the generator engines. Similarly, another scenario simulation shows that the power system redundancy ensures the required power for the propulsion system to maintain the ship position irrespective of the worst-case failure, thus enhancing the safety.

2 A Shuttle Tanker Simulator

A full-scale simulator for a shuttle tanker consists of a K-Sim® Engine and a K-Sim® Navigation simulators. This simulator is interfaced with a real Kongsberg DP software (Kongsberg Digital, 2023). The modeled ship is propelled by two main propellers with a maximum speed of 83.1 rpm each, which are driven by two propulsion electric motors (PEMs) with a power capacity of 3.25 MW each. The propulsion power is also produced by a bow tunnel thruster, two bow azimuth thruster, and a stern azimuth thruster, each of 2.2 MW capacity. The schematic of the simulated power and propulsion system is shown in the Fig. 2.

The power system consists of both AC and DC main switch boards (MSBs), interfaced using four grid converters. The AC MSB is divided into eight different buses using bus-tie breakers, out of which four main buses (Bus A, B, C, and D) are fed through a generator (4.2 MW or 5.6 MW) driven by a dual fuel (DF) engine, operating on marine diesel oil or liquefied nitrogen gas (LNG). These four main buses are divided into two sections (1 and 2) using transformers. AC main buses are operating at 690 V, 60 Hz and are feeding the propulsion loads. Other auxiliary consumers are fed via 440 V power distribution system. The DC main bus is also divided into two by the bus-tie breakers, and named hybrid drive 1 and 2. Both hybrid drives are connected with a battery system of maximum 909 kWh each. Hybrid drive 1 is also connected with a gas turbine of 1 MW capacity. The basic capacities and specifications of the major components of power and propulsion systems are listed in Table A.

Depending on the DP class, the vessel needs to have certain level of redundancy such that in case of a single failure, the redundant system ensures generation of the required propulsion power. With the optimum level of redundancy, this ship model is able to maintain its position and heading even if failure condition occurs. One azimuth thruster and a propeller with two PEMs that can be supplied by two DF generators and a battery system is placed at each side of the engine room. In addition, both the azimuth thruster and the tunnel thruster can get power
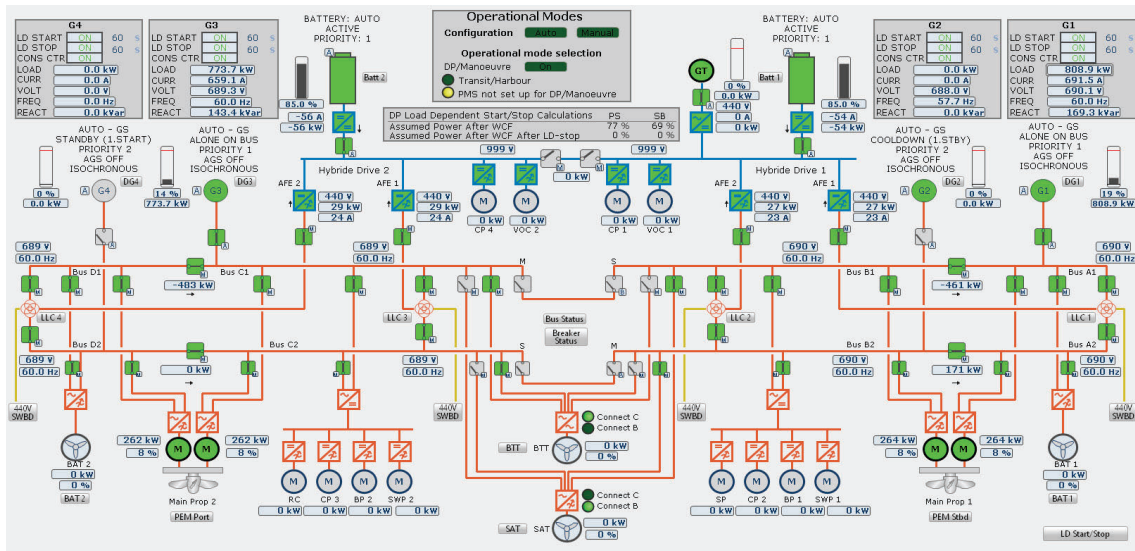
Figure 2: Power system overview of a modeled shuttle tanker.

supply from either side of the main buses.

This K-Sim® Engine simulator for the shuttle tanker is developed integrating various models; dynamic component and control system models. The simulator basically simulates two different categories present onboard a system, namely the physical components available in the engine room and control and automation systems available in the engine control room. The physics-based modeling approach is implemented while modeling the physical components such as DF engine generator set, battery systems, switch boards, breakers, pumps, valves, fluid-based pipe and node models, and so on. Similarly, simulation of control and automation system enables manual, semi-automatic, or automatic operation of a certain component or a system in addition to the alarm system. Most of the models used to develop this simulator were already available in the in-house model library. However, based on the author's previous work (Ghimire et al., 2021a,b,c; Ghimire, 2022), new models for the battery systems are developed in this work including battery management system (BMS), energy management system (EMS), DC-DC converters, DC main bus, and grid converters as shown in Fig. 3.
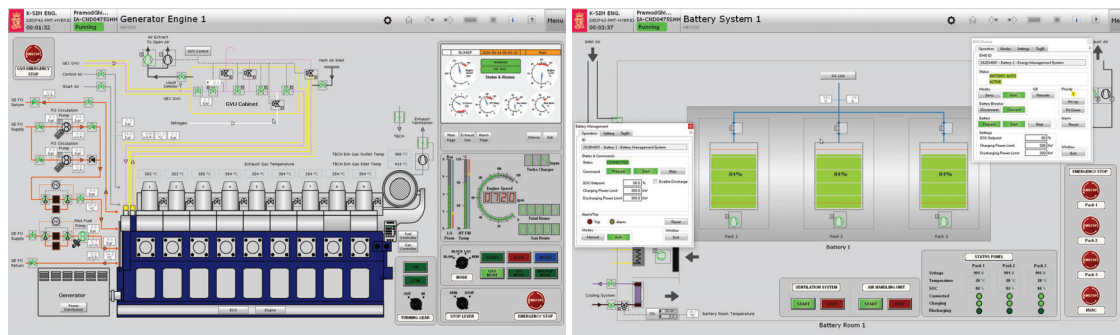
Figure 3: Simulator user interface illustrating DF generator engine operating on gas (left) and battery systems, BMS and EMS (right).

3 Simulation Scenarios

As the developed simulator is a full-scale simulator consisting of major subsystems for power and propulsion system, various simulation scenarios can be developed and presented. However, since the hybrid power system has been the focus in this paper, three different simulation scenarios are developed mainly to exemplify ability of battery systems in supporting dual fuel generators and stabilize them during the normal operation and in the occurrence of a failure.

3.1 Hybrid Power and Propulsion Scenario

In this modeled power system, the DF engine generators are major power sources used to generate required propulsion and auxiliary power. In addition, the power system is equipped with two battery systems to assist the generator sets for improved performance as shown in Fig. 4. Initially, generators are supplying the power demand by propulsion and auxiliary consumers. The batteries are adequately charged (around 81% SoC) and are in standby position. Due to the sailing conditions, the operator at the bridge moves port and starboard levers ahead demanding more power in both propellers. It resulted in sudden increase in PEMs power, which is then supported initially by the batteries. Later, battery load is transferred gradually to the generators, which took around 7 minutes. SoC of batteries decreased from around 81% to 75%. When total battery load is transferred to the generators, batteries start consuming some generator power to slowly charge up to 80% SoC which is a default SoC set point. However, in case it occurs a new load variation, batteries will act to reduce the sudden effect of load variation to the generators.
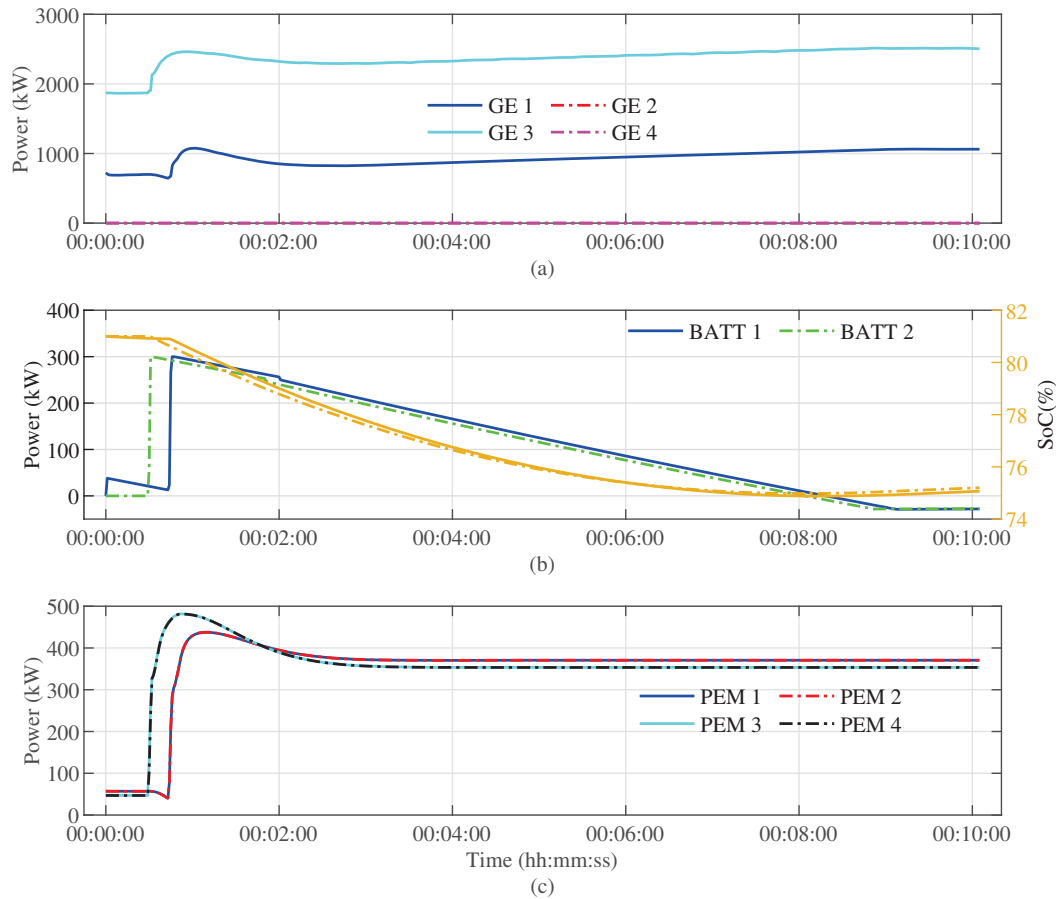
Figure 4: Simulation results illustrating the battery assistance to the generators in sudden increment of propulsion power demand. (a) Generator power (GE 1/2/3/4). (b) Battery power (BATT 1/2). (c) Propulsion electric motor power (PEM 1/2/3/4).

3.2 Power System Stabilization Scenario

Another functionality of a battery in a shipboard power system is to enhance power system stability. Due to the environment or nature of the components, electrical load onboard a vessel can be fluctuating. These fluctuating loads can easily make the power system unstable, leading to the blackout situations or create the safety issue. Therefore, it is necessary to handle the fluctuating loads. As the big engine and generators usually have higher time constants, they may not be able to respond such fluctuating loads. However, battery systems, having much faster response than the generator sets, can promptly respond these loads. In this simulation scenario, generators are supplying the total propulsion load at port and starboard sides as shown in Fig. 5. Later, heavy loads such as re-liquefaction and VOC (volatile organic compound) pumps and compressors are started. These heavy loads began to fluctuate significantly at around 5 minutes of sailing, which are effectively handled by the battery systems onboard.

This resulted in very less fluctuations in the generator power, thereby enhancing the power system stability and safety. Besides, it also decreases the maintenance cost of the rotating parts as it reduces wear and tear in engine and generators.
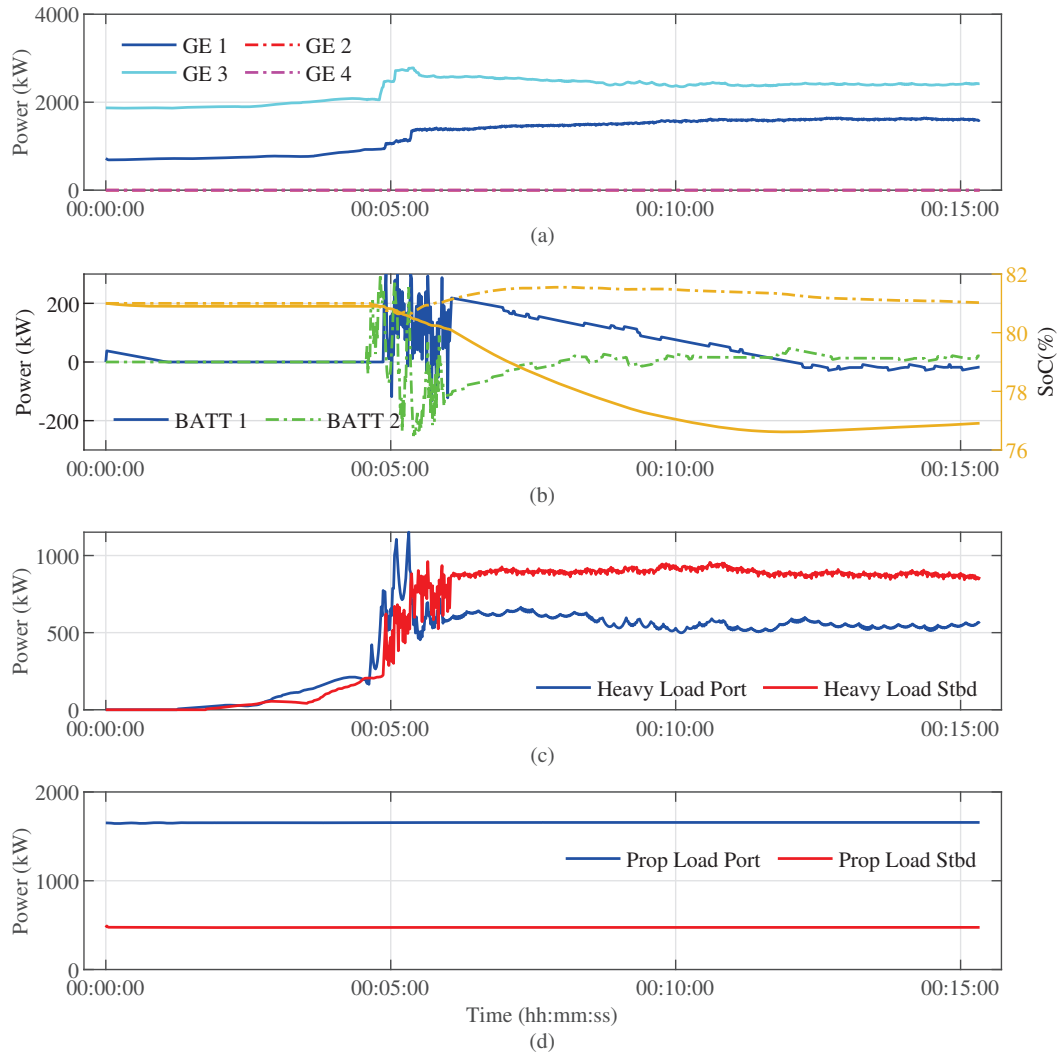
Figure 5: Simulation results illustrating the battery contribution to reduce impact of fluctuating load on the generator sets. (a) Generator power (GE 1/2/3/4). (b) Battery power (BATT 1/2). (c) Fluctuating heavy Loads (d) Stable propulsion load.

3.3 Worst Case Failure Scenario

As the modeled ship for this simulator is DP class 3 type, it has the required power system redundancy. The control system is also equipped in such a way that it can handle the sudden failure conditions without compromising the ship position and heading. In this simulation scenario, DP / Maneuver operational mode is selected, and the configuration is set to auto mode. It enables the load dependent start stop limit calculation that takes care of WCF, meaning it starts and connects the generator(s) in a bus to ensure the sufficient available power required for the propulsion in case failure condition occurs. To demonstrate WCF-based scenario with a two split power system configuration, generator start power limit for the port and starboard side together with the thruster, batteries, generator power, and bus-tie breaker positions in each side are shown in Fig. 6. The PEMs are operating, and their power level are not altered in this simulation scenario. Similarly, generators 1 and 3 are supplying the existing propulsion and auxiliary power demand.

At around 1 minutes and 30 seconds, the bow azimuth thruster 2 lever position is moved forward, which demanded the increased electrical power at the port side. Since the battery 2 was in standby, it took over the increased load demand initially and slowly transferred the load to generator 1 as it had sufficient available power.
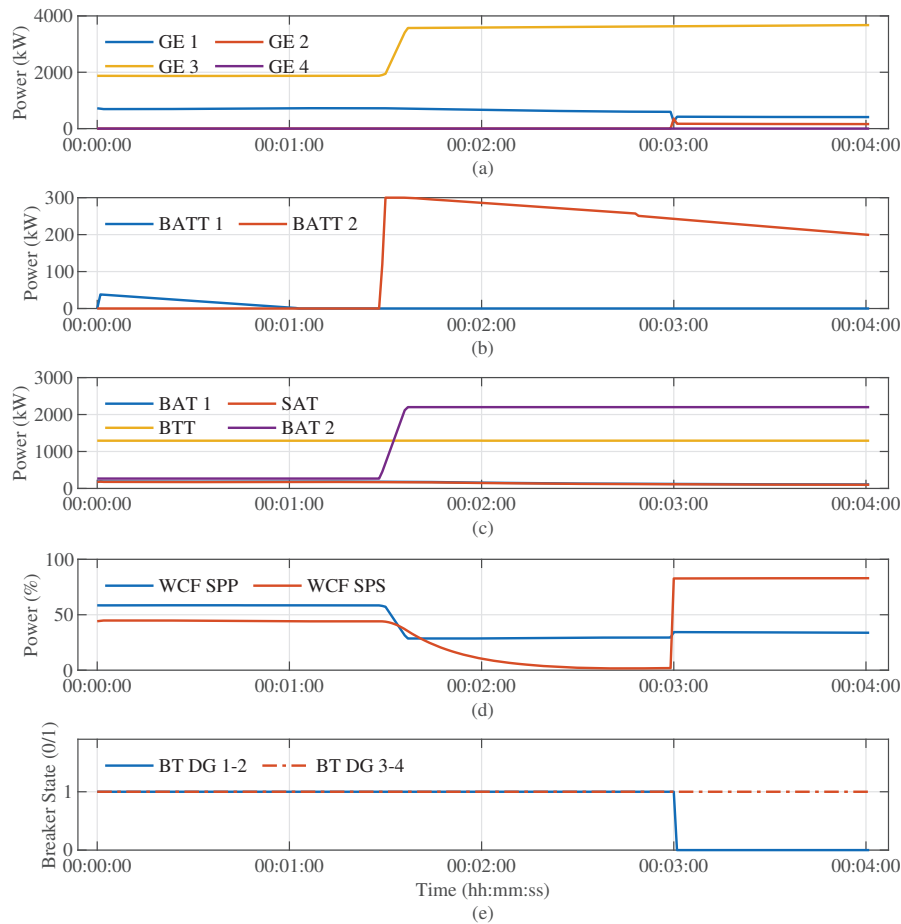
Figure 6: Simulation results illustrating WCF-based load dependent generator start test. (a) Generator power (GE 1/2/3/4). (b) Battery power (BATT 1/2). (c) Bow azimuth thruster (BAT 1/2), stern azimuth thruster (SAT), bow tunnel thruster (BTT) power. (d) Worst case failure start power limit port or starboard side (WCF SP(P/S)). (e) Bus-tie breaker states (BT (GE 1-2 / GE 3-4)).

However, this event resulted in recalculation of WCF-based load dependent start of generators. As the load in port side increased, the WCF start power limit port (SPP) and start power limit starboard (SPS) decreased. The WCF SPS decreased below 10%, initiating the start timer of 60s. Since the WCF SPS is still below 10% even after 60s, generator 2 is started in the starboard side and WCF SPS increases to around 80%. Once the generator 2 is connected to the bus, the starboard side has sufficient available power even if WCF occurs in the port side, however, both the generators in starboard side are then operating in the low load conditions. Further, bus-tie breaker(s) between the generators 1 and 2 are automatically opened resulting into the three split power system configurations.

4 Discussion

This work modeled and simulated the battery hybrid power system in a shuttle tanker, which is a fairly complex power system consisting of dual fuel generator sets, battery systems, AC switch board, DC switchboard, azimuth thrusters, propulsion electric motors, and so on. The simulator has been able to reflect various scenarios onboard a vessel with a realistic behavior. The used models in this simulator are mostly modular, flexible, and scalable such that they can be used to developed various system models appropriate for other ship types.

Besides, the maritime industry has been extensively searching and experimenting on various greener fuel types and the technologies to reduce emissions and improve efficiency ABS (2020). Similarly, reduction of maintenance

and operational cost has also been the focus while keeping intact the safety and stability. Battery-based hybrid power system can be considered as one of the greener technologies that can support the maritime industry towards a sustainable future.

The energy efficiency improvement and emissions reduction through battery hybridization is discussed in Miyazaki et al. (2016), which highlights various operational modes of the battery system to achieve the objectives. However, there can be various factors that affect the efficiency and emissions, such as mission profile, weather conditions, operating modes, battery capacity, control strategy, power system architecture, and so on. A simulation-based study done for a cruise ship scenario with a real operational profile (Ghimire et al., 2021c) shows that battery-hybridization improves the energy efficiency in both AC and DC power system architectures. It also showed that battery hybridization improves energy efficiency in rough sea compared to calm sea.

Further, (Ghimire et al., 2024) investigated the impact of battery-hybridization in four different ship types - cruise ship, Ro-Pax ferry, bulk carrier, and container ship with their real operational profiles and three different control strategies. The study showed that fuel saving is achieved by battery hybridization in all ship types. However, it also showed that proper control strategy selection is imperative to improve fuel saving and emissions reduction. It also conducted a brief techno-economic analysis to investigate the viability of battery hybridizing the existing ship power system. It arguments that proper battery size selection, such as a battery system that can supply almost the same power as an existing generator but only for an hour, make it both economically and technically feasible as one of the generators can simply be replaced with the proposed battery system.

Hence, battery-based hybrid power system can be considered as one of the technologies that can support sustainability in the maritime industry as it increases efficiency and reduces emissions in general. Therefore, implementation of battery systems onboard a vessel is increasing both in the new ship builds and in the retrofits (DNV, 2021). As the battery system is relatively a new technology in maritime industry, it also requires effective tools for design, development, testing, and training. Therefore, the developed simulator can be the effective tool (Kongsberg Digital, 2023).

5 Conclusion

In this paper, a state-of-the-art full scale simulator for a shuttle tanker is developed with a focus on the power and propulsion systems. The modeled shuttle tanker simulator consists of sophisticated power system (a battery-hybrid power system with DC and AC main buses, DC-AC grid converters, and redundant power and propulsion systems). The simulator is developed integrating the dynamic physics-based models for the components onboard together with simulated control and automation systems. The simulator is modular and flexible to be interfaced with navigation, cargo simulators and DP control system.

This work demonstrated the simulation scenarios highlighting the impact of battery systems in the power and propulsion systems. It is observed that the battery system enhances the power system stability even in the presence of highly fluctuating loads. It also discussed and demonstrated the power system capability to ensure safety during the DP operation using the worst-case failure-based load dependent start stop limits for the dual fuel generators. Moreover, this work exemplifies the recent efforts in maritime industry towards implementing more sustainable ship power system (incorporating battery systems, AC and DC buses) as well as its commitment in safe DP operations.

Further, being a committed sustainability partner organization in the maritime industry, the future research and development work includes full-scale simulators development for various ship types with greener energy and technological possibilities. This will not only help to train the crew onboard a vessel but also enhance the design, development, and testing phases of the new builds using upcoming greener fuels and technologies.

A   Specifications for a shuttle tanker simulator.

Particulars	Specifications
Propeller Speed	83.1 rpm (max)
PEMS 1 & 2	3.25 MW (each)
Generator Set 1 & 4	4.2 MW (each)
Generator Set 2 & 3	5.6 MW (each)
Gas Turbine	1 MW
Thruster (3 azimuth and 1 tunnel)	2.2 MW (each)
AC Main Bus	690V, 60 Hz
DC Main Bus	1000 V
Batteries	1000 V, 303 kWh (909 kW max)

References

ABS, 2017. ABS Advisory on Hybrid Electric Power Systems. Technical Report. American Bureau of Shipping.

ABS, 2020. Setting the Course to Low Carbon Shipping - Pathways to Sustainable Shipping. Am. Bur. Shipp. .

Arief, I.S., Fathalah, A.Z., 2022. Review Of Alternative Energy Resource For The Future Ship Power. IOP Conf. Ser. Earth Environ. Sci. 972, 012073. doi:10.1088/1755-1315/972/1/012073.

DNV, 2021. Alternative Fuels Insight. URL: https://afi.dnv.com/statistics.

Ghimire, P., 2022. Simulation-Based Ship Hybrid Power System Concept Studies and Performance Analyses. Ph.D. thesis. Norwegian University of Science and Technology. URL: https://ntnuopen.ntnu.no/ntnu-xmlui/handle/11250/3005104.

Ghimire, P., Karimi, S., Zadeh, M., Nagalingam, K.K., Pedersen, E., 2022. Model-based efficiency and emissions evaluation of a marine hybrid power system with load profile. Electr. Power Syst. Res. 212. doi:10.1016/j.epsr.2022.108530.

Ghimire, P., Park, D., Zadeh, M., Thorstensen, J., Pedersen, E., 2019. Shipboard Electric Power Conversion: System Architecture, Applications, Control, and Challenges [Technology Leaders]. IEEE Electrif. Mag. 7, 6–20. doi:10.1109/MELE.2019.2943948.

Ghimire, P., Zadeh, M., Pedersen, E., 2021a. Co-Simulation of a Marine Hybrid Power System for Real-Time Virtual Testing, in: 2021 IEEE Transp. Electrif. Conf. Expo, IEEE. pp. 1–6. doi:10.1109/ITEC51675.2021.9490050.

Ghimire, P., Zadeh, M., Pedersen, E., Thorstensen, J., 2021b. Dynamic Modeling, Simulation, and Testing of a Marine DC Hybrid Power System. IEEE Trans. Transp. Electrif. 7, 905–919. doi:10.1109/TTE.2020.3023896.

Ghimire, P., Zadeh, M., Thapa, S., Thorstensen, J., Pedersen, E., 2024. Operational Efficiency and Emissions Assessment of Ship Hybrid Power Systems with Battery; Effect of Control Strategies. IEEE Trans. Transp. Electrif. doi:10.1109/TTE.2024.3365351.

Ghimire, P., Zadeh, M., Thorstensen, J., Pedersen, E., 2021c. Data-Driven Efficiency Modeling and Analysis of All-Electric Ship Powertrain; A Comparison of Power System Architectures. IEEE Trans. Transp. Electrif. 8, 1930–1943. doi:10.1109/TTE.2021.3123886.

IMO, 2021. Fourth IMO GHG Study 2020 Full Report. Technical Report. International Maritime Organization. London.

Kongsberg Digital, 2023. K-SIM® MARITIME SIMULATION. URL: https://marsim.kongsbergdigital.com/.

Miyazaki, M.R., Sorensen, A.J., Vartdal, B.J., 2016. Reduction of Fuel Consumption on Hybrid Marine Power Plants by Strategic Loading With Energy Storage Devices. IEEE Power Energy Technol. Syst. J. 3, 207–217. doi:10.1109/jpets.2016.2621117.

Othman, M.B., Reddy, N.P., Ghimire, P., Zadeh, M., Anvari-Moghaddam, A., Guerrero, J.M., 2019. A Hybrid Power System Laboratory: Testing Electric and Hybrid Propulsion. IEEE Electrif. Mag. 7, 89–97. doi:10.1109/MELE.2019.2943982.

Shakeri, N., Zadeh, M., Bremnes Nielsen, J., 2020. Hydrogen Fuel Cells for Ship Electric Propulsion: Moving Toward Greener Ships. IEEE Electrif. Mag. 8, 27–43. doi:10.1109/MELE.2020.2985484.

Skjong, S., Rindarøy, M., Kyllingstad, L.T., Æsøy, V., Pedersen, E., 2018. Virtual prototyping of maritime systems and operations: applications of distributed co-simulations. J. Mar. Sci. Technol. 23, 835–853. doi:10.1007/s00773-017-0514-2.

Energy-Efficient Speed Planning Considering Delay and Dynamic Waterway Conditions for Inland Vessels

Ir. S Slagter[a*], Dr. Ir. Y Pang[a], Prof. Dr. R R Negenborn[a]

[a]*Delft University of Technology, The Netherlands*
*Corresponding author. Email: s.slagter@tudelft.nl

Synopsis

The inland waterway transport sector is facing increasingly stringent legislation to reduce emissions and improve energy efficiency. Speed planning methods are an attractive option as they provide energy-efficient, timely and emission-reducing voyage planning for ships. However, current methods do not consider dynamic conditions of waterways and traffic. Due to these dynamic navigational conditions the static speed planning methods do not guarantee optimality, nor do they satisfy the constraints of the optimization problem throughout the journey. In this paper we propose an optimization structure that is based on the Model Predictive Control algorithm, which uses the most current information on water depth, water speed and expected delays to re-optimize the speed planning throughout the journey. Through a use case we show a 4.31% energy reduction compared to other speed planning strategies. Additionally, we show that the constraints regarding desired arrival times and safety are satisfied throughout the journey. Therefore, the method proves useful from a logistical, energy, emissions, and safety perspective. Modelling of uncertainties, lock interactions and predictions of waterway conditions will make our method an even more attractive option for speed planning.

Keywords: Voyage optimization; Non-linear control systems; Model predictive control; Inland shipping

1 Introduction

1.1 Background

Each industry and transport sector must change in order to meet the goals set out by the European Commission in the European Green Deal. This legislation aims to reduce the net greenhouse gas emissions by 55% by 2030, and to be climate-neutral by 2050 (EC, 2020).The Commission has also set an 'energy efficiency target of reducing final energy consumption by at least 11.7% compared to projections of the expected energy use for 2030' (EC, 2022). Improving energy efficiency is a critical strategy for mitigating environmental impact, conserving natural resources, and promoting a more sustainable business practise. Using energy more efficiently reduces the amount of energy required, thereby lowering emissions and mitigating environmental damage.

For the inland waterway transport (IWT) sector the NAIADES III action plan is established which states various goals for the sector such as lowering emissions and achieving smarter waterways (EC, 2021). The IWT sector is dedicating much research into clarifying transition pathways (CCNR, 2022; Kirichek et al., 2024), developing novel technologies to facilitate the transition, and developing methods to improve the energy efficiency of ships in operation. Our interest lies in the energy efficient methods for ship operations as these solution will be immediately applicable, and remain valuable during and after the energy transition; even with zero emission technology, we still want to reduce the required energy for operations.

A method of particular interest is voyage optimization, which is a method that aims to provide safe, energy-efficient, timely and emission-reducing voyage planning for ships. Additionally, they directly contribute to achieving smarter inland waterways (EC, 2021), and are relatively cost-effective and simple to implement leading to little or no downtime upon implementation. Inland shipping frequently relies on a single route from start to finish, resulting in a focus on speed planning rather than the combined optimization of speed and route due to limited route options. For that reason, voyage optimization for inland shipping is often reduced to speed optimization.

1.2 Related works and research gap

Speed planning for inland shipping involves finding the optimal speed setpoints along the journey as a function of ship design parameters, traffic and fairway conditions, cargo, and powertrain characteristics. Methods as

---

presented in (Yan et al., 2018; WANG et al., 2019) discretize the journey in different segments or legs. Then, for each of these segments the optimal speed setting for the engine or ship is found for which the energy is minimized over the journey, resulting in a 2-5% energy reduction. Similarly, (Fan et al., 2021) determines the optimal speed setpoints between ports visited on a journey.

Speed is sometimes also co-optimized with energy directly, such as in the works of (Sun et al., 2023; Zhang et al., 2023); they consider the effect of engine setpoints on performance rather than just fairway and journey conditions. Some works take into account environmental conditions such as wind, wave, current velocity, and water depth and their effect on the resistance of the ship (Han et al., 2021; Zhang et al., 2022); others take into account the navigational conditions of the ship, ship specifications, manoeuvring and time windows constraints (Liu, 2023). (Wang et al., 2023) developed a speed planning method that considers maximum allowable SO_x emissions in emission control areas. (Gao et al., 2022) suggests a different voyage optimization, namely trim optimization leading to an energy efficiency of 1.46%.

The field of energy-efficient speed planning for inland vessels is not yet well explored compared to the maritime field. What is currently still missing in literature are methods that consider time-varying environmental and fairway conditions and their uncertainty. During an inland waterway journey the states of water depth and current will change. Additionally, the ship will run into delays at locks, or traffic delays in crowded fairways. Due to these dynamic navigational conditions the speed planning computed at the start of the journey will not remain optimal for long, nor does it guarantee to satisfy the constraints of the optimization problem. For instance, with unexpected delays or higher water speed than anticipated the journey can take substantially longer than anticipated leading to logistical problems such as late arrival times. For this reason, it is important to continually update the speed planning to take into account the most current information on water depth, current velocity, expected delays and experienced delays. Additionally, using accurate and up-to-date information on water depth is particularly important from a safety point of view; low water depths can cause grounding, higher water depths can cause safety concerns at bridges.

1.3 Aim and contribution

Dynamic waterway conditions and delays have not yet been considered in speed planning for inland vessels. It is our aim to provide a framework in which these conditions are taken into account. For that reason, in this work we propose an optimization structure that is based on the Model Predictive Control (MPC) algorithm, which continually uses the most up-to-date information throughout the journey on fairway characteristics and delays to re-optimize the speed planning, leading to improved energy efficiency, reliable arrival times, and satisfied constraints.

1.4 Structure of the paper

In Section 2 we provide the static speed planning model consisting of the resistance modelling of an inland vessel in shallow waters, models for estimating the energy consumption and the objective function and constraints of the speed planning model. Secondly, in Section 3 we introduce the MPC framework of the dynamic speed planning model and the updating procedure for different dynamic constraints and parameters. In Section 4 we define a use case and explain the dynamic parameters, journey parameters, and ship characteristics. In Section 5 the results of the case study are shown and discussed. The results are compared to other speed planning strategies to show the energy efficiency of the method. Additionally, a sensitivity analysis is included to show the effects of the dynamic parameters on the energy consumption. Finally, in Section 6 are the conclusions and suggestions for further research.

2 Speed planning model

In this paper we introduce a stretch-based speed planning model tailored for inland waterway navigation. We segment the journey from origin to destination into discrete stretches, each characterized by specific fairway features like water depth and current speed. The goal of this model is to determine the most energy-efficient speed for each stretch, minimizing the ship's overall energy consumption, while satisfying journey constraints. The speed planning model consists of three main parts: 1. Resistance models of a ship in shallow water; 2. Models for estimating resultant energy consumption; 3. An objective function and associated constraints that define the optimization problem.

2.1 Resistance modelling of an inland vessel in shallow waters

To maintain a particular sailing speed the ship's engine must provide a certain power to drive the propeller to provide a certain thrust that is able to overcome the resistances acting on the ship. The resistances on the ship can be modelled using the Holtrop and Mennen estimations (Holtrop and Mennen, 1982):

$$R_T^n = R_F^n(1+k_1) + R_W^n + R_{APP}^n + R_{TR}^n + R_A^n + R_B^n \quad \forall \ n \in \mathrm{N} \tag{1}$$

where R_T is the total resistance acting on the ship; R_F is the frictional resistance; R_{APP} is appendage resistance; R_W is the wave-making and breaking resistance, calculated based on the Froude number (Holtrop, 1984); R_B is the additional resistance due to the bulbous bow. For inland vessels $R_B = 0$ since most inland vessels do not have a bulbous bow; R_{TR} is the additional resistance due to an immersed transom; R_A is model-ship correlation resistance; and k1 is the viscous resistance factor for different ship types. All of these resistances will be calculated for each stretch n. Therefore, R_T^n is the total resistance acting on the ship on stretch n of the journey. The set of n stretches is N.

$$N = \{1, 2, 3, ..., n\} \tag{2}$$

The frictional resistance of the ship can be calculated using:

$$R_f^n = \frac{1}{2}\rho(V_s^n)^2 C_f^n S \quad \forall \ n \in \mathrm{N} \tag{3}$$

in which ρ is the density of water [kg/m³]; V_s is the speed of the vessel over water [m/s]; C_f is the friction coefficient; S is the wetted surface area of the hull [m²]. To model the friction coefficient for shallow waters as accurately as possible we use the method proposed by (Zeng, 2019). The method adjusts the friction coefficient to take into account both the additive friction resistance below the ship in shallow waters as well as the friction at the submerged flanks of the ship. The method estimates the velocity underneath the ships bottom with:

$$V_s^n + \Delta V_n = 0.4277 \cdot V_s^n \cdot \exp\left(\frac{h_n}{D_s}\right)^{-0.07634} \quad \forall \ n \in \mathrm{N}, \tag{4}$$

in which h_n is the water depth on stretch n, and D_s is the draft of the ship. The reported uncertainty of this formula is 2.5% (Zeng, 2019), and it is only suitable for $\frac{h_n}{D_s} \leq 4$. For $\frac{h_n}{D_s} \geq 4$, $V_s^n + \Delta V_n$ is assumed to be equal to V_s^n (van Koningsveld et al., 2021). The remaining resistance components are calculated according to the Holtrop and Mennen models (Holtrop and Mennen, 1982).

2.2 Models for Energy estimation

The second part of the speed planning method relates the resistances on the ship to required power, energy consumption, and travel duration. The effective power to overcome the resistances on the ship can be modelled with equation 5 (Wang et al., 2021).

$$P_E^n = k \cdot R_T^n \cdot V_s^n \quad \forall \ n \in \mathrm{N} \tag{5}$$

In which P_E^n is the effective power to overcome the resistance and k is the number of propellers. For inland shipping k is usually one. The delivered power to propellers P_D^n is larger than the required effective power because of efficiency of the propeller in open water η_O, relative rotation efficiency η_R, and the hull efficiency η_H.

$$P_D^n = P_E^n/(\eta_O \cdot \eta_R \cdot \eta_H) \quad \forall \ n \in \mathrm{N} \tag{6}$$

These three efficiencies together make up the hydrodynamic efficiency of the ship η_D^n (Simić and Radojcic, 2013).

$$\eta_D = \eta_O \cdot \eta_R \cdot \eta_H \quad \forall \ n \in \mathrm{N} \tag{7}$$

The propeller behaves differently for different water depths resulting in different efficiency ratings. In this work we assume a hydrodynamic efficiency of between 0.35 and 0.5 dependant on the water depth (Jiang et al., 2022; Simić and Radojcic, 2013). The main engine power output P_B is related to the delivered power at the propeller through the shaft efficiency η_S and the gearbox efficiency η_G.

$$P_B^n = P_D^n/(\eta_S \cdot \eta_G) \quad \forall \ n \in \mathrm{N} \tag{8}$$

The expected energy consumption on stretch n is E_n^* and can be estimated using equation 9.

$$E_n^* = P_B^n \cdot t_n^* \quad \forall \ n \in \mathrm{N} \tag{9}$$

In which t_n^* is the expected sailing duration [h] on stretch n, and can be estimated by relating distance travelled, d [m], and speed over ground, V_{og}:

$$t_n^* = \frac{d_n \cdot \phi_n^*}{3600 V_{og}^n} \quad \forall \ n \in \mathrm{N} \tag{10}$$

in which ϕ_n^* is a parameter denoting expected delay on stretch n. The speed over ground can be inferred by the ship speed and current velocity, V_c [m/s]. In this formula the current direction is taken as positive when flowing in the same sailing direction as the ship.

$$V_{og}^n = V_s^n + V_c^n \quad \forall \ n \in \mathrm{N} \tag{11}$$

The total expected energy consumption during the trip, E_{trip}^* [kWh], is the sum of the expected energy consumption on the stretches:

$$E_{trip}^* = \sum_{n=1}^{N} E_n^*. \tag{12}$$

Similarly, the total expected travel duration, t_{trip}^* [h], is the sum of the expected travel duration on each stretch n:

$$t_{trip}^* = \sum_{n=1}^{N} t_n^* \tag{13}$$

Finally, we define an expected arrival time t_{n^*} at each stretch n using the equation below.

$$t_{n^*} = \sum_{n=1}^{n^*-1} t_n^* \quad \forall \ \ n^* \in N, n^* \neq 1 \tag{14}$$

For the arrival time at stretch 1 ($n^* = 1$) the arrival time is zero $t_{n^*} = 0$. Using this formulation we can impose window arrival time constraints.

2.3 Objective function and constraints

Constraints are applied on the following state and decision variables which may be selected by end-user preference to ensure a maximum travel time (equation 15), arrival windows (equation 16), and energy consumption (equation 17).

$$t_{trip,min} \leq t_{trip}^* \leq t_{trip,max} \tag{15}$$

$$t_{n^*,min} \leq t_{n^*} \leq t_{n^*,max} \tag{16}$$

$$E_{trip}^* \leq E_{trip,max} \tag{17}$$

Constraints on the minimum and maximum speed over ground is imposed also. These bounds take into account the physical restriction on speed given the installed engines and water depth, and speed limits on fairways.

$$V_{s,min}^n \leq V_s^n \leq V_{s,max}^n \quad \forall \ \ n \in N \tag{18}$$

Indirectly, a speed limit is also imposed through a safety constraint that takes into account the squat effect of the ship, aiming to maintain a minimum clearance γ between the ship and the bottom of the fairway. We calculate squat s_n taking into account the width and depth of the river (Serban et al., 2015).

$$s_n = K \cdot C_B \cdot (V_s^n)^2 / 100 \quad \forall \ \ n \in N \tag{19}$$

In which K is function of the fairway characteristics such as depth, width and shape (Serban et al., 2015); C_B is the block coefficient. We assume a block coefficient of 0.85 for inland vessels. We pose that the sum of ship draft D_s, squat s_n and minimum clearance γ should be smaller than the depth of the river h_n; which leads to the safety constraint, equation 20.

$$D_s + s_n + \gamma \leq h_n \quad \forall \ \ n \in N \tag{20}$$

Finally, the objective function aims to minimize the energy consumption over the whole journey and has the form:

$$min_{\vec{u}} \ J = E_{trip}^*, \tag{21}$$

where $\vec{u}$ represent the set of decision variables of the problem formulation.

$$\vec{u} = \begin{pmatrix} V_s^1 \\ ... \\ V_s^n \end{pmatrix} \tag{22}$$

3 Optimization method involving dynamic fairway and delay conditions

In this work we propose an optimization structure that is based on the Model Predictive Control (MPC) algorithm, which continually uses the most up-to-date information on fairway characteristics and delays of the journey, to re-optimize the speed planning. The algorithm used for this optimization scheme is shown in Table 1. In the first step, the system is initialised; the ship parameters, journey parameters and constraints are loaded. Secondly, on the first iteration of the for-loop the speed planning is computed for the complete journey (origin to destination). The

first step of the optimal solution set $\overrightarrow{u}^*$ is carried out; the first stretch of the journey is travelled using the suggested speed from the speed planning. After each stretch of the journey the speed plan is re-optimized for the remainder of the journey, taking into account the actual delays ϕ_n, updated expected delays ϕ_n^*, and most current information on water depth h_n and current velocity V_c^n. The optimization problem shrinks after each re-optimization, since we do not to consider stretches that have already been travelled in the new speed planning. To account for the encountered delays the actual travel time t_n is calculated using:

$$t_n = \frac{d_n \cdot \phi_n}{3600 V_{og}^n} \quad \forall \quad n \in N \tag{23}$$

The actual energy consumption E_n is:

$$E_n = P_B^n \cdot t_n \quad \forall \quad n \in N \tag{24}$$

Since the optimization problem shrinks after each stretch travelled, the constraint parameters must be updated also; this ensures that the initial constraints set at the start of the journey remain satisfied throughout the dynamic changes of the journey. The updating function of these parameters are as described below in equations 25 to 29. These functions are executed in each iteration of step 6 of the algorithm described in Table 1.

$$t_{trip,max} = t_{trip,max} - t_n \tag{25}$$

$$t_{trip,min} = t_{trip,min} - t_n \tag{26}$$

$$t_{n^*,min} = t_{n^*,min} - t_n \tag{27}$$

$$t_{n^*,max} = t_{n^*,max} - t_n \tag{28}$$

$$E_{trip,max} = E_{trip,max} - E_n \tag{29}$$

The optimization problem is a constraint non-linear optimization problem. We solve the optimization problem using a sequential quadratic programming approach. A common difficulty with non-linear optimization problems is finding the global optimum since the complex solution space might lead to local optima. To overcome this issue we use a multi-start procedure; we do the optimization procedure multiple times with different initial solutions. For the use-case described in this paper this guarantees the optimal solution is found.

Table 1: The dynamic optimization algorithm based on the MPC strategy

The dynamic optimization algorithm based on the MPC strategy.
1. At timestep n=1 initialise the system; define ship parameters, set origin and destination of journey, load fairway characteristics, set the desired constraints, define the objective function, and define the problem size: z = size(N).
2. **For** n = 1:z
3. Load current information on water depth h_n, current velocity V_c^n and expected delays ϕ_n^*. Initialise the optimization problem for stretches n to z.
4. Solve the constraint non-linear optimization problem using sequential quadratic programming, and a multi-start procedure to guarantee successful convergence to the global optimum; equations 1 to 21.
5. The first step of the optimal solution set $\overrightarrow{u}^*$ is carried out. The experienced (real) delay ϕ_n and actual travel time t_n are recorded.
6. The constraints on maximum arrival times, arrival windows and maximum energy consumption are updated according to equations 25 to 29.
7. n = n + 1, return to step 2
End for-loop

4 Case study

To exemplify the method presented in the previous section and to validate the approach we study a use case; a CEMT class Va inland freight vessel sailing the Rhine upstream from Rotterdam (Netherlands) to Basel (Switzerland) for a total distance of 829 km. Graphically the journey is shown in Figure 1. The speed planning method determines the appropriate vessel sailing speed on each of the stretches of the journey, for which all imposed constraints are satisfied and energy consumption is minimized. By determining the vessel speed on a 'stretch-level', we can ensure the energy efficiency over the journey is achieved while considering the varying conditions of water depth and currents locally. The navigation circumstances of passing locks between Karlsruhe and Basel, and vessel crossings are not considered directly in this framework. However, the traffic delay parameter ϕ^* is used to model
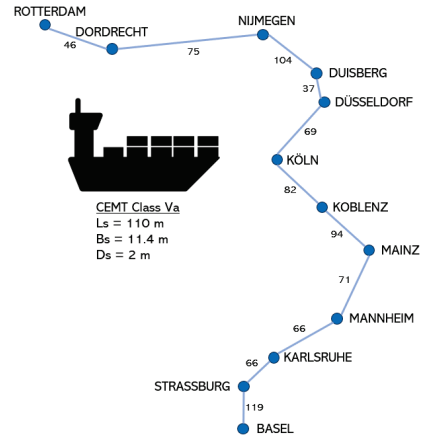
Figure 1: The journey from Rotterdam to Basel and the discretization of the journey in 11 edges; for each edge the length is displayed in km.

the expected delay on each stretch of the journey. All the relevant journey, ship, engine, and constraint parameters of the use-case are summarized in Table 2.

The water levels in the use case are initially low, with a smallest water depth of 2.4 m between Düsseldorf and Köln. These numbers are representative based on reports of CCNR and the Prominent project (TNO et al., 2016; Orlovius, 1994). Over time as the ship completes the journey the water depth changes. In Table 2 the water depth at the the final moment (t_f) of the journey is given as $h_n(t_f)$. In this use case the journey lasts 90 hours ($t_{trip,max} = t_f$). Throughout this journey the water depth slowly transitions between initial and final state. Therefore, when the ship travels stretch n the actual water depth encountered is $h_n(t_{n^*})$ which is between $h_n(0)$ and $h_n(t_f)$. The average expected water depth at $t = 0$ and the actual encountered average water depth of the use case are shown in Table 3. Similarly, the current velocity has an initial and final state and throughout the journey the states slowly change. Finally, the expected and real delay do not match exactly. The average expected and actual values for water depth, current and delay can be found in Table 3.

Table 2: The summary of all the use case parameters.

Parameter	Variable	Value
		Journey parameters
Origin		Rotterdam, Netherlands
Destination		Basel, Switzerland
Total travel distance [km]	d_{trip}	829
Set of stretches [-]	N	{1, 2, 3, 4, 5, 6, 7, 8, 9, 10, 11}
Stretch lengths [km]	d_n	[46, 75, 104, 37, 69, 82, 94, 71, 66, 66, 119]
Stretch water depth [m] at $t = 0$	$h_n(0)$	[9, 6, 5, 3, 2.4, 2.8, 3, 2.7, 3, 3, 3]
Stretch water depth [m] at $t = t_f$	$h_n(t_f)$	[9.21, 6.23, 5.26, 3.28, 2.71, 3.14, 3.36, 3.08, 3.42, 3.47, 3.50]
Stretch current velocity [m/s] at $t = 0$	$V_c^n(0)$	[-0.83, -0.83, -1.11, -1.11, -1.38, -1.66, -1.66, -1.66, -1.66, -1.94, -1.94]
Stretch current velocity [m/s] at $t = t_f$	$V_c^n(t_f)$	[-0.66, -0.66, -0.94, -0.94, -1.21, -1.49, -1.49, -1.49, -1.49, -1.77, -1.77]
Expected delay [-]	$\phi_n^* \; \forall n \in N$	1.05
Actual delay [-]	ϕ_n	[1.03, 1.05, 1.02, 1.03, 1.03, 1.03 , 1.04, 1.02, 1.04, 1.04, 1.02]
		Ship parameters
Ship type		CEMT Class Va inland freight vessel
Length at waterline [m]	L_s	110
Beam [m]	B_s	11.4
Draft [m]	D_s	2.0
Block coefficient [-]	C_B	0.85
Transom area [m^2]	A_T	4.56
Wetted area appendages [m^2]	S_{app}	72.45
Appendage resistance factor [-]	1+k2	2.5
Hydrodynamic efficiency [-]	η_d	0.35 - 0.53
		General parameters
Gravitational constant [m/s^2]	g	9.81
Water density [kg/m^3]	ρ	1000
Kinematic viscosity of water [m^2/s]	υ	$1.1296 \cdot 10^{-6}$
Wave resistance parameter [-]	d	-0.9
		Engine and powertrain parameters
Gearing efficiency [-]	η_G	0.96
Shaft efficiency [-]	η_S	0.98
		Constraint parameters
Maximum speed [km/h]	$V_{s,max}^n \; \forall n \in N$	18
Minimum speed [km/h]	$V_{s,min}^n \; \forall n \in N$	6 - $V_c^n \cdot 3.6$
Maximum arrival time [h]	$t_{trip,max}$	90
Minimum arrival time [h]	$t_{trip,min}$	0
Minimum window arrival time [h]	$t_{n^*,min} \; \forall n \in N$	$t_{trip,min}$
Maximum window arrival time [h]	$t_{n^*,max} \; \forall n \in N$	$t_{trip,max}$
Minimum clearance [m]	γ	0.3

We impose a static vessel speed limit of 18 km/h for the ship, and a minimum vessel speed of 6 km/h minus the current velocity. Therefore, for whichever current, the minimum speed over ground will be 6 km/h. The static speed constraint of 18 km/h is to take into account the maximum capabilities of the ship. The safety constraint (function 20) which imposes a minimum clearance of $\gamma = 0.3m$ (De Ruiter et al., 2023) between the ship and the river bottom considering the squat effect, indirectly imposes a dynamic speed limit also. For that reason, in shallow waters the ship will not always be able go at maximum speed because it will impose a squat effect that is considered unsafe. We impose a maximum trip duration of 90 hours as this will lead to common speed ranges of ships on the Rhine (De Ruiter et al., 2023); this makes our use case more comparable to real-world practise.

Table 3: Average values of dynamic parameters at the initial state and encountered states

Parameter	Mean value at t = 0	Mean value of actual encountered dynamic conditions	Difference [%]
Water depth h_n	3.9 m	4.07 m	4.36
Current velocity V_c^n	-5.18 km/h	-4.87 km/h	-5.98
Delay ϕ_n	1.05	1.03	-1.90

5 Results and discussion

The optimal sailing speed for each stretch of the journey at each time step along the route is shown in Table 4. At each timestep for the remaining journey the speed plan is re-optimised to find the best speed settings for which the total energy consumption is minimised. The first row of the table are the sailing speed solutions at timestep 1; this is the speed plan that is suggested at the start of the journey. If the speed planning is static, this will be the speed plan that is executed throughout the journey. The solutions of our dynamic speed planning framework are on the diagonal of the table.

Table 4: The optimal sailing speeds at each time step along the route

Time steps n	Journey segments										
	1	2	3	4	5	6	7	8	9	10	11
1	15.36	14.94	15.22	14.70	11.46	15.59	15.78	15.53	15.78	16.27	16.27
2		14.82	15.17	14.64	11.46	15.51	15.59	15.47	15.59	16.24	16.24
3			15.07	14.55	11.46	15.42	15.48	15.41	15.50	16.19	16.19
4				14.38	11.46	15.30	15.35	15.29	15.36	16.09	16.08
5					13.96	14.78	14.89	14.76	14.91	15.42	15.41
6						14.69	14.76	14.68	14.78	15.36	15.35
7							14.65	14.59	14.66	15.29	15.28
8								14.49	14.56	15.21	15.20
9									14.44	15.06	15.07
10										14.95	14.97
11											14.85

It can be noted that the speed suggestions are descending in value over time. This follows naturally from a current velocity that is decreasing over time and the overestimation of the delay, see Table 3. It should also be noted that the speed setting on journey segment 5 is lower than most setpoints. This is due to the low water depth on this stretch of the journey leading to forcing constraints on maximum vessel speed on this segment to ensure grounding does not occur. However, since the water depth is increasing over time, by the time the ship arrives at segment 5 the speed can be raised while a minimum clearance γ of 0.30 m is maintained.

We cannot directly compare the energy consumption of static and dynamic (MPC) speed planning, because this would be an 'unfair' comparison as the use-case that we choose strongly influences the amount of energy reductions achievable. In our use case the magnitude of the average current velocity and the expected delays are overestimated, and the water depth is underestimated at the start of the journey. These valuations of the states lead to relatively high speed settings to overcome these unfavorable conditions and to arrive on time. Throughout the journey the true dynamic states emerge to be more favourable: a smaller negative current acting on the ship, a higher water depth, and less traffic delay. Therefore, as we re-optimize at each timestep the speed can be lowered because we are finding that the dynamic states are less adverse than expected; this leads to a lower energy consumption. It is well known that lower velocities lead to lower energy consumption, which is basis of slow steaming techniques (Psaraftis and Kontovas, 2013). Had we chosen a use case where the velocity of the current is under-valued for instance, we would have seen an increase in suggested speed in the dynamic speed planner, and the resultant energy consumption would be higher.

To illustrate this point we show the sensitivity of the energy consumption to varying conditions of water depth, current and delay. We multiply the initial conditions of these parameters with sensitivity parameter $x \in [0.8, 1.2]$. The results can be found in Figure 2. A linear relationship between current velocity and energy consumption can be noted. Similarly, the delay variation also causes a linear response in the energy consumption. The slope of the delay is smaller because the multiplication factor x with delay parameter $\phi* = 1.05$ yields numbers relatively close to 1, and therefore a smaller change in energy. The increase in water depth has a nonlinear response, leading to lower energy consumption. We did not test a decrease in water depth as this would lead to unsafe navigable waters, and the sensitivity response would not be valid.

To make a 'fairer' comparison we compare 6 different speed planning strategies so that we can make some conclusions about the energy efficiency of the proposed MPC method. These speed planning methods, their speed setpoints, average speed, energy consumption, and travel time are shown in Table 5, and in Table 6 the comparison of the different methods is presented. The first three strategies in the table concern static speed planning. The first strategy is a speed selection by the shipper and does not involve and optimization, these speed settings lead to a total estimated travel time of 90 hours, which is the constraint we set for arrival time. The second strategy is our speed planning method without the MPC function (row 1 of Table 4), again the estimated total travel time is 90 hours. In Table 6 a quick comparison of these two methods show that a 6.56% energy efficiency can be achieved through the static speed planning method. If the shipper had chosen a different combination of speeds the energy efficiency achieved through static speed planning would also change.
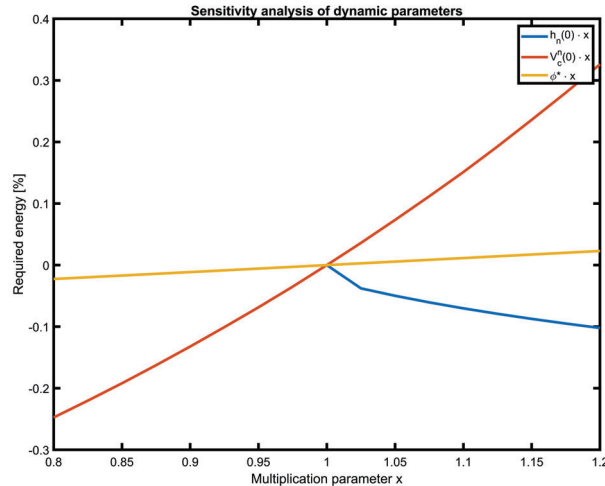
Figure 2: Sensitivity Analysis for the dynamic parameters water depth h_n, current velocity V_c^n, and delay ϕ^*. The base reference in the sensitivity analysis is the speed planning strategy 2 as indicated in Table 5.

Table 5: Overview of different speed planning strategies and their resultant energy efficiency

Speed planning strategy	1	2	3	4	5	6	7	8	9	10	11	Average speed (km/h)	Energy consumption (kWh)	Total travel time (hours)
1. Speed selection by shipper; un-assisted by optimization strategies	18.00	18.00	18.00	18.00	11.46	14.40	14.40	14.40	18.00	15.12	15.58	15.81	72525.47	90.00
2. Static speed planning: expected outcome of planning	15.36	14.94	15.22	14.70	11.46	15.59	15.78	15.53	15.78	16.27	16.27	15.27	67767.41	90.00
3. Static speed planning: actual outcome of planning	15.36	14.94	15.22	14.70	11.46	15.59	15.78	15.53	15.78	16.27	16.27	15.27	61618.61	85.10
4. Adaptive speed selection by shipper; unassisted by optimization strategies	18.00	18.00	14.40	14.40	13.00	12.28	15.48	14.40	14.83	15.12	15.58	14.98	59029.54	90.00
5. Dynamic speed planning; optimization with MPC strategy	15.36	14.82	15.07	14.38	13.96	14.69	14.65	14.49	14.44	14.95	14.85	14.71	56485.95	89.56
6. Non-causal optimization: change in water-depth, current and delay is known a priori	14.47	13.95	14.26	13.78	13.90	14.68	14.73	14.63	14.69	15.28	15.27	14.58	55866.42	90.00

Strategy 3 shows the actual outcome of the static speed planning method if the speed planning is followed regardless of the change in water depth, current and delay; it is therefore not really another strategy but rather strategy 2 corrected for dynamic conditions. We can see that the arrival time in reality is 85.10 hours, implying that the average speed could have been lowered during the journey, while still arriving on time. Additionally, due to the reduced velocity of the current, lower than anticipated delay, and higher water depths than anticipated, the energy consumption is 9.07% lower than expected.

Table 6: Comparison of speed planning strategies and their resultant comparative energy savings

Comparison	ΔAverage speed (%)	ΔEnergy use (%)	ΔTime (h)
Strategy 2 compared to 1	-3.42	-6.56	0
Strategy 3 compared to 2	0	-9.07	-4.90
Strategy 5 compared to 3	-3.67	-8.33	+4.46
Strategy 5 compared to 4	-1.80	-4.31	-0.44
Strategy 6 compared to 5	-0.88	-1.10	+0.44

Since it is likely that the shipper will sway from the static speed planning once they notice a delay we include strategy 4. This strategy assumes that the initial speed plan is from strategy 1. However, over time the shipper notices that they are ahead of schedule and that they can lower the speed while still arriving on time. Flexibly, the shipper changes the speed based on the delay experienced in real-time. Strategy 4 will be our point of comparison for the MPC strategy that we propose in the paper, which is strategy 5. Strategy 5, as discussed previously are the

solution on the diagonal of Table 4. We can note that the arrival time with this strategy is 89.56 hours; it is not exactly equal to 90 hours due to the varying conditions experienced on the final segment of the journey. Compared to strategy 4 we can see that an energy efficiency of 4.31% is achieved. Compared with the static speed planning the MPC method has a 8.33% lower energy consumption.

Finally, strategy 6 shows the non-causal optimization strategy; the exact water depth, current and delay that will be encountered by the ship is known a priori. This strategy shows a 5.36% lower energy consumption as strategy 4. Compared to the MPC strategy is has a 1.10% lower energy consumption. Using prediction models for the current and water depth a speed planning strategy resembling the non-causal optimization may be achieved. However, accurate predictions for a prediction horizon of multiple days may not be feasible. A delay that might be more predictable is at locks using lock planning methods such as described in (Buchem et al., 2022), leading to more precise speed planning. This is also one of the goals of the European (Horizon H2020) NOVIMOVE project (NOVIMOVE, 2020).

It is worth pointing out that the necessity to re-optimize the journey is a reflection of the variation experienced during the journey. Therefore, the energy efficiency percentages achieved with the MPC strategy are a function of the magnitude of the change of the dynamic parameters during the journey. For that reason, lower energy efficiencies will be achieved for journeys with less varying conditions; similarly, with more variations or larger uncertainties higher efficiencies can be achieved. The delays of the use case in this work are quite modest and in reality larger delays may be experienced, especially considering the 10 locks that are in the upper-Rhine. Also, in reality there is often a level of uncertainty about the reported current and water depth. Current velocities of the Rhine can be highly varying in bends for instance, compared to straight parts of the river. For that reason, it is always advisable to update the voyage plan continuously, and to constantly receive the most current estimations on waiting times at locks, traffic conditions, and waterway conditions.

6   Conclusions and further research

To address the need of the inland waterway transport sector to improve the energy efficiency and increase smart navigation we propose an MPC-based (dynamic) speed planning method. Currently, static speed planning methods are used for inland waterway navigation which are unable to adequately deal with dynamic waterway conditions. The proposed dynamic speed planning continually uses the most up-to-date information on water depth, current speed and expected delays of the journey to re-optimize the speed planning leading to improved energy efficiency, reliable arrival times, and accurate considerations regarding safety.

Compared to a static speed planning method we showed a 8.33% energy reduction, and compared to an adaptive speed selection by a shipper unassisted by optimization strategies we show a 4.31% energy reduction. The energy efficiency percentages achieved with the MPC strategy are a function of the magnitude of the change of the dynamic parameters during the journey. Therefore, the achievable energy reduction through this dynamic speed planning is proportional to the variability and uncertainty experienced during the journey. We also showed that using the proposed method accurate arrival times are achieved compared to static speed planning. Additionally, taking into account the most recent information on water depth and squat as a function of vessel speed, we showed that different speeds are considered safe on the segments of the journey than initially anticipated.

In future work it would be worthwhile to model the uncertainty regarding the expected dynamic conditions. Currently, the expected traffic delay is simply modelled as a proportional delay on travel time which is not accurate enough. Additionally, it would be interesting to see this framework used with prediction models for the water depth, current, and traffic; this could further improve the performance of the dynamic speed planning as indications of future states can be used in planning. Moreover, the effect of locks and their delays should be taken into account also. Considering these improvements the MPC-based speed planning becomes an even more attractive option for energy-efficient and accurate planning.

Acknowledgement

References

Buchem, M., Golak, J.A.P., Grigoriev, A., 2022. Vessel velocity decisions in inland waterway transportation under uncertainty. European Journal of Operational Research 296, 669 – 678. doi:`10.1016/j.ejor.2021.04.026`. cited by: 6; All Open Access, Hybrid Gold Open Access.

CCNR, 2022. Ccnr roadmap for reducing inland navigation emissions. URL: `https://www.ccr-zkr.org/12090000-en.html`.

De Ruiter, J.M., Bhoraskar, A., Ligterink, N.E., 2023. Meten op Schepen- Reductiepotentieel van de milieu- en klimaatimpact van binnenvaart , 1–86.

EC, 2020. The european green deal - striving to be the first climate-neutral continent. URL: `https://commission.europa.eu/strategy-and-policy/priorities-2019-2024/european-green-deal_en`.

EC, 2021. Future-proofing european inland waterway transport - naiades iii action plan. URL: `https://transport.ec.europa.eu/transport-modes/inland-waterways/promotion-inland-waterway-transport/naiades-iii-action-plan_en#:~:text=The%20core%20objectives%20are%20to,zero%2Demission%20barges%20by%202050.`

EC, 2022. Energy efficiency targets. URL: `https://energy.ec.europa.eu/topics/energy-efficiency/energy-efficiency-targets-directive-and-rules/energy-efficiency-targets_en`.

Fan, A., Wang, Z., Yang, L., Wang, J., Vladimir, N., 2021. Multi-stage decision-making method for ship speed optimisation considering inland navigational environment. Proceedings of the Institution of Mechanical Engineers, Part M: Journal of Engineering for the Maritime Environment 235, 372–382. URL: `https://doi.org/10.1177/1475090220982414`, doi:`10.1177/1475090220982414`, arXiv:`https://doi.org/10.1177/1475090220982414`.

Gao, J., Chi, M., Hu, Z., 2022. Energy consumption optimization of inland sea ships based on operation data and ensemble learning. Mathematical Problems in Engineering 2022, 1–13. doi:`10.1155/2022/9231782`.

Han, C., Liu, J., Liu, Z., Li, S., Qin, X., 2021. Research on speed optimization of inland vessels based on a shuffled frog-leaping algorithm, in: 2021 6th International Conference on Transportation Information and Safety (ICTIS), pp. 688–693. doi:`10.1109/ICTIS54573.2021.9798521`.

Holtrop, J., 1984. A statistical re-analysis of resistance and propulsion data. International Shipbuilding Progress 31.

Holtrop, J., Mennen, G., 1982. An approximate power prediction method. International Shipbuilding Progress 29.

Jiang, M., Segers, L.M., Van der Werff, S.E., Baart, F., Van Koningsveld, M., 2022. Opentnsim-energy .

Kirichek, A., Pruyn, J., Atasoy, B., R. Negenborn, R., Zuidwijk, R., van Duin, J., Tachi, K., van Koningsveld, M., 2024. Paving the way towards zero-emission and robust inland shipping URL: `https://proceedings.open.tudelft.nl/moses2023/article/view/675`, doi:`10.59490/moses.2023.675`.

van Koningsveld, M., van der Werff, S., Jiang, M., Lansen, A., de Vriend, H., 2021. Part IV - Ch 5 Performance of ports and waterway systems. TU Delft OPEN Publishing.

Liu, T., 2023. Speed optimization of inland sea vessels based on c.w saving algorithm. Applied Mathematics and Nonlinear Sciences URL: `https://sciendo.com/article/10.2478/amns.2023.2.00271`, doi:`10.2478/amns.2023.2.00271`.

NOVIMOVE, 2020. Smart and sustainable waterways. URL: `https://novimove.eu/`.

Orlovius, V., 1994. Regulations and Prescriptions for the Navigation on the Rhine , 1–16.

Psaraftis, H.N., Kontovas, C.A., 2013. Speed models for energy-efficient maritime transportation: A taxonomy and survey. Transportation Research Part C: Emerging Technologies 26, 331 – 351. doi:`10.1016/j.trc.2012.09.012`.

Serban, S., Cosmin, K., Panaitescu, V., 2015. The analysis of squat and underkeel clearance for different ship types in a trapezoidal crosssection channel 77, 205–212.

Simić, A., Radojcic, D., 2013. On energy efficiency of inland waterway self-propelled cargo vessels. FME Transactions 41, 138–145.

Sun, L., Zhang, Y., Ma, F., Ji, F., Xiong, Y., 2023. Energy and speed optimization of inland battery-powered ship with considering the dynamic electricity price and complex navigational environment. Energy Reports 9, 293–304. URL: `https://www.sciencedirect.com/science/article/pii/S2352484723006297`, doi:`https://doi.org/10.1016/j.egyr.2023.04.267`. 2022 The 3rd International Conference on Power Engineering.

TNO, VIA, PRO, DST, BAW, 2016. PROMINENT - D5.6 Land based tool for evaluation of ship efficiency and navigation performance , 1–29.

WANG, K., LI, J., HUANG, L., Ma, R., QU, X., YUAN, Y., 2019. An energy efficiency optimization method for inland ship fleet considering multiple influencing factors, in: 2019 5th International Conference on Transportation Information and Safety (ICTIS), pp. 1263–1267. doi:`10.1109/ICTIS.2019.8883776`.

Wang, K., Xu, H., Li, J., Huang, L., Ma, R., Jiang, X., Yuan, Y., Mwero, N.A., Sun, P., Negenborn, R.R., Yan, X., 2021. A novel dynamical collaborative optimization method of ship energy consumption based on a spatial and temporal distribution analysis of voyage data. Applied Ocean Research 112, 102657. URL: `https://www.sciencedirect.com/science/article/pii/S0141118721001346`, doi:`https://doi.org/10.1016/j.apor.2021.102657`.

Wang, K., Yin, M., Ayisi, A.D., 2023. Effects of reduced speed on the benefits and pollution of yangtze river ships. Transportation Research Record 2677, 783–796. URL:

https://doi.org/10.1177/03611981221150417, doi:10.1177/03611981221150417, arXiv:https://doi.org/10.1177/03611981221150417.

Yan, X., Wang, K., Yuan, Y., Jiang, X., Negenborn, R.R., 2018. Energy-efficient shipping: An application of big data analysis for optimizing engine speed of inland ships considering multiple environmental factors. Ocean Engineering 169, 457–468. URL: https://www.sciencedirect.com/science/article/pii/S0029801818316421, doi:https://doi.org/10.1016/j.oceaneng.2018.08.050.

Zeng, Q., 2019. A method to improve the prediction of ship resistance in shallow water. Ph.D. thesis. TU Delft.

Zhang, L., Peng, X., Liu, Z., Wei, N., Wang, F., 2022. An application of augmented lagrangian differential evolution algorithm for optimizing the speed of inland ships sailing on the yangtze river. International Journal of Naval Architecture and Ocean Engineering 14, 100488. URL: https://www.sciencedirect.com/science/article/pii/S2092678222000541, doi:https://doi.org/10.1016/j.ijnaoe.2022.100488.

Zhang, Y., Sun, L., Fan, T., Ma, F., Xiong, Y., 2023. Speed and energy optimization method for the inland all-electric ship in battery-swapping mode. Ocean Engineering 284, 115234. URL: https://www.sciencedirect.com/science/article/pii/S0029801823016189, doi:https://doi.org/10.1016/j.oceaneng.2023.115234.